MEASUREMENT OF NEUTRINO ABSOLUTE DEEP INELASTIC SCATTERING CROSS SECTION IN IRON, LEAD, CARBON, AND PLASTIC USING MINERVA DETECTOR AT $E_\nu = 6$ GEV

By

MARIANETTE O. WOSPAKRIK

DISSERTATION PRESENTED TO THE GRADUATE SCHOOL
OF THE UNIVERSITY OF FLORIDA IN PARTIAL FULFILLMENT
OF THE REQUIREMENTS FOR THE DEGREE OF
DOCTOR OF PHILOSOPHY

UNIVERSITY OF FLORIDA

2018

Dedicated to the memory of my father, Hans J. Wospakrik

ACKNOWLEDGEMENTS

Although only my name is printed on the cover of this dissertation, many people around me deserve credits for its completion. First of all, I would like to express my sincere gratitude to my advisor Heather Ray for the continuous support of my PhD study, related research, and career. She provided me with every bit of guidance, assistance, and expertise that I needed during the time of writing of this dissertation and also throughout my graduate year. I could not have imagined having a better advisor and mentor for my PhD study. I would also like to thank my committee members: Darin Acosta, Konstantin Matchev, James Hamlin, and Andreas Enqvist. I hope this dissertation has been an interesting read.

Many other people in the MINERvA collaboration have formed the backdrop against which this analysis was done. Thanks to Debbie Harris, Laura Fields, Kevin McFarland, Jorge Morfin, Jeff Nelson, and Dan Ruterboris for sharing your advice and wisdom. Particular thanks also to Gabe Perdue for piquing my interest in machine learning and providing me with such an interesting project to work on for this dissertation. Thank you also for Anne Norrick and Dipak Rimal for their specific works in this analysis. Especially to Anne, for sharing the journey working on the detector as well as this analysis together. I would also thank Joel Mousseau and Brian Tice for being the pioneers of the nuclear target analyses and set the ground running for my understanding of the analysis.

Second, I would like to thank my family: my mom and to my brother and extended family for supporting me throughout writing this dissertation and my life in general. This would not have been possible without their unwavering and unselfish love and support given to me at all times. Finally, thank you to all those I worked with during my PhD years in Fermilab. To Anushree Ghosh, Mehreen Sultana, Faiza Akbar, Huma Haider, Deepika Jena, Barbara Yaeggy, and Cheryl Patrick thank you for the friendship and good conversation shared over bobas and delicious foods. And also to the rest of the awesome MINERvA colleagues for your friendship and many useful and entertaining discussions.

TABLE OF CONTENTS

LIST OF TABLES

LIST OF FIGURES

Abstract of Dissertation Presented to the Graduate School
of the University Of Florida in Partial Fulfillment of the
Requirements for the Degree of Doctor of Philosophy

MEASUREMENT OF NEUTRINO ABSOLUTE DEEP INELASTIC SCATTERING CROSS SECTION IN IRON, LEAD, CARBON, AND PLASTIC USING MINERVA DETECTOR AT $E_\nu = 6$ GEV

By

Marianette O. Wospakrik

August 2018

Chair: Heather Ray
Major: Physics

Neutrino-nucleus charged-current deep inelastic scattering (DIS) provides a complementary probe to charged lepton-nucleus DIS in the study of nuclear and hadronic structure. The MINERvA experiment is a dedicated neutrino scattering experiment located on the NuMI beamline in Fermilab. With multiple nuclear targets of lead, iron, plastic, and carbon in the same beam, MINERvA will help elucidate poorly understood nuclear effects present in DIS interactions. Using the NuMI's Medium Energy beam configuration, MINERvA will be able to perform analyses of nuclear and hadronic structure with unprecedented sensitivity.

An analysis of the MINERvA DIS data on carbon, iron, lead and plastic scintillator has been conducted in the energy region $2 \leq E_\mu < 50$ GeV and $\theta_\mu < 17°$. Improvements in locating the interaction vertex in the Medium Energy data set have been achieved using a machine learning deep convolutional neural network (DCNN). Data are presented as the absolute cross section ($\sigma(E_\nu)$) as well as the differential cross section with respect to Bjorken-x ($\frac{d\sigma}{dx_{bj}}$) on carbon, iron and lead, and scintillator. These measurements are the world's first neutrino-DIS cross sections to be produced in a high statistics, systematic error limited, environment. The data distributions do not displayed significant differences with the theoretical models underlying MINERvAs MC.

CHAPTER 1
INTRODUCTION

The theoretical existence of the neutrino was first postulated in the 1930s by Wolfgang Pauli to explain conservation of energy in beta decay of an atomic nucleus. He introduced a chargeless and massless particle called the neutrino [1]. However, it took more two more decades before the particle was first directly observed in 1956 in by Frederick Reynes and Clyde Cowan [2]. In their experiment, a flux of $\overline{\nu}_e$ (coming from a beta decay) was directed into a water target. The reaction $\overline{\nu}_e p \rightarrow ne^+$ produced positrons that annihilated with electrons in the detector, resulting in two 0.5 MeV gamma rays. The neutron was captured by the water, producing an additional gamma. The observation of both processes, positron annihilation and neutron capture, confirmed the presence of $\overline{\nu}_e$. Six years later, at Brookhaven National Laboratory, the first direct observation of ν_μ occured. It was discovered that when neutrinos interact with nuclei through $\nu_\mu/\overline{\nu}_\mu + N \rightarrow \mu/\overline{\mu} + N'$, muons are produced in the final state and no electrons are observed.

In 1968, the Homestake Experiment performed the first measurement of the solar neutrino flux at Earth and discovered that it was considerably less than predicted by the best theoretical model of the time [3]. This result has been confirmed by subsequent experiments, including Kamioka Observatory [4] and Sudbury Neutrino Observatory (SNO) [5]. This deficit, also called the "solar neutrino problem", led to the discovery of neutrino oscillation and mass. The discovery prompted great theoretical and experimental interest in the properties of neutrinos. Despite the intense study of neutrino physics in the last few decades we still have many outstanding questions remaining to be answered: What is the neutrino mass hierarchy? What is the absolute neutrino mass scale? Is CP symmetry violated in the lepton sector? What is the nature of neutrinos: Dirac or Majorana particles? What is the mechanism of the origin of the neutrino mass and mixing? Do sterile neutrinos exist?

To answer these questions, current and future neutrino experiments must perform unprecedented precision measurements to extract accurate estimates of parameters describing neutrino oscillations and their properties. This requires neutrino oscillation experiments to reduce systematic errors to the level of a few percent. Reaching such a level of precision will require precisely characterizing the three leading systematic uncertainties affecting the measurement of the neutrino oscillations: the rate of neutrino interactions (cross sections), the distribution of number and energy of neutrinos entering the detector (flux), and the response of the detector to particles produced in neutrino interactions.

Figure 1-1 shows the range of neutrino energies where various current and future accelerator-based neutrino experiments will operate. In this energy region a wide variety of neutrino interaction channels are available, with a 20% uncertainty on the measurements [6]. The transitions between these interaction modes pose a significant challenge to model due to the change in the underlying physical assumptions between them. To disentangle these convolutions of parameters, a variety of independent measurements of interaction channels needs to be performed across a range of nuclei and neutrino energy. The MINERvA (Main Injector ExpeRiment for ν-A) experiment was designed to provide neutrino cross section measurements across a wide range of nuclei, with a 10% or lower uncertainty.

MINERvA is a dedicated neutrino cross section experiment that will measure the interaction of neutrinos with energy of 5-50 GeV on various nuclei, to high precision. MINERvA has accumulated high-statistics datasets in both the Low Energy (LE) and Medium Energy (ME) beam configurations (peaking at 3.5 GeV and 6 GeV, respectively). MINERvA is the only experiment operating at the energies and momentum transfers that span the first oscillation peak at the future flagship neutrino oscillation experiment, the DUNE experiment.

MINERvA simultaneously measures cross sections with five different nuclei and provides the first self-contained comparisons of interactions in different nuclei. It also

provides the necessary information required to distinguish neutrino-nucleon interactions models and nuclear medium effects. MINERvA's large collection of data has produced a detailed description of final state particles and information about the significant sources of uncertainties in the neutrino interaction, which then help to improve theoretical models used in the neutrino oscillation experiments. In addition, MINERvA's neutrino cross section measurements also yield information about the structure of protons and neutrons and the force dynamics that affect neutrino-nucleon interactions. This nuclear research contributes complementary information to the ongoing efforts at other laboratories that are studying charged lepton-nucleon interactions.

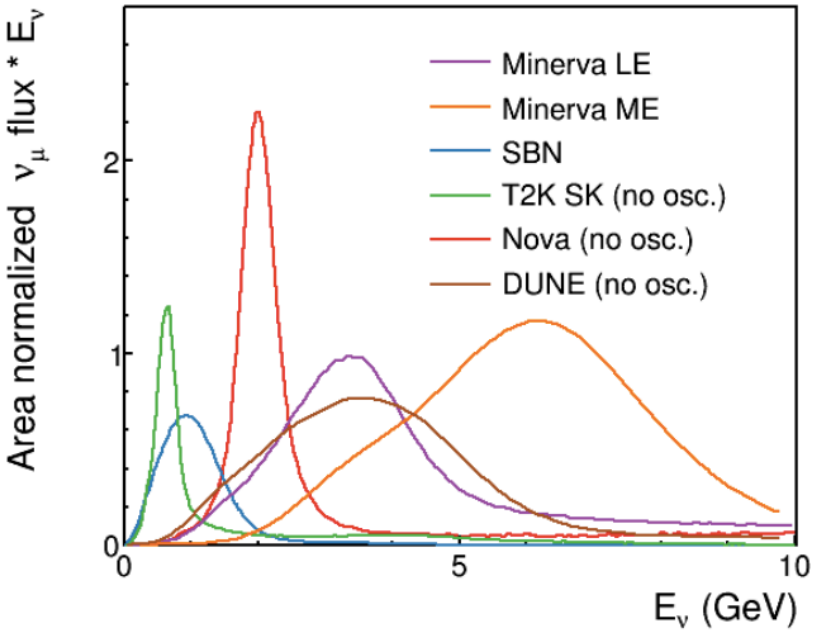

Figure 1-1: Neutrino energy spectra for the worlds accelerator-based oscillation experiments as a function of neutrino energy. No osc. label in the plot refers to the predicted neutrino spectra for no oscillation cases. All fluxes are area-normalized and then scaled by energy to reflect the scaling of interaction cross-section with energy. Figure is from [7].

CHAPTER 2
THEORY

2.1 Neutrinos in the Standard Model

Decades of theories and discoveries of physics processes have shed light on the fundamental structure of matter: everything in the universe is made from elementary building blocks of matter, called fundamental particles. The theory that describes these fundamental particles and how they interact is called the Standard Model of particle physics.

The Standard Model is comprised of 12 fundamental particles and 4 fundamental forces as shown in Figure 2-1. There are two categories of fundamental particles: quarks and leptons. There are six particles in each category. The particles are divided into three groups: first generation, second generation, and third generation. Each generation contains two quarks, two leptons, and their anti-particles. The up quark and the down quark form the first generation, followed by the charm quark and strange quark, and the top quark and bottom (or beauty) quark. The six leptons are arranged with each neutrino paired with the corresponding charged lepton: the electron and the electron neutrino in the first generation, the muon and the muon neutrino in the second generation, and the tau and the tau neutrino in the third generation.

The four fundamental forces include the strong force, the weak force, the electromagnetic force, and the gravitational force. The weak and the strong force are only effective over a finite range and dominate at the subatomic level. The electromagnetic force has infinite range and is much stronger than gravity. Particles transmit discrete amounts of energy, called quanta, among each other by exchanging force-carrying particles called bosons. Each fundamental force has its own characteristic bosons:

- The gluon carries the strong force; it "glues" quarks together.
- The photon mediates the electromagnetic force and transmits light.

- The W and Z bosons are responsible for the weak force; they facilitate different types of interactions and decays.

- The graviton (still a hypothetical elementary particle) mediates the force of gravity.

The Standard Model was built under the assumption of a massless two-component neutrino [8, 9]. If neutrinos have zero mass, then their handedness is a permanent property, and it is impossible for a neutrino to transform into another type. The neutrino oscillation observation refutes this assumption and indicates that the Standard Model of physics is still incomplete.

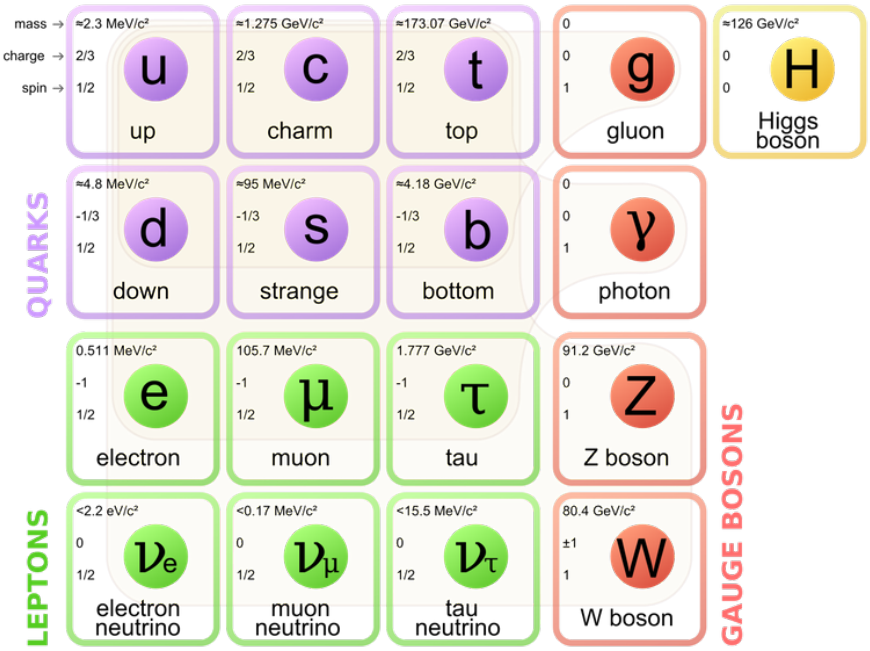

Figure 2-1: Standard model of elementary particles: the 12 fundamental fermions and 4 fundamental bosons. Brown loops indicate which bosons (red) couple to which fermions (purple and green). Taken from [10].

2.2 Neutrinos Beyond The Standard Model

Leptons, like all matter particles in the Standard Model, exhibit the peculiar feature that the states in which they engage in charged-current weak interactions, flavor states, are not mass eigenstates. Instead, the three flavor states are a superposition, or mixture, of the three mass states.

There is a freedom in defining the reference point from which the flavor states are experimentally measured. We conventionally define the quark flavor states in terms of the up-type quarks, such that all the mixing occurs in the down-type quarks. Likewise in neutrinos we define the flavor states in terms of the charged leptons with all the mixing confined to the neutrinos. There is a good reason for this choice; the fact that neutrinos interact only via weak interaction and that there are tiny differences between their masses makes it impossible to measure which mass state has been created.

It is natural to assume that, similar to the other fermions, each neutrino flavor ν_α has an anti-matter equivalent ν_α i.e. that they are Dirac particles. However, due to their neutral charge it is also possible that neutrinos are Majorana particles. If this were true, then neutrinos would be their own anti-particles. Neutrinos thus could have either Dirac or Majorana masses [11].

To date neutrino experiments have confirmed the existence of three neutrino flavor states. They are defined by the charged lepton they interact with at charged-current weak vertices: ν_e, ν_μ and ν_τ. There are also three mass states ν_1, ν_2, ν_3 with masses m_1, m_2 and m_3 respectively. In addition to the three mass states, there is also a hypothetical fourth state. This state must be mostly sterile and contain only a tiny mixture of the standard neutrino flavors [12].

Neutrino oscillation is the most productive and promising field in neutrino studies. Neutrino oscillation is a process when a neutrino produced with one of the lepton flavors (e, μ, τ) later interacts as a neutrino with a different lepton flavor. For example, a $\overline{\nu}_e$ created from the beta decay process, ${}_ZX^N \rightarrow_{Z+1} X^N + e^- + \overline{\nu}_e$, may later interact as a $\overline{\nu}_\mu$ after propagating some distance L from the point of creation in the beta decay to the location of the detector.

2.3 Neutrino Interactions

The neutrino beams in accelerator-based experiments are not monochromatic but widespread, from a few MeV to several tens of GeV. In this energy region several reaction

channels are available but the imprecise kinematic information prevents the direct comparison of measured results to theories. Since the neutrino beams are not monochromatic but widespread, the incoming neutrino energy must be reconstructed from the final state particles produced in the interaction.

The types and number of hadrons produced in a particle interaction are dependent on the scattering process, and each hadron species (*e.g.* p, n, π^+) produces a different detector response. In addition, the hadrons produced in a neutrino-nucleus interaction can themselves interact within the nucleus. In order to precisely measure the energy spectrum of the incoming neutrino beam, neutrino experiments need precise knowledge of the rates of the different neutrino-nucleus scattering processes and how the nuclear medium affects the particles produced in neutrino-nucleus interactions.

The reconstruction of neutrino energy is performed by combining the kinematic information of the outgoing lepton and the energy of all other outgoing particles:

$$E_\nu = E_l + E_{had}, \tag{2-1}$$

where E_ν is the neutrino energy, E_l is the outgoing lepton energy and E_{had} is the hadronic energy obtained by calorimetrically summing up the energy of all other outgoing particles.

The determination of neutrino energy is essential since it enters the expression of the neutrino oscillation probability. The hypothesis used to reconstruct the neutrino energy from the observed charged lepton variables (energy and scattering angle) assumes that the neutrino interaction in the nuclear target takes place on a nucleon at rest. In these interactions, a neutrino ν_l scatters off a nucleon N (proton or neutron) within the nucleus, producing a final state charged lepton l and one or more recoil hadrons X:

$$\nu_l + N \rightarrow l + X. \tag{2-2}$$

The flavor of the final state lepton identifies the flavor of the incident neutrino.

Accelerator-based neutrino oscillation experiments operate at neutrino energies E_ν in the range $1 \lesssim E_\nu \lesssim 10$ GeV. In this energy range charged current (CC) weak interactions of neutrinos with nuclei primarily occur via the following scattering processes:

- **Quasi-Elastic Scattering** ($\nu_l + N \rightarrow l + N^{'}$)

  A neutrino ν_l interacts with a nucleon N bound in a nucleus, producing a charged lepton l and a nucleon $N^{'}$ in the final state (Figure 2-2). N and $N^{'}$ have different electric charge.

- **Resonance Production** ($\nu_l + N \rightarrow l + N^{'} + \pi$)

  A neutrino interacts with a nucleon bound in a nucleus, producing a charged lepton and a baryon resonance. The resonance decays promptly before exiting the nucleus into a nucleon and a pion in the final state (Figure 2-3).

- **Shallow Inelastic Scattering** ($\nu_l + N \rightarrow l + X$)

  A neutrino interacts with a nucleon bound in a nucleus, producing a charged lepton and multiple hadrons, which often includes one more pions. Non-resonant background scattering occurs at a lower momentum transfer to the target nucleon than deep inelastic scattering.

- **Deep Inelastic Scattering (DIS)** ($\nu_l + N \rightarrow l + X$)

  A neutrino interacts with a quark of a bound nucleon producing a charged lepton and multiple hadrons X in the final states (Figure 2-4).

Measurements of the per-nucleon quasi-elastic, resonance production, and deep inelastic scattering cross sections as a function of neutrino energy for ν_μ and $\overline{\nu}_\mu$ CC interactions with isoscalar nuclei (equal numbers of protons and neutrons) are shown in Figure 2-5. Measurements of neutrino-nucleus scattering cross sections have large uncertainties due to large uncertainties on the neutrino flux, and incomplete knowledge of nuclear effects. Neutrino-nucleus cross sections are typically the largest systematic

uncertainty for neutrino oscillation measurements [13, 14]. The MINERvA experiment is performing precise measurements of neutrino-nucleus scattering cross sections for tuning neutrino-nucleus interaction models and reducing systematic uncertainties in oscillation experiments.

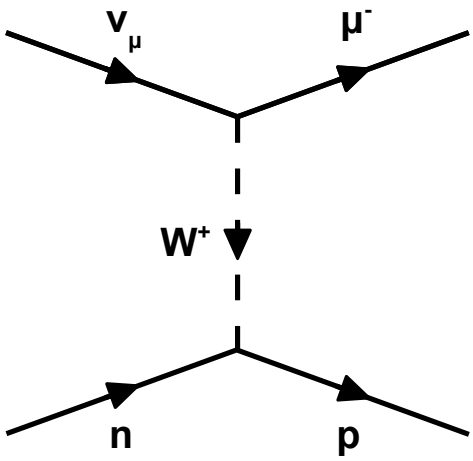

Figure 2-2: Neutrino-nucleus CC quasi-elastic scattering.

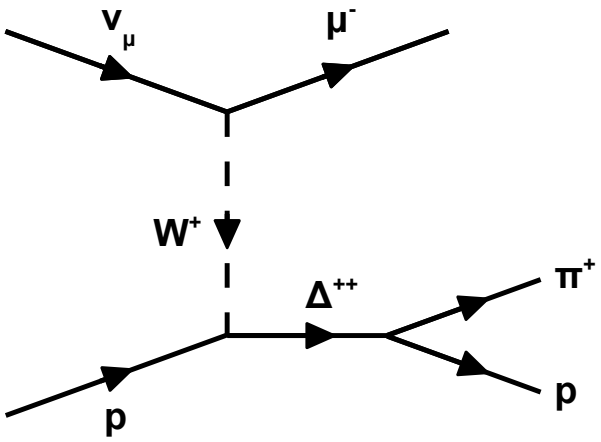

Figure 2-3: Neutrino-nucleus CC resonance production.

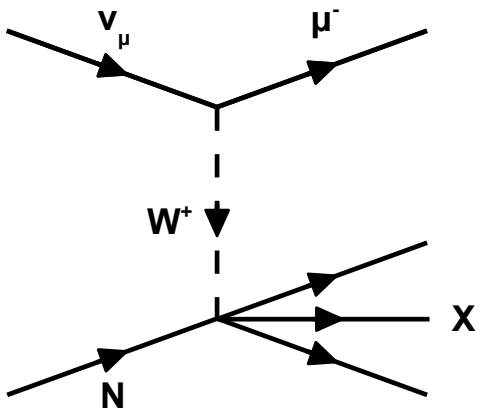

Figure 2-4: Neutrino-nucleus CC deep inelastic scattering.

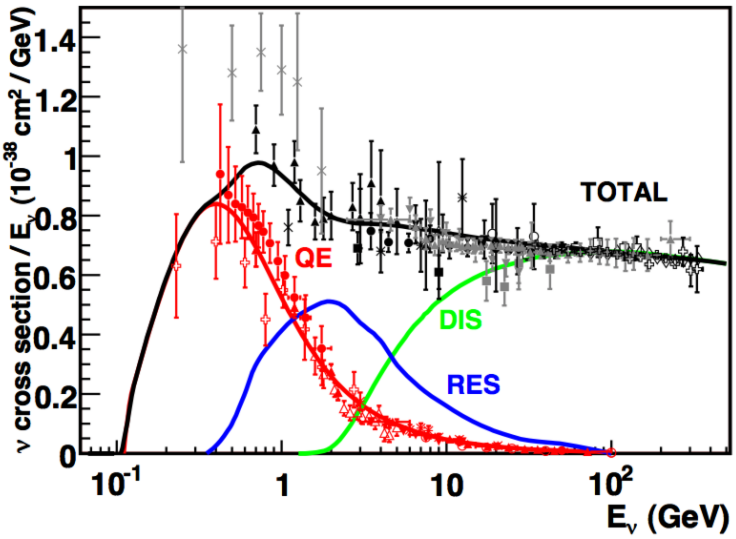

Figure 2-5: Measured and predicted per-nucleon cross sections for ν_μ CC interactions with isoscalar nuclei. CC inclusive data from ○ BEBC [15], ◇ CCFR [16], □ CDHS [17], ■ GGM-SPS [18], ▼ IHEP-ITEP [19], ▼ IHEP-JINR [20], • MINOS [21], ▲ NOMAD [22], + NuTEV [23], ▲ BNL [24], ∗ SKAT [25], ■ GGM-PS [26], and ★ SciBoone [27]. + ANL [28], ○ BEBC [29], ▲ BNL [30], ♦ FNAL [31], △ GGM [32], • MiniBooNE [33], △ NOMAD [34], ▼ Serpukhov [35], ∗ SKAT [36]. The curves are predictions for each interaction channels and are provided by the NUANCE generator [37]. Figure is from [38].

2.4 Neutrino-Nucleon DIS Interactions

At high energies ($E_\nu > 5$ GeV) the neutrino can transfer sufficient momentum to be able to resolve the internal structure of the nucleon, allowing neutrinos to scatter directly off the quarks inside in a process known as DIS. As they carry no electromagnetic charges and only interact through the weak interactions neutrinos have the unique ability to distinguish particular quark flavors and hence can significantly enhances the study of the nucleons constituents. The neutrino is able to scatter off any of the quarks that appear inside the nucleon, including those which form the sea of quarks and anti-quarks that are continually popping in and out of the vacuum. The flavor of quark seen by the neutrino depends on the four-momentum transfer available: at lower values the nucleons contain mostly up, down, and some strange quarks, but at higher values neutrinos can access the higher-mass and shorter-lived quarks too.

In DIS interactions the nucleon containing the struck quark is broken up into its constituent parts. As the struck quark recoils, the nucleon fragments and the strong force between the quarks produce a massive shower of strongly interacting particles (hadrons) in a detector, a process known as hadronization.

2.4.1 Kinematics of DIS

Neutrino CC DIS is the process in which a neutrino scatters off a quark in the nucleon via the exchange of a $W^\pm$ virtual (short-lived) vector boson, producing a corresponding lepton and a hadronic system in the final state. Figure 2-4 shows the Feynman diagram of the DIS interaction. The process under consideration can be written in the form of the momentum of each particle involved in the interaction:

$$P_\nu + P_N = P_\mu + P_X. \tag{2-3}$$

$P_\nu - P_\mu$ is the four-momentum transferred to the nucleus by the W vector boson. This variable is also represented as q. The quantity $-q^2$ is one of the important kinematic

variables that characterize DIS, and is also called Q^2. If the energy of the incoming neutrino is E_ν, and the energy and angle of the outgoing muon are E_μ, and θ respectively, then the transfer momentum is given by:

$$Q^2 = 4E_\nu E_\mu \sin^2\left(\frac{\theta_\mu}{2}\right). \tag{2-4}$$

Note that Q^2 is given purely in terms of variables on the well-defined leptonic side of the event. We will follow this convention as much as possible expressing quantities in the lab frame. Meanwhile, the invariant mass of the hadronic final state can be written as:

$$W^2 = P_X^2 = (P_\nu + P_N - P_\mu)^2. \tag{2-5}$$

Expanding W^2 yields:

$$P_\nu^2 + (P_\nu \cdot P_N) - (P_\nu \cdot P_\mu) + (P_N \cdot P_\nu) + P_N^2 - (P_N \cdot P_\mu) - (P_\mu \cdot P_\nu) - (P_\mu \cdot P_N) + P_\mu^2, \tag{2-6}$$

or

$$|P_\nu - P_\mu|^2 + (P_\nu \cdot P_N) + (P_N \cdot P_\nu) + P_N^2 - (P_N \cdot P_\mu) - (P_\mu \cdot P_N). \tag{2-7}$$

Assuming the target nucleon is at rest in the lab frame and has a rest mass of M_N, expansion of the four-vector products result in:

$$-Q^2 + 2E_\nu M_N + M_N^2 - 2E_\mu M_N. \tag{2-8}$$

The total energy of the final hadronic final state must be $E_\nu - E_\mu$ by energy conservation. Setting $E_\nu - E_\mu = E_{had}$ gives:

$$W^2 = 2M_N E_{had} + M_N^2 - Q^2. \tag{2-9}$$

The different neutrino-nucleus scattering interaction channels correspond to regions of invariant mass W, which is the center of mass energy of the final state hadronic recoil system. The multiplicity of the hadronic recoil (*i.e.* the number of hadrons in the final state hadronic recoil system) increases with W.

Both W and Q^2 are the fundamental variables characterizing DIS. There are no definite cut values for Q^2 and W to consider an event to be a DIS event; the general accepted quantities are $Q^2 \geq 1$ GeV^2 and $W \geq 2.0$ GeV. It is important to note that at the few-GeV energy region, most of the DIS events will populate the low edge region of Q^2 and W and therefore the cuts applied to these variables are chosen by considering the statistics of the sample as well. At high Q^2 the interaction has enough momentum to resolve the deep quark structure of the nucleus. Similarly, the region with $W > 2$ GeV is chosen to ensure that the interaction is safely above the resonance region and imparts sufficient energy to the nucleon to interact with a constituent quark creating a truly inelastic collision. Resonance production and non-resonant background interactions are thereby defined to have $W < 1.8$ GeV. These regions of high Q^2 and W are for interactions with a free nucleon. In a bound nucleon, the value of Q^2 and W might be smeared due to nuclear effects and therefore the DIS event sample as measured by a particle detector may contain events that are truly not DIS events.

2.4.2 CC DIS Cross Section

The cross section for neutrino DIS is derived from the matrix element

$$\mathcal{M} = \frac{G_F^2}{2} \frac{1}{1 + \frac{Q^2}{M_W^2}} (\bar{u}_\mu \gamma_\alpha (1 - \gamma_5) u_\nu) \langle X \mid J_{CC} \mid N; p, s \rangle, \tag{2-10}$$

where G_F is the Fermi coupling constant, M_W is the mass of $W^\pm$, $\bar{u}_\mu \gamma_\alpha (1 - \gamma_5) u_\nu$ is the leptonic current and $< X \mid J_{CC} \mid N; p, s >$ is the hadronic currents. Summing the leptonic

and hadronic current, the differential cross section can be written as:

$$\frac{d^2\sigma}{d\Omega_\mu dE_\mu} = \frac{G_F^2}{\left(1+\frac{Q^2}{M_W^2}\right)^2}\frac{m_\nu m_\mu}{E_\nu}\frac{E_\mu}{4\pi^2}L_{\alpha\beta}W^{\alpha\beta}, \tag{2-11}$$

where $L_{\alpha\beta}$ is the leptonic tensor and $W^{\alpha\beta}$ is the hadronic tensor.. The hadronic current is conserved $\partial_\mu J^\mu = 0$, and thus, can be written as

$$q^\alpha W_{\alpha\beta} = q^\beta W_{\alpha\beta}. \tag{2-12}$$

Contracting together the leptonic tensor and the hadronic tensor of the nucleus and neglecting any terms proportional to lepton mass, the differential cross section can be written as:

$$\begin{aligned}\frac{d^2\sigma}{dx_{bj}dy} = \frac{G_F^2 ME}{\pi\left(1+\frac{Q^2}{m_W^2}\right)^2}[&\frac{y^2 M}{2}2xW_1(\nu,Q^2)\\ &+(1-y-\frac{Mxy}{2E})\nu W_2(\nu,Q^2)\pm y(1-\frac{y}{2})\nu x W_3(\nu,Q^2)],\end{aligned} \tag{2-13}$$

where the +(-) in the third term is for neutrino (antineutrino) interactions. The change of variables $(\Omega_\mu, E_\mu \to (x,y))$ was calculated using the Jacobian form

$$d\Omega_\mu dE_\mu = \frac{2\pi M\nu}{E_\mu}dxdy. \tag{2-14}$$

The structure functions W_1, W_2, and W_3 can be written as dimensionless quantities:

$$MW_1\left(Q^2,\nu\right) = F_1\left(x\right) \tag{2-15}$$

$$\nu W_2\left(Q^2,\nu\right) = F_2\left(x\right) \tag{2-16}$$

$$\nu W_3\left(Q^2,\nu\right) = F_3\left(x\right). \tag{2-17}$$

Charged lepton deep inelastic scattering (DIS) has been used for a long time to validate the Standard Model of particle physics. The nuclear scattering mechanism for high-energy neutrinos is similar in many ways to that of the high-energy charged leptons. One important difference between the two interactions is the presence of the axial-vector current in neutrino interactions. The interference between the vector and the axial-vector current introduces a $\nu - \bar{\nu}$ cross-section asymmetry. This asymmetry gives rise to an additional structure function in neutrino-nucleon interactions, $xF_3(x, Q^2)$. The neutrino DIS cross section can be expressed in terms of $2xF_1$, F_2, and xF_3, as well as the two Lorentz invariants y and x_{bj} [39]:

$$\frac{d^2\sigma}{dx_{bj}dy} = \frac{G_F^2}{2\pi} s \left(1 + \frac{Q^2}{m_W^2}\right)^{-2} \left(x_{bj}y^2 F_1 + \left(1 - y - \frac{M x_{bj} y}{E_\nu}\right) F_2 + y(1 - \frac{y}{2}) x_{bj} F_3\right), \quad (2\text{-}18)$$

where x_{bj}, the Bjorken-x variable, is a Lorentz invariant equal to:

$$x_{bj} = \frac{-q^2}{2P_N \cdot q}, \quad (2\text{-}19)$$

and y is equal to:

$$y = \frac{P_N \cdot q}{P_N \cdot P_\nu}. \quad (2\text{-}20)$$

G_F is the Fermi constant, s is the center-of-mass energy of the interaction, m_W is the W^+ mass, and F_1, F_2, and F_3 are structure functions that describe the structure of the nucleon. The parton content of proton is not predicted by Quantum Chromodynamics (QCD), but these structure functions can be directly measured or extracted using lepton and neutrino scattering data.

In the lab frame, the target nucleon is assumed to be at rest. Equation 2-19 may then be written as:

$$x_{bj} = \frac{Q^2}{2M_N E_{had}}, \quad (2\text{-}21)$$

where $E_{had} = P_X^0$. By energy conservation, $E_{had} = E_\nu - E_\mu$. The physical interpretation of y is clearer after expanding the four-vector product in Equation 2-20. Assuming the target nucleon is at rest in the lab frame:

$$y = \frac{E_{had}}{E_\nu}. \tag{2-22}$$

y is called the "inelasticity" of the event and it measures how much of the incident neutrino's energy is transferred to the hadronic system. y is defined on the interval $0 \leq y \leq 1.0$.

2.4.3 Bjorken-x Scaling

Bjorken Scaling pertains to an underlying feature (scaling) of a large class of dimensionless physical quantities in fundamental particles; it suggests that when experimentally observed hadrons are probed at high energies, they will behave as collections of virtually independent point-like constituents. The properties of these hadrons are said to scale when they are primarily derived from dimensionless kinematic quantities, such as a scattering angle or the ratio of the energy to a momentum transfer. As energy increases the spatial resolution potentially improves, implying independence of the absolute resolution scale, and thus effectively point-like substructure [40].

The form factors of structure functions F_i depend on x_{bj} and Q^2. This implies that additional momentum transferred to the hadronic system must be changing the form factors of the target nucleon. F_i strongly depend on x_{bj} but weakly depend on Q^2 implying that there is some point-like structure inside the nucleon. This structure is point-like as it remains constant regardless of any additional momentum transfer, which should be able to resolve finer distances due to the uncertainty principle [41].

The idea of scaling was first proposed by James Bjorken in 1968 for the structure functions of deep inelastic scattering of electrons on nucleons. In 1967, at about the same time when Bjorken proposed the theoretical scaling variable, the SLAC-MIT group also discovered that the measured DIS cross section indeed exhibits the approximate scaling behavior. The SLAC-MIT group directly measured F_1 and F_2 and verified that each form

factor was only weakly dependent on Q^2 but strongly dependent on the scaling variable x_{bj} [42]. This provided direct evidence of nucleons being constructed of three point-like charges consistent with the proposed quarks [43].

In the picture of neutrinos scattering from point-like constituents of target nucleons (the parton interpretation of DIS) the variable x_{bj} is viewed as the fraction of the nucleon momentum carried by the struck quark in a frame where the target momentum is very large. The common picture of this frame is that the nucleon, as seen by the incoming lepton, is flat and static because of length contraction and time dilation, and the incoming lepton interacts with a single one of these frozen partons, carrying a momentum fraction x_{bj} [44].

2.5 Parton Distribution Function

The conditions for DIS ($Q^2 \geq 1.0$ GeV^2 $W \geq 2.0$ GeV) imply that a significant amount of energy is imparted from the neutrino to a quark inside the nucleon. The probe's resolving power is approximately $\hbar/q$, and as q increases, the resolution of the structure also become clearer. At high Q^2 ($-q^2$), it becomes easier to probe the internal structure of the nucleon. In a frame where the momentum of the target nucleon is very large, the momentum of the parton is almost colinear (parallel) with the momentum of the nucleon and so that the target can be viewed as a jet of partons, each carrying a separate fraction x_{bj} of the longitudinal momentum. The partons momentum distribution functions within the target nucleon are referred to as Parton Distribution Functions (PDFs) when the spin direction of the partons can be neglected. They represent the number densities as they are normalized to the number of partons (the probability densities) to find a parton carrying a momentum fraction x_{bj} at Q^2. DIS experiments have demonstrated that the number of partons decreases at high x_{bj} and increases at low x_{bj} with Q^2. At low Q^2 the nucleon structure function is dominated by the three valence quarks. At high Q^2 the quark-antiquark pairs carrying a low momentum fraction x_{bj} become more dominant and they form the sea quarks. PDFs describe the constituents of the nucleon in terms of sea

and valence quarks (see Figure 2-6). The relationship of structure function F_1 to F_2 satisfy the Callan-Gross relation at the lowest order of correction [45],

$$F_2(x_{bj}) = 2x_{bj}F_1(x_{bj}) \quad \Rightarrow \quad F_L(x_{bj}) = 0, \tag{2-23}$$

where F_L is the longitudinal structure function. For a given structure function F_2:

$$F_2(x_{bj}, Q^2) \approx F_2(x_{bj}) = \sum_i k_i x_{bj}(q_+(x_{bj}) + q_-(x_{bj}) + \bar{q}_+(x_{bj}) + \bar{q}_-(x_{bj})), \tag{2-24}$$

where each quark flavor i is summed, k_i is the quark's electric charge, $q_\pm$ is the momentum distribution of quarks inside a nucleon for spins aligned parallel (antiparallel) with the nucleon, and $\bar{q}_\pm$ is the momentum distribution of anti-quarks for spins aligned parallel (antiparallel) with the nucleon. Valence quarks dominate at large values of x_{bj} and form the majority of a nucleon's quarks and thus form a majority of the nucleon's momentum. Conversely, sea quarks dominate at small values of x_{bj} and will soften the valence quarks distribution as Q^2 increases.

QCD predicts that quarks are asymptotically free at high energies deep within protons and neutrons. Under this assumption, the initial four momentum (P_i) and final state four momentum (P_f) of the struck quark can be written as:

$$P_f = P_i + q. \tag{2-25}$$

Recall that since the quarks are in a boosted frame $q^0 = 0$ by definition. In this case, Equation 2-25 written as:

$$\begin{aligned} p_i^0 &= p_f^0, \\ \vec{p_i} + \vec{q} &= \vec{p_f}. \end{aligned} \tag{2-26}$$

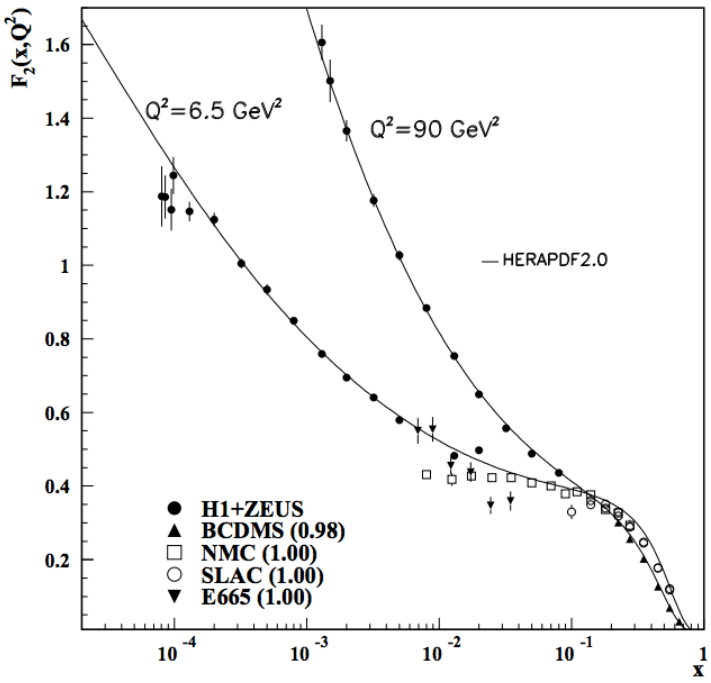

Figure 2-6: The structure function F_2 given at two fixed Q^2 values (6.5 GeV^2 and 90 GeV^2). Scaling can be seen at the pivot point $x_{bj} \sim 0.14$. Figure is from [46].

Assuming the energy of the quarks are much larger than their mass, the first half of Equation 2-26 simplifies to $|\vec{p_i}| = |\vec{p_f}|$. The transverse momentum of the quarks is also negligible. These two assumptions imply that the momentum vectors of the initial and final state quarks are either identical, or differ from each other by a sign (the momentum vectors are back to back). As $\vec{q} \neq 0$ in this frame, the only possible configuration of quark momenta is $\vec{p_i} = -\vec{p_f}$. With this information, the second expression in Equation 2-26 reduces to:

$$\vec{p_i} = \frac{-\vec{q}}{2}. \tag{2-27}$$

Using the definition of $\vec{q}$ from Equation 2-27 yields:

$$\vec{p_i} = x_{bj}\vec{p_N}. \tag{2-28}$$

It is important to note that some of the assumptions used to define x_{bj} as the quark's fractional momentum are not generally true. For instance, quarks are not massless and this "target mass" effect re-scales the scaling of quarks from x_{bj} to account for the nucleon mass M. In the Georgi-Politzer calculation [47], this is written as

$$x_{bj} \rightarrow \xi \frac{2x_{bj}}{(1+k)} \tag{2-29}$$

where $k = (1 + 4M^2x^2/Q^2)^{1/2}$. As the target mass effect involves powers of $1/Q^2$ that do not contribute to the perturbative expansion of QCD, it is frequently referred to as kinematic higher twist. When the DIS formalism is extended to lower Q^2 and W values, the "higher twist" effects as powers of $1/Q^4$ and $1/Q^6$ become significant.

The analysis in this dissertation uses data collected with the recently upgraded neutrino beam at Fermilab to produce the first measurement of a high-precision DIS absolute cross section in the energy range of $5 < E_\nu < 50$ GeV. The differential cross section as a function of Bjorken-x extracted in this thesis can be used together with the future antineutrino DIS differential cross-section analysis to measure the contribution of the antiquark PDFs relative to those of the quarks for different targets.

2.6 Partonic Nuclear Effects

If the neutrino interaction in the nuclear target takes place on a nucleon at rest, then we have all pieces needed to form a complete neutrino interaction picture. Neutrino experiments utilize neutrino-nucleus interaction models. These models calculate the cross-section for a particular neutrino-nucleon scattering process, which quantifies the probability for the scattering process to occur. Neutrino-nucleus interaction models also calculate effects of the nuclear medium, which modifies both the neutrino-nucleon cross sections and the particles produced in neutrino-nucleon interactions. The cross sections and nuclear effects cannot be calculated exactly due to the non-perturbative effects of the

strong interactions within the nucleon and nucleus. Neutrino-nucleus interaction models are therefore tuned to measured neutrino-nucleus scattering cross sections.

Equation 2-18 fully describes all DIS interactions in terms of three structure functions F_1, F_2 and F_3 for free nucleons. These structure functions are different for protons and neutrons due to the different valence quark compositions. Furthermore, atomic nuclei are made up of protons and neutrons bound together by the strong nuclear force and this binding effect must be taken into consideration when deriving the cross sections.

2.6.1 Non-Isoscalarity

Equation 2-18 can be extended in a straightforward manner to calculate the *nuclear* cross section of a nucleus with atomic mass A by combining the proton and neutron differential cross sections $\frac{d\sigma^P}{dxdQ^2}$ and $\frac{d\sigma^N}{dxdQ^2}$:

$$Z\frac{d\sigma^P}{dx_{bj}dy} + (A-Z)\frac{d\sigma^N}{dx_{bj}dy}, \tag{2-30}$$

where Z is the charge of the nucleus.

The ν_μ interacts with a down quark to conserve charge and converts to a μ^- in a CC interaction. As the proton contains only one down valence quark, the cross-section of the ν_μ + proton interaction should therefore be smaller than the ν_μ + neutron interaction, leading to a smaller proton piece as compared to the neutron piece in Equation 2-30. For an atomic nuclei with an equal number of neutrons and protons (isoscalar) this difference is negligible as the cross-section is averaged over all nucleons. However, heavier nuclei such as iron and lead have an unequal number of protons and neutrons. This unequivalence leads to a higher number of ν_μ + neutron events in the per-nucleon total cross section on lead compared to carbon. As a result, it is expected that the lead cross-section is higher than carbon when taking the lead to carbon cross section ratio. Valence quarks are more prominent at high x_{bj} resulting in larger non-isoscalar effects at higher values of x_{bj}.

Valence quarks also become dominant as A increases and the ratio of neutrons to protons in the nucleus increases.

Non-isoscalarity is observed for all x_{bj} values of DIS interactions, where it is more prominent at high x_{bj}. The partonic nuclear effects depend strongly on the x_{bj} and the size of the effect is strongly correlated to the x_{bj} of the event. As x_{bj} is the fraction of the nucleon momentum carried by the struck quark, the partonic nuclear effects thus are associated to the effects arising from sea and valence quark distributions.

2.6.2 Nuclear Structure Functions

The use of heavy targets in lepton scattering studies introduces complications, as interactions with bound nucleons are impacted by nuclear effects. These nuclear effects include how nucleons in the nuclear medium are correlated to one another before the interaction occurs, also known as the initial state nuclear effects. After the interaction occurs, the outgoing particle still needs to propagate through the nuclear medium and it may engage in additional interactions. These interactions are referred to as the final state interactions (FSI).

The measured nuclear structure function gives direct information about how nuclear binding effects modify the momentum distribution of quarks in nucleons. The next way to extend Equation 2-18 for bound nucleons is to substitute the free nucleon structure functions F_1, F_2, and F_3 with *nuclear* structure functions F_1^A, F_2^A, and F_3^A. These nuclear structure functions are related to the free nucleon structure functions by a function $f(x_{bj}, Q^2)$:

$$F_i^A(x_{bj}, Q^2) = f_i(x_{bj}, Q^2) F_i(x_{bj}, Q^2). \tag{2-31}$$

$f_i(x_{bj}, Q^2)$ may be different for different structure functions and different nuclei. The factor of Q^2 in f allows f to parametrize the target mass and higher twist effects discussed

earlier. f_i is only a function of x_{bj} and 2-31 reduces to:

$$F_i^A(x_{bj}) = f_i(x_{bj})F_i(x_{bj}), \tag{2-32}$$
$$f_i(x_{bj}) = \frac{F_i^A(x_{bj})}{F_i(x_{bj})}.$$

The most common parameterization of f is derived from charged lepton-nucleus DIS scattering experiments. It is common to use light nuclei such as ^{2}H as the denominator in Equation 2-32 in place of truly free nuclei due to the difficulties involved in using them. Figure 2-7 shows a parameterization of $f(x_{bj})$ (solid line) along with data from different charged lepton DIS experiments. There are four features in this parameterization stemming from x_{bj} dependent nuclear effects.

The PDFs nuclear medium modifications are typically described by the nuclear modification factor defined as the per-nucleon structure function ratio:

$$R = \frac{F_2^A}{F_2^D}, \tag{2-33}$$

as deuteron is approximately considered to be made up of a system of free proton and free neutron. The nuclear modifications are generally classified as:

- Nuclear shadowing: a depletion of the structure function ratio R due to interactions with hadronic fluctuations of a W boson for $x_{bj} < 0.1$.
- Anti-shadowing: an enhancement in the structure function ratio R for $0.1 < x_{bj} < 0.3$.
- The EMC effect: a second depletion in the bound nucleon structure function ratio R for intermediate x_{bj} values $0.3 < x_{bj} < 0.75$.
- Fermi motion: a sharp rise in the bound nucleon structure function ratio R as x_{bj} increases past $x_{bj} > 0.7$.

Each of these effects will be discussed in detail in the following sections.

2.6.2.1 Nuclear Shadowing

Shadowing is a depletion in the structure function ratio R due to destructive interference of interactions with multiple nucleons in a nucleus that occurs for $x_{Bj} < 0.1$. The source of the depletion is the survival probability for the force-mediating vector boson or its fluctuations to pass through the nuclear medium and reach a bound nucleon deep inside the nucleus. In other words, the interaction between a vector boson with a given bound nucleon is shaded by the probability of having preceding interactions with other nucleons, i.e. will experience multiple scattering. Nuclear shadowing occurs at low x_{bj} and at relatively low values of Q^2 because a coherence time associated with the hadronic fluctuations of the boson exceeds the mean internucleon spacing in nuclei. Derivation of this coherence time can be estimated dimensionally by:

$$l \approx \frac{E_{had}}{Q^2 + m^2}, \tag{2-34}$$

where m^2 is the effective mass of the hadronic fluctuation. As l is directly proportional to the E_{had} of the event, low E_{had} events will not have a sufficient coherence time for the hadronic fluctuation to interact with the nucleus. High E_{had} events are primarily composed of low x_{bj} by Equation 2-21, thus the shadowing effect is dominant only at low x_{bj} [48].

In the case of neutrino scattering, the W boson can interact during hadronic fluctuations. The partial conservation of axial current (PCAC) leads to the Adler relation that explains the W's fluctuation to axial-vector hadronic states [48]. In contrast to the vector meson dominance (VMD) observed in the hadronic decays of excited light mesons involving photons, many hadronic states contribute significantly to the hadronic behavior exhibited by a W [49].

Nuclear shadowing is relatively well understood in charged lepton scattering. However, there are two crucial differences expected in the shadowing mechanisms between neutrino and charged lepton scattering that will directly affect the mass term in 2-34. The

shadowing of sea quarks differs from valence quarks. Neutrinos, unlike charged leptons, are directly sensitive to the number of valence quarks through the structure function F_3. Charged lepton DIS is largely sensitive to the vector current, which contributes to effective mass terms on the order of 1 GeV^2. Meanwhile, neutrinos are also sensitive to the axial structure which brings the effective mass closer to the pion mass ($\approx$ 100 MeV^2). As a result, shadowing in neutrino scattering may occur with a longer coherence time and thus, larger values of x_{bj}. It is important to note that difference is most conspicuous at low Q^2 since the vector current is conserved and thus vanishes at $Q^2 \to 0$ GeV/c^2 while axial vector current does not.

2.6.2.2 Anti-Shadowing

Antishadowing is the enhancement in the structure function ratio R at $0.1 < x_{Bj} < 0.3$ due to the constructive interference in multiple scattering through a mechanism very similar to shadowing. However, the coherence time at such values of x_{Bj} is too small for such long-range internucleon spacing in nuclei. Therefore, the enhancement effect resulting from re-scattering is larger than the shadowing effect, which decreases faster with energy.

Some theories propose that the antishadowing effect might be related to the EMC effect (see section 2.6.2.3). As an example, one of the many models suggested to explain the EMC effect is the existence of multiquark clusters. This model assumes that the nucleus contains groups of 3N quarks [50]. While a quark in a free nucleon is restricted to have $x_{Bj} < 1$, this is not the case with a multiquark cluster. The existence of very high momentum states would subsequently deplete F_2 at lower values of x_{Bj}. This explanation is by no means a widely accepted explanation, and might become less popular with recent measurements that demonstrate a correlation between the structure functions in the EMC range and those at $x_{Bj} > 1$ [51].

2.6.2.3 The EMC Effect

Understanding the structure of nucleons in terms of quark and gluon degrees of freedom in the theory of QCD proved to be one of the greatest challenges in physics. Years of experimental and theoretical efforts have been invested in understanding how these fundamental degrees of freedom give rise to the nucleon. One of the most notable results came from the European Muon Collaboration (EMC), who reported a significant difference between the measured ratio of cross sections of iron nuclei and deuteron nuclei using a beam of muon particles [52] and the theoretically predicted value [53, 54, 55, 56]. This discovery is the first evidence for the nuclear effect known as "the EMC effect".

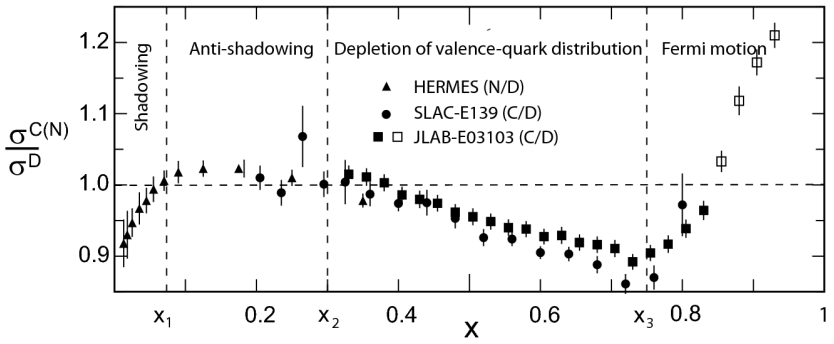

Figure 2-7: Comparisons of cross section ratios of carbon (C) or nitrogen (N) to deuterium (^2H) measured at various charged lepton experiments HERMES [57], SLAC-E139 [58], and JLAB-E03103 [59]. Results are shown as a function of Bjorken x. Figure is taken from [60].

The EMC effect is the depletion in the bound nucleon structure function ratio R in the intermediate x_{bj} region of $0.3 < x_{bj} < 0.7$. Prior to the discovery of the EMC effect, a steady increase in the bound nucleon structure functions was expected beyond the anti-shadowing region. However, the opposite effect was clearly observed in EMC [52]. The effect originates from the valence quarks of the nucleon as the EMC effect arises in the intermediate x_{bj} regime. To date, there is no universally accepted explanation for the cause of the EMC effect [61]. Numerous theories have been proposed, one of which includes the modification of free nucleon pdfs using nuclear wave functions to phenomenologically extract nuclear pdfs [62]. The EMC effect is known to be a strong function of the nuclear

density. A stronger EMC effect is observed in heavier nuclei than lighter nuclei when compared to deuterium as shown in Figure 2-8.

Some of the early neutrino-nucleus scattering experiments, mostly dominated by bubble chamber experiments, were conducted to test the EMC effects using the neutrino-nucleus interaction. One of these experiments was the Big European Bubble Chamber Collaboration (BEBCC) which published $\overline{\nu}_\mu$ neon/deuterium data. Their results agree with the muon and electron scattering results from EMC and SLAC in the kinematic region of $0.3 < x < 0.6$ and high four-momentum transfer squared (Q^2) [63]. The CERN Dortmund-Heidelberg-Saclay Collaboration (CDHS), an iron detector with a liquid hydrogen tank upstream of the detector, also reported no significant difference between the structure functions for hydrogen and iron [64]. Following these two experiments, several other neutrino-nucleus scattering experiments, namely the E545 Collaboration [65], WA25, and WA59 collaborations [66], performed additional measurements of neutrino DIS cross sections on neon and deuterium. Their results also confirmed the EMC results in $0.3 < x < 0.6$. Unfortunately, these experiments were statistically limited and thus could not provide a statistically significant comparison of the EMC effect in different nuclei. In addition, the large systematic error coming from uncertainty in the neutrino flux provides an additional complication when comparing to the charged-lepton EMC data.

The first systematic measurement of the EMC effect in neutrino scattering has been performed by MINERvA utilizing its multiple nuclear targets exposed to the identical neutrino beam [67]. This unique configuration in a neutrino experiment allows the systematic uncertainties from different fluxes and detector smearing effects to cancel in the ratio of cross section measurements.

2.6.2.4 Fermi Motion

Fermi motion is the momentum of nucleons bound inside a nucleus. As the valence quarks begin to dominate the structure functions at $x_{Bj} > 0.7$, Fermi motion becomes the dominant nuclear effect. A common nuclear model that describes this phenomenon is the

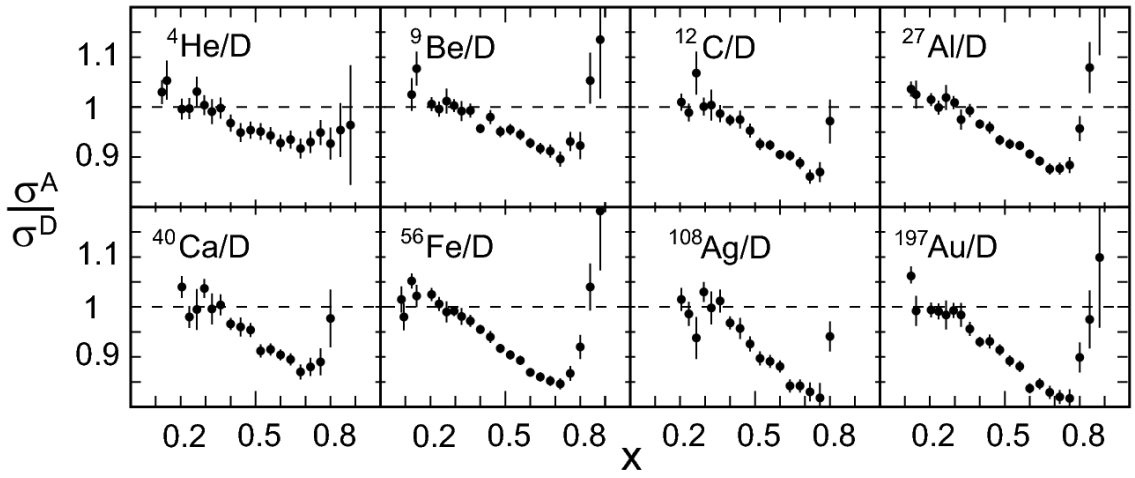

Figure 2-8: The comparisons of the EMC effect for various nuclei in charged lepton scattering. The heavier elements (gold, silver) show a sharper decrease in the x_{bj} range of $0.5 < x_{bj} < 0.8$. Data from [68] and [58]. Figure is taken from [60].

Relativistic Fermi Gas (RFG) model [69]. In this model, the nucleus is composed of two systems of free nucleons (neutrons and protons) confined in the same potential well that obey Fermi statistics. Each nucleon feels a potential due to the superposition of the potential from all other nucleons. The nucleons sit in the center of a nuclear potential wall with diameter equal to the diameter of the nucleus. The nucleons fill the lowest energy levels when it is in the ground state. The Fermi momentum p_F is the largest momentum of a nucleon bound inside an nucleus in a ground state. The momentum distribution of the nucleons is flat and goes to zero above p_F. Fermi motion can only be observed in DIS events at very high Q^2. This can be achieved by setting $x_{bj} = 1$. In that case:

$$Q^2 = 2M_N E_{had}. \tag{2-35}$$

Substituting Equation 2-35 into the definition of W^2 yields:

$$W = \sqrt{M_N^2 + 2M_N E_{had} - 2M_N E_{had}},$$
$$W = M_N. \tag{2-36}$$

$W = M_N$ indicates the event is elastic where the nucleon mass remains constant after the neutrino interaction. Increasing x_{bj} causes W to approach M_N. This evidently violates one of the DIS assumptions that sufficient energy and momentum have been transferred to the nucleon to resolve individual quarks. Large x_{bj} values are only possible in DIS events at very large Q^2. However in practice, due to the limited beam energy and angular acceptance, experiments have a limit on the maximum available Q^2.

2.7 Neutrino DIS Measurement

Contemporary neutrino-nucleus scattering experiments have utilized high-intensity neutrino beams and more finely grained detectors. Higher intensity beams produce higher statistics data samples, resulting in analyses that are no longer statistics limited but instead limited by systematic errors. Several high energy neutrino experiments have measured the DIS cross sections for specific final states, for example opposite-sign dimuon production: CHORUS ν-Pb [70], NOMAD [71], and NuTeV ν-Fe [72].

To be able to include neutrino-nucleus DIS scattering results in a global QCD fit, understanding the neutrino-nucleus nuclear effects is essential. The most precise high-statistics ν and $\bar{\nu}$ DIS measurements to date come from the NuTeV ν-Fe experiment. NuTeV reported the probability density for finding a particle with a certain longitudinal momentum fraction x at resolution scale Q^2. Using this data, the nCTEQ collaboration performed a dedicated PDF fit to neutrino-iron data by employing χ^2 analysis and extracted a set of iron nuclear correction factors for iron structure functions [73]. The results, however, shows an inconsistency between the nuclear corrections in $\nu - A$ DIS (see Figure 2-9). Compared to the theoretical predictions, NuTeV agrees well in the central x region, but exhibits inconsistency within low x at low Q^2 and high x both in shape and magnitude when compared to results from charged-lepton scattering.

The fits performed above are based on several analyses of experiments that use one heavy nuclei; therefore it is highly essential to gather data from experiments utilizing different nuclei. MINERvA with its more extensive range of nuclear targets aligned in the

same neutrino beamline has made a significant contribution toward a more detailed nuclei-dependant study of nuclear PDFs and the correction factors[67]. Neutrino DIS data with a higher energy beam (higher percentage DIS events) used in this dissertation analysis as well as the antineutrino DIS data that is currently running will provide a thorough systematic studies of the resonance-DIS transition region and the low Q^2 DIS region. This includes the extraction of high-x_{bj} parton distribution functions that will play an important role in the inclusion of neutrino-nucleus DIS data to the global QCD fit.

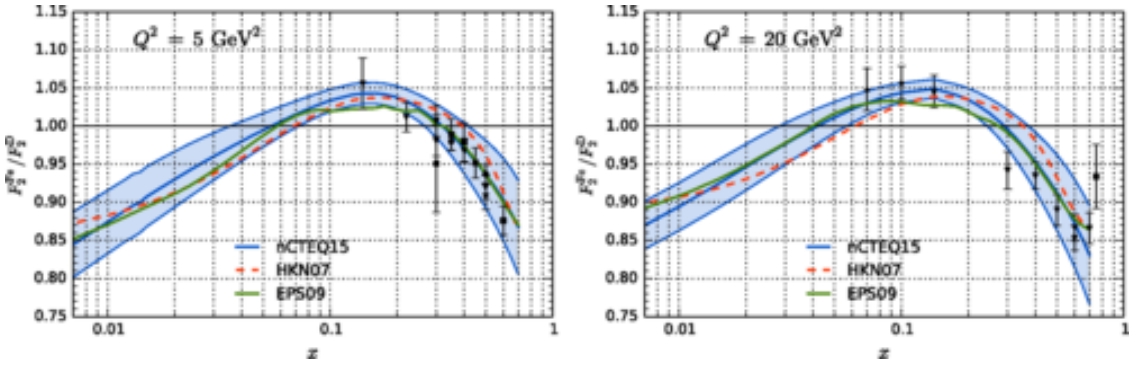

Figure 2-9: nCTEQ Global Fit of nuclear modifications on parton distribution functions (each curve represent) on neutrino cross section data from NuTeV (data points). Figure is from [74].

CHAPTER 3
NUMI BEAMLINE

Neutrinos are created naturally by various radioactive decays, cosmic rays, and during a supernova. They are a by-product of nuclear reactors and can be produced using particle accelerators. The neutrino beam used in the MINERvA experiment, as well as the oscillation experiments MINOS and NOvA, comes from the Fermilab's NuMI accelerator. NuMI delivers a high intensity, broad-spectrum neutrino beam that, depending on configuration, consists primarily of muon neutrinos or muon antineutrinos. This chapter describes the NuMI beam as it relates to this analysis, and is summarized from [75].

The neutrino beam is generated by firing 120 GeV/c protons at an angle of 58 mRad downward from Fermilabs Main Injector accelerator onto a meter long graphite target, producing mesons (predominantly pions) through interactions with nucleons in the target. A pair of pulsed toroidal magnetic horns select pions according to their electric charge while defocusing the oppositely charged ones. When the horns are running with positive (negative) polarity, positively (negatively) charged pions are selected, leading to a neutrino (anti-neutrino) enhanced beam. The sign-selected pions are then focused into the decay pipe where they are allowed to decay in the helium-filled decay pipe, producing muons and neutrinos.

A hadron absorber made of steel, aluminum, and concrete removes any leftover hadrons from the beam; over 200 meters of rock filter out the muons, leaving a beam of neutrinos that propagate in a straight line to the MINERvA detector. A schematic of the beam components is shown in Figure 3-1.

This dissertation presents results obtained using neutrinos produced in the ME beam configuration, with a peak energy around 6 GeV. The total number of protons on target (POT) for the MINERvA ME configuration for neutrinos, which corresponds to the data set used in this analysis, is 12×10^{20}. Figure 3-2 shows the data-taking periods for ν_μ for the entire ME exposure of the MINERvA detector.

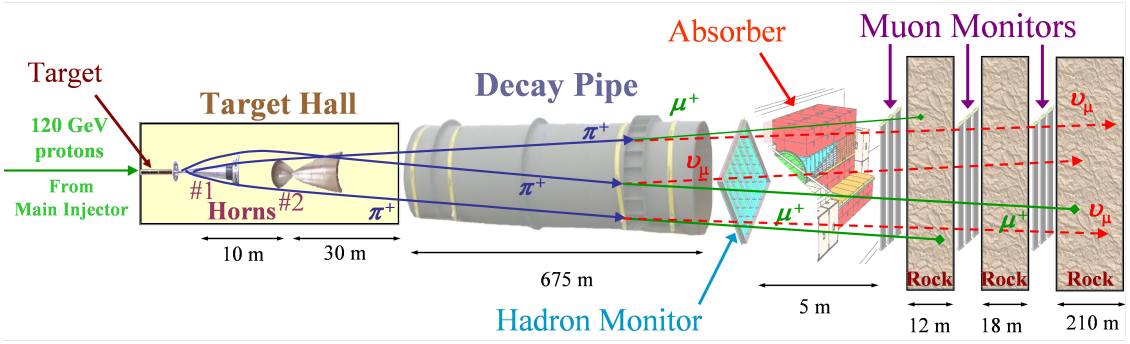

Figure 3-1: A schematic of the beam components. Figure is reprinted from [76]. Copyright (2005) with permission from R. Zwaska.

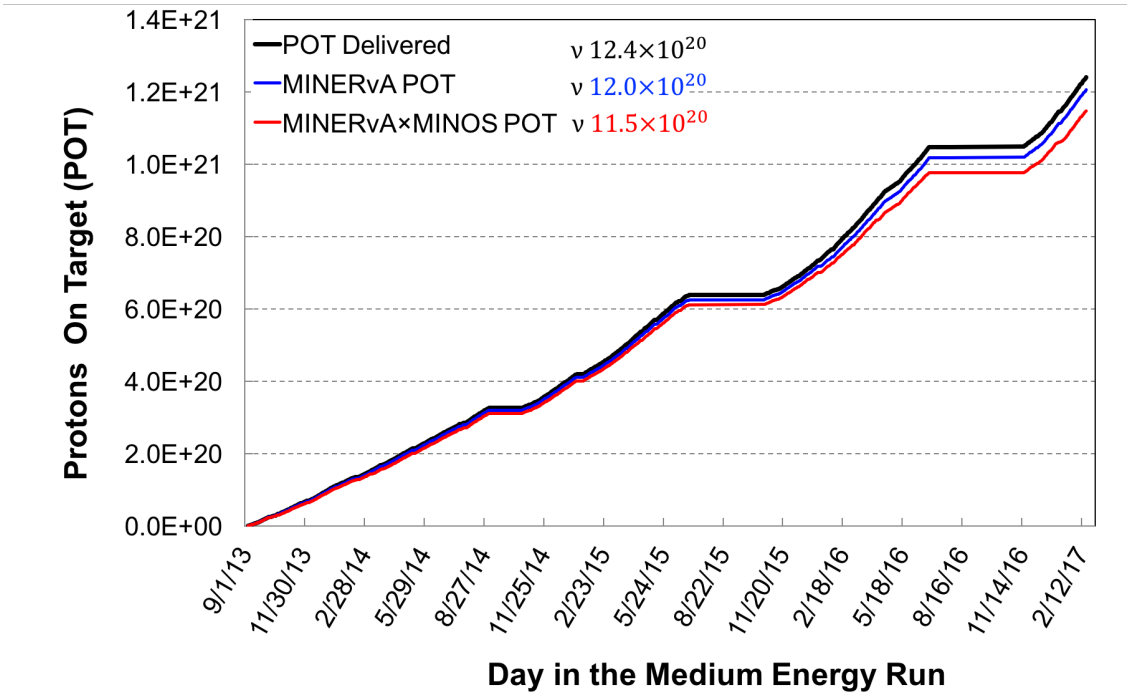

Figure 3-2: Total POT collected as a function of the number of days within the entire ME run period. The total POT for ν_μ running is 12×10^{20}. Figure is from [77].

3.1 Proton Delivery and Slip-stacking

The Fermilab Accelerator Complex is illustrated in Figure 3-3. The proton beam delivery in Fermilab starts with a H^- ion source which is accelerated from 35 keV to 750 keV, bunched into separate packets of particles, and injected into Fermilab's linear accelerator, or Linac. The 5152-meter-long Linac accelerates the H^- ions to 400 MeV. The ions enter the Booster, where they immediately pass through a carbon foil. The Booster removes electrons from the hydrogen ions, creating positively charged protons that are then accelerated to 8 GeV.

The Booster has 84 RF (radio frequency) buckets around its 474-meter-circumference which creates 84 proton bunches containing 3^{10} protons each that are 19 ns apart. The proton bunches are grouped into 1.6 μs "batches" which corresponds to one revolution around the Booster ring. The Booster accelerator delivers 8 GeV protons to the Recycler where two proton batches are stacked and squeezed into the size of one batch, doubling the proton bunch intensity.

The Main Injector, located directly underneath the Recycler, captures the proton beam from the Recycler and accelerates them from 8 GeV to 120 GeV. The Main Injector and Recycler both have 588 RF buckets and their circumferences are seven times that of the Booster which allows the injection of seven proton batches. However, one slot must stay empty to enable the extraction kicker to ramp up, so a maximum of six proton batches can be accelerated in the Main Injector. A beam spill containing all six batches lasts typically 10 μs. Roughly 15 cm before striking the NuMI target the proton beam passes through a toroid which measures the number of protons and the proton beam is focused to the desired beam spot size at the target. Target pulse-heating requires beam sizes between 1 to 2 mm in diameter.

The Main Injector was previously used to do the proton batch stacking injected from the Booster in addition to its main function as Main Injector. After the summer shutdown in 2013, the Recycler was converted to a high-intensity proton stacker using a

method called "slip-stacking". Slip-stacking approximately doubles the proton intensity by merging two proton batches into a single batch. Separating the stacking process from the role of the Main Injector allows the Main Injector to continuously ramp up, deliver beam, and ramp down at its maximum rate. This reduces the cycle time from 1.67 s to 1.33 s.

The sequence to produce a slip-stacked batch is as follows:

1. Six proton batches are injected from the Booster into the Recycler and captured by the first RF system operating at 53 MHz. The frequency of the RF system is then changed to 1260 Hz, causing the batches to decelerate to lower momentum and thus move into a smaller orbit around the Recycler.

2. An additional 6 proton batches are injected into the Recycler and captured by the RF system at 53 MHz.

3. The two six-proton-batches are separated in azimuthal space at different energy in the Recycler. The two sets of batches continue to accelerate around the Recycler until they are aligned. Then they are then injected into the Main Injector, captured and accelerated at 120 GeV.

3.2 NuMI Target

The NuMI target is one of the more delicate elements in the NuMI beam line. The target must be able to endure sustained, high-power proton beams, which induce stresses, heating and eventually radiation damage and corrosion of materials. To maximize the neutrino yield, most of the proton beam should be intercepted in the target in the smallest possible volume and re-absorption of pions produced by secondary interactions must be kept to a minimum. However, this increases the volumetric energy deposition in the target and reduces the size of the outer transverse dimensions, causing the structural rigidity of the target to decrease and resulting in a smaller surface area for cooling. To meet the thermo-mechanical requirements of a robust target design while maintaining a high fraction

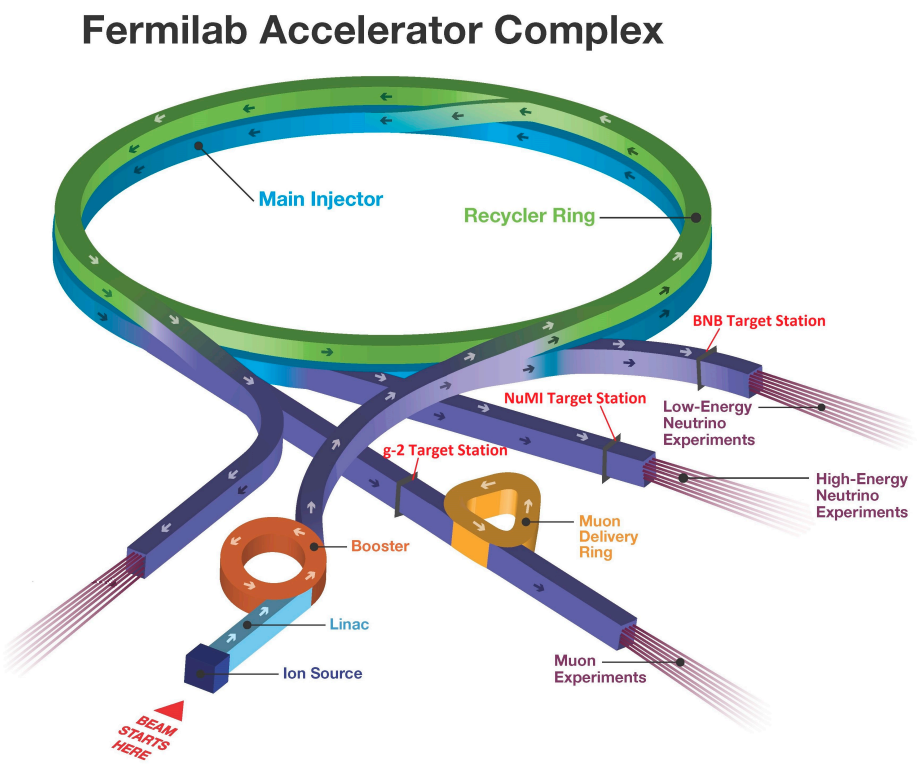

Figure 3-3: The Fermilab Accelerator Complex. Figure is taken from [78].

of the beam striking the target, the beam spot size at the target and the target itself must be increased.

3.2.1 Baffle

The NuMI beam power is so incredibly large that even a relatively small mis-steering of the beam could pose serious damage to the beam components. The target cooling and support components and the focusing horns, whose narrowest apertures (referred to as necks) are not much larger than the nominal beam spot size at their locations, are especially vulnerable to the offset parallel beam trajectories. To protect these components a baffle is installed upstream of the target. The baffle comprises a graphite core, 5.7 cm in diameter and 150 cm long in the beam direction. It is enclosed in a 6-cm-diameter aluminum tube that provides good thermal contact with the graphite. This contact is maintained under beam heating in spite of the larger thermal expansion coefficient of aluminum. A 13-mm-diameter circular hole through which the proton beam

passes is found at the center of the baffle. It is designed to endure the full intensity beam for a few pulses until mis-steering can be detected and the beam adjusted or turned off. Thermocouples mounted near the downstream end of the baffle are connected to an interlock that will turn the beam off if significant mis-steering is detected as excessive heat. This monitoring also measures how much beam is hitting the inside walls of the baffle. Since the largest temperature rise is downstream, both monitoring functions are done by measuring the temperature at the downstream end of the baffle. Beryllium windows are used to contain the radioactivated graphite target when its thermal and structural material properties degrade through exposure to high energy proton beam. The windows are also used to protect the graphite target from erosion due to the strong wind coming from the air cooling system in the target pile.

3.2.2 Target and Baffle Carrier

The NuMI neutrino beam is designed to be used in different configurations depending on the desired energy spectrum of the neutrinos, as shown in Figure 3-4. This is achieved by keeping the two focusing horns stationary and moving the target position with respect to the first horn. This results in a variety of wide band beams with peak energies ranging from 3 GeV to 9 GeV. Figure 3-4 shows two of the three beam configurations.

To tune the neutrino beam energy, the target and baffle are mounted on a rail-drive system as one unit with 2.5 m of longitudinal travel along the beam Positioning motors seated on top of the module allow motion control of the target ±8 mm in the horizontal direction, and +8/-200 mm in the vertical direction. Moving the target upstream has the effect of directing smaller-angle, higher-momentum particles into the focusing horns, resulting in a higher-energy neutrino beam.

3.3 Focusing Horn

The magnetic horns, Horn 1 and Horn 2, act as hadron lenses by focusing mesons produced from the NuMI target and directing them towards the neutrino detector located downstream. Each magnetic horn, described in Figure 3-5, is approximately 3 m long. A

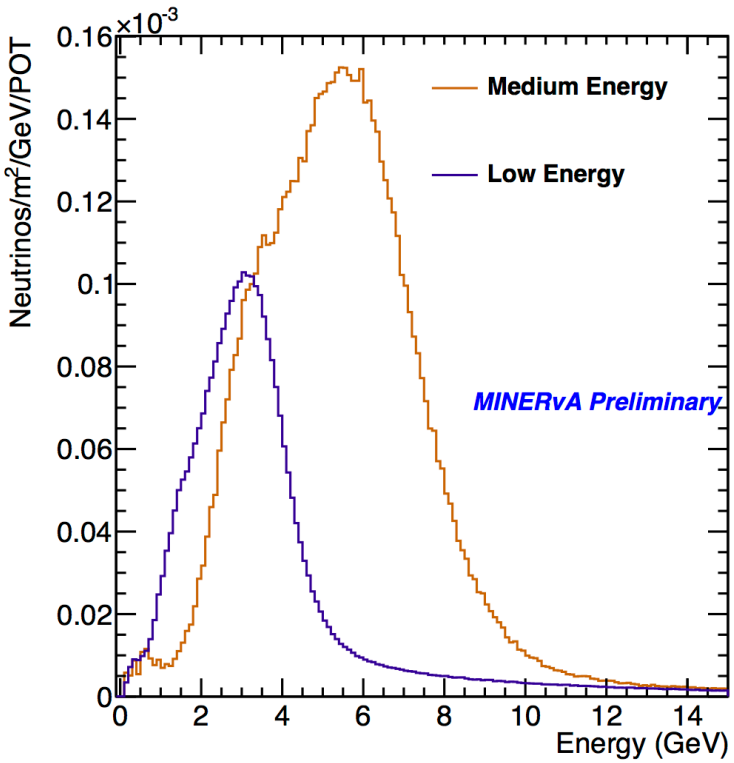

Figure 3-4: The true energy distribution of neutrino interactions in the MINERvA detector from the simulation of two beam configurations: LE and ME. This dissertation uses the ME flux denoted as the orange line in the figure. Figure is from [79].

toroidal magnetic field is generated in the volume between the conductors as the current flows in a loop from the outer conductor to the inner conductor. The data used for this analysis is taken in the Forward Horn Current configurations that select positive pions thus enhancing a ν_μ beam while reducing the $\bar{\nu}_\mu$ contribution.

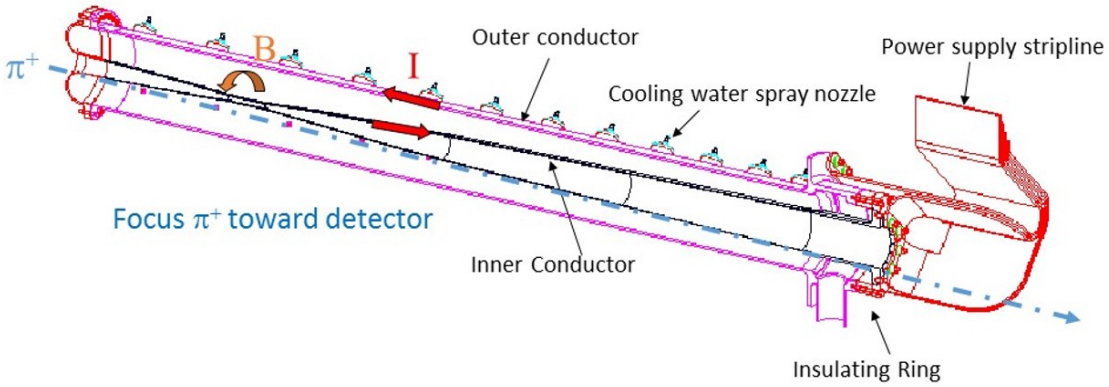

Figure 3-5: The Magnetic Horns. Figure is from [80].

From Ampere's Law,

$$B = \frac{\mu_0 I}{2\pi R}. \tag{3-1}$$

As the current I stays constant along the inner conductor, the magnetic field B generated between the inner and outer conductors should fall as the radii R increases following $1/R$ and goes to zero at radii smaller than the inner conductor. The parabolic-shaped inner conductors of the NuMI horns can act as linear lenses (in the thin-lens approximation) when the target is not too close to the first horn. The parabolic shape also causes the pathlength of particle trajectories along the magnetic field region to vary as the square of the radius at the point where the particle enters the conductor. Thus the horn appears to the incoming positive hadrons as a focusing lens with a focal length proportional to their momentum. Hadrons created in the target parallel to the beam axis pass through the horns unaffected. Hadrons that were well focused by the first horn are generally not affected by the second horn. Horn-2 acts as the "reflector" by refocusing the over-or under-focused mesons by Horn-1. Horn-2 improves the efficiency of the focusing system by 50%.

3.4 Decay Pipe and Beam Absorber

The function of the decay pipe is to provide a vacuum and low-density environment for the mesons to propagate and decay after being focused by the horns. The mesons decay into tertiary mesons, charged leptons, and neutrinos, thus producing the neutrino beam. Mass along the trajectory causes some fraction of the mesons to interact, reducing the neutrino flux. It also introduces Coulomb scattering that somewhat alters the mesons' paths.

The length of the decay pipe is chosen to be 675 m because the decay length for a 10 GeV pion, the mean energy of pions producing the ME beam, is about 700 m. The diameter of the NuMI decay pipe is chosen to be 2 m to accommodate more meson trajectories and produce more neutrinos due to the higher divergence of low-energy mesons. The decay pipe starts 46 m downstream of the NuMI target. A thin two component steel-aluminum window closes the upstream end of the decay pipe. The upstream window is thin to minimize meson interactions, while thick enough to provide sufficient strength to avoid any possibility of rupture.

The NuMI absorber is a massive aluminum, steel, and concrete structure downstream of the decay pipe whose function is to stop most of the particles still remaining in the beam. The muons remaining in the NuMI beam after the decay pipe and absorber are ranged out in the so-called muon shield. This shield consists of 240 m of solid dolomite rock between the absorber and the detector hall.

CHAPTER 4
MINERVA DETECTOR

4.1 Introduction to MINERvA

MINERvA is a dedicated high statistics neutrino scattering experiment that operates in the NuMI beamline at Fermilab. As mentioned in Chapter 1, the primary goal of MINERvA is to produce measurements of inclusive and exclusive neutrino interactions relevant to the current and future oscillation experiments, and also to study nuclear effects via measurements on different nuclei in the same beam.

The MINERvA detector employs fine-grained extruded polystyrene scintillator for tracking and calorimetry. The detector is comprised of 120 hexagonal modules stacked along the beam direction. The 5 m long hexagonal main core of the detector consists of inner and outer regions. The inner detector (ID) is arranged into four subdetectors in longitudinal direction: the nuclear targets region, the fully active tracking region, downstream electromagnetic calorimeter (ECAL), and downstream hadronic calorimeter (HCAL). The outer detector (OD) is a frame structure of hadronic calorimeter which borders and physically supports the ID. The MINOS near detector located downstream of MINERvA serves as a toroidal muon spectrometer.

Figure 4-1 shows the schematic of the MINERvA detector as viewed from along the beamline axis. The components of MINERvA detector and the calibration process in MINERvA are summarized below, and explained in detail in [81].

4.2 A Note on the MINERvA Coordinate System

The MINERvA coordinate system is defined as follows: the origin is at the center of the ID. The z-axis points in the longitudinal direction along the central axis of the detector. The y-axis points gravitationally upward, and the x-axis is orthogonal to the other two axes. The z-axis is defined to place the front face of MINOS at $z = 1200$ cm. In this system the beam central axis is in the y-z plane and points slightly downward at 3.34°.

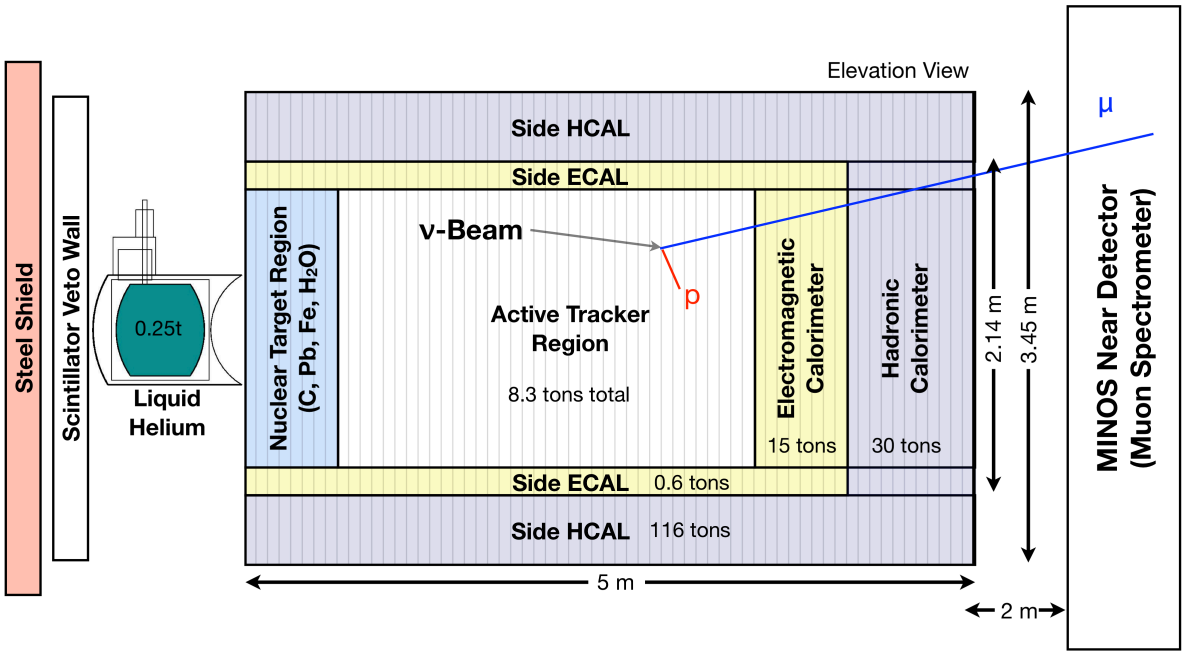

Figure 4-1: Schematic of the MINERA detector, with all sub-detectors and their masses labeled. Figure is from [81].

4.3 Tracking Modules

The core components of the MINERvA detector are 2.2 meter wide hexagonal planes composed of 127 triangular shaped bars of extruded scintillator (CH) with 33 ± 0.5 mm base and 17 ± 0.5 mm height that are glued together with 3M-DP190 translucent epoxy. The planes are covered by Lexan sheets and attached with 3M-DP190 gray epoxy to ensure that they are light tight and robust. The density and elemental composition by mass percentage for the various materials in the scintillator planes are listed in Table 4-1.

The triangular base of the scintillator bars allows charge-sharing between neighboring strips in a single plane to interpolate the coordinate position, producing 3 mm position resolution for reconstructed tracks. The extruded scintillator strips are made from polystyrene pellets (Dow Styron 663 W) doped with 1% (by weight) 2,5-diphenyloxazole (PPO) and 0.03% (by weight) 1,4-bis(5-phenyloxazol-2-yl) benzene (POPOP). PPO and POPOP are used for their spectroscopic properties as well as for their processing abilities. The strips are covered by a co-extruded white reflective coating based on 15% TiO_2 (by weight) in polystyrene. Both ends of the scintillator strips are painted with white EJ-510 TiO_2 Eljen paint. Two scintillator planes are placed in a hexagonal steel frame to form a tracking module. The inner tracking region consists of 60 tracking modules. The composition of scintillator strips and constructed planes is given in Table 4-2.

To map a charged particle's 3-D path through the detector, the scintillator planes are arranged along different orientations to the MINERvA x-y plane called "views". The hexagonal design of the plane makes a 60 degrees offset the natural axis rotation between each plane, providing three distinct views labeled X, U, and V. In the X view, the scintillator planes are arranged vertically to provide position information for the positive and negative x-directions. The U and V planes are rotated ±60 degrees relative to the X view. Each module has one X plane, and either a U or V plane. Along the z-direction, the scintillator planes are arranged in UXVX sequences to provide a stereo 3D reconstruction of multi-track events.

The scintillator planes cannot fully contain products from neutrino interactions ("events"), due to their low density. Therefore, the ID module is surrounded by a 1 mm thick lead collar that starts at roughly 90 cm from the module center and extends to the outer edge and the sides of the detector. This region is called the OD. At the energy in which MINERvA is operating, many of the neutrino interactions contain backward- and sideway-going particles. The lead collar can provide event containment for particles leaving the neutrino vertex in the fiducial region and act as a component of the EM calorimeter to slow down or stop particles. The frame itself is 56 cm wide and is instrumented with four bars of scintillator of varying lengths to span each wedge in the frame. The OD frames are 3.49 cm thick in the tracker region.

The OD scintillator bars have two different rectangular cross-sections. Approximately 90% of the OD scintillator bars have a base of 19.0 $\pm$ 0.5 mm and a height of 16.6 $\pm$ 0.5 mm. The OD steel is thicker in the hadron calorimetry region, therefore the OD scintillator bars are also thicker to improve hermicity. The ID is composed of 13,312 extruded scintillator bars and the OD is composed of 2,736 scintillator strips, including waste and spares.

Figure 4-2 shows a cross-sectional view of a module. In total, the tracking region of the detector contains 110 modules.

4.4 Veto Walls

The veto wall subsystem is located upstream of the MINERvA detector. It is comprised of alternating layers of passive steel plates interspersed with two walls of six scintillator counter panels that are arranged vertically. Each of the twelve scintillator counters are read out by two single anode PMTs. The primary purpose of the veto wall is to identify muons entering the front face of the detector. These muons are relics from muon-neutrino interactions in the rock surrounding the detector and therefore named "rock muons". Rock muon identification is extremely important for any analysis of the helium target data, located between the veto wall and the main detector. Charged current analysis

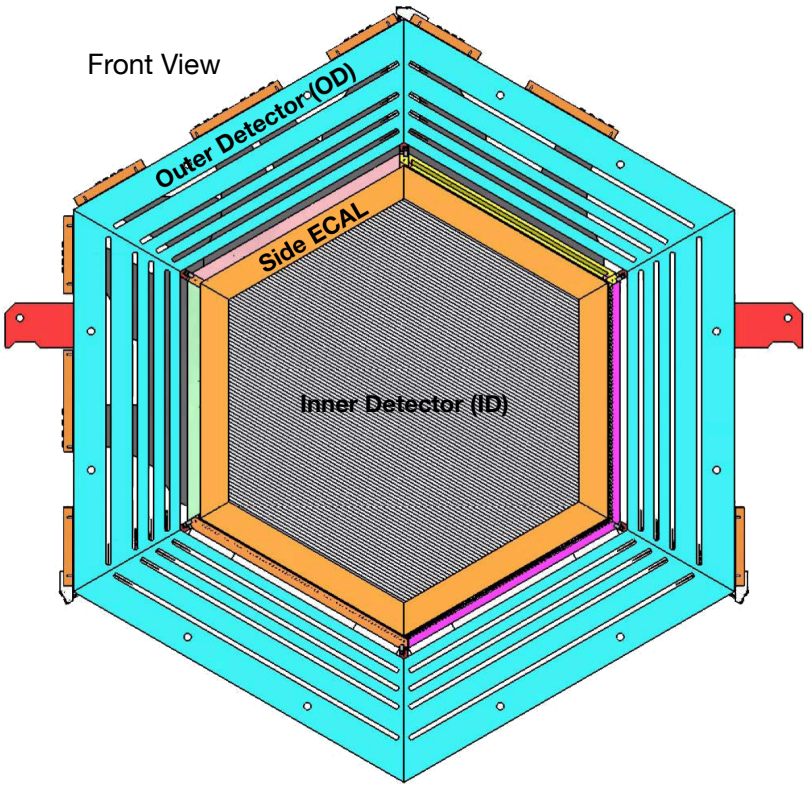

Figure 4-2: A cross-sectional schematic of a MINERvA module. The ID strips, lead collar, OD frame, and the supports for the scintillator inside the module are visible in the picture. Figure is taken from [81].

Table 4-1: The densities and composition of the various components in the detector. Table is reprinted from [81].

Material	Density (g/cm^3)	H	C	N	O	Al	Si	Cl	Ti
Scintillator	1.043 ± 0.002	7.6%	92.2%	0.06%	0.07%	-	-	-	-
Coating	1.52	6.5%	78.5%	-	6.0%	-	-	-	9.0%
Lexan	1.2	6.7%	66.7%	-	26.7%	-	-	-	-
PVC tape	1.2	4.8%	38.7%	-	-	-	-	56.5%	-
DP190 transl.	1.32	10.0%	69.0%	2.6%	17.0%	-	-	0.5%	-
DP190 gray	1.70	5.0%	47.0%	1.7%	27.0%	6.0%	6.0%	0.05%	-

Table 4-2: The composition of the constructed planes and scintillator strips given in mass percentage. Table is taken from [81].

Component	H	C	O	Al	Si	Cl	Ti
Strip	7.59%	91.9%	0.51%	-	-	-	0.77%
Plane	7.42%	87.6%	3.18%	0.26%	0.27%	0.55%	0.69%

from the most upstream nuclear target can also benefit from veto wall data. The analysis performed in this dissertation does not include the data from veto walls because the event topology of DIS events include a large hadronic shower event and not easily confused with rock muon events.

4.5 Nuclear Target Region

The nuclear target region is located in the upstream part of the detector. It contains five layers of passive targets comprised of various configurations of solid carbon, iron, and lead; this allows MINERvA to study neutrino interactions in different nuclei using the same beam. The passive targets are separated by either two or four tracking modules. This ensures good vertex position resolution for events originating in the nuclear targets as well as to measure the final state multiplicities. The identical tracking layers allows a direct comparison of interaction rates as well as hadron production and re-scattering between these targets.

For ease of detector construction and event containment, each solid nuclear target is seated in the same instrumented hexagonal steel frame as the scintillator planes. The targets are built by combining slabs of pure carbon (C), iron (Fe), and lead (Pb) that occupy different transverse areas to allow studies of acceptance differences for various regions of the detector. Target 4 is pure lead and serves as component of the electromagnetic calorimeter by slowing down or stopping final state particles. Targets 1, 2, and 5 have slabs of iron and lead that are carefully arranged to minimize systematic uncertainties due to the development of a hadronic shower. The iron slab is larger than the lead slab, with the dividing line 20.5 cm from the center. Target 3 is composed of carbon, iron, and lead. Since carbon is the lightest nuclei of the three solid targets, target 3 is

designed to be the thickest target to increase the neutrino interaction rate. The thickness of target 3 is approximately twice the thickness of targets 1 and 2. The carbon slab occupies half of the area of the hexagon module, while the iron occupies one-third, and the lead occupies one-sixth. The five targets are configured such that the thicker targets are most upstream and the thinnest targets are downstream. The thinner targets are included to study specific reactions that contain low momenta final state particles.

The orientation of the planes, as viewed looking downstream, are shown in Figure 4-3. The elemental composition of the targets is given in Table 4-3.

The fiducial area for the passive targets is an 85-cm-apothem hexagon with a 2.5 cm cut on each side of the division between materials. The z-location of the center of each target and the fiducial mass of each material for each target is given in Table 4-4. The estimated uncertainty on the fiducial masses due to density and thickness variations is less than 2%.

In addition to the solid targets, there is also a liquid water target located between targets 3 and 4. The water target comprises kevlar sheets hung from a circular steel frame. Due to design considerations there is no OD frame surrounding the target. The kevlar sheets stretch when the target is filled and the lower part expands more than the upper part, making it difficult to get a precise measurement of the water target volume. The estimation of the water target is done by comparing the measured volume when it was emptied and when it was full. The water target is not included in this dissertation analysis.

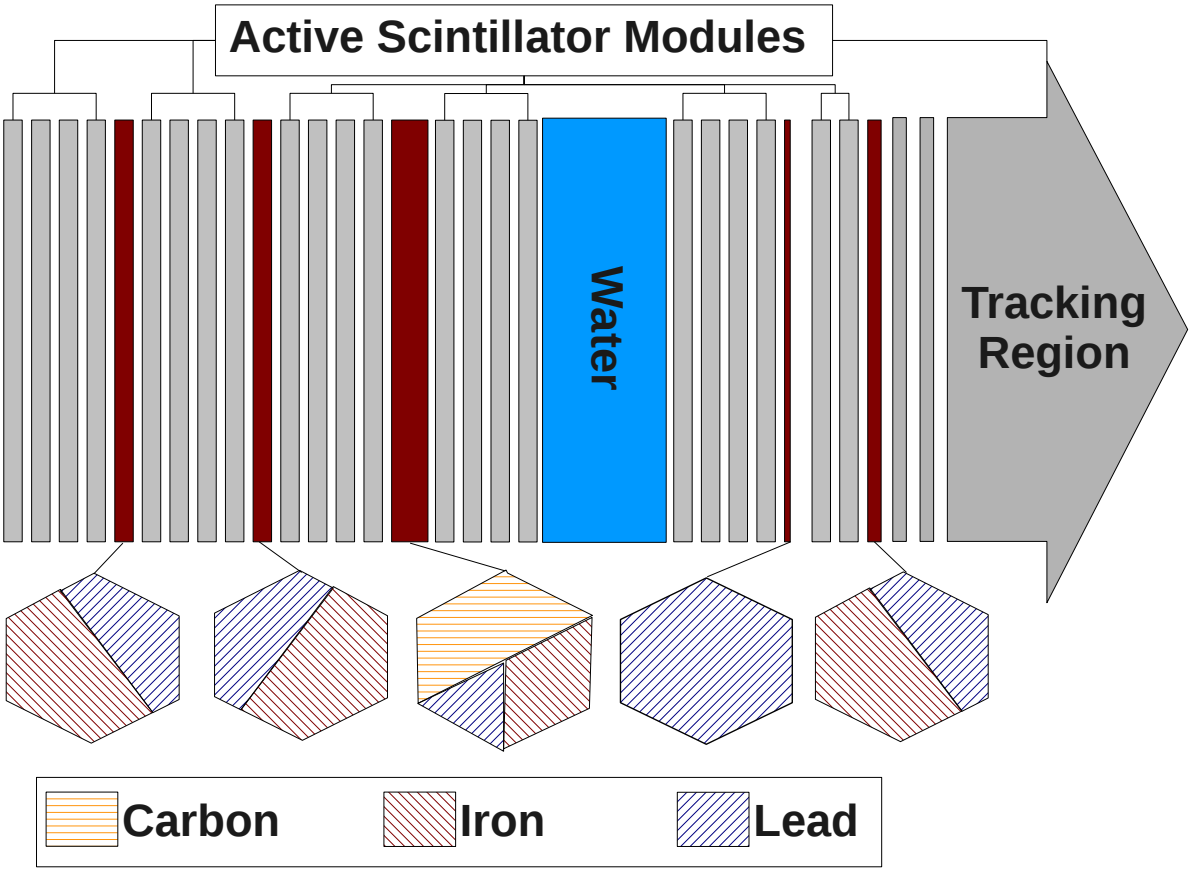

Figure 4-3: Schematic of the nuclear target region as viewed along the beamline axis. The thicker targets are located upstream while the thinner targets are located downstream. Figure is adapted from [81]

Table 4-3: The composition of nuclear target components given as mass percentage. Table is reprinted from [81].

Material	Density (g/cm^3)	C	Si	Mn	Fe	Cu	Pb
Iron	7.83 ± 0.03	0.13%	0.2%	1.0%	98.7%	-	-
Lead	11.29 ± 0.03	-	-	-	-	0.05%	99.95%
Carbon	1.74 ± 0.01	>99.5%	-	-	-	-	-

Table 4-4: Nuclear target locations, thickness and fiducial mass. The total mass refers to the entire plane of target material. Table is from [81]

Target	z-location (cm)	Thickness (cm)	Fiducial Area (cm^2)	Fiducial Mass (kg)	Total Mass (kg)
1-Fe	452.5	2.567 ± 0.006	15999	322	492
1-Pb	452.5	2.578 ± 0.012	9029	263	437
2-Fe	470.2	2.563 ± 0.006	15999	321	492
2-Pb	470.2	2.581 ± 0.016	9029	263	437
3-Fe	492.3	2.573 ± 0.004	7858	158	238
3-Pb	492.3	2.563 ± 0.004	3694	107	170
3-C	492.3	7.620 ± 0.005	12027	160	258
Water	528.4	17-24	25028	452	627
4-Pb	564.5	0.795 ± 0.005	25028	225	340
5-Fe	577.8	1.289 ± 0.006	15999	162	227
5-Pb	577.8	1.317 ± 0.007	9029	134	204

4.6 Electromagnetic and Hadronic Calorimetery

The ECAL is downstream of the tracker region. ECAL modules are similar to tracker modules except that a 0.2 cm thick sheet of lead is attached to each scintillator plane, so that lead covers the entire scintillator plane but does not extend to the OD. A transition module exists between the last tracker module and first ECAL module. This module contains a 0.2 cm thick lead sheet affixed to the front of the more upstream plane and serves as a particle absorber. The ECAL has fine granulity that allows measurement of the photon and electron energy with $\approx 5\%$ resolution as well as a directional measurement for each. There are 10 modules in the ECAL region.

The most downstream detector is the HCAL, which begins immediately following the ECAL. Modules in the HCAL are composed of a 2.54 cm thick steel absorber plane interleaved by a single scintillator plane to allow for detection of protons and pions. The scintillator planes alternate in view, having a repeating pattern of UXVX as in the tracker. In total, there are 20 modules in the HCAL.

4.7 The MINOS Near Detector

The MINOS detector is situated approximately 2 meters downstream of MINERvA in the NuMI beamline. The MINOS near detector is used as a muon spectrometer to allow reconstruction of the momentum and charge of muon tracks exiting MINERvA in the forward direction. The MINOS detector technology and readout are described in detail in [82]. The MINOS coordinate system is defined such that the Z-axis points downstream and is parallel to the coil; the positive Y-axis points upward and is orthogonal to the Z plane; the X-axis is orthogonal to the other two axes. The $x-y$ origin of the MINOS coordinate system is at the intersection point between the coil and the first steel plane. This section will focus on the detector segmentation and geometry and discuss the performance aspects that are relevant to its use in the analysis described in this dissertation.

MINOS, shown in Figure 4-4, is a tracking calorimeter composed of planes of magnetized iron and plastic scintillator with a total mass of 1 kTon. It has a toroidal

magnetic field with average strength of 1.3 T, produced by a current-carrying coil passing through the entire length of the detector. The direction of curvature in the field allows for a determination of the track charge-sign. In normal operational mode the field is set to focus the charge-sign of the primary beam component in the peak energy region.

MINOS is composed of 282 octagonal steel plates, each 2.54 cm thick, spanning a length of 16.6 m. The 120 planes located in the upstream region of the detector, the calorimeter region, are fully intrumented. The calorimeter region provides a precise picture of neutrino interactions occurring in its volume. The downstream 162 planes of the detector (the spectrometer) has full scintillator coverage but only every fifth plane is instrumented. The spectrometer region is used to track the through-going muons generated by interactions upstream and to determine their momentum. The front face of MINOS is located at $z = 1200$ cm in the MINERvA coordinate system.

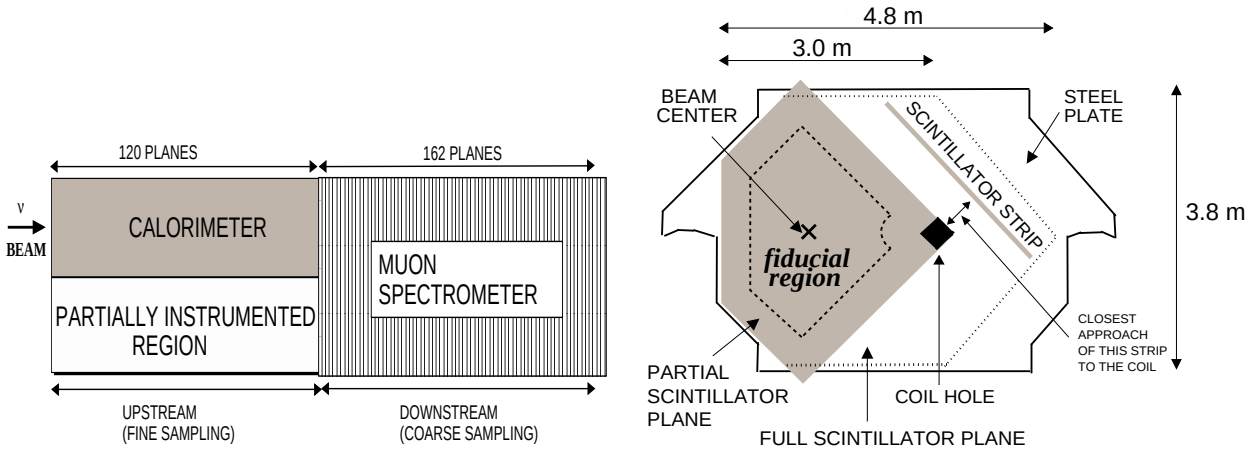

Figure 4-4: Left: the bird's eye view image of the MINOS detector with the calorimeter and muon spectrometer regions. Right: the transverse view of the MINOS detector plane. The partially instrumented active scintillator plane is denoted by the shaded area where the boundary of the fiducial region is indicated by the dotted line. Figure is taken from. [21]

4.8 MINERvA Detector Electronics

Fig 4-5 describes the process of detector readout.

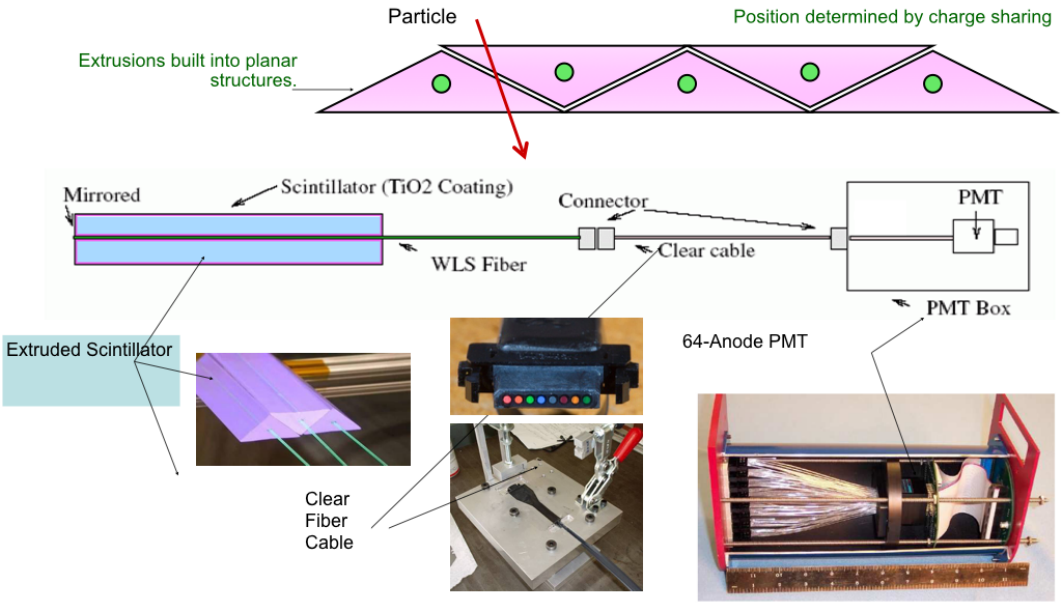

Figure 4-5: Explanation of the MINERvA Detector Readout. Figure is adapted from [83]. Photographs are courtesy of the MINERvA collaboration.

4.8.1 Scintillator and Wavelength-shifting Fibers

As mentioned in section 4.3, MINERvA uses extruded plastic scintillator technology for the ID and OD. Light produced in the scintilator is collected by a green wavelength shifting (WLS) fiber placed in the center of the strips. The plastic in these fibers is doped with fluorescent dyes that absorb the predominantly violet light ($\approx$ 425 nm) from the scintillator and emit green light (450 - 650 nm) light. The green light is partially trapped within the fiber by total internal reflection where much of the short wavelength light (<520 nm) is attenuated while traveling through a full length of a WLS fiber. The longer wavelengths are only weakly attenuated. The fiber is read out at only one end. To maximize light collection, the unread end of each fiber was mirrored using techniques developed at Fermilab.

Ice-polishing is used to prepare the fibers prior to applying the reflective coating. Ice-polishing can give a very good finish to many fibers at once. This technique is described in detail in [84]. The reflective coating is applied in a vacuum system dedicated to optical fiber mirroring. Light output is measured through the unmirrored end of a fiber with ultra-violet light incident on the fiber near the mirrored end. Then, the mirrored end is cut off at 45^o, painted black, and the light yield is remeasured with the UV light at the same place. The mirror reflectivity is measured to be about 80%. Root mean square (RMS) of the mirroring is 5.5%.

4.8.2 Photomultiplier Tubes

The light output of the detector for an energy deposition caused by a minimum ionizing partlcle (MIP) is sufficient to support a low quantum efficiency photosensor. Multi-anode photomultiplier tubes (PMTs), which have moderate gain and good linearity, were chosen to serve as MINERvA's signal readout photosensor. MINERvA uses the R8804MOD-2 photomultiplier tube manufactured by Hamamatsu Photonics [85]. This phototube has an 8 x 8 array of pixels laid out on a 2 cm x 2 cm grid. The fully instrumented MINERvA detector uses 507 PMT's. A steel tube called a PMT box houses

each PMT. A PMT box contains eight connectors that are paired to an eight fiber connector, respectively, allowing for a total of 64 fiber connections. The clear fiber cables that bring light from the scintillator and two light injection fibers used to track the PMT gain are the inputs to this box. Inside the box is a "weave" of 64 fibers that are paired to a plastic component that aligns the fibers on a "cookie". The weave is arranged in a checkerboard pattern in order to mitigate optical cross-talk between adjacent channels.

4.9 Data Acquisition

Neutrino interactions produce charged particles that travel through the detector and leave energy depositions, or hits. Information from the time and position of these hits is used to reconstruct and classify neutrino interactions. Light from the over 32,000 scintillator bars in MINERvA is converted into electrical pulses that carry accurate timing information with an amplitude proportional to the energy deposition.

Each PMT is read out by a Front End Board (FEB) utilizing six ASIC chips, also called the TriP-t chips, that amplify, digitize and convert the signals from the PMTs to a fast timing signal. The standard operating mode is to open a collection gate on the FEBs (readout gate) synchronously with the delivery of neutrino beam spills for 16 μs. Pulse-heights and latched times are recorded for all channels at the end of each 10 μs spill of the NuMI beam and any delayed detector activity, such as such as electrons from muon decays (michel electrons) is recorded in the additional 6 μs.

At the end of the spill, the readout system loops over all of the FEBs and collects data in device frames one at a time for the state of the high-voltage (HV), hit timing, and hit blocks. Each frame is passed through an FEB channel where it is stored briefly before being passed to a readout computer that writes the data into a memory buffer. Subsequently, the data can be archived to file or passed to other applications, for example, for online monitoring.

4.10 Data Processing and Calibration

In order to measure neutrino cross-sections to a high degree of accuracy, it is essential that the detector is carefully calibrated. These calibration measurements ensure that the detector components meet the experimental requirements and accurately convert the electronics output to absolute energy deposition values. The calibration data is also extremely useful for a final tuning of the parameters used in the detector simulation. Minerva calibrations are divided into two type of measurements: in-situ measurement and the ex-situ measurements.

The DIS analysis uses the latest MINERvA software framework called "Inextinguishable" in order to process all forward horn current (FHC) ME data on disk. This data was collected between September 12, 2013 to February 9, 2017. All of the data presented in this dissertation correspond to this sample. During the calibration stage, the available data are divided into several periods based on the detector configuration (for example, if water or helium target is filled) and NuMI beam slip-stacked configuration prior to be quality-checked. This results in 13 ME neutrino data samples known as playlist as listed in Table 4-5. It is important to note that the data samples used in this dissertation do not include playlist minervame1M listed in Table 4-5.

4.10.1 Ex-situ Measurements

The ex situ measurements were conducted before the MINERvA detector was assembled. These measurements provide several of the constants required to reconstruct energy depositions in the MINERvA detector and ensure that the components met the experimental requirements.

4.10.1.1 Front end board response

The purpose of calculating the constants of the front end board response is to convert the output signal of the FEB (ADC) into the equivalent charge for the low, medium, high gain ADC channels. The constants cannot be characterized by a simple

Table 4-5: MINERvA ME neutrino playlists based on detector and NuMI beam slip-stacked configuration. There are 4 slip-stacked configuration: 6+0 refers to no slip stacked batches, 6+2 refers to 2 NuMI slip-stacked batches out of the 6 batches, 6+4 refers to 4 NuMI slip-stacked batches out of the 6 batches, and 6+6 refers to 6 NuMI slip-stacked batches.

Playlist	Data Taken	NuMI Batch Configuration	Detector Configuration
minervame1A	09/12/2013-01/14/2014	6+0	Empty water target; Empty Helium target
minervame1B	01/14/2014-02/06/2014	6+0	Empty water target; Filling Helium target
minervame1C	02/06/2014-04/08/2014	6+0	Empty water target; Filled Helium target
minervame1D	04/08/2014-09/05/2014	6+0	Empty water target; Filled Helium target
minervame1E	10/24/2014-02/06/2015	6+0	Empty water target; Filled Helium target
minervame1F	02/06/2015-06/10/2015	6+2	Empty water target; Filled Helium target
minervame1G	10/23/2015-02/22/2016	6+4	Empty water target; Empty Helium target
minervame1H	02/22/2016-02/22/2016	6+4	Filling water target; Empty Helium target
minervame1L	02/22/2016-03/01/2016	6+4	Filled water target; Empty Helium target
minervame1M	03/01/2016-06/29/2016	6+4	Filled water target; Empty Helium target
minervame1N	11/14/2016-01/19/2017	6+6	Filled water target; Empty Helium target
minervame1O	01/19/2017-01/31/2017	6+6	Filled water target; Filling Helium target
minervame1P	01/31/2017-02/20/2017	6+6	Filled water target; Filled Helium target

linear function of the input charge. In order to characterize the non-linearity, a fit is performed between the high, medium, and low gain response of each channel that consists of three distinct linear segments:

$$PE(c,t) = ADC \times FEB(c) \div \text{gain}(c,t). \tag{4-1}$$

Three sets of six parameters that describe the electronic channel's high, medium, and low gain response are extracted and stored in the offline database to correct the raw ADC response to linearized charge. If the corresponding digitized output drops below the saturation of the electronics (below $\tilde{2}500$ ADC counts), the charge is calculated from the high, medium, or low gain response, respectively.

4.10.1.2 Module mapping

The purpose of module mapping is to provide the final quality check on the module construction and also to map the light response of strips as a function of transverse and longitudinal position. The module mapping is done as follows. Modules are scanned throughout using Cs-137 sources. The strip response is mapped at a number of transverse distances from the strip. Subsequently the strip response at each longitudinal position is also mapped. The pedestal shift is plotted as a function of the transverse position, which is then fitted to a Lorentzian profile in order to find the maximum response amplitude at the center of the fiber position. An attenuation response curve is then determined from the maximum response as a function of longitudinal position along the strip and is used to account for the attenuation when the tracking algorithms determine the position of a hit along a strip.

4.10.2 In-situ Measurements

Calibration of ADC data is necessary to give an estimate of the energy deposited in each of the scintillator strips. Several factors needed to convert ADC counts to an energy deposition are best measured in the assembled detector. Because these factors can vary

over the course of a multi-year run, the time dependence must be accounted for in the reconstruction and the detector simulation.

4.10.2.1 Pedestal monitoring

Regular monitoring of detector noise during beam-absent time periods is necessary to establish the reference point, or pedestal, against which beam signals are compared. During standard beam-on operation pedestal levels are measured for all ∼32k channels during a special mixed beam/pedestal subrun that occurs twice every 40 subruns, about 10.5 hours apart. This subrun collects ∼750 gates from each channel over the course of ∼27 minutes. Each readout gate is open for 16 μs [86] and captures the activity from rock muons, radioactivity, and electronic sources. Background activity in a large sample of pedestal gates was measured to be 18 Hz. The main contributor is the rock muons. Rock muon events produce a single high pedestal gate for the illuminated channels. An example of a single gate well above the normal pedestal distribution for a representative channel is shown in Figure 4-6.

An outlier removal method known as Peirce's Criterion [87] is utilized to identify the high-side pedestal readings that occur from background particle entry into the detector and from spurious electronic readout. These outliers are removed prior to the mean and RMS being calculated for each channel during the subrun. The pedestal mean values are found to vary 7% across all channels, and each channel's pedestal is stable to within 2% during the pedestal subrun. See Table 4-6 for a summary of the pedestal variation for the entire detector during a single pedestal subrun.

No organized drift of pedestal values has been observed over long time scales. The pedestal mean computed from the mixed pedestal/beam subrun is used as the reference point against which all signal levels are calculated for the 10.5 hours until the next pedestal sample is taken. The RMS of pedestal means over time is much smaller than the RMS of the pedestal values within one subrun, justifying the use of the latter as an estimate of the uncertainty on the actual pedestal at the moment a beam signal is recorded.

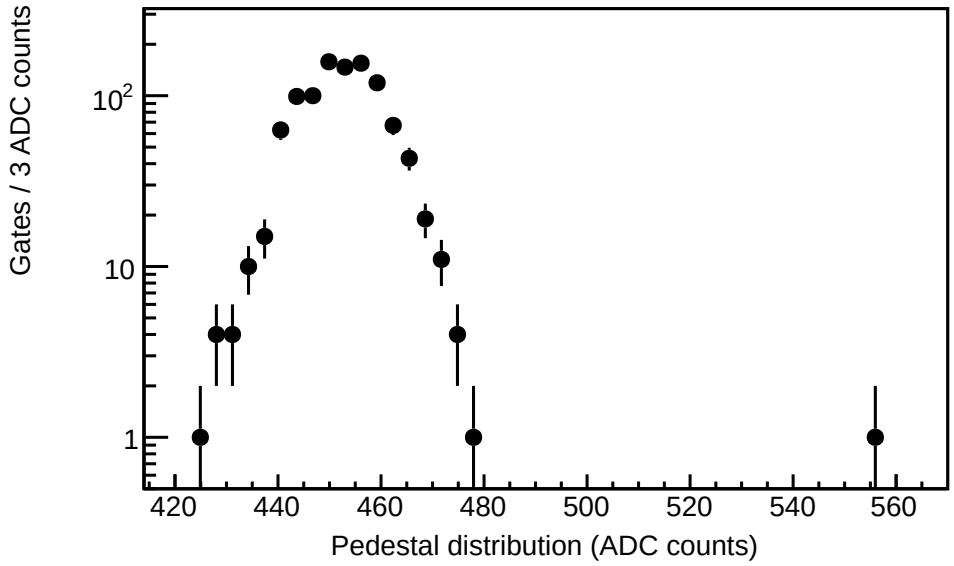

Figure 4-6: Example of a channel demonstrating a single pedestal gate with a measured signal ∼100 ADC above the pedestal level. Gates such as this are removed from the distribution before calculating pedestal statistics. Figure is from [81]

Table 4-6: Pedestal variation across more than 32,000 detector channels for a representative subrun (Run 3721, Subrun 1).

	mean (ADC)	RMS (ADC)	gates
High gain	432±30	7.76±0.41	746±5
Medium gain	436±30	6.65±0.29	745±5
Low gain	440±29	6.36±0.27	746±5

4.10.2.2 PMT gain monitoring

The PMT gains are key to determining the amount of light detected and subsequently, the energy of the incoming neutrino. MINERvA uses in situ calibration data to measure the pixel gains of each PMT. A light injection system is utilized to measure the single photo-electron gain of each of the less than 32000 channels. The light-injection system is based upon pulsed blue light-emitting diodes (LEDs). The light from each LED is fanned out to 50 PMT boxes in a cone/collar assembly. The entire system is controlled

as part of the data acquisition program. Groups of PMTs are pulsed together and all PMTs are read out each time the calibration system is triggered.

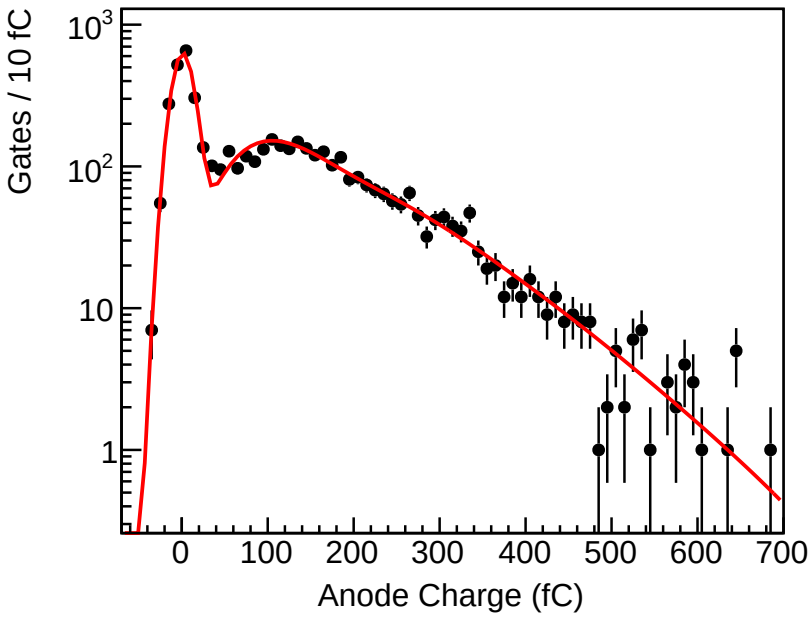

Figure 4-7: An example of fitting a photoelectron distribution. The x-axis is in units of ADC counts. Figure is from [81]

Figure 4-7 shows the results from the data taken in one channel, where the light injection system was set to pulse at a voltage that, on average, delivers about one photoelectron (p.e) per pulse to most PMTs. The highest peak is the pedestal. The second highest peak is the single p.e peak. Subsequent peaks cannot be distinguished from each other since they smear together. The gain is set in the following way:

1. Calculate the gain of all 64 pixels on a tube. Label pixels with a gain less than 8×10^4 as dead.

2. Calculate the average gain of the 8 lowest gain pixels on the tube that are not dead.

3. Calculate the required HV value such that the 8 lowest gain pixels have an average gain of 4.38×10^5.

The resulting gains of 473 of the 507 phototubes after this tuning procedure is done are shown in Figure 4-8.

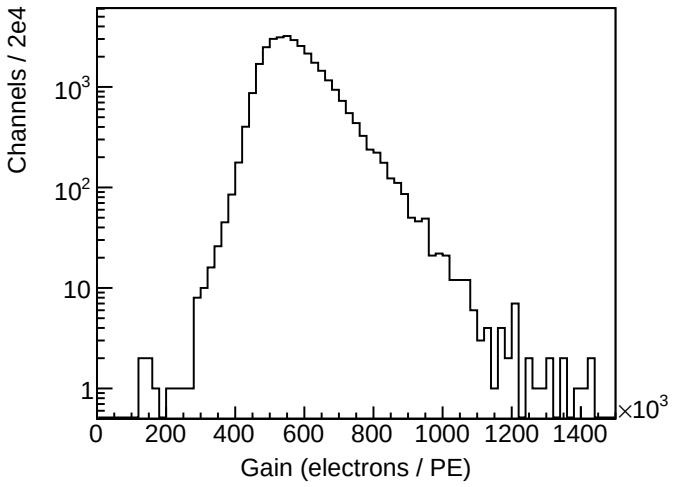

Figure 4-8: A histogram as a funtion of gain for all channels in the MINERvA Detector. Figure is from [81]

4.10.2.3 Relative channel to channel response variations

The light level between ID strips might vary due to several factors, for instance, due to the differences in the composition of batches of scintillator, air bubbles in the epoxy used to fill the fiber hole, or couplings between the optical fibers and photomultiplier tube. A correction is applied to address these variations by applying a multiplicative constant to strip energy deposits to make the response uniform throughout the detector. To derive the constants, the rock muon sample is used to provide a relative energy scale for the muon MIP energy per length. The initial step is to perform alignment of strips to correctly measure the path length corrected charge. One iteration of alignment is adequate to align all the planes [88]. After applying the calibration, the plane-to-plane peak energy is consistent with flat with a p-value of 0.90, shown in Figure 4-9.

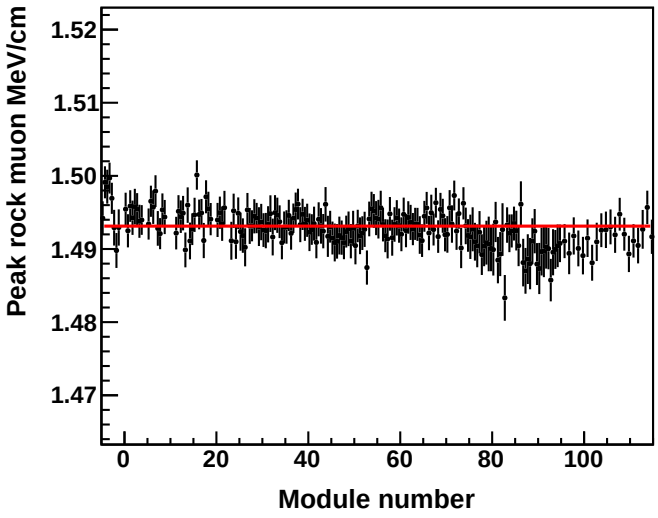

Figure 4-9: The peak energy per unit path length is fitted for each plane. Figure is taken from [81]

4.10.2.4 Muon Equivalent Unit

The Muon Equivalent Unit (MEU) technique is used to determine the absolute energy scale of the detector, using a rock muon sample. The peak number of photoelectron for each PMT is tuned to be the same in the data and simulation to ensure the same statistical fluctuations. Rock muons that are matched to the MINOS near detector are used to measure the energy and photoelectrons deposition in the strip.

4.10.2.5 Timing calibration

A timing calibration is performed to account for transport time in the optical fiber, time slewing, and channel-to-channel time offsets. Time slewing is defined as a function of hit p.e and primarily caused by the scintillator decay times. The FEBs are wired together in sequence, and thus the channel-to-channel time offsets include cable delays between FEBs along a chain and time offsets between the sequences. Time slewing and the channel-to-channel offsets are measured in an iterative procedure using hit time and PE along rock muon tracks. They are measured relative to the truncated mean hit time along

the rock muon track, which is corrected for muon time-of-flight, transport time in the optical fiber, and time-slewing and channel-to-channel offsets. Transport time in the optical fiber is corrected using the fiber length and the speed of light in the fiber. The measured time slewing as a function hit p.e (Figure 4-10) is parameterized by a 3rd order polynomial in $\frac{1}{\sqrt{hitPE}}$, which is used to correct for time slewing in data. One time offset is measured for each group of FEB channels read out by the same high-gain TriP-t chip. This accounts for channels that have low statistics and takes advantage of the small time offsets between channels on the same FEB. The time offset between channels on different FEBs is as large as 30 ns. Since hardware swaps change the channel-to-channel time offsets, the timing calibration is performed after each hardware change.

The calibrated time resolution is determined from calibrated hit times along rock muon tracks. A Gaussian fit to the region above half-height gives a width of 3.0 ns that represents the timing resolution of the detector.

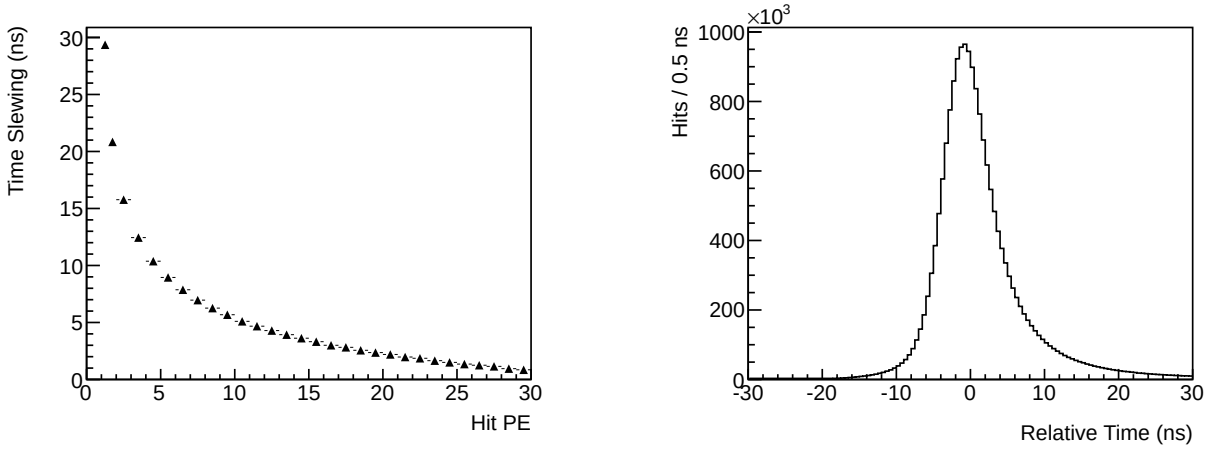

Figure 4-10: Left: Measured time slewing vs. hit p.e along rock muon tracks. Right: Calibrated hit time along rock muon tracks relative to the truncated mean calibrated hit time along the track. Figure is taken from [81]

4.10.2.6 Cross-talk

Cross-talk is a term used to describe several different effects that cause signal migration from one channel into another. Because cross-talk can affect the final event topology reconstructed by the software algorithms, it is important to have a system that identifies and rejects cross-talk activity. In principle, these effects can be differentiated by testing in laboratory prior to installation. However, once the detector components are assembled and installed it is practically impossible to separate the different types of cross talk from one another with any significant confidence, specifically at large pulse-heights.

The dominant types of cross-talk in MINERvA are optical (fiber-to-PMT coupling) and PMT internal (dynode chain). Ideally, the probe to measure either cross-talk in the detector is by illuminating individual pixels with a well-defined light pulse. However, this method is inaccessible once the PMTs are installed on the detector. The LI system discussed in Section 4.10.2.2 cannot be used because it illuminates multiple pixels at once. The next best probe is to utilize data produced by neutrino interactions. For this measurement, the rock muons data sample is used.

The measurement starts by classifying hits that are within a time window (known also as time slice, see Section 6.1) as signal or noise based on whether or not they have been associated to the muon track by the track reconstruction software. This is done to account for the optical cross talk where the careful positioning between the PMT holder and the fiber cookie was compromised. Crosstalk hits are distinguished from other noise by assuming that they must occur in the same PMT as on-track activity, and each cross talk hit is associated with the on-track hit that is nearest to it on the PMT pixel grid. A sketch of how this process would work for a typical muon event is shown in Figure 4-11.

Once hits are identified as either signal or cross-talk, an average cross-talk fraction for the PMT is formed. This is defined as

$$f_{\text{xt}} = \frac{\text{energy of cross-talk hits}}{\text{energy of on-track hits}}. \tag{4-2}$$

Most often various permutations of this metric, such as a "nearest-neighbor" pixel cross-talk average for each PMT (since the strongest cross-talking pixels are generally nearest-neighbors) $f_{\mathrm{xt,NN}}$ are reported.

The measured values of $f_{\mathrm{xt,NN}}$ for the PMTs are shown as the black points in figure 4-12. The red curve in Figure 4-12 depicts the simulation's prediction for the optical cross-talk component only. Although the simulation implements a technique to individually scale the cross-talk for each simulated channel to what was measured from the data, agreement is modest at best. The disagreement is likely to be driven by individual channels in PMTs whose response deviates significantly from the underlying model used in the simulation (based on detailed measurements taken by MINOS [89]). Though the simulation's per-PMT averages do not identically match the data, the individual pulse height spectrum for simulated cross-talk hits agrees much better as shown in Figure 4-13.

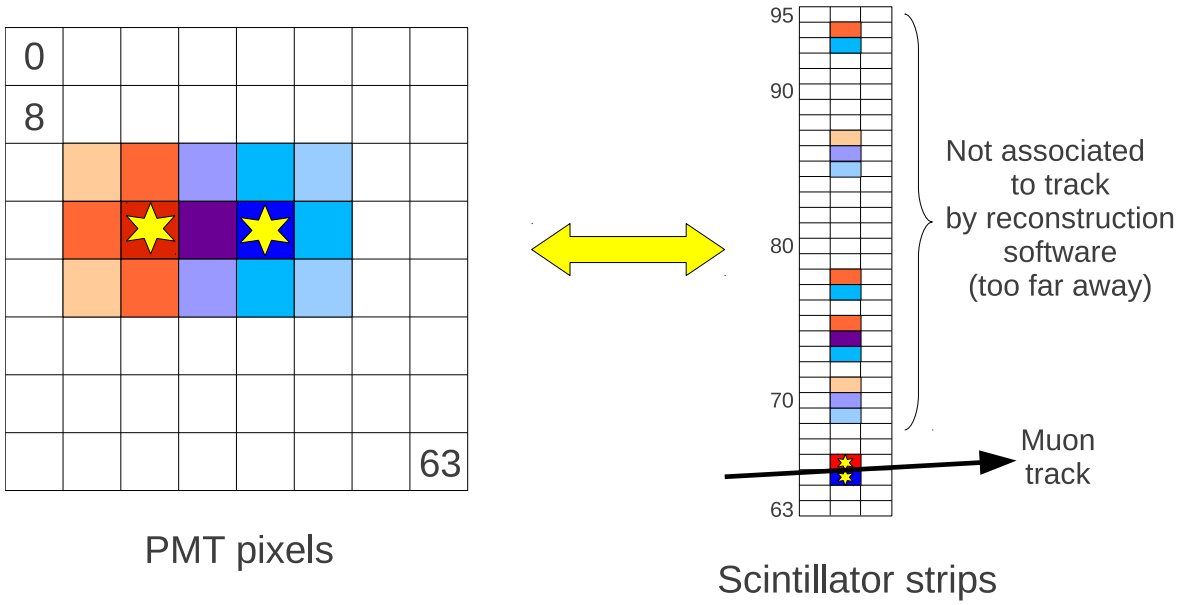

Figure 4-11: Cartoon depicting how cross-talk on the PMT face maps to scintillator strips. The darkest blue and red (stars on the PMT diagram; strips 65 and 66 in the scintillator sketch) are the original signal from a muon track; the cross-talk energy is colored according to which original signal hit it will be associated with by the algorithm described in the text (darker means stronger cross-talk). Purple represents cross-talk that will randomly be associated to either hit due to its ambiguity. Figure is from [81]

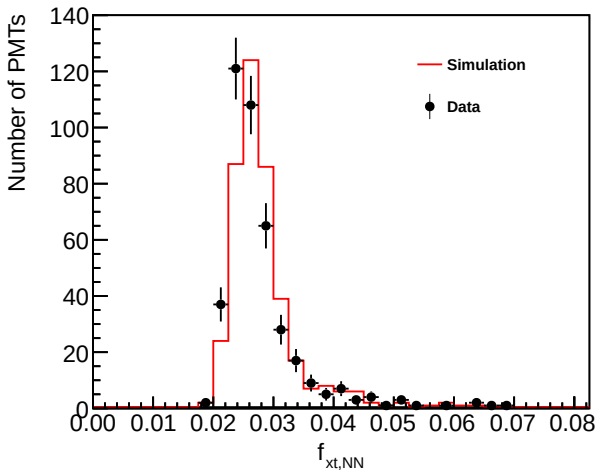

Figure 4-12: Measured $f_{\mathrm{xt,NN}}$ in data (black points) vs. optical cross-talk simulation (red curve). Figure is from [81]

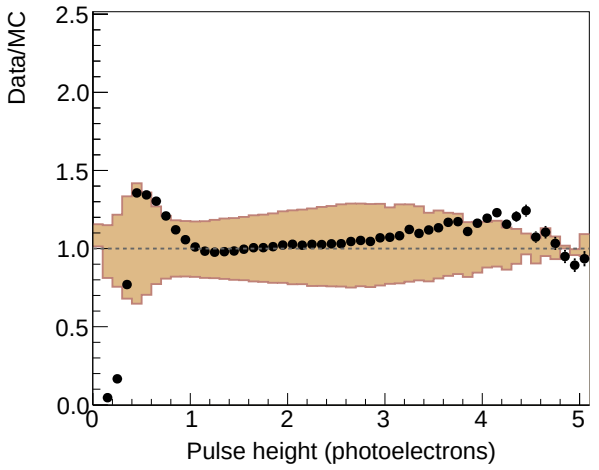

Figure 4-13: Ratio of data to simulation for the photoelectron pulse-height spectrum of measured cross-talk hits. The shaded region corresponds to the systematic uncertainty assigned to cross-talk in neutrino analyses. Within the 1-3.5 photoelectron range (where cross-talk is most important), the divergence between data and simulation is less than 10%. Figure is from [81]

CHAPTER 5
SIMULATION

Accurate simulation of the interactions of particles with matter and modeling of detector geometries are essential in order to analyze and interpret experimental data. In order to identify the produced particles and estimate their energies, the behavior of different types of particles in our detector must be simulated. Simulation software in neutrino experiments is designed to produce, in an ideal scenario, events which are identical to those resulting from the actual experiment. The output data format is typically the same for simulated and real events (data), so that event reconstruction and physics analysis can be performed in the same way and with the same tools on both samples.

Event simulation in MINERvA is referred to as the Monte Carlo (MC) simulation. The simulation contains several stages as illustrated in Figure 5-1. As the energy spectrum of the incoming neutrinos cannot be measured, the simulation process starts with the NuMI beam simulation to determine the incoming neutrino flux, followed by the simulation of neutrino interactions with the nuclei in the detector. The particles exiting the nucleus are then sent to a detector simulation package that propagates the particles through the MINERvA detector. Finally, custom simulation software is used to imitate the readout of the detector and generate time-stamped, calibrated hits similar to what is seen in data. Once this is done, identical reconstruction and analysis software is run on data and simulation.

The DIS analysis uses the MINERvA "Inextinguishable" MC simulation processing. The simulation of the physics processes within the detector is based on the neutrino interaction event generator GENIE (**G**enerates **E**vents for **N**eutrino **I**nteraction **E**xperiments) [90] version 2.8.4. GENIE is a MC event generator that is adept in modeling neutrino flavor interactions over a range of energies from the MeV to several hundred GeV scale. In particular, it focuses on the few-GeV energy range that is relevant to

accelerator-based oscillation experiments. All of the MC presented in this dissertation corresponds to approximately a factor of 2 larger than the data sample.

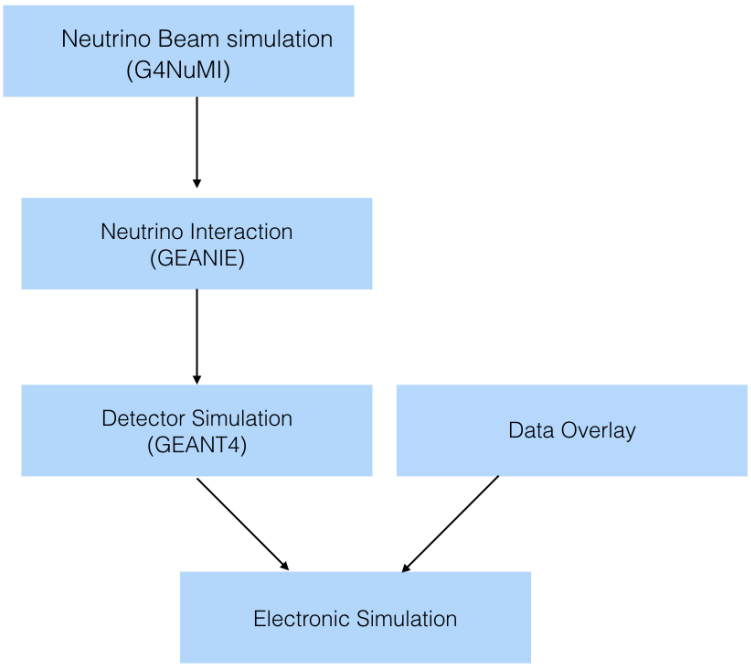

Figure 5-1: A schematic of MINERvA simulation chain.

5.1 NuMI Flux Simulation

The NuMI neutrino beam has been simulated to provide an estimate of the flux of neutrinos incident upon the MINERvA detector. The energy spectrum of the neutrino flux used in this dissertation is shown in figure 3-4. The components that go into producing this flux simulation are summarized below, and explained in detail in [91].

5.1.1 Hadron Production

The NuMI beamline simulation starts with a GEANT4 based [92] beamline simulation to predict the neutrino flux. The G4Numi package is used to build a representation of the NuMI beamline geometry and interface it with the GEANT4 physics tools. A model of the incoming proton beam is used as a source of initial particles. The primary output of this code is a file containing information that represents the decays of secondaries that give rise to neutrinos. We use theoretical and experimental inputs to constrain the flux model. Interactions not constrained by the experimental data are predicted using the FTFP_BERT hadron shower model. It uses the Bertini intranuclear cascade model [93] for hadrons with energies less than 5 GeV. The Fritiof with Precompound (FTFP) model [94] that assumes binary reactions for all hadron-hadron interactions is used for high energy hadrons.

Two experimental measurements are used to constrain the hadron production. One measurement, from NA49 [95], uses a replica of NuMI thin target and with an incident proton energy of 158 GeV. The other measurement, from Main Injector Particle Production (MIPP) [96], uses protons of 120 GeV impinging on a spare target that was eventually used in the NuMI beamline after the MIPP data run [97]. For the thin target prediction NA49's measurement of the invariant cross-section for pion production, $E_\pi \frac{\mathrm{d}^3\sigma}{\mathrm{d}p^3}$, is used to calculate the $\pi^\pm$ yield per absorption interaction [95]:

$$f_{Data} = \frac{1}{\sigma_{\mathrm{abs}}} E_\pi \frac{\mathrm{d}^3\sigma}{\mathrm{d}p^3}, \tag{5-1}$$

where E_π is the energy of the pion. The absorption cross-section σ_{abs} is the sum of the inelastic cross-section measured by NA49, σ_{inel}, and the quasi-elastic cross-section, σ_{qel}, as measured on a series of nuclei from different experiments in [98]. The prediction from the simulation for the same quantity, f_{MC}, is used to generate weights to be applied to the simulated pion production yield:

$$w(x_F, p_T, E) = \frac{f_{Data}(x_F, p_T, E)}{fMC(x_F, p_T, E)} \times s(x_F, p_T, E), \tag{5-2}$$

where $s(x_F, p_T, E)$ is the Feynman scaling [99]. The cross sections and weights are functions of the Feynman variable x_F and the transverse momentum p_T.

FLUKA MC simulation [100] is used to translate NA49 measurements to proton energies of 120 GeV using Feynman scaling [99],

$$s(x_F, p_T, E) = \frac{\sigma_{FLUKA}(x_F, p_T, E)}{\sigma_{FLUKA}(x_F, p_T, 158\ GeV)}. \tag{5-3}$$

As a check of this method, NA49 pion production data at 158 GeV is scaled to NA61 data taken at 31 GeV [101]. The difference between the two was negligible.

The weights are directly applied from the NA49 data for $x_F < 0.5$ and leverage the dataset of Barton [102] for $0.5 < x_F < 0.88$ and $0.3 < p_T < 0.5\,\text{GeV/c}$. The Barton and NA49 datasets differ by 25% where the data sets overlap, while the uncertainties on each are only a few percent.

The flux uncertainty is further corrected by using the ratios of pion and kaon cross sections data published by the MIPP experiment [96]. The MIPP data is used by classifying pions leaving the simulated target as a function of x_F and p_T. Each function is then weighted by the ratio of the yield measured by MIPP and the yield predicted by the simulation. These weights are used to account for pions produced by the original proton and also for reinteractions in the target. The MIPP statistical uncertainties range from

approximately 2-6% in the kinematic bins of interest, and have a roughly 5% systematic uncertainty that we assume is 75% correlated, bin-to-bin.

The K/π production ratio from the NuMI target measured in the region $0.2 < x_F < 0.5$ is also used with the NA49 pion yields to estimate the kaon yields [103]. The data have statistical errors generally in the 5-20% range and systematic uncertainties in the several percentage range, which are added in quadrature.

The Package to Predict the Flux (PPFX) is a package used to implement the hadron production corrections described above. The package provides a correction for hadron production mis-modeling using almost all relevant external data. A file of hadrons and muons that decay to neutrinos for each neutrino event is passed as input and a set of correction values to be used as weights to calculate the right neutrino yield is returned.

PPFX is also used to propagate uncertainties of the NuMI beam line as well as the uncertainty in several components of hadron production. The uncertainty is computed using the many-universe method, where the model uncertainties are evaluated by varying model parameters within a Gaussian width of the uncertainty of the relevant parameter (for further discussion on the multi-universe method see Chapter 13). The contributions of each model uncertainty to the total flux estimate are presented in Figure 5-2 and they are as follows:

- **Meson incident correction**: due to scarcity of applicable data on interactions in which mesons are the projectile. 40% uncertainty is applied in 4 x_F uncorrelated regions: $0. < x_F \leq 0.25$, $0.25 < x_F \leq 0.5$, $0.5 < x_F \leq 0.75$, and $0.75 < x_F \leq 1.0$.
- $\boldsymbol{pC \rightarrow \pi X}$: uncertainty on pion production cross section, as reported by NA49 [95] measurements and scaled with FLUKA [100, 104].
- $\boldsymbol{pC \rightarrow KX}$: uncertainty on kaon production cross section, as reported by NA49 [95] pion production measurements and tuned with MIPP ratios [96].

- **Target attenuation**: uncertainty on the attenuation for the particles that pass through the target (C). The uncertainty arises when the particle interacts and leaves the target.

- $\boldsymbol{nC \rightarrow \pi X}$: uncertainty on neutron induced pion production off of carbon. The neutrino interaction cross section is estimated by extending isoscalar symmetry: $\boldsymbol{\sigma(pd \rightarrow \pi^{+} X d) = \sigma(nd \rightarrow \pi^{-} p X)}$ to carbon.

- $\boldsymbol{pC \rightarrow}$ **nucleon** $\boldsymbol{X}$: uncertainty on nucleon production, as reported by NA49 measurements [105].

- **Absorption**: similar to target attenuation, but for the inner conductors of the magnetic horns (Al), the decay pipe volume (He) and the decay pipe walls (Fe).

- **Nucleon-A**: uncertainty on the nucleon interactions on nuclei that are not carbon and outside the kinematic range of the available experimental data. The uncertainty is estimated by using an $\boldsymbol{A}$ dependent scaling in bins of momentum and angle. This scaling is extracted by comparing the $\boldsymbol{K^0, \Lambda^0, \bar{\Lambda}^0}$ production data using a 300 GeV proton beam [106] to the of $\boldsymbol{pA \rightarrow \pi X}$ and $\boldsymbol{pA \rightarrow KX}$ measurement data collected at 100 GeV on different materials [102].

5.1.2 Beam Focusing

The hadrons produced in the target are propagated through the inner conductors and magnetic fields of the focusing system and through the decay pipe. For this dissertation, the horn current was set up so as to prioritize the focusing of pions that produce a neutrino beam energy peak around 6-6.5 GeV. The horn focusing system is modeled in GEANT4 [92] using the G4Numi package. During the hadron propagation there are a considerable number of parameters that will alter the neutrino energy seen at MINERvA, and those parameters must be carefully measured and then included in the neutrino beam simulation. These parameters are as follows:

1. **Target and horns misalignment**: on the primary proton beam trajectory, target, and horns as described in [75].

2. **Target and horns position.**

3. **Shape of the inner conductor**: the precise shape of the inner conductor and the current itself is only known to 1%.

4. **Baffle scraping**: small non-gaussian tails on even a perfectly steered beam that will hit (scrape) the baffle and produce pions. These pions can get focused in the two-horn system. The uncertainty in the tails contribute to the uncertainty on the flux that comes from the baffle and is estimated to be 0.25% uncertain [107].

5. **Water layer**: uncertainty from the residual water layer on the inner conductor that remains from the horn cooling system between proton pulses. The water layer has thickness of 1.0 ± 0.5 mm and can deflect or absorb pions.

Figure 5-2 shows the uncertainty on the neutrino flux at MINERvA as a function of neutrino energy that comes from each of these effects. While most of these effects are less than the hadron production uncertainties they tend to be largest at the falling edge of the focusing peak, so it is precisely at about that energy where the focusing uncertainties dominate the total flux uncertainty.

5.1.3 Neutrino Electron Scattering Constraint

This flux constraint technique is described in detail in [110]. This technique was previously used to constrain the flux uncertainty in the LE data set and the identical constraint method is applied to the ME data set. Neutrino-electron elastic scattering can be precisely predicted in the standard electroweak model because it exclusively involves fundamental lepton scattering without the use of neutrino-nucleus scattering information. In the electroweak standard model and in the limit that $m_e \ll E_\nu \ll \frac{M_W^2}{2m_e}$, the $\nu e \to \nu e$

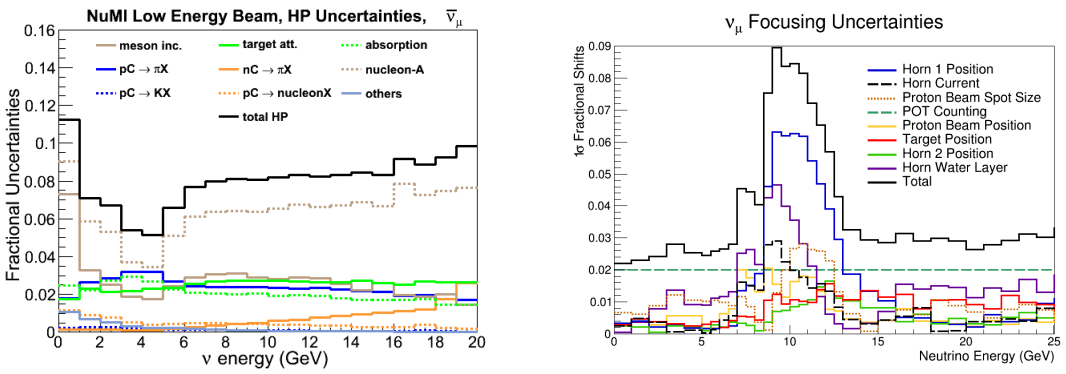

Figure 5-2: Contributions to flux uncertainty from hadron uncertainties (left) and beam focusing uncertainties (right). Figures are from [108] and [109]

cross section for all active neutrinos and antineutrinos is given generically by:

$$\frac{d\sigma(\nu e^- \to \nu e^-)}{dy} = \frac{G_F^2 s}{\pi}\left[C_{LL}^2 + C_{LR}^2(1-y)^2\right], \tag{5-4}$$

where G_F is the Fermi weak coupling constant, s is the Mandelstam invariant representing the square of the center-of-mass frame total energy and $y \equiv T_e/E_\nu$, where T_e is the kinetic energy of the electron. C_{LL} and C_{LR} are constants that depend on the neutrino flavor and determine if the initiating particle is a neutrino or anti-neutrino. For muon and tau neutrinos, $C_{LL} = \frac{1}{2} - \sin^2\theta_W$ and $C_{LR} = \sin^2\theta_W$, where θ_W is the Weinberg angle. For anti-neutrinos the values for C_{LL} and C_{LR} are swapped.

A sample of 800 background-subtracted and efficiency-corrected neutrino-electron elastic scattering candidates are isolated in the scintillator tracker of the MINERvA detector. Since the total number of background-subtracted and efficiency-corrected neutrino-electron scattering events is simply the product of the neutrino-electron scattering cross section, detector mass, and flux, the total uncertainty on the number of signal events collected can be thought of as one measurement of an energy-weighted flux integral. This sample is used to improve the uncertainty on the predicted NuMI flux to $\approx 6\%$. This

constraint is applicable to any neutrino experiment utilizing the NuMI neutrino beam, and may be extended to experiments with multi-GeV accelerator-based neutrino beams.

Although some of the neutrino's initial energy is lost to the final state neutrino in neutrino-electron scattering, the final state electron's energy spectrum can constrain both the overall normalization and shape of the neutrino flux. This can be done by using Bayes theorem to relate the probability of a particular flux model (M) given an observed electron spectrum ($N_{\nu e \to \nu e}$) to the *a priori* model and the probability of the data given the model:

$$P(M|N_{\nu e \to \nu e}) \propto P(M)P(N_{\nu e \to \nu e}|M). \tag{5-5}$$

Assuming a Gaussian approximation of the Poisson-distributed data, the probability of the data spectrum given the model is proportional to:

$$P(N_{\nu e \to \nu e})|M) \propto e^{-\chi^2_M}, \tag{5-6}$$

where χ^2_M is the chi-square statistic comparing the observed electron energy distribution to that predicted by model M. The flux is constrained by weighting each universe's distributions by $e^{-\chi^2_M}$.

5.1.4 Low ν Constraint

Neutrino interactions with low nuclear recoil energy (ν) have a nearly constant cross section as a function of incident neutrino energy. Consequently a measurement of low-ν interactions as a function of energy can be used as to extract the shape of the neutrino flux as a function of energy. This technique is described in [111].

The low-ν restricted cross section deviates from constant both due to the finite value of ν_0 (a recoil energy cutoff value, where $\nu_0 \ll E_\nu$) in practical application and due to the small Q^2 dependence (Bjorken scaling violation) of the structure functions [112]. Therefore, the yield of neutrino interactions with $\nu < \nu_0$ as a function of E_ν is a measurement of the neutrino flux shape as function of E_ν. An absolute normalization is

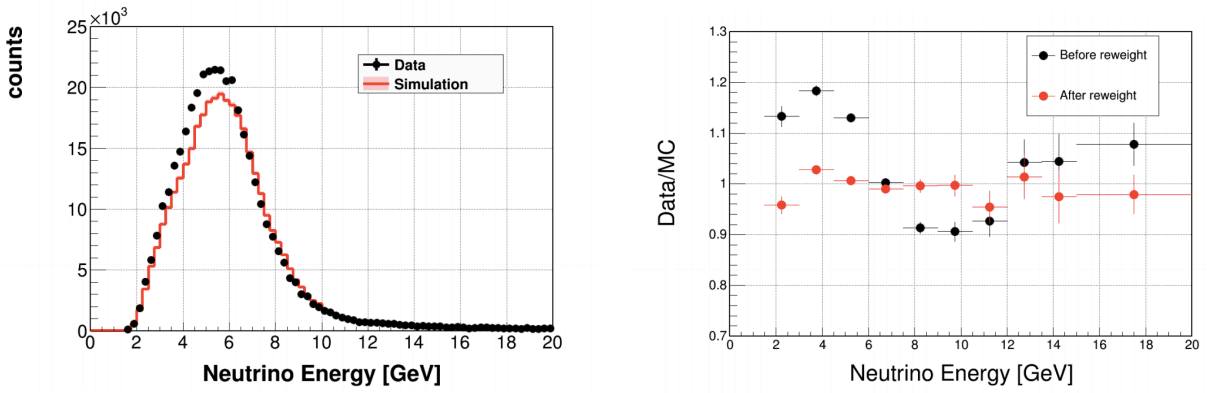

Figure 5-3: Beam focusing fit using a sample of neutrino events with hadronic recoil less than 800 MeV and a number of possible focusing system effects. Left: Neutrino energy distribution. Right: The ratio of data to simulation as a function of neutrino energy before and after the reweighting is applied. Figure is from [113]

determined by scaling the low-ν flux such that the extracted inclusive cross section matches the world average of σ_ν/E at high energy.

5.1.5 Beam Focusing Fit

After constraining the flux using the methods mentioned above, the prediction for the peak of the flux in the ME beam still appears to be shifted by a fraction of a GeV relative to data, as shown in Figure 5-3. This figure shows the event distribution for data and simulation of the low-ν events whose cross-section is nearly independent of the neutrino energy. Thus, the shape discrepancy of this distribution indicates a problem in the flux simulation rather than cross section. However, this discrepancy is not observed in a data set where the horns are turned off, suggesting a focusing mismodeling rather than a hadron production mismodeling. To compensate for this discrepancy MINERvA has developed a fitting technique between the distribution on the left panel of Figure 5-3 and a number of possible focusing system effects: alignment, horn current, and primary beam parameters. The different alignment offsets that will affect the neutrino energy spectra in various transverse regions of MINERvA are also taken into consideration. The data to simulation ratio before and after this fit are shown on the right panel of Figure 5-3.

5.2 GENIE MC Event Generator

GENIE randomly selects neutrino events from an input neutrino flux distribution to simulate neutrinos from MINERvA's energy spectrum. GENIE's physics models simulate the relative probabilities of different interactions along with a simulation of the MINERvA detector to generate a simulated interaction chain for each neutrino. A description of the MINERvA geometry, modeled in GEANT4, tells GENIE what materials make up the detector and where they are positioned.

A description of the MINERvA detector geometry that includes the scintillator planes, the nuclear targets, the helium target, and even the air gaps inside the detector is constructed. The interactions in the calorimeters are not simulated since the backgrounds from events coming from the outer detector or downstream calorimeters are negligible. In addition, simulating events in the calorimeters in proportion to that in the tracker region is computationally expensive since their masses are approximately 18 times heavier.

There are three main parts of GENIE physics modeling of neutrino interactions: the nuclear physics model, the cross section model, and hadron production.

5.2.1 Nuclear Physics Model

The nuclear model used in GENIE is the Relativistic Fermi Gas model. It treats the nucleus as quasi-free independent nucleons with Fermi motion in a uniform binding potential. GENIE uses the version of Bodek and Ritchie [114] which has been modified to include high-momentum tails resulting from short range nucleon-nucleon correlations. In the nuclear medium the initial-state momentum of the nucleon is derived from this distribution.

The most important physics process in this dissertation analysis is DIS. Baryon resonance production also has a significant contribution as the background model to the DIS process. GENIE uses the Bodek and Yang model that accounts for higher twist effects and target mass corrections [115]. For the baryon resonance production, the Rein and Sehgal model that incorporates electroweak interaction by the minimal coupling scheme is

used [116]. A nuclear modification factor is also incorporated to correct for the differences between nuclear and free nucleon structure functions. This modification factor includes shadowing, anti-shadowing, and the EMC effect which are the important nuclear effects in deep inelastic scattering, where $x_{Bj} < 0.8$ [115]. GENIE also provides a record of intranuclear scatterings of induced particles in the neutrino interaction (see Section 5.2.3).

5.2.2 Cross Section Model

There are two cross section models that are relevant in this dissertation analysis:

1. The DIS cross section is calculated using an effective leading order (LO) calculation that incorporates the modifications in the Bodek and Yang model [115] to describe scattering at low Q^2. The model uses a new scaling variable to account for the higher twist and target mass corrections that modifies the low Q^2 parton distributions. The DIS cross sections are computed on the struck parton in the nucleus, where the cross section for $\nu q \to lq'$ for all pertinent sea and valence quarks are taken into account. This model incorporates the Whitlow R ($R = F_L/2xF_1$) parameterization that accounts for the longitudinal structure function [117], in which the default parameters are based on the GRV98 LO parton distributions [118]. The Bodek-Yang model has identical treatment for the modifications of the axial and vector form resulting in imprecise simulation of neutrino data. To correct for this discrepancy for the neutrino cross section at high energy (100 GeV), a scale factor of 1.032 is applied. Since the DIS scale factor is extracted from the comparison of the model and available neutrino data, the value of the scale factor will change when the underlying cross section model is changed.

2. GENIE incorporates the Rein-Sehgal model to describe the production of baryon resonances in charged and neutral current channels. The model uses the Feynman Kislinger Ravndal (FKR) model of baryon resonances, which gives wavefunctions for the resonances as excited states of a 3-quark system in a relativistic harmonic oscillator potential with spin-flavor symmetry [116]. The baryon resonance cross

sections are constructed using the helicity amplitudes calculated from the FKR model and 16 different unambiguous resonance parameters where the interference between neighboring resonances has been ignored [119]. The effect of lepton mass is taken into account despite not included in the calculation. Resonant baryon production includes an axial mass parameter, M_A^{RES}, which GENIE takes to be 1.12 GeV/c^2 based on the global fit performed in [120]. The resonant baryon production cross section is the dominant background for this dissertation.

5.2.3 Neutrino-Induced Hadron Production

The hadronization model (or fragmention model) describes the formation and propagation of neutrino-induced hadronic showers as well as determines the final state particles and the interaction kinematics such as the four-momentum transfer, Q^2, the hadronic invariant mass W, and Bjorken-x. The formation of hadrons in DIS scattering events is described using the Andreopoulos-Gallagher-Kehayias-Yang (AGKY) model originally developed for the MINOS experiment. The model incorporates the Koba-Nielsen-Olesen (KNO) based low-hadronic invariant mass model [121] that is tuned to bubble chamber data for ν interactions on hydrogen and deuterium. At higher invariant mass, a PYTHIA model [122] is used to generate high-energy collisions. The PYTHIA model, based on the Lund string fragmentation framework [123], comprises a library of hard processes and models for initial- and final-state parton showers, multiple parton-parton interactions, beam remnants, string fragmentation and particle decays. The interaction probability can be dramatically reduced due to the different re-interactions that quarks may undergo as they transverse through the nuclear environment. This re-interaction process is taken into account in GENIE before they are passed to the intranuclear rescattering model; it is known as the formation zone. The width of the formation zone is determined by the characteristic formation time of 0.523 fm/c as reported by the SKAT experiment [124]. Similarly, the hadrons produced in the nuclear environment of a heavier nuclear target have to propagate through the nuclear medium and

may re-scatter before exiting the nucleus. This re-scattering process modifies the energy and event topologies resulting in distortion of the observable seen by the detector as well as the reconstructed cross section processes.

5.3 Detector Simulation

The MINERvA detector simulation starts with the GEANT4-based simulation of the particles propagation and energy deposition through the material of the detector. A custom simulation is used to convert the energy deposits to simulated hits that can be analyzed in an identical fashion to MINERvA data.

5.3.1 GEANT4 Simulation

As mentioned in Section 4.1, once neutrino scattering interactions and a set of final-state particles have been generated by GENIE, the next step in the simulation process is to propagate the particles through the material of the detector. The full detector geometry is used for this stage including the outer detector and the downstream calorimeters. In the MINERvA simulation, GEANT propagates (steps) particles 1 mm at a time where a random decision is made to have the particle interact, decay, or continue to propagate and deposit energy in each scintillator strip. This is decided based on the QGSP BERT list, which includes the quark gluon string precompound (QGSP) model [125] and the Bertini cascade model [93, 126] tuned to available hadron-nucleus scattering data. The QGSP portion of the model is used for pion, proton, and neutron interactions with momentum above 10 GeV/c. The Bertini cascade is used for those with momentum below 10 GeV/c. There can be multiple simulated hits in one strip as the step size in GEANT4 is much smaller than the strip size (17 mm).

5.3.2 Readout Simulation

The readout simulation is necessary to make the simulated quantities as close to data as possible. The simulation starts by converting the true energy deposits in active materials from GEANT4 back to the raw ADC counts so that the lower-level quantities such as suppression and discriminator thresholds can be applied as in data. Then

calibration is applied to the raw counts following the same procedure as in the data, to construct reconstructed simulated energy:

- Optical model converts energy deposit to a number of p.e.
- PMT model converts p.e into a charge, applies noise hits, crosstalk and afterpulsing.
- Discriminator model determines the charges that should fire the discriminator.
- ADC model digitizes the charges, and applies the pedestal suppression.

5.3.3 Data Overlay

Pile-up occurs when multiple neutrino interactions overlap in the same time window in the data gate. It is an important effect to be simulated because pile-up can either confuse the reconstruction or cause an event to not be reconstructed. To do this, POT weighted data gates are randomly selected to be overlaid on the simulated events. This is done before the event is reconstructed and before the hits are sorted based on their hit time (this will be described in Section 6.1). In the data overlay stage we also apply time-dependent calibration constants to the simulation. Simulated events that are overlaid with data gate are calibrated following the same procedure as data. This results in two vital time-dependent effects appearing in the simulation: light levels and dead channels. The light level decreases with time due to scintillator degradation. The decrease in light levels reduces the number of observed p.e and increases the statistical fluctuations in the number of p.e. Dead channels found in the overlaid data are hidden, and the GEANT4 simulated energy depositions are ignored.

CHAPTER 6
RECONSTRUCTION

Reconstruction is the process of converting the energy depositions in the the detector into collections of measurements associated to particles created in the neutrino interaction. In order to analyze the patterns in the measurements and identify particle tracks, a general reconstruction algorithm is run on all of MINERvA's data and simulation. The reconstruction algorithm outputs a set of derived measurements corresponding to the properties of the particle.

There are several layers of reconstruction such that the output of one reconstruction algorithm is often used as an input to another reconstruction algorithm. The ultimate purpose of reconstruction is to produce a collection of objects associated to particles that can be used in physics analyses. Reconstruction begins by separating individual event interactions from the larger readout window into groupings known as time slices, forming clusters of hit activity in the detector, performing tracking, and matching tracks into MINOS. These steps are explained below; more detail can be found in [81].

6.1 Time Slicing

Neutrino interactions in MINERvA have time profiles much narrower than the 16 μs width of a gate. Within this narrow time window multiple neutrino interactions can take place in the detector simultaneously in a so-called pile-up event. Pile-up is mitigated by forming time slices, clusters of activity in time formed without considering any spatial information. This slicing serves as the foundation for the following reconstruction stages. Hits within a gate are sorted by calibrated time, which takes into account light propagation to the center of a strip. Time slices are initiated when hits firing the discriminator exceed a charge threshold of 10 photoelectrons in an 25-nanosecond window in time. The window then slides forward until the threshold is no longer met. Hits which do not fire the discriminator are then added if they share a TriP-t with a hit already in the slice. With the

exception of electrons from the decay of stopped muons, activity from a single neutrino interaction is contained in a single time slice.

6.2 Cluster Formation

Charged particles that transverse through the plane typically pass through two strips in a plane. They will deposit energy in a minimum of two strips and form a group of neighboring hits within the same time slice called a cluster. An isolated strip without neighbors that recorded a hit is also labeled as a cluster. The position of the cluster is determined based on its energy deposition in the strips and the position is weighted by the sum of energy of all hits in the cluster. The cluster time is determined by the time of the hit with the highest energy in the cluster.

Based on the hit energy sum and the size and distribution of the hits (see Figure 6-1), clusters can be classified as low activity, trackable, heavy ionizing, superclusters, or cross-talk:

- **Low activity clusters**: clusters with hit energy sum less than 1 MeV.
- **Trackable clusters**: the energy deposit in each hit is between 1-8 MeV and a maximum of 12 MeV in the sum of hits.
- **Heavy ionizing clusters**: hit energy sum greater than 1 MeV and one to three hits have energy greater than 0.5 MeV. The high energy single hits must be adjacent to each other. Heavy ionizing clusters are essential in forming high angle tracks.
- **Superclusters**: hits distribution is broad or double peaked. Typically contains more than 5 hits in a cluster.
- **Cross-talk clusters**: low energy hits within a cluster typically induced by the optical cross talk in PMT (see Section 4.10.2.6).

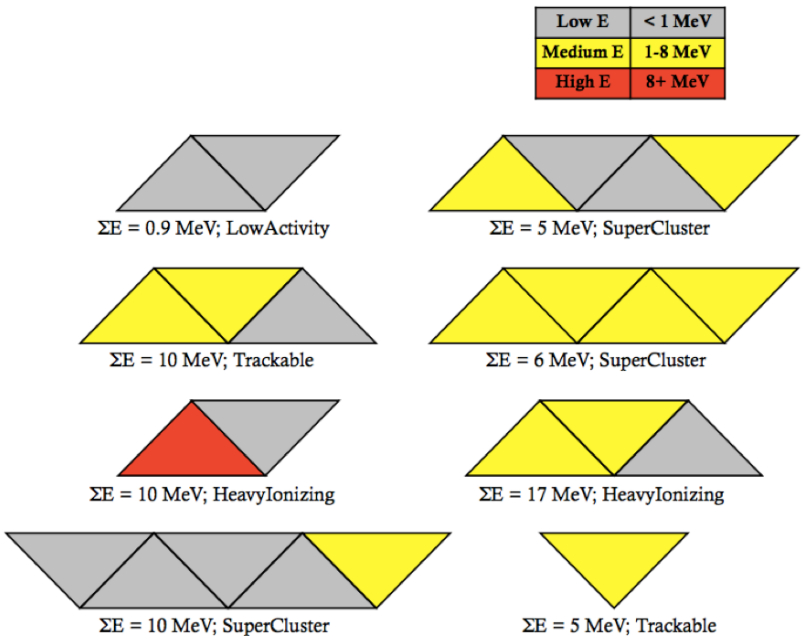

Figure 6-1: A schematic of cluster classification based on the hits topology. Figure is taken from [127].

6.3 Track Reconstruction

Track reconstruction is the process of using the clusters to construct the estimates for the position parameters of the charged particles inducing the hits (tracks). Unless a particle undergoes a large angle scattering or decays into another charged particle, only one track is needed to reconstruct the particle trajectory. A reconstructed track is used to determine the origin, direction, and momentum of a charged particle.

The track pattern recognition scheme starts with the exhaustion of trackable and heavy-ionizing clusters within a time slice to form a collection of objects called seeds. Each seed is comprised of three clusters with the following requirements:

- Clusters must occupy different scintillator planes.
- Clusters must have the same plane orientation (X, U, or V).
- Clusters must occupy consecutive scintillator planes along the longitudinal position of the detector.

- Clusters must be successfully fitted to a two-dimensional straight line.

Based on the requirements above, two-dimensional seeds are formed using at least three hits in each view (X, U, or V) and enforces at least a minimum of 9 planes for 3-view tracks. The merging process moves from the downstream end of the detector towards upstream to avoid possible high amounts of activity near the start point of the track or vertex. Larger two-dimensional track-like objects called track candidates are built from the seeds within the same plane orientation that are in line. The linearity of the seeds is based on doing a least squares fit to a line where a minimum χ^2 value for the fit is enforced. If the track seeds pass this linearity cut, they are then considered in the next step of tracking.

A single track candidate is built from track candidates with similar slope and slope intercepts. A track candidate is required to contain only a single cluster per plane. This results in a number of track candidates composed of clusters from a single detector view.

The two dimensional track candidates from different views are subsequently combined into a three dimensional track. A χ^2 value is extracted from a least squares fit of the three dimensional track to a straight line and it is used as a requirement to select co-linear tracks. The amount of overlap in the longitudinal-direction is also checked and it is also used as a requirement. If the track passes the χ^2 cut and sufficient overlap is found, the track candidates are combined into a track object.

The track is fit using a custom Kalman fitter implementation that takes multiple scattering into account as the track propagates through the detector [128, 129]. The mass of the muon is used to calculate multiple scattering when we are searching for a muon track. The fit is required to converge despite no constraint placed on the fit χ^2. Using the fit, the track is projected upstream and downstream to extend the track with any cluster object. It is also extrapolated to the planes with no clusters within the track projection. If a cluster is found in such a plane, it is added to the track. At this stage the cluster objects are not limited to only trackable and heavily ionizing, but low activity clusters and superclusters are also included. If superclusters are included in the muon track, they are

split into at least two clusters to ensure that each cluster energy is consistent with a minimum-ionizing particle energy deposition along the path of the track.

This method ensures that:

- All the clusters consistent with MIP energy are associated with the muon track and do not go into the recoil energy calculation (described in Section 6.6).
- The muon track is extended upstream to the interaction vertex.
- The muon track is extended to the downstream end of the detector which will help in the MINOS track matching later, as explained in Section 6.4.

6.4 Track Matching with the MINOS Near Detector

Approximately 72% of muons created by neutrino interactions in the MINERvA detector pass into the MINOS detector. MINERvA uses reconstruction information from both the MINERvA and MINOS detectors for these muons to enable complete reconstruction of the muon trajectory and energy. For this reconstruction to be feasible, both detectors must successfully find a track and the tracks must be matched to each other. For tracks in MINERvA and MINOS to be considered for this procedure, the two tracks under consideration must be within 200 ns of each other in time. MINERvA tracks must stop within the last five modules of the detector, and the MINOS vertex must be located within one of the first four planes of MINOS.

The track-matching is done via two separate methods: a track projection method and a closest approach method. The track projection method takes the vertex of the MINOS track and extrapolates it to the plane where the MINERvA track stops. The distance between the extrapolated point and the end point of the MINERvA track, also known as the match residual, is then computed. Similarly, the MINERvA track is also extrapolated to the plane that contains the vertex of the MINOS track and match residual in MINOS is computed. If both match residuals are smaller than 40 cm the MINERvA

track is considered to be MINOS-matched. If more than one possible match is found, the track with the smallest individual match residual is assigned as the MINOS-matched track.

The closest approach method is performed when no match residuals smaller than 40 cm are found using the track projection method. This method extrapolates the MINOS track towards MINERvA, and likewise, extrapolates the MINERvA track towards MINOS, and finds the point of closest approach of the two tracks via an Euclidean distance minimization for the the two points in the x and y plane. If the minimization value does not converge after 1000 steps, then it is decided that the MINERvA track is not matched to MINOS. This method can be useful if the muon undergoes a hard scatter in any of the passive material between the two detectors. The MINERvA tracks that are MINOS-matched are almost exclusively muons.

6.5 Charge Determination and Energy Reconstruction

MINERvA uses the MINOS detector as a spectrometer to reconstruct the energy of muons escaping MINERvA. The MINOS detector can be subdivided into two sections. The calorimeter region is designed to accurately measure the muon momenta and hadronic shower. Due to its coarser granularity, the spectrometer region is only used for tracking high energy muons only. Typically, MINOS-matched muons produced within an energy range between 0.5 to 6 GeV/c at their MINERvA event vertex are contained in the MINOS calorimeter region. Meanwhile, more energetic muons completely pass through the calorimeter and stop in the downstream spectrometer region (Figure 6-2) or exit the MINOS detector (Figure 6-3) [130].

The magnetic coil deflects the charged particles traversing MINOS. Information about the charge and momentum of the particle can be extracted from this deflection. The muon is negatively charged if it is deflected towards the coil, and the muon is positive if it is deflected away from the coil. The details of the charge and momentum measurements procedure in the MINOS detector can be found in [131].

Two methods are used to determine the muon momentum: range and curvature. For muons that are contained inside the calorimeter region, a measurement of their momenta is obtained from a range measurement (P_{range}). The range method calculates the muon momenta using the total energy loss through interactions in the detector. For muons that pass through the calorimeter region, the curvature method (P_{curve}) is used to reconstruct the muon momenta. This method utilizes a track fitting algorithm developed by the MINOS collaboration as follows,

$$K \equiv \frac{1}{R} = \frac{0.3\ B}{P}, \tag{6-1}$$

where K is the curvature of the track, B is the magnetic field, P is the momentum component perpendicular to the field, and R is the radius of curvature [132].

Figures 6-4 and 6-5 illustrate the differecence between the two methods in their ability to reconstruct momentum. The estimated systematic uncertainty on the P_{range} method is 2% based from the errors of the simulation of the MINOS geometry, detector mass and track finding [131]. We add an offset of 16.9235 MeV/c to the value of the P_{range} because MINOS considers the initial interaction vertex at the middle of the steel plane. This is different from MINERvA, where we require the range estimation to start at the front face of MINOS.

MINERvA has developed an approach to calculate the systematic uncertainty of the P_{curv} method that is different from the method used by the MINOS collaboration. This procedure compares the P_{curv} distributions to the P_{range} distributions. For this method only muon tracks that were contained in the fully instrumented part are used, so that information is available from both the P_{range} and P_{curv} methods.

The systematic error of P_{curv} as a function of the momentum is determined by dividing the $1/P_{curv} - 1/P_{range}$ distributions of data and the simulation by the total number of events in six P_{range} bins of 0.5 GeV/c of length, except for the first (< 1 GeV/c)

and last (> 3 GeV/c) bins. The curvature difference, defined as $\Delta K = |\bar{\mu}_{data} - \bar{\mu}_{MC}|$, is obtained using the arithmetic means of the data, $\bar{\mu}_{data}$, and MC, $\bar{\mu}_{MC}$, distributions:

$$\frac{1}{P_{curv}} \rightarrow \frac{1}{P_{curv}} \pm \Delta K = \frac{1 \pm P_{curv}\Delta K}{P_{curv}}. \tag{6-2}$$

Expressing this in terms of error on P_{curv},

$$P_{curv} \rightarrow \frac{P_{curv}}{1 \pm P_{curv}\Delta K} \approx P_{curv}(1 \pm P_{curv}\Delta K) = P_{curv} \pm (P_{curv})^2 \Delta K, \tag{6-3}$$

where the error on P_{curv} is given by $\Delta P = (P_{curv})^2 \Delta K$. Based on a sample of MINERvA charged current inclusive events taken from March to July 2010 and November 2010 to February 2011, the estimated systematic errors for muon momentum are overall less than 3% (See Table 6-1).

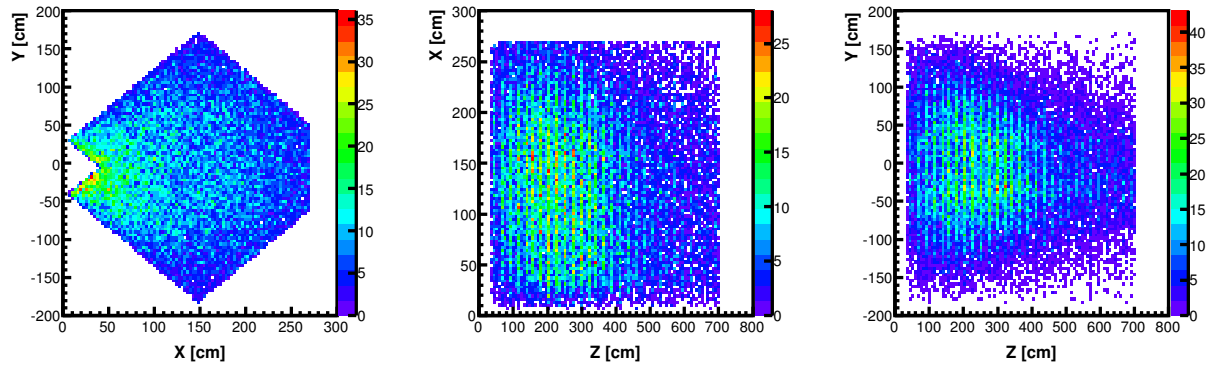

Figure 6-2: Final muon track positions in XY, ZX and ZY planes of μ^- contained inside the MINOS calorimeter region. Figure is reprinted from [81].

Table 6-1: Summary of systematic errors regarding muon momentum reconstruction. Table is reprinted from [81].

Reconstructed $< P_{curv} >$ (GeV/c)	Percentage syst. error on P_{curv} with respect to P_{range}	Percentage syst. error on P_{range}
Less than 1.0	2.5%	2%
More than 1.0	0.6%	2%

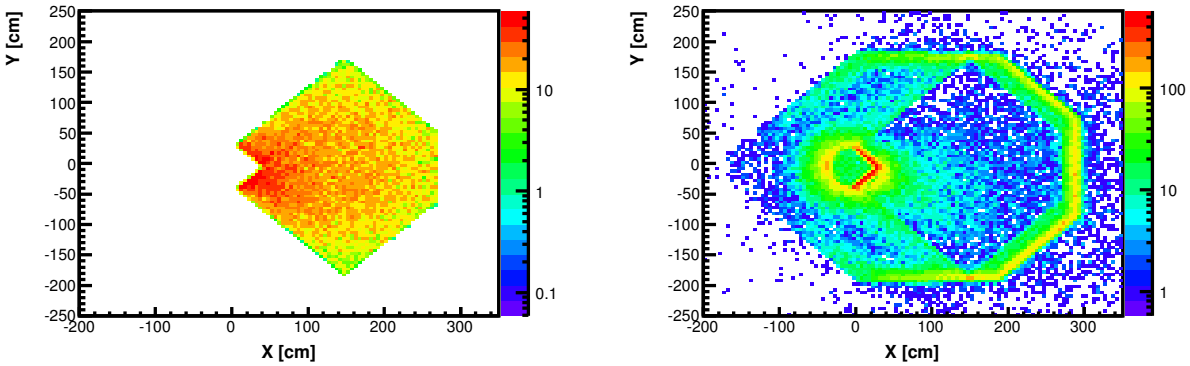

Figure 6-3: Final muon track positions extrapolated to XY plane of MINOS for muons contained inside the calorimeter region of near detector (left) and for muons that escape the calorimeter region (right). The muon events were produced by neutrino CC inclusive interactions in MINERvA from March to July 2010 and November 2010 to February 2011 and they are the same events used in Figure 6-2. Figure is reprinted from [81].

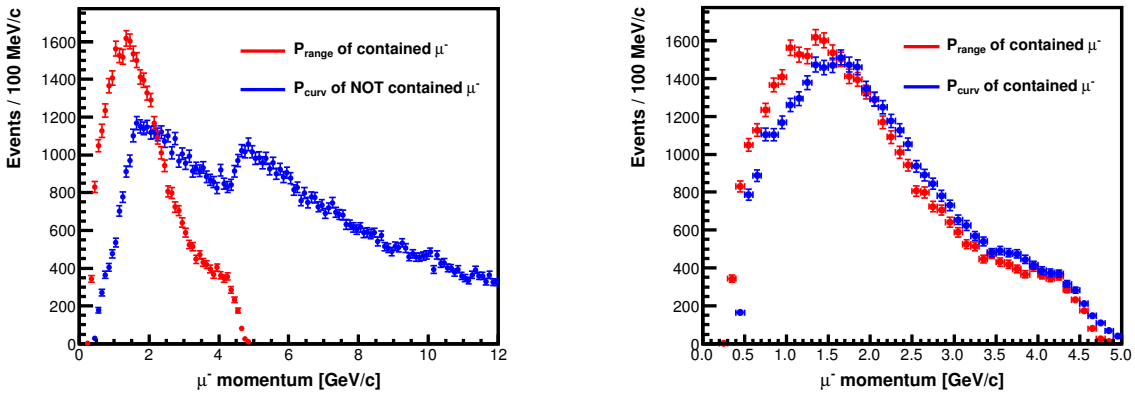

Figure 6-4: Left: P_{range} distribution of contained muons contrasted with P_{curv} distribution of not contained muons. Right: P_{range} and P_{curv} distributions of contained muons. Note the differences in the shape, even though both distributions are based on the same event sample. Figure is taken from [81].

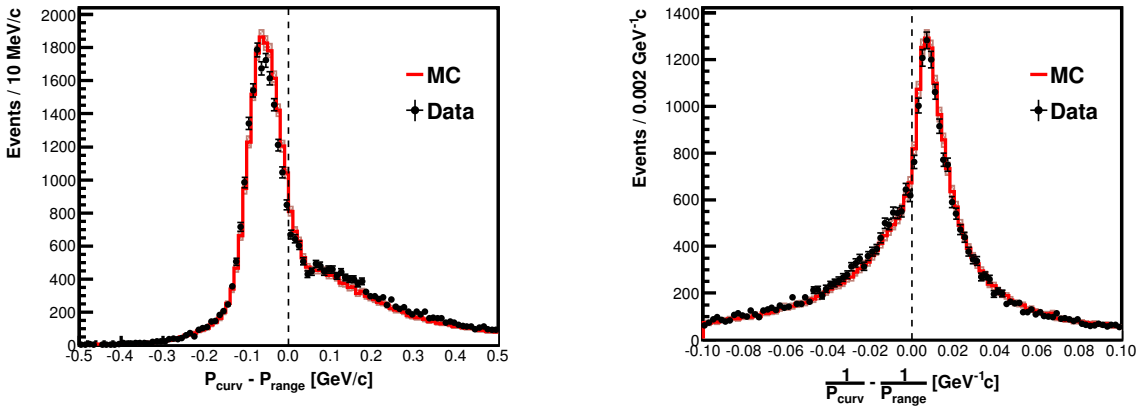

Figure 6-5: Left: Residual $P_{curv} - P_{range}$ distribution of all CC inclusive contained muon events. Right: Residual $1/P_{curv} - 1/P_{range}$ distribution of the same events. Figure is reprinted from [81].

6.6 Recoil Energy Reconstruction

The energy of the recoil system (everything other than the primary lepton) is reconstructed by summing the calorimetrically corrected energy depositions within the detector. For charged-current interactions, clusters within a -25 to 35 ns window around the event time (defined by the muon) and not identified as low activity or cross-talk are included in the sum. This time window is narrower than a typical time slice to remove pile-up from adjacent in-time neutrino interactions and background events. While cross-talk is a real energy deposition in the detector and should ideally be included in the reconstruction of the recoil system, we have chosen to ignore all cross-talk clusters to prevent energy from the muon track being included in the recoil energy sum.

MINERvA currently employs a simple sum in which energy deposits in the ECAL, HCAL, and OD are weighted to account for the additional passive absorber. These weights, or calorimetric constants, are determined by the dE/dx of a minimum ionizing particle at normal incidence in an idealized detector consisting of 17 mm polystyrene scintillator planes with 2 mm lead absorber planes in the ECAL and 25 mm steel absorber planes in the HCAL. The calculation produces a constant of 2.01 for the ECAL and 10.31 for the HCAL, with the tracker constant defined as 1.0. The constant for the OD is

likewise calculated assuming normal incidence into the OD (orthogonal to the beam axis). A material assessment of the MINERvA detector yields improved constants, lowering the ECAL and HCAL constants relative to the tracker, but in practice it is found that the calorimetric energy resolution is minimally affected by these improved constants.

The calorimetric-corrected reconstructed recoil energy is fit to true recoil energy for simulated events to obtain an overall calorimetric scale. True recoil energy is obtained by subtracting the energy of the outgoing lepton from the energy of the neutrino, and ignoring the final state interactions:

$$\text{true}\, E_{\text{recoil}} \equiv E_{\nu} - E_{\text{lepton}}. \tag{6-4}$$

Calorimetric reconstructed recoil energy can be written as:

$$\text{calorimetric}\, E_{\text{recoil}} \equiv \alpha \times \sum_{i} c_i E_i, \tag{6-5}$$

where α is the overall scale, $i = \{\text{tracker}, \text{ECAL}, \text{HCAL}, \text{OD}\}$, c_i is the calorimetric constant for sub-detector i, and E_i is the total energy in sub-detector i from clusters passing the time, low activity and cross-talk selection criteria. α is determined by minimizing the error:

$$\text{error} = \sum \frac{\left[\arctan(\text{calorimetric}/\text{true}) - \pi/4\right]^2}{N}, \tag{6-6}$$

where the summation is over events of true recoil energy between 1.0 and 10.0 GeV and N is the total number of such events. This error definition is less susceptible to the asymmetric tails of the calorimetric/true distribution. The tail is bounded on the left at zero, but trails off on the right due to energetic hits in the calorimeters that are weighted up by the calorimetric constants, and overlapping events. $\Delta E/E_{\text{recoil}} = (\text{calorimetric} - \text{true})/\text{true}$ is plotted in bins of true recoil energy after fitting α.

Simulated events that start in the tracker fiducial volume with MINOS-matched muons have $\alpha = 1.22$ with a calorimetric energy resolution of $\sigma/E = 0.152 \oplus 0.265/\sqrt{E}$

(see Figure 6-6). The calorimetric energy resolution is a sum of various effects: final state interactions, electromagnetic shower, hadronic and neutral components, passive absorber deposition, scintillator, attenuation along scintillator strips, PMT and electronics response, containment in the detector and pile-up events.

The simulation of MINERvA's calorimetric response to single final state particles was validated with a test beam program at the Fermilab Test Beam Facility. The test beam facility is a scaled-down replica of the solid scintillator tracking and sampling calorimeter regions of the MINERvA detector. It comprised of a stack of 40 scintillator planes of $\sim$1 m^2 active area that was exposed to a beam of pions and protons of momentum 400 MeV/c to a few GeV/c. The calorimetric response to protons, pions, and electrons are determined from the test beam data. The proton sample is used to measure the parameter in Birks' law and estimate the tracking efficiency. The details about the test beam program can be found in [133]. Overall, it has verified that the data and the simulation of the detector and particle interactions agree to 4%.

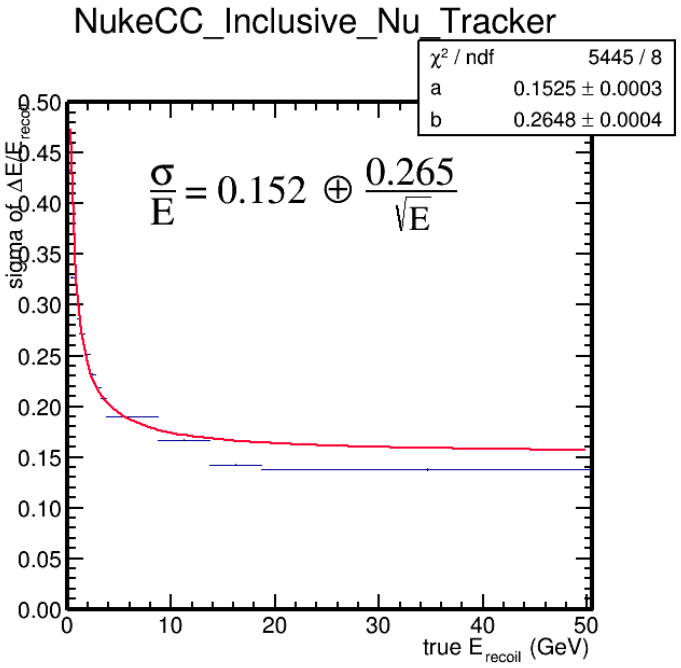

Figure 6-6: Calorimetric energy resolution for charged-current inclusive events in the MINERvA detector.

CHAPTER 7
MACHINE LEARNING VERTEXING

Vertexing is the primary tool used to identify the target nucleus when studying A-dependent nuclear effects. Therefore, it is very important for the nuclear target analysis to precisely determine the neutrino interaction vertex. Traditional vertex reconstruction methods in MINERvA rely only on tracking information. For events with high hadronic energy such as DIS this method can fail when the shower activity occludes the vertex location or when tracks created by secondary interactions or decays bias the vertex location (see Figure 7-1). While in tracker analyses one can misreconstruct the interaction vertex by a few centimeters, for a nuclear target analysis a few centimeters will cause you to mis-identify the material where the neutrino interaction took place. This can have a dramatic impact on the purity and efficiency of the event sample, thus biasing the measured cross section.

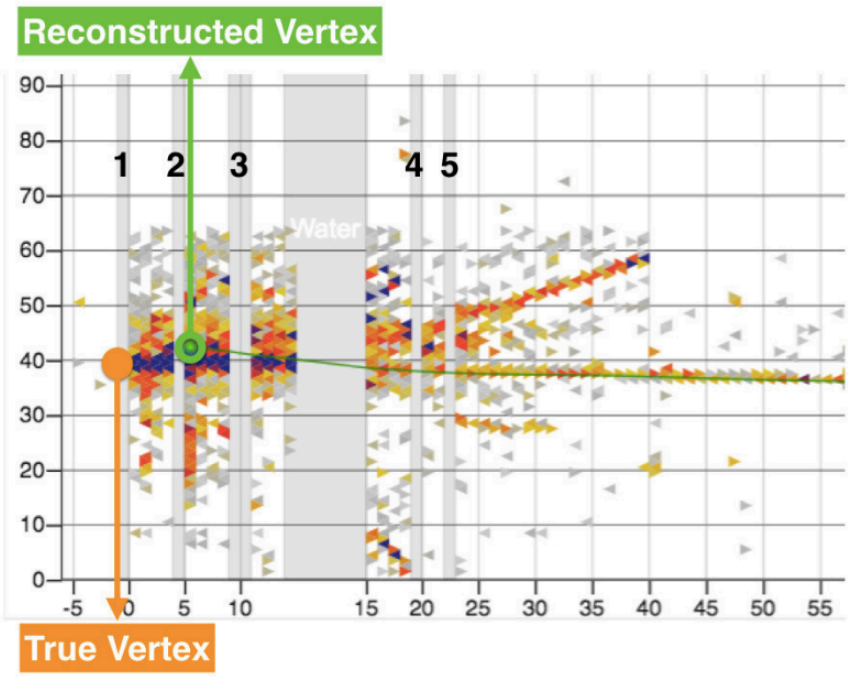

Figure 7-1: An example when an event vertex position is misreconstructed to the wrong target due to the large hadronic shower that confuses the traditional vertex reconstruction algorithm.

The general strategy to manage this type of vertex misreconstruction is by applying a set of event selection criteria, or cuts, to reject these misreconstructed events. With the increased neutrino beam energy in the ME configuration not only is the neutrino flux per POT higher, but the number of POT per beam spill is higher and the neutrino events themselves are more energetic than in the LE configuration. This may lead to more events being rejected from the selection sample, resulting in lower efficiencies across all passive targets.

As events in MINERvA can be represented as images, the vertex finding can be viewed as an image classification problem that is well suited for a machine learning application (See Figure 7-2). As the image space is not linear, regression techniques don't work well and therefore classification is employed to solve this localization problem. In particular, we utilize deep convolutional neural networks (DCNN) to identify neutrino interaction vertices in the MINERvA nuclear target region.

While machine learning techniques utilized in this dissertation analysis are described in this chapter, it is well beyond the scope of this thesis to provide a complete introduction to computational physics. It must be assumed that the reader has some familiarity with the language used to discuss machine learning algorithms and applications. Please see [134, 135, 136] for a more thorough primer on this topic.

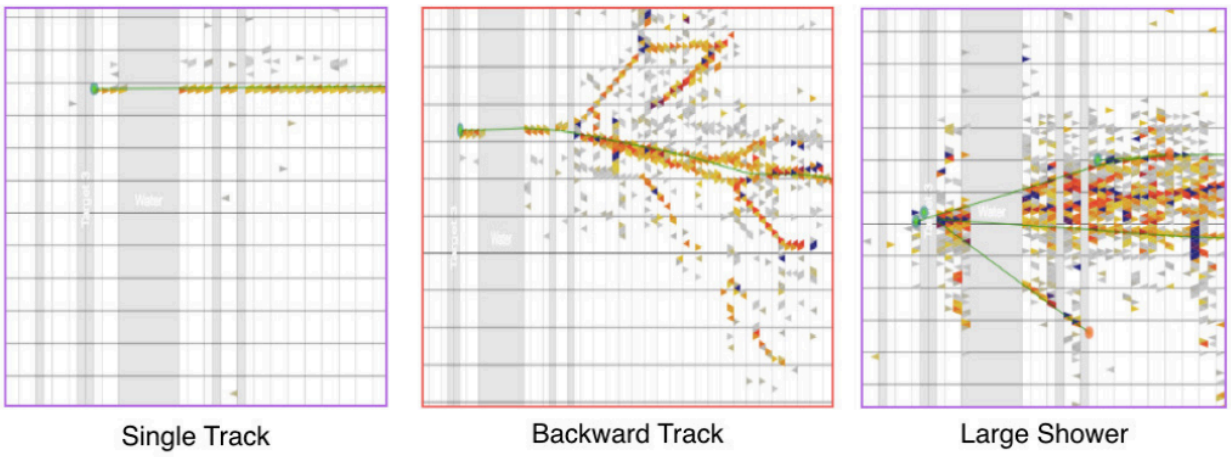

Figure 7-2: Different types of events in MINERvA can be represented as labeled images for training machine learning models.

7.1 Machine Learning

Machine learning is an application that combines statistics and computer science to enable computers to learn how to execute given tasks without being programmed to do so. Analog to how a human's brain improves on performing a task the more experience they have, computers can also do the same. Input data is fed to computers, which learn how to complete a task by looking for statistical patterns in the data and representing information numerically in space.. The most important advantage of machine learning is that it reduces the amount of hand-tuning done by the programmer. Instead, it utilizes the computer to extract the crucial features from the data and establishes the algorithms by which future data will be sorted.

Machine learning is suitable to solve a classification problem. Classification is a supervised learning approach in which the computer program learns from the data input given to it and then uses this learning to correctly classify unseen data [137]. To simplify the task of classifying a large set of data, a method called feature extraction is utilized to reduce the amount of variables necessary to describe a complex set of data [138]. Interesting features are extracted from the data and subsequently used as input to the machine learning algorithm.

The learning algorithms have to be general enough to be able to handle unseen data. If the training model is too simple, it will not adequately capture essential features of the data [139]. Meanwhile, if the model is too complicated, it can model irrelevant information that results in overfitting [140]. When a model overfits, it learns to model the known data but does not understand the underlying patterns that connect them. As a result, the algorithm performs impeccably well during the training but will deteriorate when shown unknown data.

The performance of a model can be evaluated by a summation of errors for each example in training, or validation set. A loss function, for example mean square errors or softmax function, is utilized to assign penalty to the errors [141]. The objective of the

training process is to acquire the best parameter values of the model by minimizing this loss.

After the model parameters are optimized and no learning is taking place, the accuracy of a model can be calculated. Test samples are subsequently fed to the model and the fraction of correct predictions is determined.

A confusion matrix is a summary of prediction results on a classification problem [142]. As the name alludes, a confusion matrix shows the way in which the classification model is confused when it makes predictions. It gives insight not only into the errors being made by the classifier but more importantly the types of errors that are being made. Confusion matrices are used in conjunction with the classification algorithm to overcome limitations of using the classification alone.

7.2 Neural Network

Machine learning can be carried out through the use of a neural network. A neural network is a set of algorithms designed to enable a computer to mimic pattern-based thought processes similar to the human brain. Neural networks are comprised of three layers: input layer, hidden layer(s), and output layer [134].

The input layer typically passes data along without modifying it. Most of the computation happens in the hidden layers. The output layer converts the hidden layer into an output, such as a classification. Each layer has one or more nodes. The node represents a computational unit of the model and the network describes the connections of one node to another.

A node is loosely analogous to a neuron, in the sense that it receives input from many other units and computes its own interest score of a function (concept), or activation value. Each node takes in a set of inputs, combines them with a set of coefficients of weights and bias that either will decrease or increase that input and therefore assign a significance to inputs for the task the algorithm is trying to learn. The weighted input

products are summed, and the result is passed through an activation function to determine the outcome that will affect the classification.

With deep learning, there is less need for hand-tuned machine learning solutions that were used previously. A classical pattern detection system, for example, includes a hand-tuned feature detection phase before a machine learning phase. The deep learning equivalent consists of a single neural network. The lower layers of the neural network learn to recognize the basic features which are then fed forward to higher layers of the network. A hierarchical representation of a data model can be built by chaining together copious numbers of these nodes.

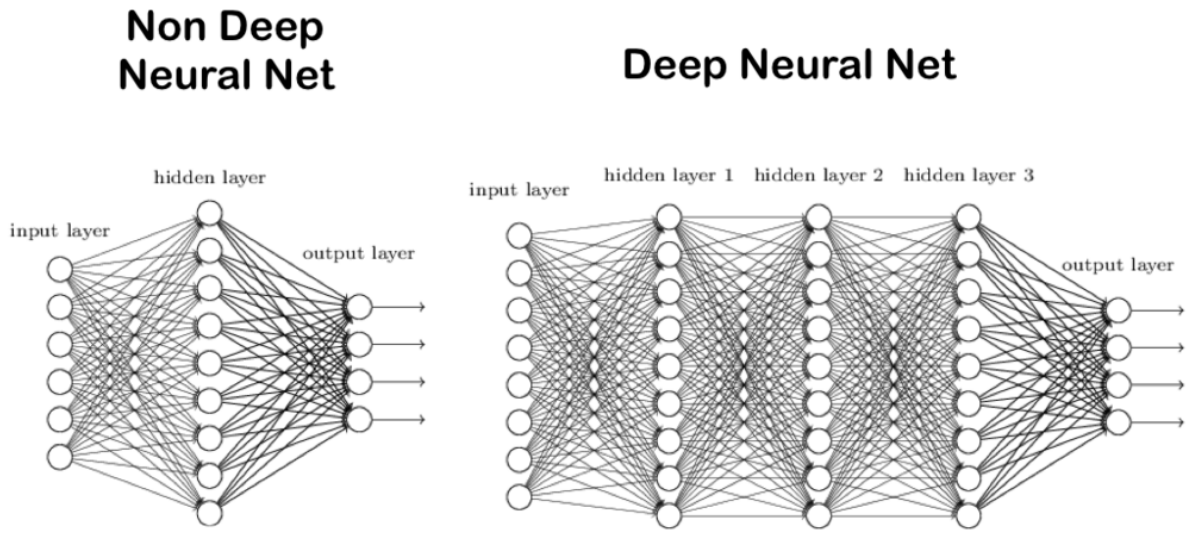

Figure 7-3: Difference between neural network and deep neural network. Illustration adapted from [136].

Neural networks evolve into a deep neural network when the outputs of one network become the inputs of another, creating many hidden layers in the network (see Figure 7-3). The multitude layers enable the hierarchical representation of the data required for "deep learning". Deep Convolutional Neural Networks (DCNN) are a type of deep neural networks where the inputs of each layer are mapped into outputs by convolving a small matrix, or kernel, with the inputs [143, 144].

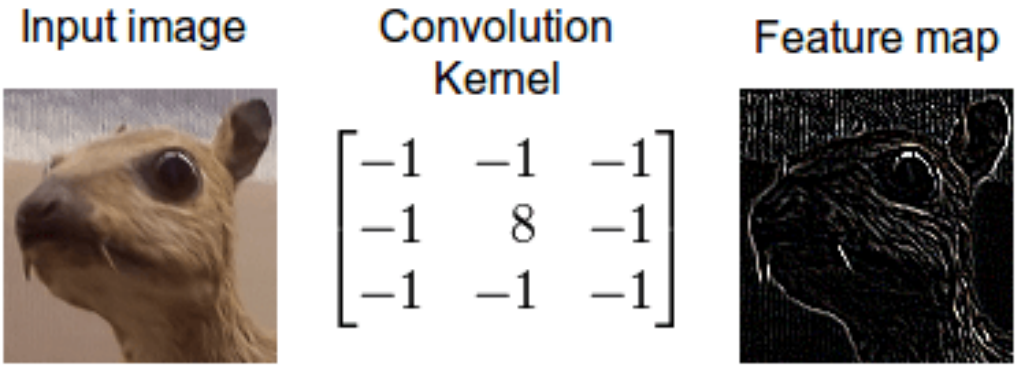

Figure 7-4: An example of detecting horizontal edges from an input image using convolution kernel. Image sources: [145, 146].

The term convolution in machine learning is related to a form of mathematical convolutions, which is the process of adding each element of the image (sub-image) to its local neighbors, weighted by the kernel. Convolution is used in image processing to filter images to produce different visible effects as demonstrated in Figure 7-4. This method involves taking a small sub-image and shifting it up and down with some overlaps. A convolutional filter that is tuned by hand detects horizontal edges from an image. The convolution operation between a sub-image f and a filter matrix g is denoted as follows:

$$h[x, y] = f[x, y]\dot{g}[x, y] = \sum_{n} \sum_{m} f[n, m]g[x - y, y - m]. \tag{7-1}$$

The sub-image f has the same dimensions as g. The dot product of the filter g and a sub-image of f centered on coordinates (x, y) produces the pixel value of h at coordinates (x, y). The size of the feature map is adjusted by the size of the filter matrix. Arranging the filter consecutively with each sub-image of f produces the of output pixel matrix h which is also called a feature map.

Image edges are handled as a special case. A method called padding is used to preserve the image dimensionality and allow the output matrix dimension to only decreases slightly with every convolution. Padding improves performance by keeping information at the edges of image.

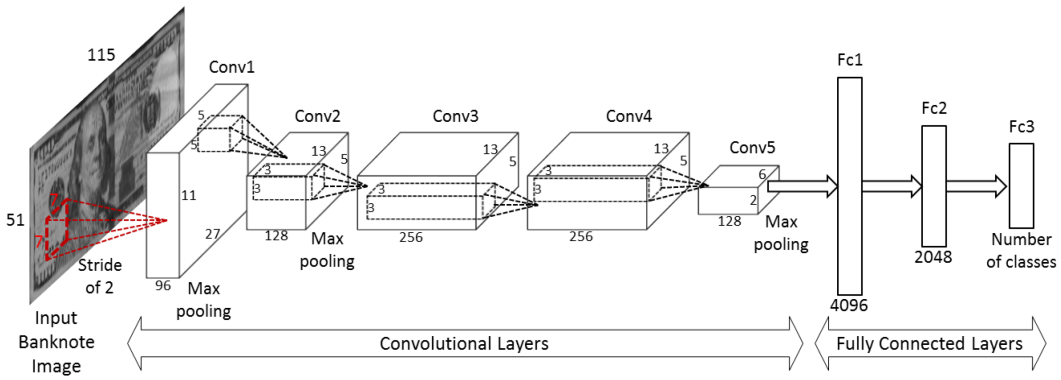

Figure 7-5: An example of convolutional neural net [148].

A convolutional layer of a neural network is formed by combining a set of convolutional filters [147]. The matrix values of the filters are treated as neuron parameters and trained using machine learning. The convolution operation replaces the multiplication operation of a regular neural network layer.

The output of the layer is usually described as a volume. The height and width of the volume depends on the dimensions of the feature map. The depth of the volume depends on the number of filters. The number free parameters are reduced drastically compared to a fully-connected neural layer since the same filters are utilized for all parts of the image [135]. The same parameters are shared by the neurons of the convolutional layer which are only connected to a local region of the input to ensure translation invariance.

A convolutional neural network (CNN) is formed by consecutive convolutional layers. An example of a convolutional network is shown in Figure 7-5. There is evidence that the layers closer to the input learn to identify low-level features of the image, such as edges and corners, and the layers closer to the output learn to combine these features to distinguish more meaningful shapes [147]. In this dissertation, the method of deep convolutional network is applied to find the location of the interaction vertex.

Since the deep layers of the network require more filter matrices to distinguish various high-level patterns, the feature map size in the deep end of the network can be reduced to make the network more adaptable for classification.

To increase depth of the network while keeping the computation time efficient, the dimensionality of the feature map can be reduced by adding a pooling layer after a convolutional layer [134]. The most common type of pooling layer is a max pooling layer, where the feature map is down-sampled in such a way that the maximum value within a sub-image of the activation map is retained. Max pooling causes the loss of spatial information by selecting the maximum value in the activation in a sub-image, which subsequently forces the detectors to be less precise and allows the resulting network to be more "translation invariant".

A neural network is trained by adjusting the weights of all neurons so that the network learns to predict the target outputs from known inputs. Analytically solving the neuron weights of a multi-layer network has proven to be a difficult task, however an algorithm called back propagation can provide an effective iterative solution for solving the weights [149]. Back propagation is a form of supervised learning for multi-layer nets using gradient descent, also known as the generalized delta rule. The error values at the output layer are back propagated through the network to compute the error values of the hidden layers, allowing incoming weights to these layers to be updated. It is most often used as a training algorithm in current neural network applications.

To introduce non-linearity into the network, the convolutional layer typically includes a non-linear activation function. Since the activation function ϕ decides the final output of each neuron, it is essential to select the function properly in order to create an effective network. One of the acivation functions is the rectified linear activation function. The Rectified linear units (ReLu) is an effective method to introduce non-linearity to the network. This method produces an output using a ramp function such as:

$$\phi(s) = max(0, s). \tag{7-2}$$

This type of function is easy to compute and differentiate for back-propagation. The function is not differentiable at zero, but this has not prevented its use in practice. ReLus have become quite popular lately, often replacing sigmoidal activation functions which have smooth derivatives but suffer from gradient saturation problems and slower computation.

To solve multi-class classification problems, the softmax activation function is employed in the output layer of the network:

$$\phi(s) = \frac{exp(s_k)}{\sum_{k=1}^{K} \exp s_k}. \tag{7-3}$$

The softmax function computes the probabilities distribution of the event over k different events over all possible K events and outputs a vector of K values ranging between 0...1 that sums to 1. The output values of the softmax function can be used as class probabilities, where the target class will have the high probability.

The final hidden layers of a CNN are typically fully-connected layers [134]. The output from the convolutional layers describes high-level features in the data. Whereas the output can be flattened and connected to the output layer, adding a fully-connected layer is an inexpensive computationally way of learning about the non-linear combinations of these features.

The weights between the connected layers are learned with back propagation. The error "back-propagates" through the fully-connected layer to the convolutional and pooling layers allowing non-linear combination of features. The activations of the most outer layers can also be used directly to generate a hierarchical representation of an image.

A typical way to minimize overfitting in a machine learning algorithm is to employ a regularization term that assigns penalty to large weights or non-sparse weights. One of the techniques used for this purpose is called dropout [150]. Dropout switches off some neurons from neural network during training and subsequently forces other active neurons to learn harder and to make predictions for the missing neurons. This results in a network

that is capable of better generalization because it is less sensitive to a specific weights of neurons and therefore it will be less likely to overfit the training data. In convolutional networks, dropout is typically used in the final fully-connected layers [151].

7.3 Methodology

Stacking multiple hidden layers with many kernels per layer allows a DCNN to automatically extract features that describe the input image as it creates a hierarchical representation of data. In the DCNN application, the localization is effectively treated as a classification problem.

The vertex identification in MINERvA is treated as a classification of multi-class problem. The finely segmented detector is categorized into 173 segments, where each scintillator plane and passive target is assigned a number starting from segment 0 for the region upstream of the detector all the way to segment 173 which is located in the upstream end of the ECAL region. Figure 7-6 shows the schematic of the segment assignment. The segment number will then mapped into the plane number in the detector space, where each passive target will occupy at least two planes. See Table 7-1.

A neural network takes numbers as input. To a computer, an image is merely a grid of numbers that represent the darkness of each pixel. For the image classification for vertex finding in MINERvA, each unit of grid or lattice stores the energy deposited by the charged particle and the time when that energy is deposited. The muon vertex time is used as the reference time and to teach the network that the time associated with the track that is matched to MINOS detector is special.

The machine learning machinery starts by creating input files that can be passed on to machine learning software packages, for instances, Theano [152], Caffe [153], or TensorFlow [154]. The input files are created by having all the digits in the inner detector and downstream ECAL region encoded into a two-dimensional array that is handled in the MINERvA Gaudi framework. The 127x50 pixel image is treated as an array of 6400 numbers in order to feed an image into the neural network.

MC datasets were drawn from the ME data configurations of the NuMI beam. A three-way split for training, validation, and testing is employed, with test data saved until training was finished to provide a final evaluation. The simulated datasets are split based on a list of MINERvA runs/subruns corresponding to a specific beam and detector configuration. For instance, we use playlists minervame1F and minervame1G as the datasets for the training models to test or classify events in playlist minervame1A. We perform the same splitting method to classify other ME playlists. Two-channel images are built using deposited energy and hit time. Each event contains images for the X, U, and V views that are fed into different convolutional towers in the DCNN.

The second step is to run a ROOT [155] script to produce a set of file formats designed to store and organize large amounts of data with support in deep learning frameworks called HDF5 [156]. The next step is to use the HDF5 and the model file (DCNN) as image input files (shown in Figure 7-7) to create an sqlite database comprising the DCNN vertexing. This database will then be used to split the analysis sample based on the vertex prediction.

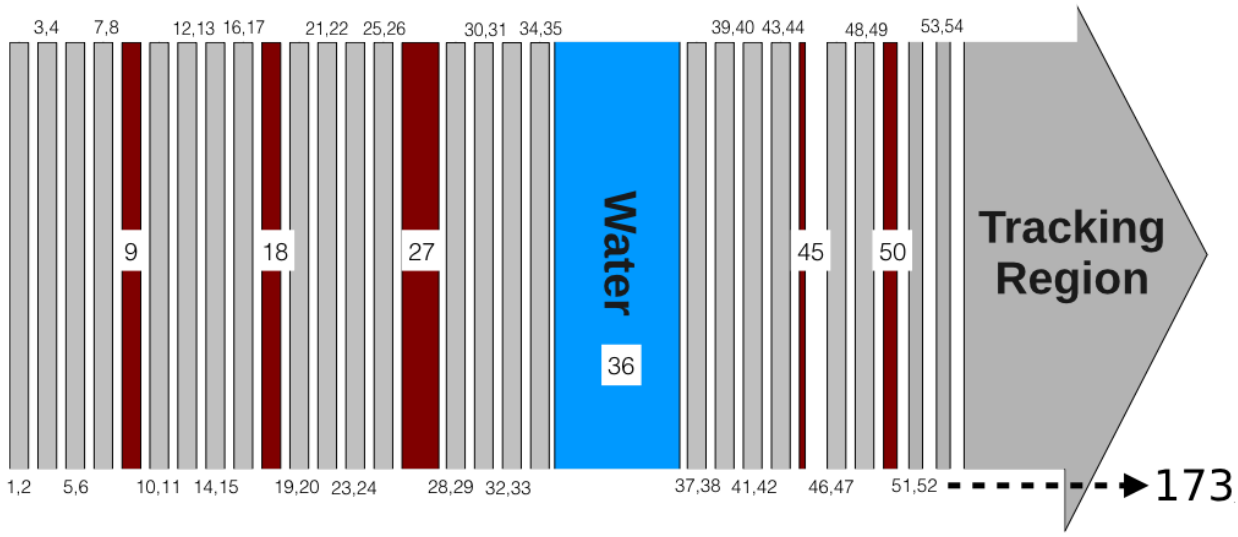

Figure 7-6: Schematic of the target class (segment) assignment for nuclear target region extending from segment 1 all the way to segment 173 in the downstream end of ECAL. Note that segment 0 is assigned for region upstream of the nuclear target.

Table 7-1: Segment/plane number assignment for the passive targets.

Target	Segment number	Plane Number (Detector)
1	9	9,10
2	18	19, 20
3	27	29, 30, 31, 32
4	44	49, 50
5	49	55, 56

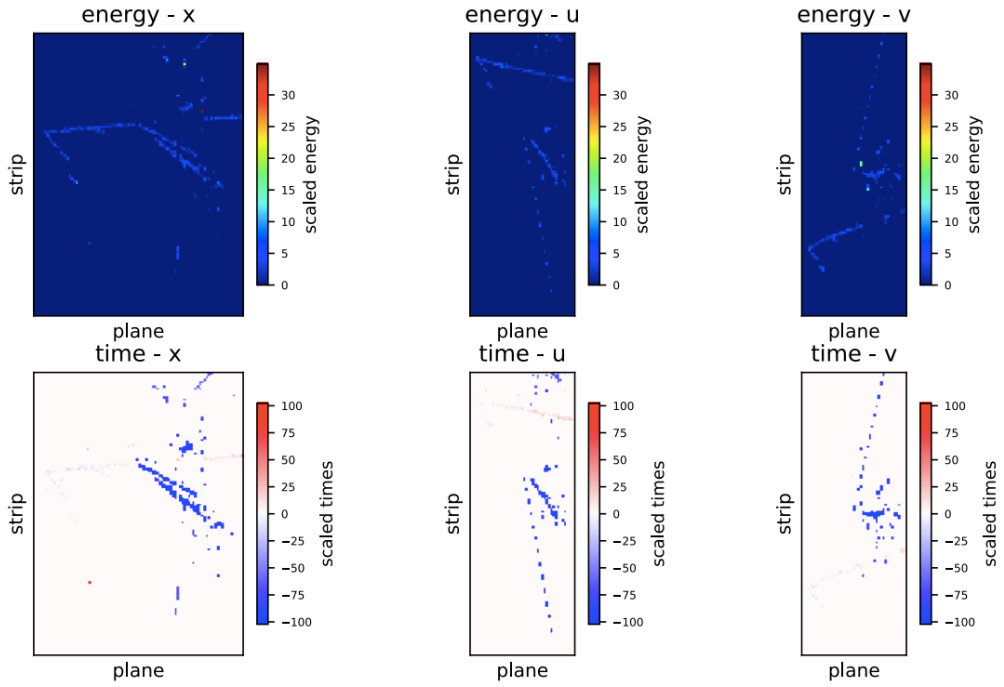

Figure 7-7: Plots from HDF5 that encode the energy and timing information. Top: Energy Lattice only - there are two overlapping neutrino events but it's hard to tell if both are true neutrino events or if one of them comes from overlay. Bottom: Time lattice information. Now it can be clearly seen that one of the events have different timing information as those that are not coming from overlay.

7.4 Network Topology

The goal of the DCNN is to predict the location of the interaction vertex along the beam axis. The incoming neutrino beam is nearly parallel to the z-axis of MINERA and the three views that define the detector geometry all include the z-axis. Due to this, pooling is only performed along the X, U and V view along the z-axis using a non-square kernels to extract the features (the kernels are larger along the transverse direction than they are along the z-direction). It is found that there is a significant advantage in using non-square kernels and non-square pooling units. By using the non-square kernels we conserve the image aspect size along the z-axis and allow the network to simultaneously learn the features concerning where an activity stops, starts, and peaks. The network is viewed as a hybrid-classifier-localizer with classification elements operating along the transverse axis and localization elements operating along the z-axis.

As shown in Figure 7-8, the network is comprised of three separate towers corresponding to the "X", "U", and "V" views. Four iterations of convolution and max pooling layers with ReLUs are performed for each tower. Each pooling layer comprises a kernel that shrinks the dimension along the transverse axis by one. A fully connected layer with 196 semantic output features is attached at the end of four iterations. The outputs for the three views are concatenated and fed to another fully connected layer with 98 outputs which in turn is input for a final fully connected layer with an 173-output softmax.

Training was performed with cross-entropy loss that treated all mistakes as equally important, but a localization function in the network is achieved by using convolutional kernels that are larger in the transverse direction than in the beam direction. Images of neutrino interactions are then utilized to train the neural network so that the network will be able to learn how to tell them apart.

The class probabilities will be returned in a form of a vector of plane or segment probabilities. The index of the vector refers to the segment number, while each element will represent (on a scale of 0 to 1) how confident the DCNN is that the vertex is

originating from that segment number. For instance, an output of [0.02; 0.03; 0.95,...] would mean that the network is about 2% confident that the interaction is coming from segment 0, 3% confident that it is coming from segment 1, and 95% confident that it is originating from segment 2, and so on. The segment with the highest confidence is then chosen as the primary vertex of interaction. In a case where the network is not confident of its predictions, there usually are two or three competing segments to choose from. For example, an output of [0.35,0.33,0.32,...] would imply that the network is having a "confusion" in determining the origin of the real events as coming from segment 0, segment 1, or segment 2. Out of a handful of "confused vertex" events scanned by eye, we found that this happens when we have a large hadronic shower events that would even confuse human eyes.

These confidence measures are then employed to build a more reliable system by automatically processing only those images that the networks are confident about. To decide on the confidence threshold, the lowest accuracy (probability) threshold of 40% is chosen based on the DIS Figure of Merit (Signal divided by square root of Signal and Background) and DIS Purity, as shown in Figure 7-9. The purpose of this study is to optimize the signal (correct segment events) selection while maintaining a statistically significant distribution. Once the 40% threshold has been applied the segment prediction can be performed and the segment prediction can be then assigned as the new vertex plane. The segment number is subsequently used to split the analysis samples based on the vertex location.

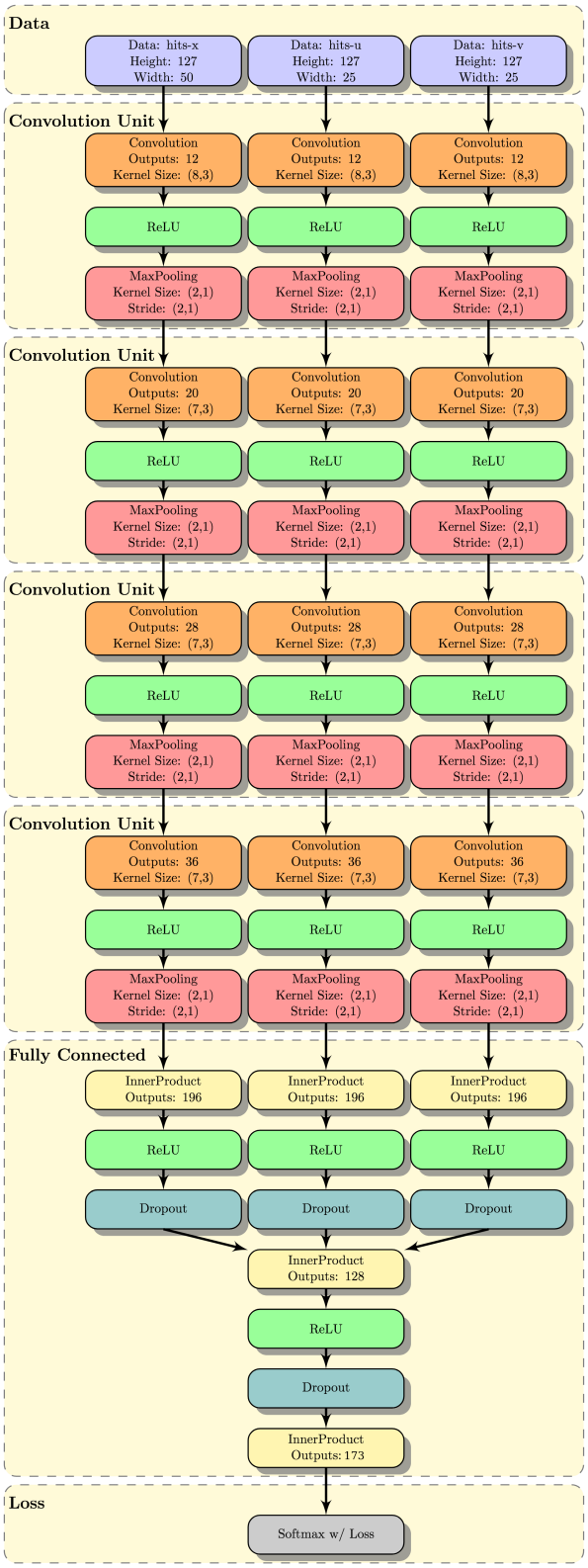

Figure 7-8: Structure of the 173 target class network used to predict the location of the interaction vertex.

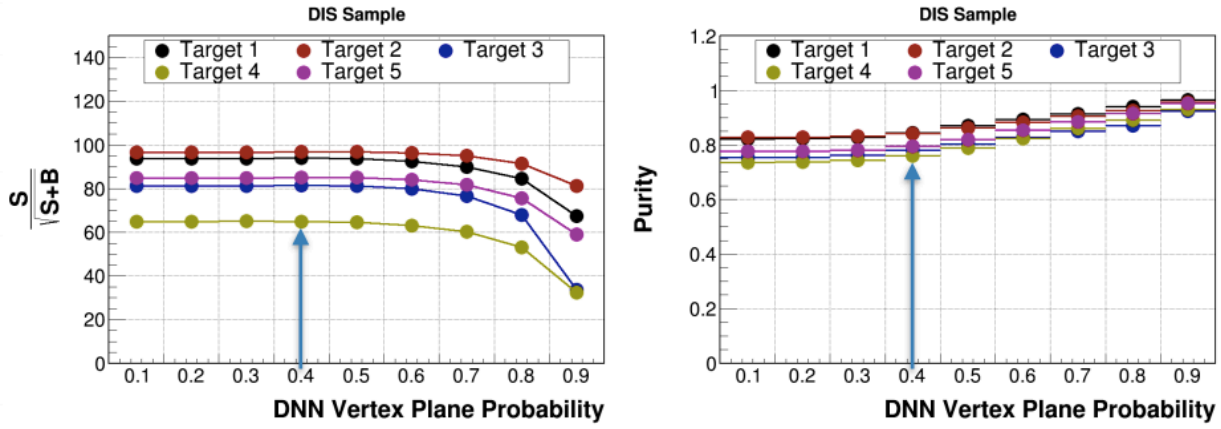

Figure 7-9: Left: DIS Figure of Merit. The lines are mostly constant between 40 to 50% for most of the targets except for target 4 where a decline between 40 to 50% is observed. Right: DIS Purity. The higher the the threshold, the more confident the network is of its predictions and therefore the higher the purity. Some improvements in purity are gained at 40% threshold.

7.5 Comparison to Track Based Vertexing

The results obtained from implementing DCNN for vertex finding are then compared to the track-based vertexing. The comparison is done using MC so that one can get the true information about where the neutrino interacted and compare to where it was reconstructed. The metric for comparison is given as a function of plane number that defines the z-position of the vertex of interaction.

In DCNN vertexing, an event is a candidate DIS event if it originated in the same target location as predicted by the DCNN. For track-based vertexing, an event is a a candidate DIS event if it comes from either one plane upstream or two planes downstream of the passive target. The wider "correct target" selection in the track-based algorithm is done to account for the event smearing surrounding the passive target due to activities around the vertex. An improvement in event selection after applying the DCNN method for vertexing can be seen in Figure 7-10. There is less signal leakage from the passive target region to the surrounding scintillator tracker and less contamination coming from the scintillator tracker around the passive target.

Figures 7-10 and 7-11 compare the perforance of the two vertexing methods for the DIS analysis. Plots in Figure 7-10 show the the event distributions as a function of plane number and separated by the type of target where the vertex originated. The green color represents true DIS events. In the track based vertex reconstruction, there are are more true DIS events (signal) being incorrectly reconstructed as having come from the planes upstream and downstream of the passive target. In order to retain these true DIS events, a wider cut is applied to define the passive target region as shown by arrow in the figure. On the other hand, DCNN based vertexing shows cleaner separation between plastic scintillator upstream and downstream of the target compared to the track-based method. DCNN predicts the correct location of the interaction vertex more often, and there is almost no signal leakage to the neighboring planes. Hence, we can apply a tighter selection for our event sample by only taking events that are predicted to be coming from the target.

Figure 7-11 shows the improvement in the vertex-z resolution seen in DCNN vertexing in comparisons to the track-based vertexing. The samples used in these resolution plots are selected as follows:

1. Events that are truly originating from the target and predicted to be coming from either the target region or 8 modules upstream or 8 modules downstream of the target are selected for the DNN vertexing resolution plot.

2. Events that are truly originating from the target and reconstructed in the target region or 8 modules upstream or 8 modules downstream of it are selected for the track-based vertexing resolution plot.

3. For the DNN vertexing, the vertex-z residual is taken as the difference between the true vertex of interaction and the center of the plane where an event is predicted to occur.

4. For the track-based vertexing, the vertex-z residual is taken as the difference between the true vertex of interaction and vertex-z location as given by the reconstruction algorithm.

A study to examine the impact of DNN vertexing on the signal efficiency and purity was performed. Background subtraction and unfolding, steps usually performed prior to calculating purity and efficiency, are not implemented in this study to compare vertexing methods. Background subtraction and unfolding as they relate to this dissertation analysis are described in more detail in Chapters 10 and 11.

A signal event is defined as an event that is truly DIS and truly originating from the passive target. True DIS is defined as true reconstructed $Q^2 > 1.0$ GeV$^2/c^2$ and true reconstructed $W > 2.0$ GeV$/c$ where true reconstructed (true reco) means the variables are calculated using the true charged lepton kinematics variables. The purity and efficiency are defined as follow:

$$\text{DIS Purity} = \frac{\text{DIS signal events passing all reco cuts}}{\text{All reco DIS events truly in the passive target}} \tag{7-4}$$

$$\text{DIS Efficiency} = \frac{\text{DIS signal events passing all reco cuts}}{\text{All generated DIS events truly in the passive targets}}. \tag{7-5}$$

The improvement on the signal efficiency and purity for the DIS analysis is shown in Figure 7-12. The improvements are largely coming from better handling of events with high shower topology in the DNN vertexing. This leads to an improvement in distinguishing events that truly originate in passive targets from events that truly originate in the scintillator between the passive targets.

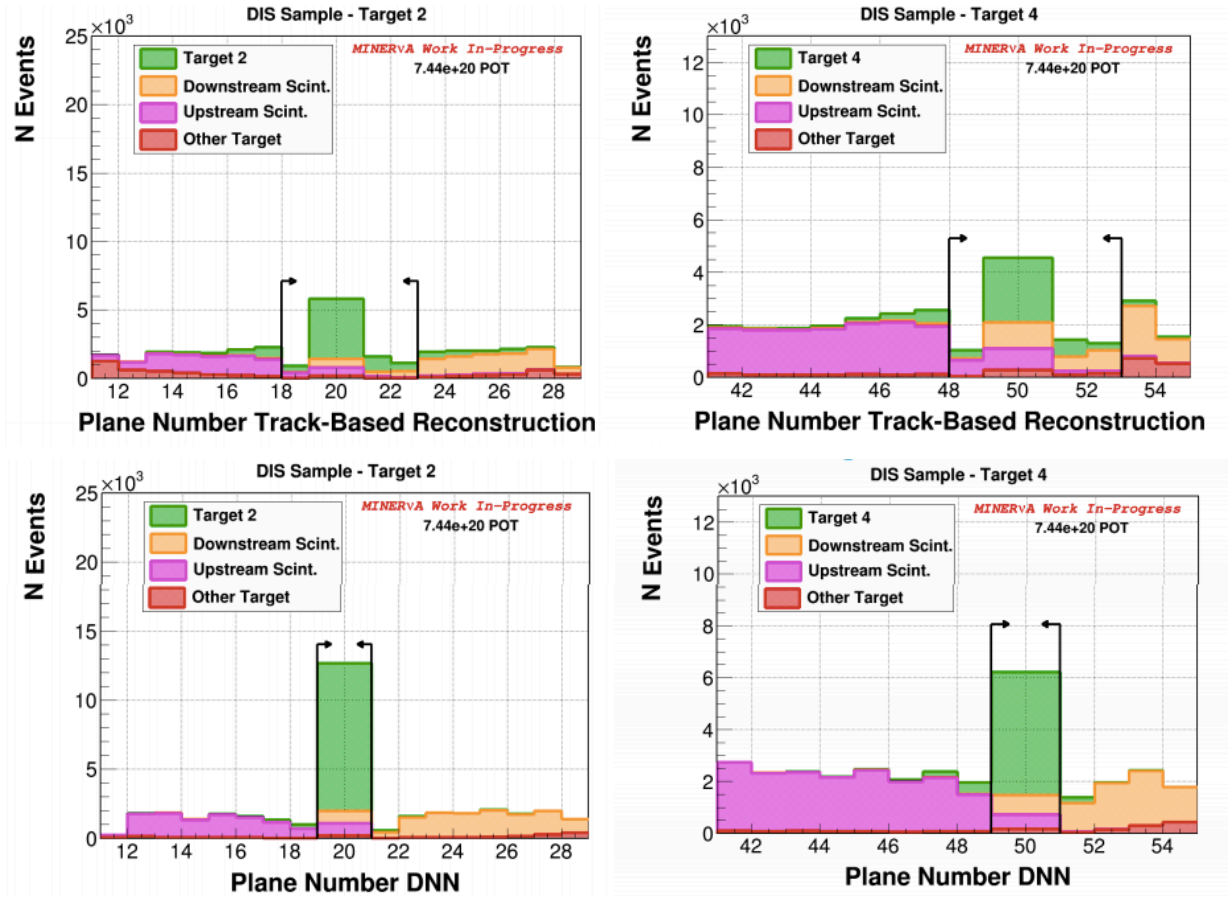

Figure 7-10: Comparisons between track-based vertexing and machine learning vertexing as a function of plane number. Top: Track-based vertexing. Target 2 covers plane number 18 to 22 while target 4 covers the plane number 48 to 52. Bottom: DCNN vertexing. Target 2 covers plane number 19 to 20 while target 4 covers plane number 49 to 50. The color represents the location of the true interaction vertex.

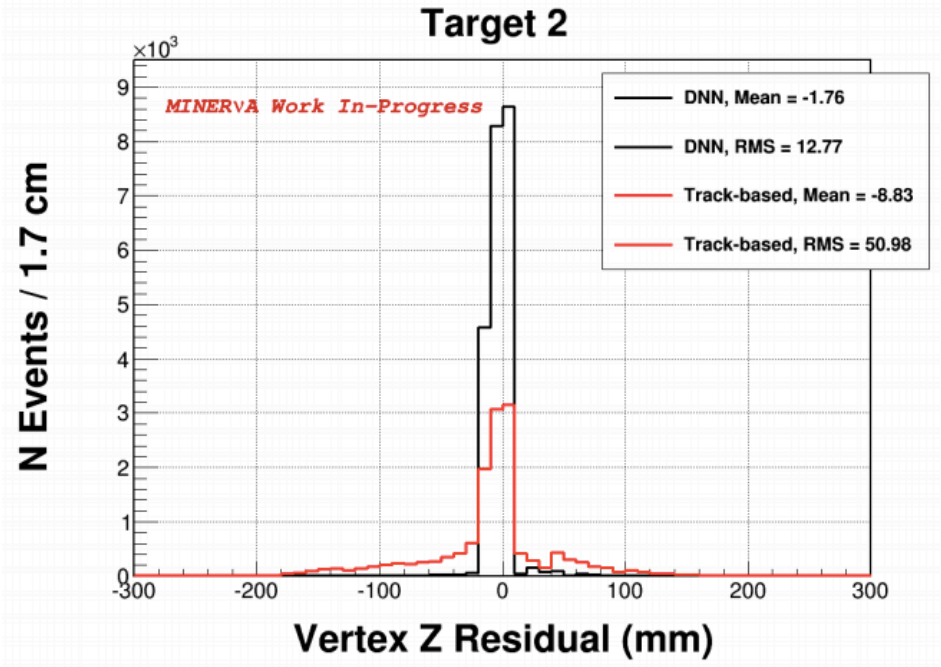

Figure 7-11: Plots of vertex z residual for Target 2. Black line on the plot corresponds to the vertex-z residual of DNN vertexing, while the red line corresponds to the vertex z residual for track-based vertexing.

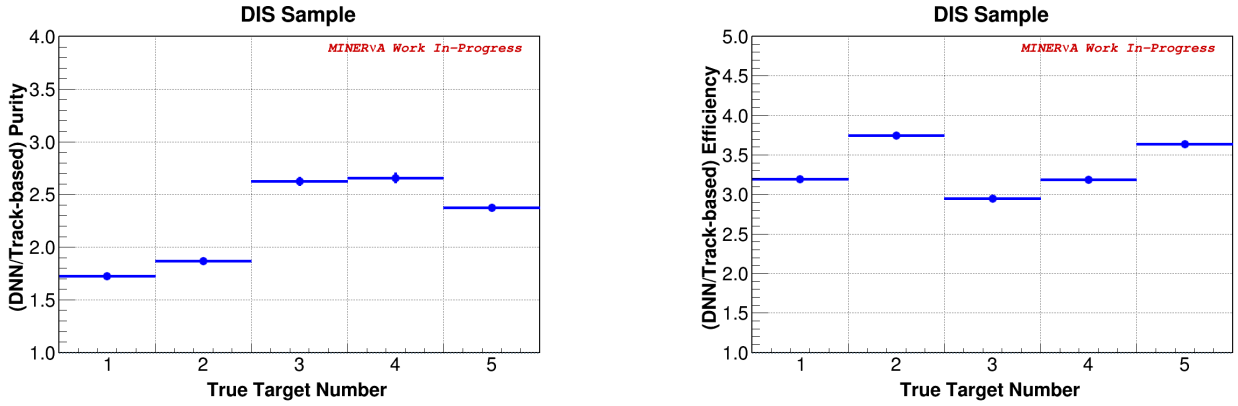

Figure 7-12: Left: Purity improvements of DNN vertexing to track-based vertexing as a function of target number. Sample in DNN is defined as all of the events that are predicted to be coming from the plane of the passive target. Sample in track based vertexing is defined as all the events that are reconstructed in 1 plane/2 planes downstream of the passive target. Right: Efficiency improvements of DNN vertexing to track-based vertexing as a function of target number.

CHAPTER 8
OVERVIEW OF THE MEASUREMENT

This dissertation presents a measurement of the charged current muon-neutrino deep inelastic cross section on iron, lead, carbon, and plastic. The analysis focuses on a neutrino interaction channel whose final-state particles are a muon and a variety of hadrons. The interaction equation is:

$$\nu_\mu + N \rightarrow \mu + X,$$

where most of the interactions involve target neutrons ($\nu_\mu + n$) bound within iron, lead, carbon, and plastic nuclei.

8.1 A Note on Units

The DIS sample used in this dissertation is isolated using two kinematic variables, the transfer momentum squared Q^2 and the invariant mass W. Thus, this analysis comprises many studies of backgrounds in Q^2 and W kinematic regions that differ from the canonical $Q^2 > 1.0$ (GeV/c)^2 and $W > 2.0$ (GeV/c^2) region. To clearly distinguish between the transfer momentum squared and invariant mass, SI units will be used in the remainder of this document; momentum squared has units of (GeV/c)^2 and mass has units of (GeV/c^2).

8.2 Cross Section Formula

The total DIS cross section is measured as a function of neutrino energy using the standard cross-section formula:

$$\sigma_i = \frac{U_{ij}\,(N_j - b_j)}{\Delta_i\,\epsilon_i\,\Phi_i\,N}, \tag{8-1}$$

where N_j is the total number of selected events in data in the reconstructed energy bin j, b_j is the number of background events in the reconstructed energy bin j, U_{ij} is an unfolding matrix which maps events reconstructed in the jth bin to their true ith bin, Δ_i is

the width of bin i, ϵ_i is the total event selection efficiency, Φ_i is the neutrino flux (measured in bins of neutrino energy), and N is the number of scattering centers (nucleons) in a particular target, C, Fe, Pb, or CH.

The differential cross section may be measured in terms of a variable x. In this case the per-bin flux Φ_i is replaced with the integrated flux Φ as follows:

$$\frac{d\sigma}{dx}_i = \frac{U_{ij}\,(N_j - b_j)}{\Delta_i\,\epsilon_i\,\Phi\,N}, \tag{8-2}$$

where d, b, U, and ϵ are now all functions of the variable x. The differential DIS cross section presented in this dissertation is measured in terms of Bjorken-x (x_{bj}).

The signal definition and event selection as well as their purity and efficiency are given in Chapter 9. The background classifications for the selected sample and sideband studies are presented in Chapter 10. The unfolding method used to obtain measurements independent of detector effects is presented in Chapter 11. The efficiency correction and target normalization of the unfolded DIS sample is discussed in Chapter 12. Finally, the systematic uncertainties attached to the measurements and the DIS cross sections results are given in Chapters 13 and 14, respectively.

CHAPTER 9
EVENT SELECTION

The first step to measure a cross section is to count the number of events passing a set of signal selection cuts. This set of selection cuts is used to isolate the DIS events from all the events recorded by the detector and distribute them into bins of E_ν and x_{bj} based on the reconstruction. Recalling the formula for total cross section (Equation 8-1):

$$\sigma_i = \frac{U_{ij}\,(N_j - b_j)}{\Delta_i\,\epsilon_i\,\Phi_i\,N}, \tag{9-1}$$

where N_j refers to the number of candidate DIS events found in data.

9.1 Event Selection Requirements

The DIS nuclear target analysis inherits a set of event selection cuts from the previously published nuclear target inclusive analysis [157] and the DIS analysis in the LE era [67]. The cuts that are inherited by this analysis are as follows:

- Only MINOS matched muons tracks are reconstructed and analyzed.
- The MINOS matched muons must have a negative curvature in the MINOS magnet field to ensure that the muon is negatively charge and thus a ν_μ event.
- The interaction vertex must be contained in an 850 mm apothem hexagonal fiducial area in x and y.
- For the passive target sample, the z position of the interaction vertex must be located within 1 plane upstream and 2 planes downstream of the passive targets 1, 2, 3, 4 and 5.
- For events in targets 1, 2, 3 or 5, the interaction vertex must not be within 25 mm from the barrier of materials.
- To mitigate the rate of rock muons mis-reconstructed in the fiducial volume, a cut is applied on the maximum allowed dead time upstream of the interaction vertex. An

event is rejected if it has more than one dead TriP-t upstream of the projected muon track.

- Reject events if there are more than 7 planes upstream of the interaction vertex with average energy between 1.5 and 6.5 MeV. This selection cut ensures that events where the vertexing algorithm mis-identified an event in an upstream target as coming from a target downstream are removed.

- Muons reconstructed by curvature in the MINOS magnetic field must have a curvature significance of at least 5 σ.

- The endpoints of muon tracks in MINOS must be at least 210 mm away from the MINOS magnetic coil, but within 2500 mm from the coil ($210 < R < 2500$ mm).

- Events must have a neutrino energy within $5 \leq E_\nu < 50$ GeV, and a muon angle $\theta_\mu \leq 17°$. The muon angle cut is imposed due to the acceptance to the MINOS detector.

The ME DIS cross section analysis requires several modifications to this set of inherited event selection cuts. A modification to the reconstruction-based vertexing cut is required for this analysis as we employ machine learning vertexing. For the ME DIS analysis, we removed the cut applied on the neutrino energy and instead we apply the cut on the kinematic variable that is directly measured in the detector, muon energy. The muon must have a minimum energy of 2 GeV. This is the minimum energy necessary for a muon coming from the most upstream passive target (target 1) to exit the back of the MINERvA detector and travel a minimum of 100 mm in the MINOS fiducial region. The maximum muon energy cut is kept at 50 GeV to retain a large statistics DIS sample, as the DIS events dominate at the high energy tail of the flux.

The ME DIS analysis also removes the upstream energy cut which depends on the reconstruction-based vertexing algorithm. This upstream cut is employed to account for

the fact that hadronic energy from showers obscuring the muon were far more likely to cause failures in the vertexing algorithm than muon tracks which are mis-reconstructed. The machine learning vertexing performed well in handling this type of vertexing failure.

As the machine learning vertexing performs better in clearly distinguishing between plastic events and passive targets, we modified the requirement that the interaction vertex must have a z location between 1 plane upstream and 2 planes downstream of the nuclear targets 1, 2, 3, 4 and 5. Instead, we only accept events with a reconstructed vertex position located in the passive nuclear targets region. This narrower region cut results in an improved purity of the sample as the reconstructed DIS events that truly come from interactions in the scintillator immediately upstream and downstream of the target are removed.

Summarizing all the modifications described above, the updated set of event selection cuts used for the DIS analysis using ME data are presented below. Cuts that differ from the DIS analysis using LE data are listed in *italics*:

- Only MINOS matched muons tracks are reconstructed and analyzed.
- The MINOS matched muons must have a negative curvature in the MINOS magnet field to ensure that the muon is negatively charge and thus a ν_μ event.
- The interaction vertex must be contained in an 850 mm apothem hexagonal fiducial area in x and y.
- *For the passive target sample, the z position of the interaction vertex must be located within the passive targets 1, 2, 3, 4 and 5.*
- For events in targets 1, 2, 3 or 5, the interaction vertex must not be within 25 mm from the barrier of materials.
- To mitigate the rate of rock muons mis-reconstructed in the fiducial volume, a cut is applied on the maximum allowed dead time upstream of the interaction vertex. An

event is rejected if it has more than one dead TriP-t upstream of the projected muon track.

- Muons reconstructed by curvature in the MINOS magnetic field must have a curvature significance of at least 5 σ.

- The endpoints of muon tracks in MINOS must be at least 210 mm away from the MINOS magnetic coil, but within 2500 mm from the coil ($210 < R < 2500$ mm).

- *Events must have a muon energy within* $2 \leq E_\mu < 50$ *GeV and a muon angle* $\theta_\mu \leq 17°$. *The minimum muon energy and angle cuts are imposed due to the acceptance to the MINOS detector.*

Kinematic cuts on the reconstructed Q^2 and W of the event are employed in order to isolate a DIS sample from the inclusive nuclear target sample. An event is selected as a DIS event if the reconstructed $Q^2 \geq 1$ (GeV/c)^2 and the reconstructed $W \geq 2$ GeV/c^2. A MC event is considered to be a true DIS event if it had a true generated $Q^2 \geq 1$ (GeV/c)^2, a true generated $W \geq 2$ GeV/c^2, and a GENIE channel = 3 (i.e. DIS). The additional cut on GENIE channel = 3 is required to eliminate CCQE events that produce charm quarks that could potentially pass the Q^2 and W cuts. Table 9-1 provides a breakdown of the number of events remaining after each selection cut.

Events which pass the W and Q^2 cuts based on *reconstructed* W and Q^2 are called "reco events," events which pass based on the *true* W and Q^2 are called "true events," and events which pass both are called "true reco events." Events in data may only be reco events or not reco events. Events in MC may be any (or all) the three types.

9.2 Event Efficiencies and Purities

We considered two types of efficiency when choosing event selection cuts to isolate the DIS sample. The first efficiency describes the efficiency of the DIS cut compared to the existing Inclusive sample. This efficiency is defined as the number of events in the true material passing the reconstructed CCInclusive cuts, the reconstructed *and* truth DIS cut,

Table 9-1: A breakdown of event rates after each cut for the iron events in nuclear target 3. These numbers are scaled to represent the size of our data sample, 8.89×10^{20} POT.

	Number of Events	Survival Rate (%)
Total Generated DIS Events in the target with true $\theta_\mu < 17$ degrees	2789	100
Matched to MINOS	1274	46
Reco $\theta_\mu < 17$ degrees	1248	45
MINOS track quality < 9.0	1016	36
MINOS coil cut	942	34
Helicity cut	931	33
In fiducial area	793	28
Dead time cut < 1	769	28
Muon Energy Cut 2-50 GeV	761	27
Reconstructed as W > 2 GeV	697	25
Reconstructed as $Q^2 > 1\ GeV^2$	700	25
Reconstructed as DIS	633	23

divided by the number of events in the true material passing the reconstructed CCInclusive cuts and the truth DIS cut. Since the Q^2 and W are calculated from the reconstructed observable quantities, this efficiency depends on the resolution of the hadronic and muon reconstruction. This efficiency is referred to as the "inelastic efficiency" in the text.

An "inelastic purity" is related to inelastic efficiency. The number of events in the true material passing the reconstructed CCInclusive cuts, the reconstructed *and* truth DIS cut is divided by the number of events in the true material passing the reconstructed CCInclusive cuts and the reconstructed DIS cut. Both inelastic purity and inelastic efficiency quantify the efficacy of the DIS cuts.

The second type of efficiency is the "overall efficiency". This quantity has the same numerator: the number of events in the true material passing the reconstructed CCInclusive cuts, the reconstructed *and* truth DIS cut. However, the denominator is instead *all* true generated CC DIS events in the true fiducial volume with true muon angle $< 17^o$. This quantity describes the overall efficiency of the DIS cut, the MINOS matching, and the algorithm which builds vertices in the nuclear targets. The overall efficiency is lower than the inelastic efficiency since the number of generated events in the denominator

is much larger. The overall efficiency is used in the calculation of the total and differential cross-sections, as described in Section 12.1.

The "overall purity" is related to the overall efficiency. It is defined as the number of events in the true material passing the reconstructed CCInclusive cuts, the reconstructed *and* truth DIS cut, divided by the number of events passing the reconstructed CCInclusive cuts and reconstructed DIS cut. The overall purity accounts for the loss of events mis-reconstructed in the fiducial volume, which was not considered in the inelastic purity.

The inelastic and overall efficiencies and purities for the DIS cuts are listed in Table 9-2. The errors are statistical only. The inelastic efficiency along with the numbers of events that correspond to this efficiency is given in Table 9-3. The contamination (1 minus the inelastic purity) is given in Table 9-4.

Table 9-2: Inelastic and overall efficiencies and purities of the DIS cut for the five nuclear targets. These numbers are scaled to represent the size of our data sample, 8.89×10^{20} POT.

Target / Z	Inelastic Efficiency	Inelastic Purity	Overall Efficiency	Overall Purity
1/26	$82 \pm 0.9\%$	$75 \pm 1\%$	$14 \pm 0.3\%$	$58 \pm 1\%$
1/82	$82 \pm 1\%$	$73 \pm 1\%$	$15 \pm 0.4\%$	$61 \pm 1\%$
2/26	$82 \pm 0.9\%$	$75 \pm 1\%$	$15 \pm 0.3\%$	$63 \pm 1\%$
2/82	$80 \pm 1\%$	$75 \pm 1\%$	$15 \pm 0.4\%$	$66 \pm 1\%$
3/6	$83 \pm 1\%$	$78 \pm 1\%$	$20 \pm 0.5\%$	$67 \pm 1\%$
3/26	$81 \pm 1\%$	$77 \pm 1\%$	$17 \pm 0.5\%$	$67 \pm 1\%$
3/82	$82 \pm 2\%$	$74 \pm 2\%$	$14 \pm 0.6\%$	$69 \pm 2\%$
4/82	$82 \pm 0.9\%$	$77 \pm 1\%$	$18 \pm 0.4\%$	$61 \pm 1\%$
5/26	$86 \pm 1\%$	$78 \pm 1\%$	$21 \pm 0.6\%$	$65 \pm 1\%$
5/82	$81 \pm 1\%$	$79 \pm 1\%$	$20 \pm 0.6\%$	$67 \pm 1\%$

9.3 Event Sample (Data and MC)

The DIS analysis produces histograms by running over the inclusive events (tuples) created by the NukeCCInclusive algorithm twice. The NukeCCInclusive algorithm is run first to create a set of lattice information describing event topology that will be passed to the machine learning algorithm. The machine learning algorithm will produce predictions of the location of the vertex for each of the inclusive events. The predictions are converted

into a set of tuples containing all of the necessary event information and prediction of vertex-z location and how confident the algorithm is of its prediction. The NukeCCInclusive algorithm is then run again with the vertex location prediction, where it will correct the event vertex position by moving it to the vertex location prediction. The energy related to the muon and hadronic system must also be corrected to account for the energy loss or gain due to vertex location displacement. The algorithm then will produce a set of NukeCCInclusive tuples and divide the entire sample into different sub-samples depending on the predicted z vertex of the event. The machine learning initially sorts each event based on their predicted plane numbers into nuclear target 1, 2, 3, 4 or 5, or the tracker. An event is then classified according to its' target nuclei based on the x, y position of the vertex in each target.

Histograms are produced target by target and material by material, so each of tracker modules in the tracker region (36 modules) and 5 nuclear targets are analyzed separately. Figure 9-1 shows the DIS selection of recontructed events for data and MC as a function of neutrino energy. The MC is broken down into its constituent channels. Each MC channel is defined in terms of *true* W and Q^2 (except for the QE channel, which is all QE events regardless of W or Q^2). The true DIS signal is colored dark purple. The full collection of these histograms are found in Appendix A.

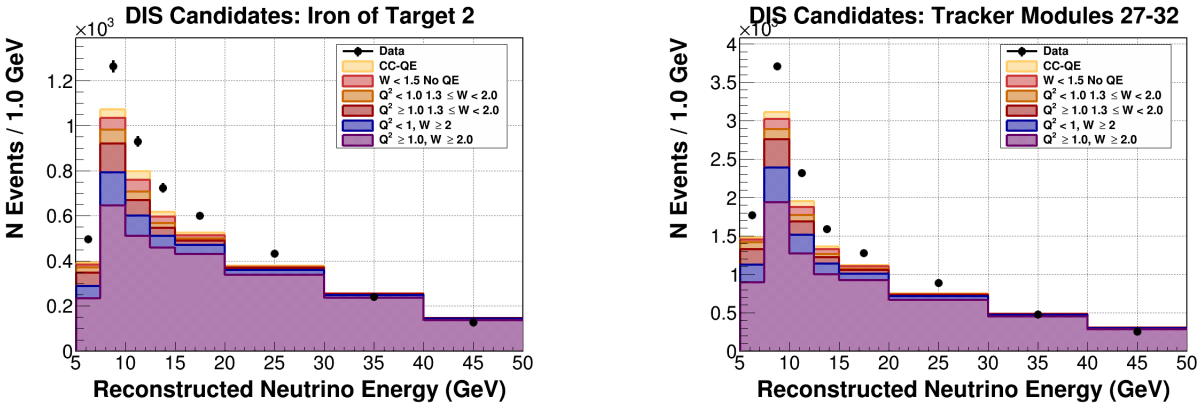

Figure 9-1: The reconstructed DIS events for data (black points) and MC (various colored bands) in the iron of target 2 (left) and tracker modules 27-32 (right). The data and MC correspond to 8.89×10^{20} POT.

Table 9-3: The number of true DIS events (True Events), the number of true DIS events passing the reconstructed DIS cuts (True Reco Events) and the inelastic efficiency of the nuclear targets. These numbers are for an energy range of $2 \leq E_{\mu} < 50$ GeV, and correspond to 8.89×10^{20} POT.

Target	Target Z	True Events	True Reco Events	Inelastic Efficiency (%)
1	26	940	760	$82 \pm 0.9\%$
1	82	800	660	$82 \pm 1\%$
2	26	970	800	$82 \pm 0.9\%$
2	82	850	680	$80 \pm 1\%$
3	6	660	550	$83 \pm 1\%$
3	26	550	450	$81 \pm 1\%$
3	82	320	260	$82 \pm 2\%$
4	82	920	750	$82 \pm 0.9\%$
5	26	670	570	$86 \pm 1\%$
5	82	570	460	$81 \pm 1\%$

Table 9-4: The number of reconstructed DIS events (Reco Events), the number of true DIS events passing the reconstructed DIS cuts (True Reco Events) and the non-DIS contamination of the nuclear targets. These numbers are for an energy range of $2 \leq E_\mu < 50$ GeV, and correspond to 8.89×10^{20} POT.

Target	Target Z	Reco Events	True Reco Events	Contamination (%)
1	26	1000	760	$24 \pm 1\%$
1	82	900	660	$26 \pm 1\%$
2	26	1100	800	$24 \pm 1\%$
2	82	910	680	$24 \pm 1\%$
3	6	710	550	$22 \pm 2\%$
3	26	580	450	$22 \pm 2\%$
3	82	350	260	$23 \pm 2\%$
4	82	980	750	$21 \pm 1\%$
5	26	730	570	$21 \pm 2\%$
5	82	590	460	$19 \pm 2\%$

CHAPTER 10
BACKGROUNDS

The inelastic purity described in Section 9.2 indicates the DIS cuts will also select events with a reconstructed $Q^2 \geq 1.0$ and $W \geq 2.0$ when in fact the true $Q^2 < 1.0$ or the true $W < 2.0$. This is considered a source of contamination, or background, to our DIS sample. These contamination events must be removed from the reconstructed DIS sample before extracting a cross section. Backgrounds in the jth bin of E_ν and x_{bj} are expressed as b_j in cross section expression:

$$\sigma_i = \frac{U_{ij}\,(N_j - b_j)}{\Delta_i\,\epsilon_i\,\Phi_i\,N}. \tag{10-1}$$

We estimate the amount of background to subtract using the MC sample. To minimize model dependency on the background in the measurement, we constrain the MC background to data before subtraction.

For any analysis with low purity, the model dependence of the background is critical and additional background-enhanced control samples are used to ensure the background is properly accounted for. These background-enhanced control samples are referred to as sidebands. Sidebands are regions to the side of a peak in some variable that can be used to constrain the background under the peak. Applying the same principle for the DIS cross-section measurements we select a region distinct from the signal selection. This region is then used to constrain the backgrounds present in the signal region and reduce the modeling uncertainty.

The goal of the background subtraction is to eliminate background components in a selected DIS sample. We select a distribution of reconstructed DIS events predicted to be originating from a nuclear target, T_r, and transform that distribution to a distribution of true DIS events truly originating from the nuclear target, T_t. The reconstructed DIS event sample contains backgrounds from events that truly originate in the plastic scintillator surrounding the nuclear targets. Kinematically, it also contains events that don't truly pass

the Q^2 and W cut. As a result, the background subtraction is more complicated than analyses done in the tracker fiducial region and special care must be taken.

We classify the background events for this DIS analysis into two types: according to target where the interaction took place and according to the kinematics background. The background subtraction is performed to address these two background components, as illustrated in Figure 10-1.

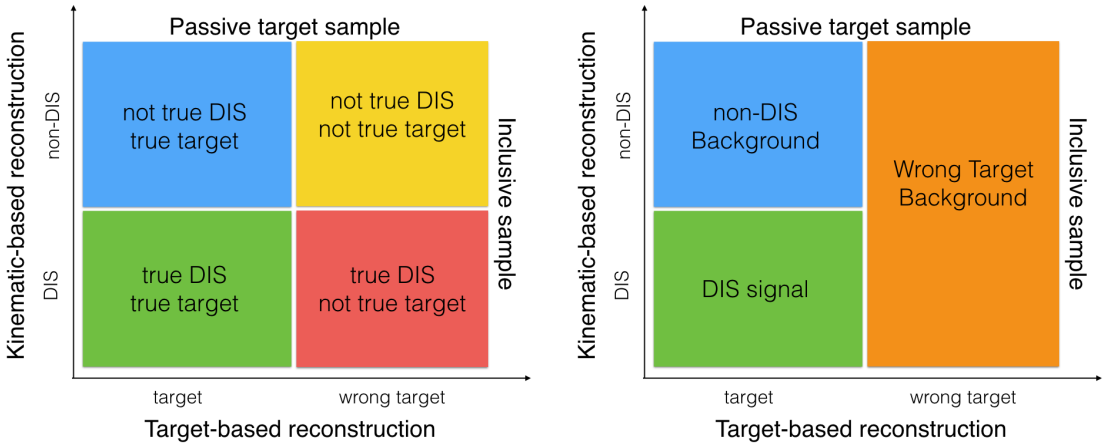

Figure 10-1: Left: The four sub-categories of the DIS sample based on their physical and kinematics space. Green box is the DIS signal, while the other boxes refer to three main type of backgrounds to this analysis. Right: The type of background subtraction performed on the three backgrounds. Plastic background subtraction handles the two types of backgrounds in physical space (wrong target) while non-DIS background subtraction handles the backgrounds in the kinematic space (non-DIS).

10.1 Wrong Target Background

10.1.1 Constructing Plastic Background Sidebands

Figure 10-2 presents the event distribution for the combination of all the passive targets that contain lead as one of its target material. This refers to target 1, 2, 3, 4, and 5. It is important to note that the plastic background sideband construction described in this section uses the inclusive sample and not the DIS sample. This can be done because the wrong target background subtraction is performed before subtracting the non-DIS background. Therefore, we don't have to discriminate the sample based on its kinematics

space at this stage. It is preferable to combine targets materials to obtain a more precise measurement of the background contamination since per target per material sideband is statistically limited. The procedure to combine the material is performed as follows:

1. Loop over each passive target for specific nuclei.

2. For each event where the vertex is predicted to be originating from the upstream sidebands region of the target or downstream sideband of the target (6 planes upstream only or 6 planes downstream only), we make histogram of the true material of the vertex.

Each of these sidebands is based on the nuclei where the vertex originated for the upstream region only or downstream region only. For this sideband construction method, we exclude the scintillator region upstream of target 1 from the merged sideband template. We perform the exclusion because our data is very statistically limited in that region due to the rock muon rejection cut (we reject events where the interaction vertices originate in the first 2 modules of the detector). An example of the sideband distribution is shown in Figure 10-3.

To perform the background subtraction, we have to ensure that the kinematic properties of events in the sideband region (scintillator region) are representative of those in the signal region (passive target region). As the kinematic shapes between the sideband region and the signal region are similar enough (shown in Figure 10-4), we can use these sideband regions to estimate the contribution from this background to the signal region.

Please note that the body of this dissertation includes only a representative set of plots to illustrate the analysis techniques. The complete set of distributions used to estimate the wrong target background are found in Appendix C.

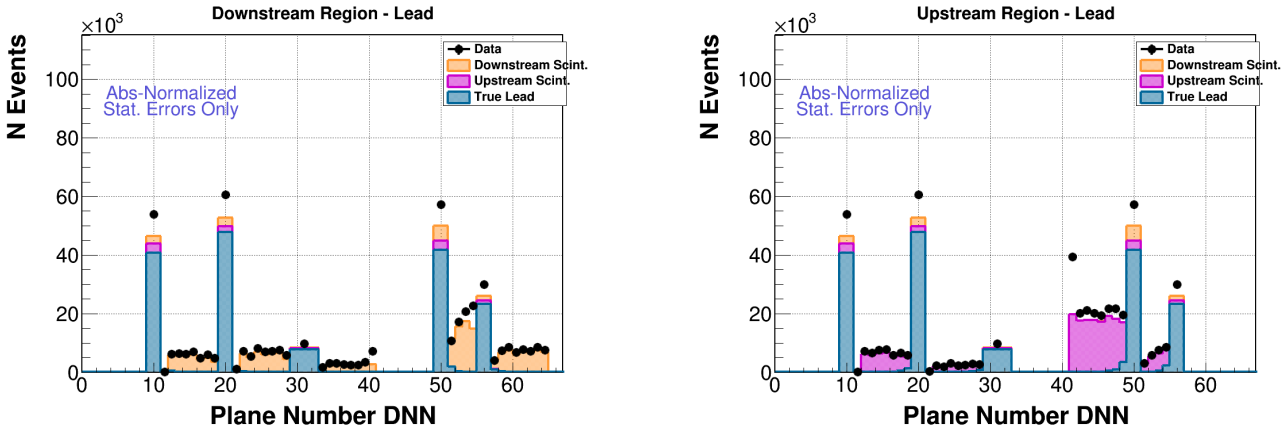

Figure 10-2: Event distribution of the DIS sample in the nuclear target region. Downstream plastic and passive target (left). Upstream plastic and passive target (right).

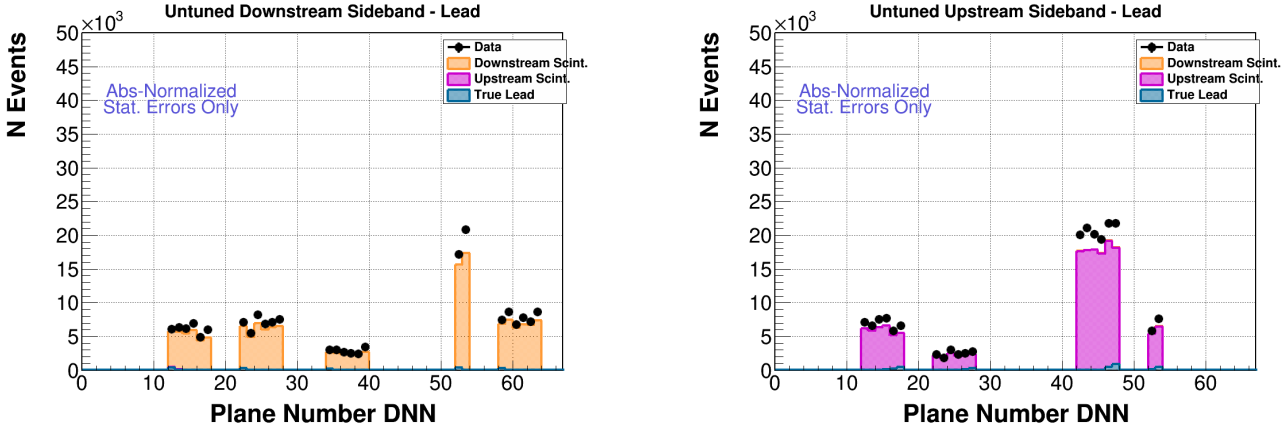

Figure 10-3: Event distribution of the DIS sample in the sideband region of a target material. Downstream plastic region (left). Upstream plastic sideband region (right). Note that a few events that truly originate in our target nuclei do make it in to the sideband sample, but this contribution is negligible.

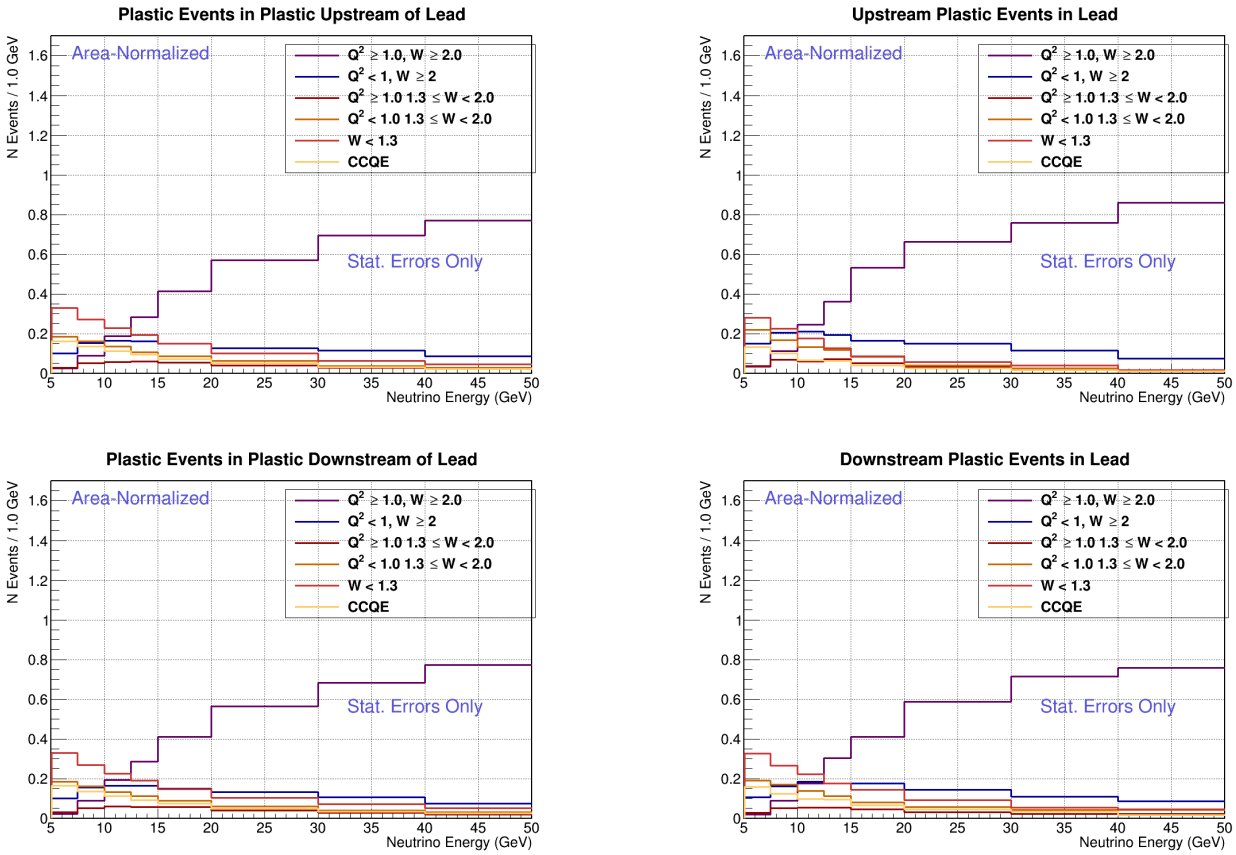

Figure 10-4: The shape of the upstream plastic backgrounds as a function of E_ν, separated by their true vertex interaction, in the sideband region (top left) compared to the signal region (top right). The shape of the downstream plastic backgrounds as a function of E_ν, separated by their true vertex interaction, in the sideband region (bottom left) compared to the signal region (bottom right). The colors represent the true material.

10.1.2 Plastic Background Fitting Prescription

For events in the Inclusive sample, two MC plastic background templates are fit to the data. The first template (upstream plastic template) consists of the sum of all events where the interaction vertex is reconstructed in the plastic region that is shadowing the target material upstream. The second template (downstream plastic template) consists of the sum of all events where the interaction vertex is reconstructed in the plastic region that is shadowing the target material downstream. The two templates are fit simultaneously to the data in both sidebands using a χ^2 minimization for each plane number bin i,

$$\chi^2 = \sum_{\text{bin i}} \frac{(N_{\text{DATA}} - N_{\text{MC}})^2}{\sigma^2_{\text{DATA}}}. \tag{10-2}$$

The fits are performed for each passive target material between plane number 11 to 65. This set of plane numbers encompasses the plastic scintillator tracker immediately downstream of passive target 1 through four scintillator modules downstream of target 5. The results of the fits are two scale factors for each material (Table 10-1). We extract the scale factor as follows:

- Extract upstream plastic scale factors using the ROOT Minuit2Minimizer function [158] by allowing the amount of events occurring in the upstream plastic to float while keeping the signal, the event from other passive targets upstream of the reconstructed target, and downstream plastic events fixed.

- Extract downstream plastic scale factors using the ROOT Minuit2Minimizer function by allowing the amount of events occurring in the downstream plastic to float while keeping the signal, the event from other passive targets downstream of the reconstructed target, and upstream plastic events fixed.

- MC is scaled to data using POT normalization, then the data to MC ratio is compared before the tuning and after the tuning (Figure 10-5). The fitting procedure is considered acceptable if the χ^2 is close to 1,

$$\chi^2 = \sum_{\text{bin i, bin j}} (N_{\text{bin i,Data}} - N_{\text{bin i,MC}}) \times \sigma M_{\text{bin i, bin j}} \times (N_{\text{bin j,Data}} - N_{\text{bin j,MC}}) \,. \quad (10\text{-}3)$$

Table 10-1: Upstream and downstream scale factors for each material.

Material	Upstream	Downstream
Carbon	1.08 ± 0.01	1.09 ± 0.01
Iron	1.09 ± 0.01	1.01 ± 0.01
Lead	1.1 ± 0.01	1.09 ± 0.01

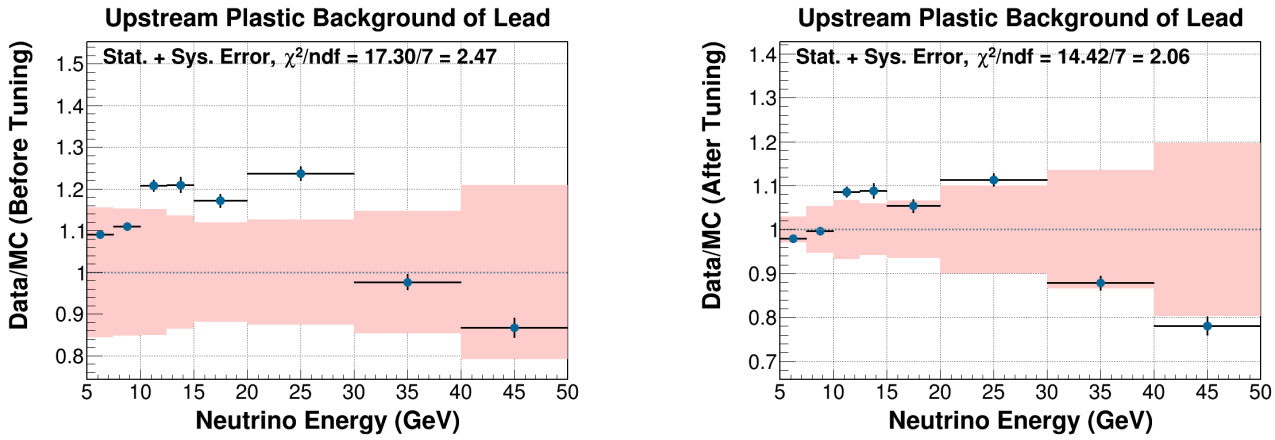

Figure 10-5: Data to MC ratio before the plastic background tuning (left). Data to MC ratio after the plastic background tuning (right).

10.1.3 Tuning Plastic Background

We apply the scale factors in Table 10-1 to the upstream plastic background templates and downstream plastic background templates in each of the nuclei in the passive targets. After the plastic backgrounds are tuned, the tuned plastic backgrounds are subtracted from data. This procedure is illustrated in Figure 10-6.

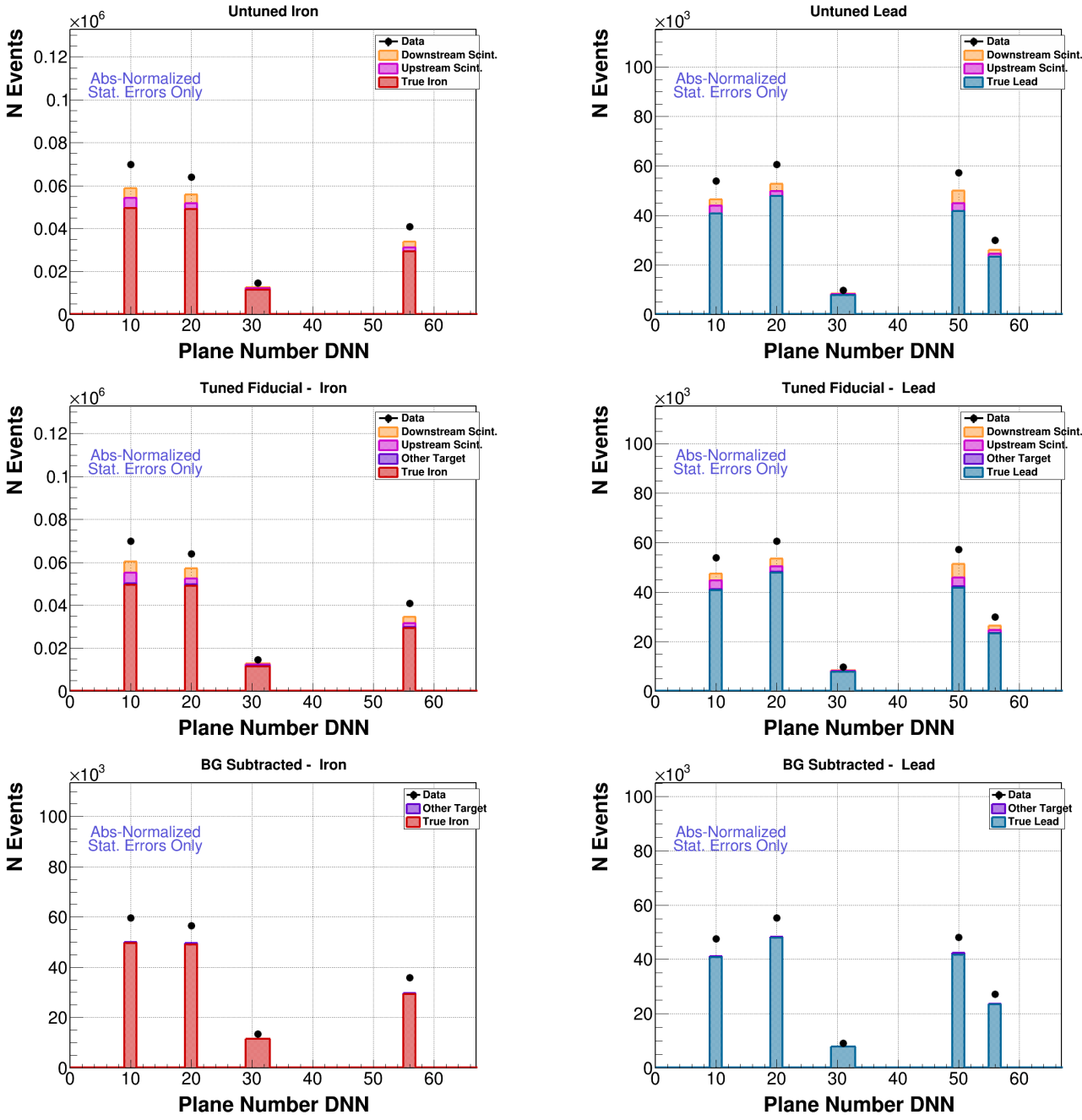

Figure 10-6: Top row: Event distribution as a function of plane number before the MC plastic background is tuned. Middle row: Event distribution as a function of plane number after the MC plastic background is tuned. Bottom row: Event distribution as a function of plane number after the MC plastic background is tuned and the tuned background is subtracted from data.

10.1.4 Plastic Background Fit Results

The upstream and downstream distribution of the plastic background is modeled using simulation. To improve the statistical precision each material is combined across all passive targets. This procedure is validated in sideband and fiducial regions that contain events from the signal and sideband regions. As demonstrated in Figure 10-5, the fit at higher energy (30 GeV $< E_\nu <$ 50 GeV) tends to lead to higher discrepancy between data and MC as those bins tend to underestimate the number of plastic events in the sideband region as opposed to the overestimation seen in lower energy bins.

The table of the χ^2 for each material as a function of various kinematics variables before and after the tuning are presented in Table 10-2 and Table 10-3. It is important to note that the χ^2 calculated here includes the errors coming from systematic uncertainties. Figure 10-5 shows that the systematic uncertainties improve across all energy spectrum but significantly so at the low energy bins. This causes the ratio after the fit at the two last bins to sit just outside the systematic errors band and increases the value of the χ^2 after the fit.

The fit can be improved by increasing the statistical size of the MC sample. The MC sample used in this dissertation is less than 20% of the projected MC sample that is going to be utilized for the nuclear target DIS analysis publication. Despite some discrepancy, the plastic background procedure works sufficiently well in removing most of the plastic background in data prior to cross-section extraction.

Table 10-2: χ^2/ndf for Upstream Plastic Sideband.

Variable	Carbon		Iron		Lead	
	Before Fit	After Fit	Before Fit	After Fit	Before Fit	After Fit
Neutrino Energy	2.06	2.28	2.08	2.42	1.08	0.88
Muon Energy	3.17	3.13	2.28	2.26	0.85	0.62
Hadronic Energy	1.23	2.89	2.09	0.87	0.61	0.38
Muon Angle	0.80	0.78	0.37	0.37	1.30	0.34
Q^2	1.06	1.18	1.72	0.69	0.61	0.54
W	2.08	1.94	2.11	2.10	0.99	0.47
Bjorken-x	0.93	0.77	0.66	0.16	1.59	1.43
y	0.94	0.73	0.83	0.40	1.12	1.06

Table 10-3: χ^2/ndf for Downstream Plastic Sideband.

Variable	Carbon		Iron		Lead	
	Before Fit	After Fit	Before Fit	After Fit	Before Fit	After Fit
Neutrino Energy	1.56	1.53	1.67	1.71	1.69	1.76
Muon Energy	3.08	2.96	2.70	2.58	2.96	2.87
Hadronic Energy	1.90	2.42	1.58	1.68	2.25	1.30
Muon Angle	2.18	2.12	0.65	0.62	0.70	0.67
Q^2	1.39	1.57	1.19	1.42	0.88	0.88
W	1.62	1.76	2.67	2.13	1.45	1.69
Bjorken-x	1.31	1.13	1.50	1.29	1.65	1.36
y	1.33	1.12	0.85	0.51	0.78	0.47

10.2 Non-DIS Background

The DIS sample is selected by isolating events with reconstructed $Q^2 < 1$ (GeV/c)^2 and reconstructed $W > 2$ GeV/c^2. The non-DIS background events are the events that erroneously pass the kinematic selection cuts but that are not truly DIS events. These backgrounds can be separated into two categories with comparable statistics. Comparing across the target materials, the largest background within the non-DIS category consists of events with true $W > 2$ GeV/c^2, but true $Q^2 < 1$ (GeV/c)^2, known as the continuum region. The next background comes from events having true $W < 2$ GeV/c^2, referred to as the transition region. Table 10-4 gives the breakdown of the different components of each category.

It is observed that with this method of classification, backgrounds that include $Q^2 < 1$ are the larger contributor for passive targets located further downstream. These type of events are typically dominated by events with low muon energy. As the interaction vertex moves further downstream, muons with lower reconstructed energy (compared to true muon energy) are more likely to exit the detector and reach the MINOS detector to be charged analyzed. Initially, two sidebands with *reconstructed* $0.4 < Q^2 < 0.8$, $W \geq 2.0$ (low Q^2 sideband) and $1.5 \leq W < 1.9$, $Q^2 \geq 1.0$ (low W sideband) were selected to estimate the background present in the signal region (see Figure 10-7).

The true number of DIS events, truly occurring in a nucleus N, T_N, is equal to the number of reconstructed DIS events reconstructed in a nucleus N, R_N, minus the number of reconstructed DIS events truly in the surrounding scintillator CH, R_{CH}, and minus the true *non*-DIS events reconstructed in the nucleus N, C_N :

$$T_N = (R_N - R_{CH}) - C_N \tag{10-4}$$

R_{CH} is estimated from the MC. This MC simulation is tuned to the data following the procedure outlined in Section 10.1.1. R_{CH} is measured for the data and MC, by using the plastic-enriched sideband region of the scintillator modules surrounding the passive target. The number R_{CH} is obtained by constraining the sideband region to data using the procedure described in section 10.1.2.

Table 10-4: Breakdown of contamination events which passed the reconstructed DIS cuts. The percentage quoted is the percentage of total contamination events falling into that W and Q^2 region. The W and Q^2 values are true values.

Target / Z	$W < 2.0$ All Q^2	$W \geq 2.0$ $Q^2 < 1.0$
1 / 26	51.%	48.5%
1 / 82	52.8%	46.9%
2 / 26	48.1%	51%
2 / 82	53.5%	45.3%
3 / 6	40.06%	58.5%
3 / 26	44.6%	55.1%
3 / 82	43.16%	56.2%
4 / 82	46.7%	51.7%
5 / 26	45.32%	54.2%
5 / 82	46.2%	52.9%

10.2.1 Constructing Non-DIS Background Sidebands

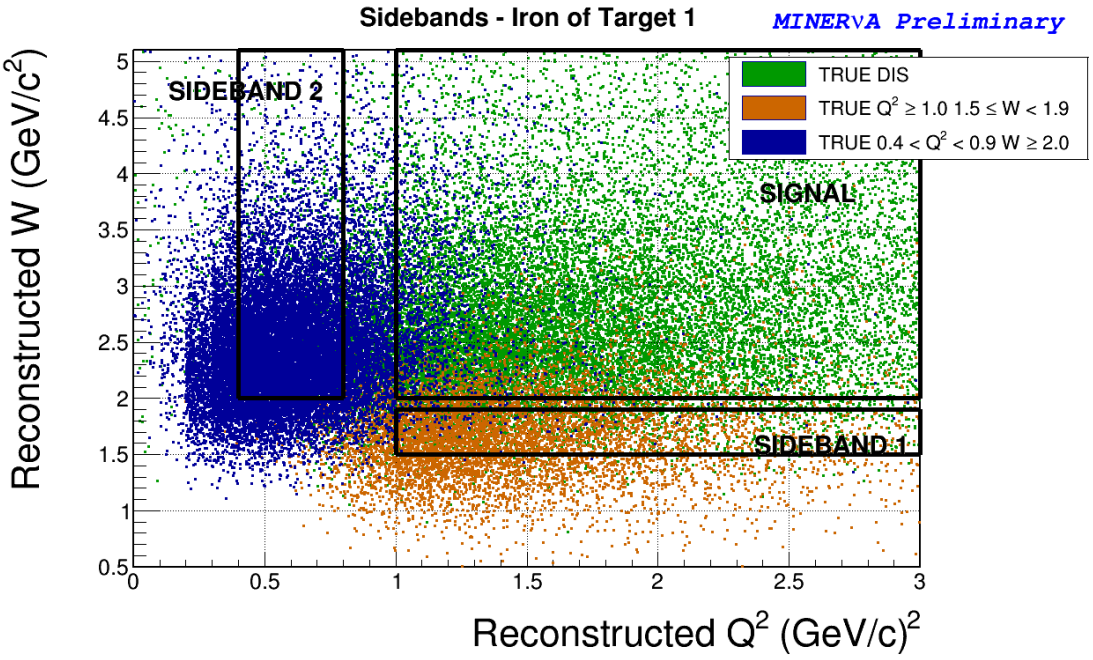

Figure 10-7: Reconstructed W vs. reconstructed Q^2, with the two sidebands labeled. The green dots are true DIS events. The blue and orange dots in the top-right box labeled signal are from non-DIS backgrounds.

The boundary on the reconstructed sideband regions are adjusted to reduce the amount of signal events in the sideband, while still ensuring the kinematics of the sideband sufficiently emulate the kinematics of the true non-DIS background present in the signal region. The procedure for DIS sideband construction in ME inherits the framework from the LE, with several updates. The higher statistics in the ME allows the regions for reconstructed sidebands in low W and low Q^2 to be reduced and moved closer to the reconstructed signal region as shown in Figure 10-7. Subsequently, this allows the events in the sidebands region to better model the background in the signal region.

The low Q^2 sideband boundary region is further adjusted to determine the lowest Q^2 boundary where the kinematics of the sideband still resemble the kinematics of the true contamination. The boundary of the low Q^2 sideband is lowered to $Q^2 = 0$. The shape of this sample ($Q^2 < 0.9$ $W \geq 2.0$) is compared to the shape of the backgrounds. It is

concluded that the shape of the backgrounds in W with an extension to the $Q^2 < 0.4$, $W \geq 2.0$ events closely resembles the shape of the W of the true contamination in the signal region, and the Q^2 cut of the sideband may be lowered to $Q^2 = 0$. This is demonstrated in Figures 10-8 and 10-9.

The MC is separated into each of the different true components. The reconstructed low Q^2 band contains 20 % true DIS events, and the low W band contains approximately 5 % true DIS events. The MC templates were fit by keeping the true signal template fixed at the default GENIE prediction and allowing the fit to change the amount of the low W and low Q^2 background events. Plots of the POT normalized data and MC of each sideband as a function of E_ν, x_{bj}, Q^2, E_μ and θ_μ may be found in Appendix C.

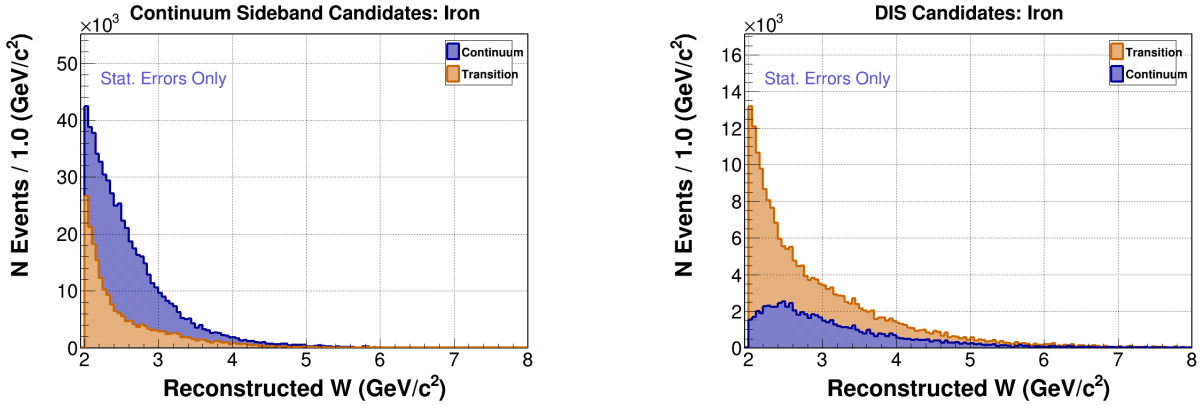

Figure 10-8: The shape of the backgrounds as a function of W in the sideband region compared to the signal region. The overall shape of the backgrounds in the sideband regions closely resembles the shape of the true contamination found in the signal region as a function of W.

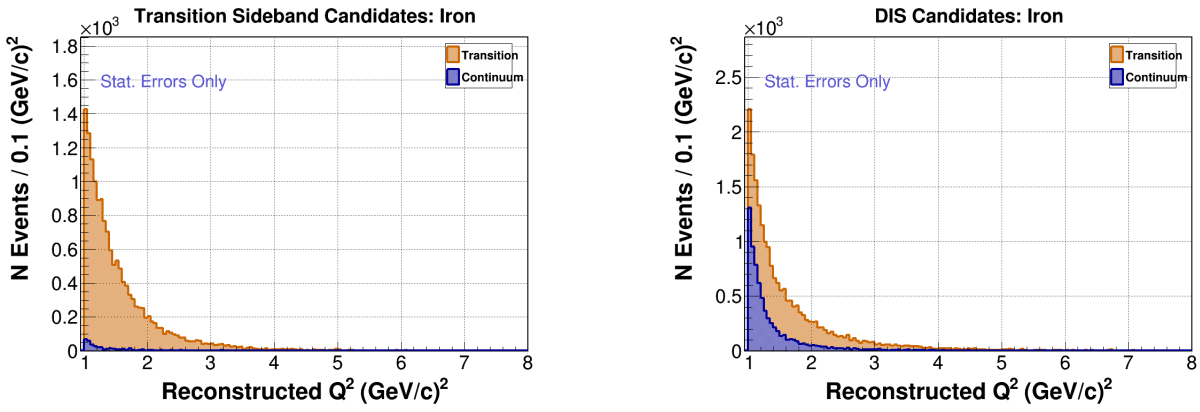

Figure 10-9: The shape of the backgrounds as a function of Q^2 in the sideband region compared to the signal region. The overall shape of the backgrounds in the sideband regions closely resembles the shape of the true contamination found in the signal region as a function of Q^2.

10.2.2 Non-DIS Background Fitting Prescription

We fit the two MC background templates to the data after we subtract the true plastic background from each sideband. The first template (template 1) consists of the sum of all events with $W < 2.0$. The second template (template 2) consists of all events with $W \geq 2.0$ but $Q^2 < 1.0$. We simultaneously fit the two templates to the data in both sidebands using a χ^2 minimization technique, with χ^2 defined as:

$$\chi^2 = \sum^{i} \frac{(N_{data} - N_{MC})^2}{\sigma^2_{data}}, \tag{10-5}$$

for each energy bin i.

We perform the fits for each passive target material combination and tracker region as a function of E_μ over the energy range $2 \leq E_\mu < 50$ GeV. The results of the fits for each target are two scale factors α and β. We use the fit results to scale template 1 and template 2 respectively.

Once again, since each sideband is statistics limited, it is preferable to combine materials from passive targets to obtain a more precise measurement of each scale factor. To prove that the fits to each target individually were consistent with a fit to the sum, a

statistical analysis was performed for each material with multiple targets (CH, Fe and Pb). The procedure and the results of the study is described in more detail in [159]. This analysis compares the consistency of α ($W < 2.0$) and β ($W \geq 2.0$, $Q^2 < 1.0$) of each target material combination to the error-weighted mean α and β of each material. In all but two cases, the average and individual scale factors did not differ by more than 1 σ.

10.2.3 Non-DIS Background Fit Results

After summing targets of identical materials, scale factors were derived for each material and each MC template. The extracted scale factors can be found in Table 10-5. The scale factors are applied to non-DIS events passing the DIS event selection cuts in the MC. This re-weighted MC is then subtracted from the candidate DIS events in data. For this fitting procedure, the plastic (wrong-nuclei) background subtraction is performed before subtracting the non-DIS events. In this sense, the plastic background predicted at each nuclear target comprises both DIS and non-DIS predictions. This is explained in further detail in Section 10.1.1. Data to MC comparisons of selected DIS events before and after background tuning are in Figure 10-10. These plots sum the different background components into true $W < 2.0$ and true $Q^2 < 1.0$ $W \geq 2.0$.

The complete set of distributions used to evaluate the non-DIS background are found in Appendix C.

Table 10-5: Scale factors of the two templates, derived from data and MC tuning for each material analyzed. The errors quoted in the table are statistical errors.

Material	low W scale (α)	low Q^2 scale (β)
CH	1.21 ± 0.14	1.29 ± 0.15
C	1.14 ± 0.21	1.11 ± 0.21
Fe	1.07 ± 0.1	1.03 ± 0.97
Pb	1.04 ± 0.99	1.02 ± 0.97

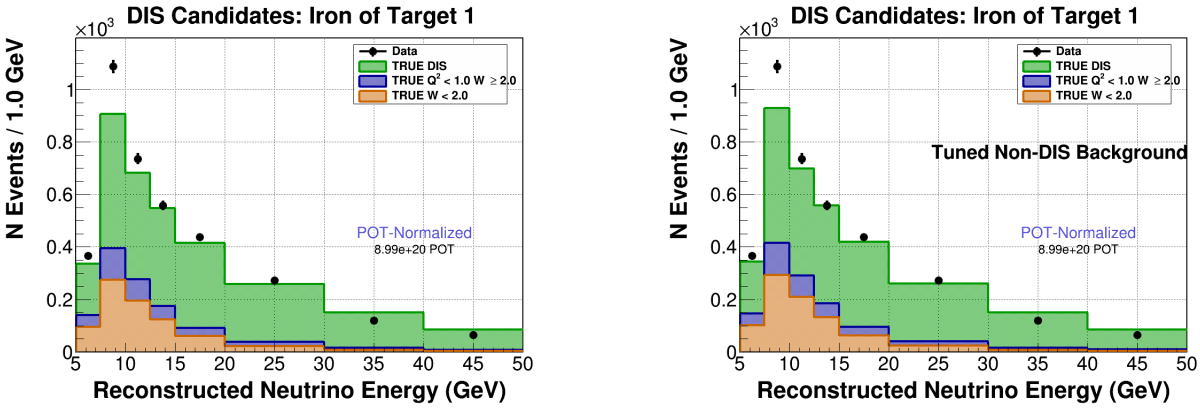

Figure 10-10: Events passing the DIS selection cuts in data (black points) as well as the MC signal (green) and background (orange and blue). The left plot is prior to the background tuning to data, and the right plot is after tuning.

CHAPTER 11
UNFOLDING

The final piece required for the numerator to calculate a cross-section is the unfolding matrix. Unfolding is the general term for removing the effect of a measuring device from a measurement. Following Equation 8-1, this means taking a measurement in bins of the reconstructed variable, j, and producing a result in bins of the true variable, i. This process is performed by the unfolding matrix U_{ij}, which describes the mapping between true and reconstructed bins.

11.1 Introduction to Unfolding

The act of measuring a physics observable will introduce smearing, or deviations away from the true value of the observable. What is measured is the reconstructed value of the observable, not the true value. To facilitate comparison with theoretical models and between experiments, physics analyses must unfold their distributions, removing detector effects from their results. Some examples of detector effects are losses due to the efficiency of the detector (acceptance), and smearing due to the finite resolution of the measuring device.

To understand smearing, consider a neutrino energy spectrum as a function of neutrino energy bin number. If the resolution is not perfect, some neutrinos with true incoming energy falling in one bin will be reconstructed in the neighboring bin instead (demonstrated in Figure 11-1).

In MINERvA, the smearing is somewhat complicated. Bin widths and resolution vary as a function of neutrino energy. As neutrino energy is reconstructed from summing up the muon energy and the recoil energy, edge effects in the smearing may occur since muons with true energy less than 2 GeV are not likely to reach the MINOS detector. An example of the edge effect is demonstrated in Figure 11-1 where events have been allowed to smear out of the distribution to the left and right while no events are permitted to

smear in, resulting in a suppressed spectrum at the low edge. In the data, edge effects and efficiency turn-on result in suppressing the low end of the neutrino spectra.

The reconstructed and true variable quantities are related by the migration matrix M_{ij}:

$$x_i = M_{ij} x_j. \tag{11-1}$$

M_{ij} is separately computed for each target from the MC. The goal of unfolding is to find the inverse of the migration matrix, the unfolding matrix, such that:

$$x_j = M^{-1}_{ji} x_i. \tag{11-2}$$

Typically, a migration matrix is not directly invertible. Inverting the migration matrix often causes the statistical uncertainty in bins of the reconstructed variable to inflate, leading to large fluctuations in the data. This is because neighboring bins in true space have very similar responses in reconstructed space. Thus, a small fluctuation in reconstructed space will, upon inversion, result in a large fluctuation of one true bin, with compensating changes in neighboring true bins to preserve the total normalization. This gives the characteristic bin-to-bin anti-correlations between adjacent bins where higher values of one bin tend to be associated with lower values of the adjacent bin.

The Bayesian unfolding method is employed in this analysis to regularize the unfolded results. This unfolding method is fully described in [160] and will be summarized in Section 11.3. This method restricts the allowed solutions to those in which the result fits some prior expectation. The two variables selected for unfolding were neutrino energy E_ν and Bjorken-x x_{bj}.

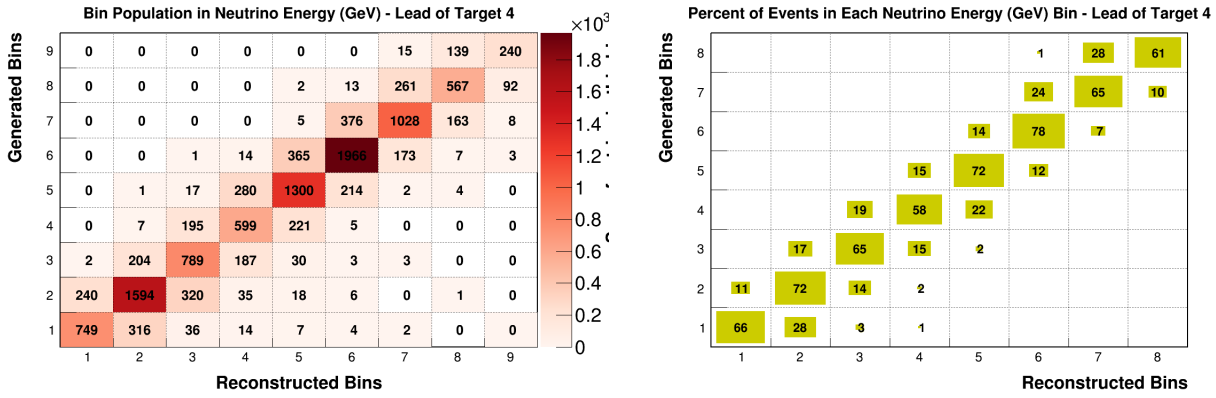

Figure 11-1: E_ν smearing effect on a neutrino energy spectrum as a function of neutrino energy bin number. Left: Each generated bin records the number of events smeared across the reconstructed bins. Right: Each generated bin records the fraction of events migrating across the reconstructed bins.

11.2 Bin Width Optimization

Unfolding is mostly affected by choice of the bin width. If the bin size of the unfolded distribution is too narrow compared to the resolution, the migration matrix has large off-diagonal elements. On the other hand, if the bin size is too large, the unfolded distribution will lose the sensitivity to high-frequency components of the true distribution. To determine the binning on the unfolded distribution, we start by choosing a reasonably large size of bin and then decrease the size in subsequent steps. We stop the process before the correlation between adjusted bins become too big.

The procedure described above is performed for all variables of interest in this analysis, except for x_{bj}. Specifically for x_{bj}, we have chosen the bin width based on the three regions of nuclear effects in DIS: shadowing ($0.01 < x_{bj} < 0.1$), anti-shadowing ($0.1 < x_{bj} < 0.3$), and the EMC effect ($0.3 < x_{bj} < 0.8$). We then divide the bin size in two to increase the sensitivity of the unfolded distribution. The statistics and the smearing effects in one bin are taken into consideration to decide the bin width in these regions of interest.

11.3 Unfolding Procedure

MINERvA employs the D'Agostini unfolding technique [160] that has been characterized as an algorithm for maximum-likelihood estimation with early stopping. When the algorithm converges, the result is equivalent to a matrix inversion in the Gaussian limit.

Unfolding is based on the Bayesian statistics, so bias is introduced to this method due to uncertainties in the underlying theoretical models of our MC. The unfolding matrix is calculated based on Bayes theorem [160]:

$$P(C_i \mid E) = \frac{P(E \mid C_i)\dot{P}(C_i)}{\sum_{l=1}^{n_e} P(E \mid C_i)\dot{P}(C_i)}, \tag{11-3}$$

where C_i is the ith cause that can produce an effect E. In this case, the C_i represents the true kinematic variables, and the effect is the measured kinematic observable. $P(E \mid C_i)$ is the same as M_{ij} in Equation 11-1; the probability that an event in a reconstructed bin representing E comes from a true bin i. We can apply this method for several effects or several reconstructed variable bins, by noting that:

$$P(C_i \mid E_j) = \frac{P(E_j \mid C_i)\dot{P}(C_i)}{\sum_{l=1}^{n_e} P(E_j \mid C_i)\dot{P}(C_i)}, \tag{11-4}$$

where E_j represents the reconstructed variable bin j. Unfolding the reconstructed variable spectrum should yield the true spectrum, or the number of events in each true bin $\hat{n}(C_i)$. The number of events in each bin must be given by:

$$\hat{n}(C_i) = \sum_{j=1}^{N_j} P(E_j \mid C_i)\dot{\hat{n}}(E_j). \tag{11-5}$$

The procedure for obtaining $\hat{n}(C_i)$ is as follows:

- Select an initial distribution for $P_0(C_i)$, the initial guess at the unfolded distribution, subject to the constraint that

$$\sum_{j=1}^{N_j} P_0(C_i) = 1. \tag{11-6}$$

  In this analysis, the true MC distribution (true signal distribution) functions as the "best" initial guess at the spectrum. This guess also selects the initial expected number of events $\hat{n}_0(C_i) = P_0(C_i)\dot{N}_{obs}$.

- Calculate $\hat{n}(C_i)$ and $P(C_i)$

- Perform a χ^2 comparison between $\hat{n}(C_i)$ and $\hat{n}_0(C_i)$.

- Replace $P_0(C_i)$ with $P(C_i)$ and $\hat{n}_0(C_i)$ with $\hat{n}(C_i)$ and restart the process. After the second iteration, if the χ^2 value < 0.001, stop the iteration; otherwise we will repeat step 2.

Unfolding using the Bayesian method provides several advantages over other methods. First, the method does not depend on the shape of the distribution being unfolded. Second, although a realistic starting guess produces the best results, the method can still provide a satisfactory result from a uniform initial distribution. Finally, the Bayesian unfolding does not require matrix inversion which can fail when the migration matrix is singular.

A systematic error will be assigned to cover the signal model dependence. This is calculated by varying the M_{ij} matrix by changing systematics so uncertainties in the signal cross section is part of the final error. This method, however, will fail if M_{ij} is highly non-diagonal.

The entire reconstructed MC sample used for building the migration matrix is composed of events that are truly DIS and truly originating from the measured target. The migration matrices of each target and material combination are constructed from the reconstructed and true (generated) x_{bj} and E_ν. The number of unfolded iterations was

tuned using fake data studies described in section 11.4. The reconstructed data from each target combination is then unfolded using the MinervaUnfold package with Bayesian unfolding described above.

Each event in the migration matrix passed all reconstruction cuts, as well as the true DIS and true material cuts. In general, the measured migrations are similar from target to target (see Figure 11-2 and 11-3).

Plots of migration matrix variables target by target may be found in Appendix D

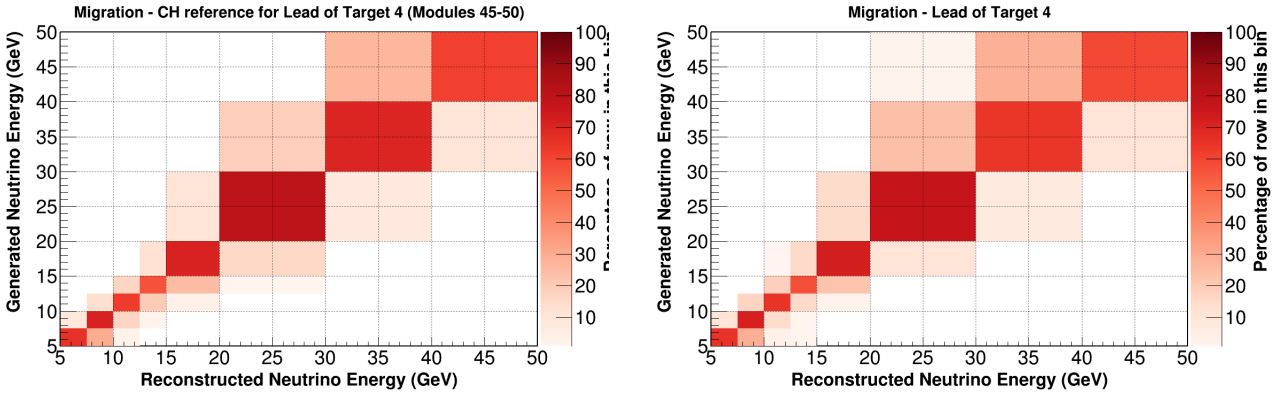

Figure 11-2: Neutrino energy migration for tracker modules 45 - 50 (left) and target 4 (right). The y-axis is generated (true) E_ν and the x-axis is reconstructed E_ν. Each cell records the percent of true and reconstructed DIS events.

11.4 Unfolding Tuning

Prior to unfolding, a fake data study is conducted to determine the number of unfolding iterations as well as to monitor any biases that may occur in unfolding. The study re-weights the non-DIS background data tuned MC and uses the migration matrices that are reconstructed following the procedure described in Section 11.3. Fake data is generated by re-weighting the MC according to a re-weighting function $f(x_{bj})$, which mimics the data to MC ratio in each bin. The details of this procedure are given in [159]. The analysis generates 500 universes of fake data and unfolds the fake data using 0 to 6 iterations. For each iteration, the difference between the mean unfolded and true number of events is calculated. As the number of iterations increases, the mean tends to stay

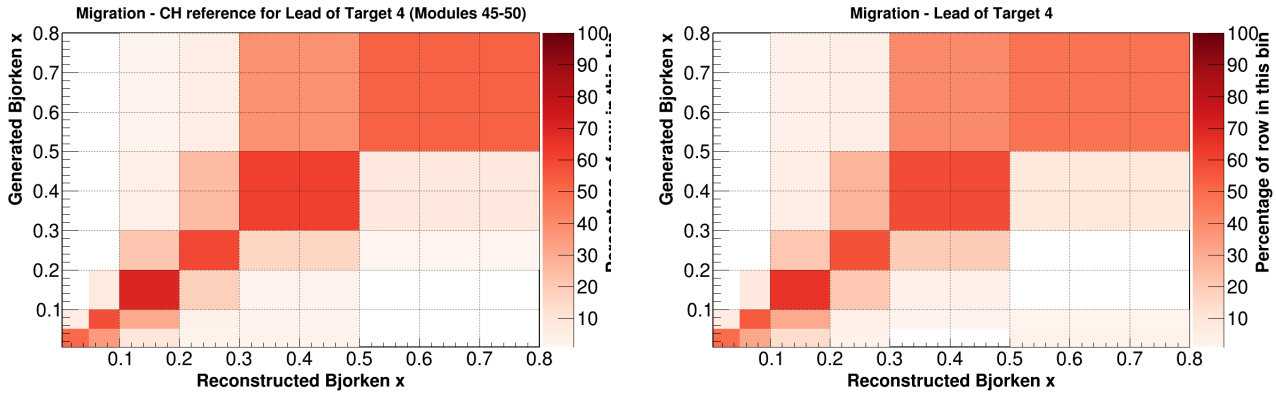

Figure 11-3: Bjorken-x migration for tracker modules 45 - 50 (left) and target 4 (right). The y-axis is generated (true) x_{bj} and the x-axis is reconstructed x_{bj}. Each cell records the percent of true and reconstructed DIS events.

constant. However, it is important to note that with each successive iteration, statistical uncertainty is introduced to the distribution. This fake data study shows that using one iteration as a minimum number of iterations is sufficient to stabilize the unfolding.

11.5 Event Yields Prior to Unfolding

After finalizing all event selection cuts, the background estimations (CH and non-DIS), and unfolding, the analysis measures the number of DIS events per E_ν and x_{bj} bin for the nuclei C, CH, Fe, and Pb. The targets are summed material-by-material prior to making these plots. The C originates from nuclear target 3, the Fe from nuclear targets 1, 2, 3, 5, the Pb from nuclear targets 1, 2, 3, 4 and 5, and the CH from tracker modules 26 through 80.

Figures 11-4 through 11-7 show the DIS event distributions for C, CH, Fe, and Pb as a function of reconstructed neutrino energy along with the extracted plastic and non-DIS background. In each case, the non-DIS events and CH events are not yet subtracted. Figures 11-8 through 11-11 present the same information as a function of reconstructed Bjorken-x. The extracted CH and non-DIS backgrounds are then subtracted. Distributions after background subtraction, but still prior to unfolding, are shown in 11-12 through 11-19.

All figures do include a systematic error band, and a plot of the errors included in that band. Further discussion of the systematic errors is found in Chapter 13.

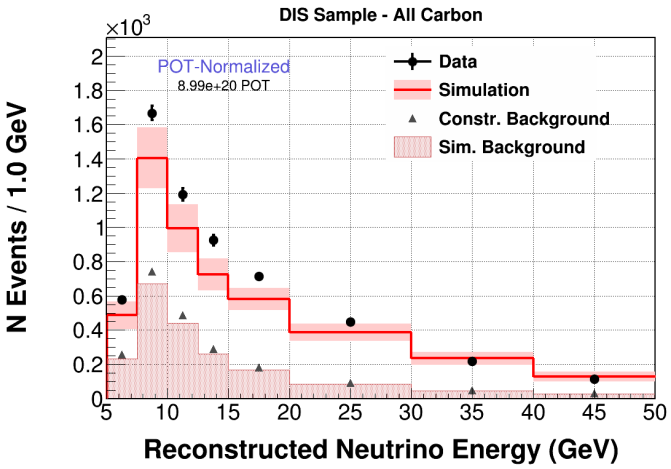

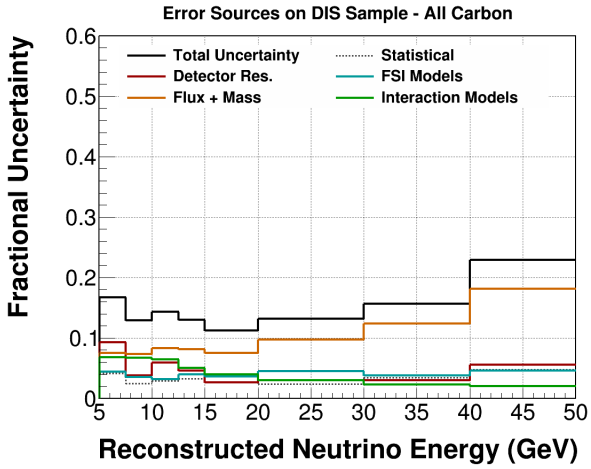

Figure 11-4: DIS events reconstructed in carbon per neutrino energy in data (black points) and Monte Carlo (red line) prior to background subtraction. The pink band around the line is the systematic error displayed on the right. The extracted CH background from the data (triangles) and MC (hatched plot) are drawn as well.

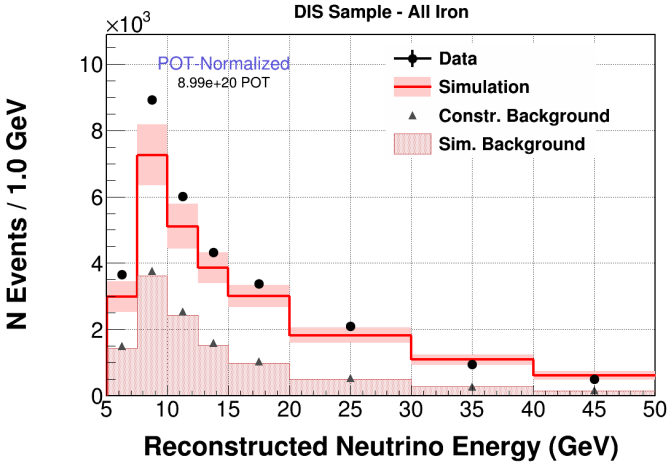

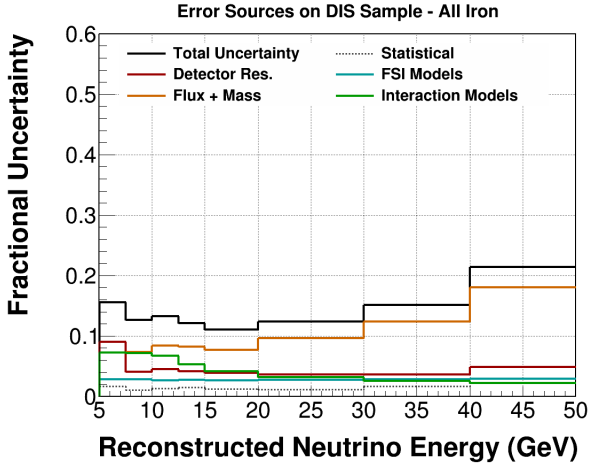

Figure 11-5: DIS events reconstructed in iron per neutrino energy in data (black points) and Monte Carlo (red line) prior to background subtraction. The pink band around the line is the systematic error displayed on the right. The extracted CH background from the data (triangles) and MC (hatched plot) are drawn as well.

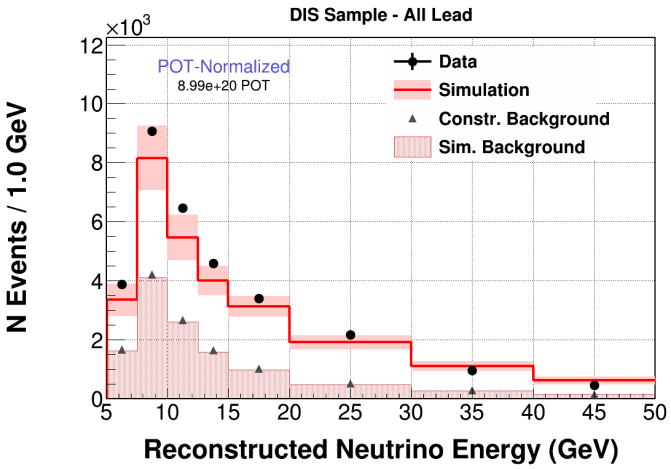

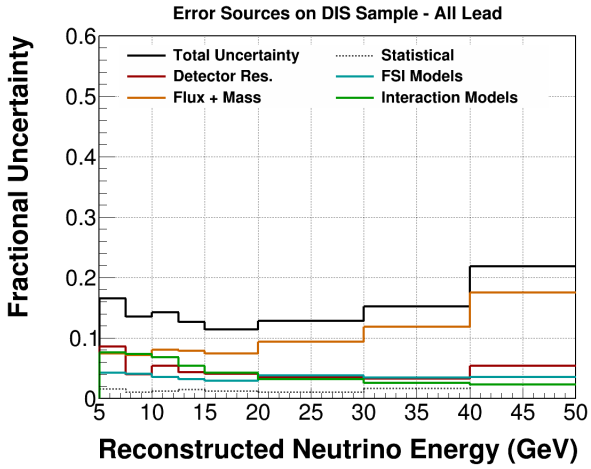

Figure 11-6: DIS events reconstructed in lead per neutrino energy in data (black points) and Monte Carlo (red line) prior to background subtraction. The pink band around the line is the systematic error displayed on the right. The extracted CH background from the data (triangles) and MC (hatched plot) are drawn as well.

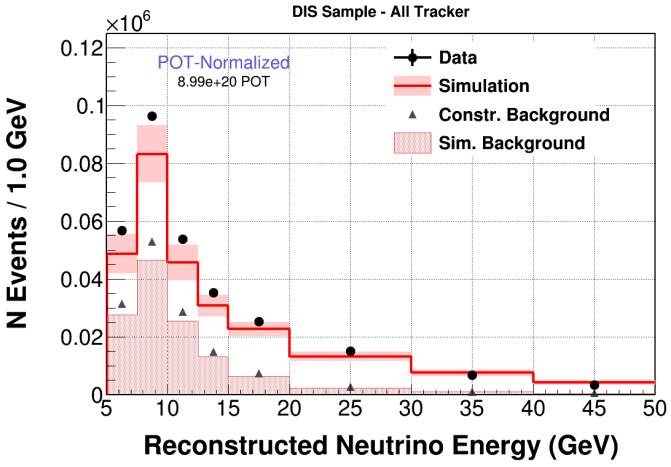

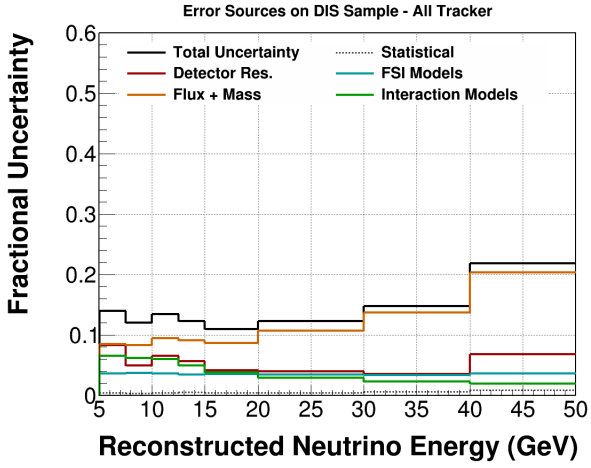

Figure 11-7: DIS events reconstructed in scintillator per neutrino energy in data (black points) and Monte Carlo (red line) prior to background subtraction. The pink band around the line is the systematic error displayed on the right. The extracted CH background from the data (triangles) and MC (hatched plot) are drawn as well.

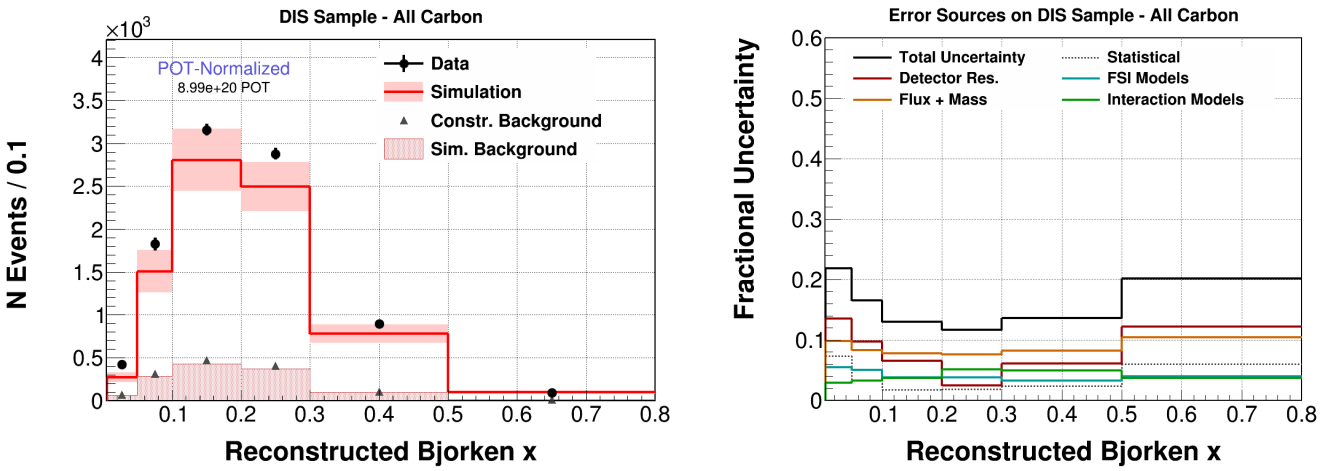

Figure 11-8: DIS events reconstructed in carbon per Bjorken-x in data (black points) and Monte Carlo (red line) prior to background subtraction. The pink band around the line is the systematic error displayed on the right. The extracted CH background from the data (triangles) and MC (hatched plot) are drawn as well.

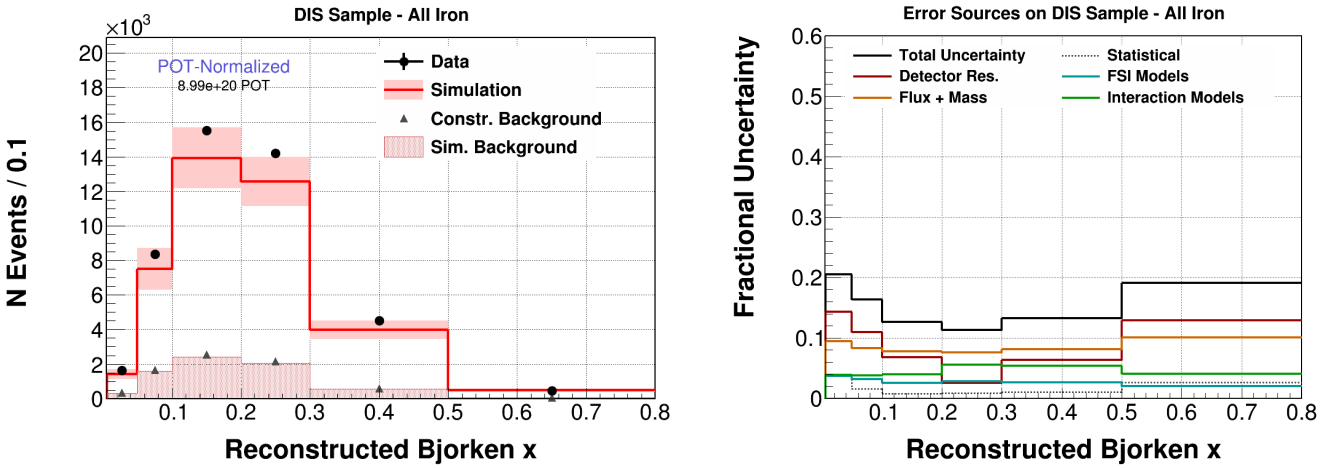

Figure 11-9: DIS events reconstructed in iron per Bjorken-x in data (black points) and Monte Carlo (red line) prior to background subtraction. The pink band around the line is the systematic error displayed on the right. The extracted CH background from the data (triangles) and MC (hatched plot) are drawn as well.

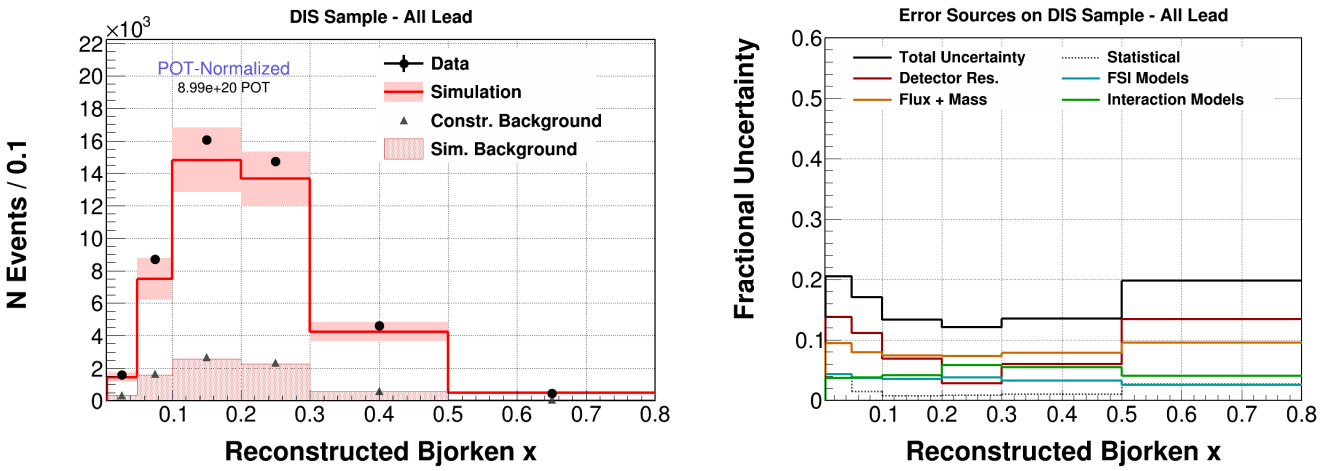

Figure 11-10: DIS events reconstructed in lead per Bjorken-x in data (black points) and Monte Carlo (red line) prior to background subtraction. The pink band around the line is the systematic error displayed on the right. The extracted CH background from the data (triangles) and MC (hatched plot) are drawn as well.

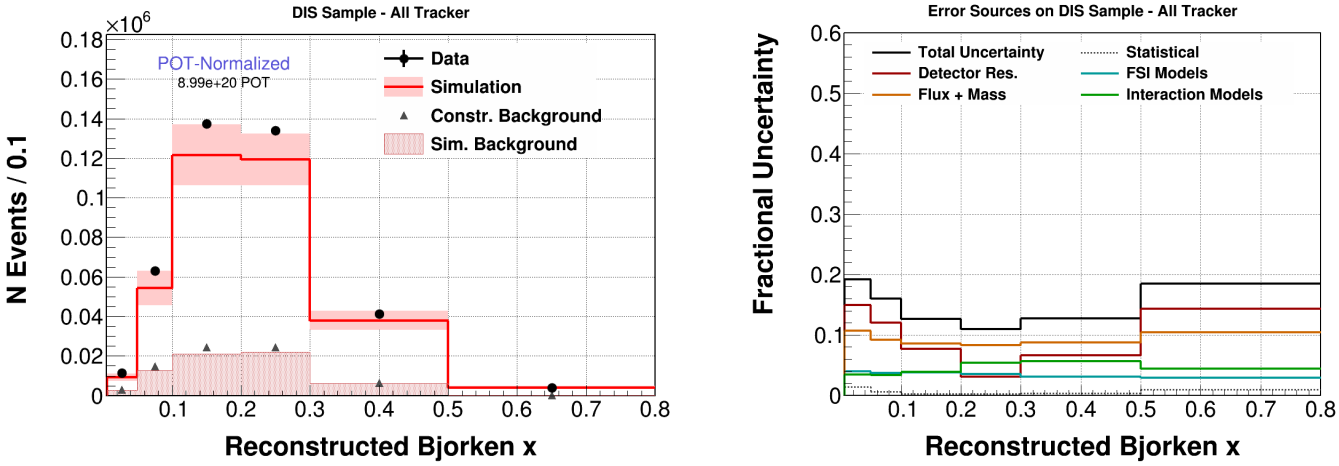

Figure 11-11: DIS events reconstructed in scintillator per Bjorken-x in data (black points) and Monte Carlo (red line) prior to background subtraction. The pink band around the line is the systematic error displayed on the right. The extracted CH background from the data (triangles) and MC (hatched plot) are drawn as well.

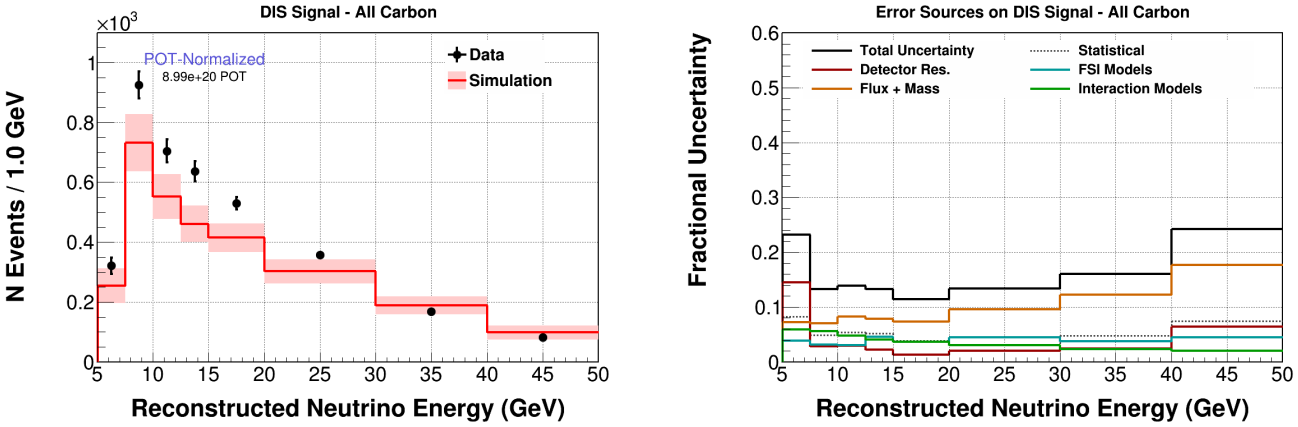

Figure 11-12: DIS events in carbon per neutrino energy in data (black points) and Monte Carlo (red line) after background subtraction. The pink band around the line is the systematic error displayed on the right.

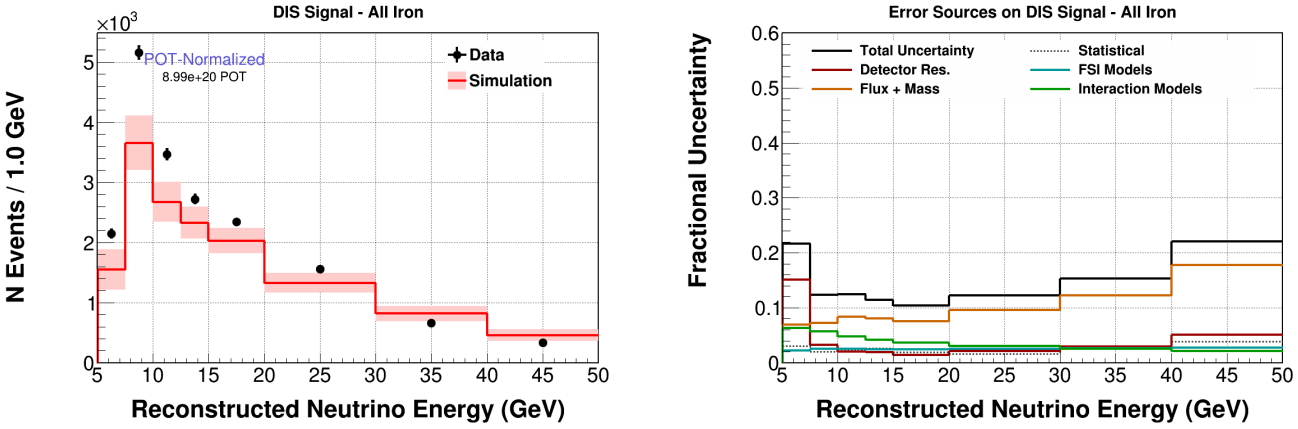

Figure 11-13: DIS events in iron per neutrino energy in data (black points) and Monte Carlo (red line) after background subtraction. The pink band around the line is the systematic error displayed on the right.

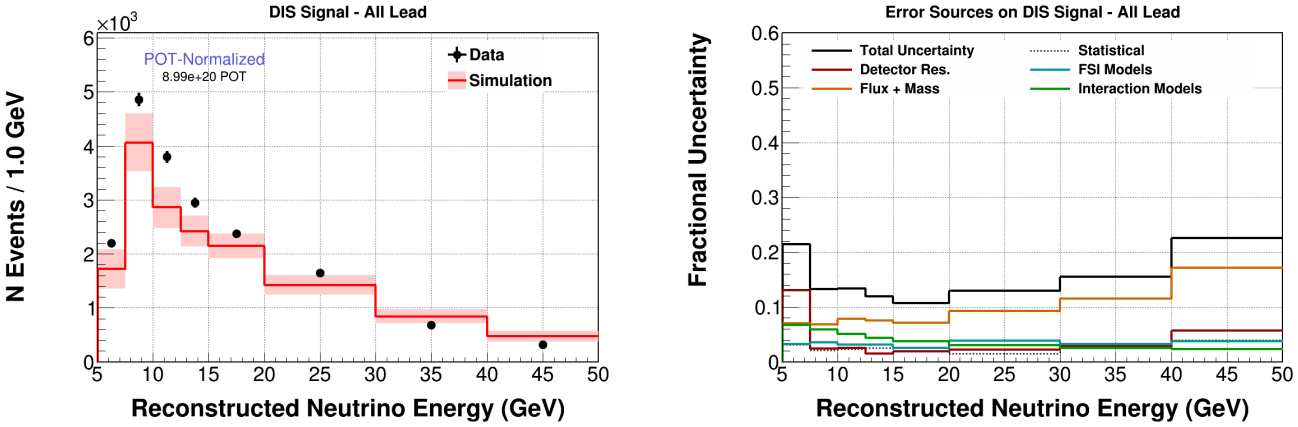

Figure 11-14: DIS events in lead per neutrino energy in data (black points) and Monte Carlo (red line) after background subtraction. The pink band around the line is the systematic error displayed on the right.

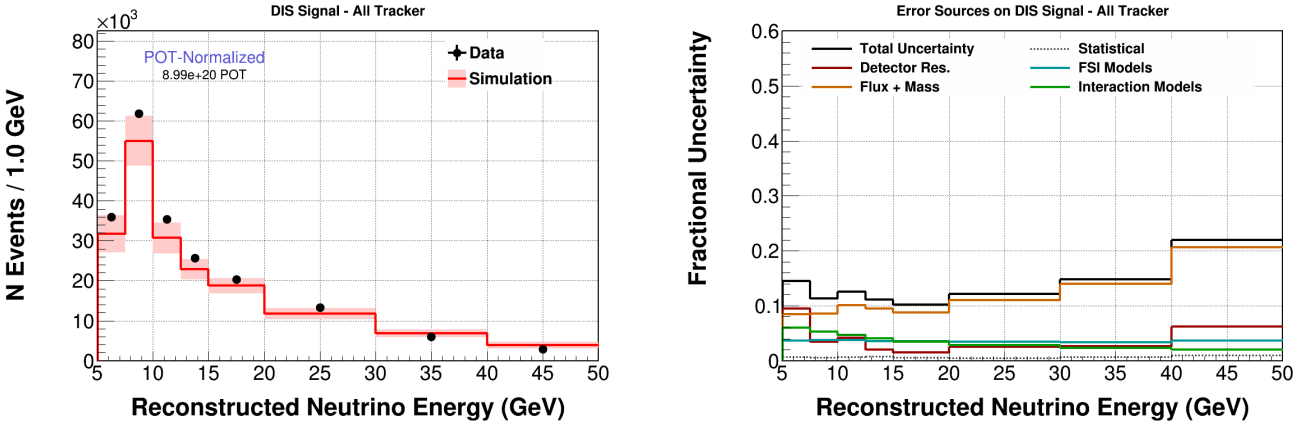

Figure 11-15: DIS events in scintillator per neutrino energy in data (black points) and Monte Carlo (red line) after background subtraction. The pink band around the line is the systematic error displayed on the right.

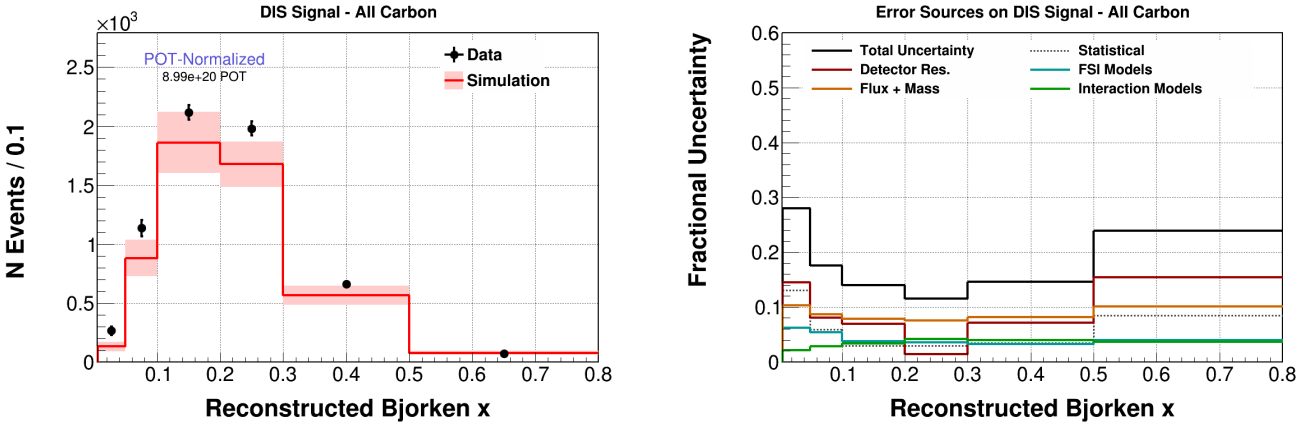

Figure 11-16: DIS events in carbon per Bjorken-x in data (black points) and Monte Carlo (red line) after background subtraction. The pink band around the line is the systematic error displayed on the right.

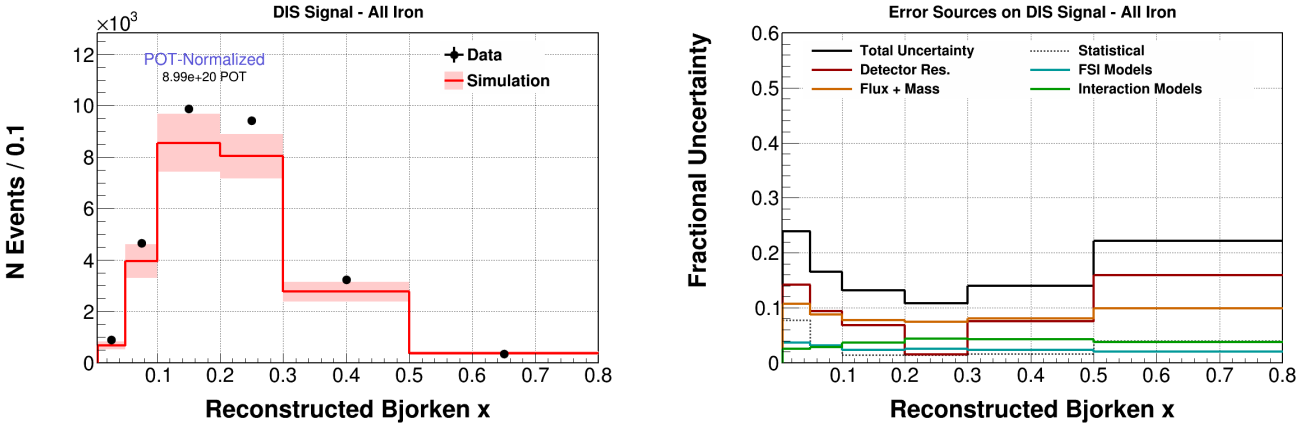

Figure 11-17: DIS events in iron per Bjorken-x in data (black points) and Monte Carlo (red line) after background subtraction. The pink band around the line is the systematic error displayed on the right.

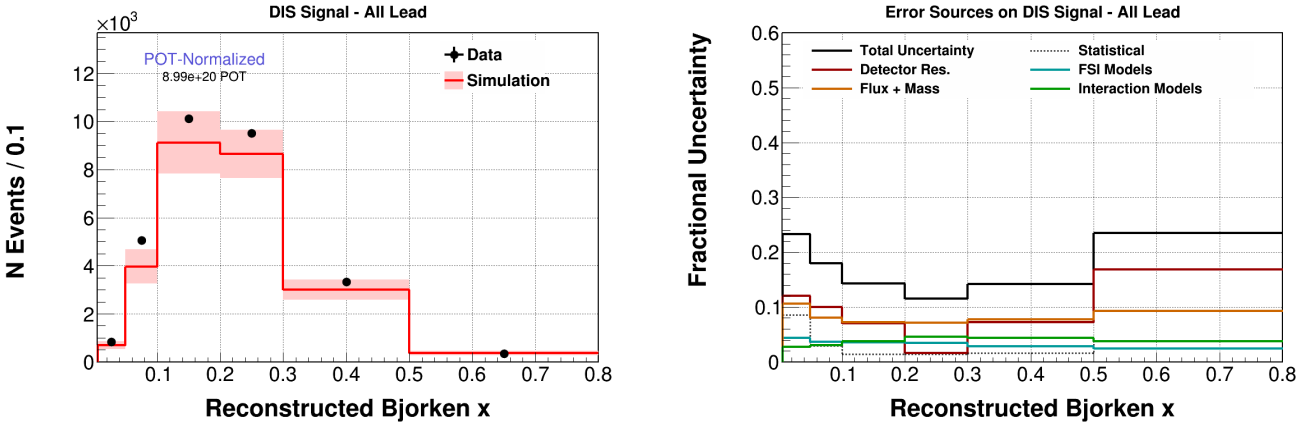

Figure 11-18: DIS events in lead per Bjorken-x in data (black points) and Monte Carlo (red line) after background subtraction. The pink band around the line is the systematic error displayed on the right.

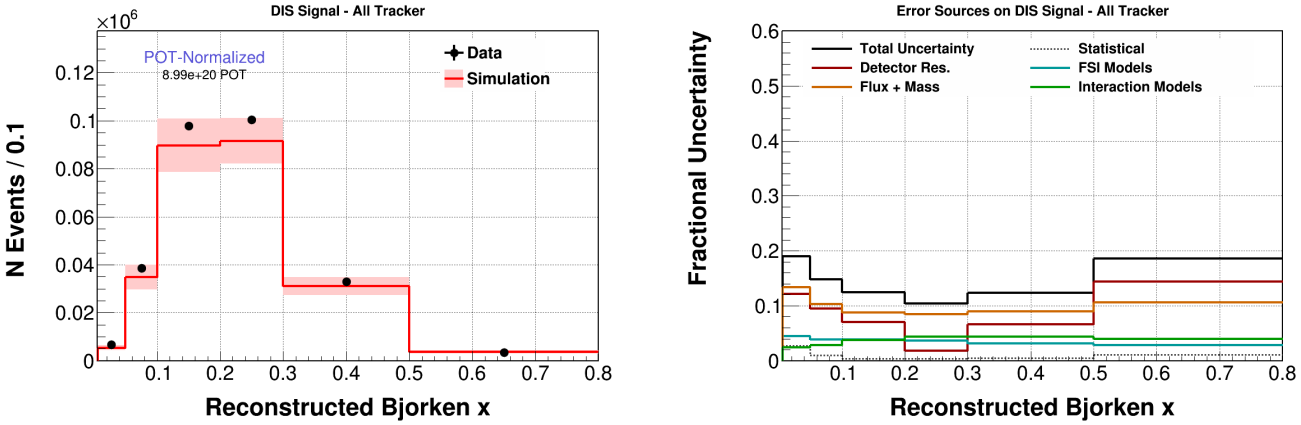

Figure 11-19: DIS events in scintillator per Bjorken-x in data (black points) and Monte Carlo (red line) after background subtraction. The pink band around the line is the systematic error displayed on the right.

11.6 Unfolded Kinematics

Unfolding is performed after subtracting the non-DIS and CH backgrounds. The neutrino energy and Bjorken-x distributions are unfolded separately for each target and nuclei, however for brevity only the plots of the sum of each nuclei after unfolding are presented.

Plots of the events in C, CH, Fe, Pb as a function of unfolded neutrino energy and Bjorken-x, along with the uncertainty are displayed in Figures 11-20 through 11-27. The process of unfolding introduces correlations into the statistical uncertainty. As a result, the statistical error of the data, calculated only from the *diagonal* errors, appears to decrease post unfolding. The separate universes used in calculating the systematic uncertainties are unfolded using a separate migration matrix calculated in that universe.

To gain a better understanding of the effect of unfolding, the reconstructed and unfolded versions are plotted side by side in Figures 11-28 through 11-35. Two trends are observed. In the case of E_ν, the unfolding does very little. The neutrino energy distribution has large bins necessary to get sufficient statistics in each bin. These bins, at least 5 GeV wide, are much larger than the neutrino energy resolution of the event sample. As a result, there is not much smearing bin to bin in neutrino energy. In the case of x_{bj}, most events are smeared from the peak of the x_{bj} distribution ($0.2 < x_{bj} < 0.4$) to the high x_{bj} tail ($0.4 < x_{bj} < 0.75$). This effect is seen across all nuclei.

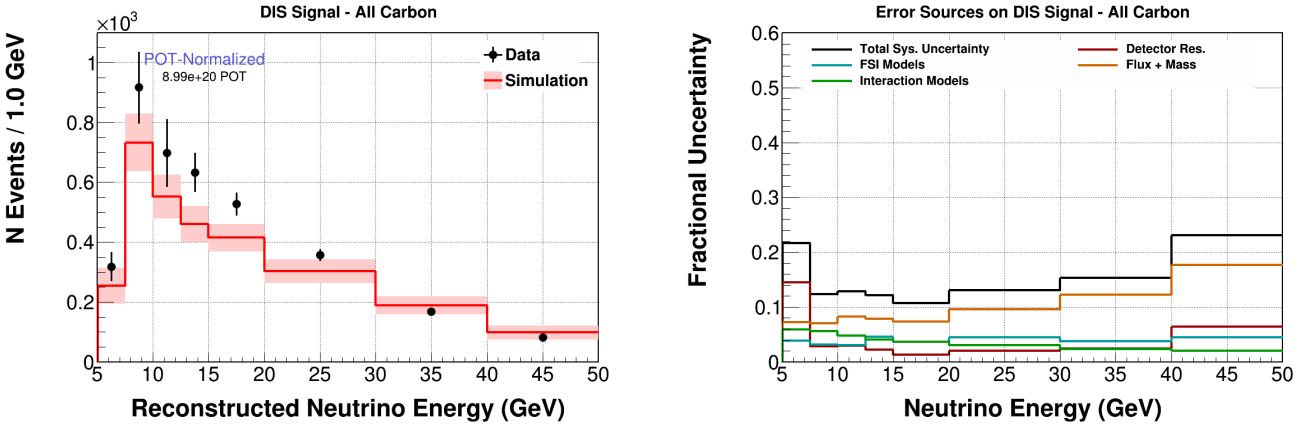

Figure 11-20: DIS events in carbon per unfolded neutrino energy in data (black points) and Monte Carlo (red line) after background subtraction. The pink band around the line is the systematic error displayed on the right.

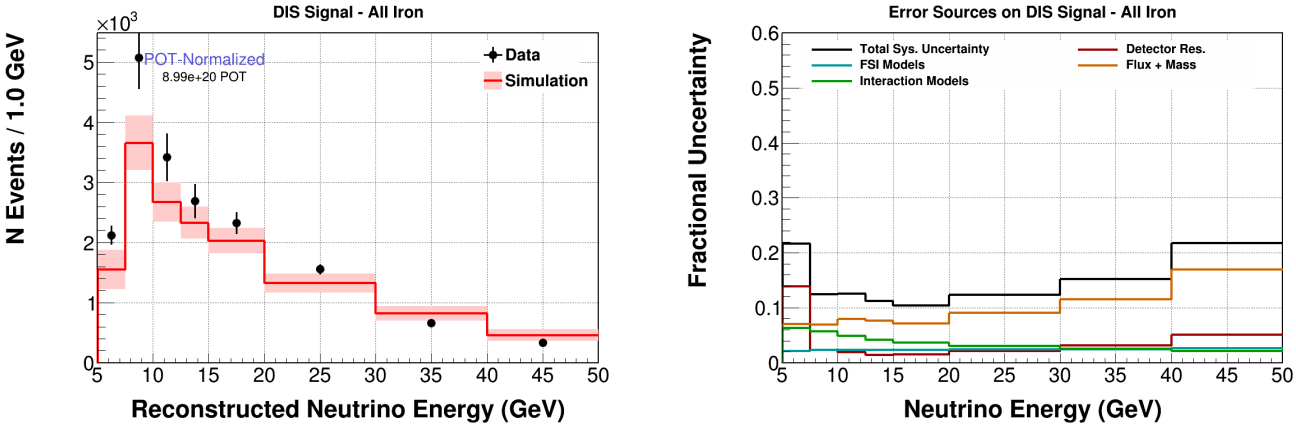

Figure 11-21: DIS events in iron per unfolded neutrino energy in data (black points) and Monte Carlo (red line) after background subtraction. The pink band around the line is the systematic error displayed on the right.

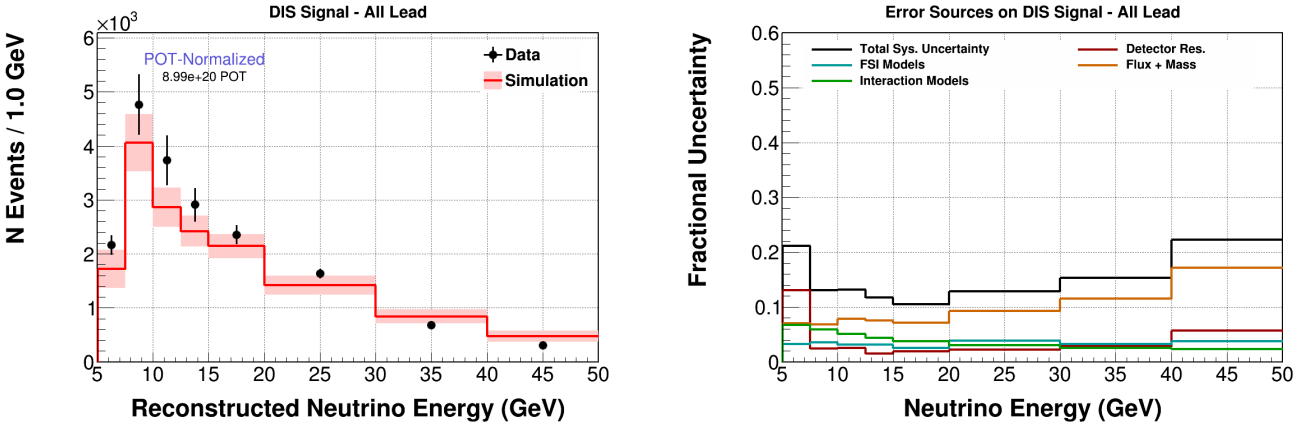

Figure 11-22: DIS events in lead per unfolded neutrino energy in data (black points) and Monte Carlo (red line) after background subtraction. The pink band around the line is the systematic error displayed on the right.

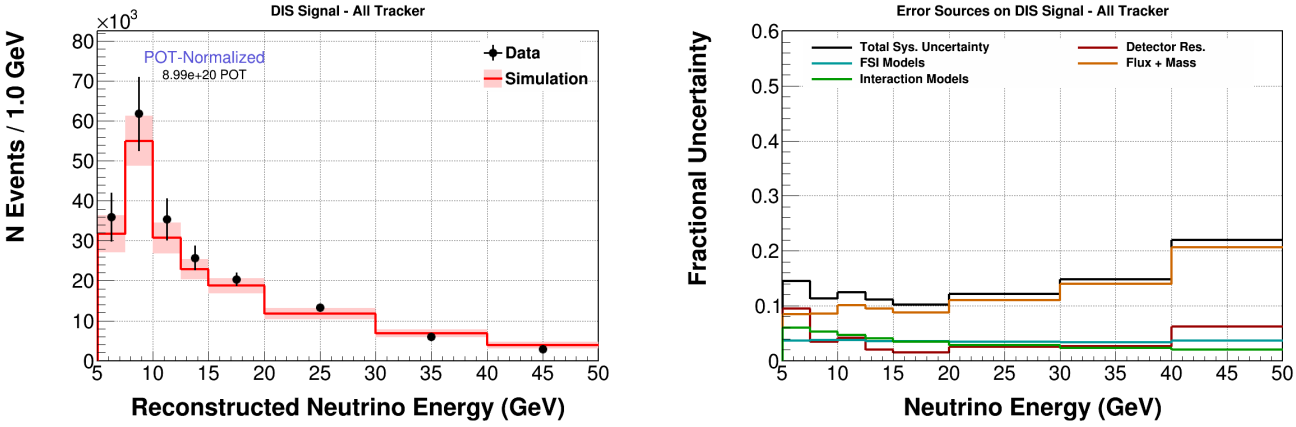

Figure 11-23: DIS events in scintillator per unfolded neutrino energy in data (black points) and Monte Carlo (red line) after background subtraction. The pink band around the line is the systematic error displayed on the right.

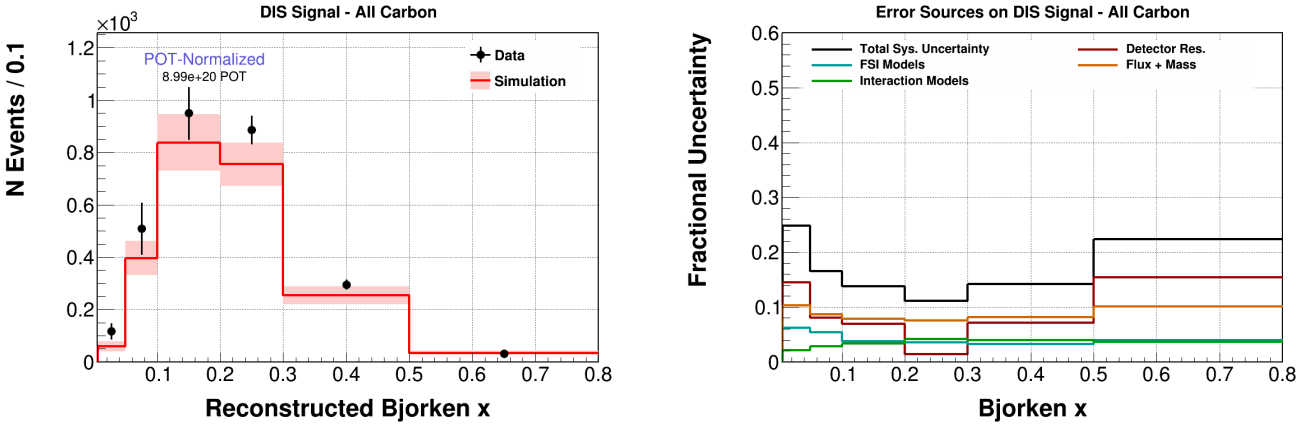

Figure 11-24: DIS events in carbon per unfolded Bjorken-x in data (black points) and Monte Carlo (red line) after background subtraction. The pink band around the line is the systematic error displayed on the right.

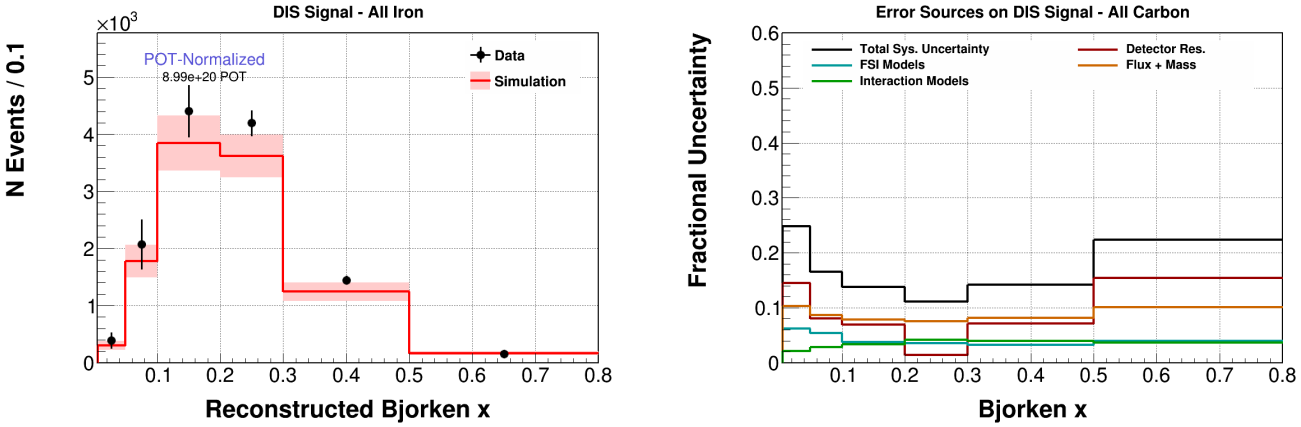

Figure 11-25: DIS events in iron per unfolded Bjorken-x in data (black points) and Monte Carlo (red line) after background subtraction. The pink band around the line is the systematic error displayed on the right.

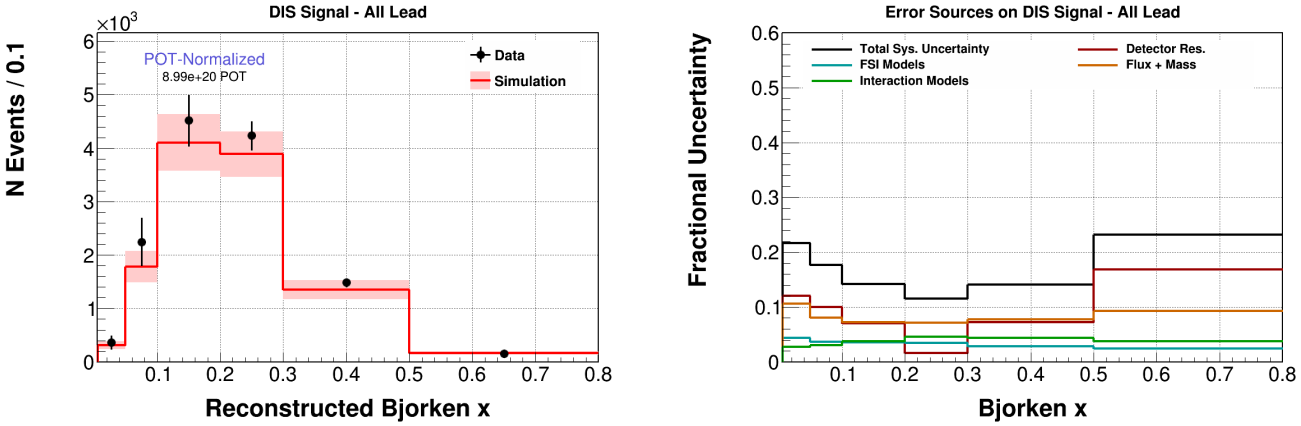

Figure 11-26: DIS events in lead per Bjorken-x in data (black points) and Monte Carlo (red line) after background subtraction. The pink band around the line is the systematic error displayed on the right.

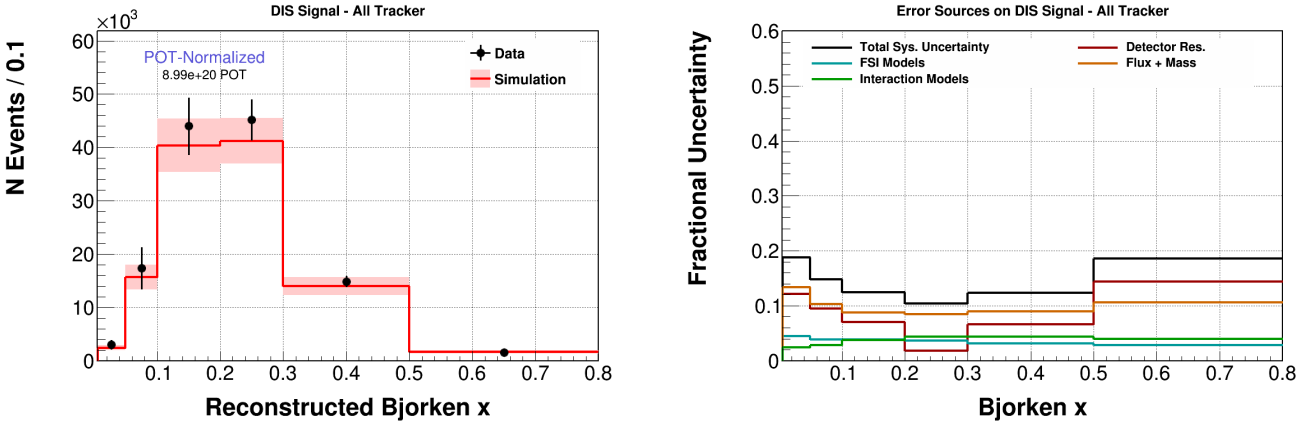

Figure 11-27: DIS events in scintillator per unfolded Bjorken-x in data (black points) and Monte Carlo (red line) after background subtraction. The pink band around the line is the systematic error displayed on the right.

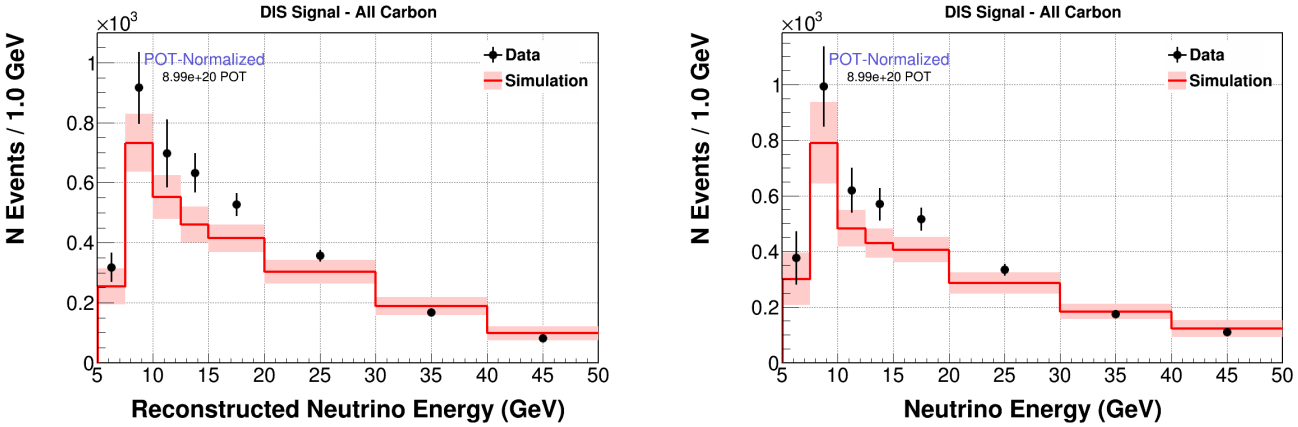

Figure 11-28: DIS events in carbon per reconstructed E_ν (left) and unfolded E_ν (right).

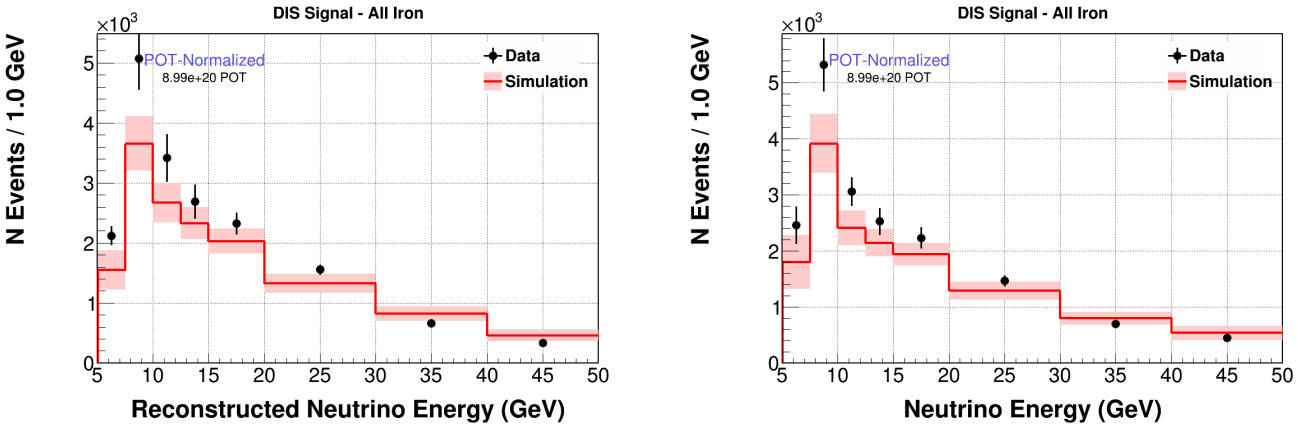

Figure 11-29: DIS events in iron per reconstructed E_ν (left) and unfolded E_ν (right).

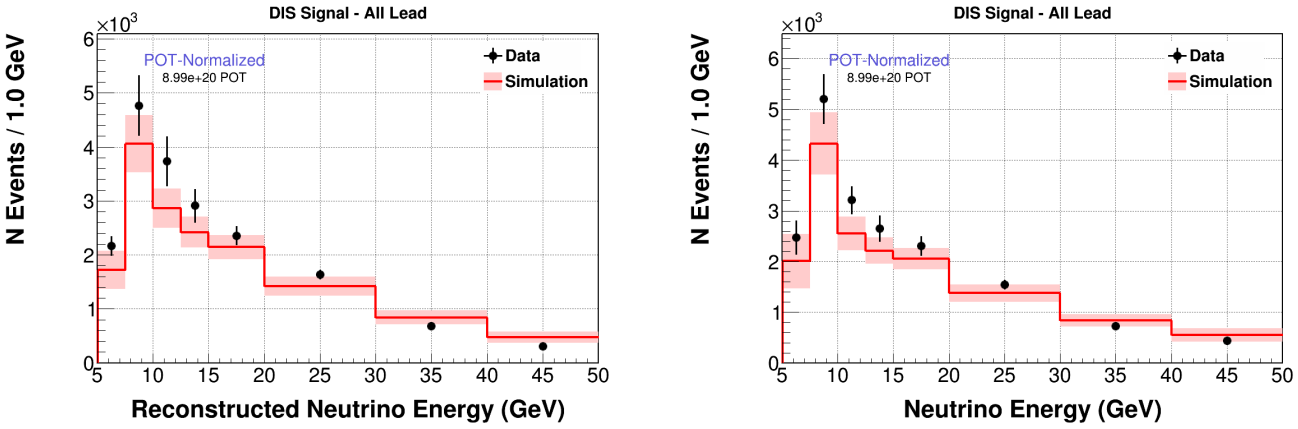

Figure 11-30: DIS events in lead per reconstructed E_ν (left) and unfolded E_ν (right).

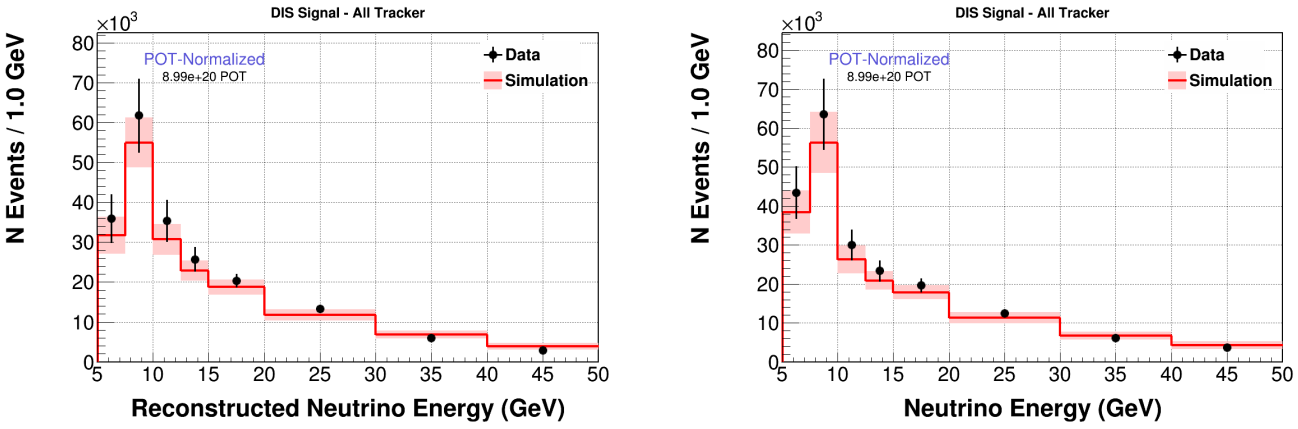

Figure 11-31: DIS events in scintillator per reconstructed E_ν (left) and unfolded E_ν (right).

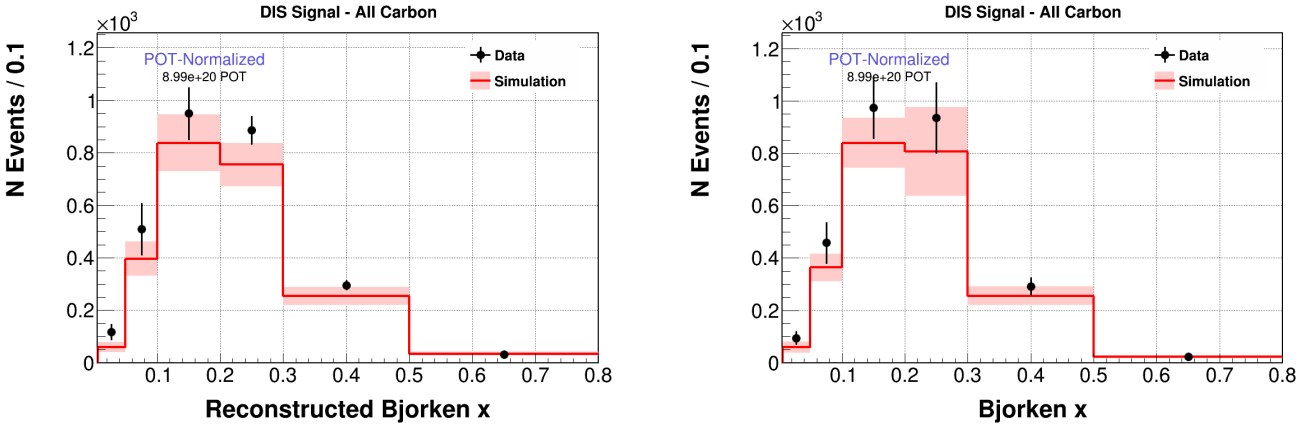

Figure 11-32: DIS events in carbon per reconstructed x_{bj} (left) and unfolded x_{bj} (right).

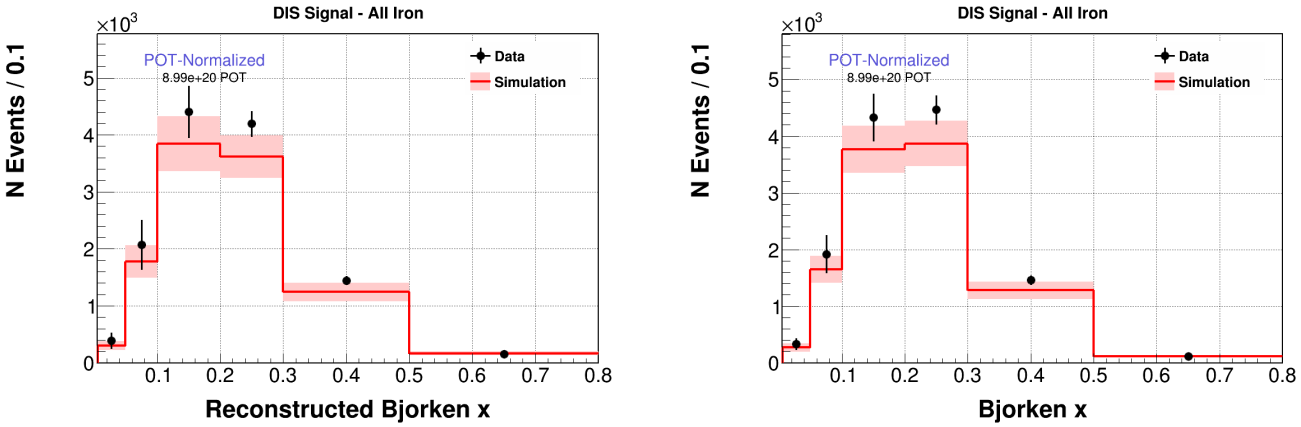

Figure 11-33: DIS events in iron per reconstructed x_{bj} (left) and unfolded x_{bj} (right).

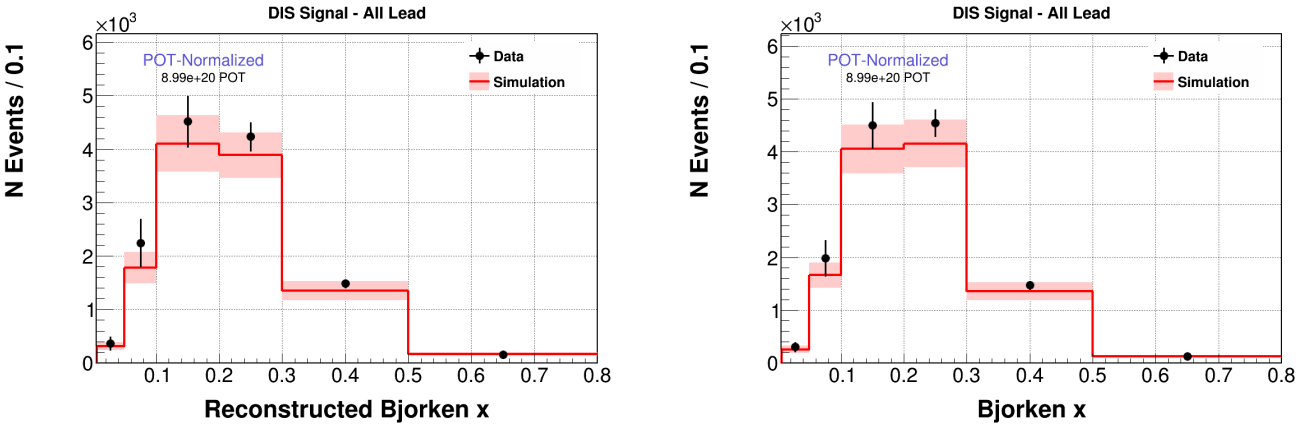

Figure 11-34: DIS events in lead per reconstructed x_{bj} (left) and unfolded x_{bj} (right).

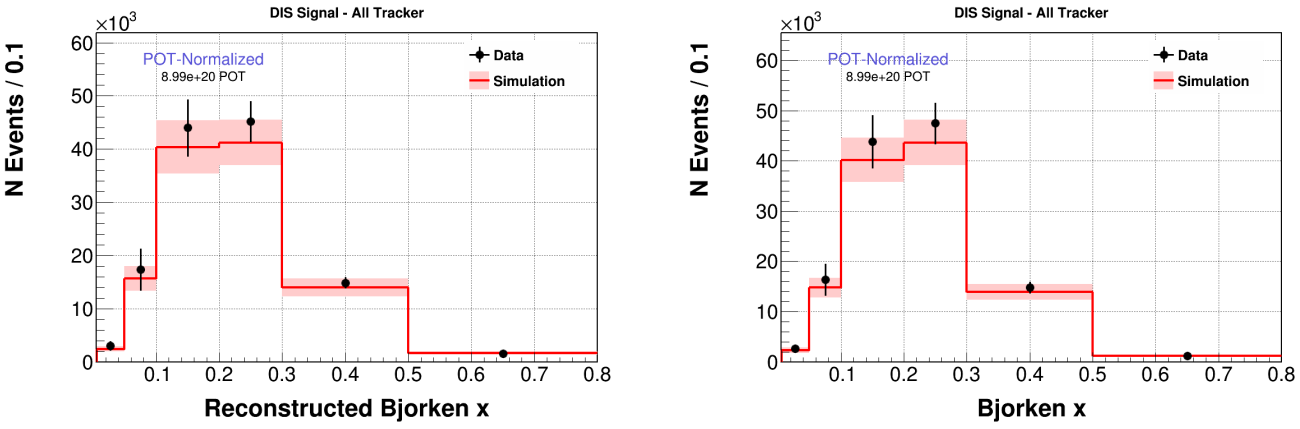

Figure 11-35: DIS events in scintillator per reconstructed x_{bj} (left) and unfolded x_{bj} (right).

CHAPTER 12
EFFICIENCY CORRECTION AND FLUX DIVISION

The final step in converting event yields to cross-sections is to divide by the overall efficiency, flux, and the number of targets.

12.1 Efficiency Correction

The set of event selection cuts used to isolate the DIS signal in Chapter 9 is unable to reconstruct some fraction of the signal events. The reconstruction efficiency for signal events is approximately 15% in this analysis. Therefore, an efficiency correction is applied to the cross-section calculation to recover the true signal distribution. For the efficiency correction, two true signal distributions are used. The first distribution is the true distribution for the reconstructed signal events and the second one is the true distribution for all the signal events. The efficiency is calculated completely from the MC, and defined the same way as in Section 9.2:

Overall Efficiency 1 *Reconstructed DIS events that pass the true DIS cuts, truly in a nuclear target A / the total number of DIS events generated by the MC in nuclear target A.*

Each nuclear target has its own efficiency correction as a function of true x_{bj} and E_ν. Figure 12-1 shows the efficiency correction as a function of E_ν for the lead of target 4, as well as the uncertainty on the efficiency correction. The efficiency and its uncertainty as a function of true x_{bj} are plotted in Figure 12-2.

Plots of the overall efficiency correction, as well as the systematic error on the correction, may be found in Appendix E.

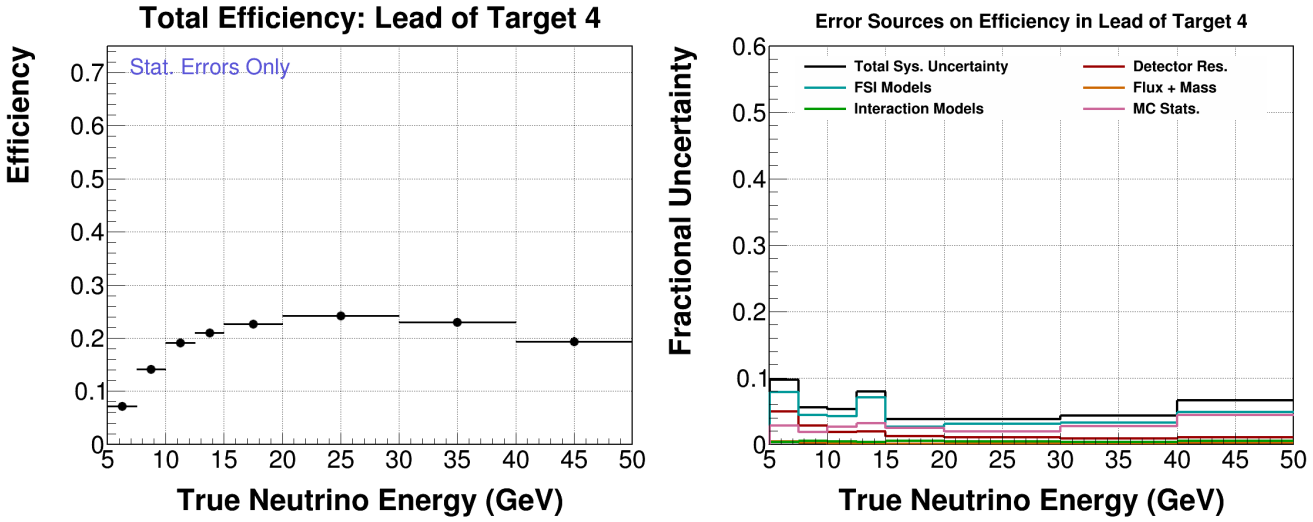

Figure 12-1: Overall efficiency of events in the lead of target 4 as a function of true E_ν (left) and the systematic uncertainty on the overall efficiency (right).

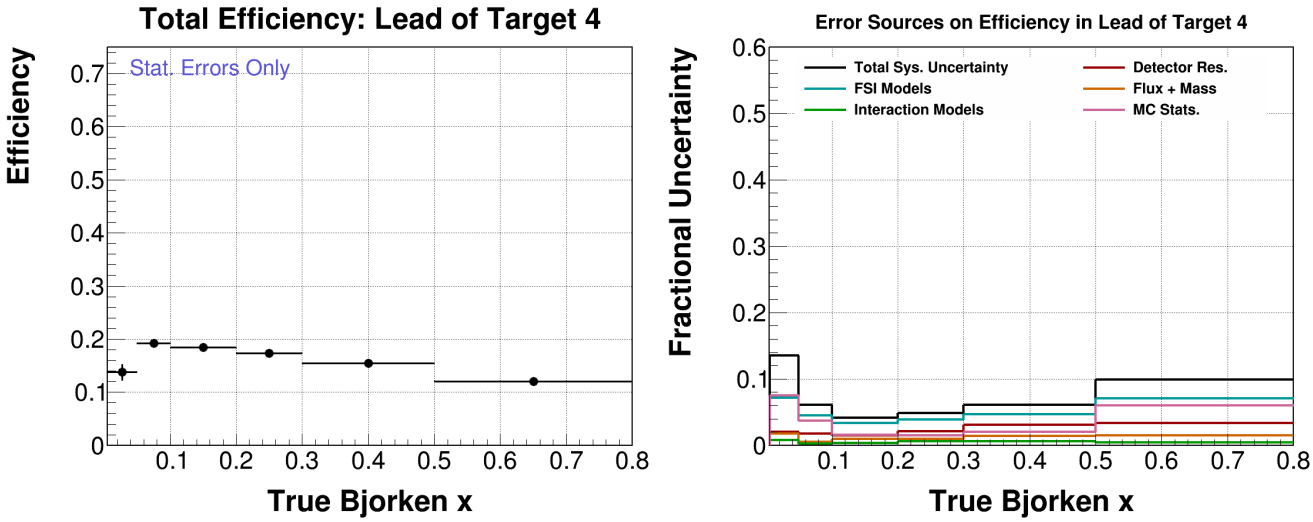

Figure 12-2: Overall efficiency of events in the lead of target 4 as a function of true x_{bj} (left) and the systematic uncertainty on the overall efficiency (right).

12.2 Flux Division, Target Counting, and Bin Width Normalization

In the case of the total cross section, $\sigma(E_\nu)$, the flux is *averaged* over each E_ν bin i:

$$\sigma_i = \frac{U_{ij}\,(N_j - b_j)}{\Delta_i\,\epsilon_i\,\Phi_i\,N}. \tag{12-1}$$

The flux distribution is rebinned to match the binning of the neutrino energy measurement. In contrast, the differential cross section with respect to Bjorken-x ($\frac{d\sigma}{dx}$) is divided by the *integrated* flux over $2 \leq E_\nu < 120$ GeV, and each bin is divided by its bin width (Δ_i) to express the result in the appropriate units:

$$\frac{d\sigma}{dx}_i = \frac{U_{ij}\,(N_j - b_j)}{\Delta_i\,\epsilon_i\,\Phi\,N}, \tag{12-2}$$

The final step in the calculation of the cross-section is the application of normalization factors. These factors appear in the denominator of Equations 12-1 and 12-2 and they refer to the flux normalization, the target number normalization, and the bin width normalization (for x_{bj}).

The cross-section results of this dissertation are reported per nucleon. Consequently, the cross-section calculation includes division by the number of nucleons inside the fiducial volume (T_n). The number of nucleons in each target is computed from the measured density of each material. The number is converted into a mass by multiplying by the fiducial area and thickness of each target.

CHAPTER 13
SYSTEMATICS UNCERTAINTIES

Systematic uncertainties arise from uncertainties related to the limitation of the measurement apparatus, or the model utilized to draw conclusion based on the observed data. Due to the limited and incomplete theoretical understanding to interpret these uncertainties in hypothesis testing, these uncertainties are typically correlated from one measurement to another. Systematic errors on the cross section measurement in MINERvA can be separated into three broad categories: flux, reconstruction, and the theoretical cross sections used in the simulation.. These uncertainties are sub-categorized into different error groups: Detector Resolution, Flux and Mass, Interaction Models, and FSI Models.

13.1 Calculating Systematic Uncertainties

The standard MINERvA method of computing the systematic uncertainty on the distribution of any parameter is used in this analysis. We use the baseline simulation to produce a "central value" distribution as a function of parameter x. To calculate the systematic uncertainty, we vary the model parameters with a known covariance matrix to produce shifted distributions. The uncertainty is the difference between the central value distribution and the mean of the varied distributions in each bin of the distribution. The error band represents the effect of model uncertainties on any distribution influenced by the model.

A multi-universe method is used in MINERvA to asses uncertainty with many correlated parameters, such as flux. In order to ensure the accurate measurement of uncertainty, we vary each of the parameters randomly within a $\pm 1\sigma$ Gaussian width distribution. This is performed up to n times, generating up to n shifted distributions of x, also known as universes. For each set of parameters in each universe, a new simulated distribution is generated. The RMS of the resulting n universes in one bin is then taken to be the uncertainty on x in that bin. The total uncertainty comprises the sum of the

uncertainties on each parameter, and correlation between parameters are also taken into account when relevant.

13.2 GENIE Uncertainties

Ideally, a neutrino cross section measurement should only depend on data and the detector response model, not the neutrino interaction model used by a particular experiment. The cross-section calculation process relies on the Monte Carlo simulation to estimate background fractions, unfolding, efficiency correction, and flux estimation.

The GENIE uncertainties affect the cross section model in two different ways:

- Primary interaction rate uncertainties.
- Final-state interaction rate uncertainties.

GENIEs parameter values and their uncertainties come from the results of previous experiments. The model dependence in this analysis comes from the background model that enters into cross section measurements, resulting in larger uncertainties on the measurement. The use of background enhanced control regions (sideband method) helps reduce some of the dependence on the background model, although the extrapolation of the background constraint into the signal region still relies on the model. This model dependence is mitigated by utilizing a sideband regions with similar underlying kinematics to the background in the signal region.

13.2.1 GENIE FSI Uncertainties

The GENIE event generator uses the INTRANUKE (hA) intranuclear hadron transport model to model the final-state interaction. Some of the quantum effects incorporated in the model are the Pauli blocking, formation time, and nucleon correlations. A description of the operation of GENIE'S FSI model is described briefly in [161].

The uncertainties affecting the INTRANUKE (hA) intranuclear hadron transport model can be classified into two types:

- Uncertainties in the sum of the rescattering probabilities (mean free path) for hadrons as they travel through the nuclear medium.

- Uncertainties in each of the hadron rescattering mode probabilities if rescattering did occur. The re-scaterring modes include the pion production and absorption, charge exachange, inelastic, elastic, and other re-scattering modes.

All of the GENIE parameters associated with final state interactions are assigned a $\pm 1\ \sigma$ systematic uncertainty in the cross-section measurements.

13.2.2 Reweightable GENIE Uncertainties

The GENIE uncertainties in the interaction model can modify the probability for a particular type of interaction to occur and thus, the uncertainties for a physics quantity x must be calculated via an event reweighting procedure. In this procedure, a systematic parameter s_x is used to modify the physics quantity x as follows,

$$x \to x' = x\left(x + s_x * \frac{\delta x}{x}\right). \tag{13-1}$$

In the GENIE framework in MINERvA, the systematic parameter is changed by $\pm 1\ \sigma$. Thus, the corresponding physics quantity x is modified by $\pm \delta x$.

For the DIS cross section model, the most important parameters of the Bodek-Yang (BY) model, CV1uBY and CV2uBY, are considered. To avoid overlapping uncertainties with the transition/resonance region, these BY uncertainties are taken into account only for events with $Q^2 > 1$ and $W > 2$. For the uncertainties related to the neutrino-induced hadronization, the uncertainties in the in-medium modifications of the hadronization process are considered.

The default GENIE $\pm 1\ \sigma$ uncertainty is included in the error budget for the cross-section measurements. The uncertainty is calculated from the mean of the two universes. The GENIE cross section uncertainties in MINERvA are explained in detail in [162]. The calculation of the GENIE weights is decribed in [161]. The GENIE systematic

uncertainties are evaluated on the efficiency, as well as the wrong target and non-DIS background events and the reconstructed signal.

13.2.3 Non-Reweightable GENIE Uncertainties

Some GENIE uncertainties can modify the particle "fates" as they propagate through the nuclear medium and cannot be modeled simply by the re-weighting method or by assigning a simple error band as in the case of the FSI. To accommodate cases like this, it is necessary to generate an alternative simulated sample in which these models have been altered.

There are three GENIE uncertainties that are categorized into the non-reweightable uncertainties:

- Formation-zone uncertainties. In deep inelastic interactions, the neutrino scatters directly off a quark. As the quark travels through the nuclear medium it will have a low probability of interaction as it has not materialized as hadrons yet, and this therefore reduces the probability of final-state interactions. The formation zone is directly related to the formation time, τ_0, via,

$$f_z = \frac{pc\tau_0}{m}, \tag{13-2}$$

  where p is the momentum of the hadron, m is the mass of the hadron, and c is the speed of light. The formation time is the time required to form fully developed hadron and is estimated from experiment. GENIE uses a formation time of 0.342 fm/c as reported by the SKAT experiment [124]. When the formation zone is reduced, it increases the amount of nuclear matter the hadron must propagate through before it escapes the target nucleus. Thus, the hadron has a higher probability to undergo a final state interaction.

  When the formation zone is included in the simulation, there is less possibility for any strong interaction to occur until a hadron is formed. Therefore a hadron is more

likely to escape the nucleus without undergoing final state interactions. This results in higher average energy and narrower transverse momentum, p_T, of particles exiting the nucleus.

- Effective nuclear radius correction. The nuclear radius affects the probability of particles to undergo FSI. When the nuclear radius is increased, the probability of a particle to undergo FSI is also increased as they will have to propagate through a longer distance before escaping the nucleus. GENIE uses $R_{nucl} = R_0 A^{1/3}$, where $R_0 = 1.4$ fm is the fermi radius, to calculate the effective nuclear radius for different nuclei depending on their atomic masses A.

- Alternative hadronization model. The AGKY hadronization model is employed by GENIE for deep inelastic scattering processes. It includes a phenomenological description of the low invariant mass region based on Koba-Nielsen-Olesen (KNO) scaling [121]. As the invariant mass increases gradually, it transitions to PYTHIA/JETSET [122] at the intermediate invariant mass. To calculate the uncertainties arising from the hadronization model, the inclusive analysis is performed on alternative hadronization model samples between an E_{had} of 2 and 20 GeV. As the peak of the DIS sample falls in this region, it is expected that the inclusion of the high energy tail from DIS will have a trivial effect. The procedure to calculate the systematic related to the hadronization model is described in [163].

13.3 Flux

Flux uncertainty comes from three sources. The first source of uncertainty is the error introduced by the interaction of the proton beam and the target to create pions and kaons. The production rate is estimated using data from CERN's NA49 experiment, but since it must be extrapolated from their energy range to MINERvA's range of energy, it leads to uncertainties. The second source of uncertainty is related to the possibility of re-interaction of particles created in the target as they traverse the long target. This is

called the tertiary particle production, and results in an uncertainty on the production rate. The third source of uncertainty comes from the beam focusing with the magnetic horns. This is an uncertainty on how well particles at each energy will be focused into our beam.

All of the components of the flux error are estimated by varying the flux model parameters to produce 100 different universes for beam focusing, PPFX uncertainties (see Chapter 3), and flux effects. In each universe, the underlying model parameters are shifted and the flux prediction is calculated again generating 100 different weights for each uncertainty. These individual uncertainties are then summed in quadrature producing a single systematic uncertainty.

The flux uncertainty in the DIS nuclear target analysis is assigned to the yield of events in each bin. This is done due to historical reasons as the inclusive framework that this analysis inherits from used to serve as a cross-check on detector calibrations and reconstruction algorithms. Assigning the flux uncertainty to the event distribution allows us to check if the differences seen in normalization could be attributed to the flux model.

The flux uncertainty remains on distributions of event yields for the reconstructed and unfolded distributions. Dividing by the flux to obtain the absolute cross sections as outlined in Chapter 14 therefore does not cause additional uncertainty. The uncertainties on the absolute cross section are similar to the uncertainties on the unfolded distribution and they differ only due to the efficiency correction.

13.4 Absolute Normalization

Uncertainty on the absolute normalization arises from the uncertainty on the detector mass, POT counting, and MINOS and MINERvA tracking efficiency. The mass uncertainty comes from the discrepancy between the estimated mass in the MINERvA geometry model and the actual mass of the detector. In the study performed in [164], it was found that the mass model overestimates the amount of mass by approximately 2%.

POT counting is the uncertainty attached to the counting precision of the number of primary protons orginating from the NuMI beam. It was found that the precision is approximately 1%. Details of these uncertainties may be found in [163].

MINOS and MINERvA tracking efficiency uncertainties comes from how well the MC can reconstruct muons. In this study, we look at how many tracks escaping the back of MINERvA and pointing towards the fiducial volume of the MINOS detector are matched to MINOS tracks. The MC event must be corrected to account for for this inefficiency in tracking. MINERvA's tracking efficiency varies accross all playlists. For the minervame1A dataset used in this analysis, it was found that we do not have to apply a correction for MINERvA's tracking efficiency, while a scale factor of 0.96 and 0.99 needs to be applied to MC to correct for muons with momenta below 3 GeV and muons with higher momenta, respectively.

13.5 Detector Resolution

Reconstruction uncertainties can arise due to the limitations of the detector, the reconstruction algorithms, or the fact that some particles can mimic others. Detector resolution uncertainties include the uncertainties associated with the tracking and energy estimation for muon energy, muon angle, and hadronic energy.

Uncertainties on derived quantities (Q^2, W, etc.) are largely affected by the detector's reconstruction of E_μ, θ_μ and E_{had}. Since Q^2 and W are used to isolate the reconstructed DIS events from the sample, the number of DIS events reconstructed will also be affected by these shifts.

The same multi-universe method as the flux uncertainties is also used to calculate the uncertainties for detector resolution. Since the excursions in each universe of detector resolution are expected to be smaller than for the flux model, the number of universes used was only 60 instead of 100. In addition, weights are not calculated for detector resolution uncertainties. Instead, each basic quantity E_μ, θ_μ and E_{had} is shifted individually according to a Gaussian random number with variance equal to the $\pm 1\sigma$ variance of the variable in

question. All the derived quantities and their effects on the analysis selection cuts are then re-calculated, and the RMS of all the shifted quantities in the universe is assigned as the uncertainty.

Shifts in Q^2, W, and E_μ can cause events to move in or out of the selected DIS sample. If an event passed the DIS selection cut in the central value universe or any of the 60 shifted universes, then the events will be included in the calculation for the error band. However, if an event passed the DIS selection cut in the central value universe but not any of the 60 shifted universes, then the event will be skipped in the calculation for the error band.

13.6 Plastic Background Subtraction

After fitting and extracting the scale factor for the central-value histogram, we use our same cuts and plot another histogram for each of our universes. Each event is reweighted by its shifted value for the corresponding universe. The value of the uncertainty in each bin is the difference between the central-value event count in the bin and the shifted one. With two universes, it is the average difference between each shifted histogram and the central value.

In order to calculate the systematic uncertainties on the plastic background, we start by filling the histograms of reconstructed DIS events with the shifted value in 100 flux universes, 60 hadronic energy universes, 60 muon energy universes, 60 muon angle universes, 40 GENIE interaction model universes, and 40 final state interactions universes. The systematic error before data tuning is calculated in each universe. We then fit the MC event distribution in each universe to the data for both plastic background templates (upstream plastic events and downstream plastic events) and extract the scale factors separately for each template in each of the universes. We then use the scale factors to tune the upstream and downstream tempate respectively in each of the universes and calculate the systematic uncertainties after the tuning. The fractional error summary plots for all the systematic uncertainties associated with the plastic backgrounds in iron are shown in

Figure 13-1. The fractional error summary plots for all of the systematic uncertainties associated with the plastic backgrounds in lead are shown in Figure 13-2.

The dominant uncertainties as a function of neutrino energy in this procedure come from our flux estimate. The hadronic energy resolution drives the uncertainty in Detector Resolution. The two dominant uncertainties in the Interaction Model are the CV1uBY and axial mass for resonant production. Meanwhile, the pion inelastic and absorption interactions are the dominant uncertainties in FSI models.

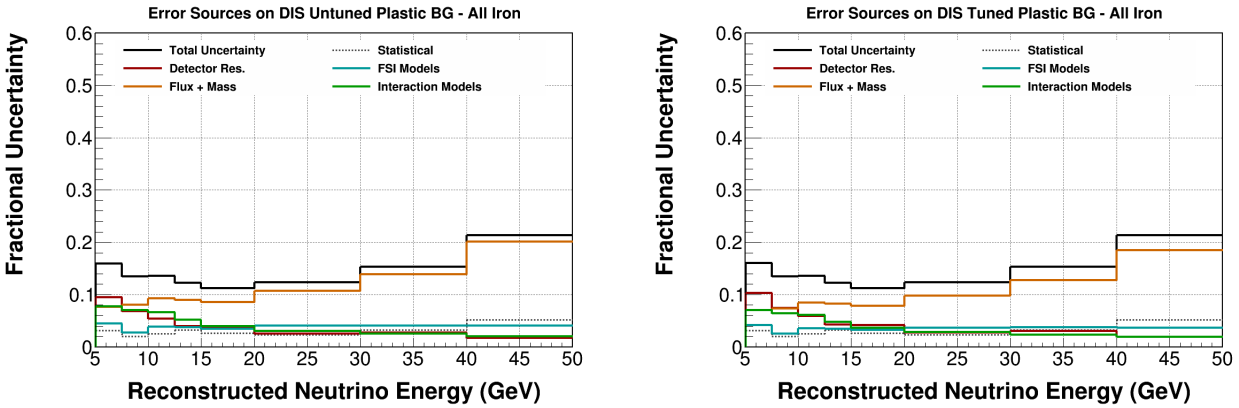

Figure 13-1: Uncertainty on the wrong target event prediction in iron before data tuning (left) and after data tuning (right). The majority of the improvement is below 30 GeV, where the neutrino electron and low-ν constraints are applied to the flux.

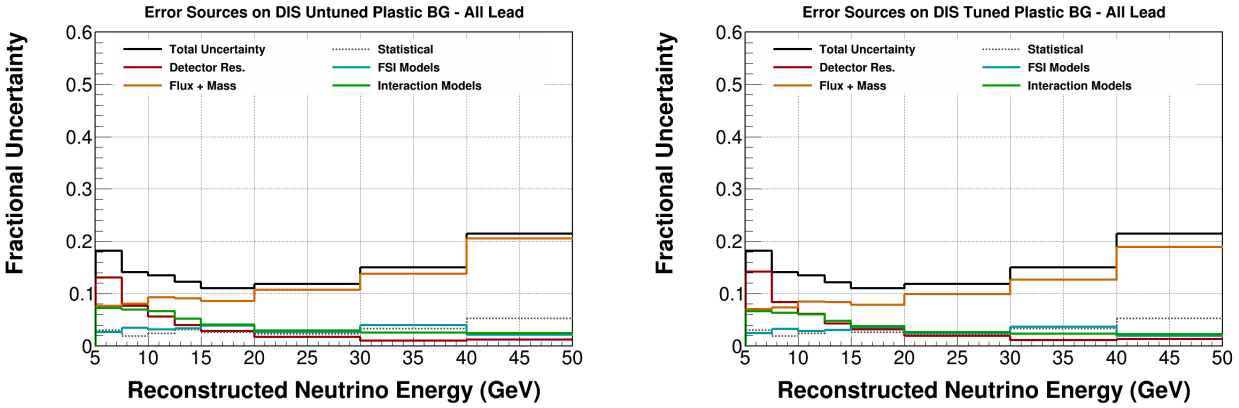

Figure 13-2: Uncertainty on the wrong target event prediction in lead before data tuning (left) and after data tuning (right). The majority of the improvement is below 30 GeV, where the neutrino electron and low-ν constraints are applied to the flux.

13.7 Non-DIS Background Subtraction

The systematic error for the non-DIS background tuning is calculated by re-running the fits to the sidebands in each different universe. In the case of GENIE and FSI errors, each universe corresponds to the $\pm 1\sigma$ change to one of GENIE's reweightable parameters. In the case of flux errors, each universe corresponds to one of the 100 shifted flux universes. The weight derived for each universe is applied to the two different sidebands described in Section 10.2. After applying the weights, the fit is re-run over the same data set and MC templates. In the end, a set of fit values are derived for each universe and each variation.

At the creation of each distribution of the predicted non-DIS events, each universe which makes up the systematic error was scaled by the scale factor derived for that universe. In this way, each universe (and its universe central value) of the non-DIS events is pinned to the data in some way. This procedure reduced systematic errors considerably (see Figures 13-3 and 13-4).

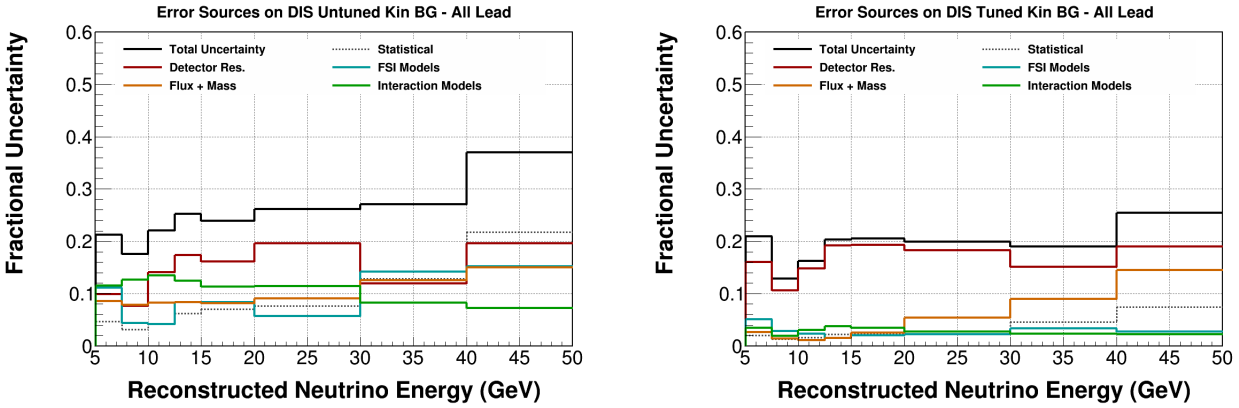

Figure 13-3: Uncertainty on the non-DIS event prediction in lead before data tuning (left) and after data tuning (right). The majority of the improvement is below 20 GeV, where the data sidebands are well populated.

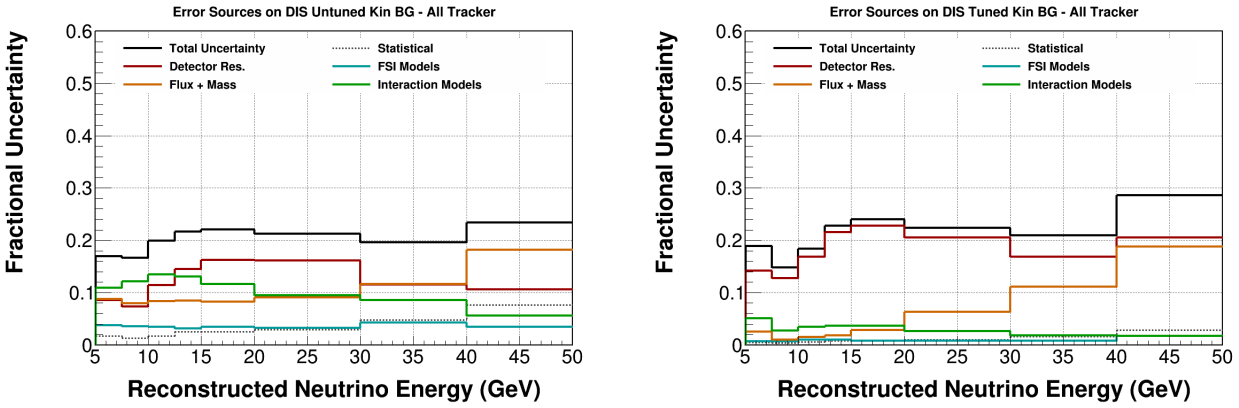

Figure 13-4: Uncertainty on the non-DIS event prediction in plastic before data tuning (left) and after data tuning (right). The majority of the improvement is below 20 GeV, where the data sidebands are well populated.

CHAPTER 14
CROSS SECTION RESULTS

14.1 Closure Tests

A method called closure tests is performed to validate the internal consistency of the analysis. In a closure test, the analyzed MC events are treated as fake data and are compared to the truth values at each analysis stage. The first closure test is performed at the background estimation stage. A reconstructed MC sample is used as fake data to estimate the plastic and non-DIS background. Then this estimated background is compared to the true MC background distribution. The second closure test is performed at the background subtraction stage. Again, a reconstructed MC sample is used as fake data for the plastic and non-DIS background subtraction, and the result is compared with the true signal distribution of the MC sample. The third closure test is performed at the unfolding step. The reconstructed MC sample is used as fake data which is then unfolded, and the result is compared to the truth distribution of selected signal events. The final closure test is performed at the efficiency correction step. A reconstructed MC sample is used as fake data, it is efficiency-corrected, and the result is compared to the truth distribution of all signal events. Distributions in E_ν and x_{bj} are subjected to these closure tests and the closure tests are performed for all individual passive target material and the scintillators in the trackers. As an example, the closure plots for carbon are shown in Figure 14-1. The ratio between the fake data and the simulation is close to one in the closure tests.

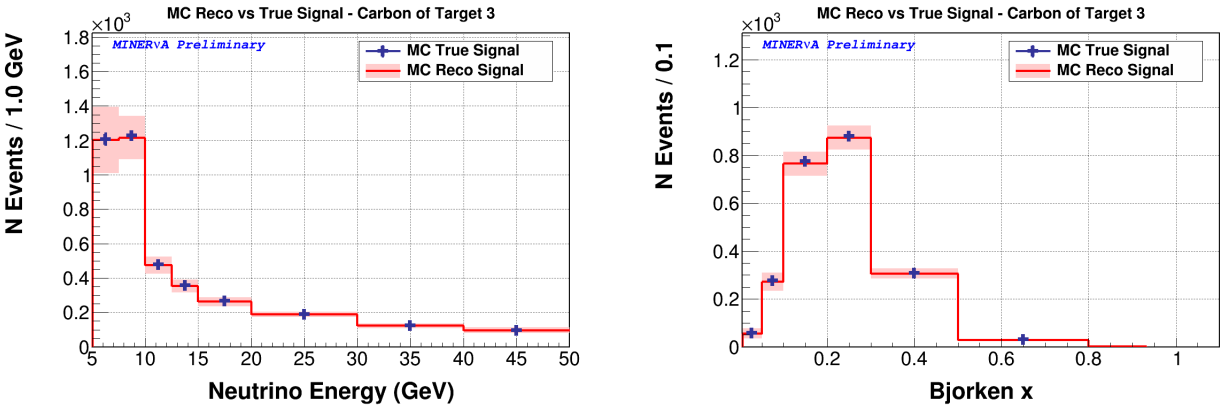

Figure 14-1: Left: Neutrino energy closure test plots for background subtracted, unfolded, and efficiency corrected MC sample. Right: Bjorken x closure test plots for background subtracted, unfolded, and efficiency corrected MC sample.

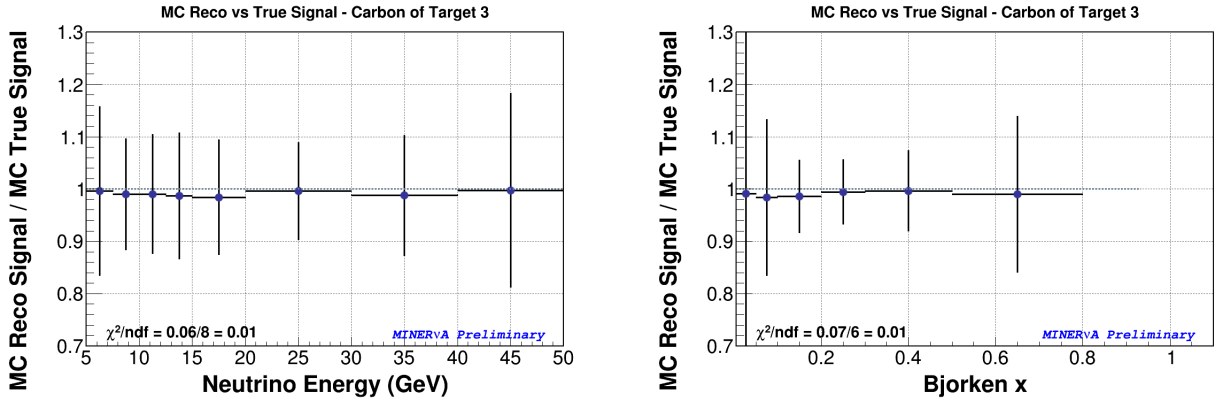

Figure 14-2: Left: Neutrino energy closure test plots ratio for background subtracted, unfolded, and efficiency corrected MC sample. Right: Bjorken x closure test ratio plots for background subtracted, unfolded, and efficiency corrected MC sample. The ratio for reconstructed MC to true MC for both distributions are close to 1.

14.2 Absolute Cross Sections

The absolute cross section per nucleon as a function of neutrino energy is calculated for C, CH, Fe, and Pb. In each nuclei, the data is compared to the simulation. Each of the data points contains the statistical uncertainty on the cross section measurement. The red band surrounding the MC contains all of the systematic errors, including those on the MC statistics. The cross sections and the breakdown of uncertainties as a function of unfolded E_ν are in Figures 14-3 through 14-6. In general, the MC tends to under-predict the cross section at low energies ($E_\nu < 30$ GeV) and over-predict at high energies ($E_\nu \geq 30$ GeV). None of these differences are significant taking into account the systematic uncertainty assigned to each bin. Since this trend is observed across the different nuclei, a likely explanation is a shape-difference between the actual and predicted neutrino flux.

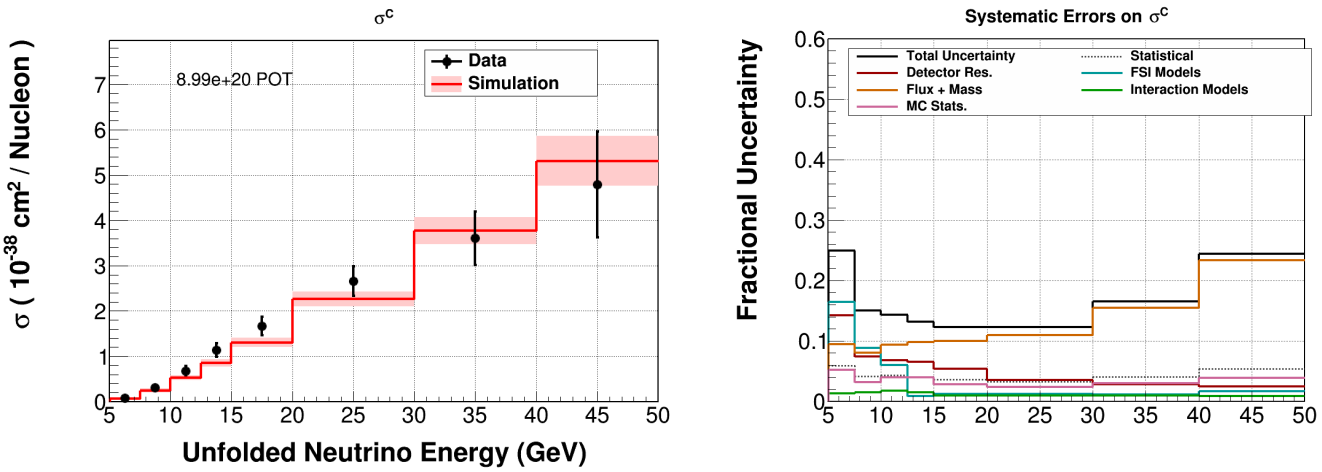

Figure 14-3: The absolute DIS cross section per nucleon on carbon as a function of unfolded neutrino energy for data (black points) and simulation (red line). The total systematic error is shown as a red band around the simulation, and the breakdown of the systematic errors is shown in the right hand plot.

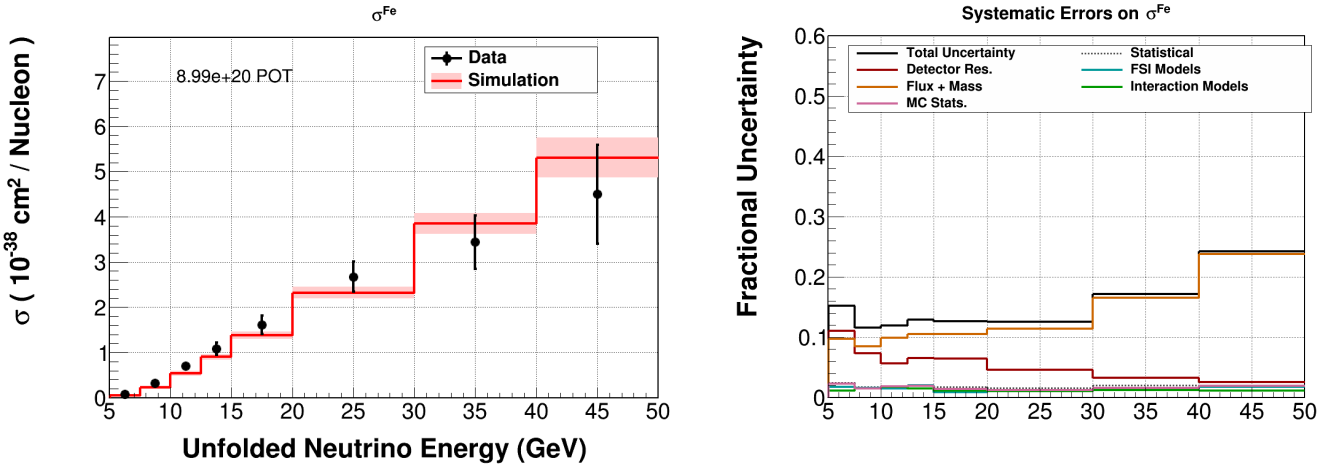

Figure 14-4: The absolute DIS cross section per nucleon on iron as a function of unfolded neutrino energy for data (black points) and simulation (red line). The total systematic error is shown as a red band around the simulation, and the breakdown of the systematic errors is shown in the right hand plot.

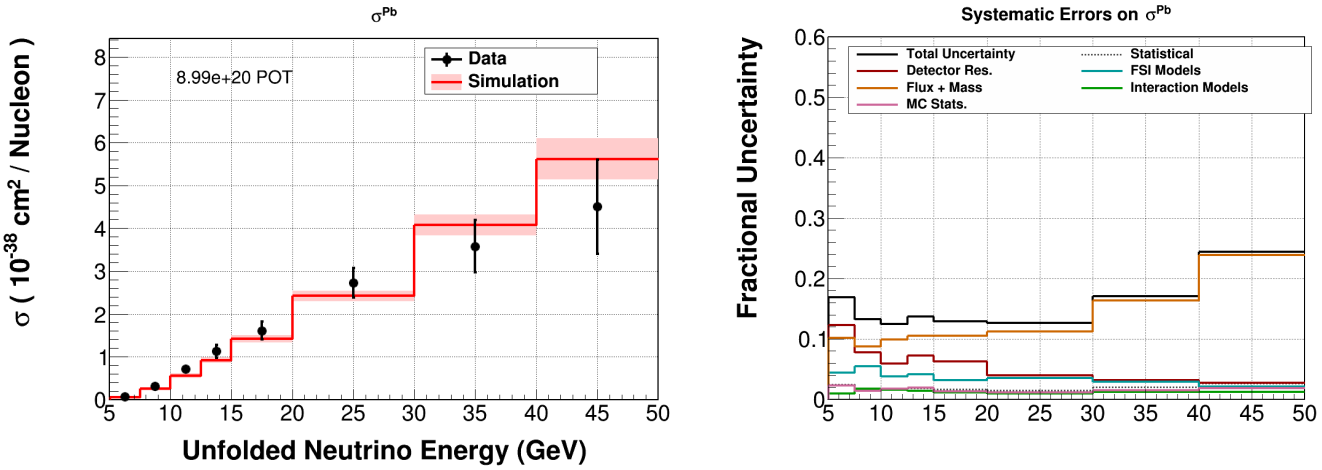

Figure 14-5: The absolute DIS cross section per nucleon on lead as a function of unfolded neutrino energy for data (black points) and simulation (red line). The total systematic error is shown as a red band around the simulation, and the breakdown of the systematic errors is shown in the right hand plot.

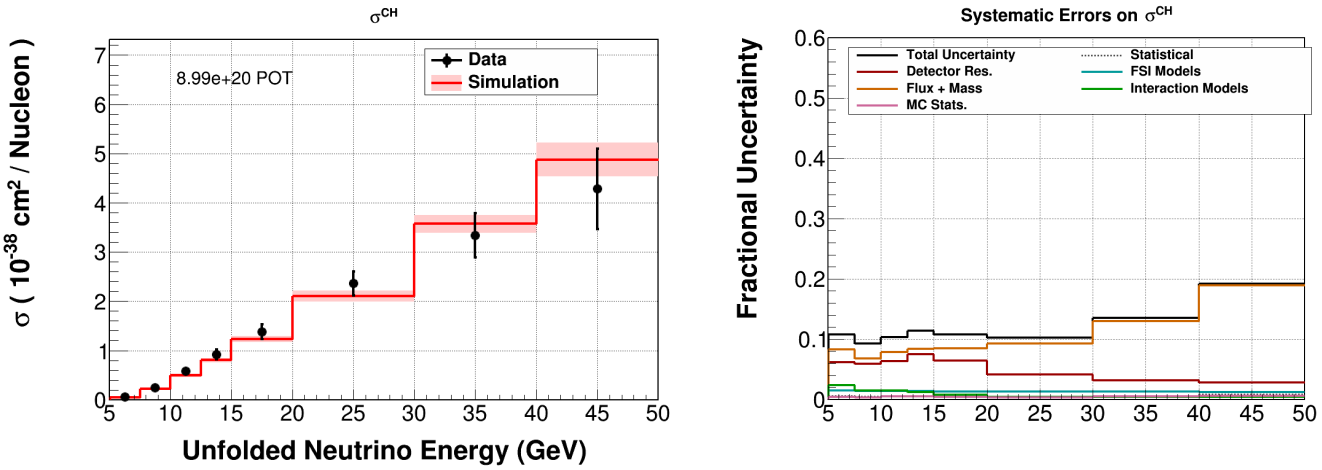

Figure 14-6: The absolute DIS cross section per nucleon on scintillator as a function of unfolded neutrino energy for data (black points) and simulation (red line). The total systematic error is shown as a red band around the simulation, and the breakdown of the systematic errors is shown in the right hand plot.

14.3 Differential Cross Section

The differential cross section per nucleon as a function of Bjorken-x is calculated for C, CH, Fe, and Pb. Similar to absolute cross section, the data is compared to the simulation in each nuclei. Each of the data points contains the statistical uncertainty on the cross section measurement. The red band surrounding the MC contains all of the systematic errors, including those on the MC statistics. In general, the MC tends to under-predict the cross section. None of these differences are significant taking into account the systematic uncertainty assigned to each bin.

Figures 14-7 through 14-10 show the differential cross section as a function of Bjorken-x. No significant differences between the data and MC are observed.

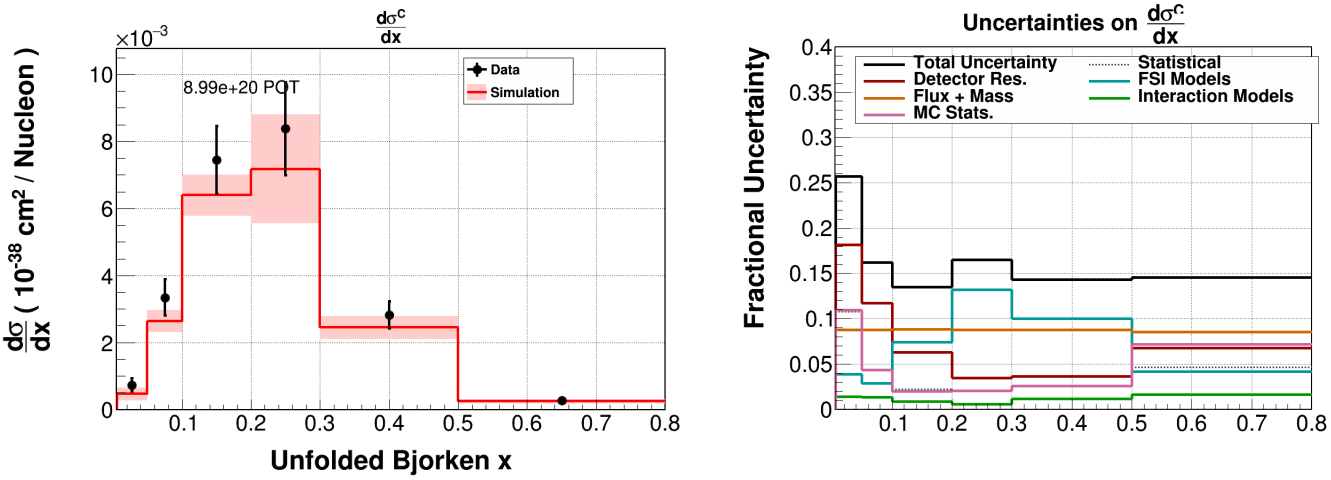

Figure 14-7: The differential DIS cross section per nucleon on carbon as a function of unfolded neutrino energy for data (black points) and simulation (red line). The total systematic error is shown as a red band around the simulation, and the breakdown of the systematic errors is shown in the right hand plot.

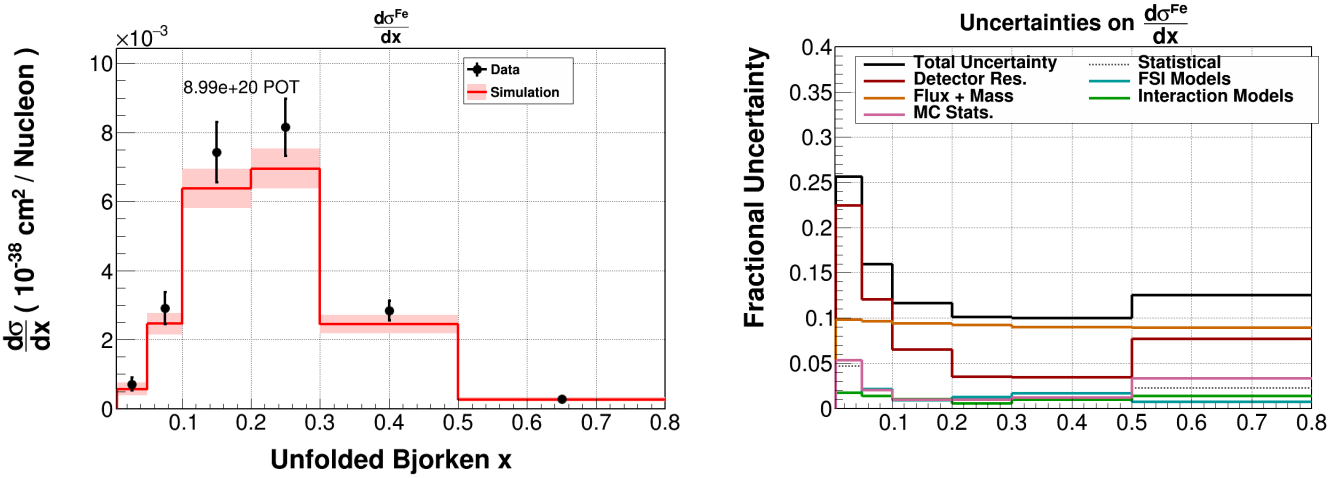

Figure 14-8: The differential DIS cross section per nucleon on iron as a function of unfolded Bjorken-x for data (black points) and simulation (red line). The total systematic error is shown as a red band around the simulation, and the breakdown of the systematic errors is shown in the right hand plot.

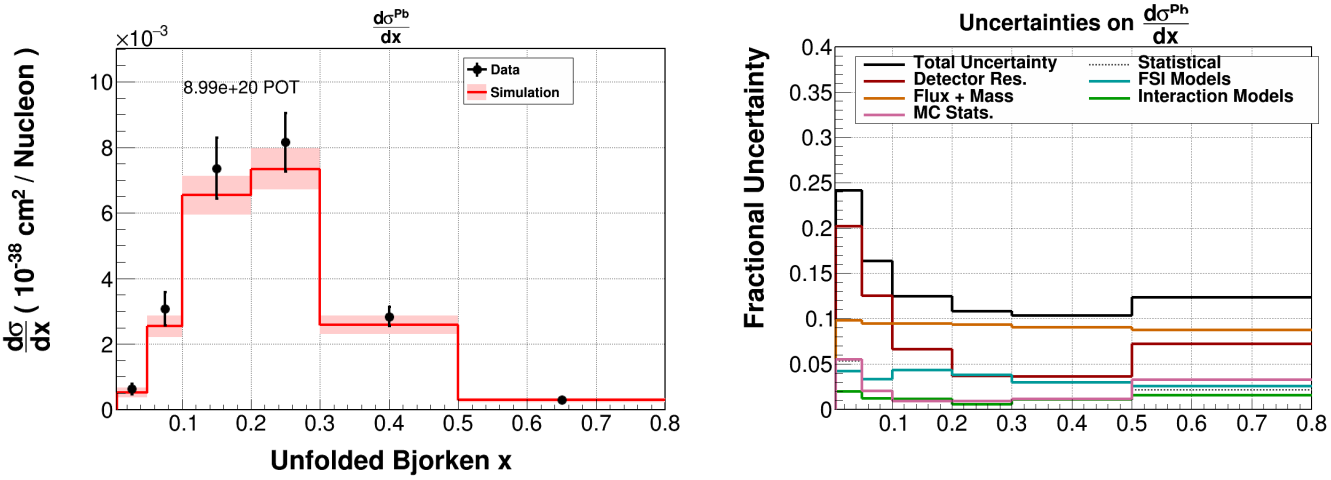

Figure 14-9: The differential DIS cross section per nucleon on lead as a function of unfolded Bjorken-x for data (black points) and simulation (red line). The total systematic error is shown as a red band around the simulation, and the breakdown of the systematic errors is shown in the right hand plot.

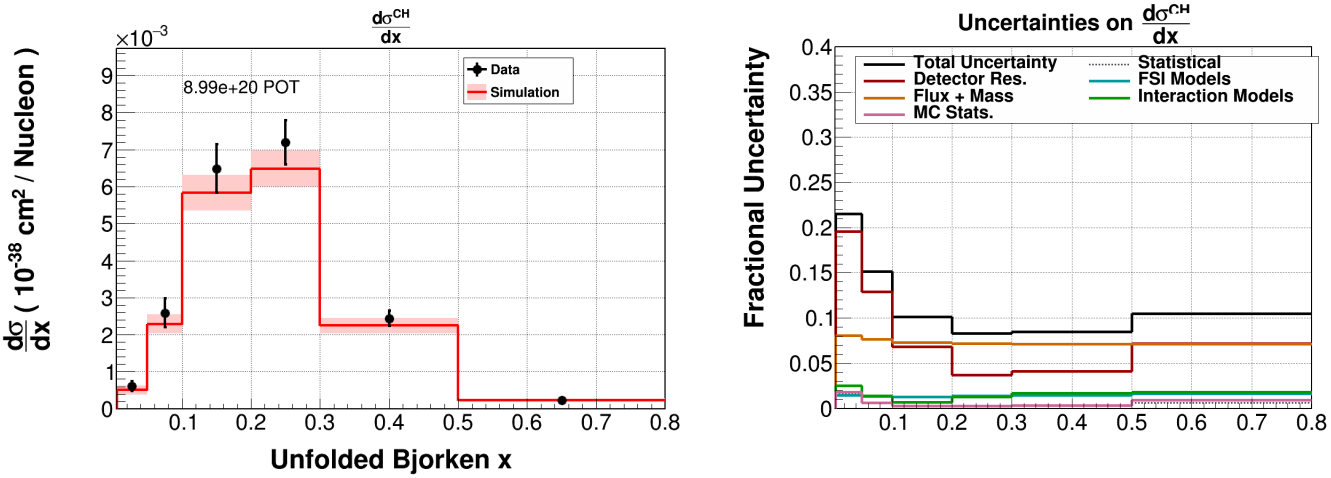

Figure 14-10: The differential DIS cross section per nucleon on scintillator as a function of unfolded Bjorken-x for data (black points) and simulation (red line). The total systematic error is shown as a red band around the simulation, and the breakdown of the systematic errors is shown in the right hand plot.

CHAPTER 15
CONCLUSIONS

A deep inelastic sample is selected from the nuclear charged current inclusive analysis, by requiring reconstructed $Q^2 \geq 1.0$ (GeV/c)^2 and $W \geq 2.0$ GeV/c^2. The neutrino energy range of $5 < E_\nu < 50$ previously applied to this analysis in the LE analysis is removed and the energy range cut is imposed on the muon energy from $2 < E_\mu < 50$ GeV. Machine learning vertexing is used to improve the track-based vertexing resulting in higher purity and efficiency of the sample. A local sideband method is utilized to remove the plastic background for the events reconstructed in the target. After plastic backgrounds and non-DIS backgrounds are subtracted, the reconstructed neutrino energy and Bjorken-x are unsmeared to their true quantities via Bayesian unfolding. The unfolded distributions of carbon, iron, lead, and plastic are efficiency corrected and then divided by the flux and the number of nucleons in the target to produce the absolute cross section as a function of E_ν and differential cross section as function of x_{bj}.

The results of the analysis show good agreement between data and MC for E_ν and x_{bj} (see Figures 14-3 through 14-10). None of the distributions displayed significant differences with the theoretical models underlying MINERvAs MC. None of the differences between the data and MC observed have significances greater than 3σ.

For the updated results using complete set of MINERvA Monte Carlo simulation, please refer to: For the updated results using complete set of MINERvA Monte Carlo simulation, please refer to: https://ccd.fnal.gov/techpubs/fermilab-reports-thesis.html

APPENDIX A
DIS CANDIDATE PLOTS

A.1 Reconstructed DIS events as a function of E_ν

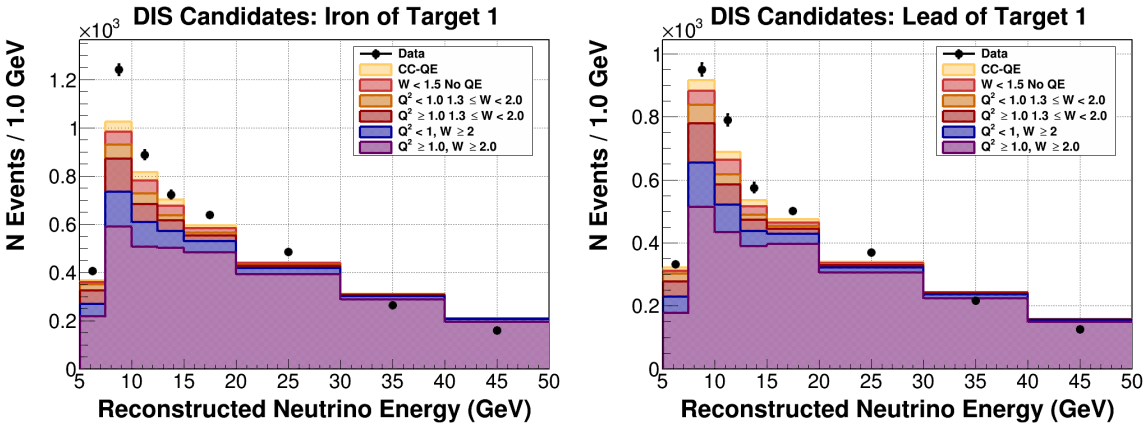

Figure A-1: The reconstructed DIS events for data (black points) and MC (various colored bands) in the iron of target 1 (left) and lead of target 1 (right). The data and MC correspond to 8.89×10^{20} POT.

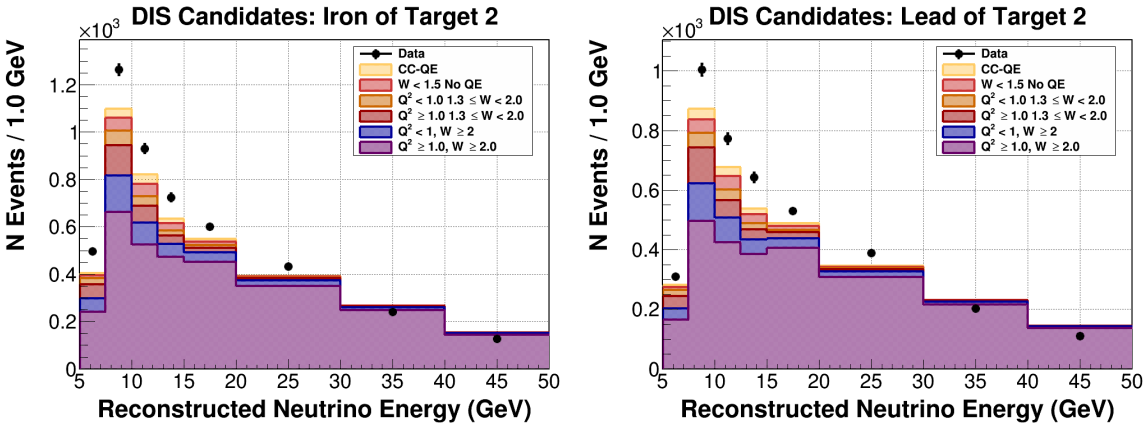

Figure A-2: The reconstructed DIS events for data (black points) and MC (various colored bands) in the iron of target 2 (left) and lead of target 2 (right). The data and MC correspond to 8.89×10^{20} POT.

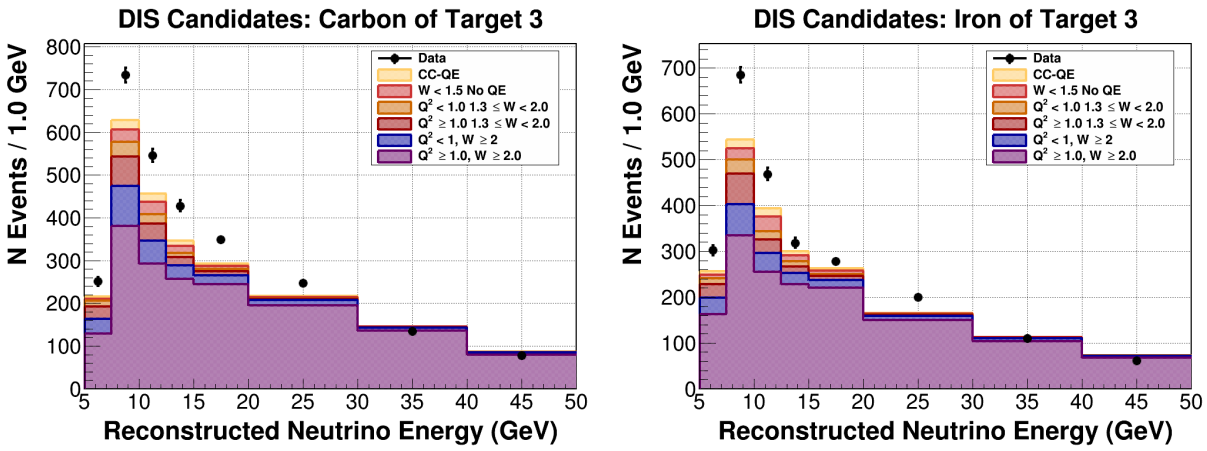

Figure A-3: The reconstructed DIS events for data (black points) and MC (various colored bands) in the carbon of target 3 (left) and iron of target 3 (right). The data and MC correspond to 8.89×10^{20} POT.

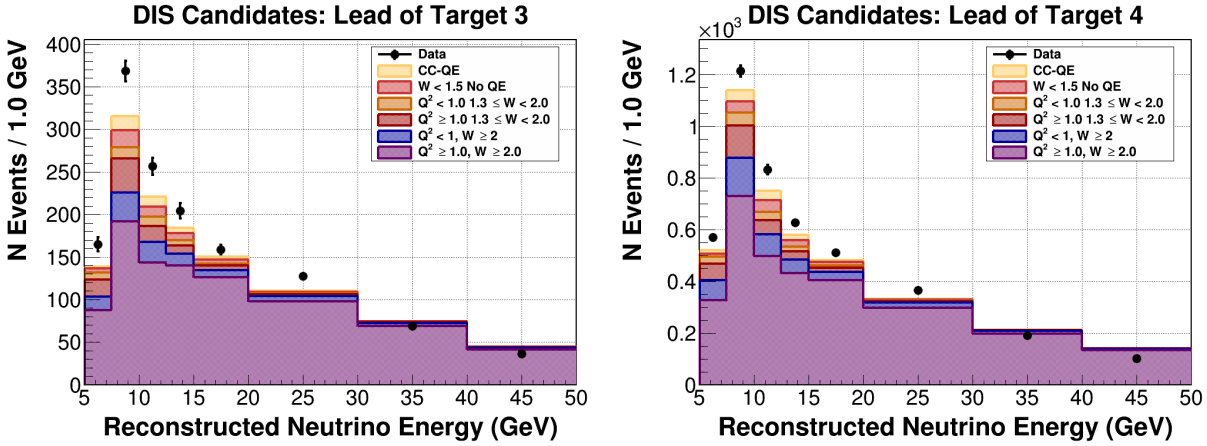

Figure A-4: The reconstructed DIS events for data (black points) and MC (various colored bands) in the lead of target 3 (left) and lead of target 4 (right). The data and MC correspond to 8.89×10^{20} POT.

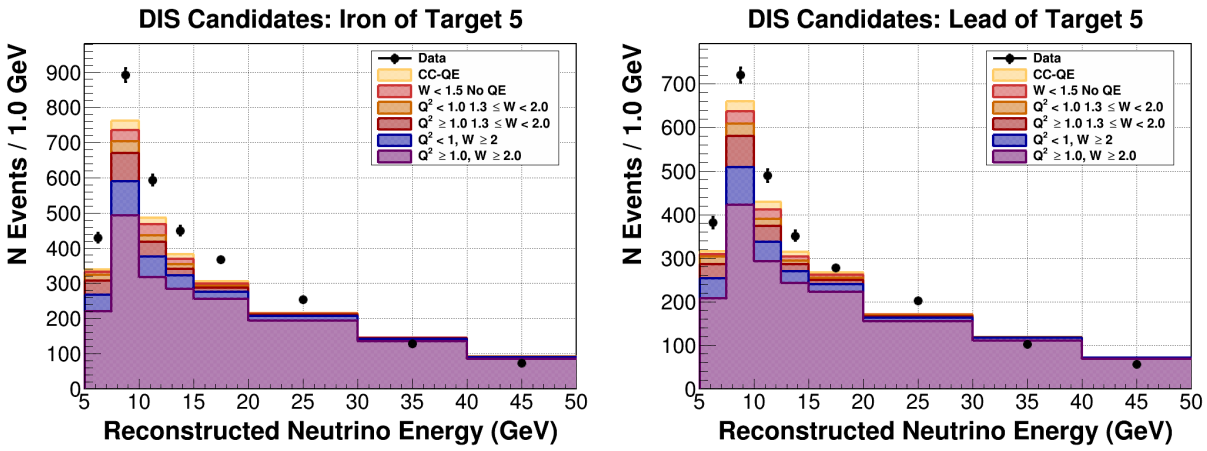

Figure A-5: The reconstructed DIS events for data (black points) and MC (various colored bands) in the iron of target 5 (left) and lead of target 5 (right). The data and MC correspond to 8.89×10^{20} POT.

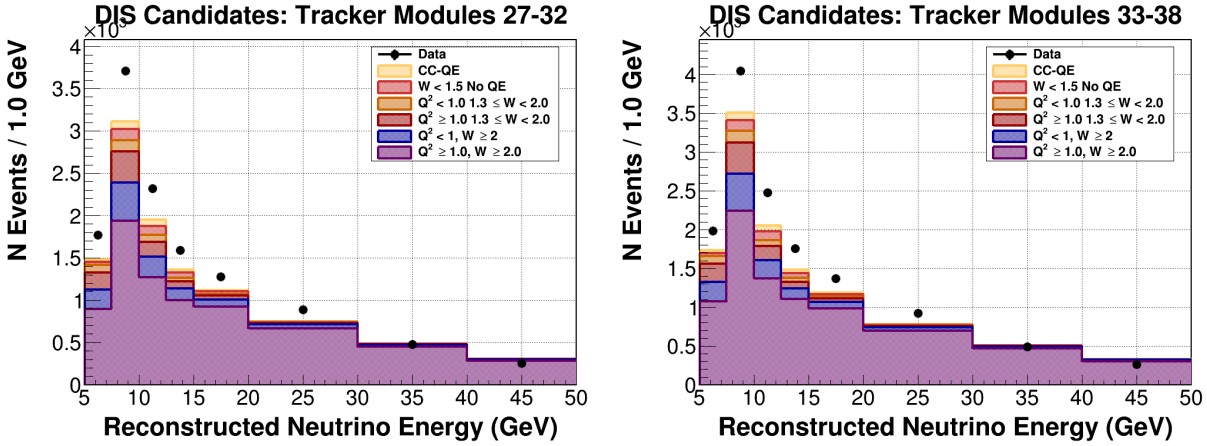

Figure A-6: The reconstructed DIS events for data (black points) and MC (various colored bands) in the scintillator tracker moduless 27-32 (left) and scintillator tracker moduless 33-38 (right). The data and MC correspond to 8.89×10^{20} POT.

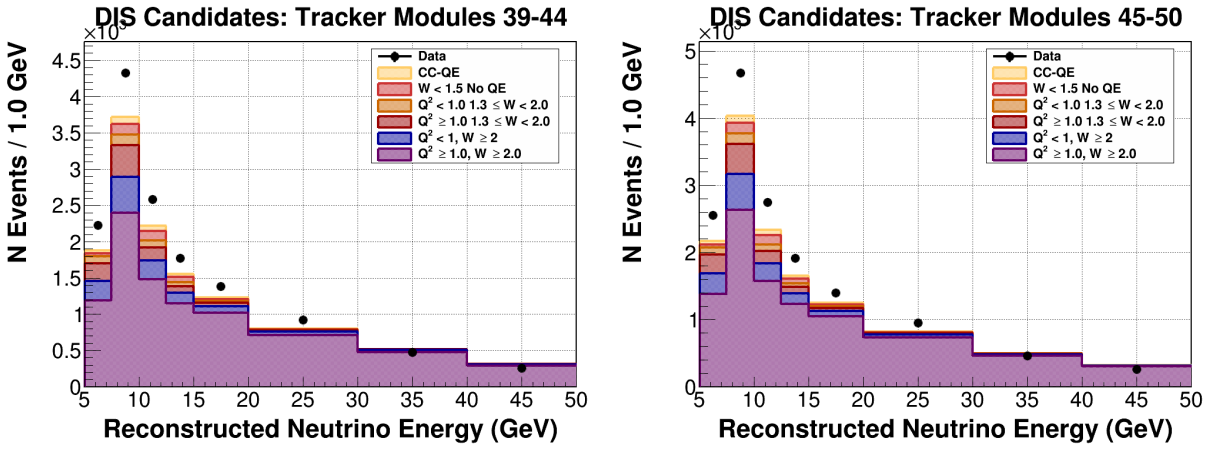

Figure A-7: The reconstructed DIS events for data (black points) and MC (various colored bands) in the scintillator tracker moduless 39-44 (left) and scintillator tracker moduless 45-50 (right). The data and MC correspond to 8.89×10^{20} POT.

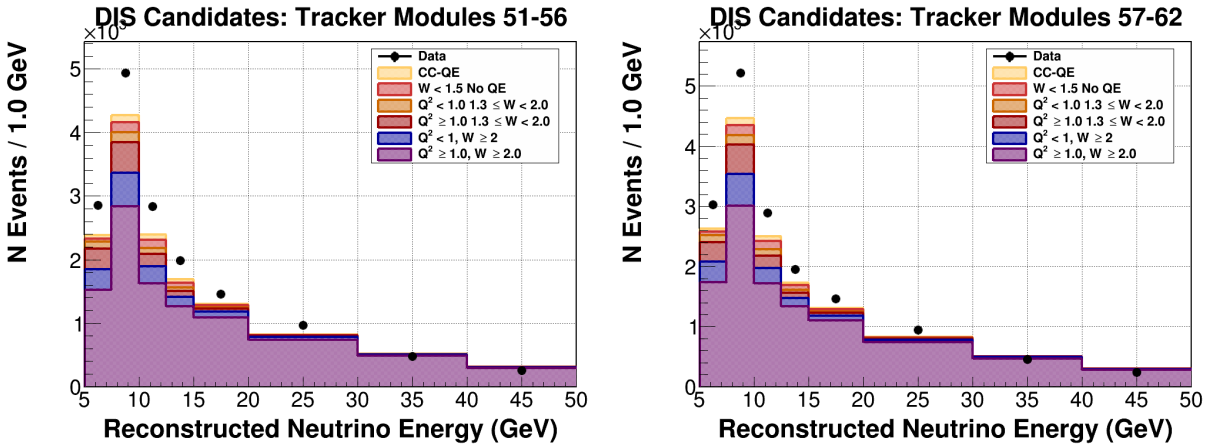

Figure A-8: The reconstructed DIS events for data (black points) and MC (various colored bands) in the scintillator tracker moduless 51-56 (left) and scintillator tracker moduless 57-62 (right). The data and MC correspond to 8.89×10^{20} POT.

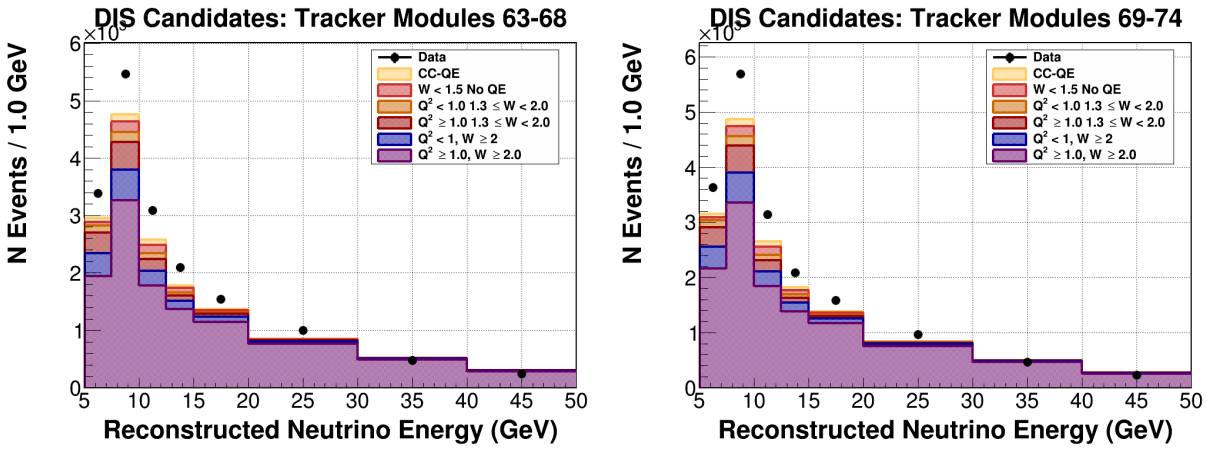

Figure A-9: The reconstructed DIS events for data (black points) and MC (various colored bands) in the scintillator tracker moduless 63-68 (left) and scintillator tracker moduless 69-74 (right). The data and MC correspond to 8.89×10^{20} POT.

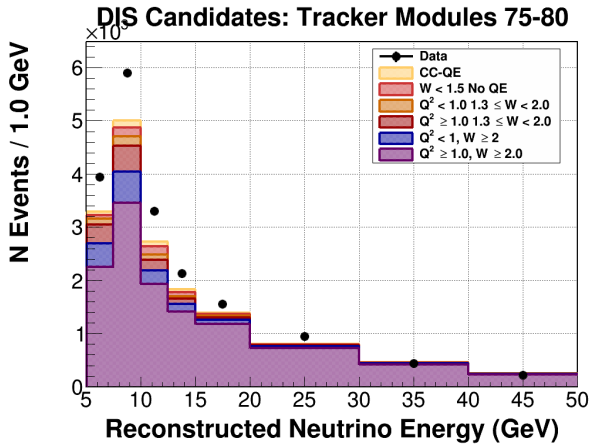

Figure A-10: The reconstructed DIS events for data (black points) and MC (various colored bands) in the scintillator tracker moduless 75-80 (right). The data and MC correspond to 8.89×10^{20} POT.

A.2 Reconstructed DIS events as a function of x_{bj}

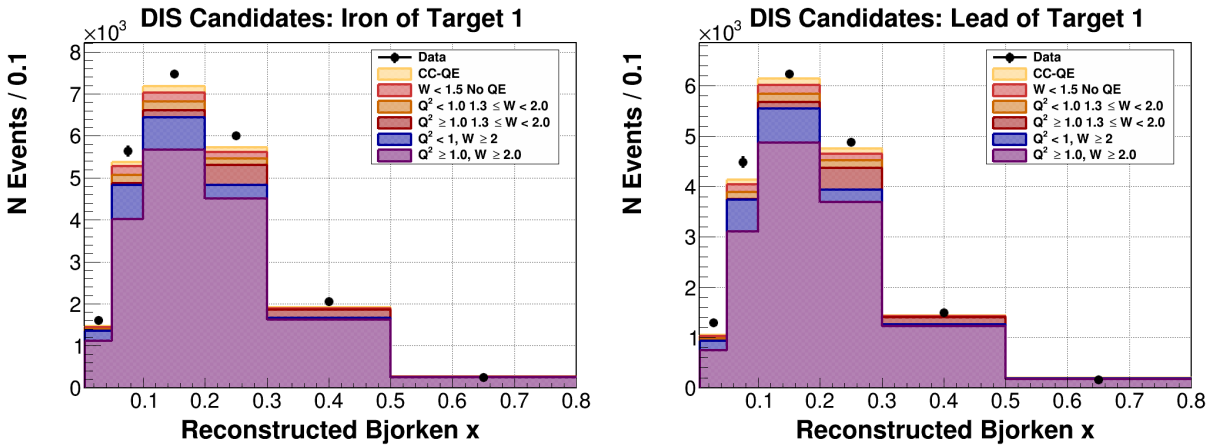

Figure A-11: The reconstructed DIS events for data (black points) and MC (various colored bands) in the iron of target 1 (left) and lead of target 1 (right). The data and MC correspond to 8.89×10^{20} POT.

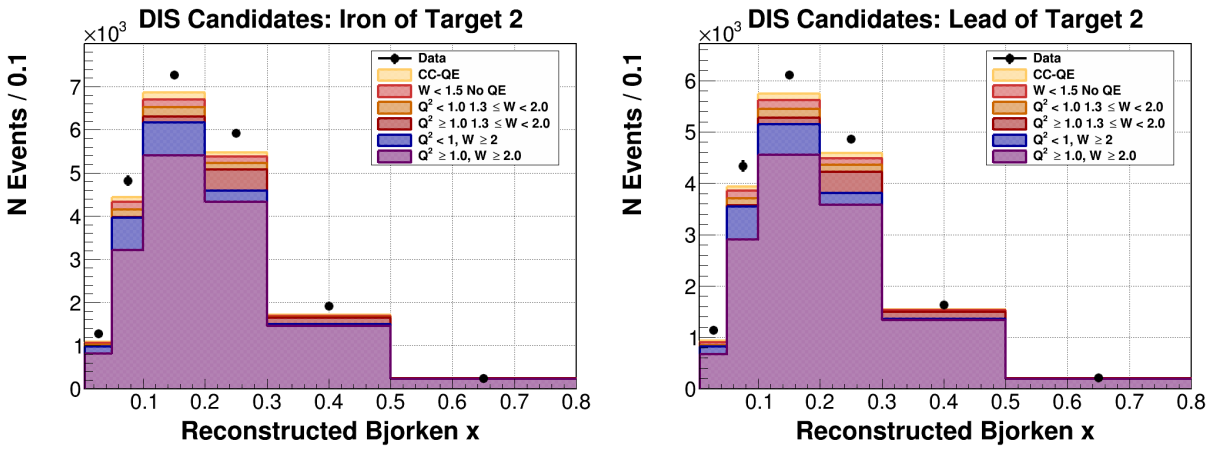

Figure A-12: The reconstructed DIS events for data (black points) and MC (various colored bands) in the iron of target 2 (left) and lead of target 2 (right). The data and MC correspond to 8.89×10^{20} POT.

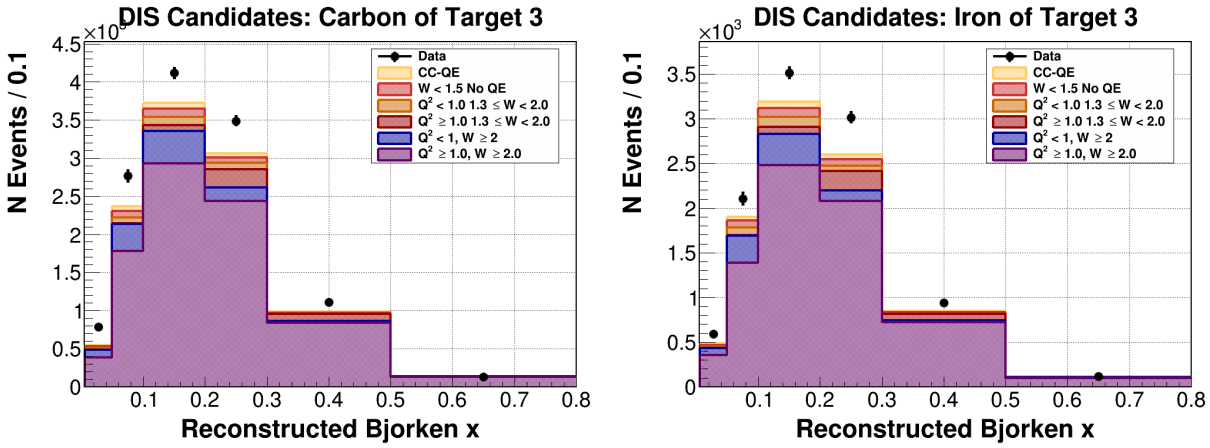

Figure A-13: The reconstructed DIS events for data (black points) and MC (various colored bands) in the carbon of target 3 (left) and iron of target 3 (right). The data and MC correspond to 8.89×10^{20} POT.

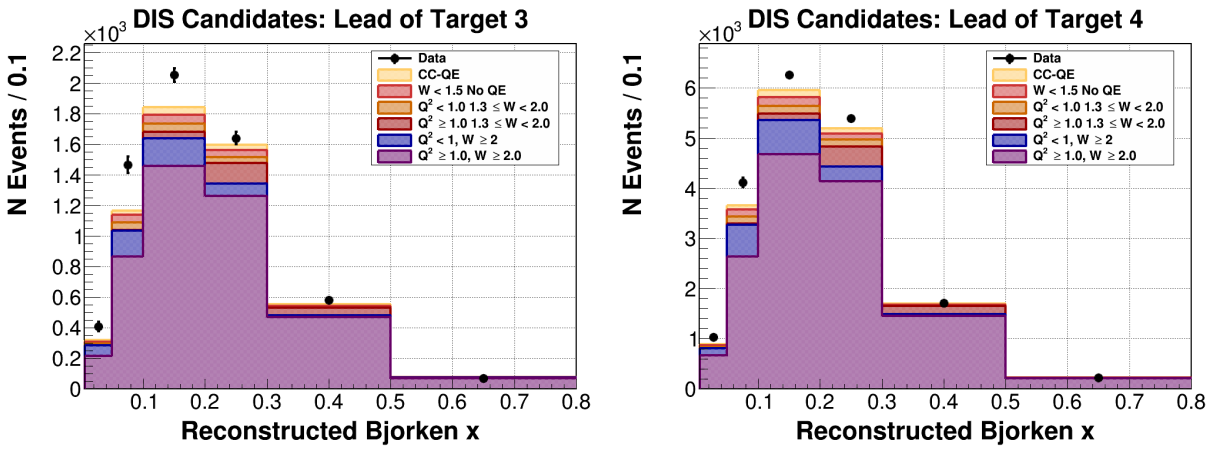

Figure A-14: The reconstructed DIS events for data (black points) and MC (various colored bands) in the lead of target 3 (left) and lead of target 4 (right). The data and MC correspond to 8.89×10^{20} POT.

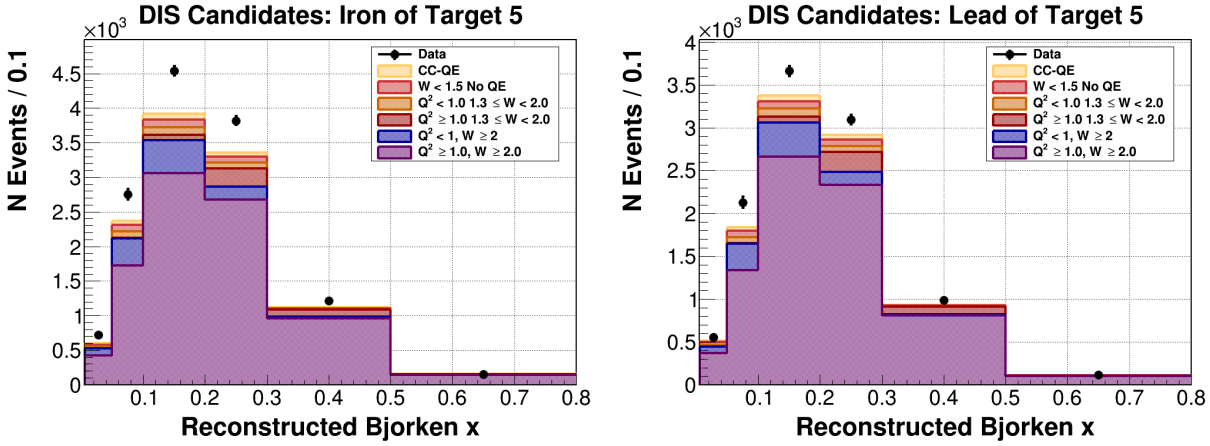

Figure A-15: The reconstructed DIS events for data (black points) and MC (various colored bands) in the iron of target 5 (left) and lead of target 5 (right). The data and MC correspond to 8.89×10^{20} POT.

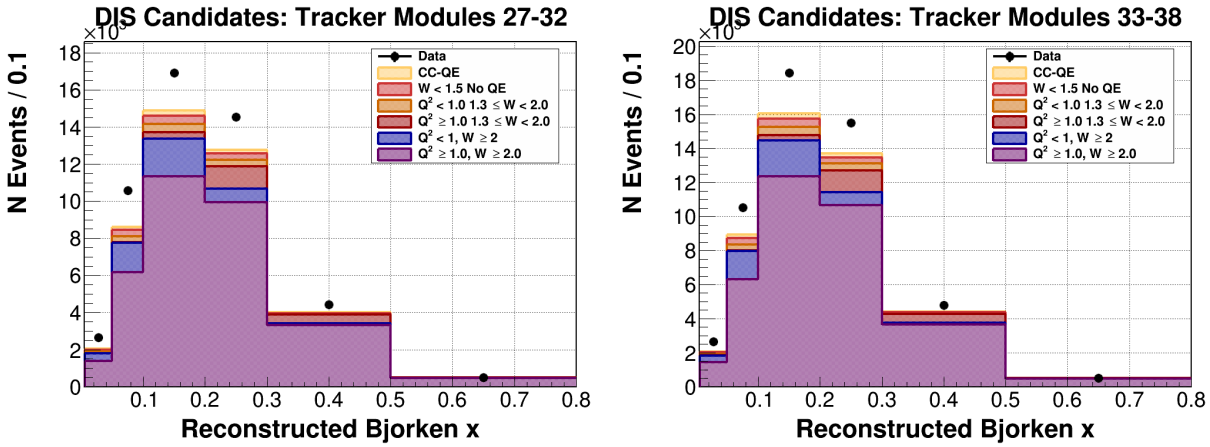

Figure A-16: The reconstructed DIS events for data (black points) and MC (various colored bands) in the scintillator tracker moduless 27-32 (left) and scintillator tracker moduless 33-38 (right). The data and MC correspond to 8.89×10^{20} POT.

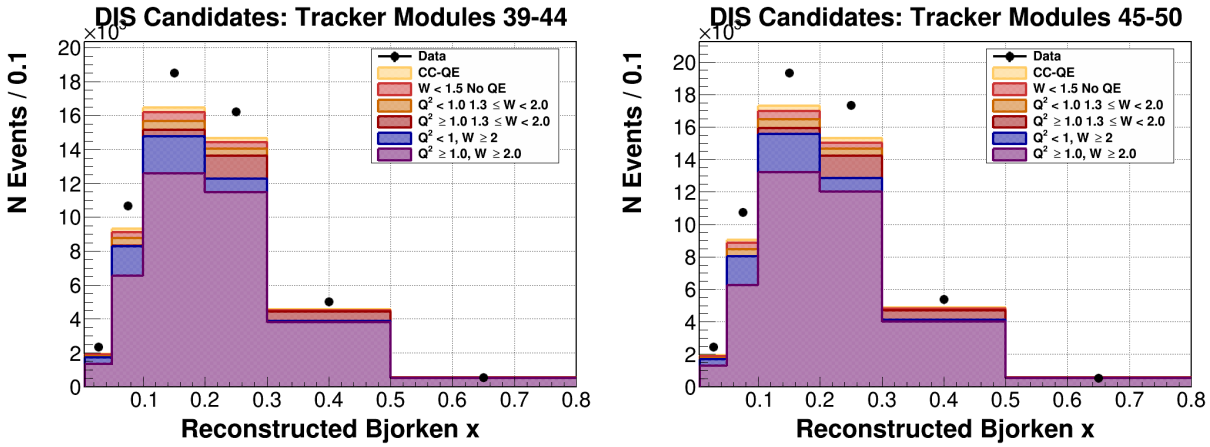

Figure A-17: The reconstructed DIS events for data (black points) and MC (various colored bands) in the scintillator tracker moduless 39-44 (left) and scintillator tracker moduless 45-50 (right). The data and MC correspond to 8.89×10^{20} POT.

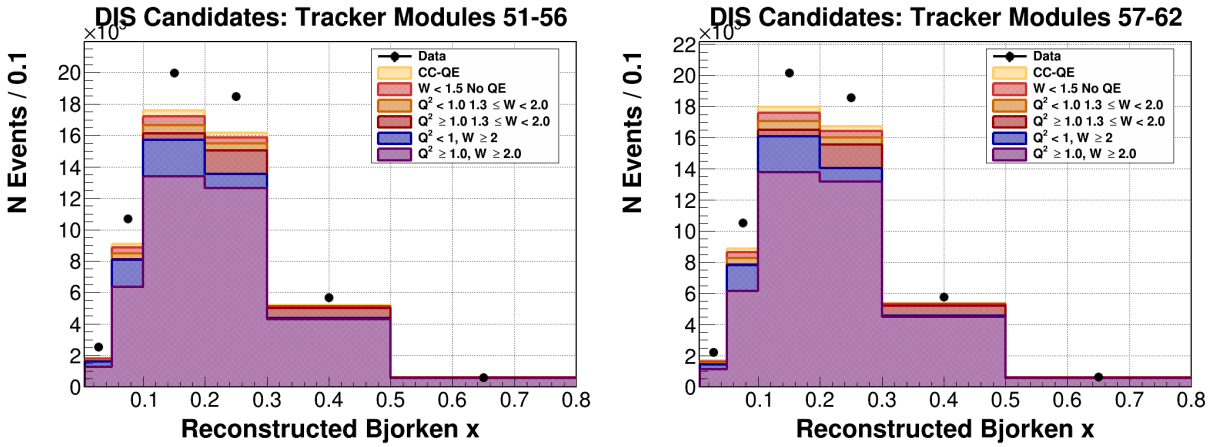

Figure A-18: The reconstructed DIS events for data (black points) and MC (various colored bands) in the scintillator tracker moduless 51-56 (left) and scintillator tracker moduless 57-62 (right). The data and MC correspond to 8.89×10^{20} POT.

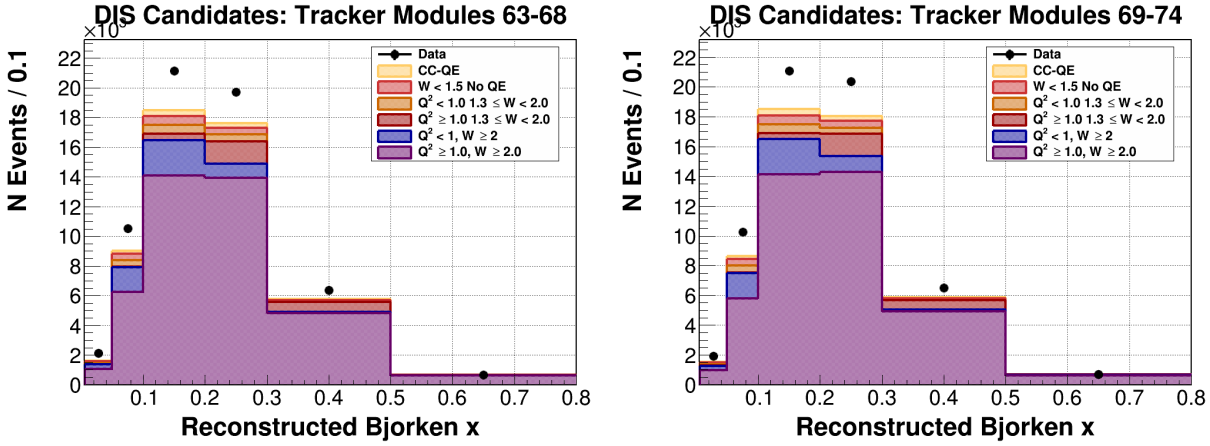

Figure A-19: The reconstructed DIS events for data (black points) and MC (various colored bands) in the scintillator tracker moduless 63-68 (left) and scintillator tracker moduless 69-74 (right). The data and MC correspond to 8.89×10^{20} POT.

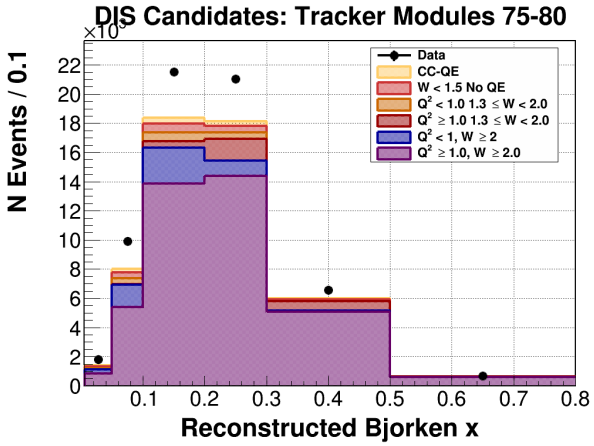

Figure A-20: The reconstructed DIS events for data (black points) and MC (various colored bands) in the scintillator tracker moduless 75-80 (right). The data and MC correspond to 8.89×10^{20} POT.

APPENDIX B
PLASTIC BACKGROUND

B.1 Event distribution of the DIS sample in the nuclear target region as a function of plane number

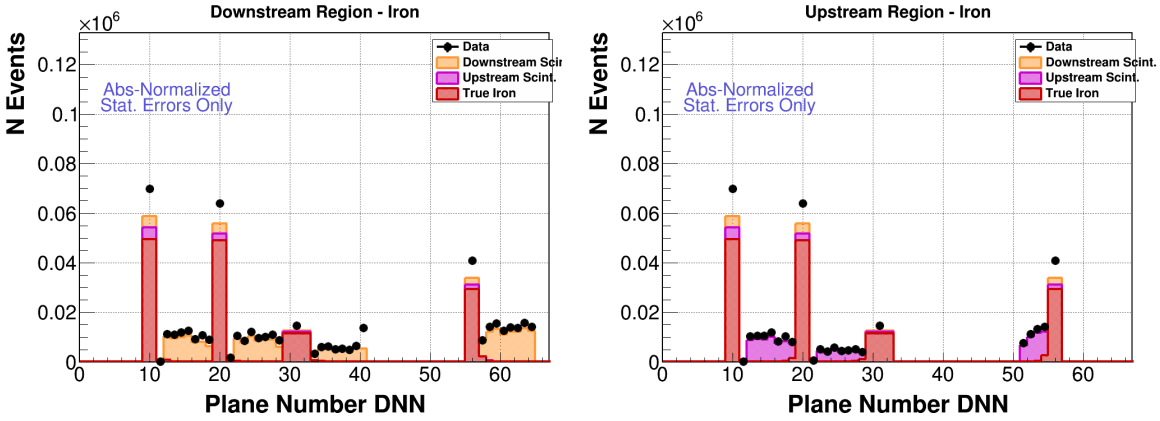

Figure B-1: Event distribution of the DIS sample in the nuclear target region. Downstream plastic and passive target (left). Upstream plastic and passive target (right).

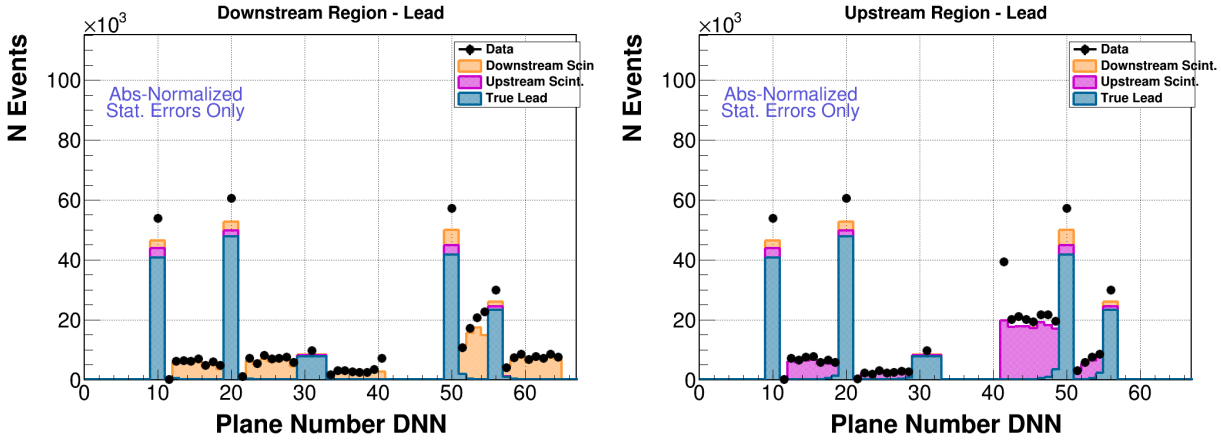

Figure B-2: Event distribution of the DIS sample in the nuclear target region. Downstream plastic and passive target (left). Upstream plastic and passive target (right).

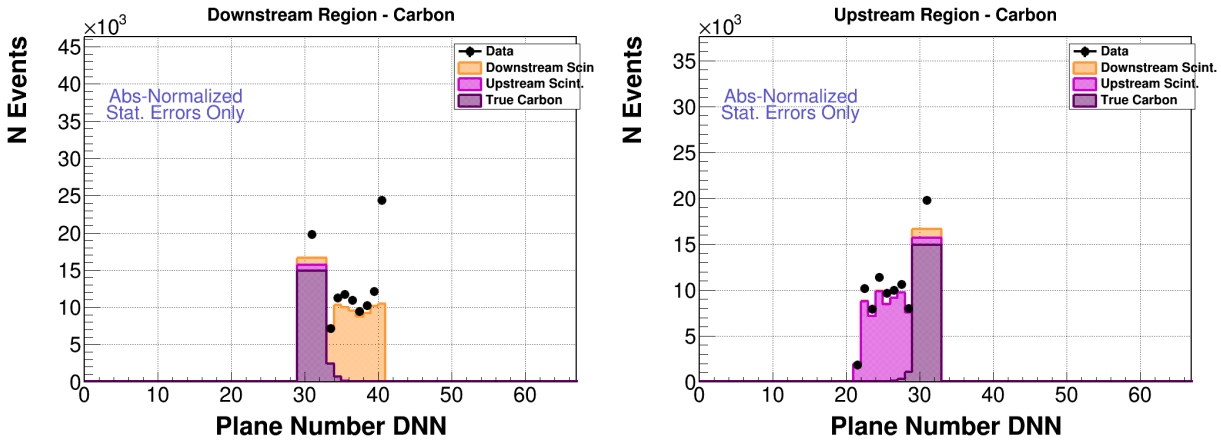

Figure B-3: Event distribution of the DIS sample in the nuclear target region. Downstream plastic and passive target (left). Upstream plastic and passive target (right).

B.2 Event distribution of the DIS sample in the sideband region of a target material

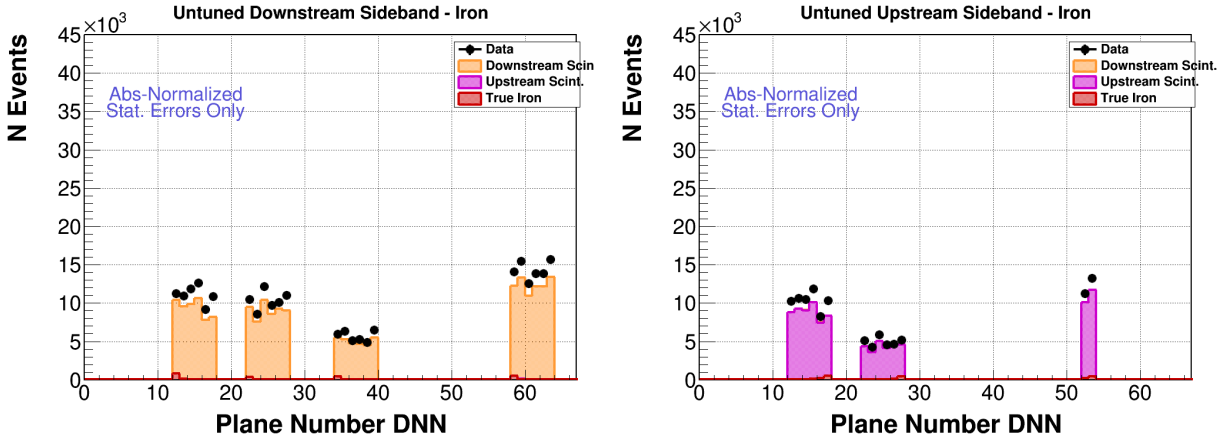

Figure B-4: Event distribution of the DIS sample in the sideband region of a target material. Downstream plastic region (left). Upstream plastic sideband region (right). Note that a few events that truly originate in our target nuclei do make it in to the sideband sample, but this contribution is negligible.

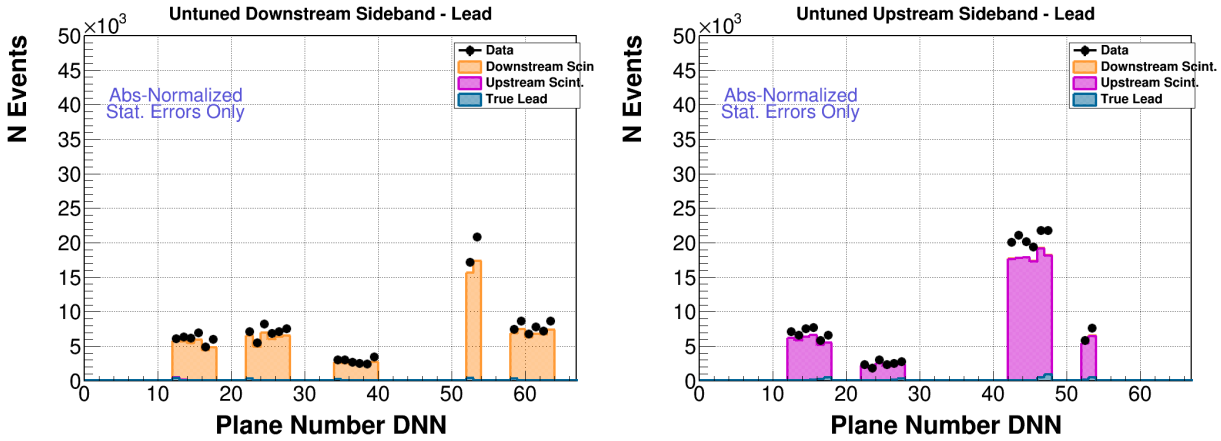

Figure B-5: Event distribution of the DIS sample in the sideband region of a target material. Downstream plastic region (left). Upstream plastic sideband region (right). Note that a few events that truly originate in our target nuclei do make it in to the sideband sample, but this contribution is negligible.

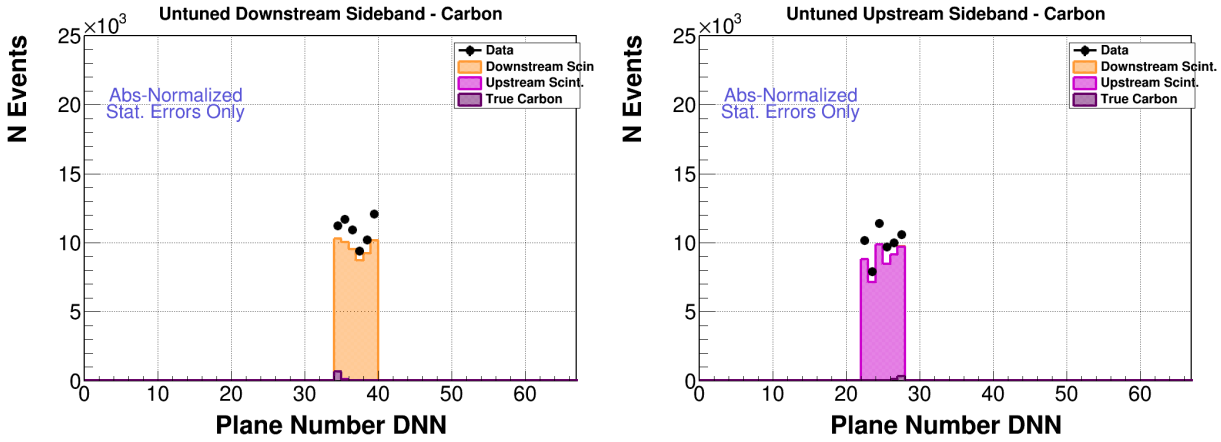

Figure B-6: Event distribution of the DIS sample in the sideband region of a target material. Downstream plastic region (left). Upstream plastic sideband region (right). Note that a few events that truly originate in our target nuclei do make it in to the sideband sample, but this contribution is negligible.

B.3 Breakdown of Kinematics for sideband and passive target region

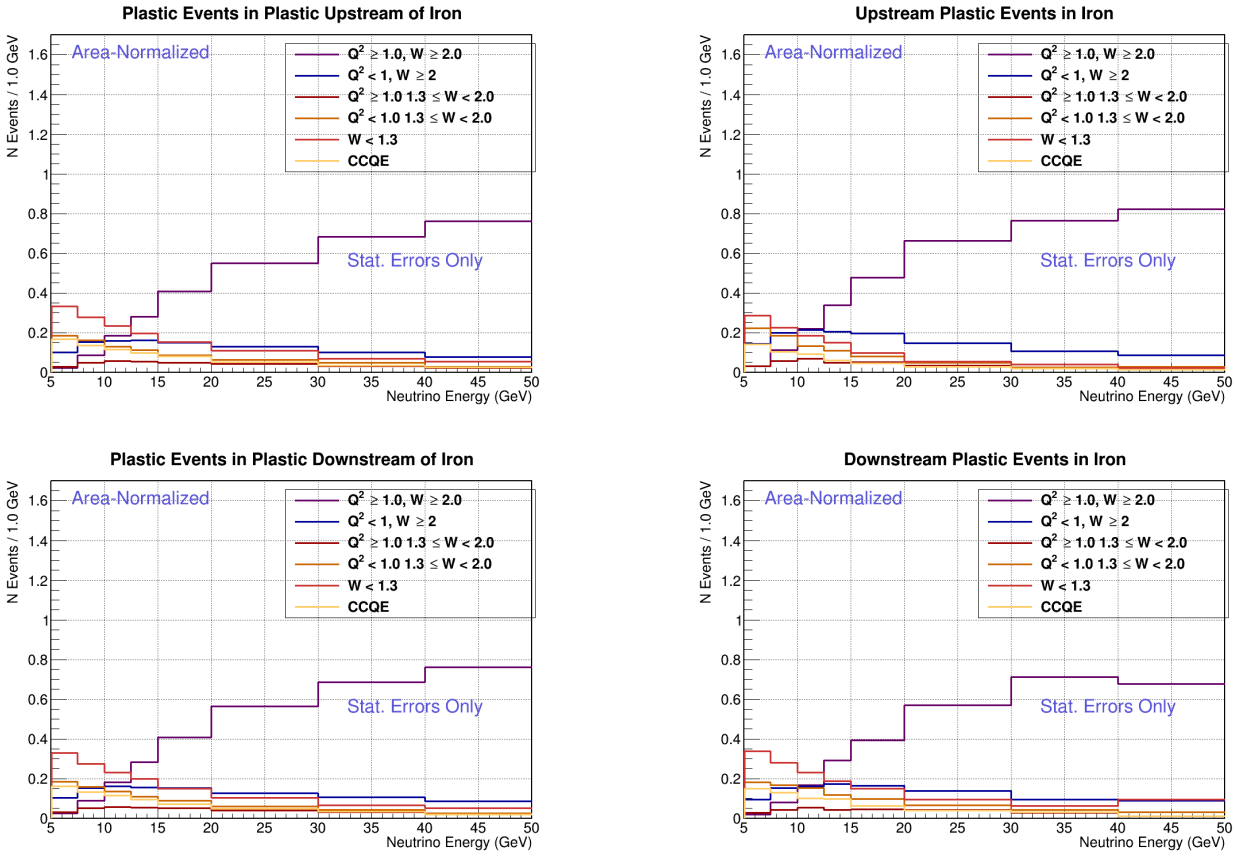

Figure B-7: The shape of the upstream plastic backgrounds as a function of E_ν, separated by their true vertex interaction, in the sideband region (top left) compared to the signal region (top right). The shape of the downstream plastic backgrounds as a function of E_ν, separated by their true vertex interaction, in the sideband region (bottom left) compared to the signal region (bottom right). The colors represent the true material.

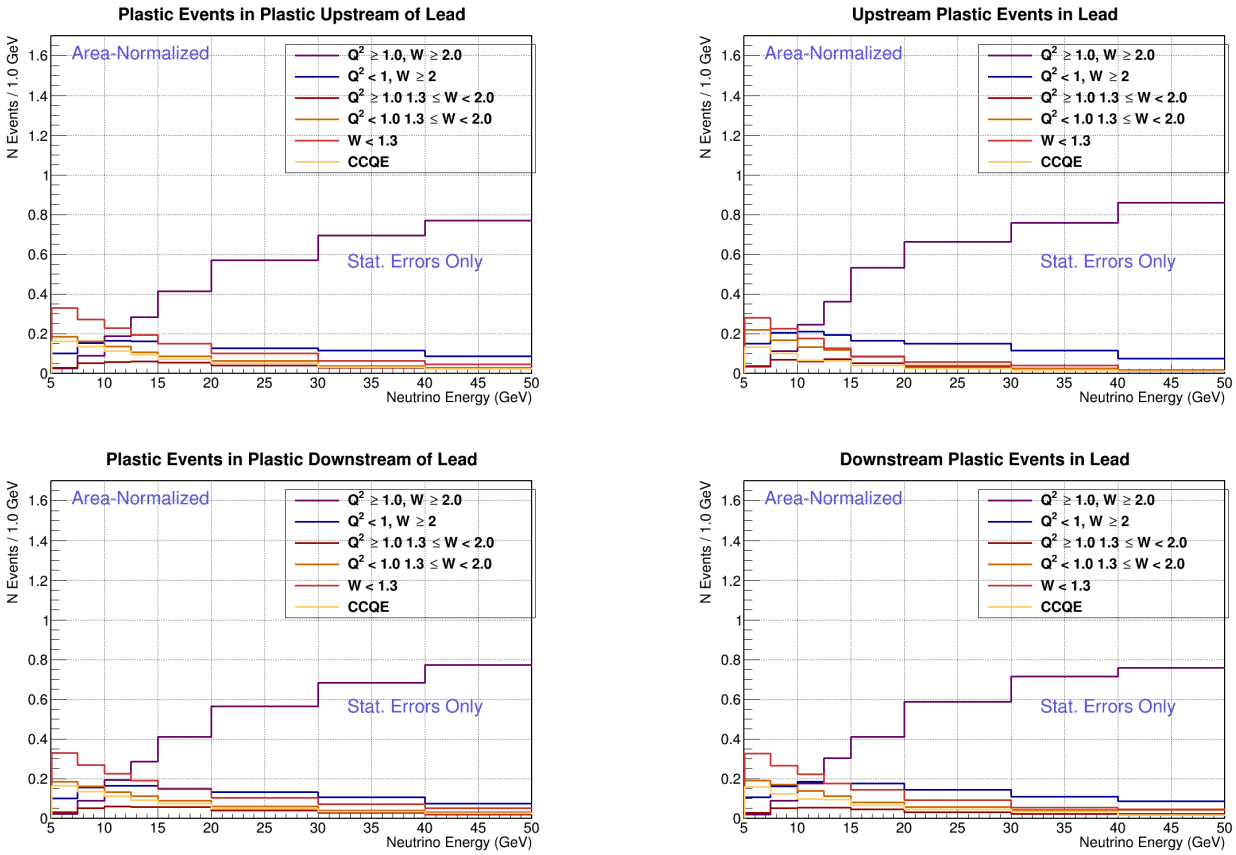

Figure B-8: The shape of the upstream plastic backgrounds as a function of E_ν, separated by their true vertex interaction, in the sideband region (top left) compared to the signal region (top right). The shape of the downstream plastic backgrounds as a function of E_ν, separated by their true vertex interaction, in the sideband region (bottom left) compared to the signal region (bottom right). The colors represent the true material.

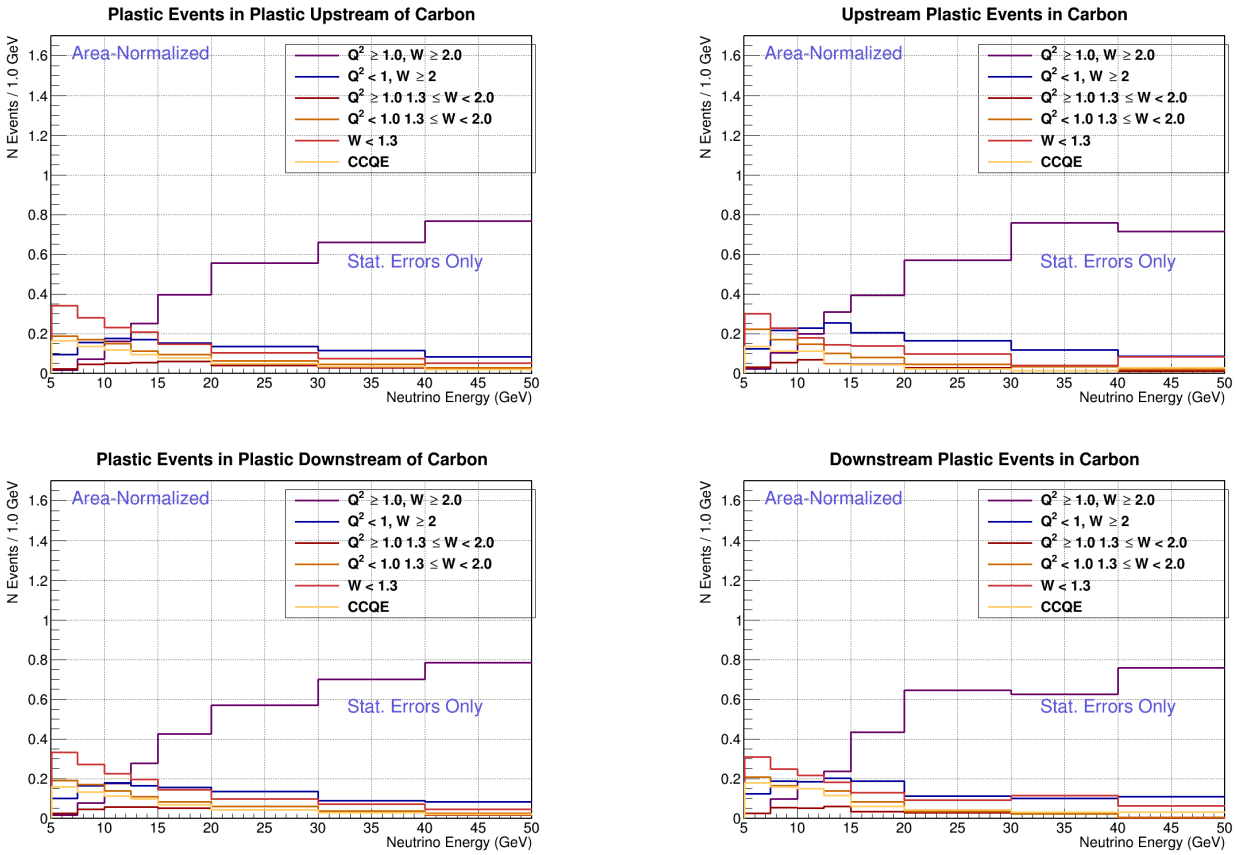

Figure B-9: The shape of the upstream plastic backgrounds as a function of E_ν, separated by their true vertex interaction, in the sideband region (top left) compared to the signal region (top right). The shape of the downstream plastic backgrounds as a function of E_ν, separated by their true vertex interaction, in the sideband region (bottom left) compared to the signal region (bottom right). The colors represent the true material.

B.4 Data To MC Ratio Before And After The Background Constraint In The Sideband Region.

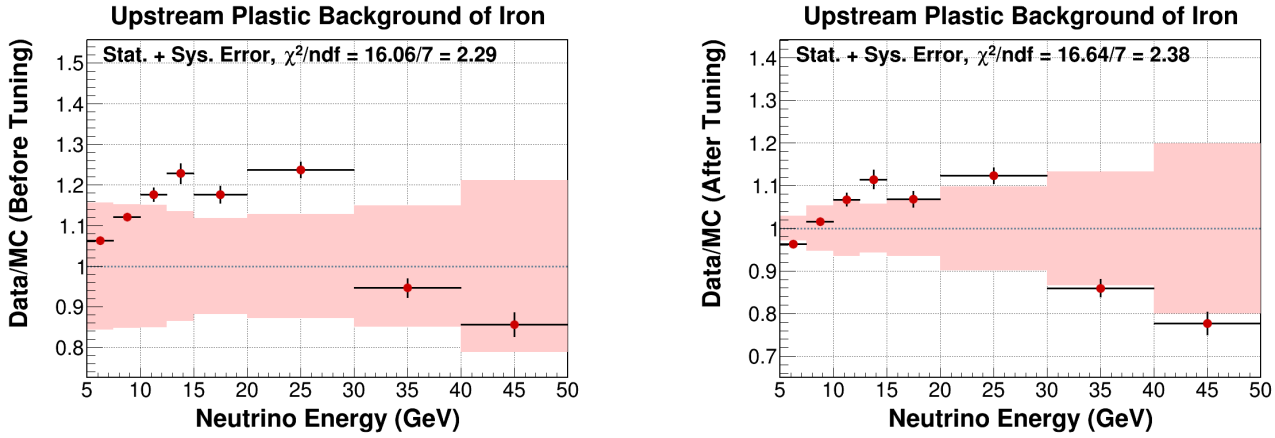

Figure B-10: Data to MC ratio before the plastic background tuning (left). Data to MC ratio after the plastic background tuning (right).

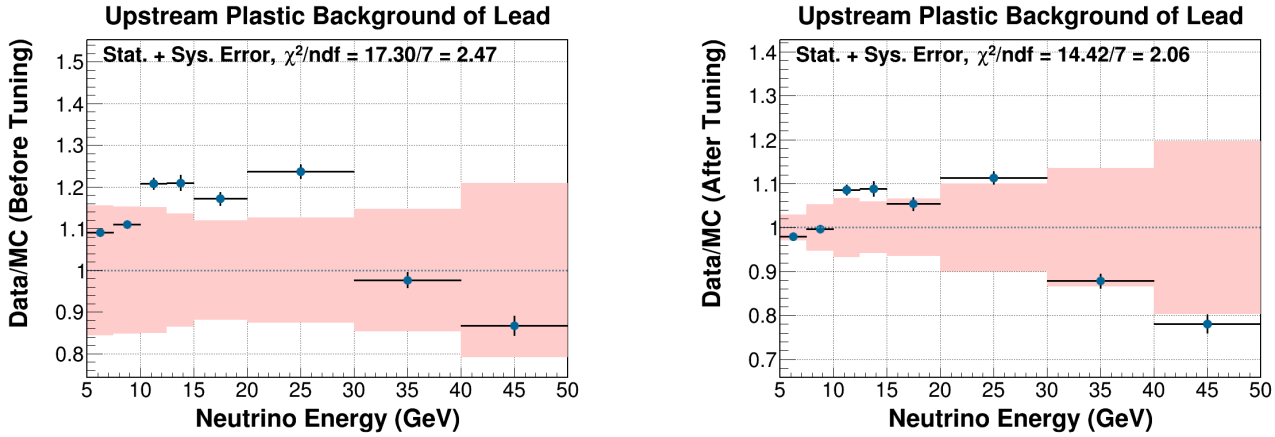

Figure B-11: Data to MC ratio before the plastic background tuning (left). Data to MC ratio after the plastic background tuning (right).

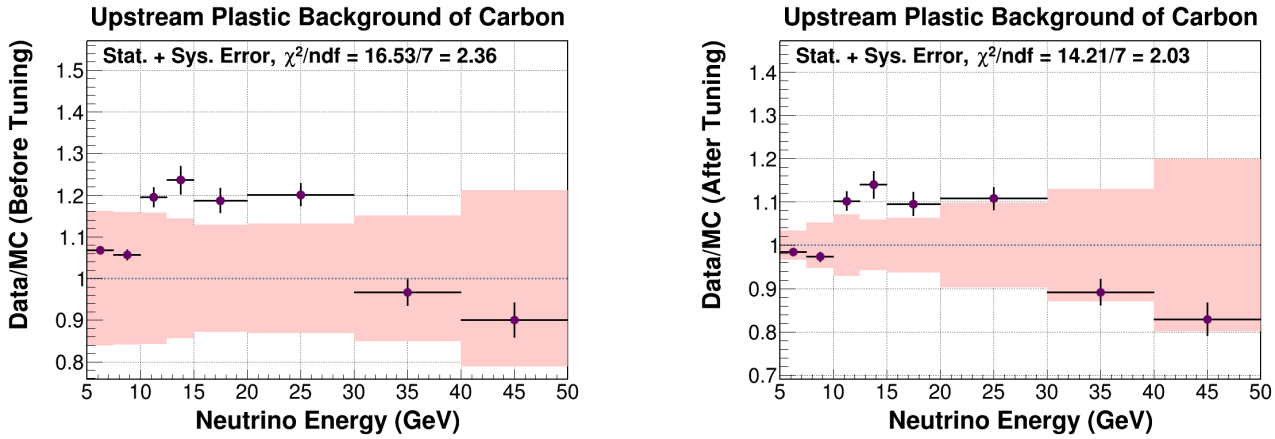

Figure B-12: Data to MC ratio before the plastic background tuning (left). Data to MC ratio after the plastic background tuning (right).

B.5 Data To MC Ratio Before And After The Background Constraint In The Sideband Region.

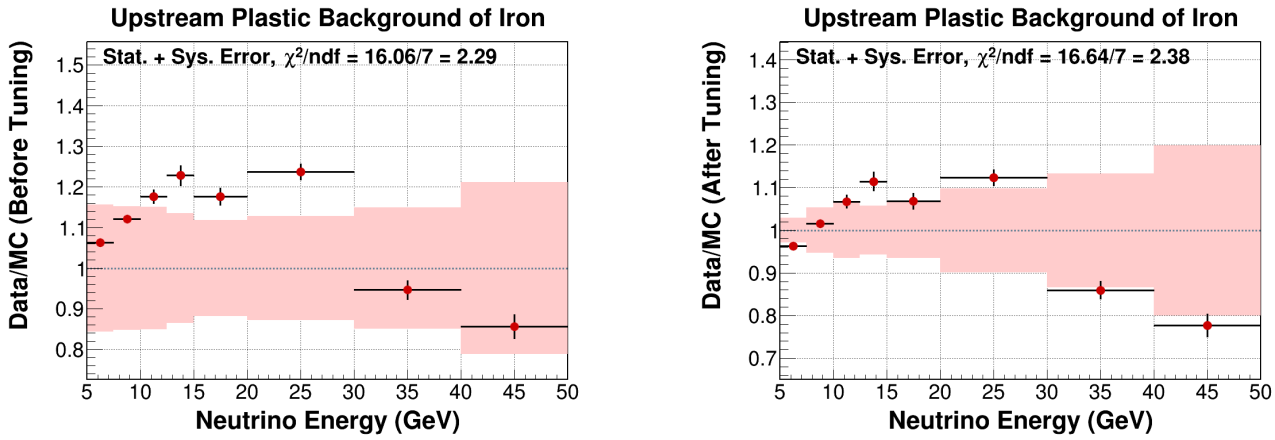

Figure B-13: Data to MC ratio before the plastic background tuning (left). Data to MC ratio after the plastic background tuning (right).

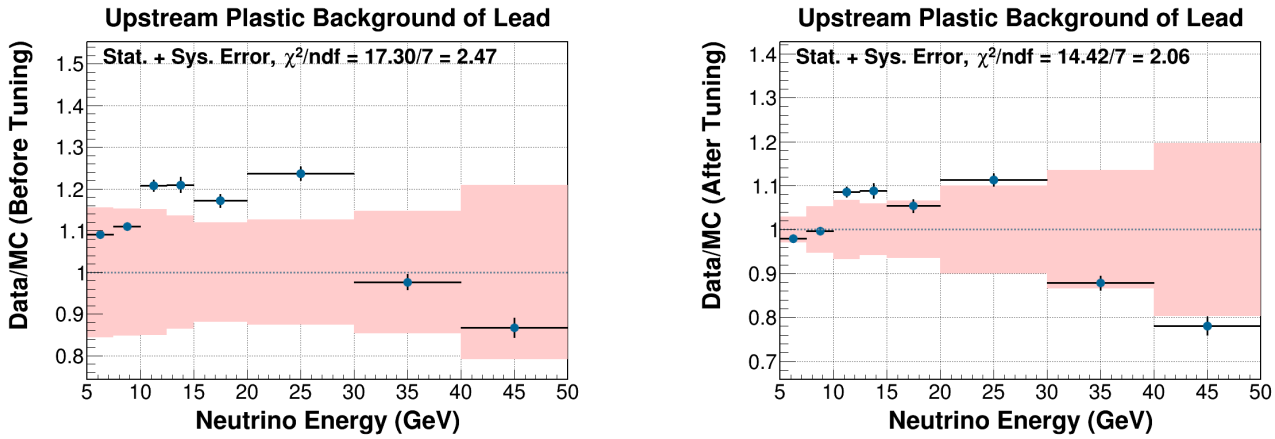

Figure B-14: Data to MC ratio before the plastic background tuning (left). Data to MC ratio after the plastic background tuning (right).

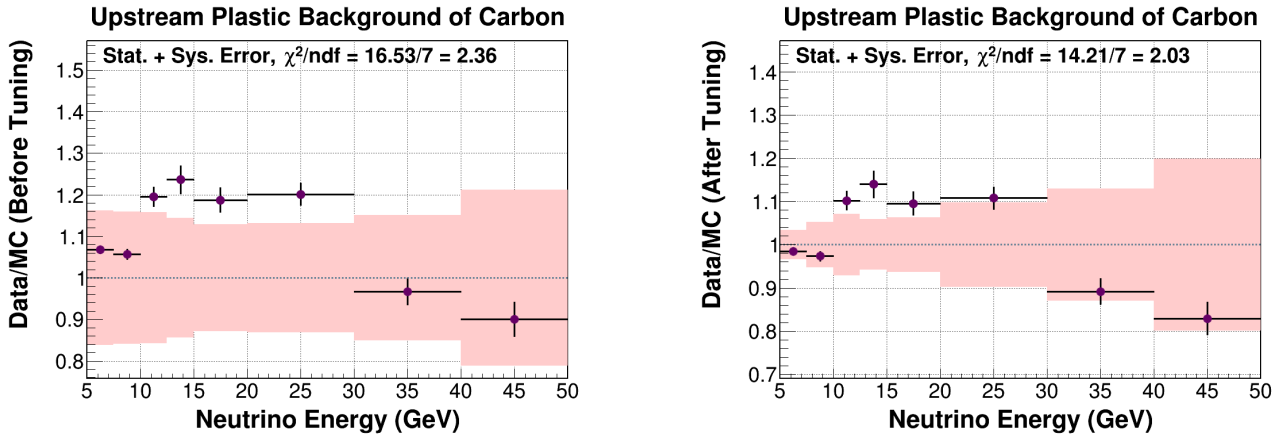

Figure B-15: Data to MC ratio before the plastic background tuning (left). Data to MC ratio after the plastic background tuning (right).

B.6 Data and MC ratio before and after the background constraint in the target material region.

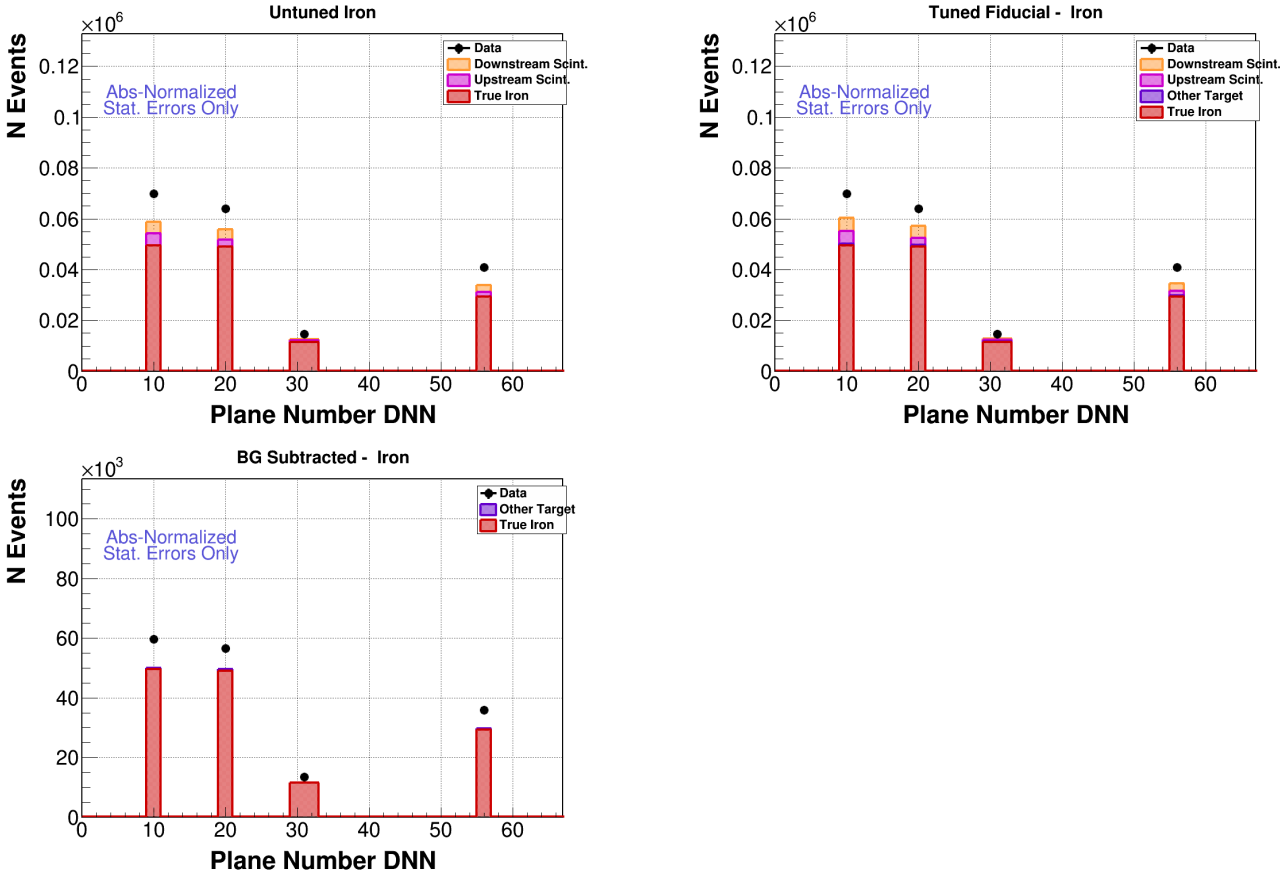

Figure B-16: Top row: Event distribution as a function of plane number before the MC plastic background is tuned. Middle row: Event distribution as a function of plane number after the MC plastic background is tuned. Bottom row: Event distribution as a function of plane number after the MC plastic background is tuned and the tuned background is subtracted from data.

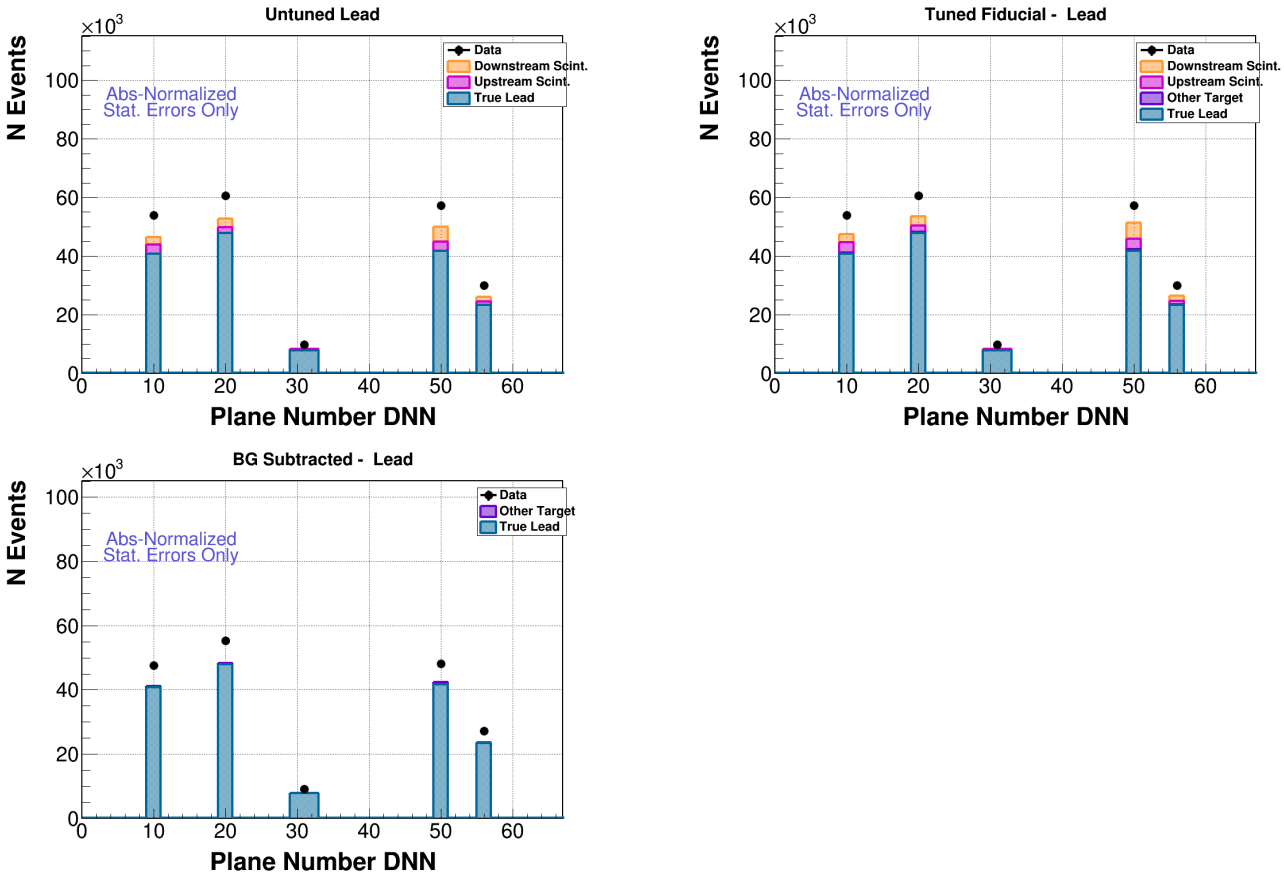

Figure B-17: Top row: Event distribution as a function of plane number before the MC plastic background is tuned. Middle row: Event distribution as a function of plane number after the MC plastic background is tuned. Bottom row: Event distribution as a function of plane number after the MC plastic background is tuned and the tuned background is subtracted from data.

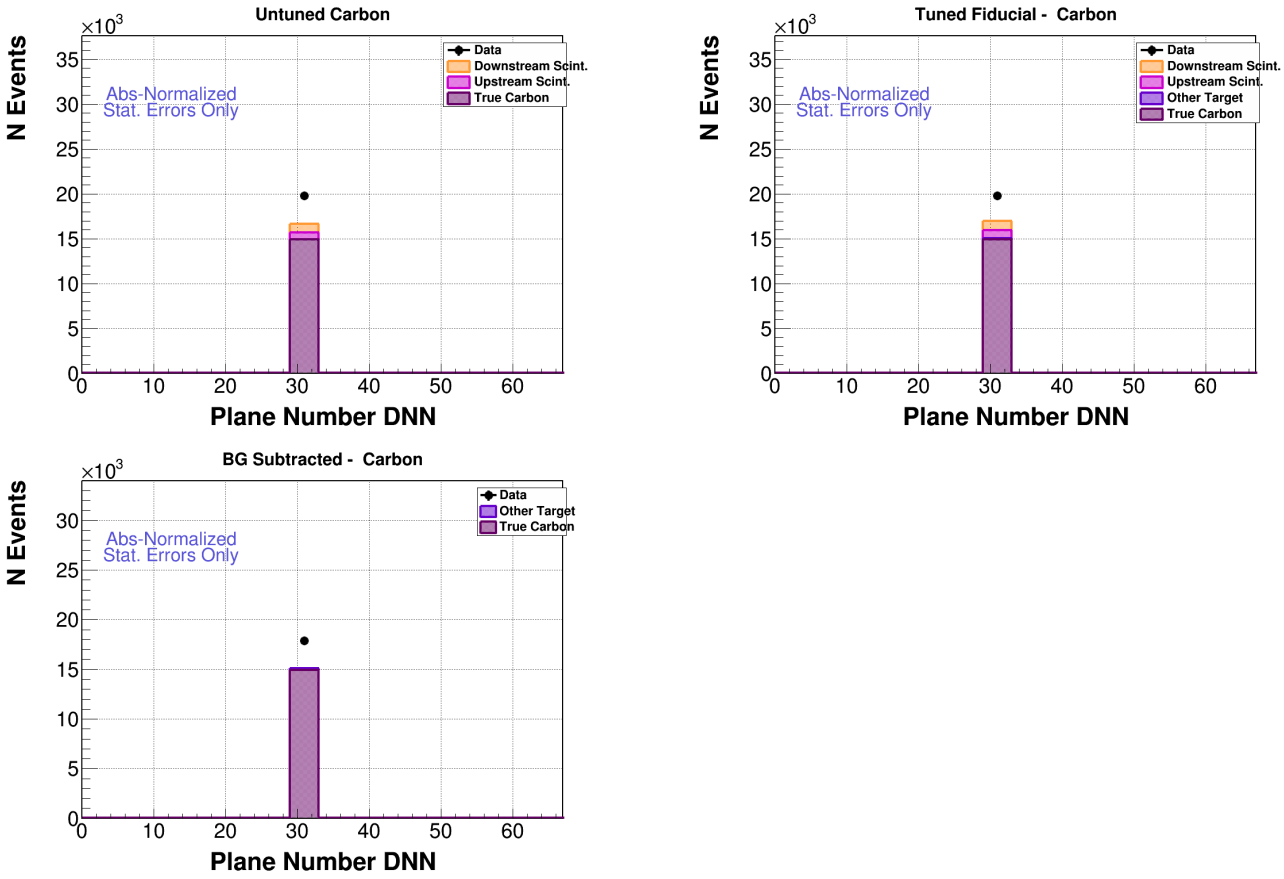

Figure B-18: Top row: Event distribution as a function of plane number before the MC plastic background is tuned. Middle row: Event distribution as a function of plane number after the MC plastic background is tuned. Bottom row: Event distribution as a function of plane number after the MC plastic background is tuned and the tuned background is subtracted from data.

APPENDIX C
NON-DIS BACKGROUND

C.1 DIS signal and background before and after background tuning as a function of E_ν

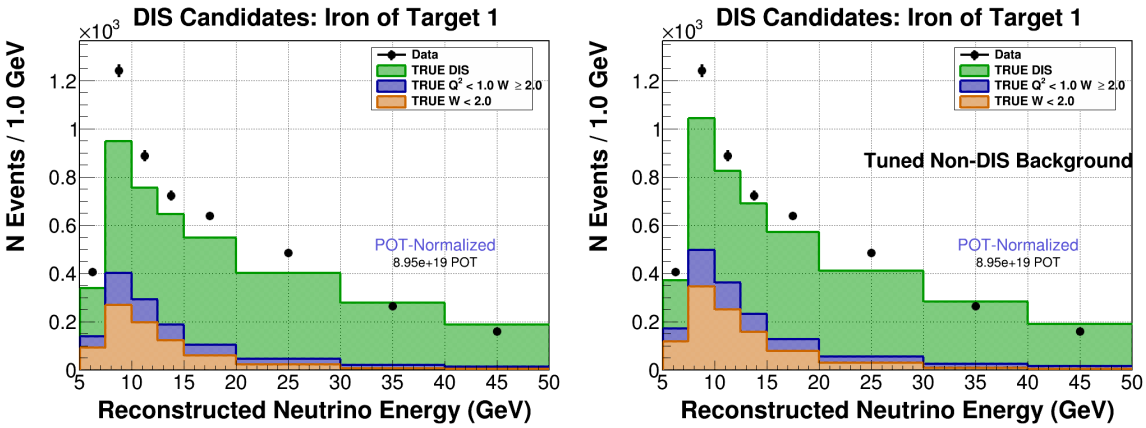

Figure C-1: Events passing the DIS selection cuts in data (black points) as well as the MC signal (green) and background (orange and blue). The left plot is prior to the background tuning to data, and the right plot is after tuning.

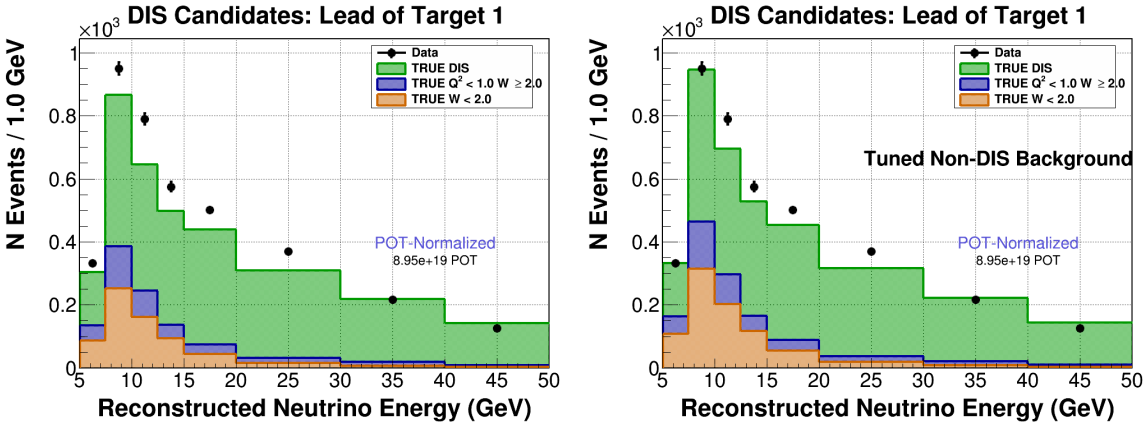

Figure C-2: Events passing the DIS selection cuts in data (black points) as well as the MC signal (green) and background (orange and blue). The left plot is prior to the background tuning to data, and the right plot is after tuning.

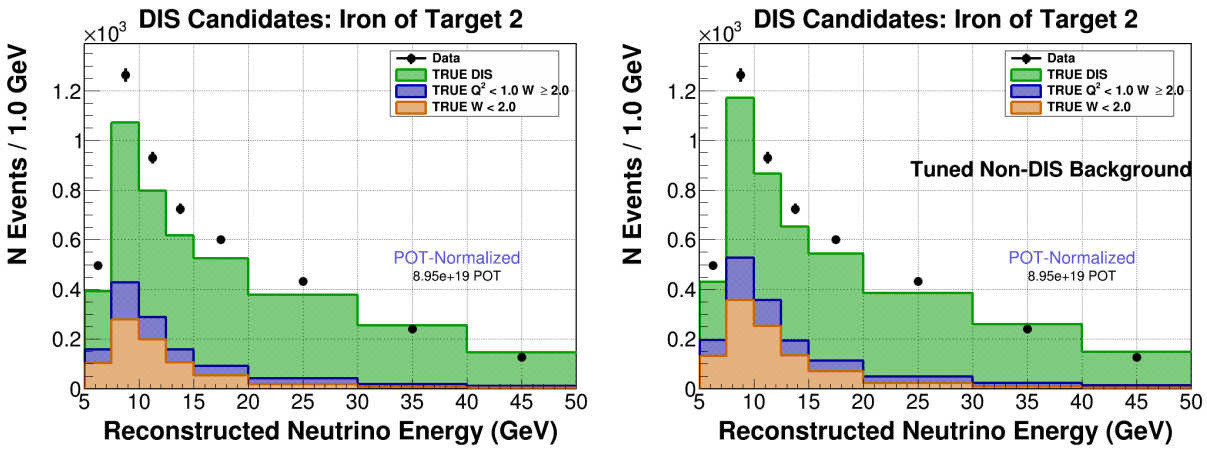

Figure C-3: Events passing the DIS selection cuts in data (black points) as well as the MC signal (green) and background (orange and blue). The left plot is prior to the background tuning to data, and the right plot is after tuning.

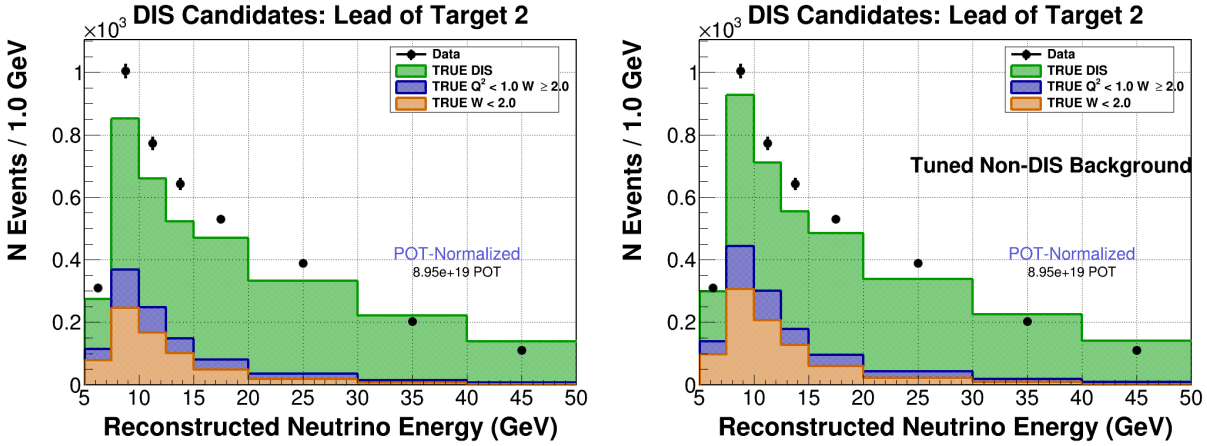

Figure C-4: Events passing the DIS selection cuts in data (black points) as well as the MC signal (green) and background (orange and blue). The left plot is prior to the background tuning to data, and the right plot is after tuning.

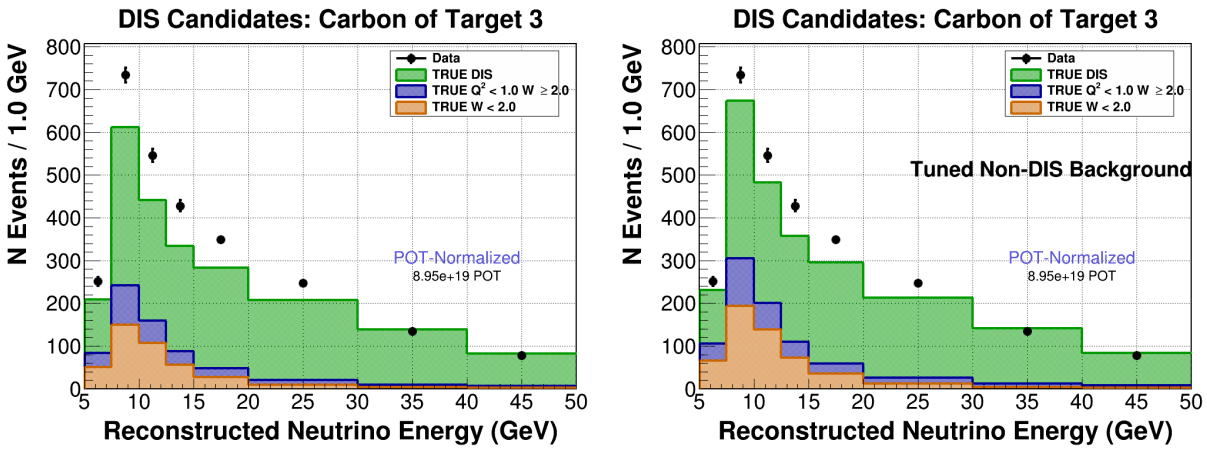

Figure C-5: Events passing the DIS selection cuts in data (black points) as well as the MC signal (green) and background (orange and blue). The left plot is prior to the background tuning to data, and the right plot is after tuning.

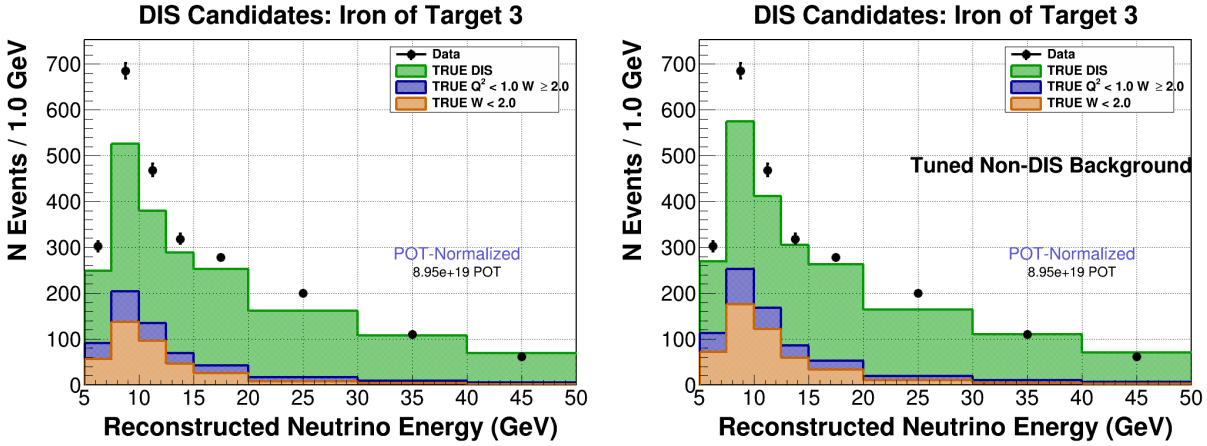

Figure C-6: Events passing the DIS selection cuts in data (black points) as well as the MC signal (green) and background (orange and blue). The left plot is prior to the background tuning to data, and the right plot is after tuning.

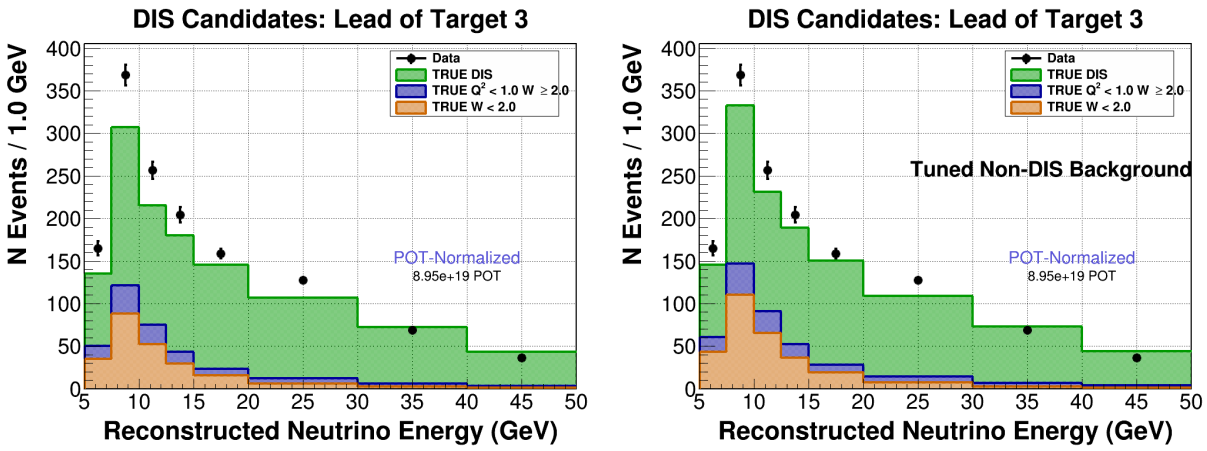

Figure C-7: Events passing the DIS selection cuts in data (black points) as well as the MC signal (green) and background (orange and blue). The left plot is prior to the background tuning to data, and the right plot is after tuning.

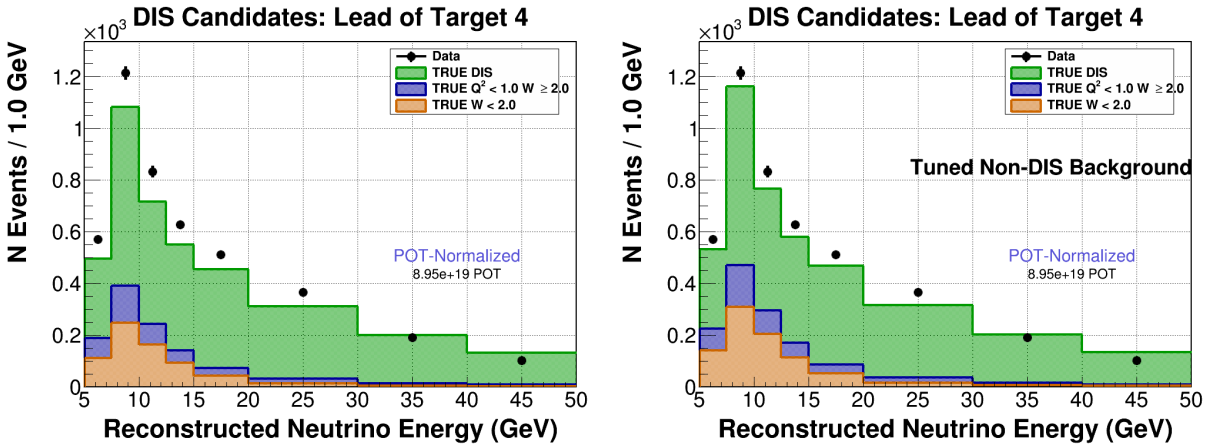

Figure C-8: Events passing the DIS selection cuts in data (black points) as well as the MC signal (green) and background (orange and blue). The left plot is prior to the background tuning to data, and the right plot is after tuning.

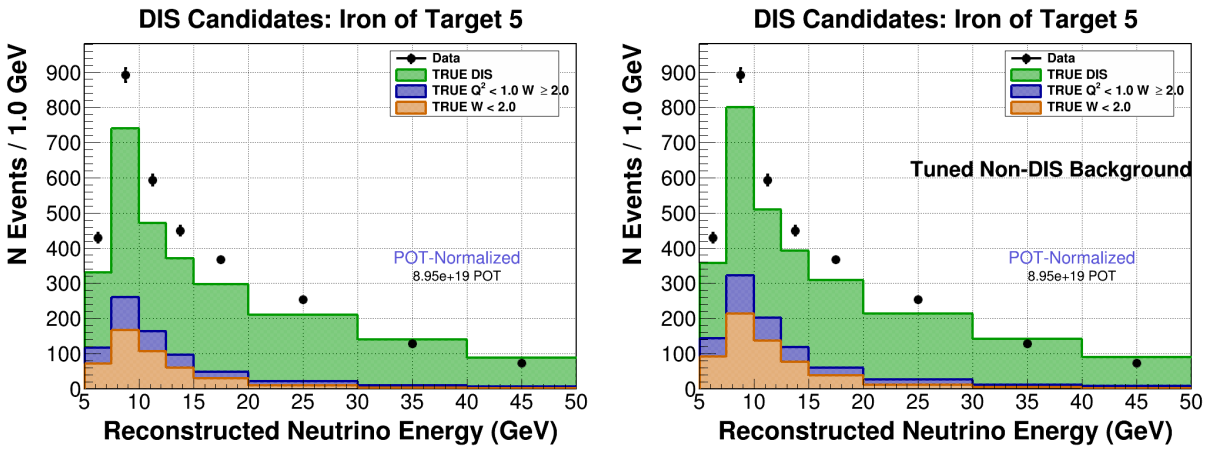

Figure C-9: Events passing the DIS selection cuts in data (black points) as well as the MC signal (green) and background (orange and blue). The left plot is prior to the background tuning to data, and the right plot is after tuning.

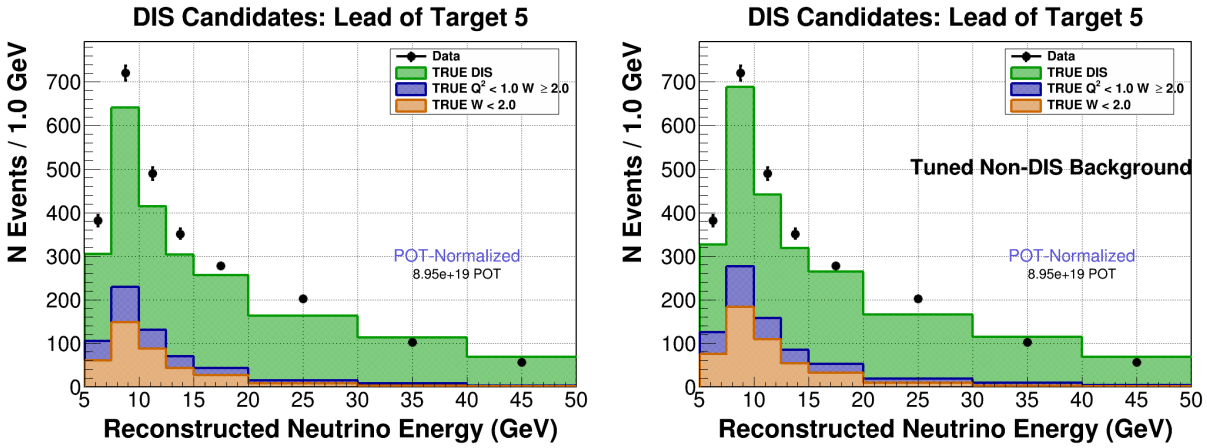

Figure C-10: Events passing the DIS selection cuts in data (black points) as well as the MC signal (green) and background (orange and blue). The left plot is prior to the background tuning to data, and the right plot is after tuning.

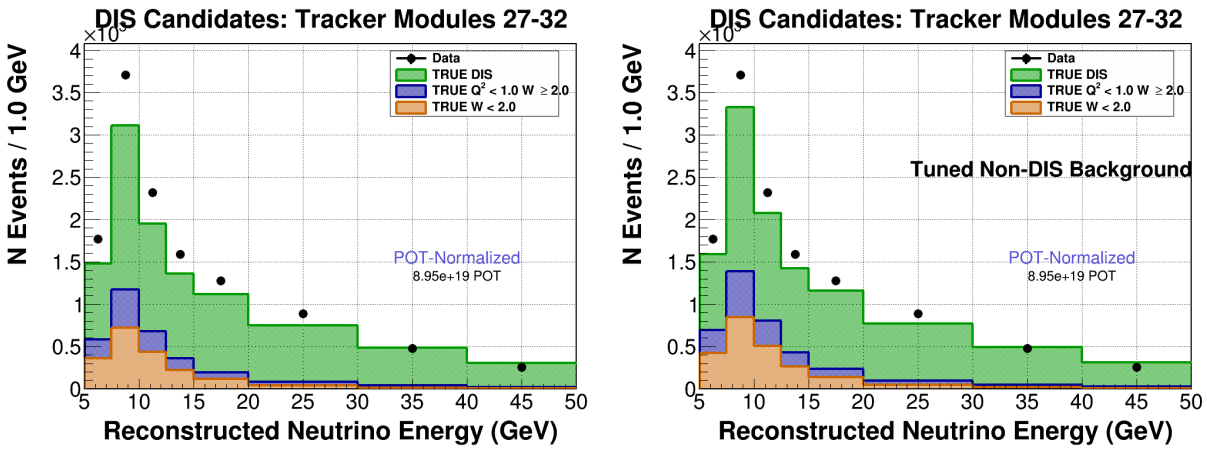

Figure C-11: Events passing the DIS selection cuts in data (black points) as well as the MC signal (green) and background (orange and blue). The left plot is prior to the background tuning to data, and the right plot is after tuning.

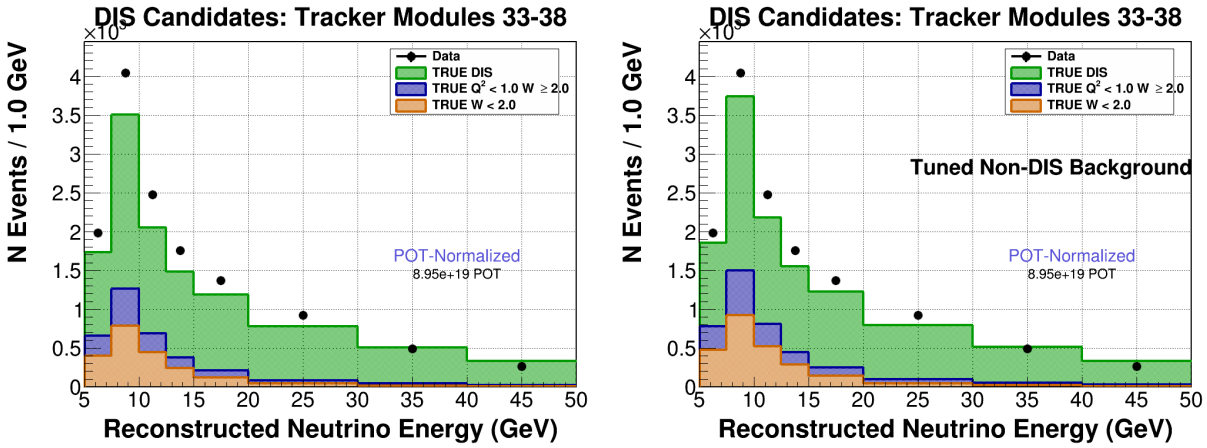

Figure C-12: Events passing the DIS selection cuts in data (black points) as well as the MC signal (green) and background (orange and blue). The left plot is prior to the background tuning to data, and the right plot is after tuning.

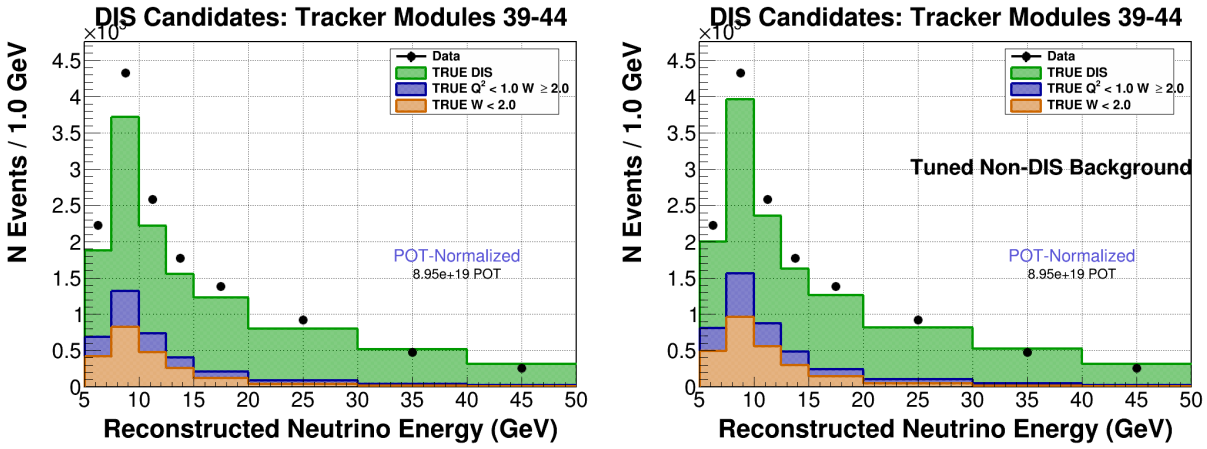

Figure C-13: Events passing the DIS selection cuts in data (black points) as well as the MC signal (green) and background (orange and blue). The left plot is prior to the background tuning to data, and the right plot is after tuning.

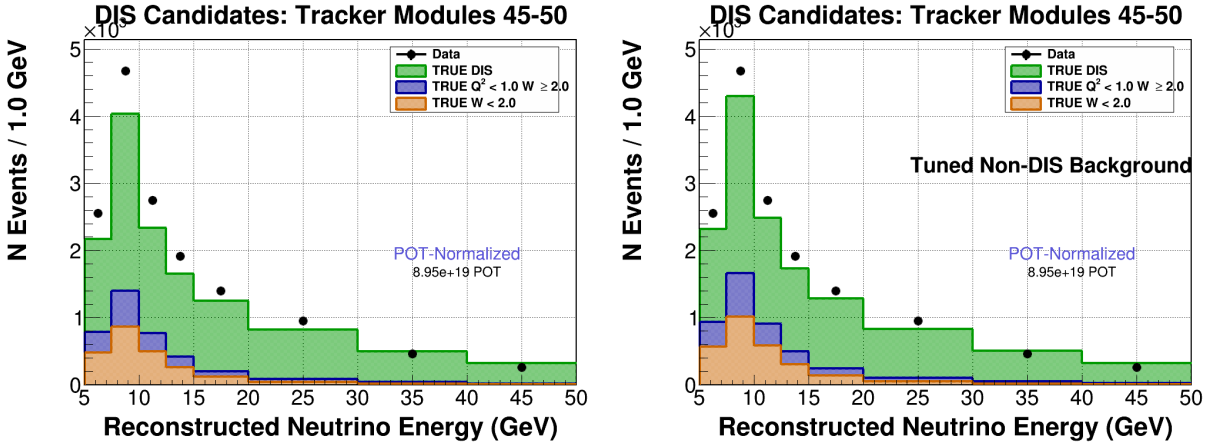

Figure C-14: Events passing the DIS selection cuts in data (black points) as well as the MC signal (green) and background (orange and blue). The left plot is prior to the background tuning to data, and the right plot is after tuning.

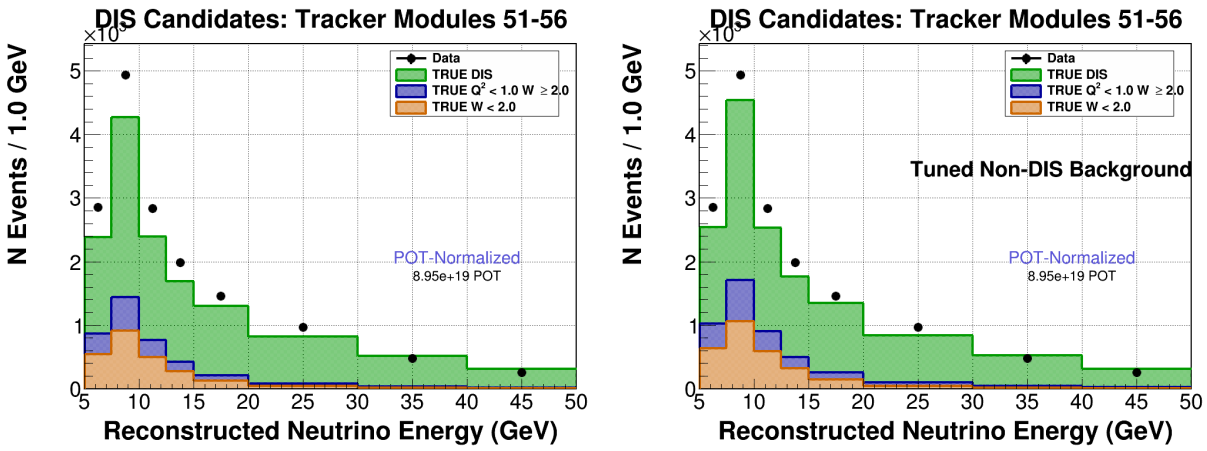

Figure C-15: Events passing the DIS selection cuts in data (black points) as well as the MC signal (green) and background (orange and blue). The left plot is prior to the background tuning to data, and the right plot is after tuning.

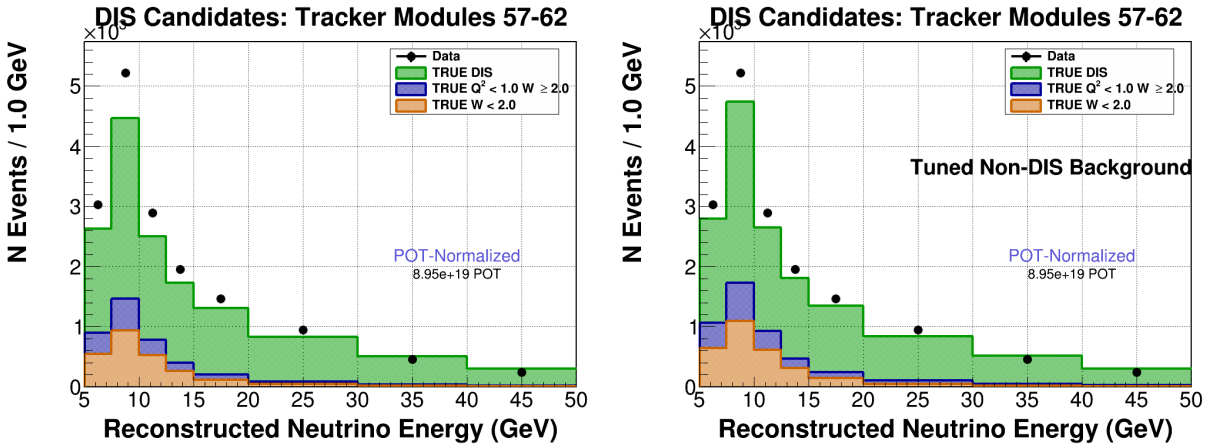

Figure C-16: Events passing the DIS selection cuts in data (black points) as well as the MC signal (green) and background (orange and blue). The left plot is prior to the background tuning to data, and the right plot is after tuning.

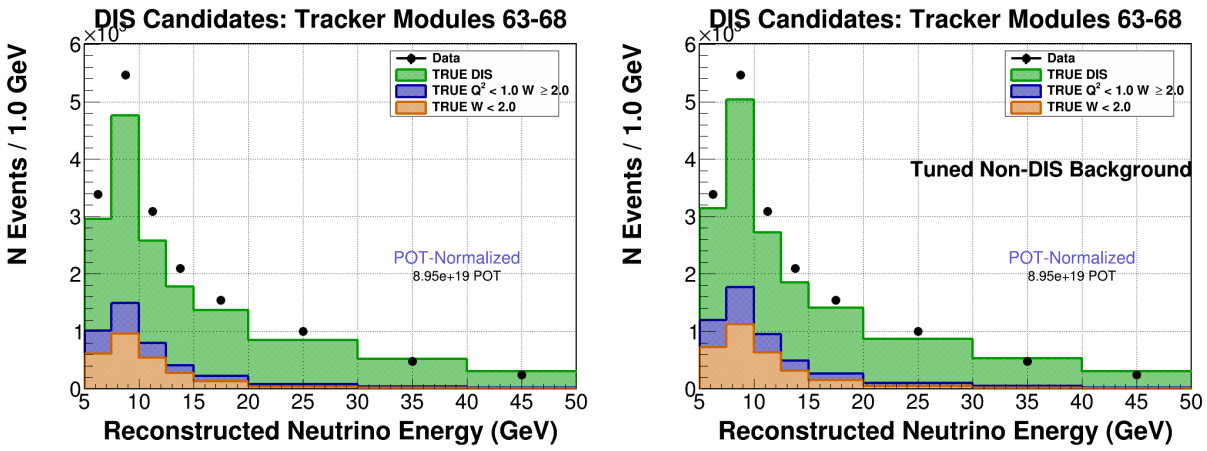

Figure C-17: Events passing the DIS selection cuts in data (black points) as well as the MC signal (green) and background (orange and blue). The left plot is prior to the background tuning to data, and the right plot is after tuning.

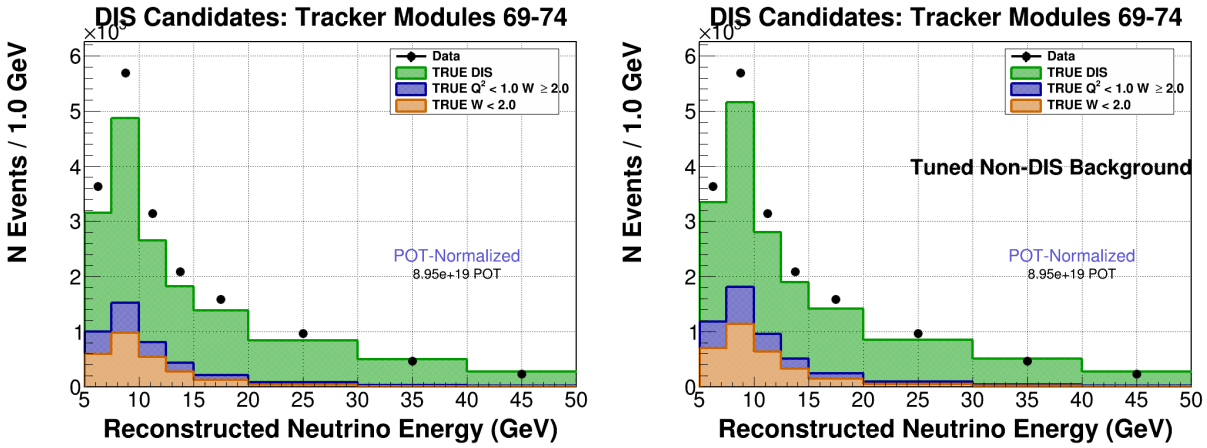

Figure C-18: Events passing the DIS selection cuts in data (black points) as well as the MC signal (green) and background (orange and blue). The left plot is prior to the background tuning to data, and the right plot is after tuning.

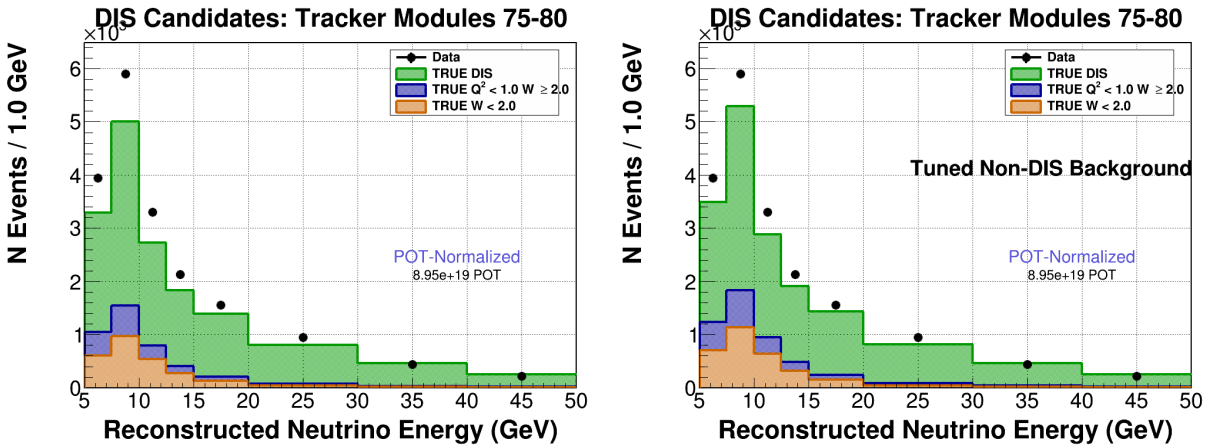

Figure C-19: Events passing the DIS selection cuts in data (black points) as well as the MC signal (green) and background (orange and blue). The left plot is prior to the background tuning to data, and the right plot is after tuning.

C.2 DIS signal and background before and after background tuning as a function of E_μ

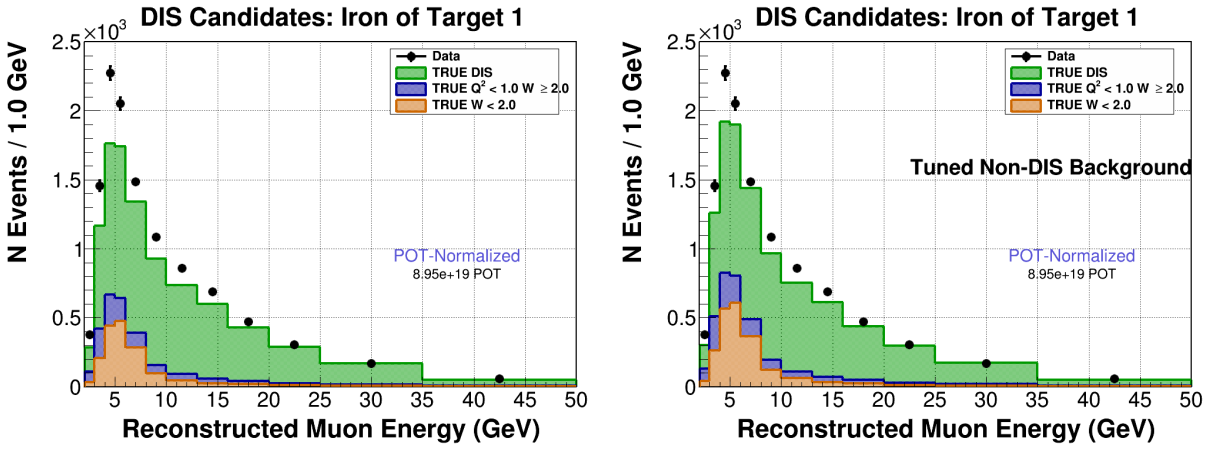

Figure C-20: Events passing the DIS selection cuts in data (black points) as well as the MC signal (green) and background (orange and blue). The left plot is prior to the background tuning to data, and the right plot is after tuning.

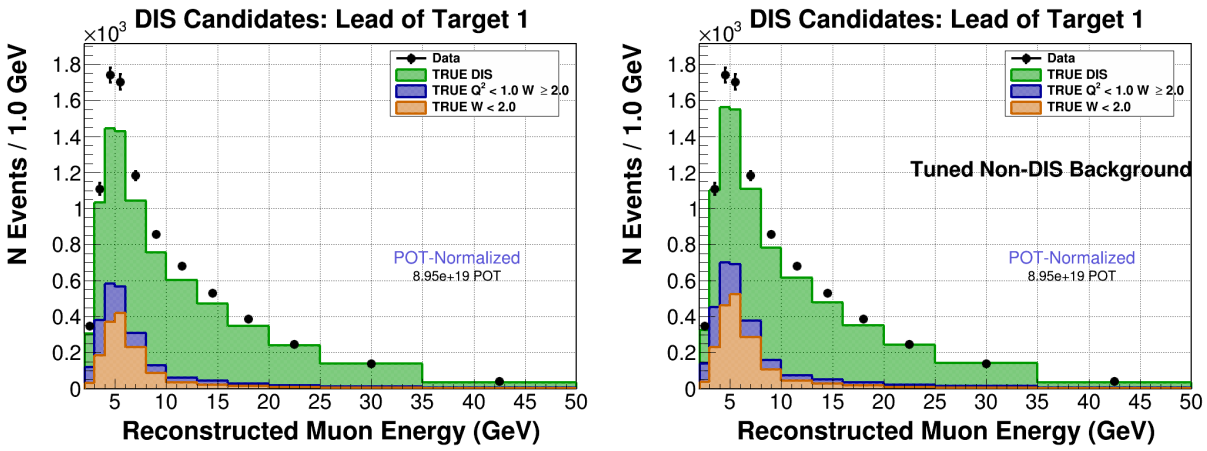

Figure C-21: Events passing the DIS selection cuts in data (black points) as well as the MC signal (green) and background (orange and blue). The left plot is prior to the background tuning to data, and the right plot is after tuning.

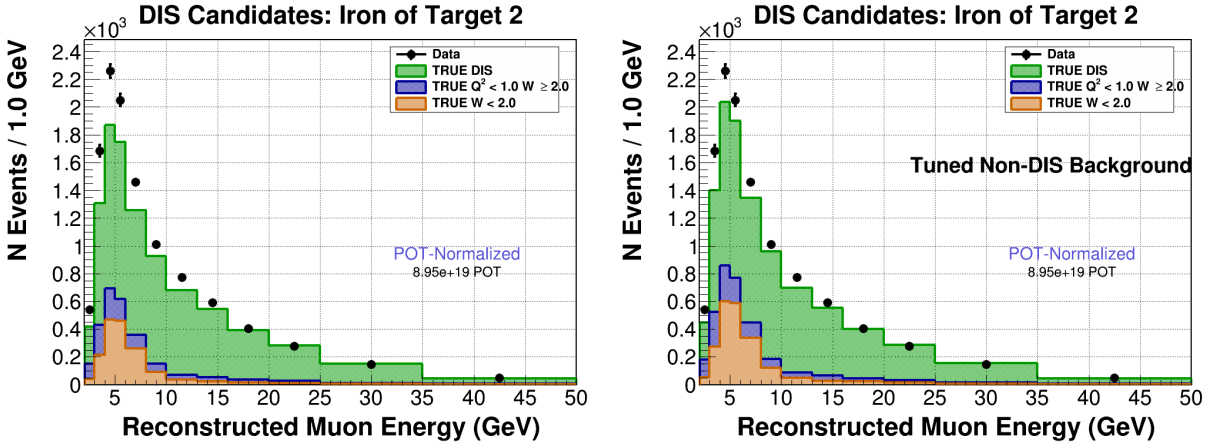

Figure C-22: Events passing the DIS selection cuts in data (black points) as well as the MC signal (green) and background (orange and blue). The left plot is prior to the background tuning to data, and the right plot is after tuning.

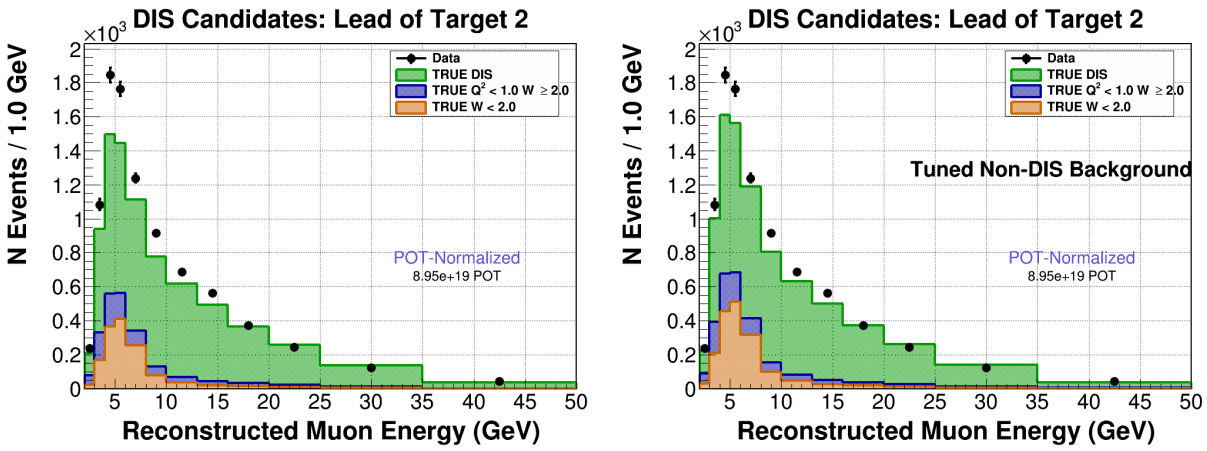

Figure C-23: Events passing the DIS selection cuts in data (black points) as well as the MC signal (green) and background (orange and blue). The left plot is prior to the background tuning to data, and the right plot is after tuning.

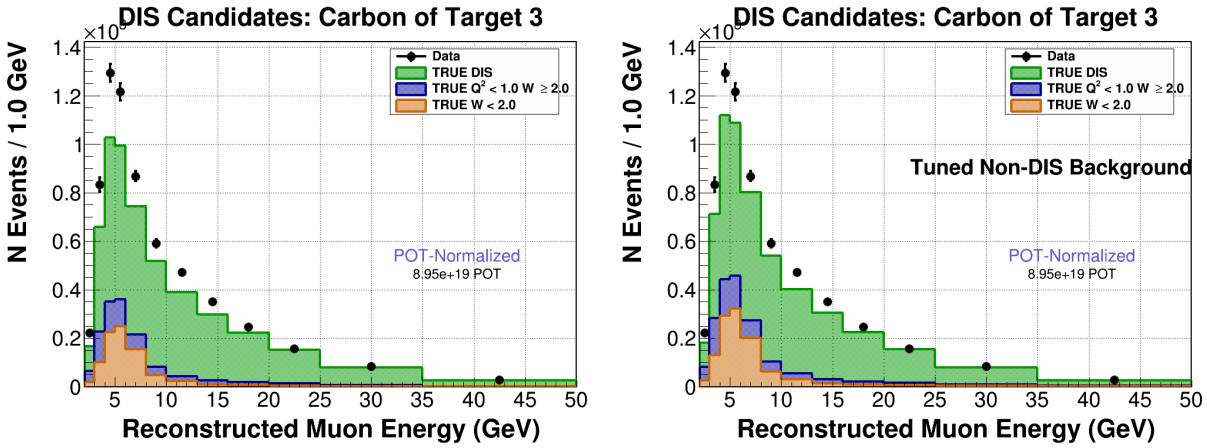

Figure C-24: Events passing the DIS selection cuts in data (black points) as well as the MC signal (green) and background (orange and blue). The left plot is prior to the background tuning to data, and the right plot is after tuning.

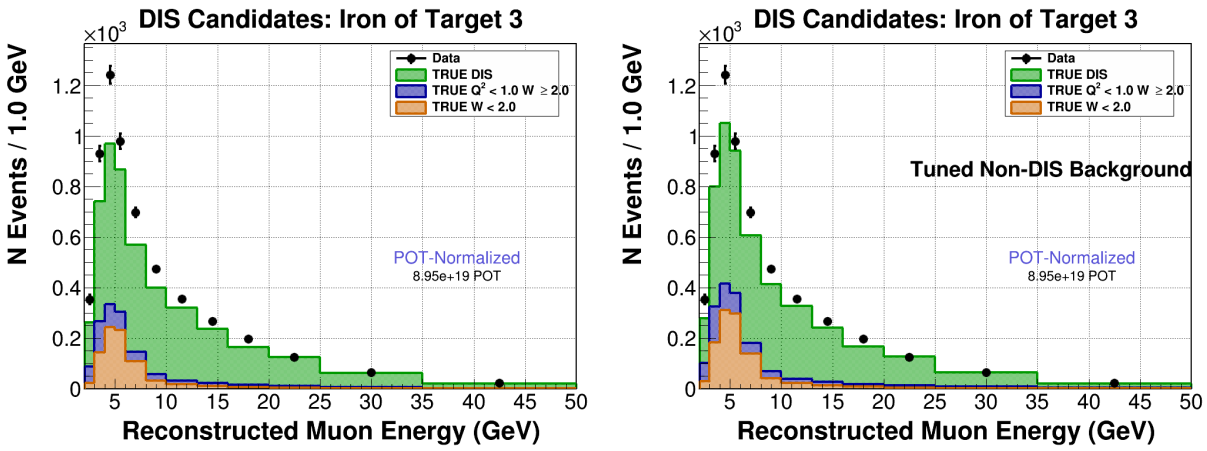

Figure C-25: Events passing the DIS selection cuts in data (black points) as well as the MC signal (green) and background (orange and blue). The left plot is prior to the background tuning to data, and the right plot is after tuning.

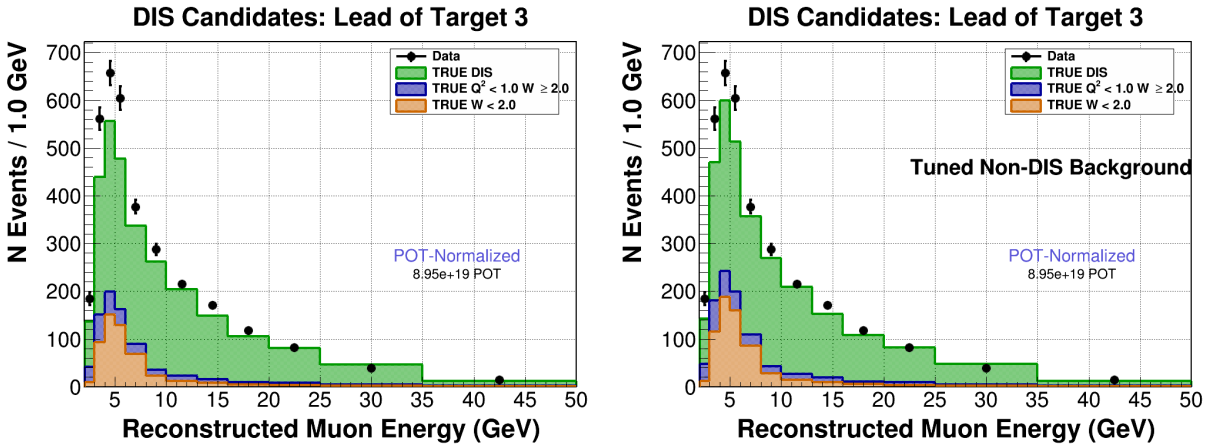

Figure C-26: Events passing the DIS selection cuts in data (black points) as well as the MC signal (green) and background (orange and blue). The left plot is prior to the background tuning to data, and the right plot is after tuning.

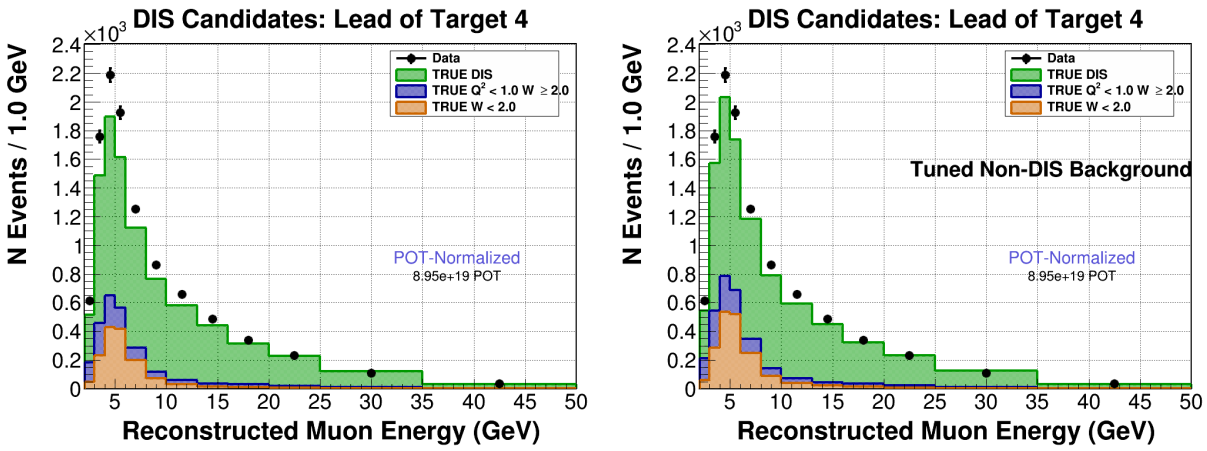

Figure C-27: Events passing the DIS selection cuts in data (black points) as well as the MC signal (green) and background (orange and blue). The left plot is prior to the background tuning to data, and the right plot is after tuning.

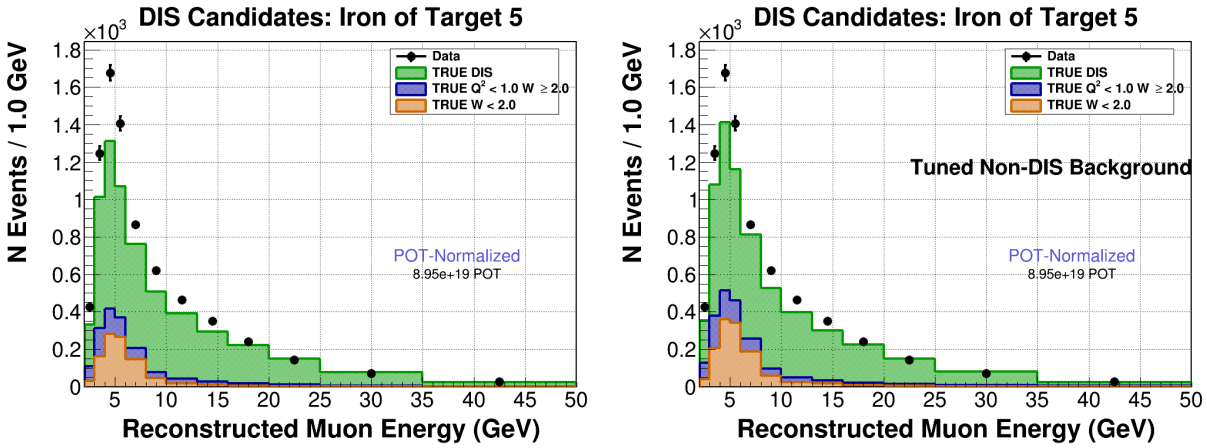

Figure C-28: Events passing the DIS selection cuts in data (black points) as well as the MC signal (green) and background (orange and blue). The left plot is prior to the background tuning to data, and the right plot is after tuning.

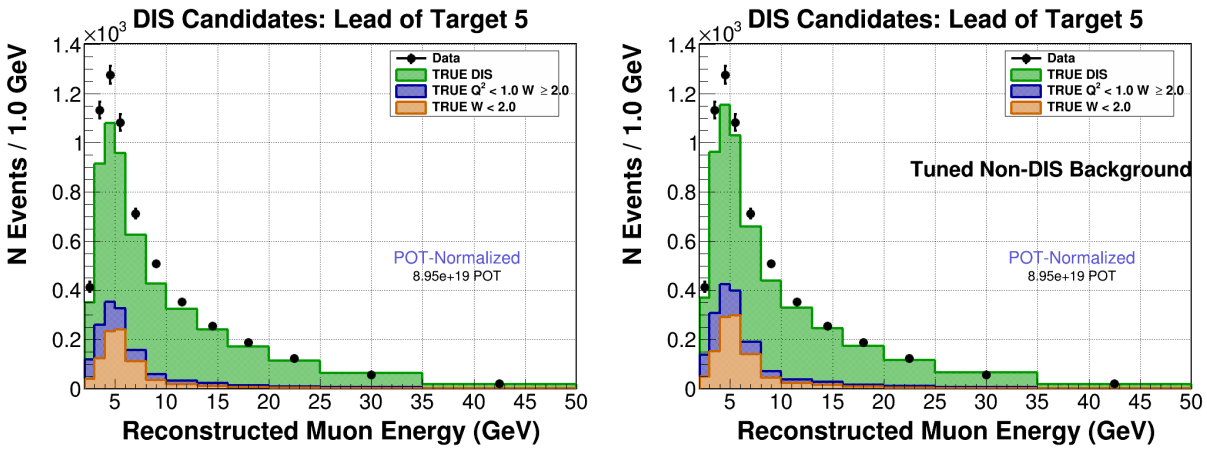

Figure C-29: Events passing the DIS selection cuts in data (black points) as well as the MC signal (green) and background (orange and blue). The left plot is prior to the background tuning to data, and the right plot is after tuning.

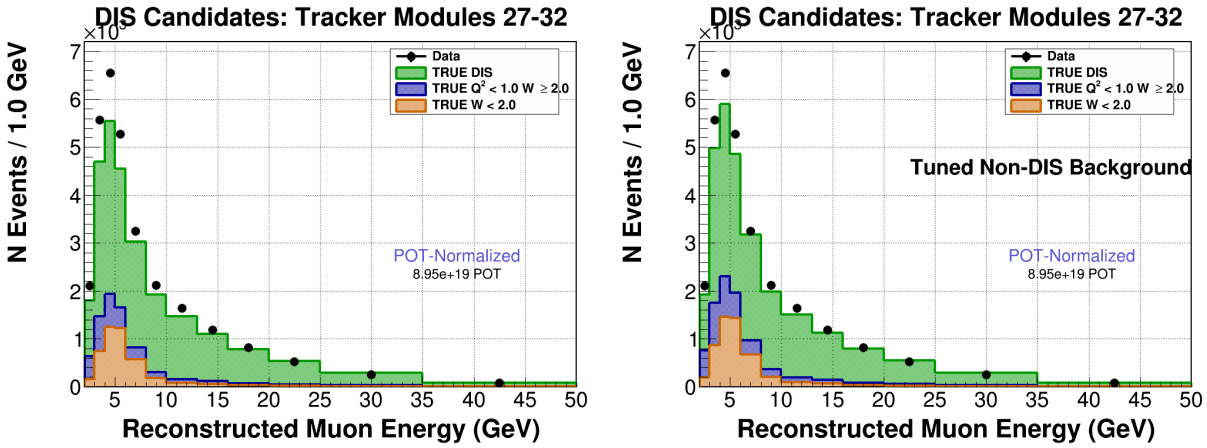

Figure C-30: Events passing the DIS selection cuts in data (black points) as well as the MC signal (green) and background (orange and blue). The left plot is prior to the background tuning to data, and the right plot is after tuning.

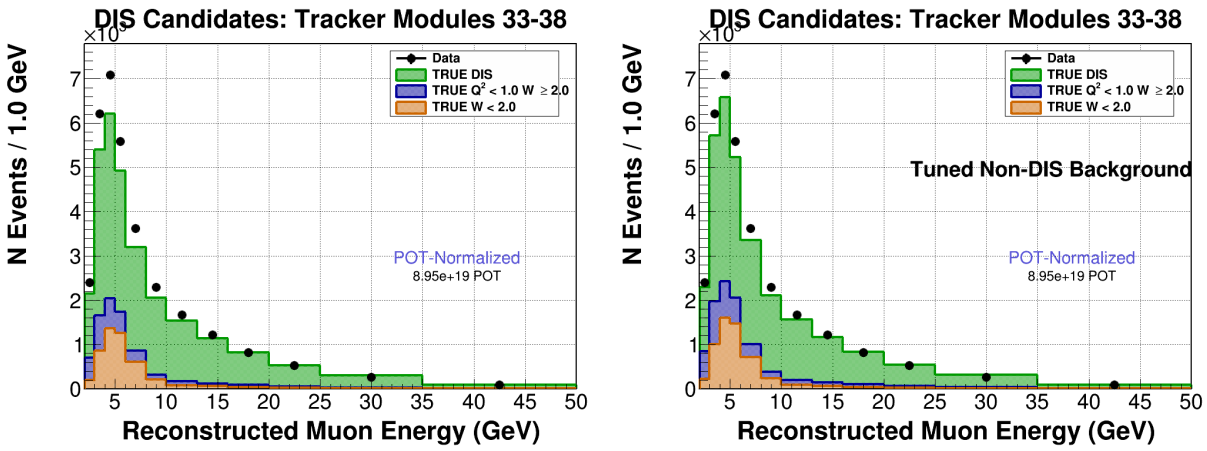

Figure C-31: Events passing the DIS selection cuts in data (black points) as well as the MC signal (green) and background (orange and blue). The left plot is prior to the background tuning to data, and the right plot is after tuning.

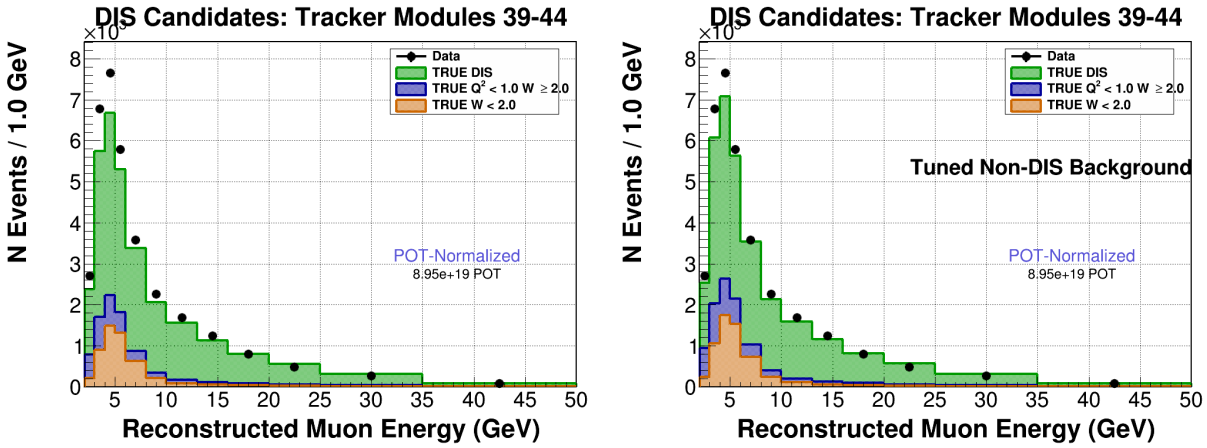

Figure C-32: Events passing the DIS selection cuts in data (black points) as well as the MC signal (green) and background (orange and blue). The left plot is prior to the background tuning to data, and the right plot is after tuning.

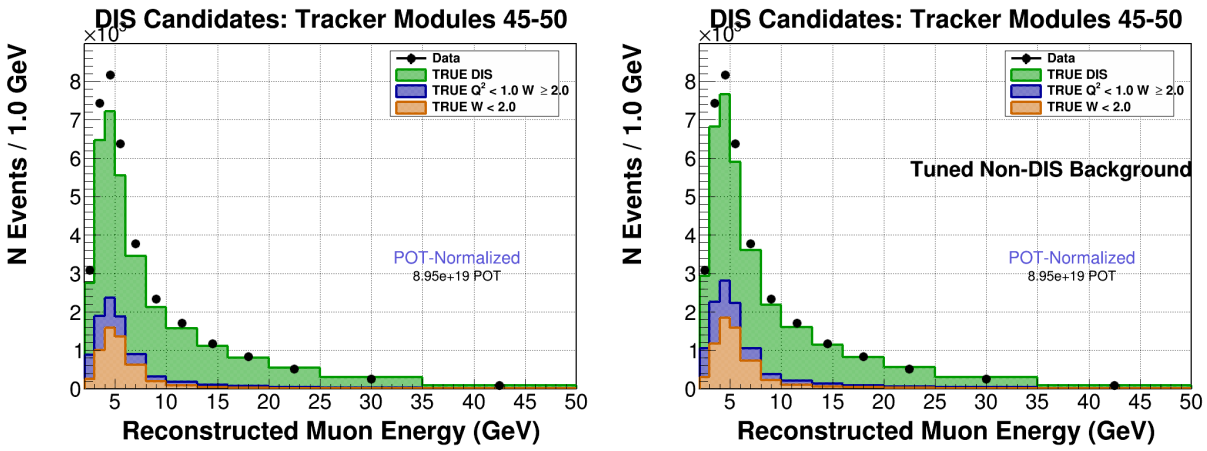

Figure C-33: Events passing the DIS selection cuts in data (black points) as well as the MC signal (green) and background (orange and blue). The left plot is prior to the background tuning to data, and the right plot is after tuning.

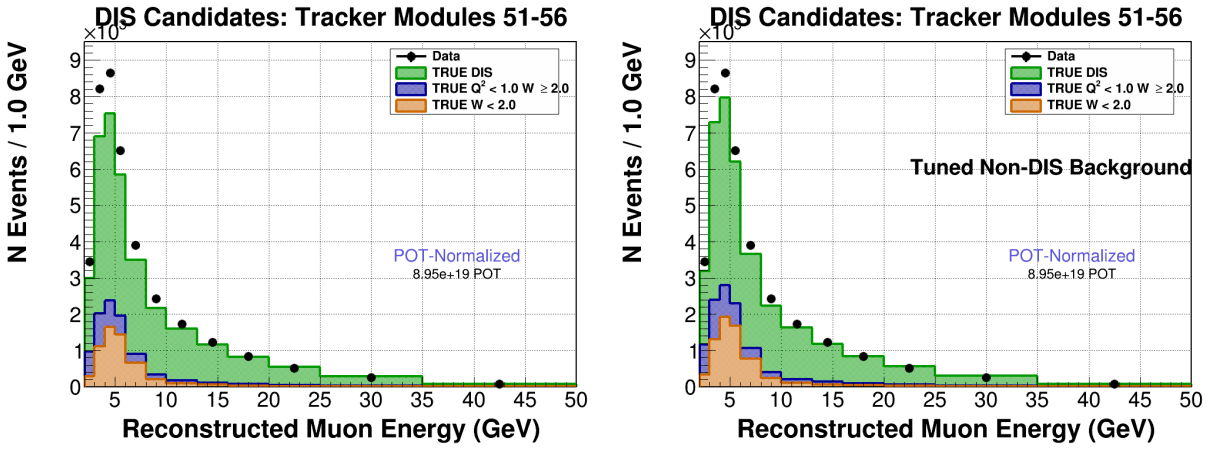

Figure C-34: Events passing the DIS selection cuts in data (black points) as well as the MC signal (green) and background (orange and blue). The left plot is prior to the background tuning to data, and the right plot is after tuning.

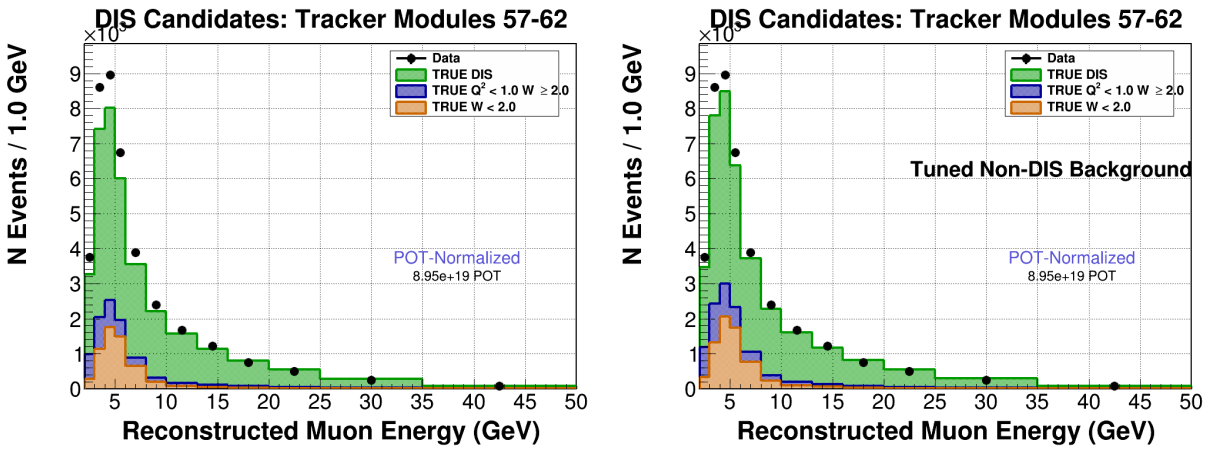

Figure C-35: Events passing the DIS selection cuts in data (black points) as well as the MC signal (green) and background (orange and blue). The left plot is prior to the background tuning to data, and the right plot is after tuning.

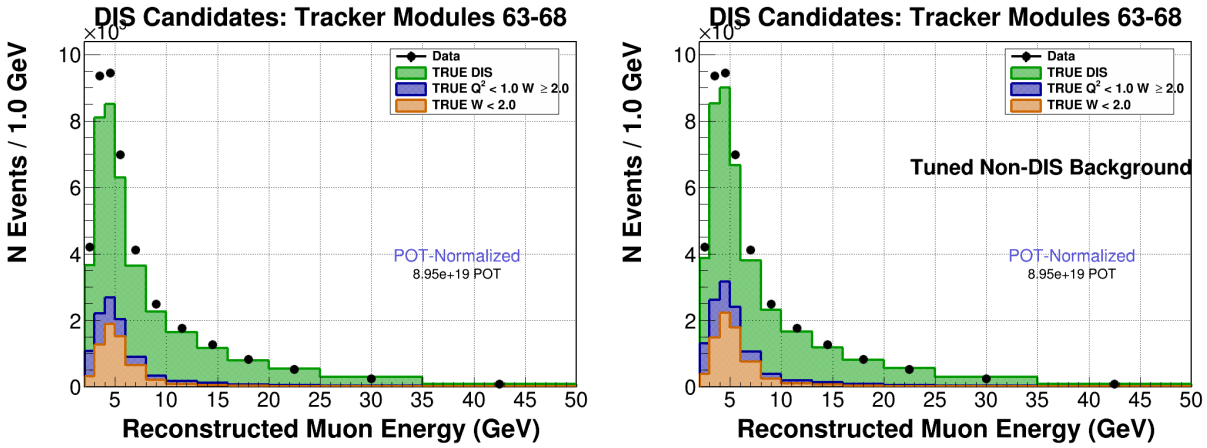

Figure C-36: Events passing the DIS selection cuts in data (black points) as well as the MC signal (green) and background (orange and blue). The left plot is prior to the background tuning to data, and the right plot is after tuning.

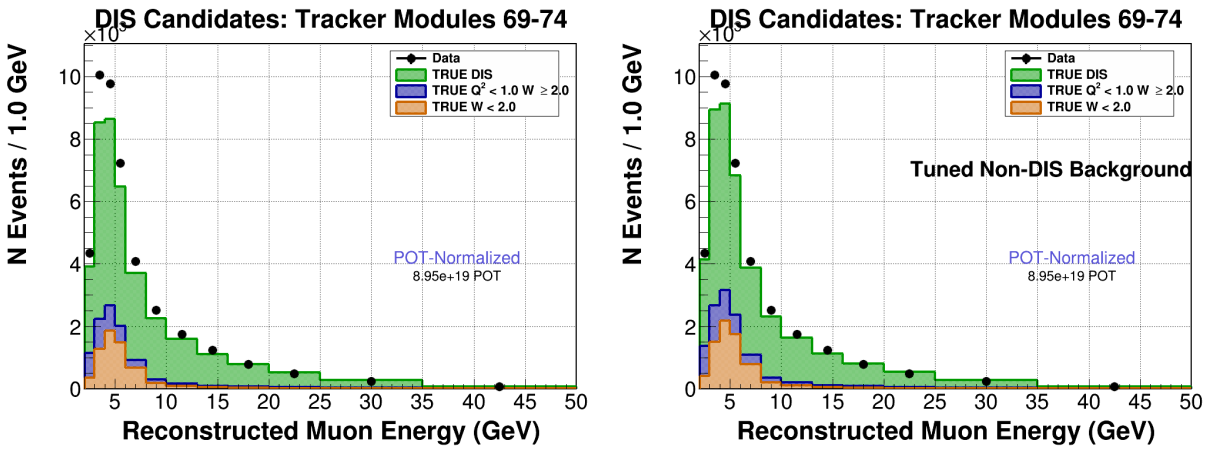

Figure C-37: Events passing the DIS selection cuts in data (black points) as well as the MC signal (green) and background (orange and blue). The left plot is prior to the background tuning to data, and the right plot is after tuning.

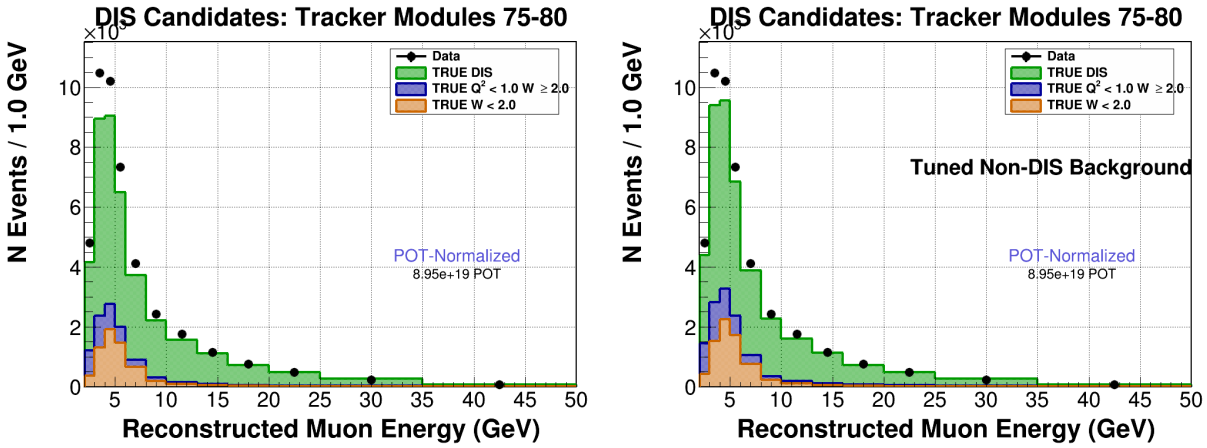

Figure C-38: Events passing the DIS selection cuts in data (black points) as well as the MC signal (green) and background (orange and blue). The left plot is prior to the background tuning to data, and the right plot is after tuning.

C.3 DIS signal and background before and after background tuning as a function of Bjorken x

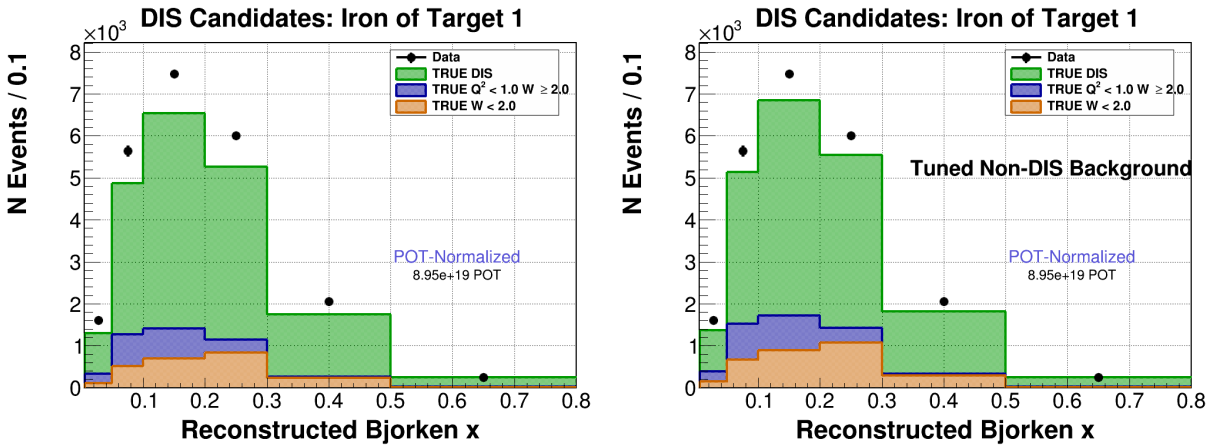

Figure C-39: Events passing the DIS selection cuts in data (black points) as well as the MC signal (green) and background (orange and blue). The left plot is prior to the background tuning to data, and the right plot is after tuning.

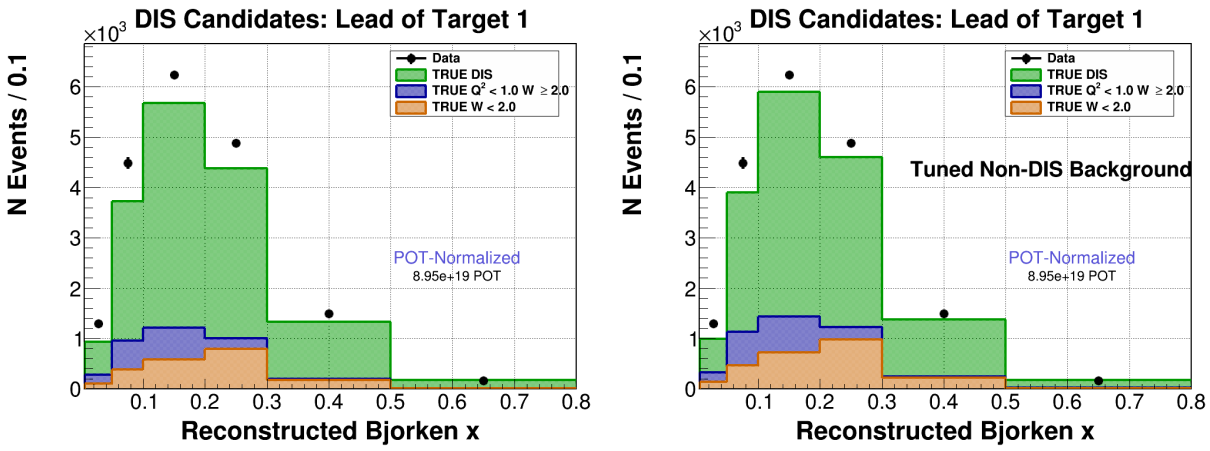

Figure C-40: Events passing the DIS selection cuts in data (black points) as well as the MC signal (green) and background (orange and blue). The left plot is prior to the background tuning to data, and the right plot is after tuning.

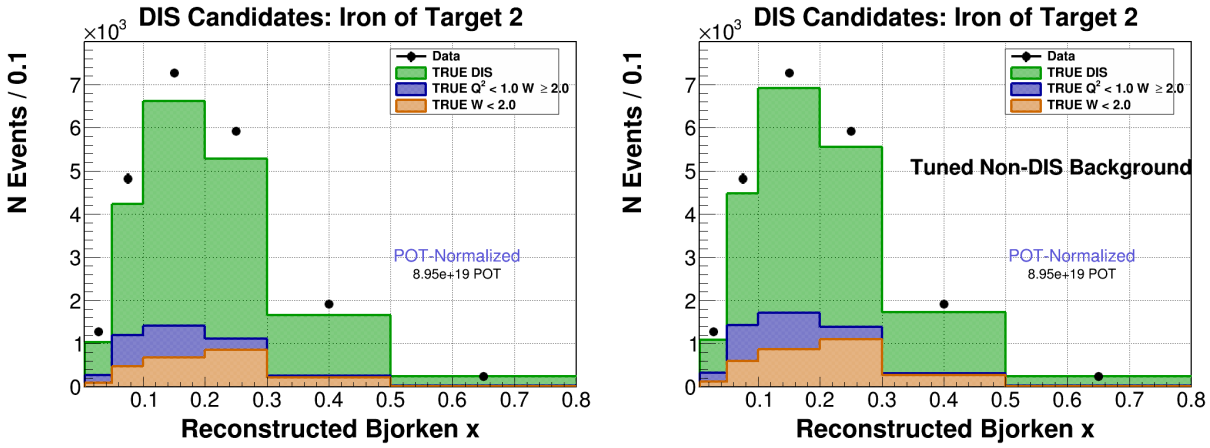

Figure C-41: Events passing the DIS selection cuts in data (black points) as well as the MC signal (green) and background (orange and blue). The left plot is prior to the background tuning to data, and the right plot is after tuning.

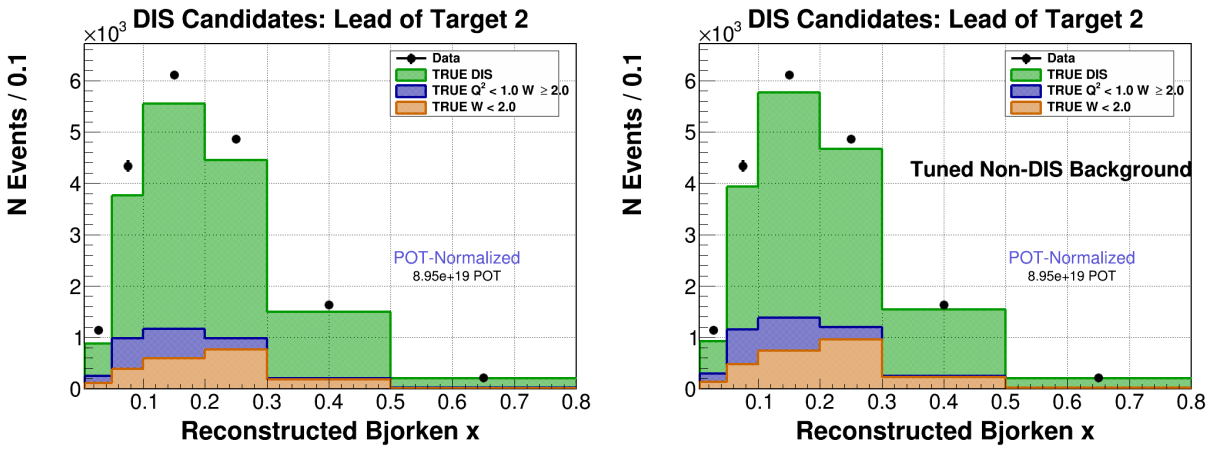

Figure C-42: Events passing the DIS selection cuts in data (black points) as well as the MC signal (green) and background (orange and blue). The left plot is prior to the background tuning to data, and the right plot is after tuning.

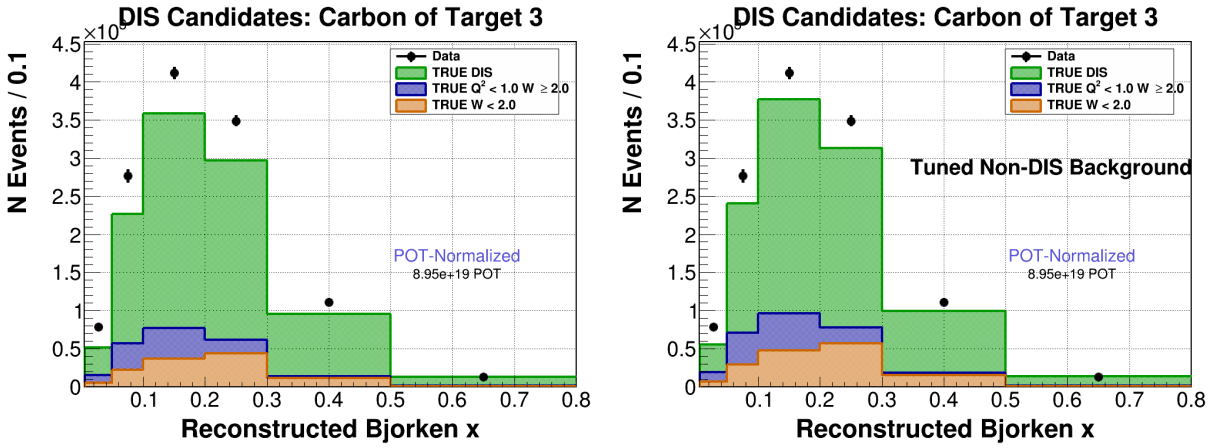

Figure C-43: Events passing the DIS selection cuts in data (black points) as well as the MC signal (green) and background (orange and blue). The left plot is prior to the background tuning to data, and the right plot is after tuning.

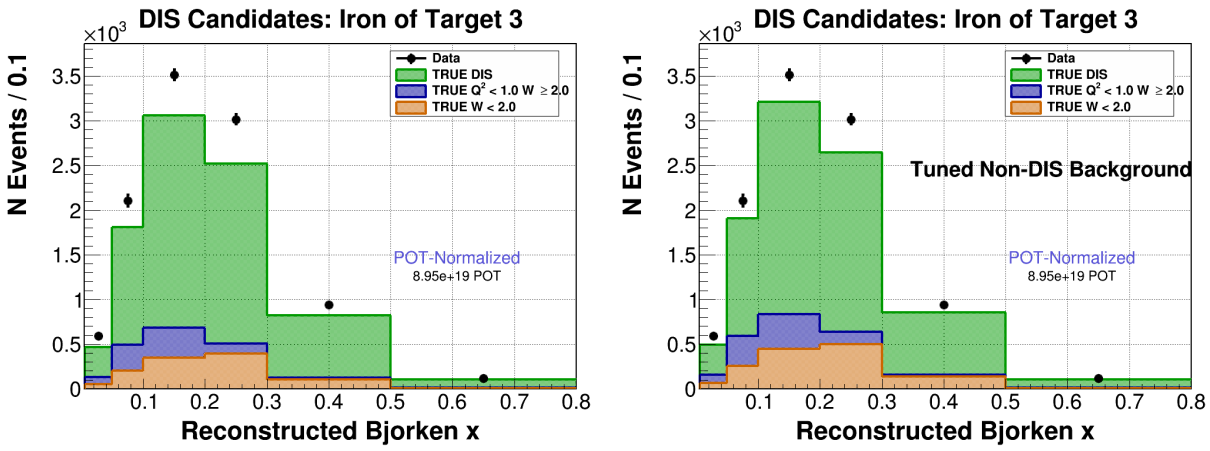

Figure C-44: Events passing the DIS selection cuts in data (black points) as well as the MC signal (green) and background (orange and blue). The left plot is prior to the background tuning to data, and the right plot is after tuning.

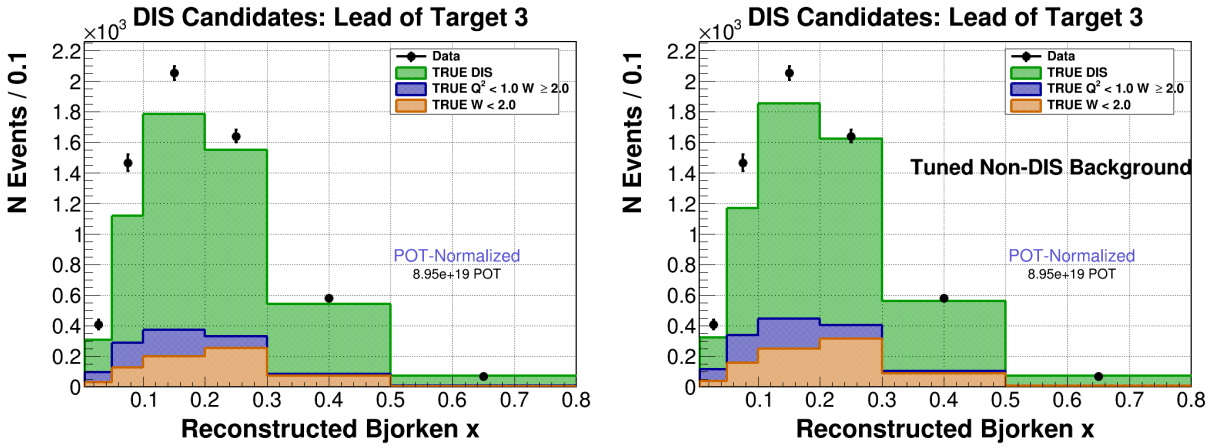

Figure C-45: Events passing the DIS selection cuts in data (black points) as well as the MC signal (green) and background (orange and blue). The left plot is prior to the background tuning to data, and the right plot is after tuning.

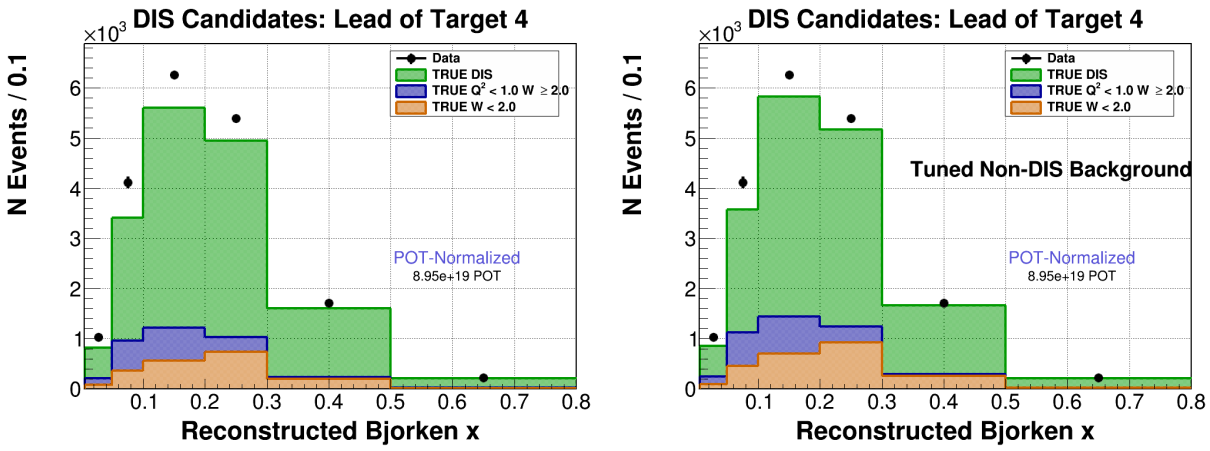

Figure C-46: Events passing the DIS selection cuts in data (black points) as well as the MC signal (green) and background (orange and blue). The left plot is prior to the background tuning to data, and the right plot is after tuning.

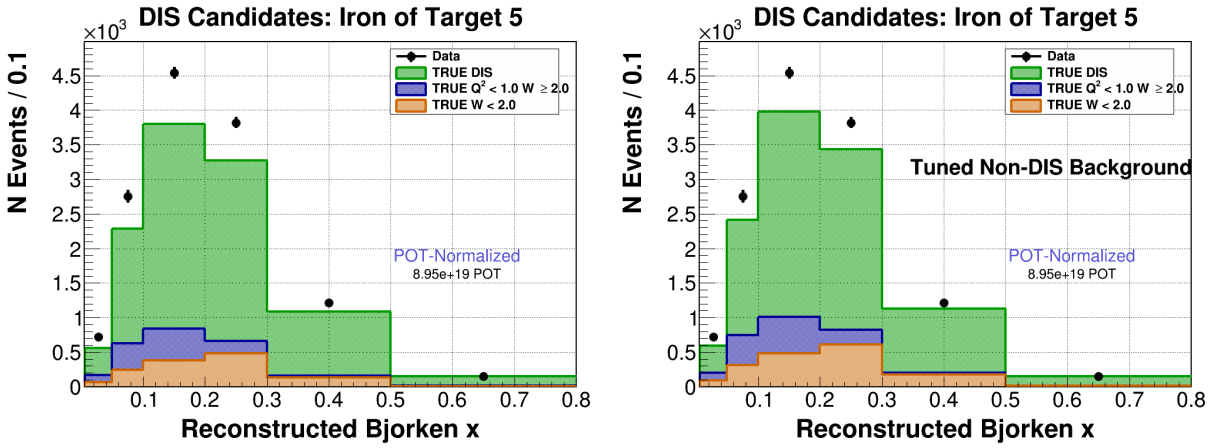

Figure C-47: Events passing the DIS selection cuts in data (black points) as well as the MC signal (green) and background (orange and blue). The left plot is prior to the background tuning to data, and the right plot is after tuning.

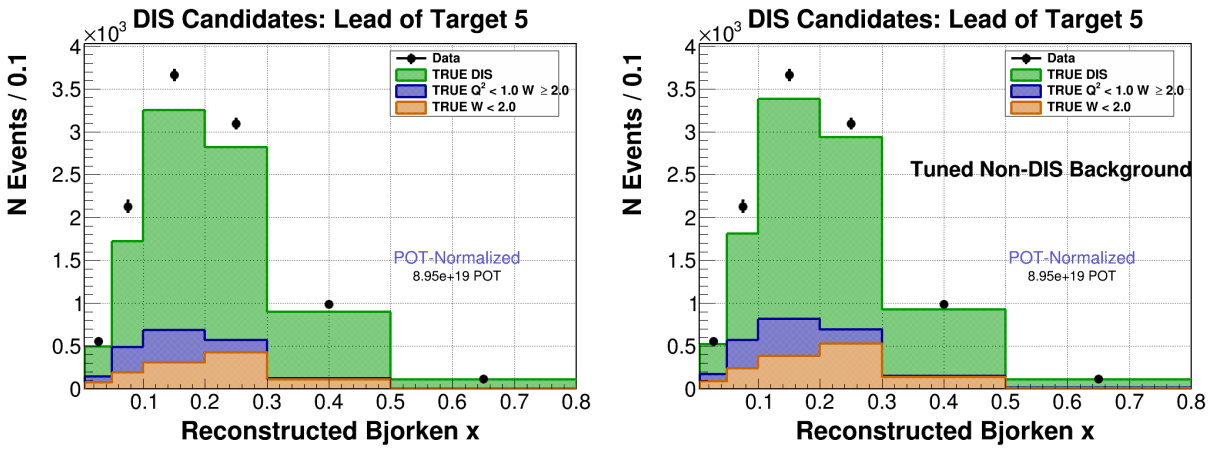

Figure C-48: Events passing the DIS selection cuts in data (black points) as well as the MC signal (green) and background (orange and blue). The left plot is prior to the background tuning to data, and the right plot is after tuning.

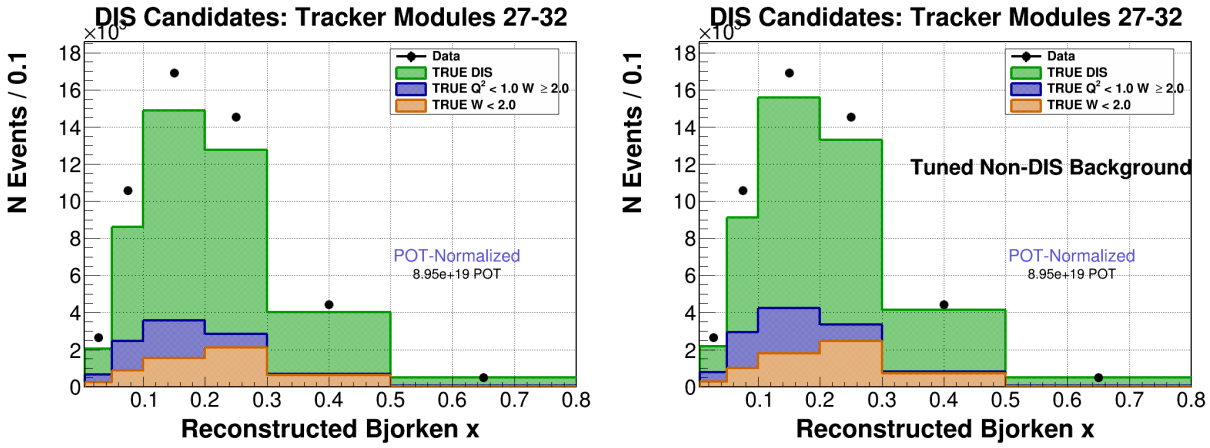

Figure C-49: Events passing the DIS selection cuts in data (black points) as well as the MC signal (green) and background (orange and blue). The left plot is prior to the background tuning to data, and the right plot is after tuning.

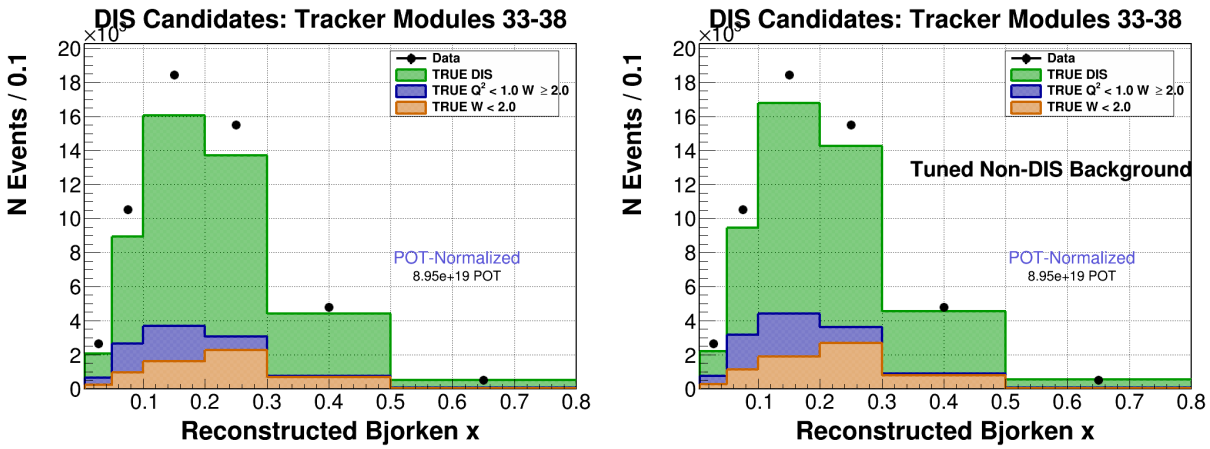

Figure C-50: Events passing the DIS selection cuts in data (black points) as well as the MC signal (green) and background (orange and blue). The left plot is prior to the background tuning to data, and the right plot is after tuning.

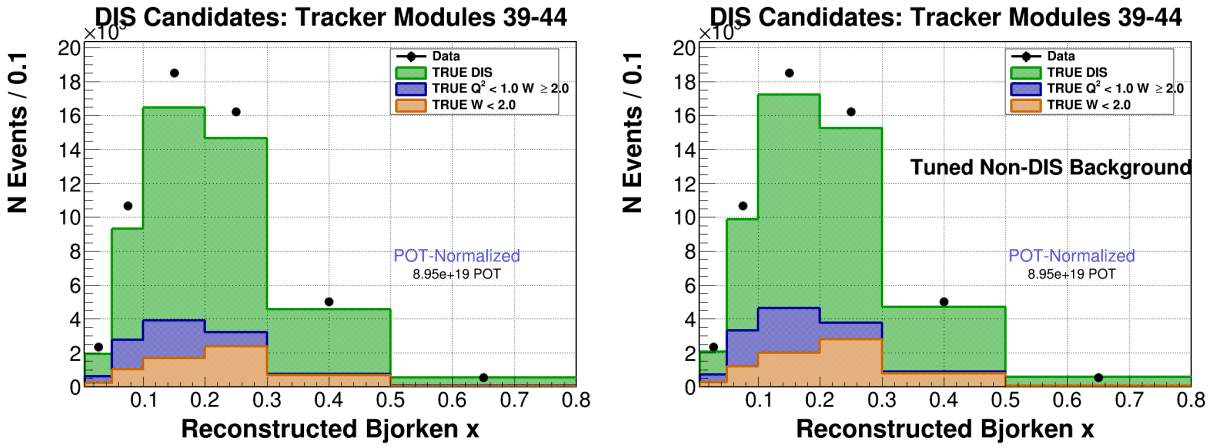

Figure C-51: Events passing the DIS selection cuts in data (black points) as well as the MC signal (green) and background (orange and blue). The left plot is prior to the background tuning to data, and the right plot is after tuning.

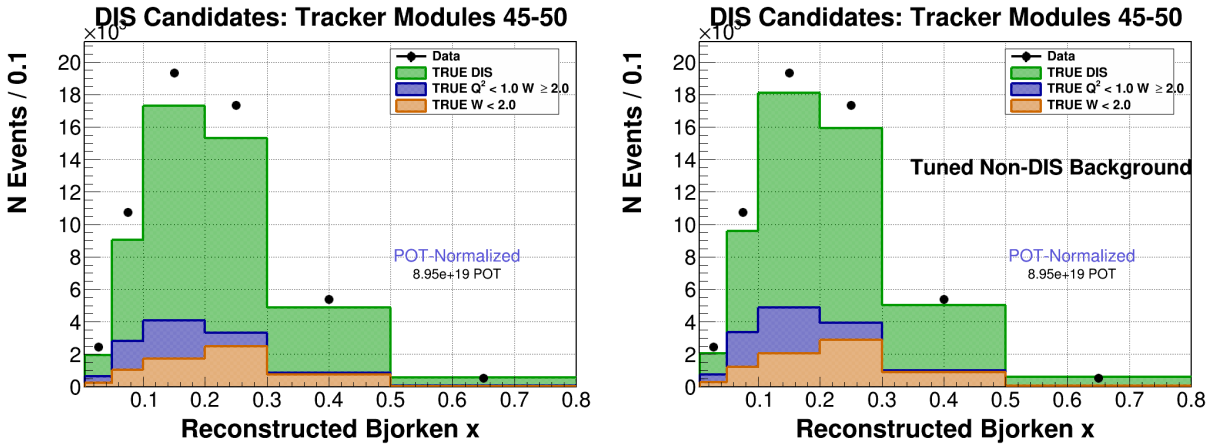

Figure C-52: Events passing the DIS selection cuts in data (black points) as well as the MC signal (green) and background (orange and blue). The left plot is prior to the background tuning to data, and the right plot is after tuning.

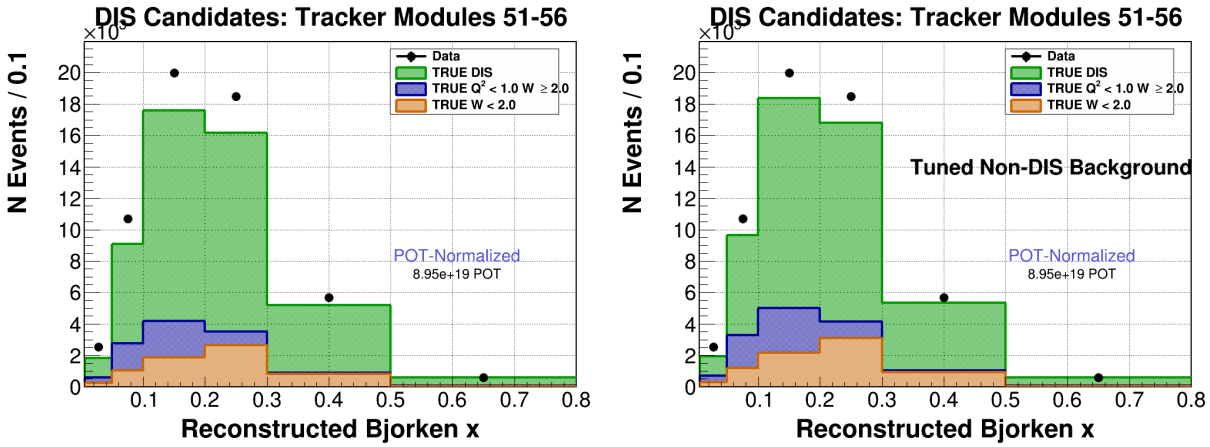

Figure C-53: Events passing the DIS selection cuts in data (black points) as well as the MC signal (green) and background (orange and blue). The left plot is prior to the background tuning to data, and the right plot is after tuning.

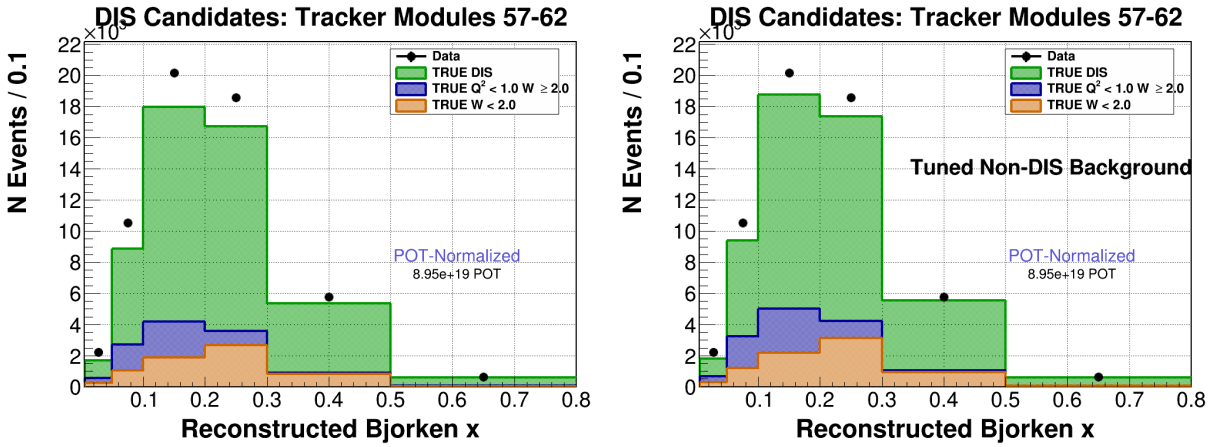

Figure C-54: Events passing the DIS selection cuts in data (black points) as well as the MC signal (green) and background (orange and blue). The left plot is prior to the background tuning to data, and the right plot is after tuning.

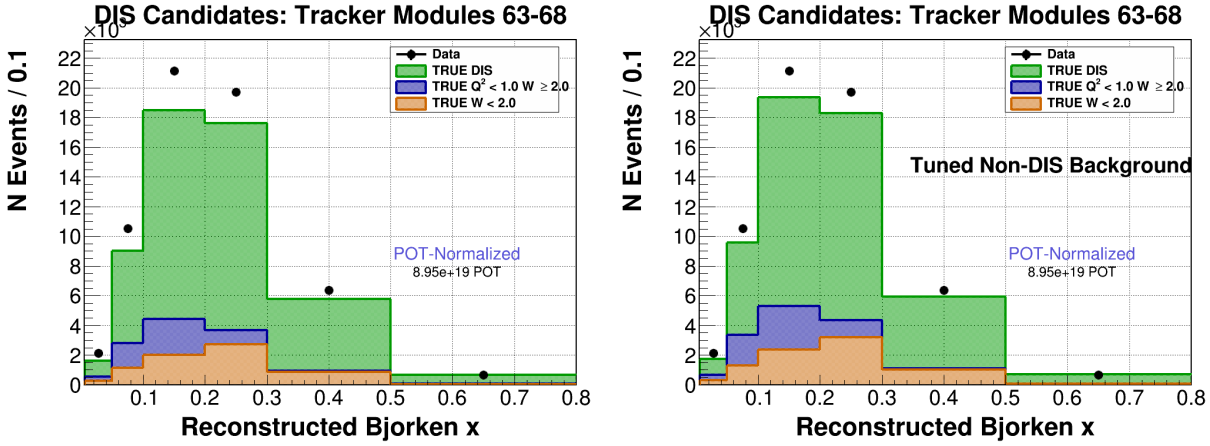

Figure C-55: Events passing the DIS selection cuts in data (black points) as well as the MC signal (green) and background (orange and blue). The left plot is prior to the background tuning to data, and the right plot is after tuning.

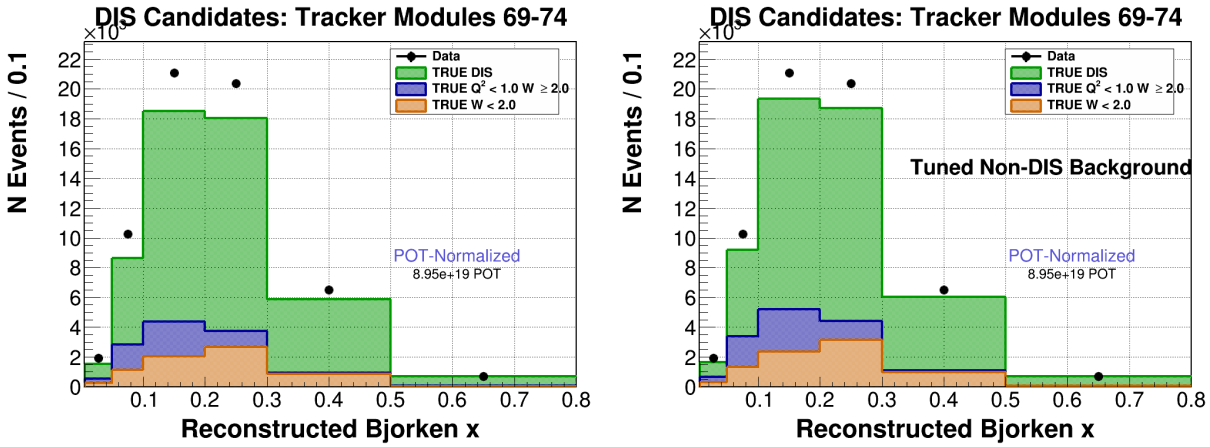

Figure C-56: Events passing the DIS selection cuts in data (black points) as well as the MC signal (green) and background (orange and blue). The left plot is prior to the background tuning to data, and the right plot is after tuning.

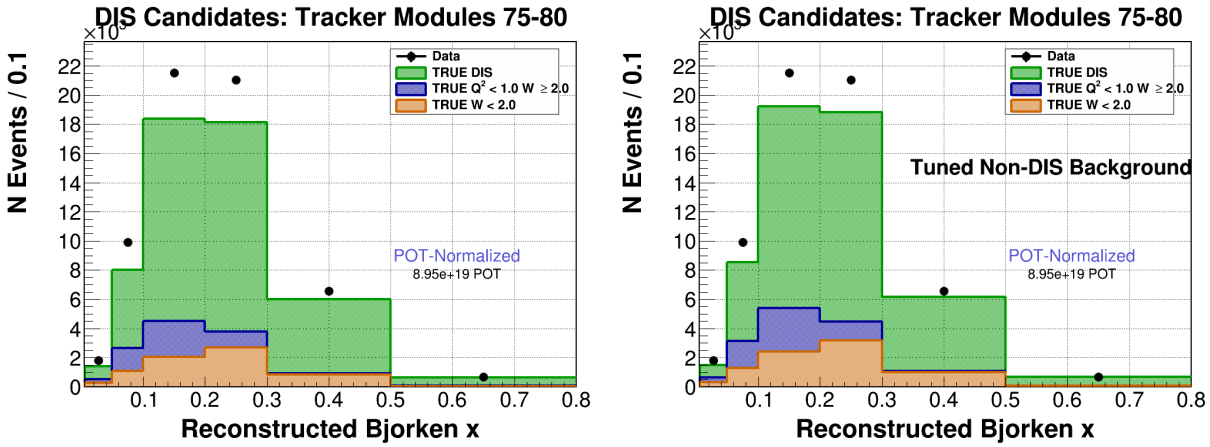

Figure C-57: Events passing the DIS selection cuts in data (black points) as well as the MC signal (green) and background (orange and blue). The left plot is prior to the background tuning to data, and the right plot is after tuning.

APPENDIX D
MIGRATION MATRICES

D.1 Migration matrix fraction as a function of E_ν

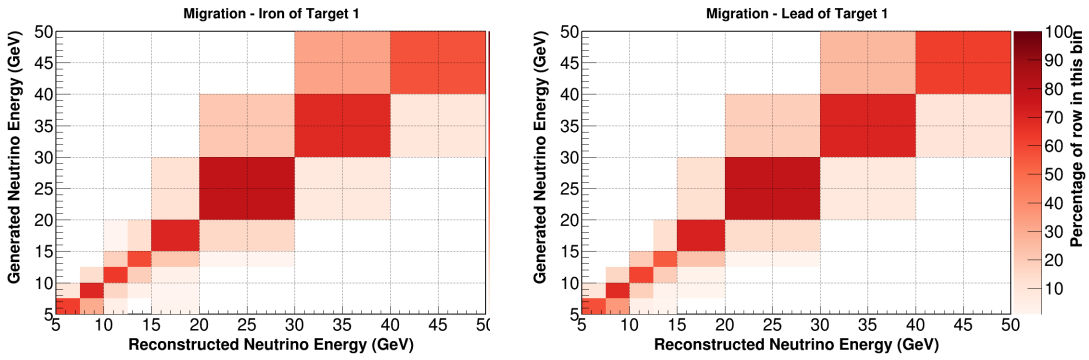

Figure D-1: E_ν migration matrix for iron of target 1 (left) and lead of target 1 (right). The y-axis is generated (true) E_ν and the x-axis is reconstructed E_ν. Each cell records the percent of true and reconstructed DIS events.

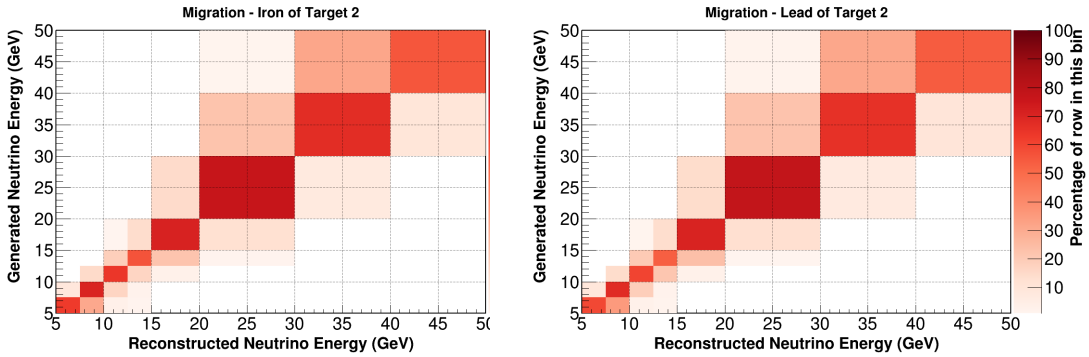

Figure D-2: E_ν migration matrix for iron of target 2 (left) and lead of target 2 (right). The y-axis is generated (true) E_ν and the x-axis is reconstructed E_ν. Each cell records the percent of true and reconstructed DIS events.

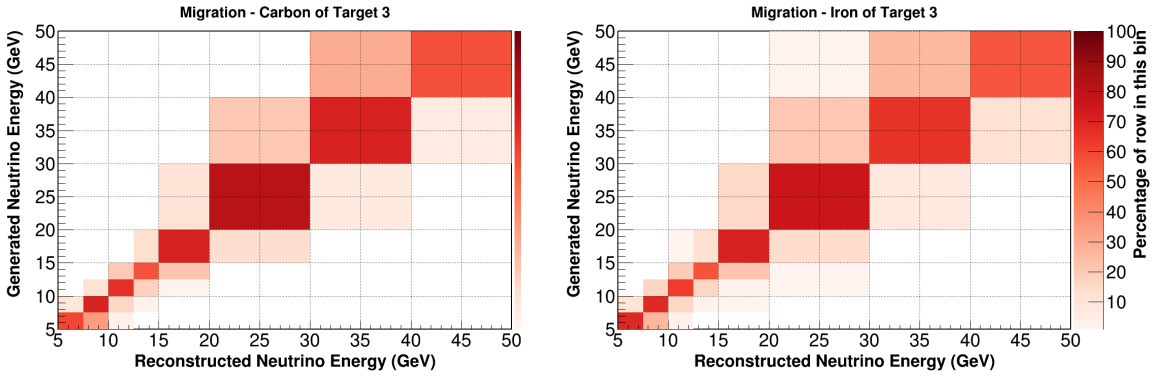

Figure D-3: E_ν migration matrix for carbon of target 3 (left) and iron of target 3 (right). The y-axis is generated (true) E_ν and the x-axis is reconstructed E_ν. Each cell records the percent of true and reconstructed DIS events.

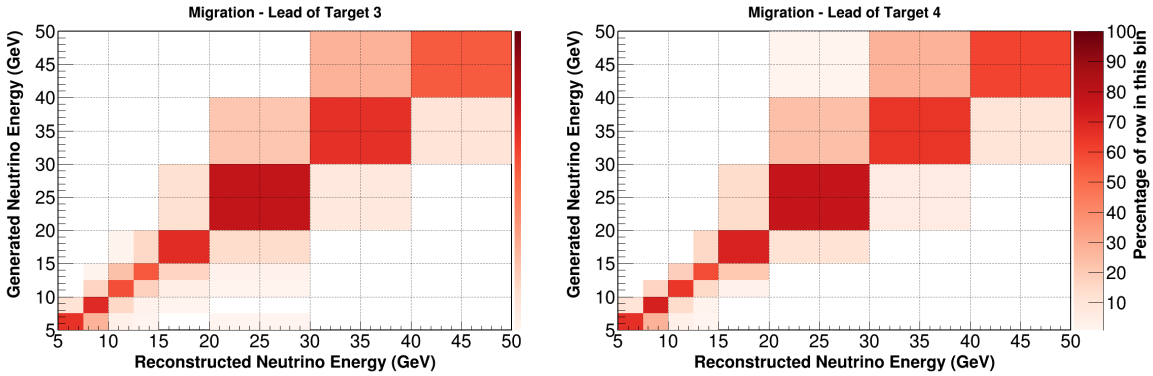

Figure D-4: E_ν migration matrix for lead of target 3 (left) and lead of target 4 (right). The y-axis is generated (true) E_ν and the x-axis is reconstructed E_ν. Each cell records the percent of true and reconstructed DIS events.

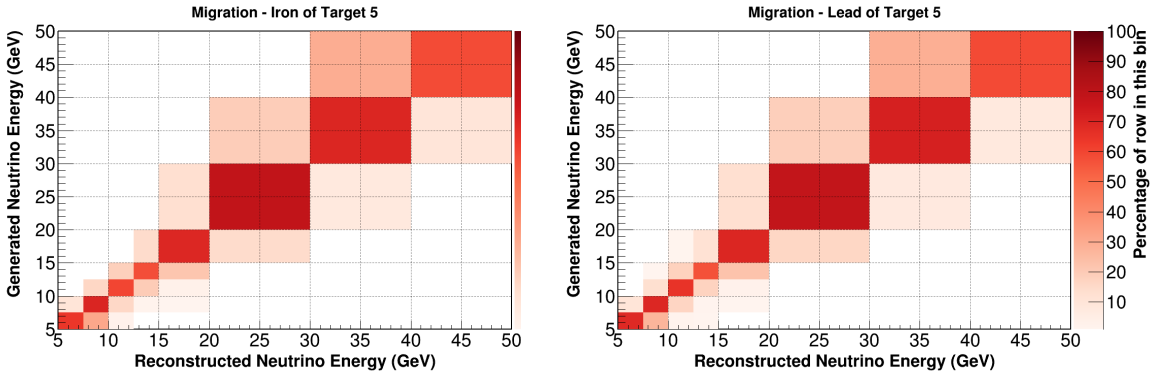

Figure D-5: E_ν migration matrix for iron of target 5 (left) and lead of target 5 (right). The y-axis is generated (true) E_ν and the x-axis is reconstructed E_ν. Each cell records the percent of true and reconstructed DIS events.

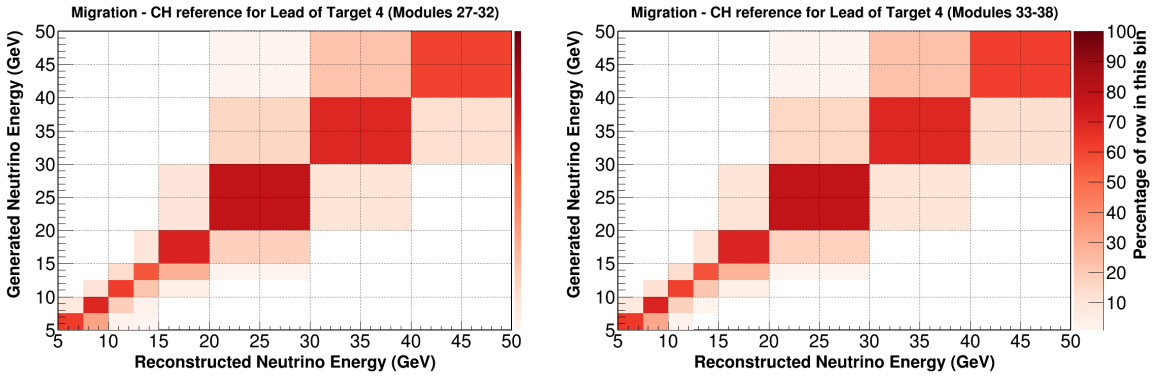

Figure D-6: E_ν migration matrix for scintillator tracker modules 27-32 (left) and scintillator tracker modules 33-38 (right). The y-axis is generated (true) E_ν and the x-axis is reconstructed E_ν. Each cell records the percent of true and reconstructed DIS events.

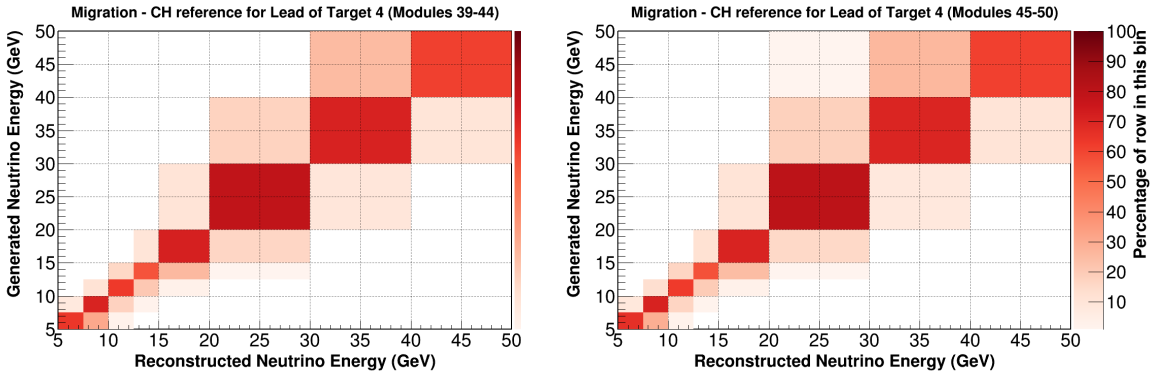

Figure D-7: E_ν migration matrix for scintillator tracker modules 39-44 (left) and scintillator tracker modules 45-50 (right). The y-axis is generated (true) E_ν and the x-axis is reconstructed E_ν. Each cell records the percent of true and reconstructed DIS events.

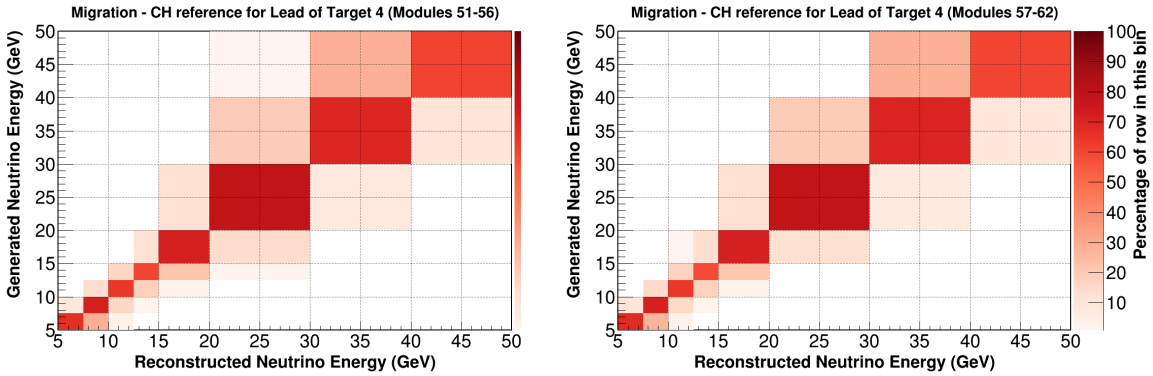

Figure D-8: E_ν migration matrix for scintillator tracker modules 51-56 (left) and scintillator tracker modules 57-62 (right). The y-axis is generated (true) E_ν and the x-axis is reconstructed E_ν. Each cell records the percent of true and reconstructed DIS events.

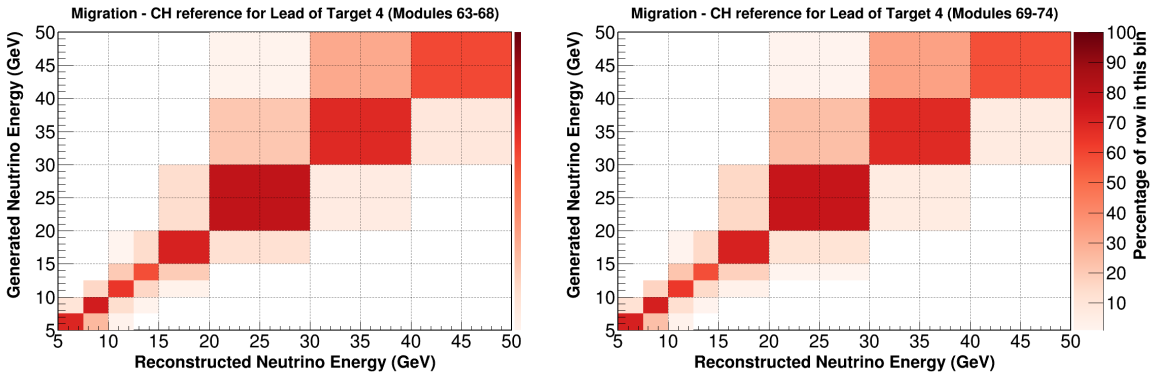

Figure D-9: E_ν migration matrix for scintillator tracker modules 63-68 (left) and scintillator tracker modules 69-74 (right). The y-axis is generated (true) E_ν and the x-axis is reconstructed E_ν. Each cell records the percent of true and reconstructed DIS events.

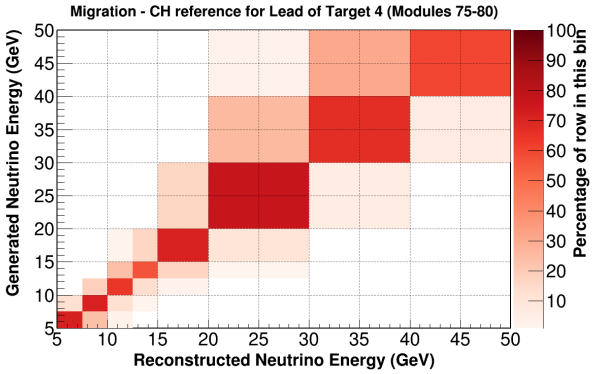

Figure D-10: E_ν migration matrix for scintillator tracker modules 75-80. The y-axis is generated (true) E_ν and the x-axis is reconstructed E_ν. Each cell records the percent of true and reconstructed DIS events.

D.2 Migration matrix fraction as a function of x_{bj}

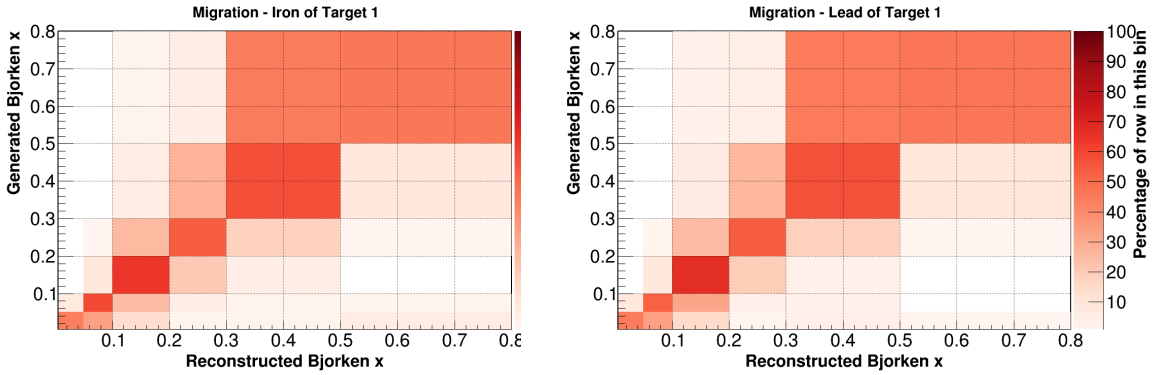

Figure D-11: x_{bj} migration matrix for iron of target 1 (left) and lead of target 1 (right). The y-axis is generated (true) x_{bj} and the x-axis is reconstructed x_{bj}. Each cell records the percent of true and reconstructed DIS events.

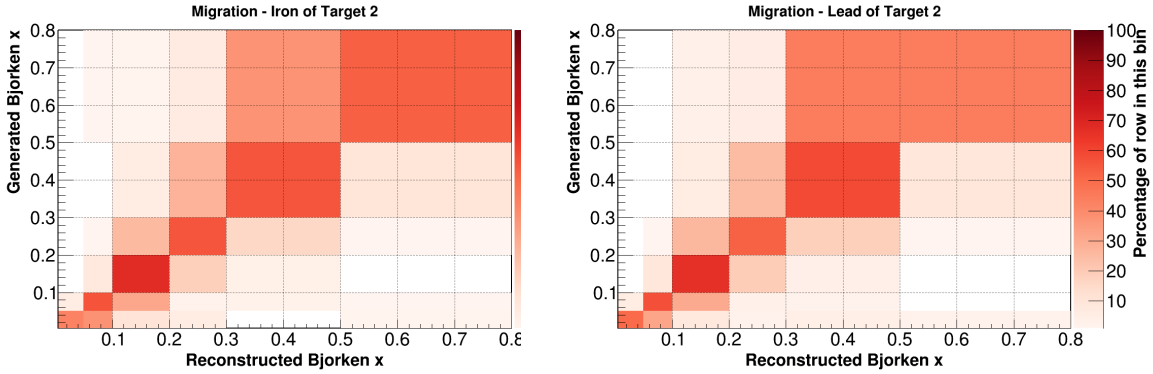

Figure D-12: x_{bj} migration matrix for iron of target 2 (left) and lead of target 2 (right). The y-axis is generated (true) x_{bj} and the x-axis is reconstructed x_{bj}. Each cell records the percent of true and reconstructed DIS events.

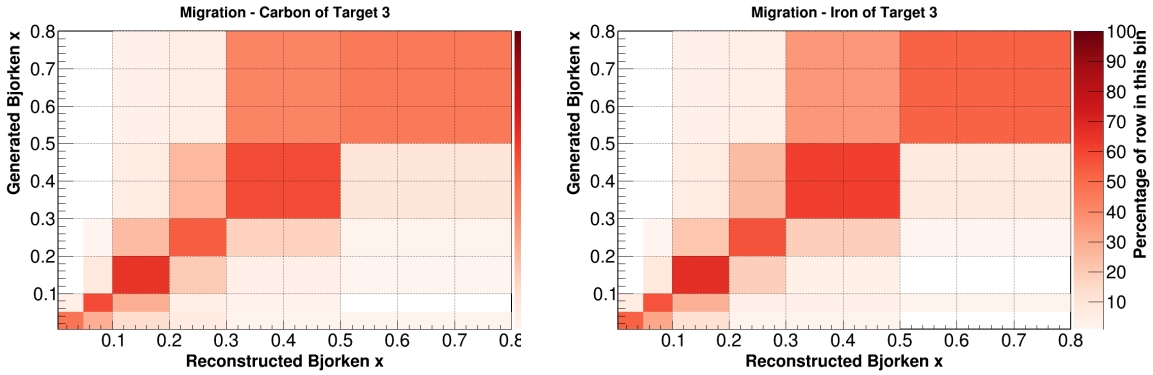

Figure D-13: x_{bj} migration matrix for carbon of target 3 (left) and iron of target 3 (right). The y-axis is generated (true) x_{bj} and the x-axis is reconstructed x_{bj}. Each cell records the percent of true and reconstructed DIS events.

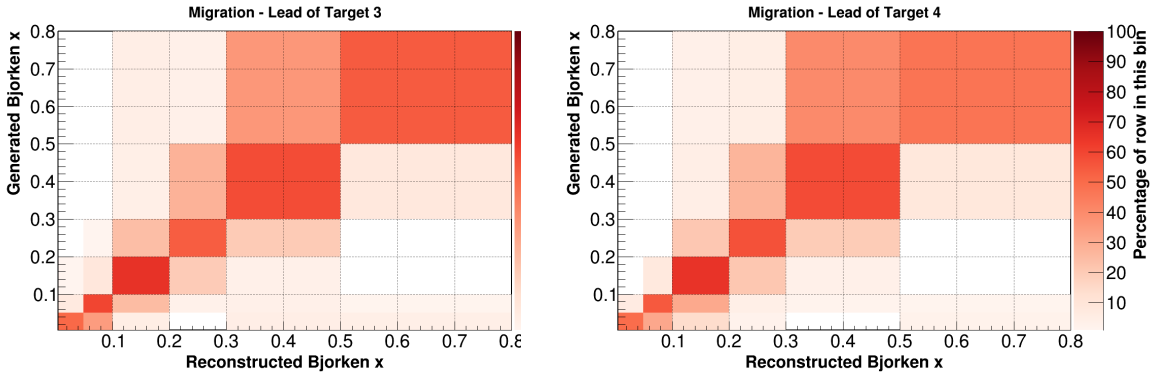

Figure D-14: x_{bj} migration matrix for lead of target 3 (left) and lead of target 4 (right). The y-axis is generated (true) x_{bj} and the x-axis is reconstructed x_{bj}. Each cell records the percent of true and reconstructed DIS events.

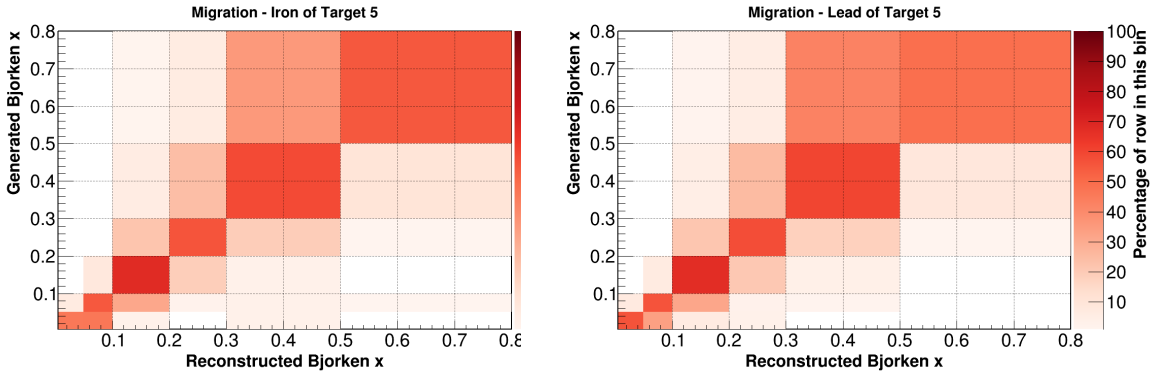

Figure D-15: x_{bj} migration matrix for iron of target 5 (left) and lead of target 5 (right). The y-axis is generated (true) x_{bj} and the x-axis is reconstructed x_{bj}. Each cell records the percent of true and reconstructed DIS events.

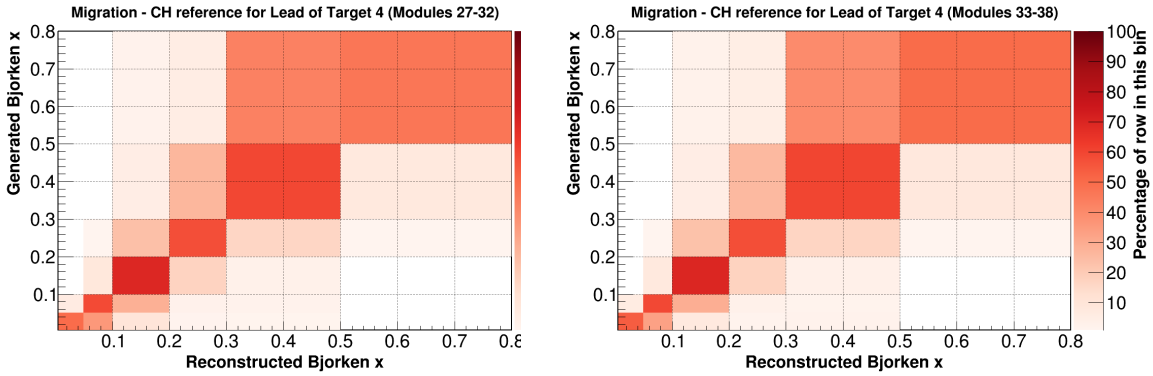

Figure D-16: x_{bj} migration matrix for scintillator tracker modules 27-32 (left) and scintillator tracker modules 33-38 (right). The y-axis is generated (true) x_{bj} and the x-axis is reconstructed x_{bj}. Each cell records the percent of true and reconstructed DIS events.

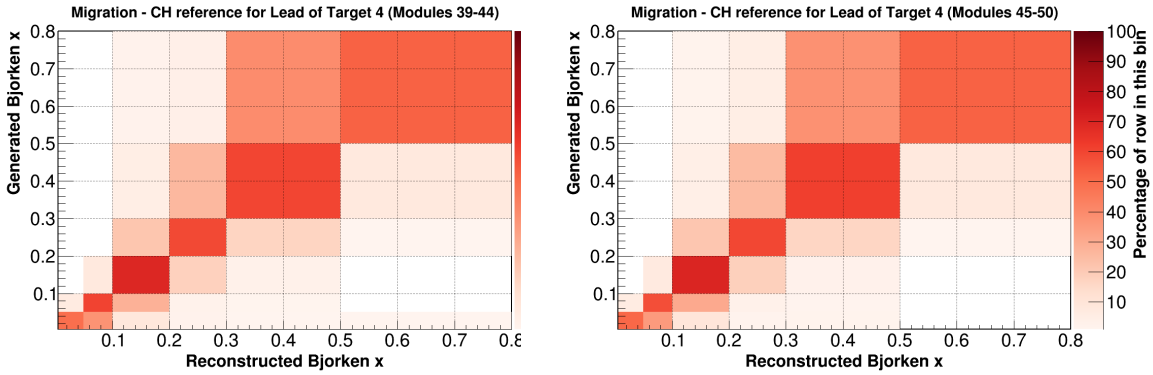

Figure D-17: x_{bj} migration matrix for scintillator tracker modules 39-44 (left) and scintillator tracker modules 45-50 (right). The y-axis is generated (true) x_{bj} and the x-axis is reconstructed x_{bj}. Each cell records the percent of true and reconstructed DIS events.

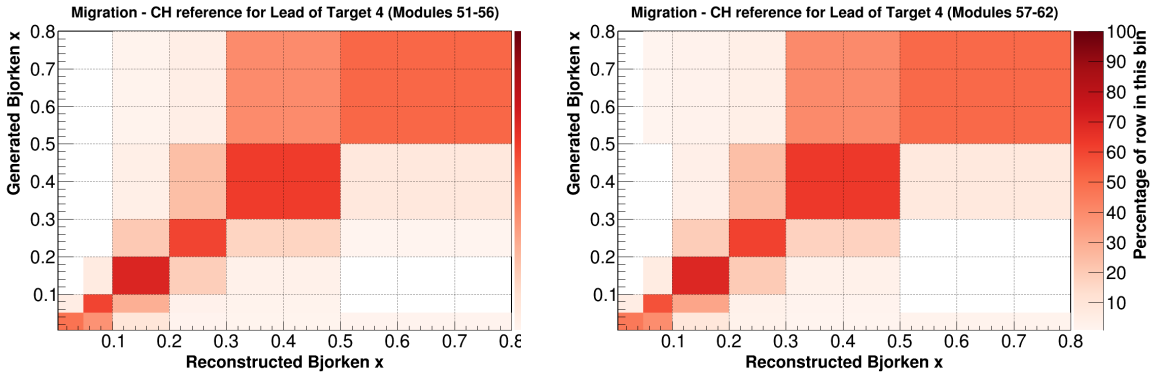

Figure D-18: x_{bj} migration matrix for scintillator tracker modules 51-56 (left) and scintillator tracker modules 57-62 (right). The y-axis is generated (true) x_{bj} and the x-axis is reconstructed x_{bj}. Each cell records the percent of true and reconstructed DIS events.

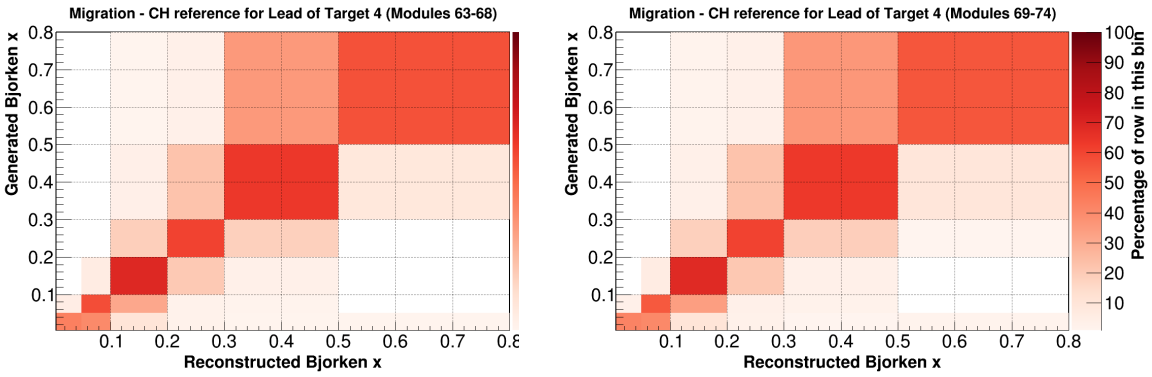

Figure D-19: x_{bj} migration matrix for scintillator tracker modules 63-68 (left) and scintillator tracker modules 69-74 (right). The y-axis is generated (true) x_{bj} and the x-axis is reconstructed x_{bj}. Each cell records the percent of true and reconstructed DIS events.

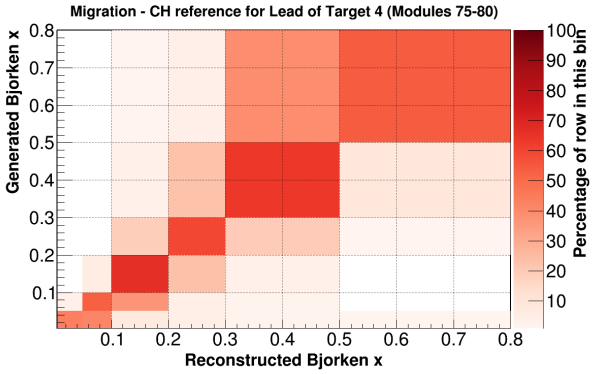

Figure D-20: x_{bj} migration matrix for scintillator tracker modules 75-80. The y-axis is generated (true) x_{bj} and the x-axis is reconstructed x_{bj}. Each cell records the percent of true and reconstructed DIS events.

D.3 Migration matrix fraction as a function of E_μ

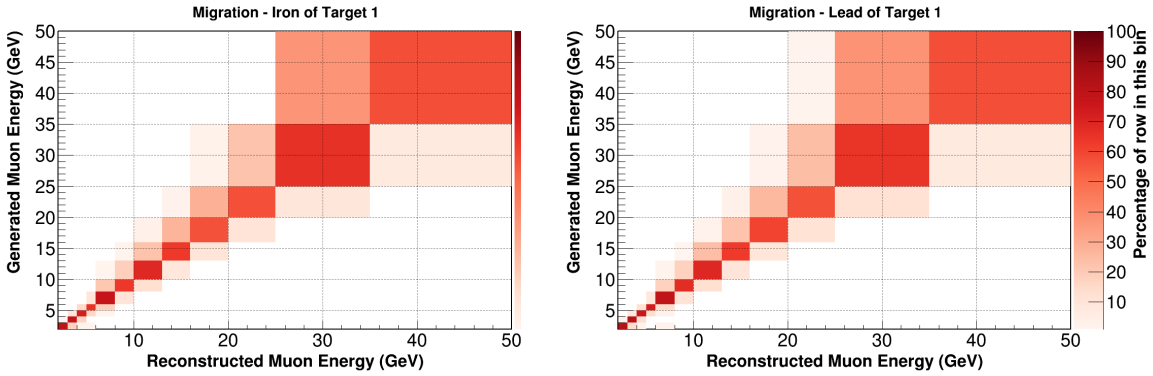

Figure D-21: E_μ migration matrix for iron of target 1 (left) and lead of target 1 (right). The y-axis is generated (true) E_μ and the x-axis is reconstructed E_μ. Each cell records the percent of true and reconstructed DIS events.

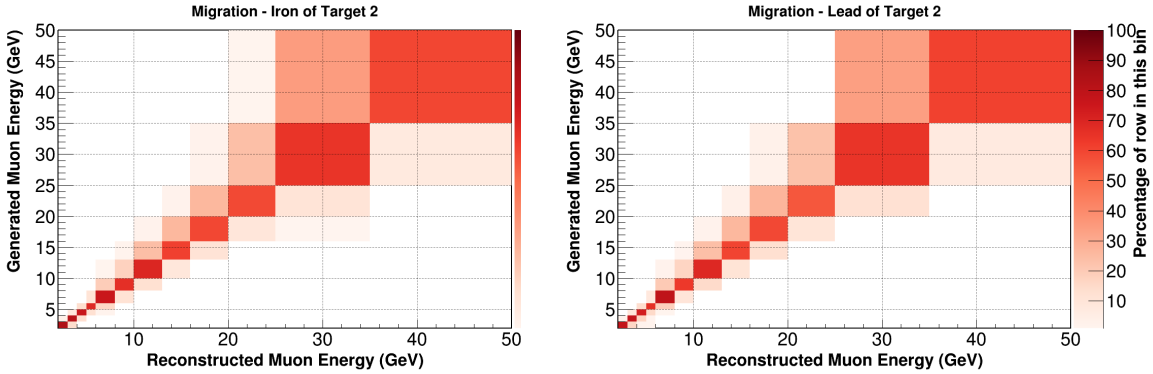

Figure D-22: E_μ migration matrix for iron of target 2 (left) and lead of target 2 (right). The y-axis is generated (true) E_μ and the x-axis is reconstructed E_μ. Each cell records the percent of true and reconstructed DIS events.

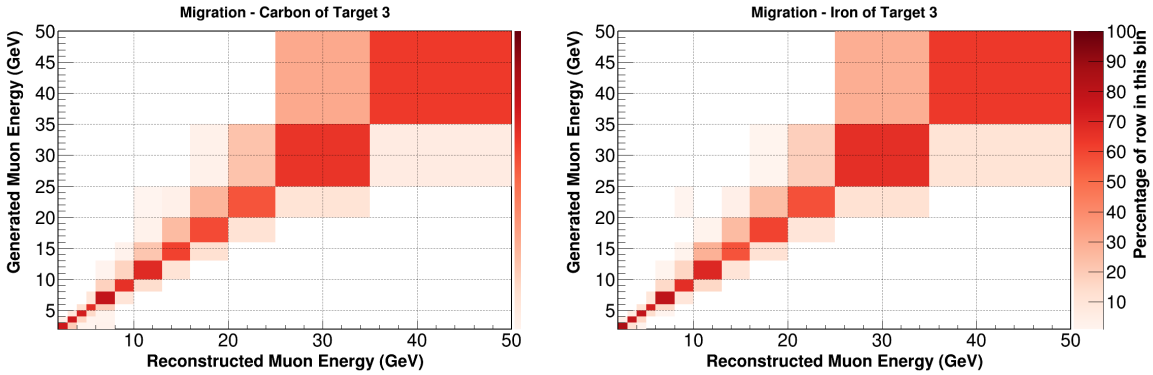

Figure D-23: E_μ migration matrix for carbon of target 3 (left) and iron of target 3 (right). The y-axis is generated (true) E_μ and the x-axis is reconstructed E_μ. Each cell records the percent of true and reconstructed DIS events.

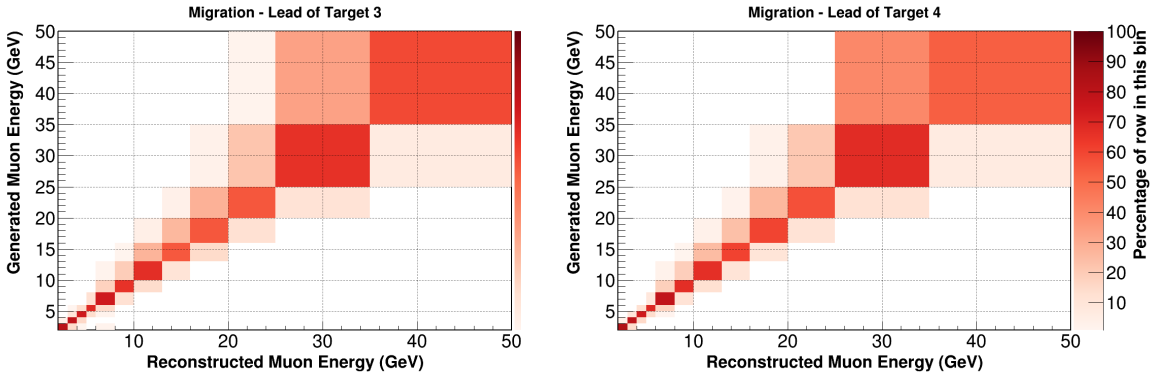

Figure D-24: E_μ migration matrix for lead of target 3 (left) and lead of target 4 (right). The y-axis is generated (true) E_μ and the x-axis is reconstructed E_μ. Each cell records the percent of true and reconstructed DIS events.

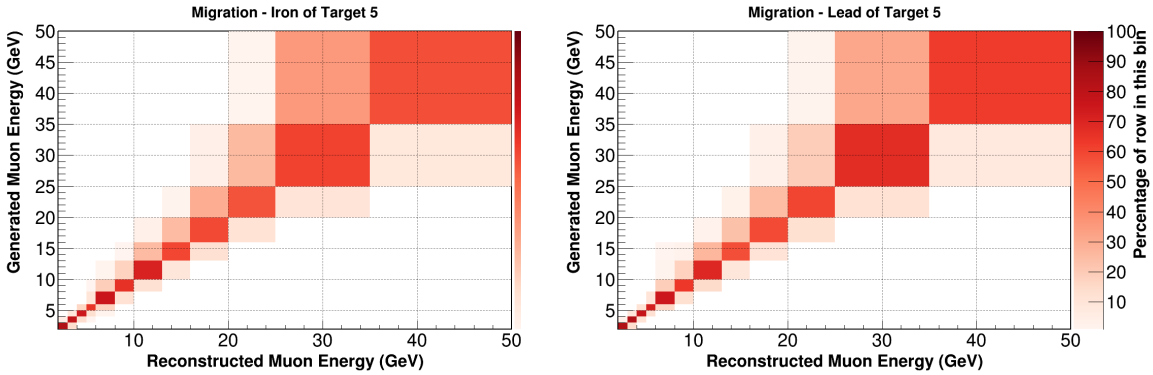

Figure D-25: E_μ migration matrix for iron of target 5 (left) and lead of target 5 (right). The y-axis is generated (true) E_μ and the x-axis is reconstructed E_μ. Each cell records the percent of true and reconstructed DIS events.

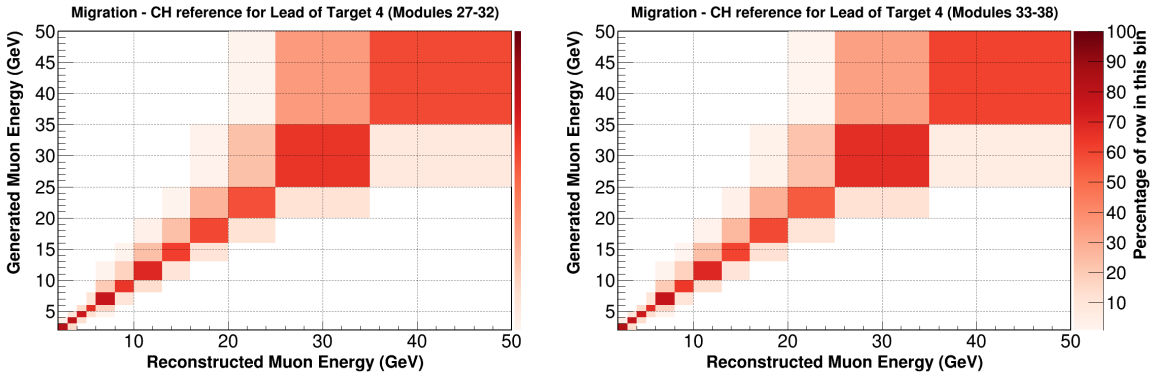

Figure D-26: E_μ migration matrix for scintillator tracker modules 27-32 (left) and scintillator tracker modules 33-38 (right). The y-axis is generated (true) E_μ and the x-axis is reconstructed E_μ. Each cell records the percent of true and reconstructed DIS events.

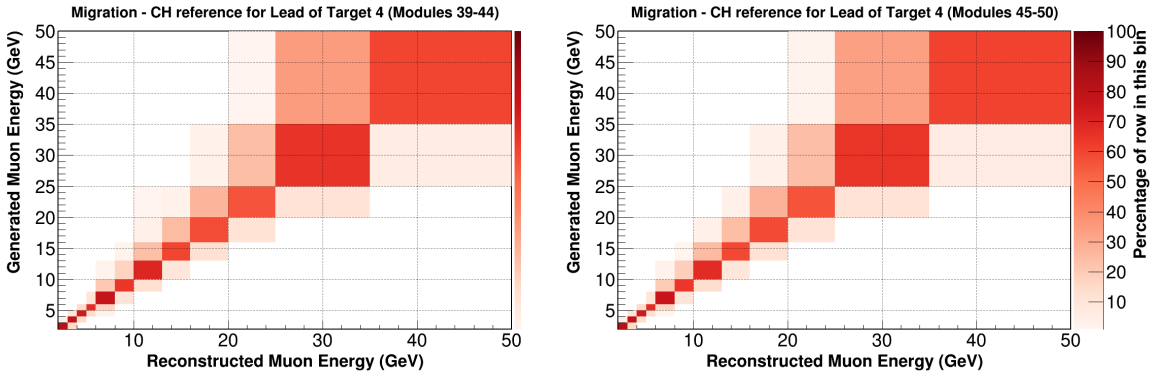

Figure D-27: E_μ migration matrix for scintillator tracker modules 39-44 (left) and scintillator tracker modules 45-50 (right). The y-axis is generated (true) E_μ and the x-axis is reconstructed E_μ. Each cell records the percent of true and reconstructed DIS events.

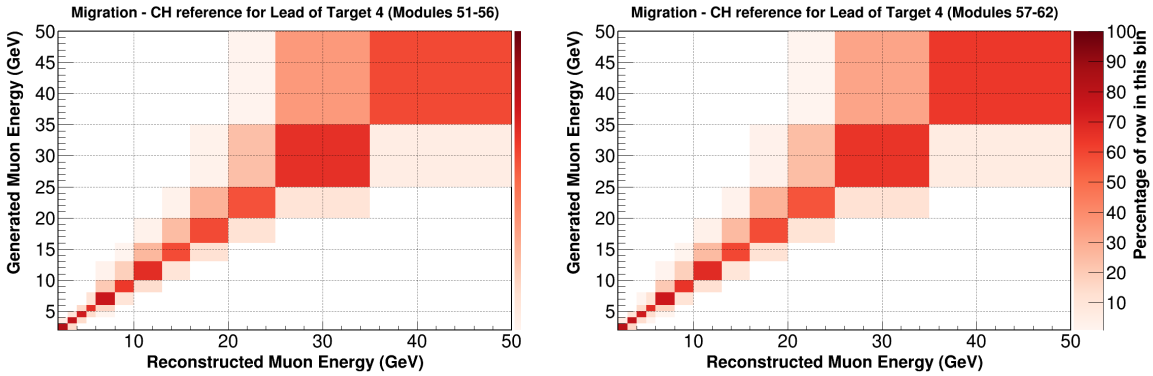

Figure D-28: E_μ migration matrix for scintillator tracker modules 51-56 (left) and scintillator tracker modules 57-62 (right). The y-axis is generated (true) E_μ and the x-axis is reconstructed E_μ. Each cell records the percent of true and reconstructed DIS events.

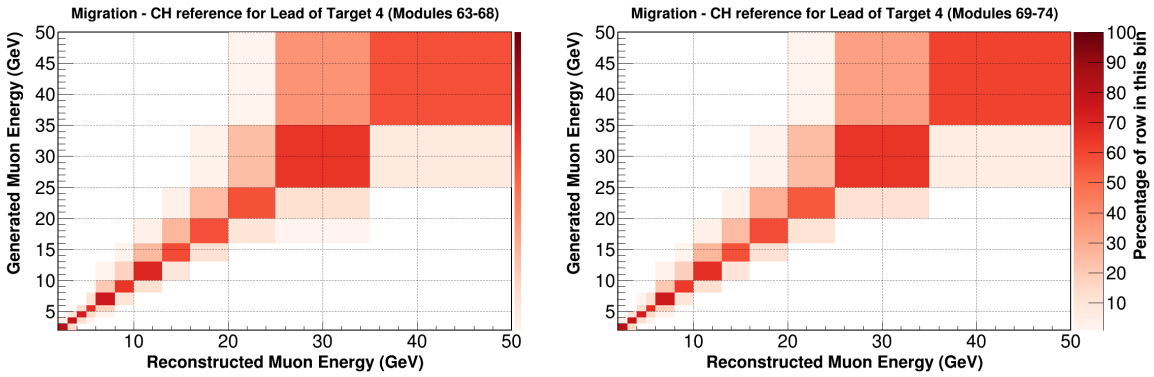

Figure D-29: E_μ migration matrix for scintillator tracker modules 63-68 (left) and scintillator tracker modules 69-74 (right). The y-axis is generated (true) E_μ and the x-axis is reconstructed E_μ. Each cell records the percent of true and reconstructed DIS events.

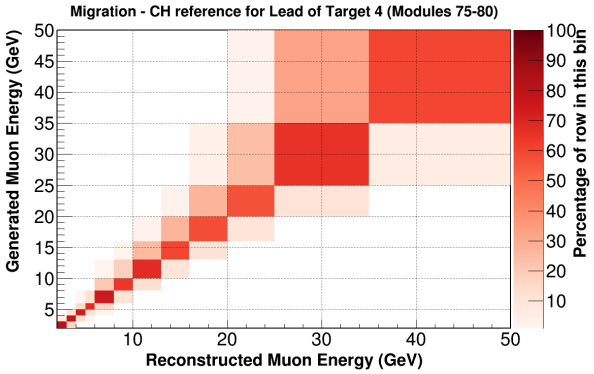

Figure D-30: E_μ migration matrix for scintillator tracker modules 75-80. The y-axis is generated (true) E_μ and the x-axis is reconstructed E_μ. Each cell records the percent of true and reconstructed DIS events.

D.4 Migration matrix fraction as a function of θ_μ

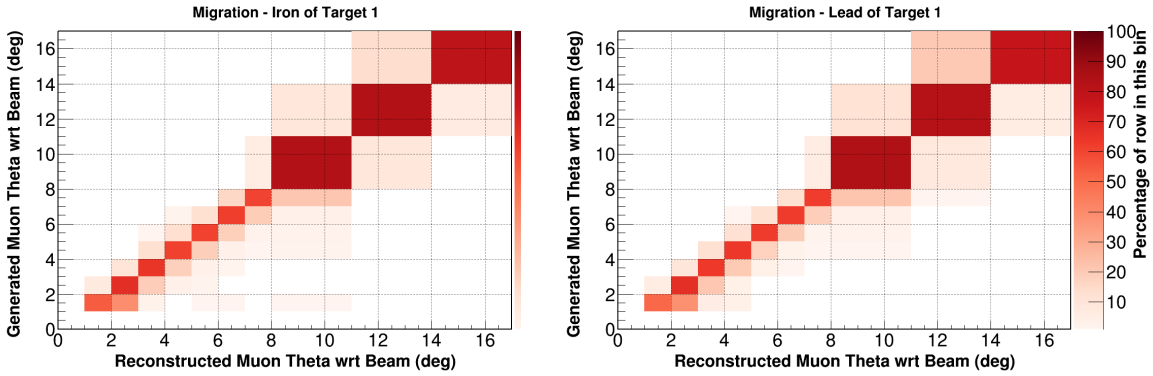

Figure D-31: θ_μ migration matrix for iron of target 1 (left) and lead of target 1 (right). The y-axis is generated (true) θ_μ and the x-axis is reconstructed θ_μ. Each cell records the percent of true and reconstructed DIS events.

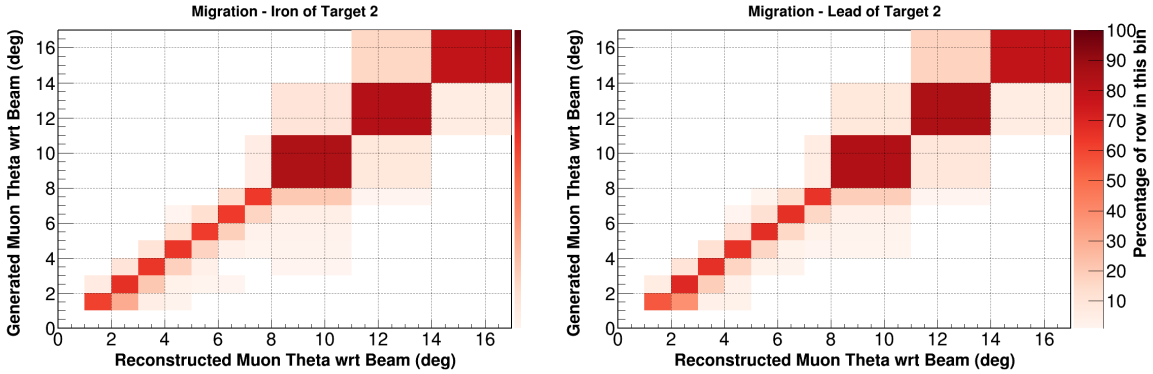

Figure D-32: θ_μ migration matrix for iron of target 2 (left) and lead of target 2 (right). The y-axis is generated (true) θ_μ and the x-axis is reconstructed θ_μ. Each cell records the percent of true and reconstructed DIS events.

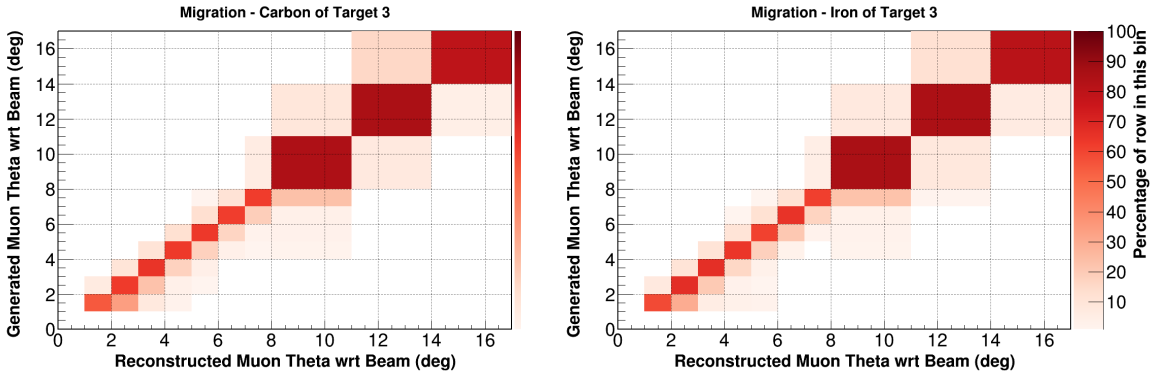

Figure D-33: θ_μ migration matrix for carbon of target 3 (left) and iron of target 3 (right). The y-axis is generated (true) θ_μ and the x-axis is reconstructed θ_μ. Each cell records the percent of true and reconstructed DIS events.

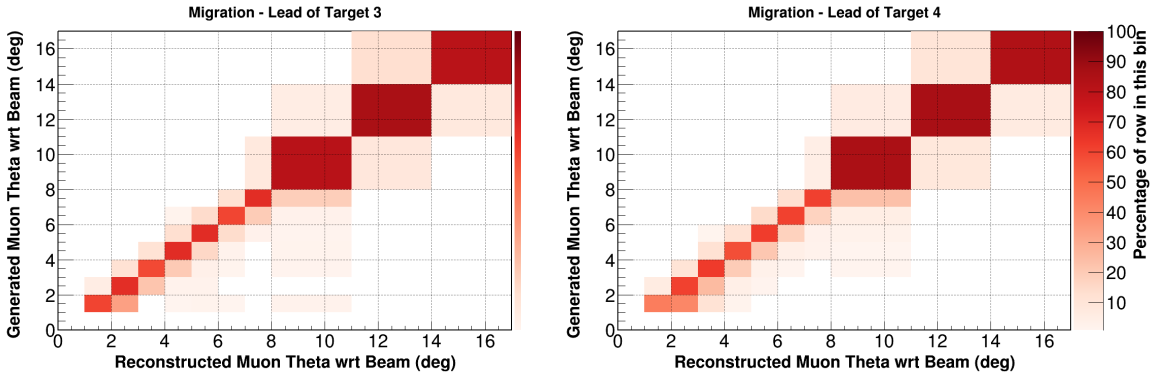

Figure D-34: θ_μ migration matrix for lead of target 3 (left) and lead of target 4 (right). The y-axis is generated (true) θ_μ and the x-axis is reconstructed θ_μ. Each cell records the percent of true and reconstructed DIS events.

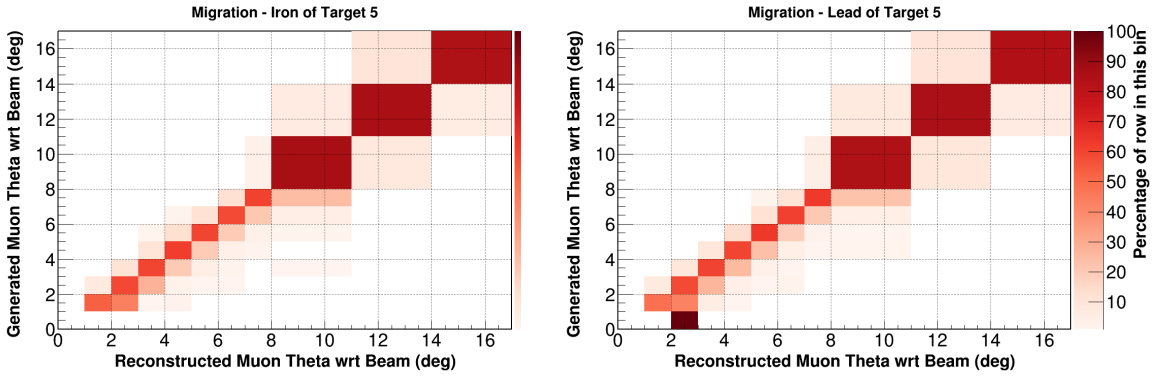

Figure D-35: θ_μ migration matrix for iron of target 5 (left) and lead of target 5 (right). The y-axis is generated (true) θ_μ and the x-axis is reconstructed θ_μ. Each cell records the percent of true and reconstructed DIS events.

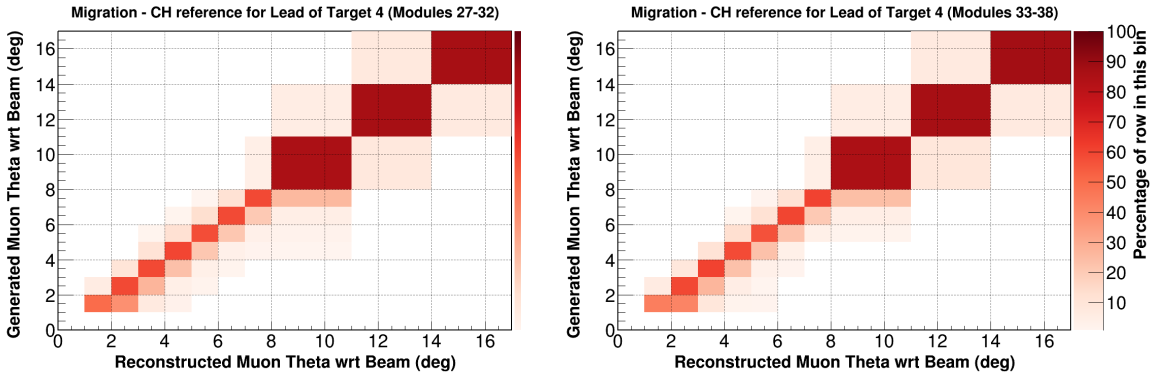

Figure D-36: θ_μ migration matrix for scintillator tracker modules 27-32 (left) and scintillator tracker modules 33-38 (right). The y-axis is generated (true) θ_μ and the x-axis is reconstructed θ_μ. Each cell records the percent of true and reconstructed DIS events.

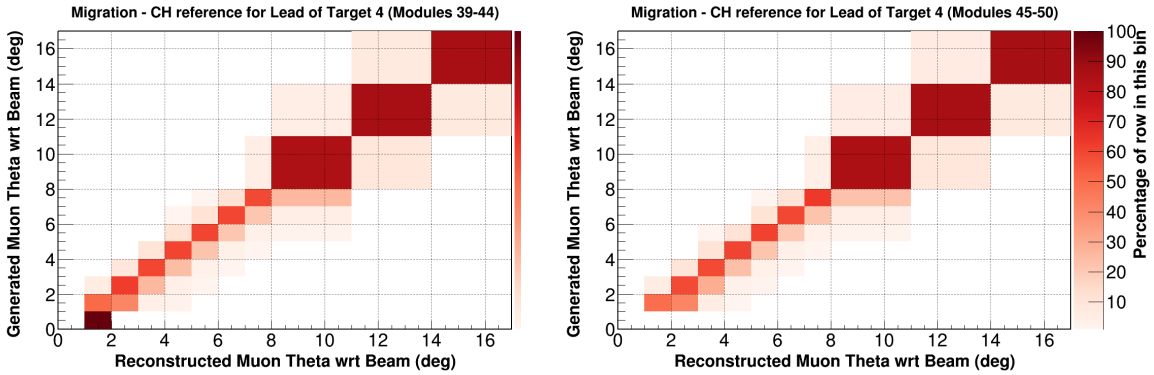

Figure D-37: θ_μ migration matrix for scintillator tracker modules 39-44 (left) and scintillator tracker modules 45-50 (right). The y-axis is generated (true) θ_μ and the x-axis is reconstructed θ_μ. Each cell records the percent of true and reconstructed DIS events.

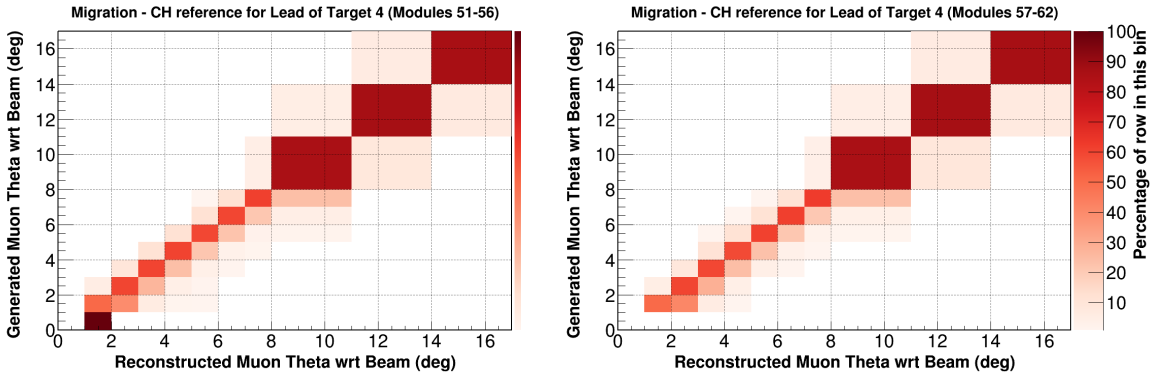

Figure D-38: θ_μ migration matrix for scintillator tracker modules 51-56 (left) and scintillator tracker modules 57-62 (right). The y-axis is generated (true) θ_μ and the x-axis is reconstructed θ_μ. Each cell records the percent of true and reconstructed DIS events.

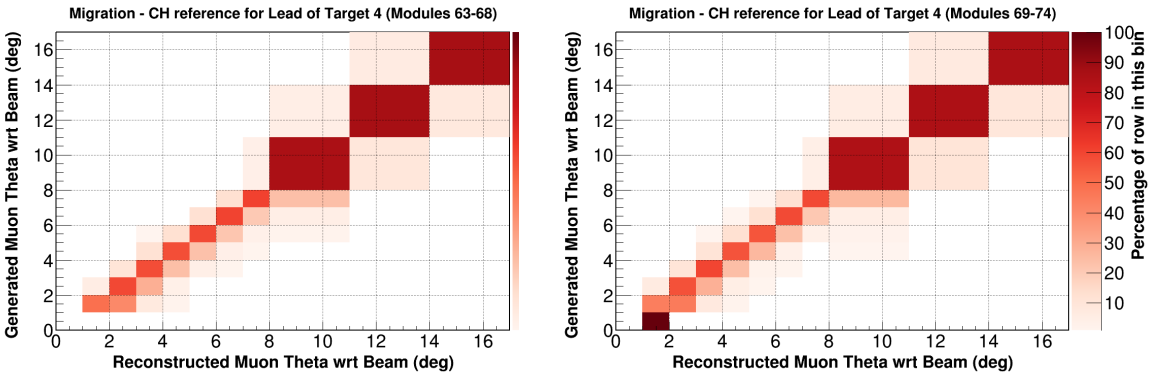

Figure D-39: θ_μ migration matrix for scintillator tracker modules 63-68 (left) and scintillator tracker modules 69-74 (right). The y-axis is generated (true) θ_μ and the x-axis is reconstructed θ_μ. Each cell records the percent of true and reconstructed DIS events.

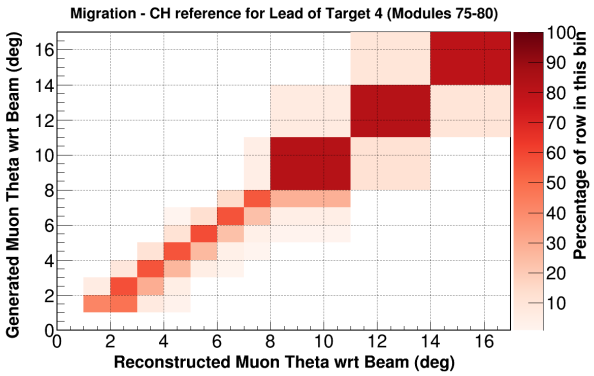

Figure D-40: θ_μ migration matrix for scintillator tracker modules 75-80. The y-axis is generated (true) θ_μ and the x-axis is reconstructed θ_μ. Each cell records the percent of true and reconstructed DIS events.

D.5 Migration matrix fraction as a function of Q^2

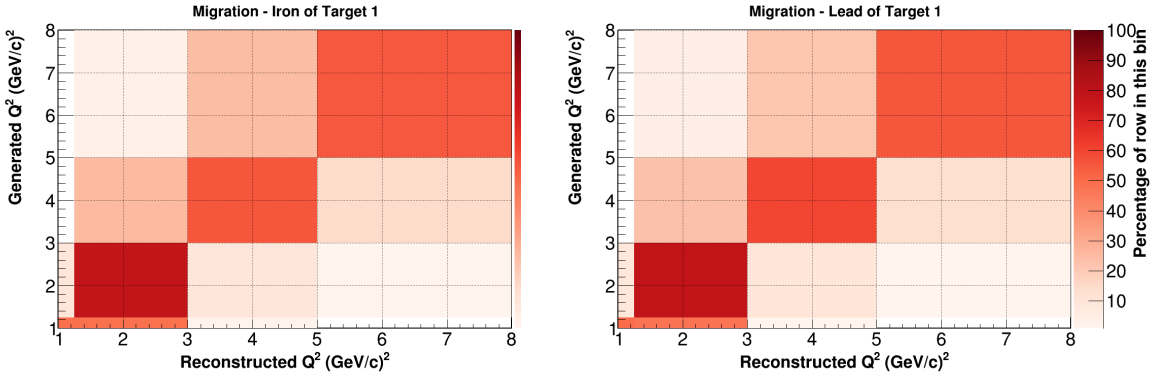

Figure D-41: Q^2 migration matrix for iron of target 1 (left) and lead of target 1 (right). The y-axis is generated (true) Q^2 and the x-axis is reconstructed Q^2. Each cell records the percent of true and reconstructed DIS events.

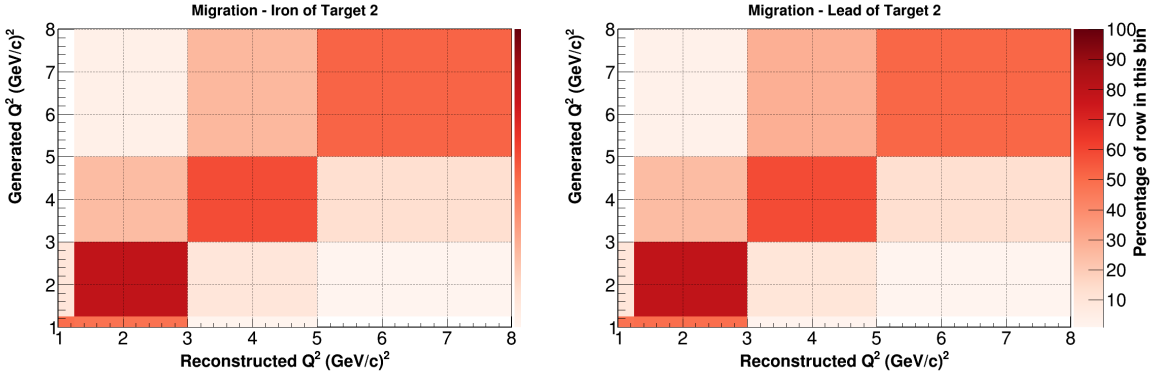

Figure D-42: Q^2 migration matrix for iron of target 2 (left) and lead of target 2 (right). The y-axis is generated (true) Q^2 and the x-axis is reconstructed Q^2. Each cell records the percent of true and reconstructed DIS events.

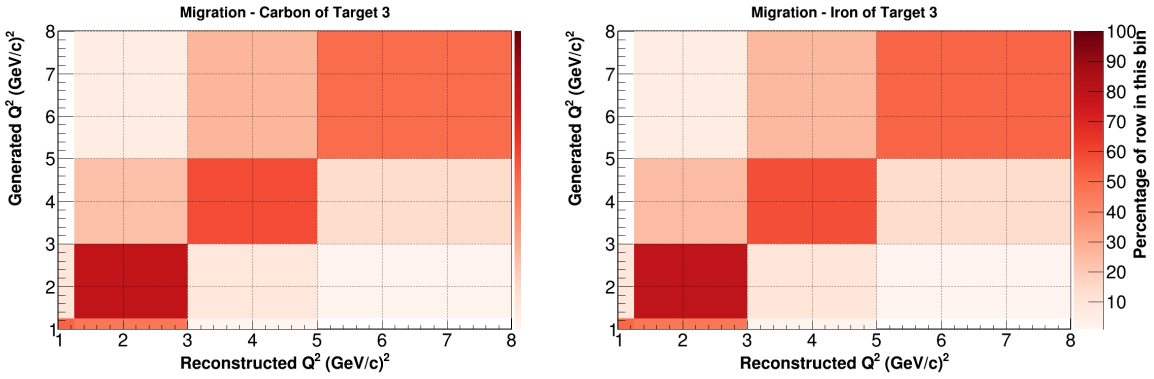

Figure D-43: Q^2 migration matrix for carbon of target 3 (left) and iron of target 3 (right). The y-axis is generated (true) Q^2 and the x-axis is reconstructed Q^2. Each cell records the percent of true and reconstructed DIS events.

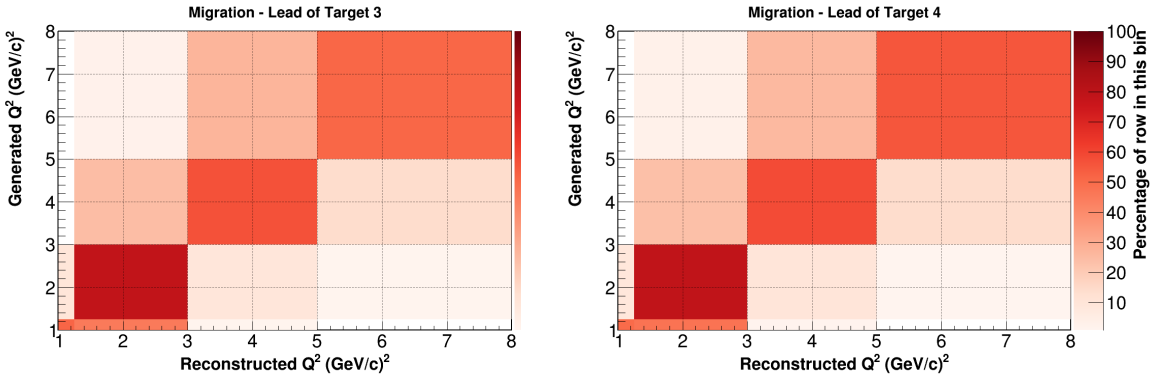

Figure D-44: Q^2 migration matrix for lead of target 3 (left) and lead of target 4 (right). The y-axis is generated (true) Q^2 and the x-axis is reconstructed Q^2. Each cell records the percent of true and reconstructed DIS events.

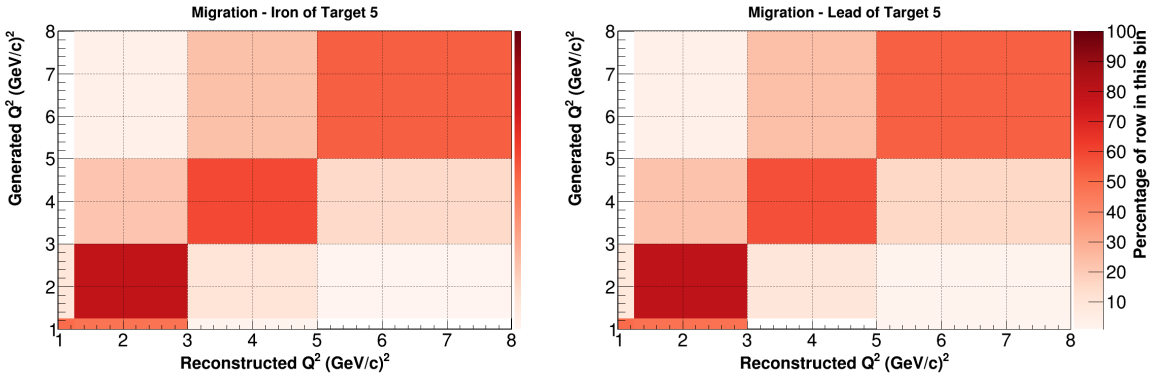

Figure D-45: Q^2 migration matrix for iron of target 5 (left) and lead of target 5 (right). The y-axis is generated (true) Q^2 and the x-axis is reconstructed Q^2. Each cell records the percent of true and reconstructed DIS events.

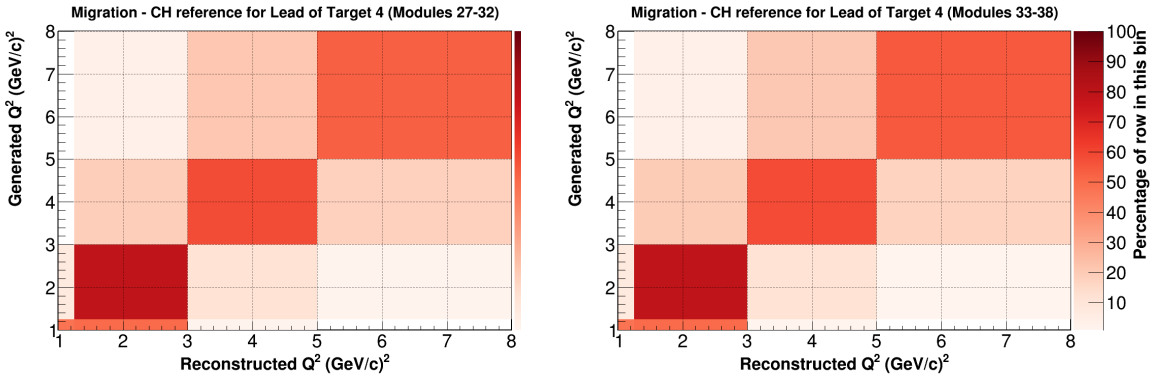

Figure D-46: Q^2 migration matrix for scintillator tracker modules 27-32 (left) and scintillator tracker modules 33-38 (right). The y-axis is generated (true) Q^2 and the x-axis is reconstructed Q^2. Each cell records the percent of true and reconstructed DIS events.

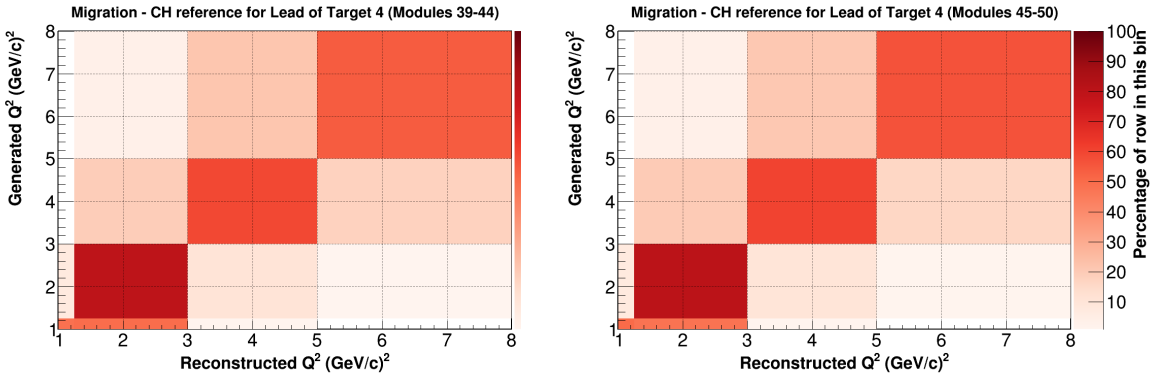

Figure D-47: Q^2 migration matrix for scintillator tracker modules 39-44 (left) and scintillator tracker modules 45-50 (right). The y-axis is generated (true) Q^2 and the x-axis is reconstructed Q^2. Each cell records the percent of true and reconstructed DIS events.

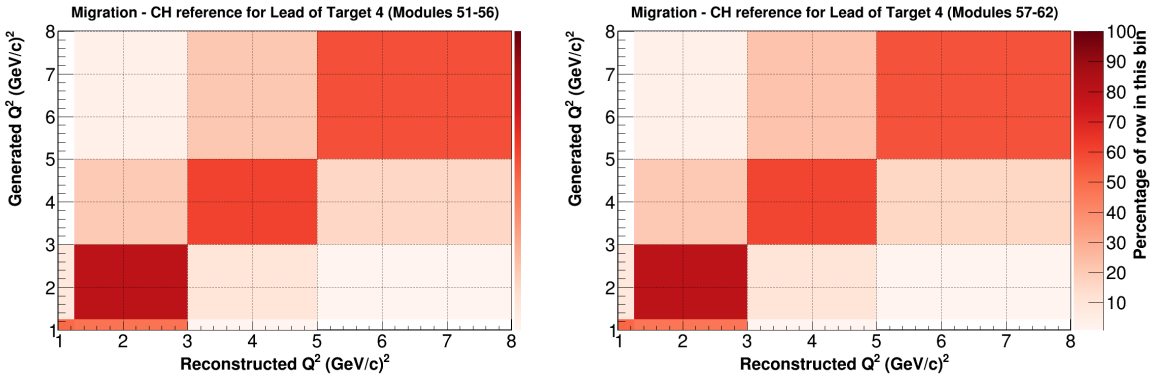

Figure D-48: Q^2 migration matrix for scintillator tracker modules 51-56 (left) and scintillator tracker modules 57-62 (right). The y-axis is generated (true) Q^2 and the x-axis is reconstructed Q^2. Each cell records the percent of true and reconstructed DIS events.

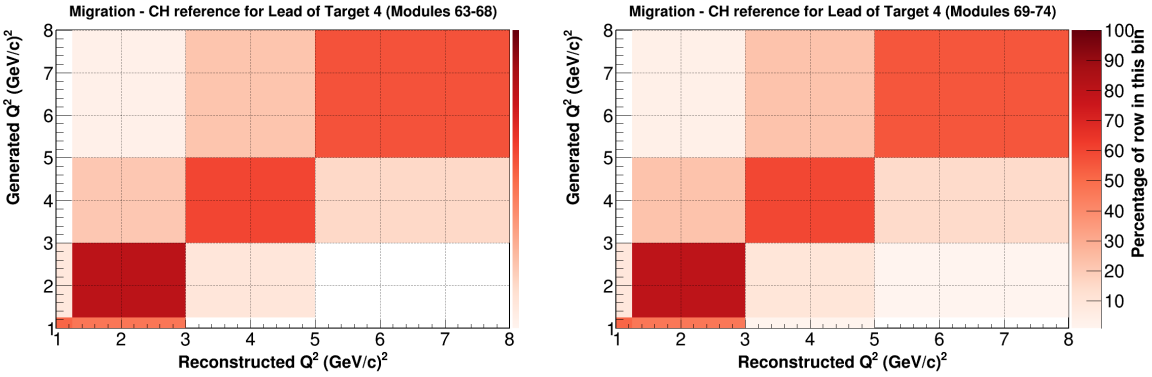

Figure D-49: Q^2 migration matrix for scintillator tracker modules 63-68 (left) and scintillator tracker modules 69-74 (right). The y-axis is generated (true) Q^2 and the x-axis is reconstructed Q^2. Each cell records the percent of true and reconstructed DIS events.

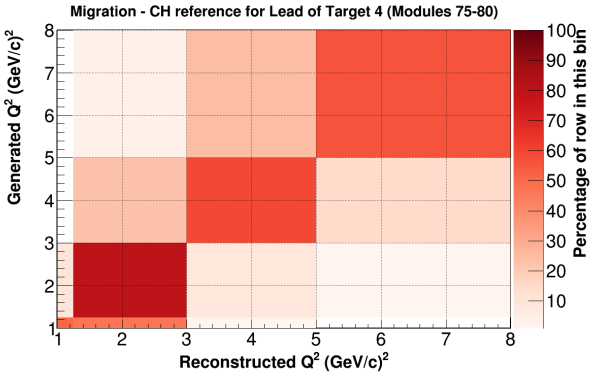

Figure D-50: Q^2 migration matrix for scintillator tracker modules 75-80. The y-axis is generated (true) Q^2 and the x-axis is reconstructed Q^2. Each cell records the percent of true and reconstructed DIS events.

D.6 Migration matrix fraction as a function of W

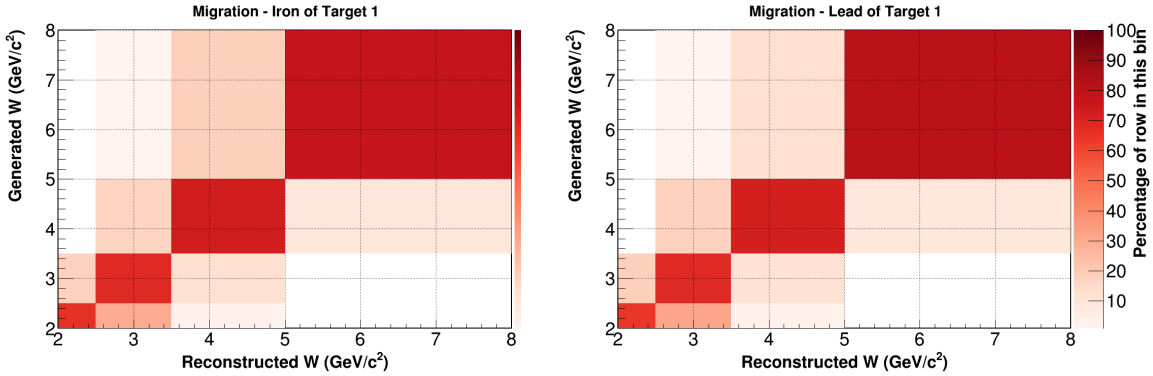

Figure D-51: W migration matrix for iron of target 1 (left) and lead of target 1 (right). The y-axis is generated (true) W and the x-axis is reconstructed W. Each cell records the percent of true and reconstructed DIS events.

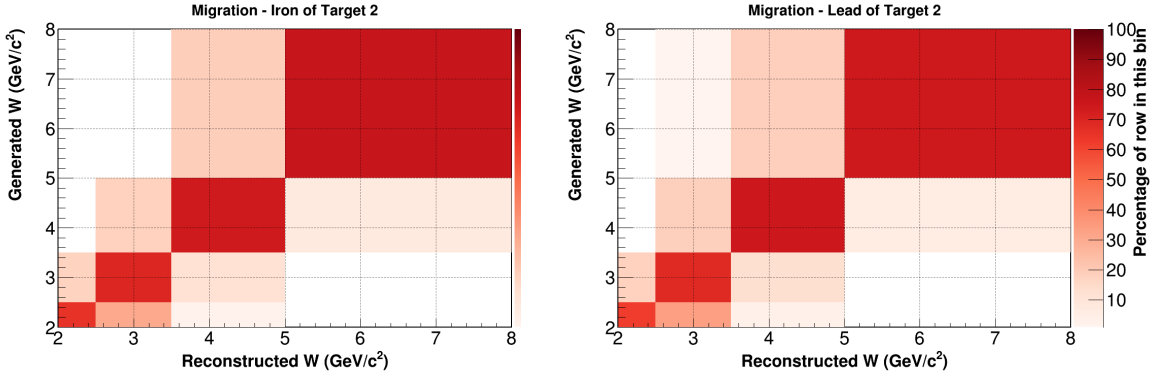

Figure D-52: W migration matrix for iron of target 2 (left) and lead of target 2 (right). The y-axis is generated (true) W and the x-axis is reconstructed W. Each cell records the percent of true and reconstructed DIS events.

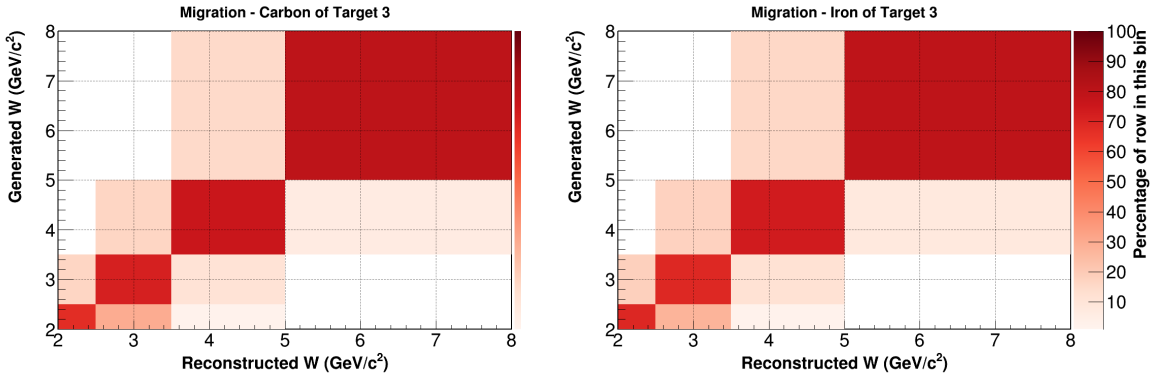

Figure D-53: W migration matrix for carbon of target 3 (left) and iron of target 3 (right). The y-axis is generated (true) W and the x-axis is reconstructed W. Each cell records the percent of true and reconstructed DIS events.

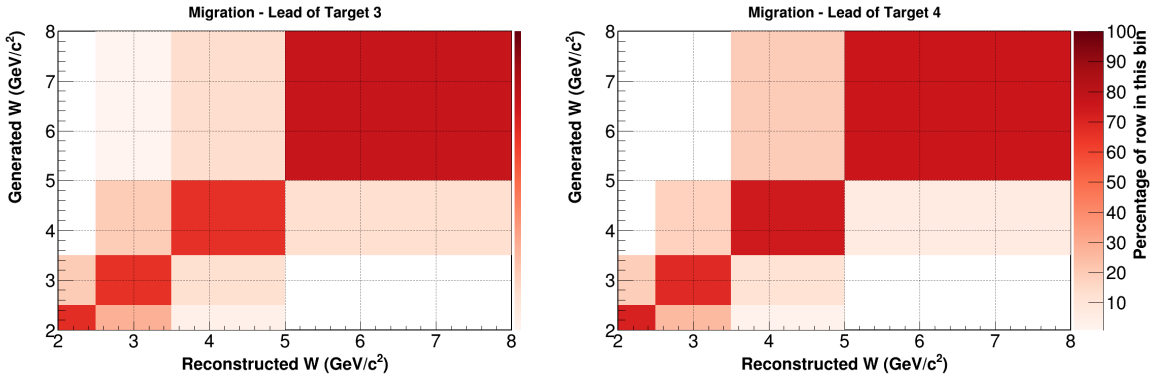

Figure D-54: W migration matrix for lead of target 3 (left) and lead of target 4 (right). The y-axis is generated (true) W and the x-axis is reconstructed W. Each cell records the percent of true and reconstructed DIS events.

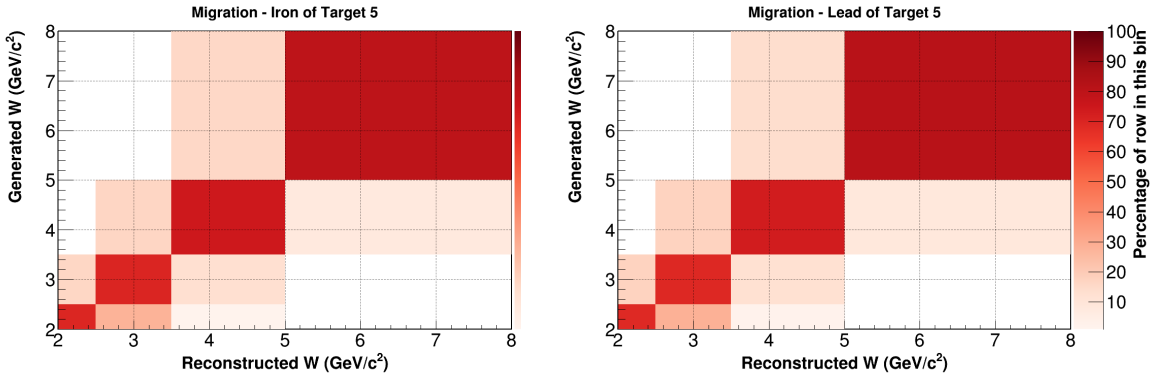

Figure D-55: W migration matrix for iron of target 5 (left) and lead of target 5 (right). The y-axis is generated (true) W and the x-axis is reconstructed W. Each cell records the percent of true and reconstructed DIS events.

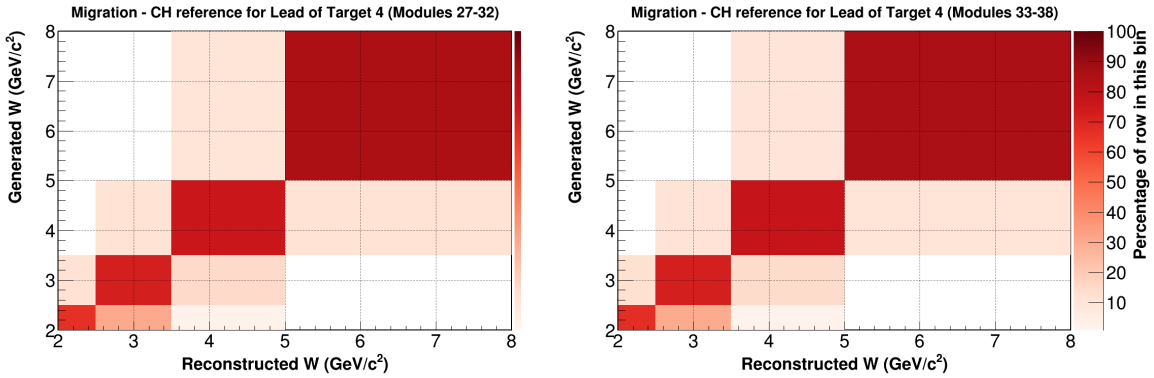

Figure D-56: W migration matrix for scintillator tracker modules 27-32 (left) and scintillator tracker modules 33-38 (right). The y-axis is generated (true) W and the x-axis is reconstructed W. Each cell records the percent of true and reconstructed DIS events.

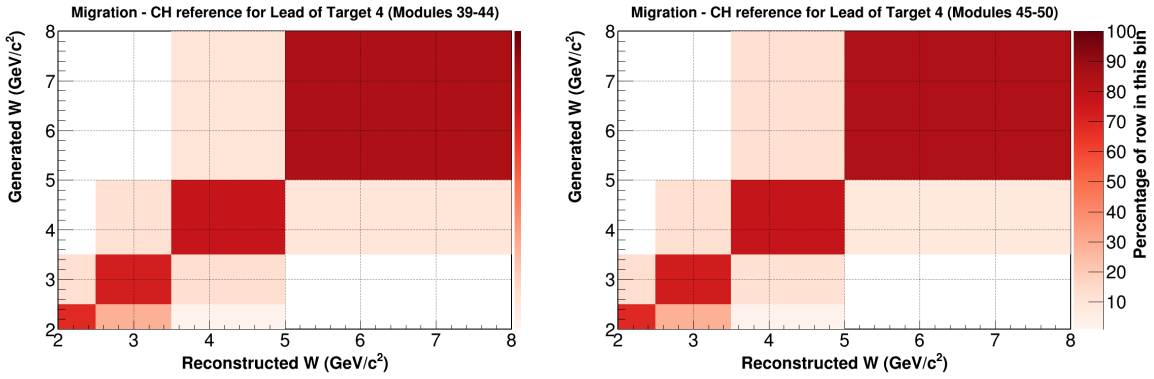

Figure D-57: W migration matrix for scintillator tracker modules 39-44 (left) and scintillator tracker modules 45-50 (right). The y-axis is generated (true) W and the x-axis is reconstructed W. Each cell records the percent of true and reconstructed DIS events.

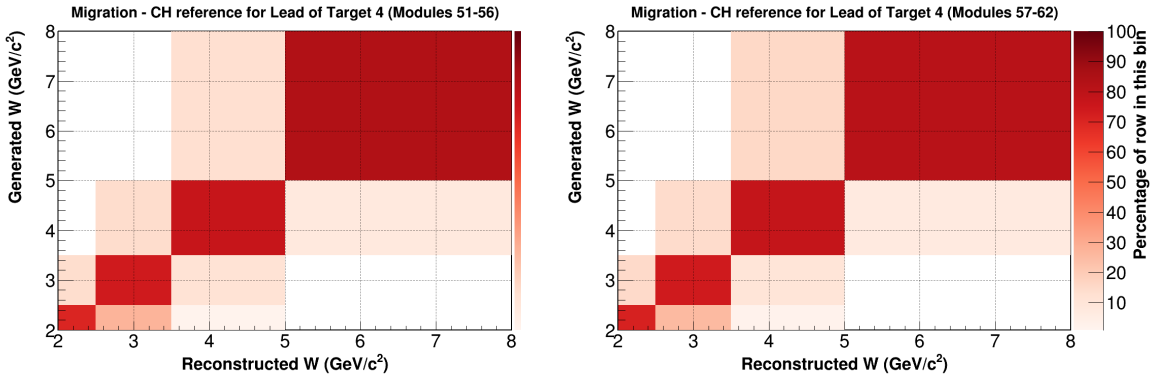

Figure D-58: W migration matrix for scintillator tracker modules 51-56 (left) and scintillator tracker modules 57-62 (right). The y-axis is generated (true) W and the x-axis is reconstructed W. Each cell records the percent of true and reconstructed DIS events.

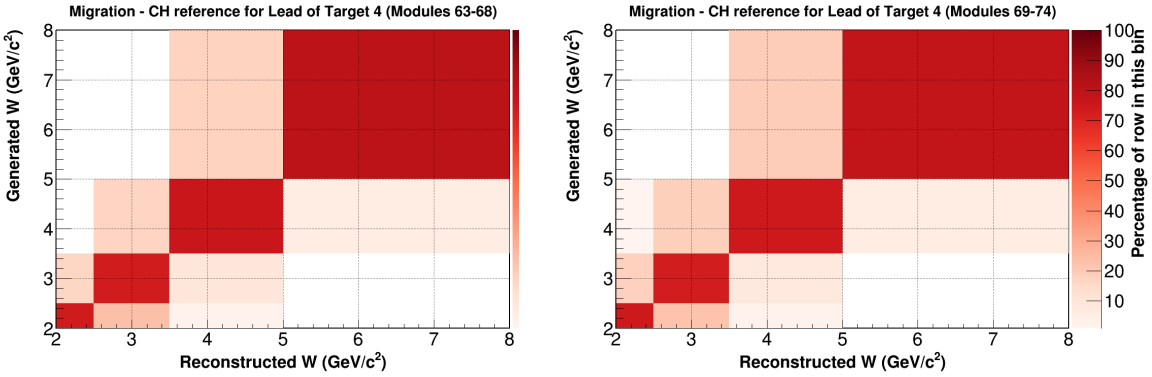

Figure D-59: W migration matrix for scintillator tracker modules 63-68 (left) and scintillator tracker modules 69-74 (right). The y-axis is generated (true) W and the x-axis is reconstructed W. Each cell records the percent of true and reconstructed DIS events.

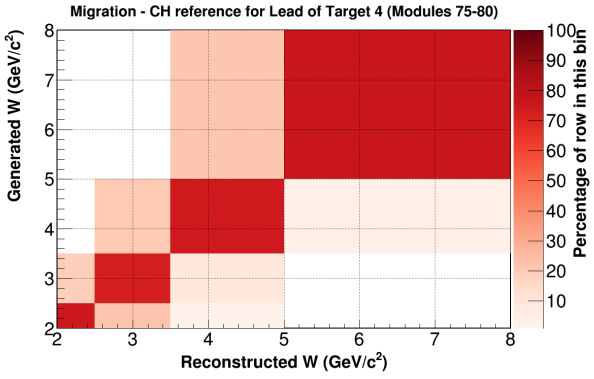

Figure D-60: W migration matrix for scintillator tracker modules 75-80. The y-axis is generated (true) W and the x-axis is reconstructed W. Each cell records the percent of true and reconstructed DIS events.

APPENDIX E
OVERALL EFFICIENCY

E.1 Overall Efficiencies as a function of E_ν

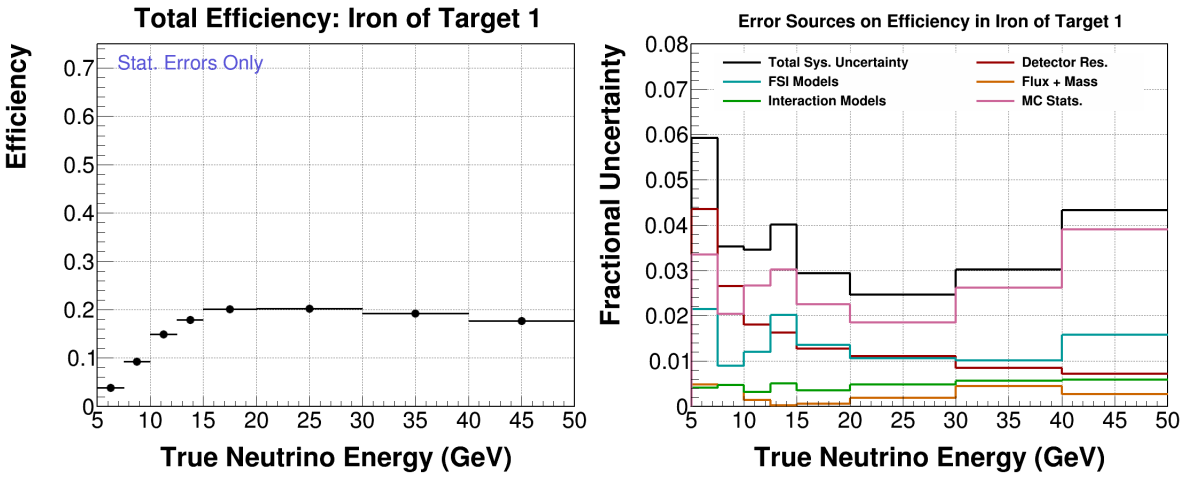

Figure E-1: Overall efficiency of events in the iron of target 1 as a function of true E_ν (left) and the systematic uncertainty on the overall efficiency (right).

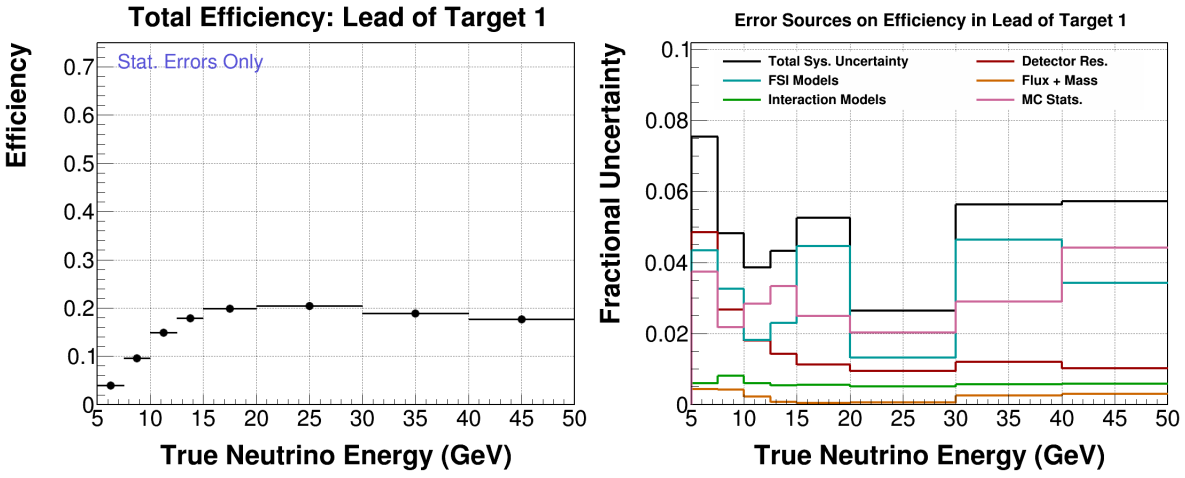

Figure E-2: Overall efficiency of events in the lead of target 1 as a function of true E_ν (left) and the systematic uncertainty on the overall efficiency (right).

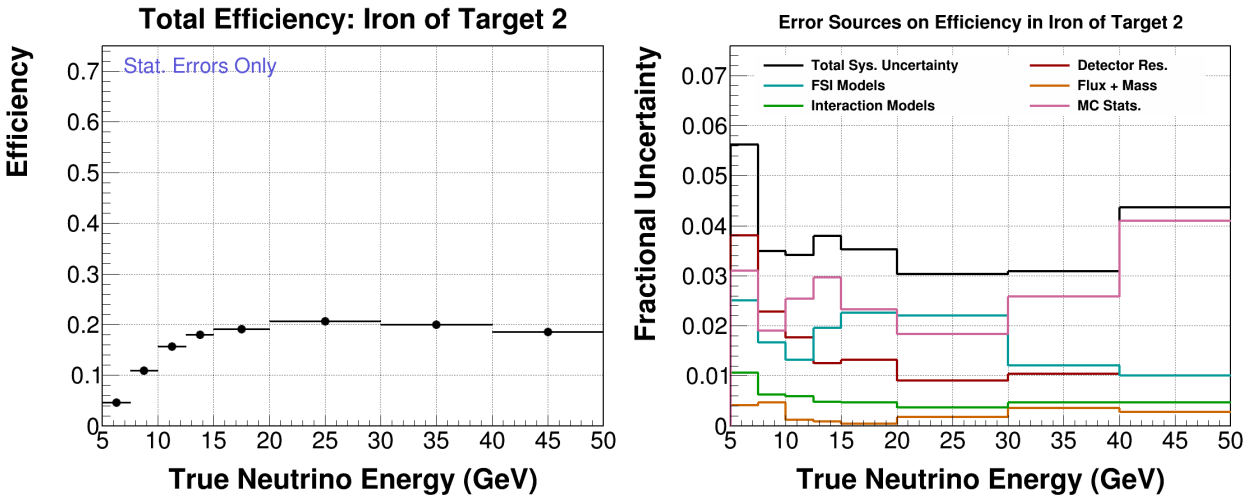

Figure E-3: Overall efficiency of events in the iron of target 2 as a function of true E_ν (left) and the systematic uncertainty on the overall efficiency (right).

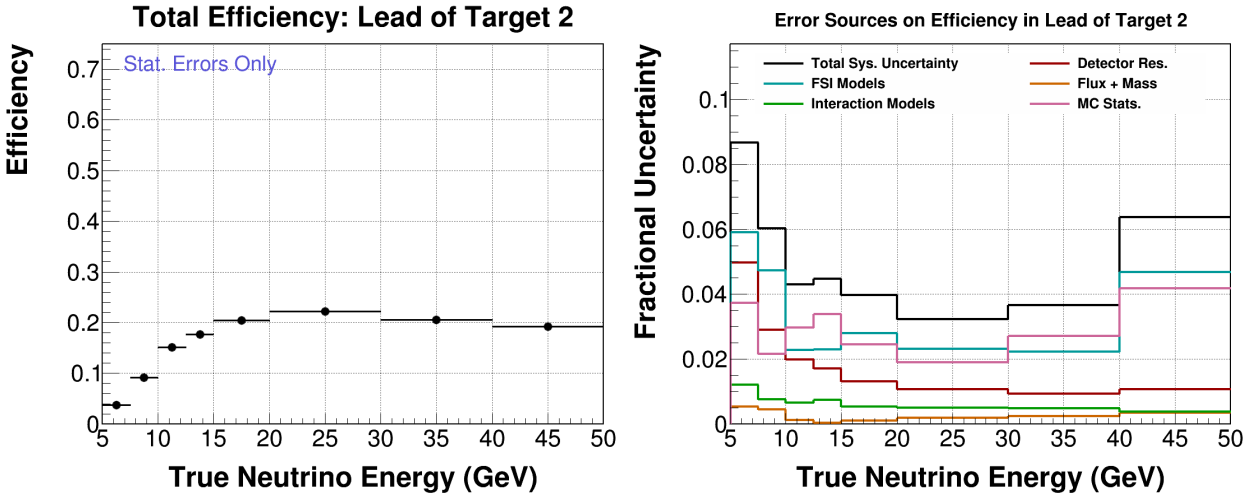

Figure E-4: Overall efficiency of events in the lead of target 2 as a function of true E_ν (left) and the systematic uncertainty on the overall efficiency (right).

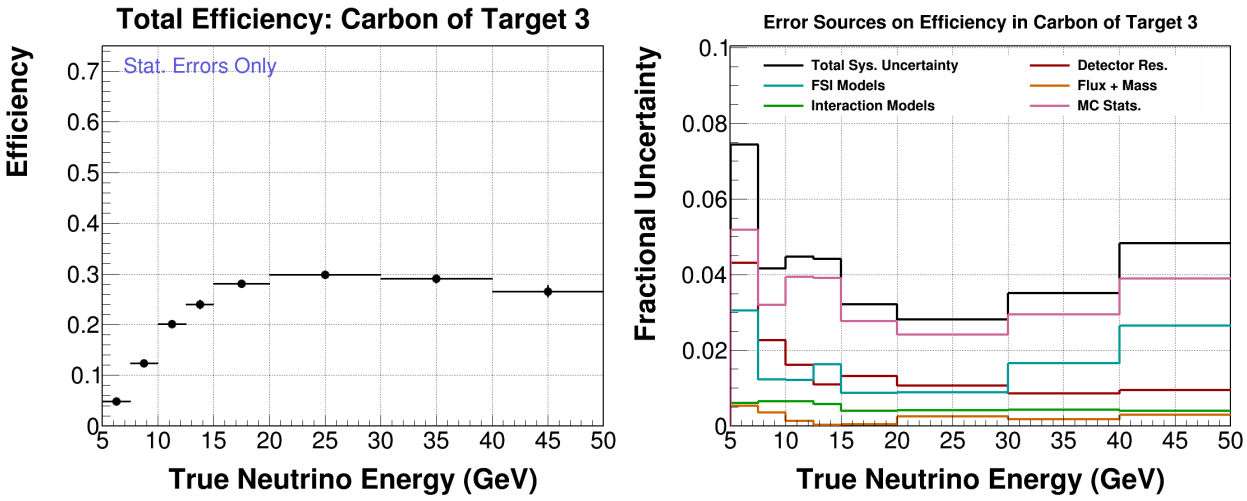

Figure E-5: Overall efficiency of events in the carbon of target 3 as a function of true E_ν (left) and the systematic uncertainty on the overall efficiency (right).

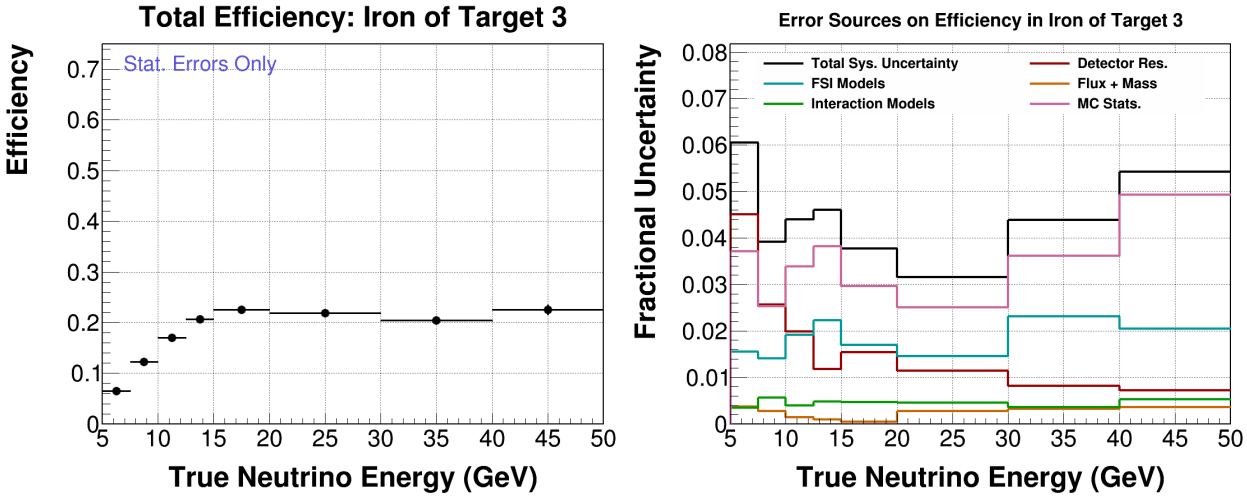

Figure E-6: Overall efficiency of events in the iron of target 3 as a function of true E_ν (left) and the systematic uncertainty on the overall efficiency (right).

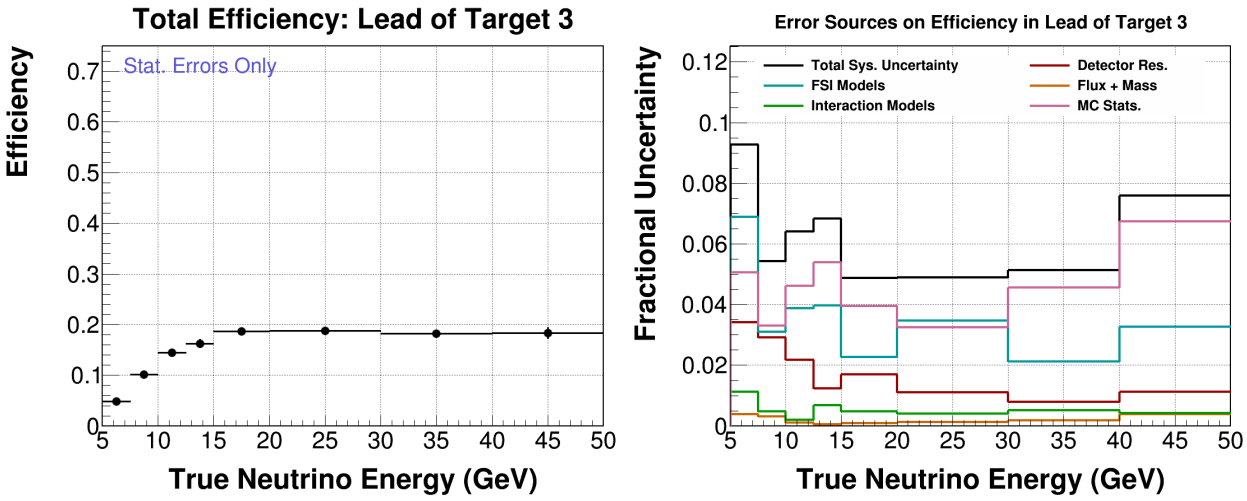

Figure E-7: Overall efficiency of events in the lead of target 3 as a function of true E_ν (left) and the systematic uncertainty on the overall efficiency (right).

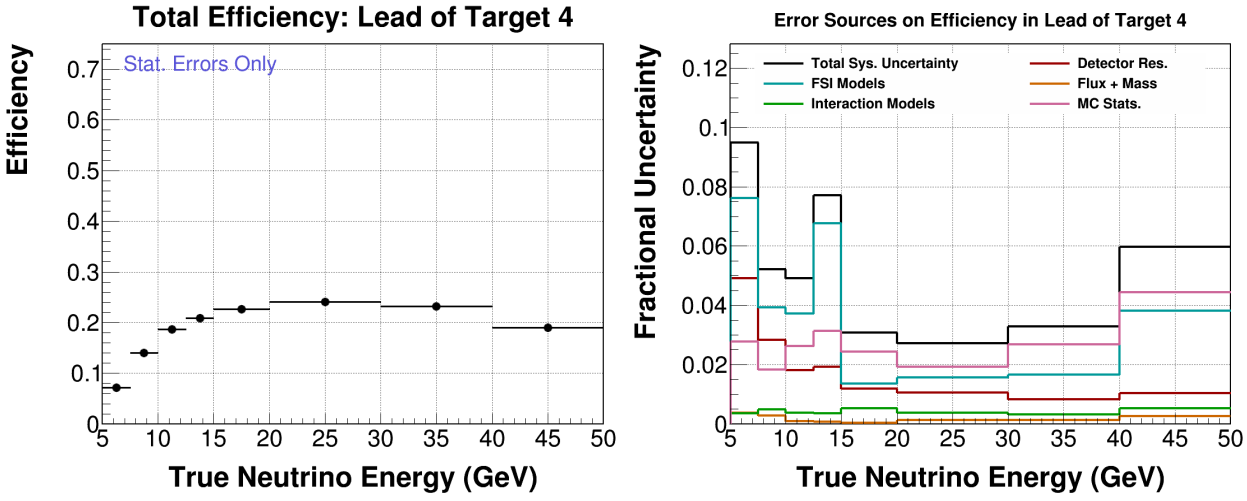

Figure E-8: Overall efficiency of events in the lead of target 4 as a function of true E_ν (left) and the systematic uncertainty on the overall efficiency (right).

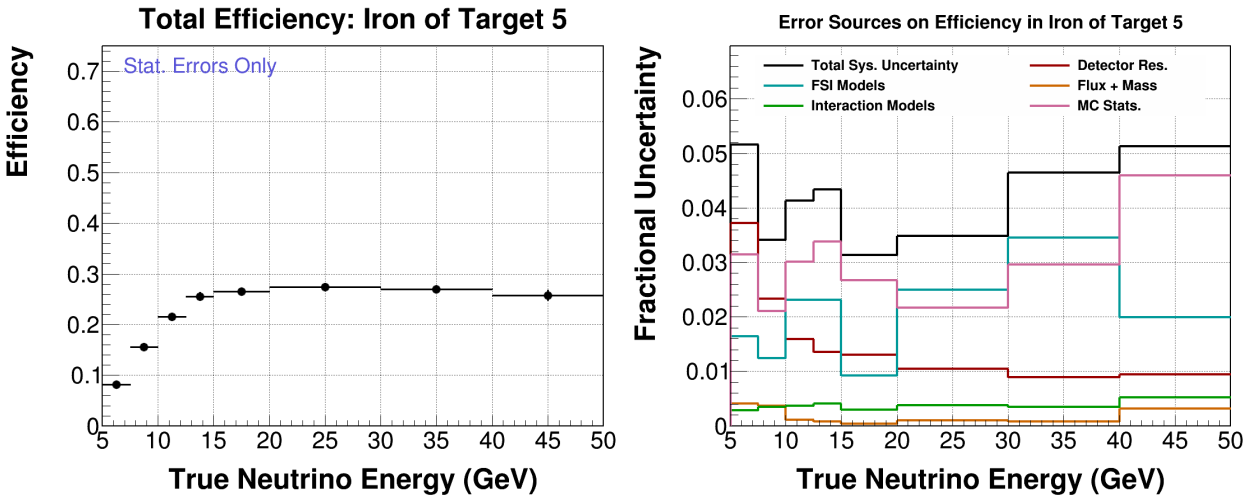

Figure E-9: Overall efficiency of events in the iron of target 5 as a function of true E_ν (left) and the systematic uncertainty on the overall efficiency (right).

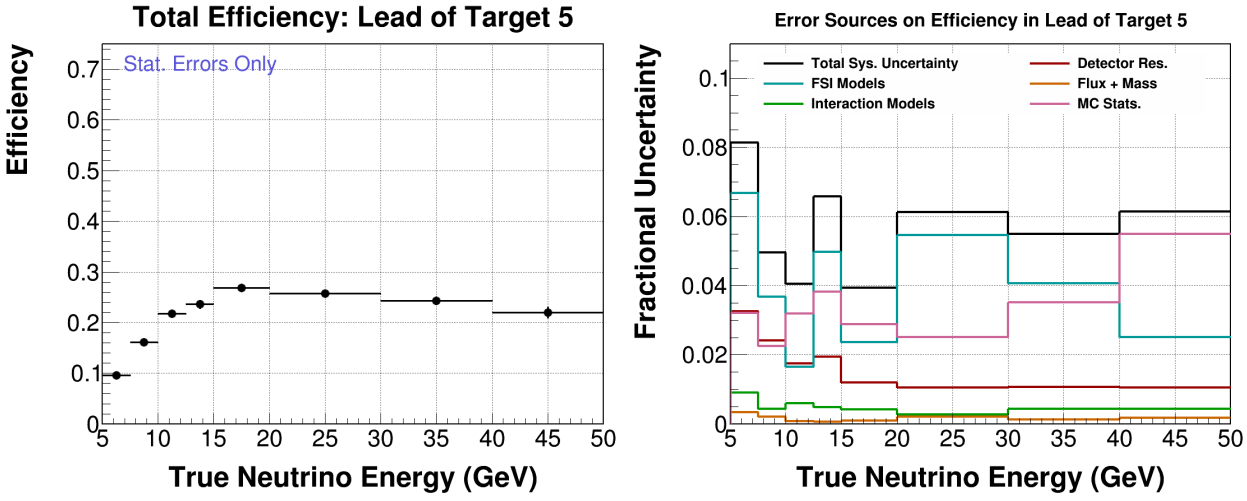

Figure E-10: Overall efficiency of events in the lead of target 5 as a function of true E_ν (left) and the systematic uncertainty on the overall efficiency (right).

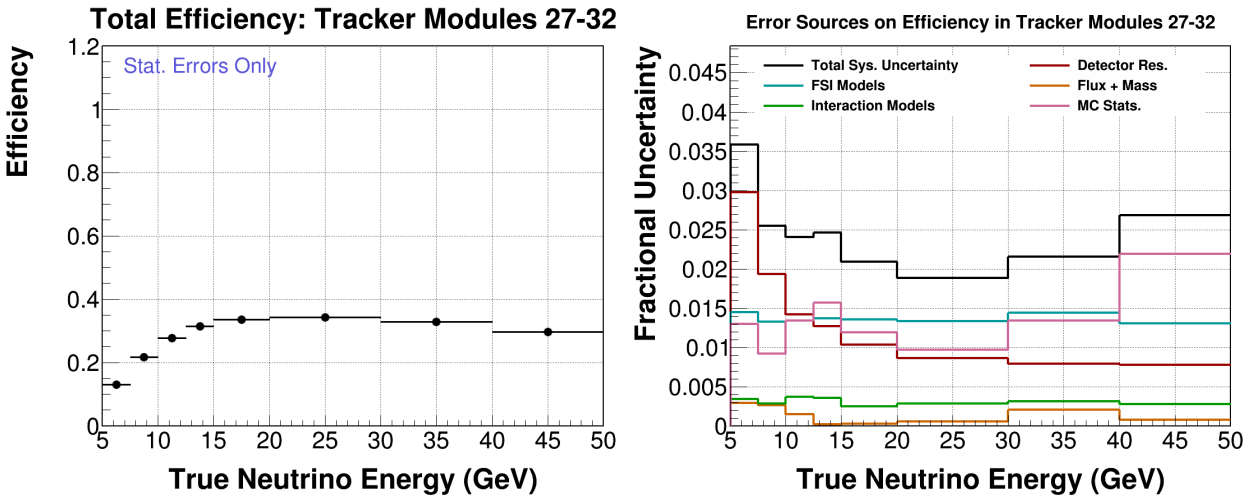

Figure E-11: Overall efficiency of events in the scintillator tracker module 27-32 as a function of true E_ν (left) and the systematic uncertainty on the overall efficiency (right).

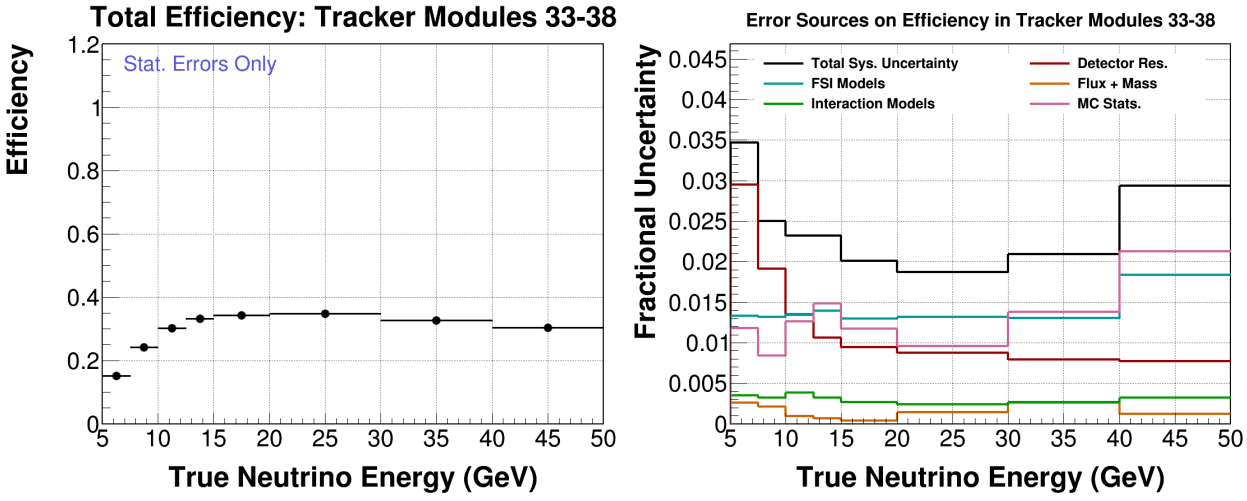

Figure E-12: Overall efficiency of events in the scintillator tracker module 33-38 as a function of true E_ν (left) and the systematic uncertainty on the overall efficiency (right).

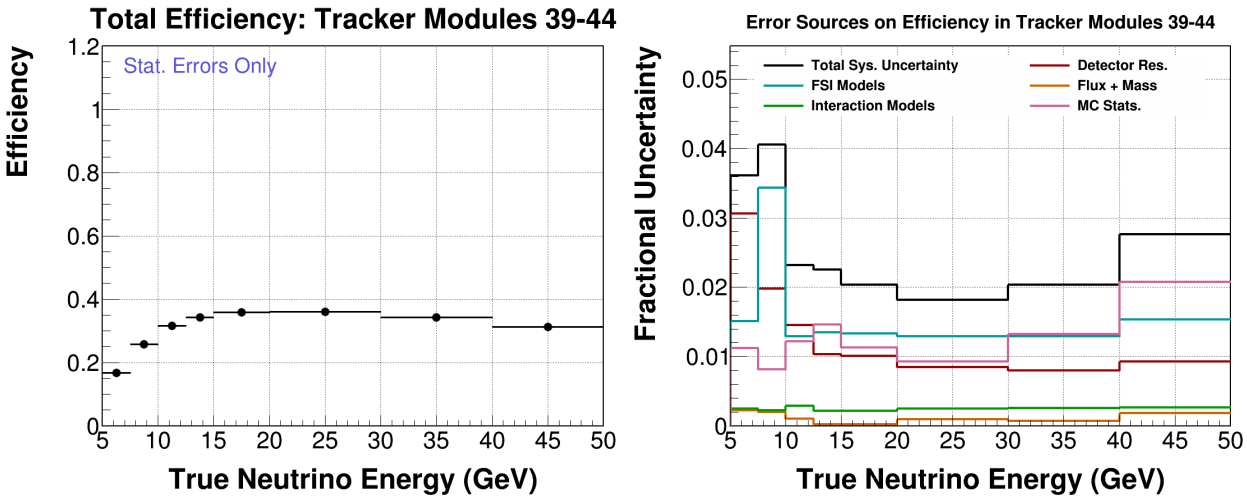

Figure E-13: Overall efficiency of events in the scintillator tracker module 39-44 as a function of true E_ν (left) and the systematic uncertainty on the overall efficiency (right).

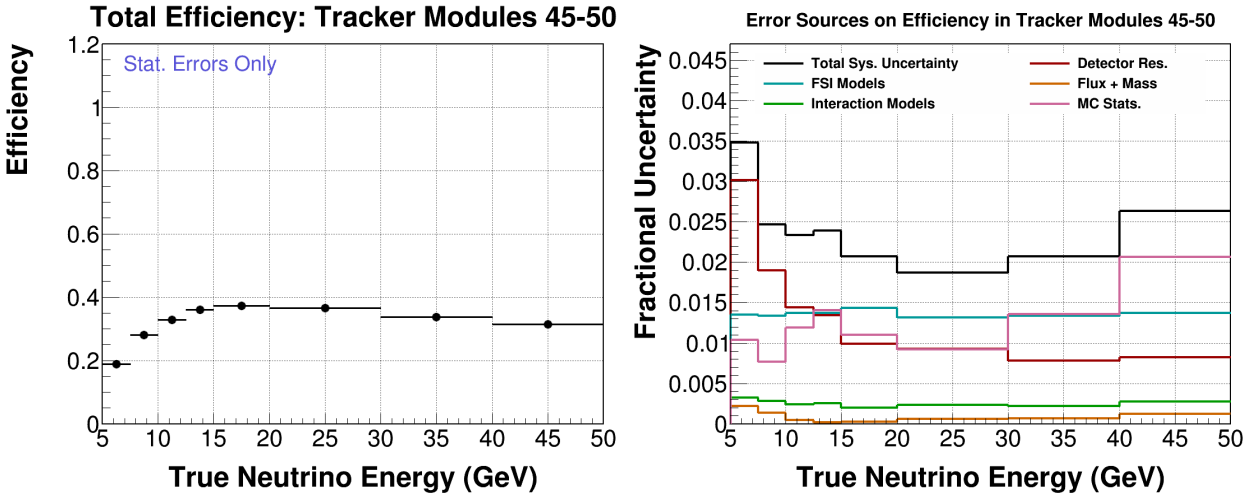

Figure E-14: Overall efficiency of events in the scintillator tracker module 45-50 as a function of true E_ν (left) and the systematic uncertainty on the overall efficiency (right).

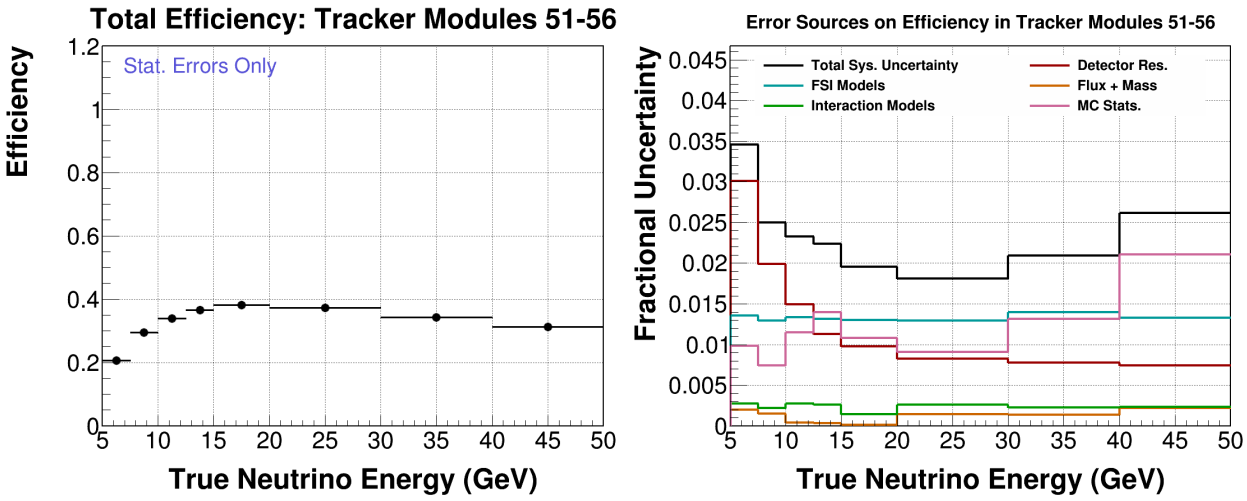

Figure E-15: Overall efficiency of events in the scintillator tracker module 51-56 as a function of true E_ν (left) and the systematic uncertainty on the overall efficiency (right).

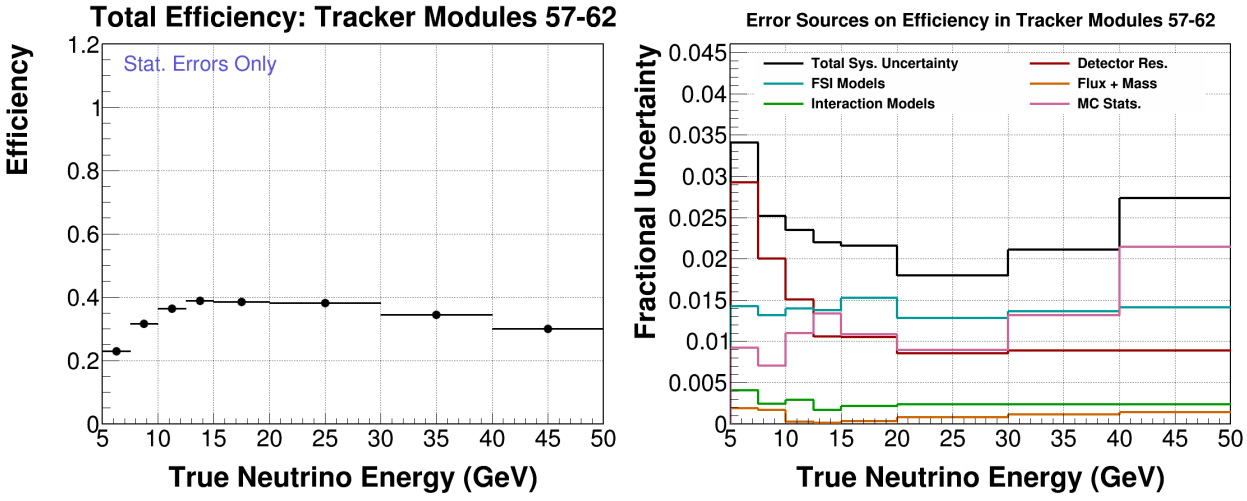

Figure E-16: Overall efficiency of events in the scintillator tracker module 57-62 as a function of true E_ν (left) and the systematic uncertainty on the overall efficiency (right).

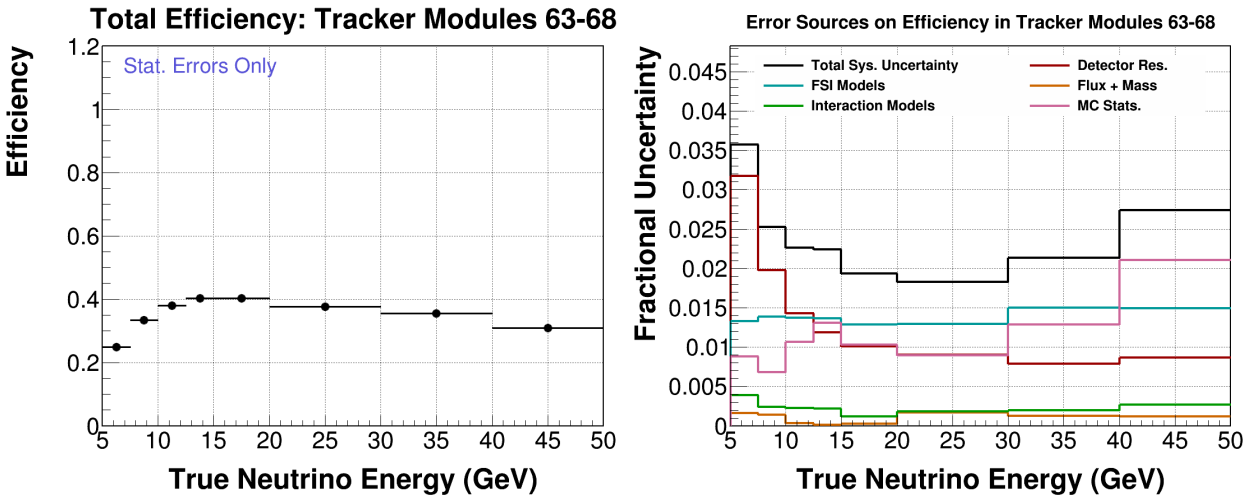

Figure E-17: Overall efficiency of events in the scintillator tracker module 63-68 as a function of true E_ν (left) and the systematic uncertainty on the overall efficiency (right).

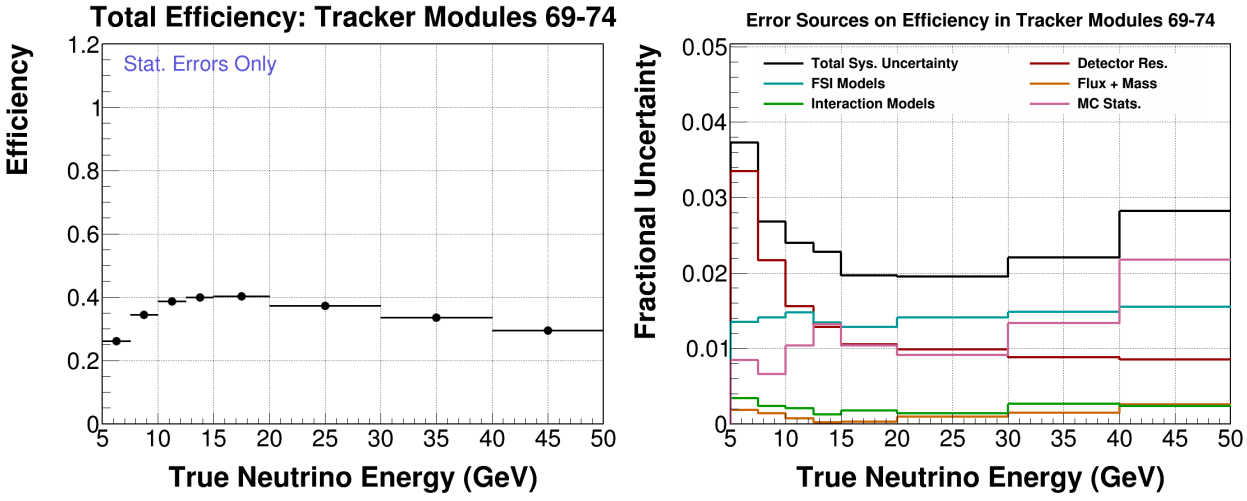

Figure E-18: Overall efficiency of events in the scintillator tracker module 69-74 as a function of true E_ν (left) and the systematic uncertainty on the overall efficiency (right).

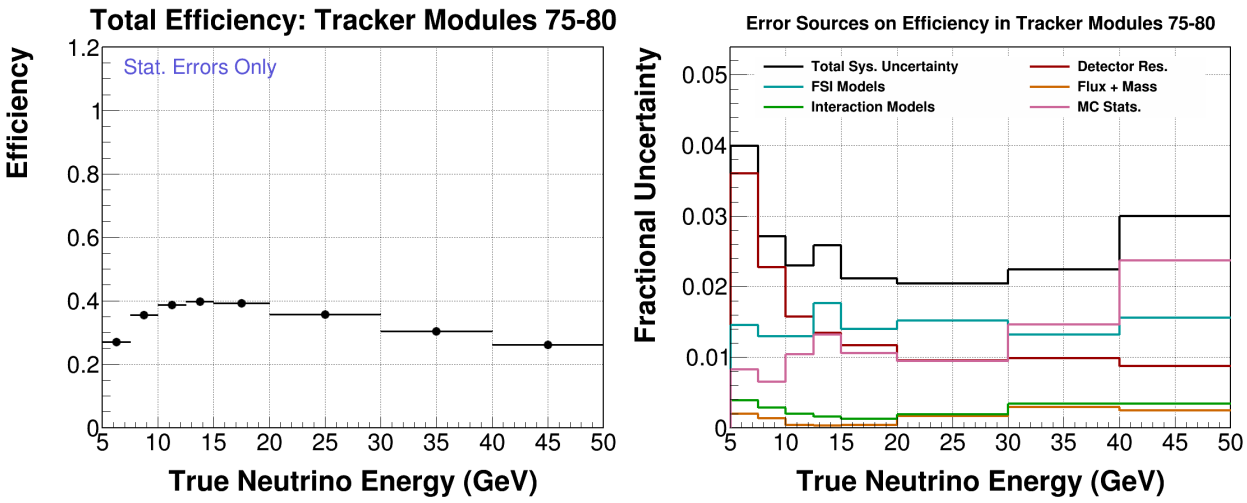

Figure E-19: Overall efficiency of events in the scintillator tracker module 75-80 as a function of true E_ν (left) and the systematic uncertainty on the overall efficiency (right).

E.2 Overall Efficiencies as a function of x_{bj}

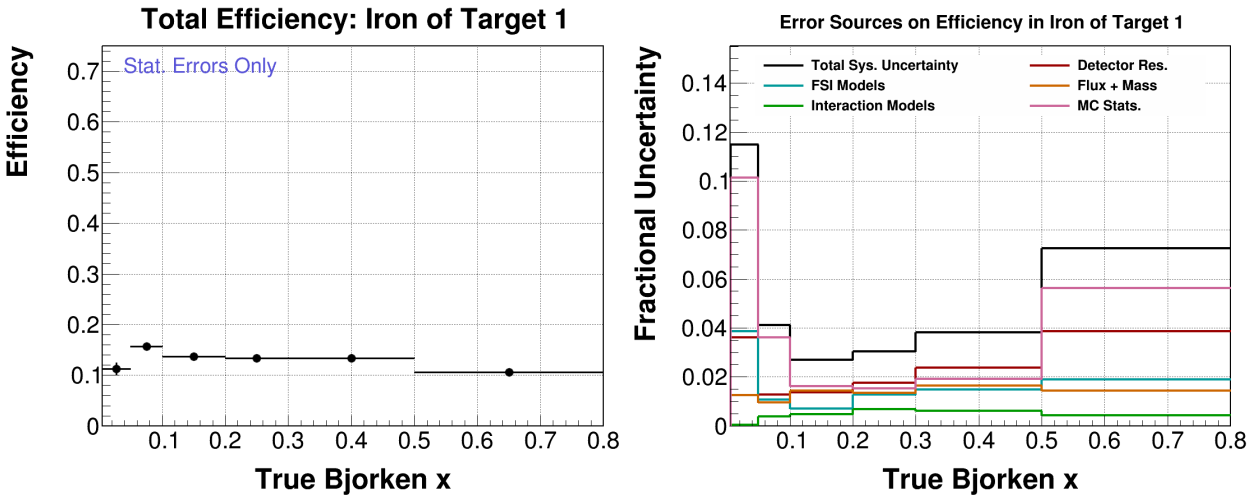

Figure E-20: Overall efficiency of events in the iron of target 1 as a function of true x_{bj} (left) and the systematic uncertainty on the overall efficiency (right).

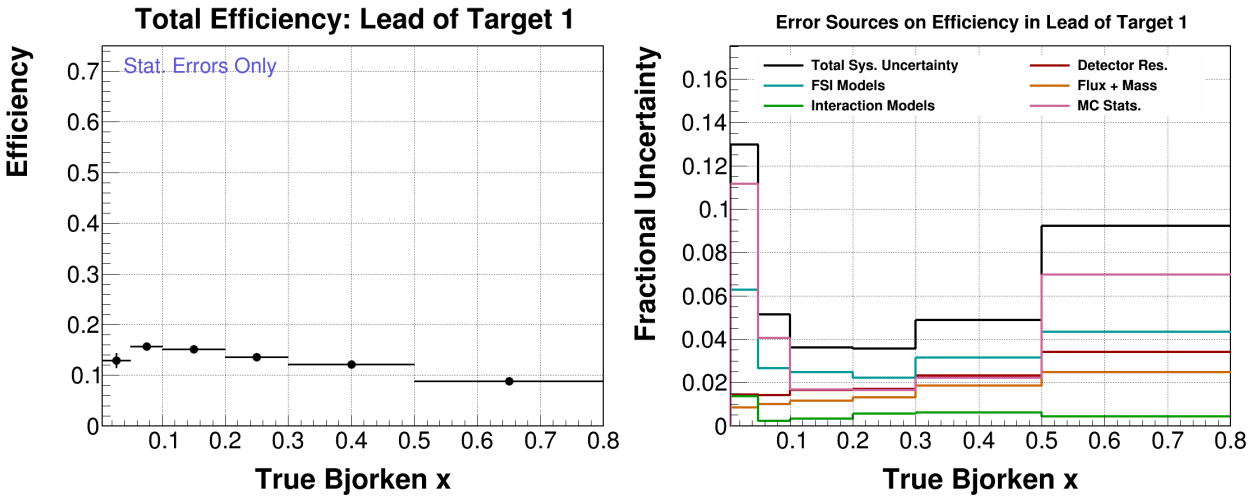

Figure E-21: Overall efficiency of events in the lead of target 1 as a function of true x_{bj} (left) and the systematic uncertainty on the overall efficiency (right).

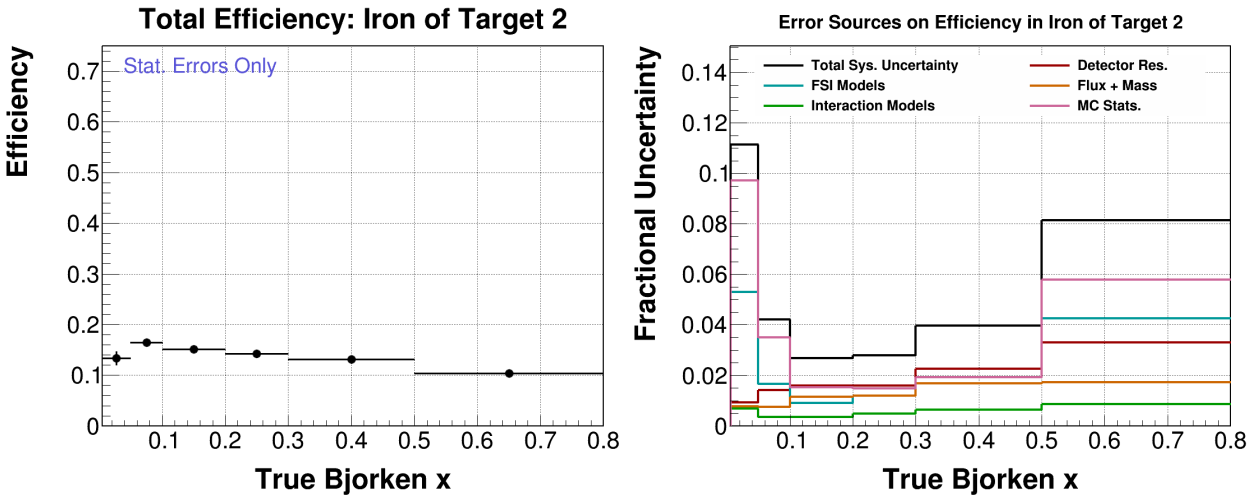

Figure E-22: Overall efficiency of events in the iron of target 2 as a function of true x_{bj} (left) and the systematic uncertainty on the overall efficiency (right).

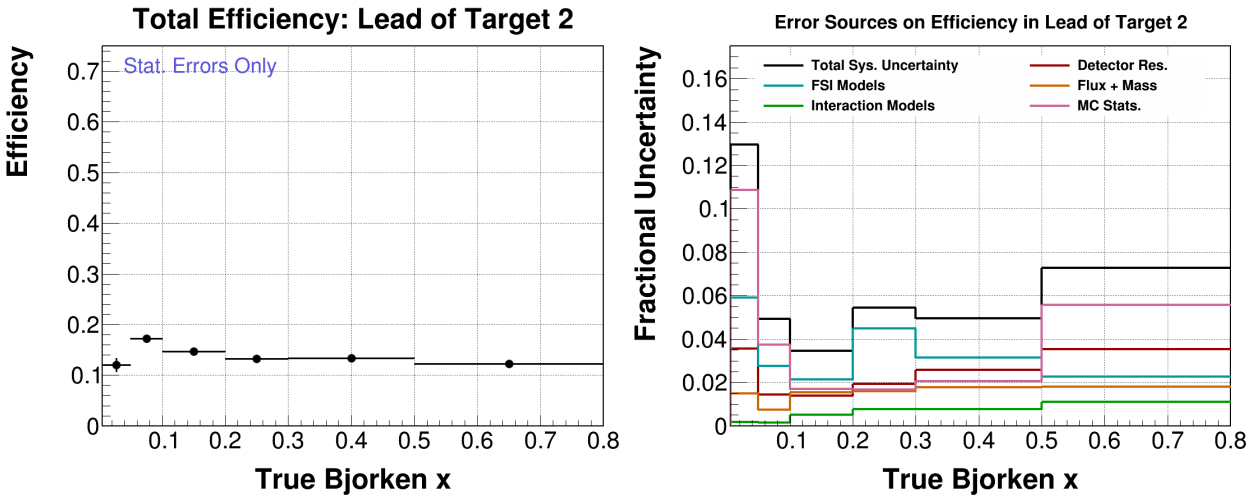

Figure E-23: Overall efficiency of events in the lead of target 2 as a function of true x_{bj} (left) and the systematic uncertainty on the overall efficiency (right).

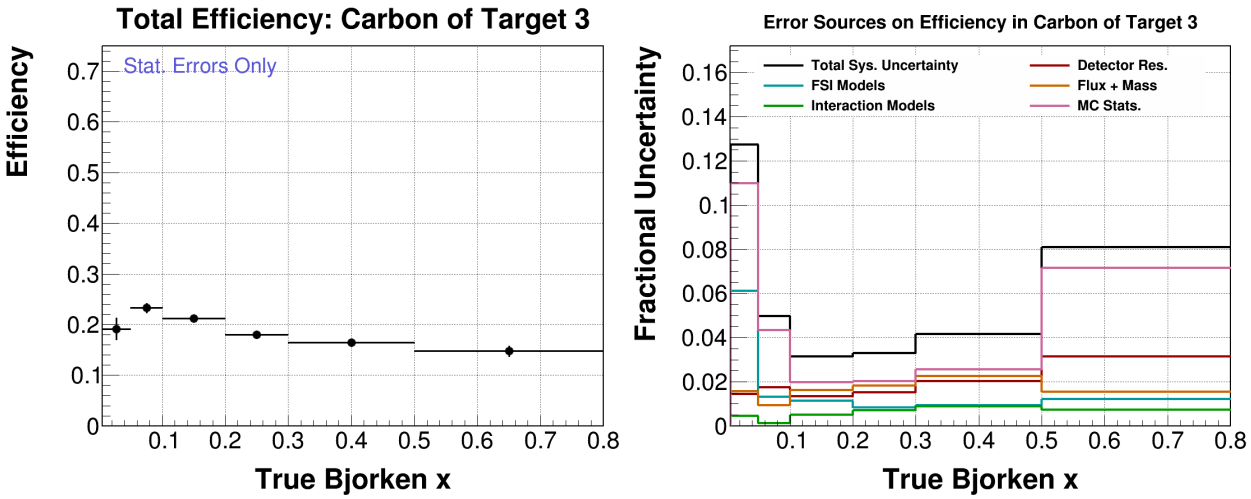

Figure E-24: Overall efficiency of events in the carbon of target 3 as a function of true x_{bj} (left) and the systematic uncertainty on the overall efficiency (right).

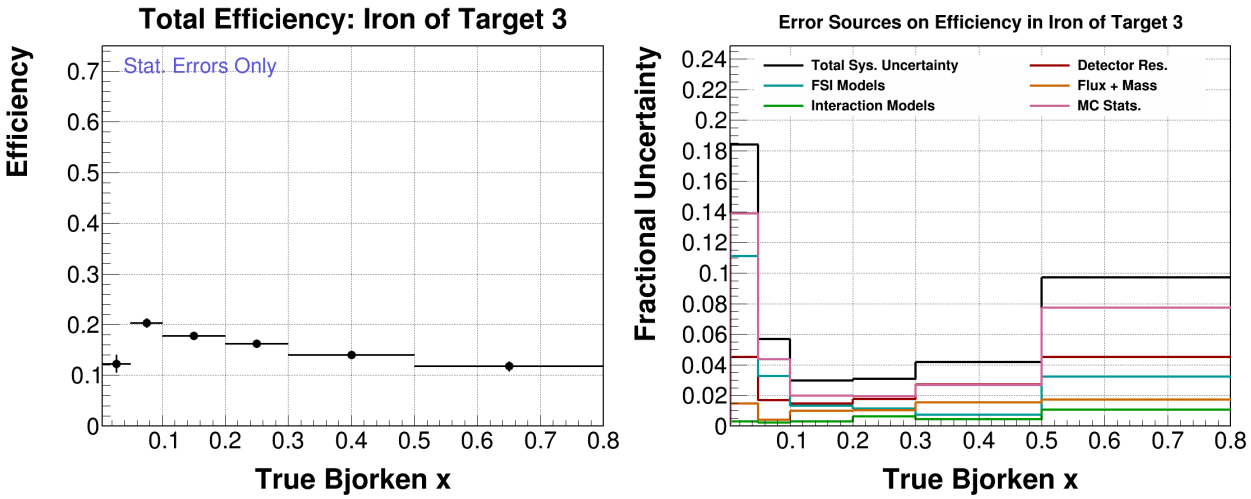

Figure E-25: Overall efficiency of events in the iron of target 3 as a function of true x_{bj} (left) and the systematic uncertainty on the overall efficiency (right).

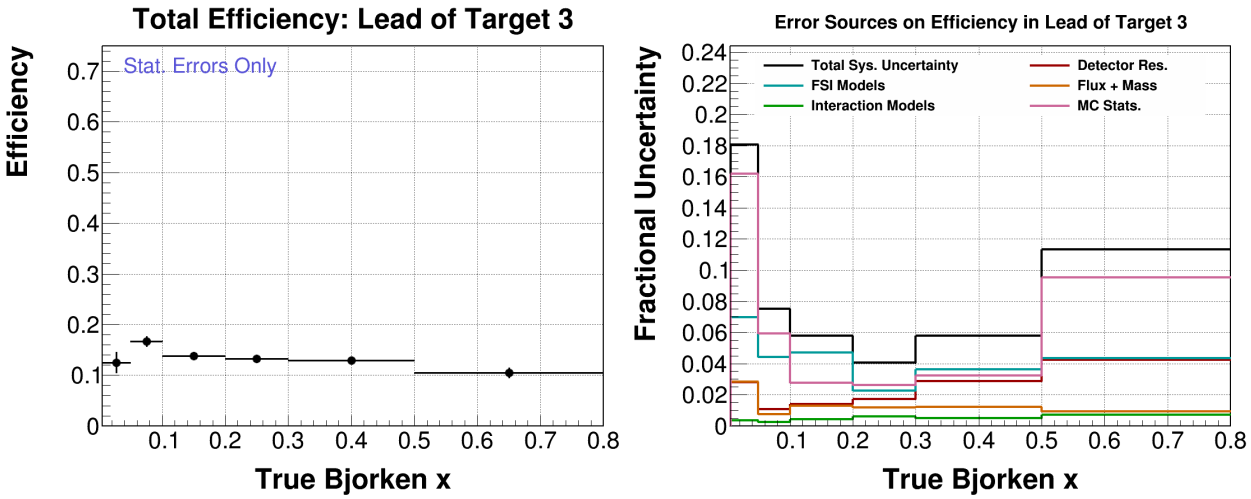

Figure E-26: Overall efficiency of events in the lead of target 3 as a function of true x_{bj} (left) and the systematic uncertainty on the overall efficiency (right).

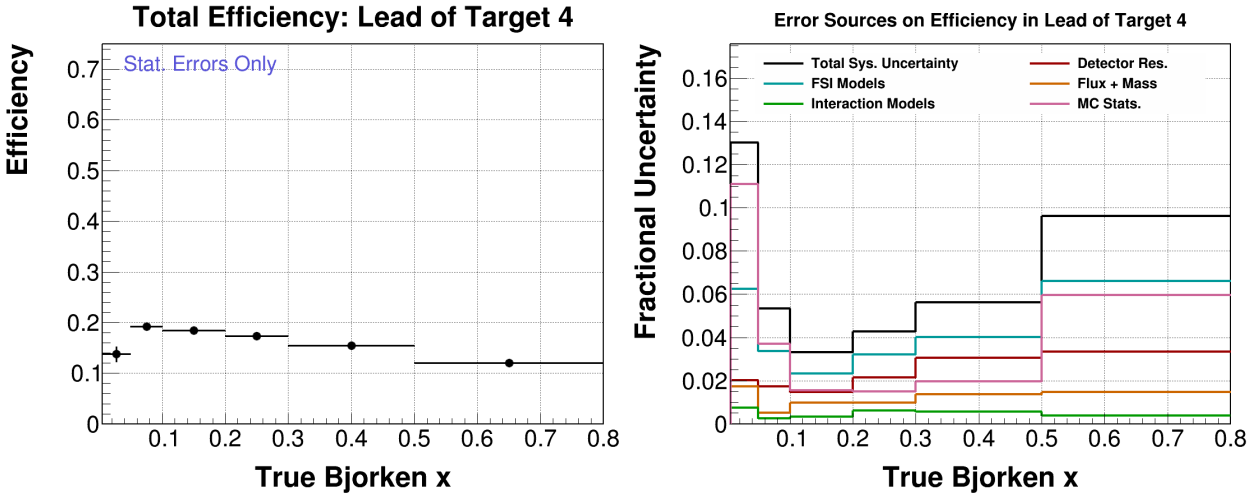

Figure E-27: Overall efficiency of events in the lead of target 4 as a function of true x_{bj} (left) and the systematic uncertainty on the overall efficiency (right).

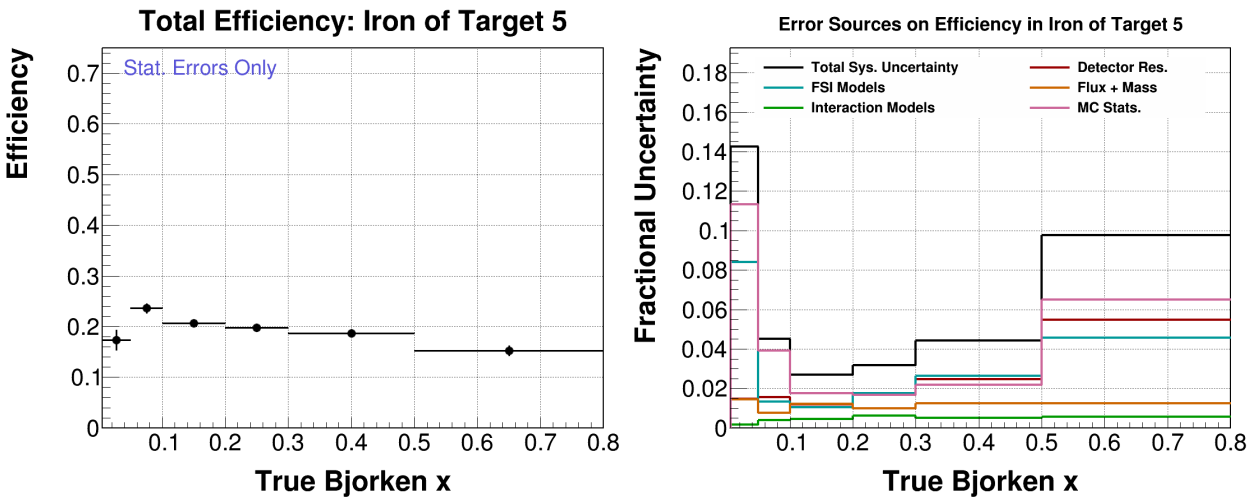

Figure E-28: Overall efficiency of events in the iron of target 5 as a function of true x_{bj} (left) and the systematic uncertainty on the overall efficiency (right).

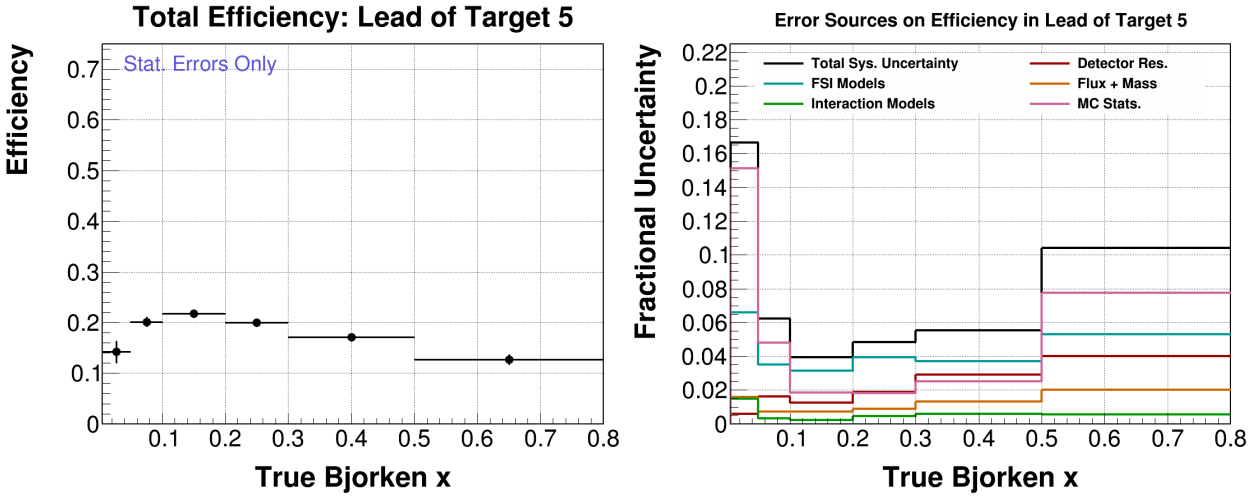

Figure E-29: Overall efficiency of events in the lead of target 5 as a function of true x_{bj} (left) and the systematic uncertainty on the overall efficiency (right).

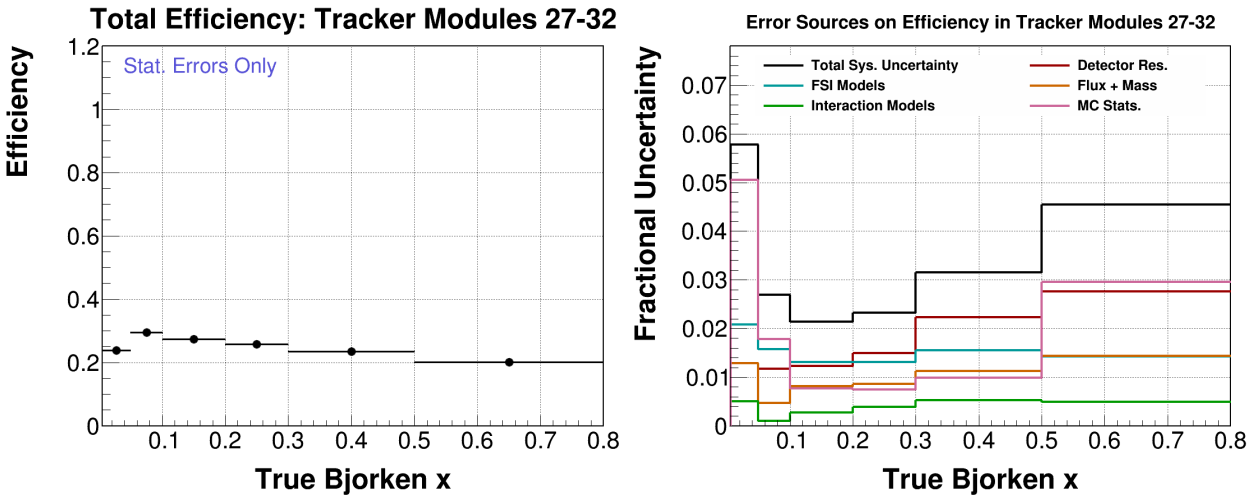

Figure E-30: Overall efficiency of events in the scintillator tracker module 27-32 as a function of true x_{bj} (left) and the systematic uncertainty on the overall efficiency (right).

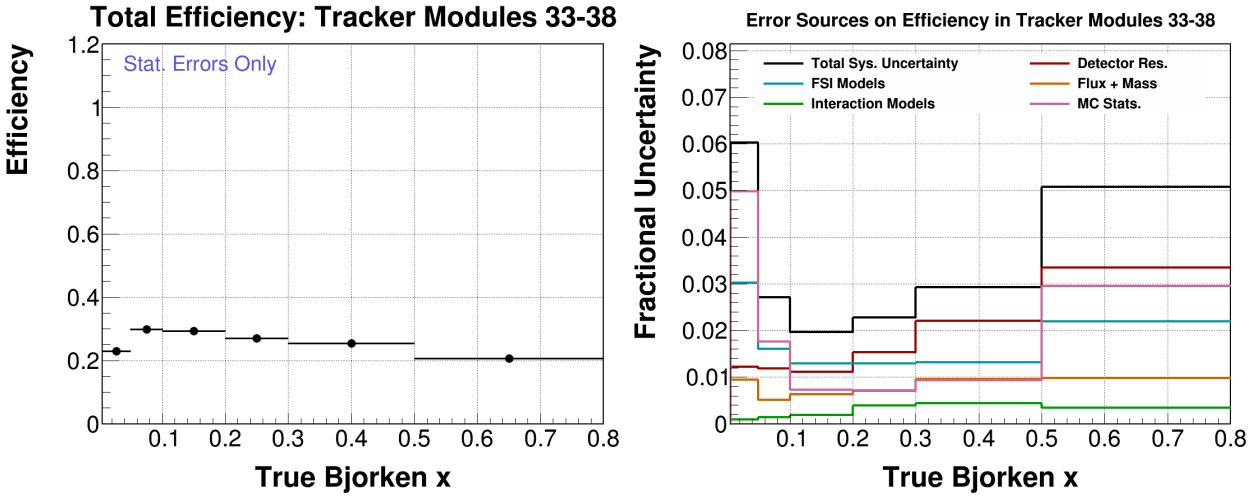

Figure E-31: Overall efficiency of events in the scintillator tracker module 33-38 as a function of true x_{bj} (left) and the systematic uncertainty on the overall efficiency (right).

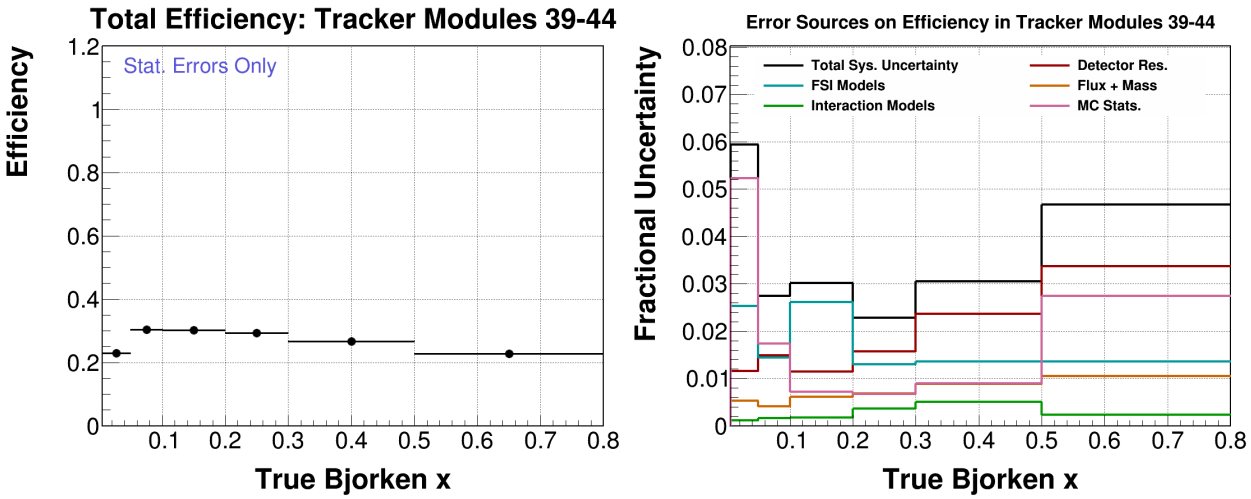

Figure E-32: Overall efficiency of events in the scintillator tracker module 39-44 as a function of true x_{bj} (left) and the systematic uncertainty on the overall efficiency (right).

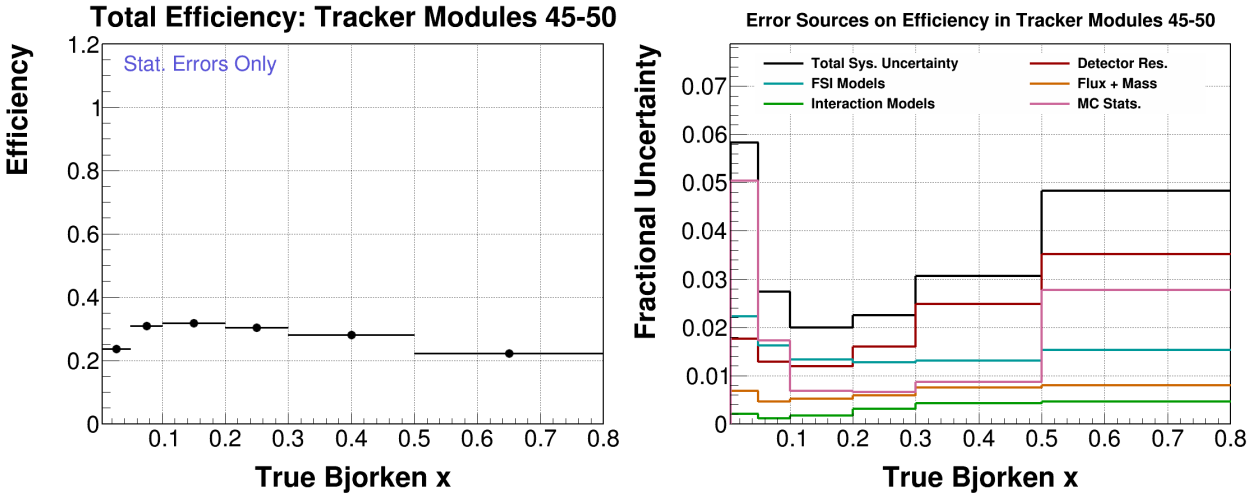

Figure E-33: Overall efficiency of events in the scintillator tracker module 45-50 as a function of true x_{bj} (left) and the systematic uncertainty on the overall efficiency (right).

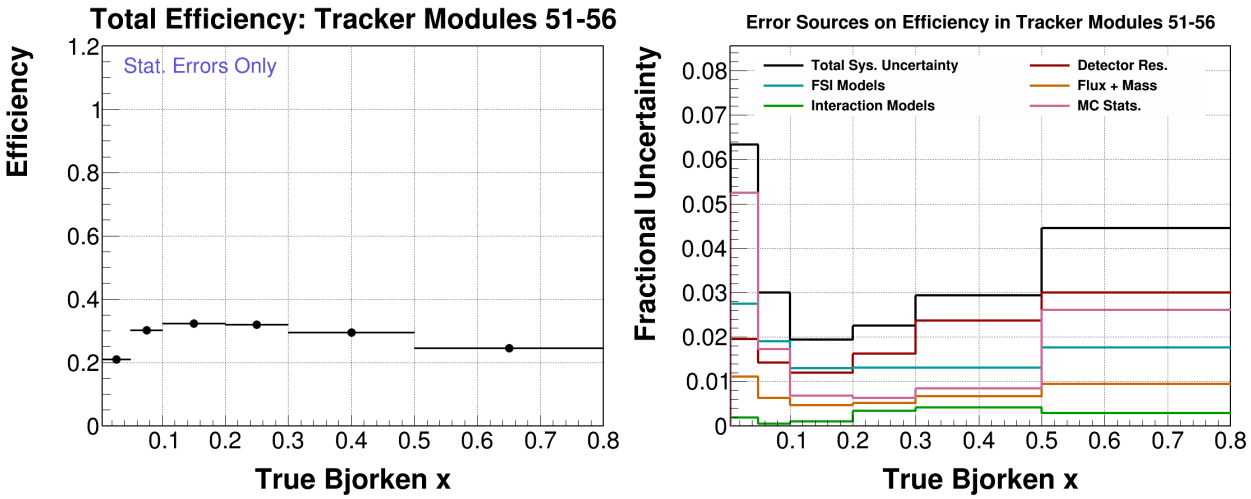

Figure E-34: Overall efficiency of events in the scintillator tracker module 51-56 as a function of true x_{bj} (left) and the systematic uncertainty on the overall efficiency (right).

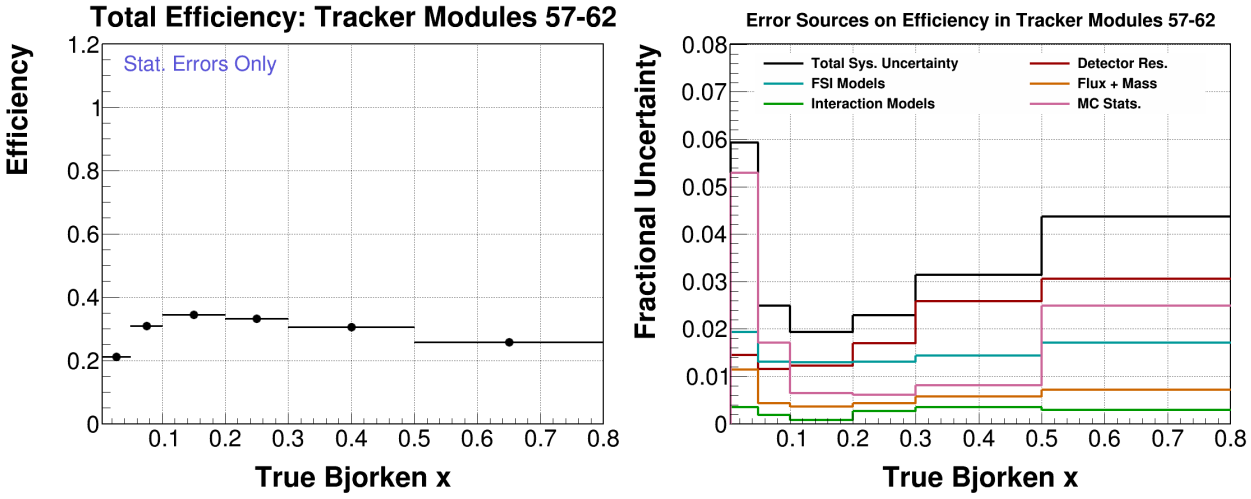

Figure E-35: Overall efficiency of events in the scintillator tracker module 57-62 as a function of true x_{bj} (left) and the systematic uncertainty on the overall efficiency (right).

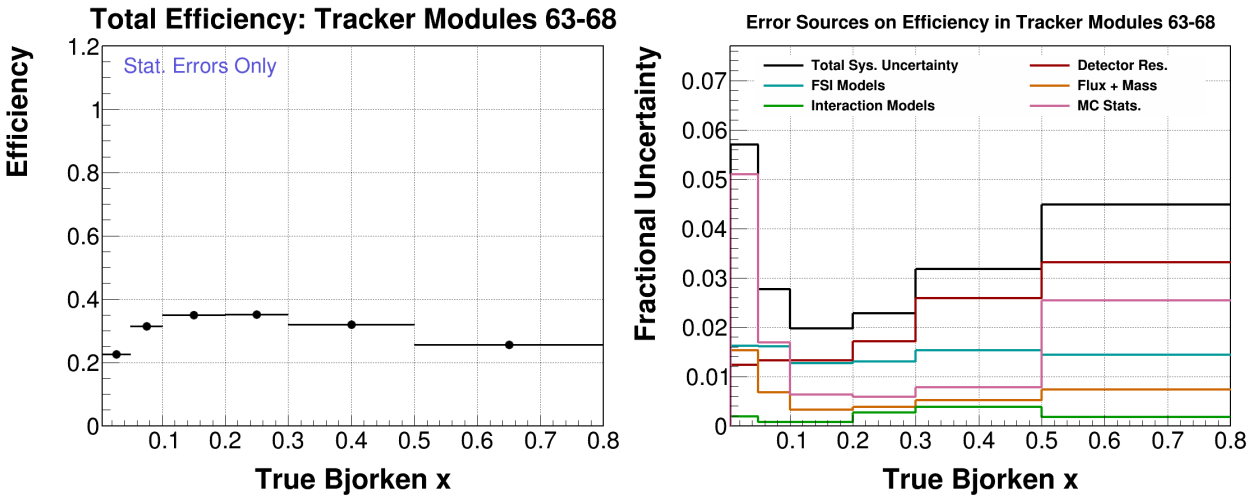

Figure E-36: Overall efficiency of events in the scintillator tracker module 63-68 as a function of true x_{bj} (left) and the systematic uncertainty on the overall efficiency (right).

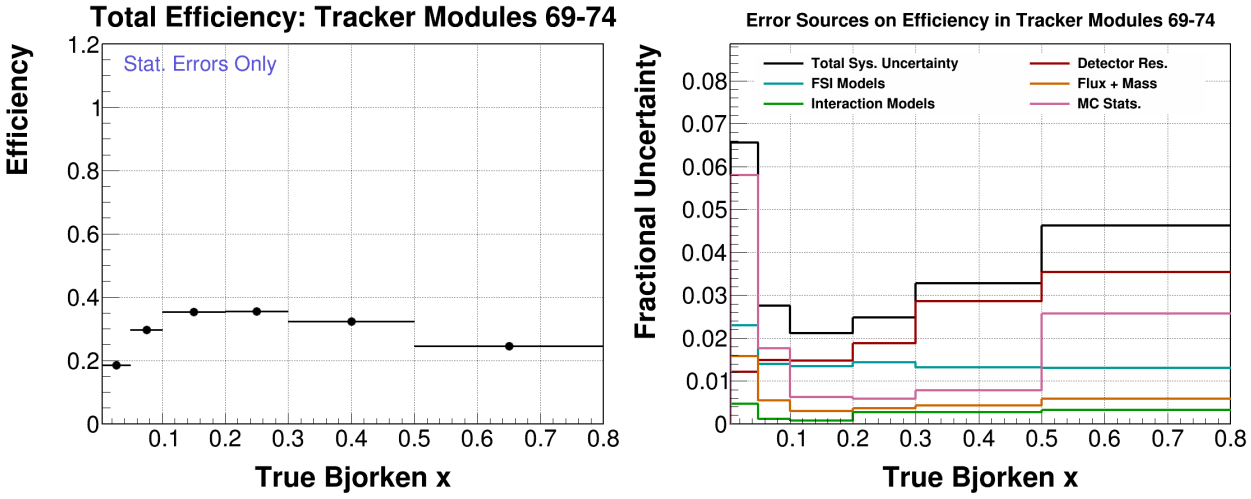

Figure E-37: Overall efficiency of events in the scintillator tracker module 69-74 as a function of true x_{bj} (left) and the systematic uncertainty on the overall efficiency (right).

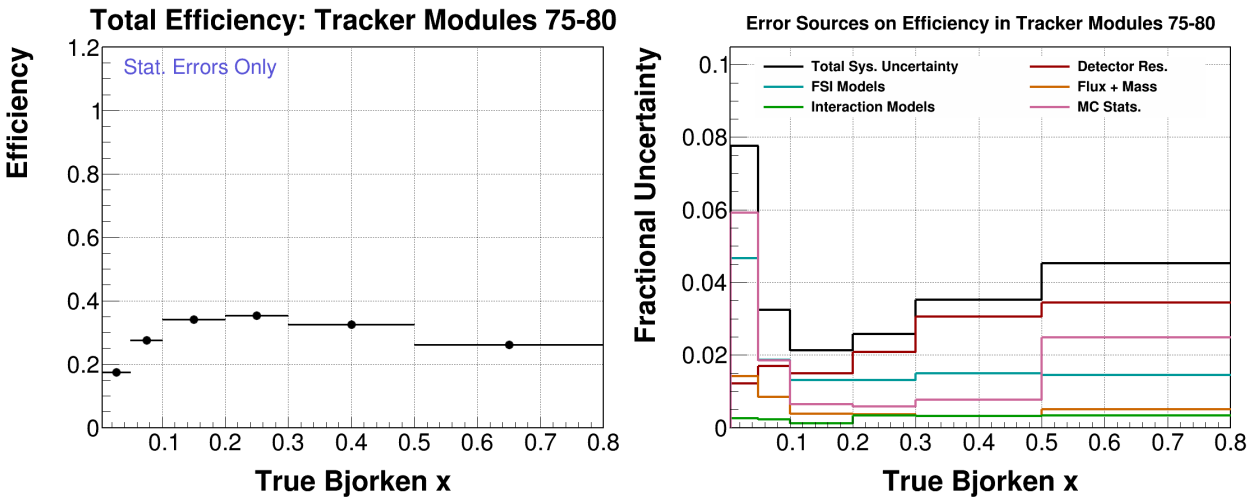

Figure E-38: Overall efficiency of events in the scintillator tracker module 75-80 as a function of true x_{bj} (left) and the systematic uncertainty on the overall efficiency (right).

E.3 Overall Efficiencies as a function of E_μ

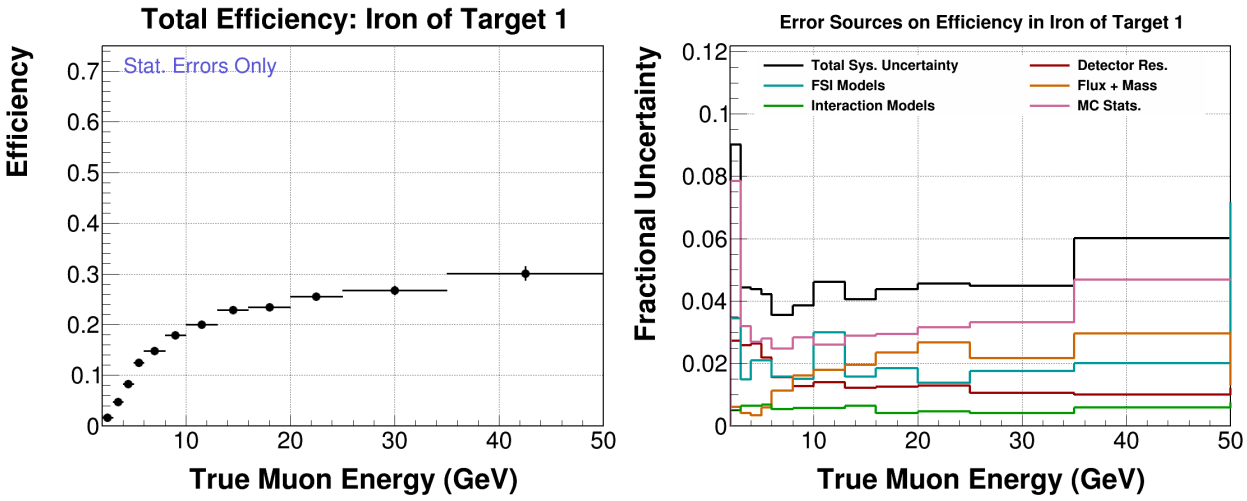

Figure E-39: Overall efficiency of events in the iron of target 1 as a function of true E_μ (left) and the systematic uncertainty on the overall efficiency (right).

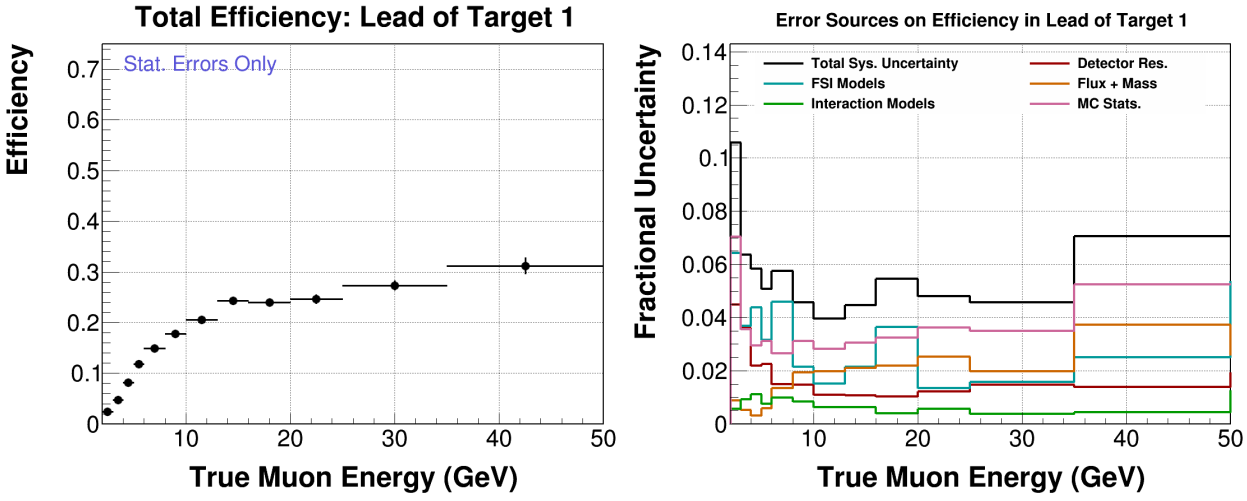

Figure E-40: Overall efficiency of events in the lead of target 1 as a function of true E_μ (left) and the systematic uncertainty on the overall efficiency (right).

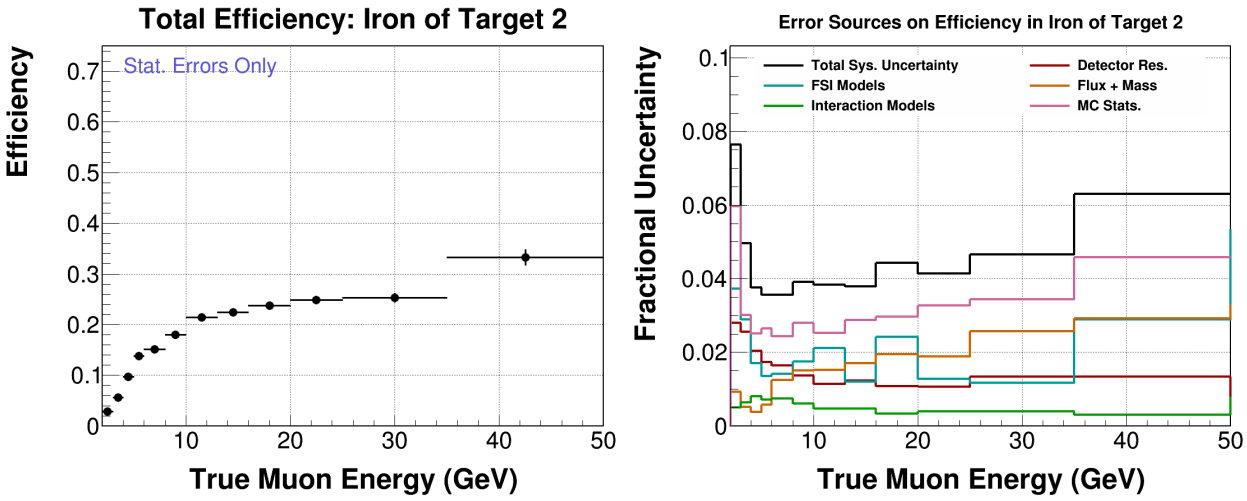

Figure E-41: Overall efficiency of events in the iron of target 2 as a function of true E_μ (left) and the systematic uncertainty on the overall efficiency (right).

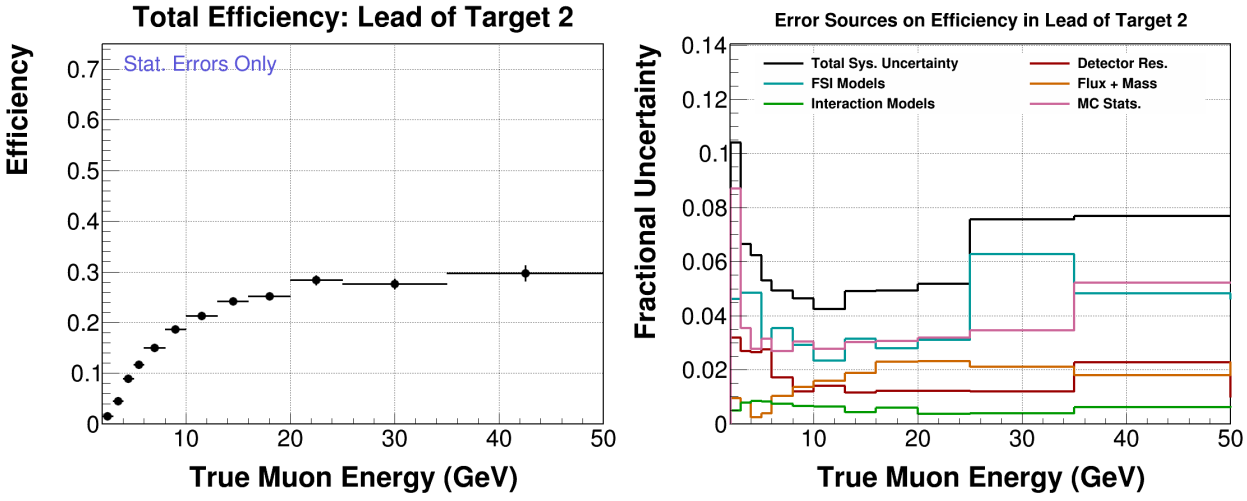

Figure E-42: Overall efficiency of events in the lead of target 2 as a function of true E_μ (left) and the systematic uncertainty on the overall efficiency (right).

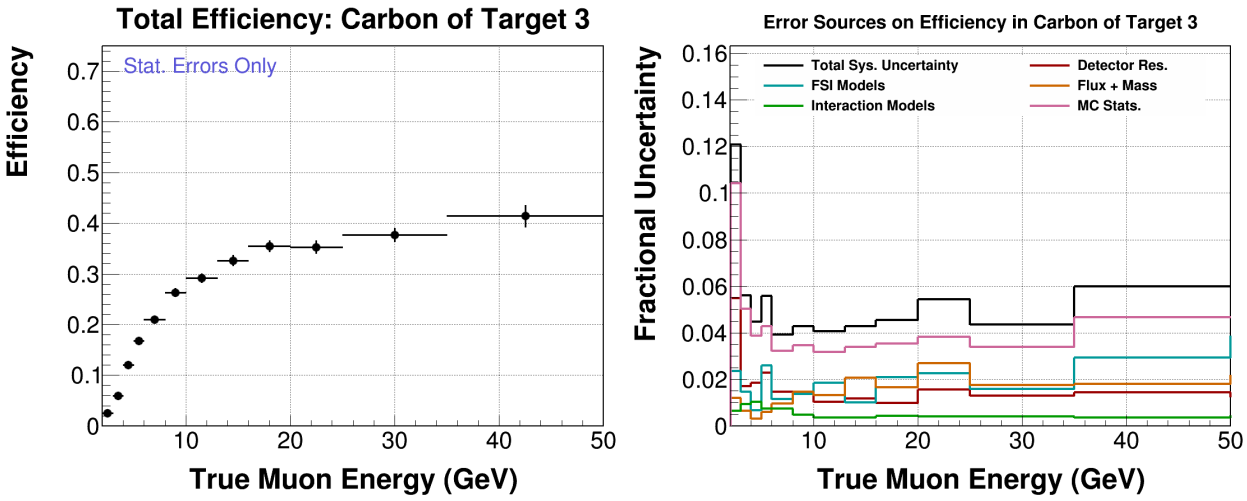

Figure E-43: Overall efficiency of events in the carbon of target 3 as a function of true E_μ (left) and the systematic uncertainty on the overall efficiency (right).

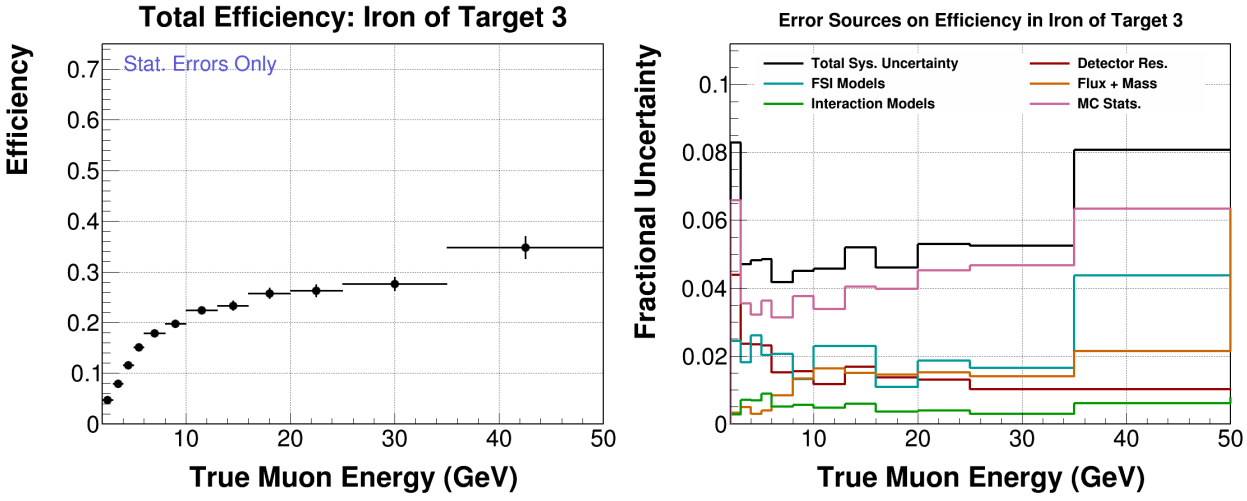

Figure E-44: Overall efficiency of events in the iron of target 3 as a function of true E_μ (left) and the systematic uncertainty on the overall efficiency (right).

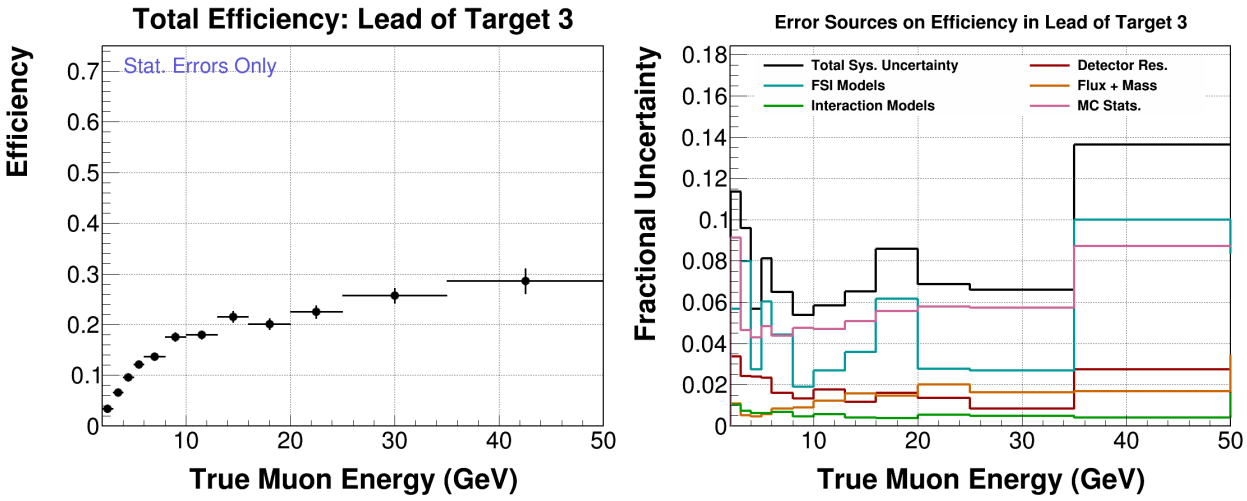

Figure E-45: Overall efficiency of events in the lead of target 3 as a function of true E_μ (left) and the systematic uncertainty on the overall efficiency (right).

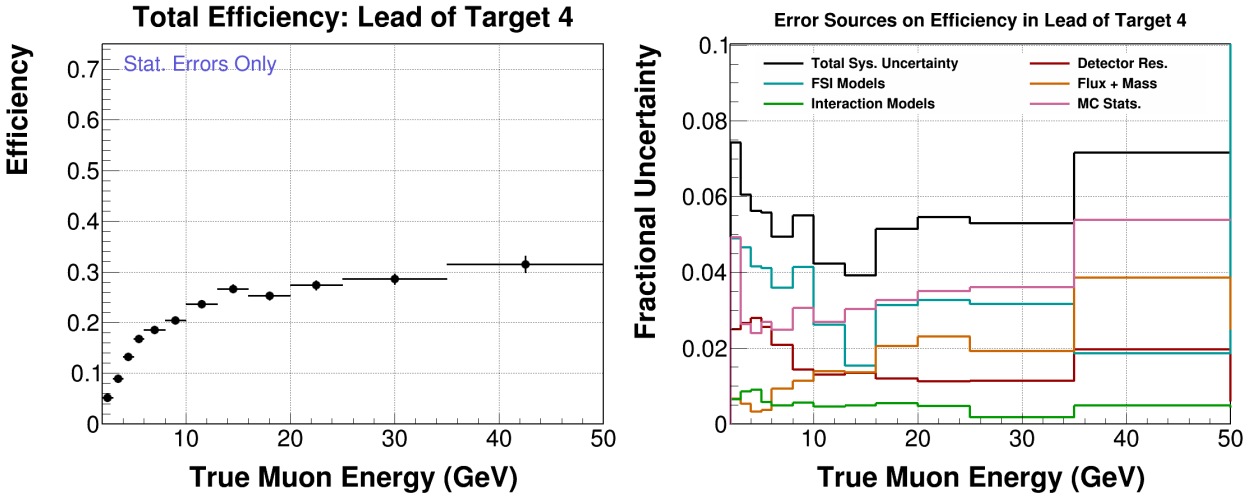

Figure E-46: Overall efficiency of events in the lead of target 4 as a function of true E_μ (left) and the systematic uncertainty on the overall efficiency (right).

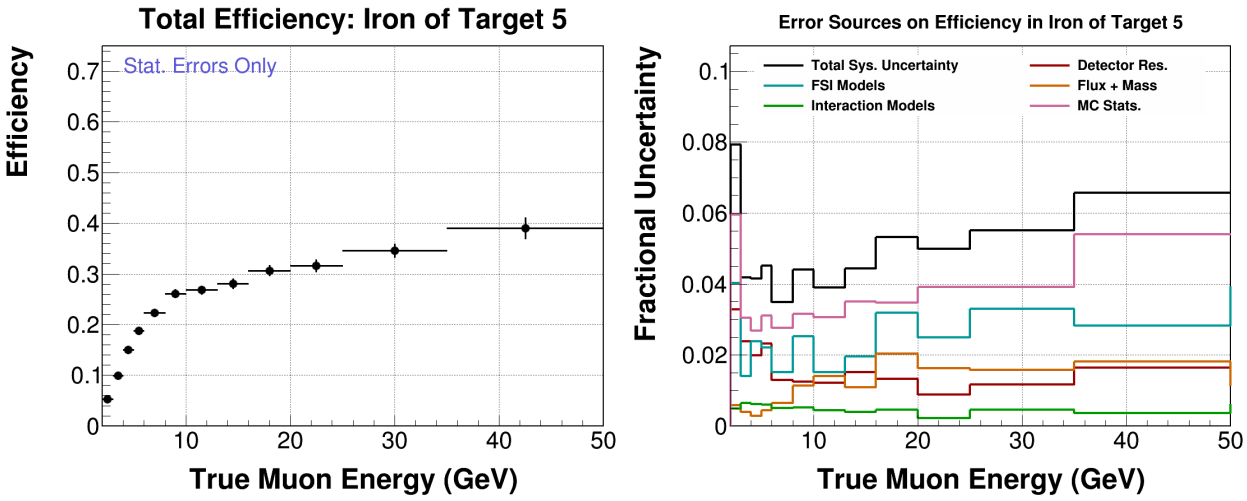

Figure E-47: Overall efficiency of events in the iron of target 5 as a function of true E_μ (left) and the systematic uncertainty on the overall efficiency (right).

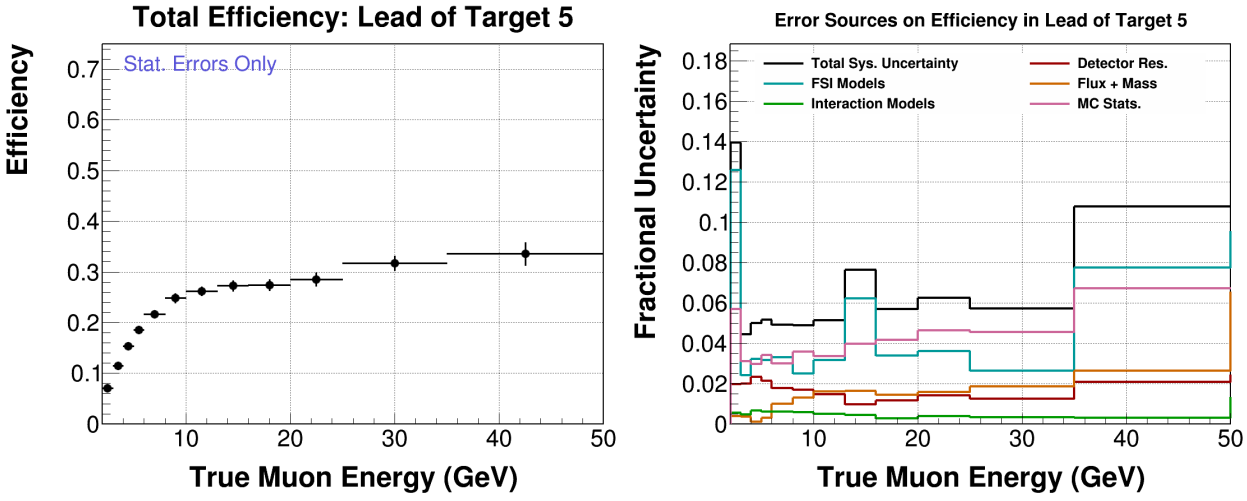

Figure E-48: Overall efficiency of events in the lead of target 5 as a function of true E_μ (left) and the systematic uncertainty on the overall efficiency (right).

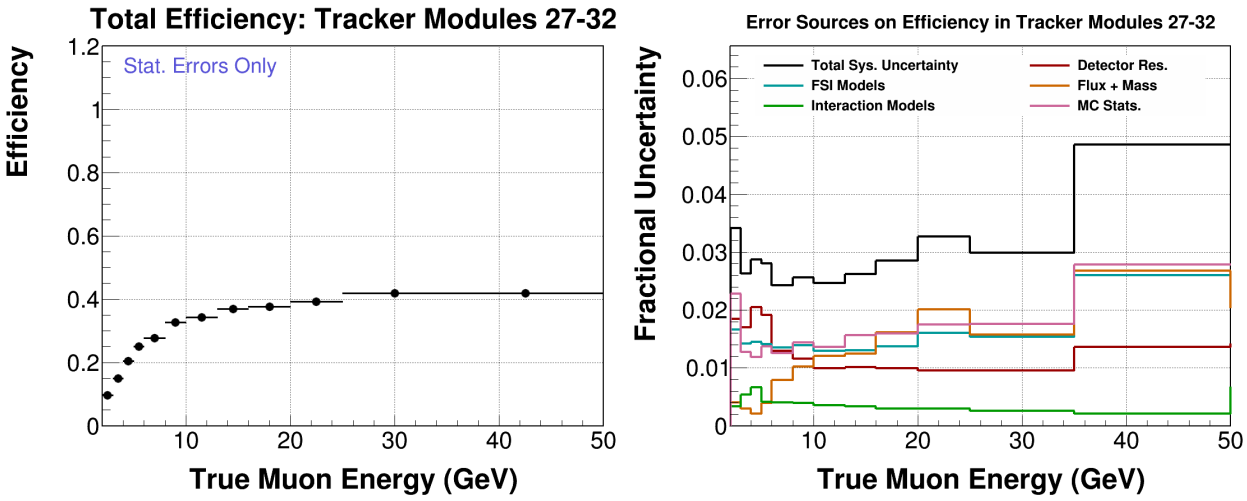

Figure E-49: Overall efficiency of events in the scintillator tracker module 27-32 as a function of true E_μ (left) and the systematic uncertainty on the overall efficiency (right).

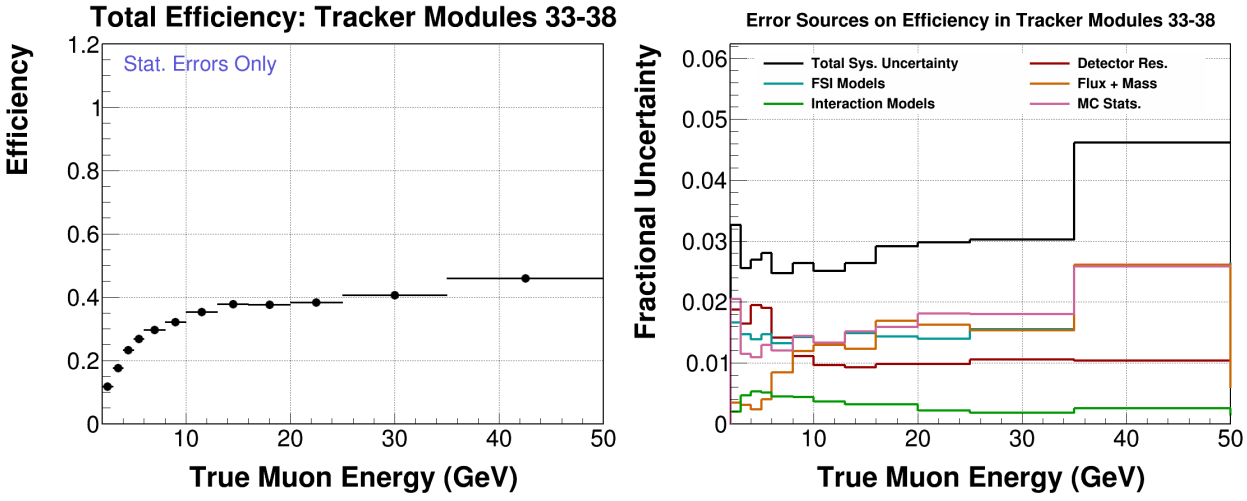

Figure E-50: Overall efficiency of events in the scintillator tracker module 33-38 as a function of true E_μ (left) and the systematic uncertainty on the overall efficiency (right).

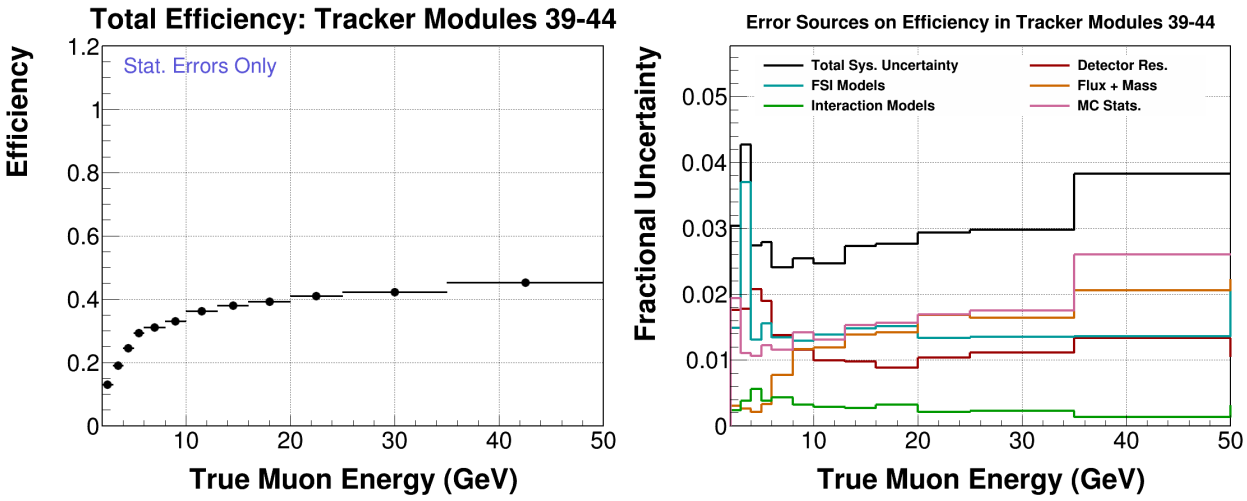

Figure E-51: Overall efficiency of events in the scintillator tracker module 39-44 as a function of true E_μ (left) and the systematic uncertainty on the overall efficiency (right).

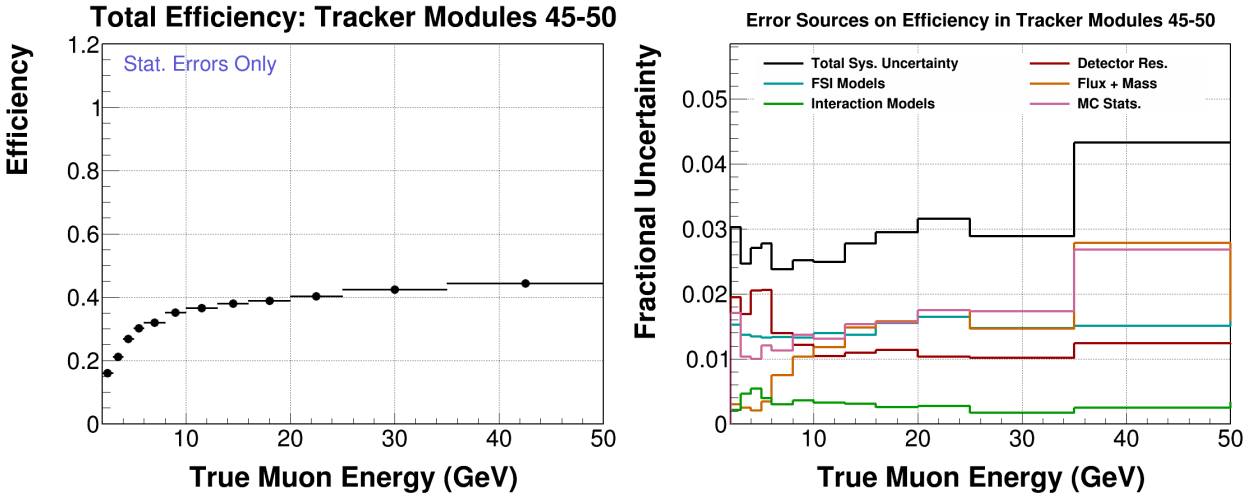

Figure E-52: Overall efficiency of events in the scintillator tracker module 45-50 as a function of true E_μ (left) and the systematic uncertainty on the overall efficiency (right).

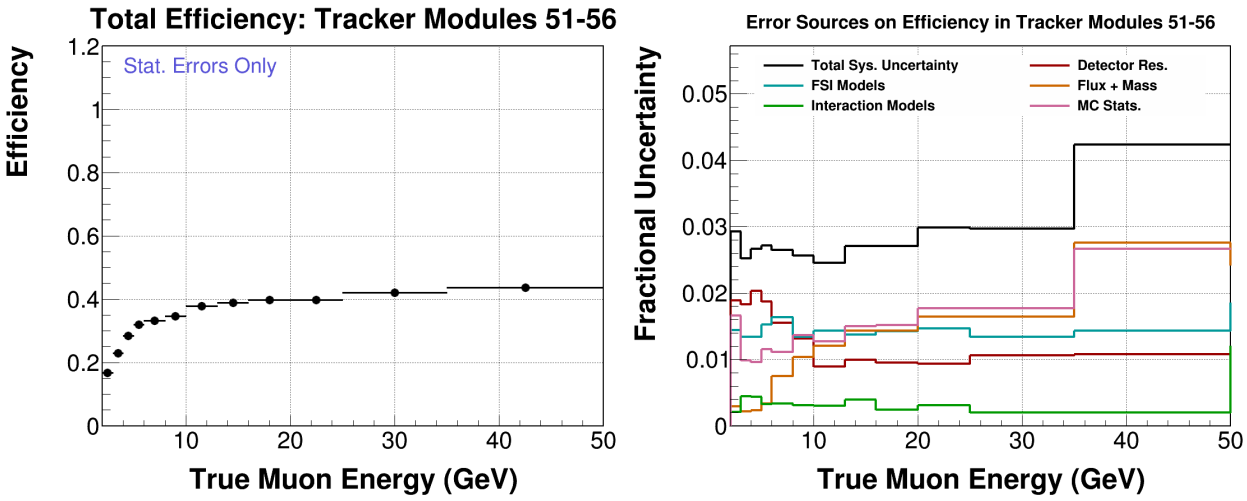

Figure E-53: Overall efficiency of events in the scintillator tracker module 51-56 as a function of true E_μ (left) and the systematic uncertainty on the overall efficiency (right).

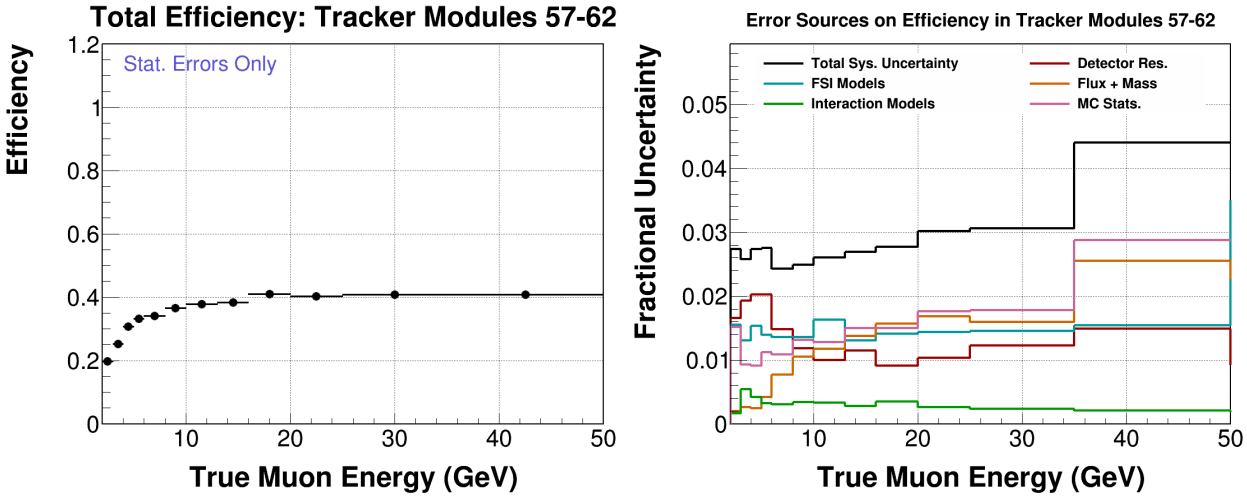

Figure E-54: Overall efficiency of events in the scintillator tracker module 57-62 as a function of true E_μ (left) and the systematic uncertainty on the overall efficiency (right).

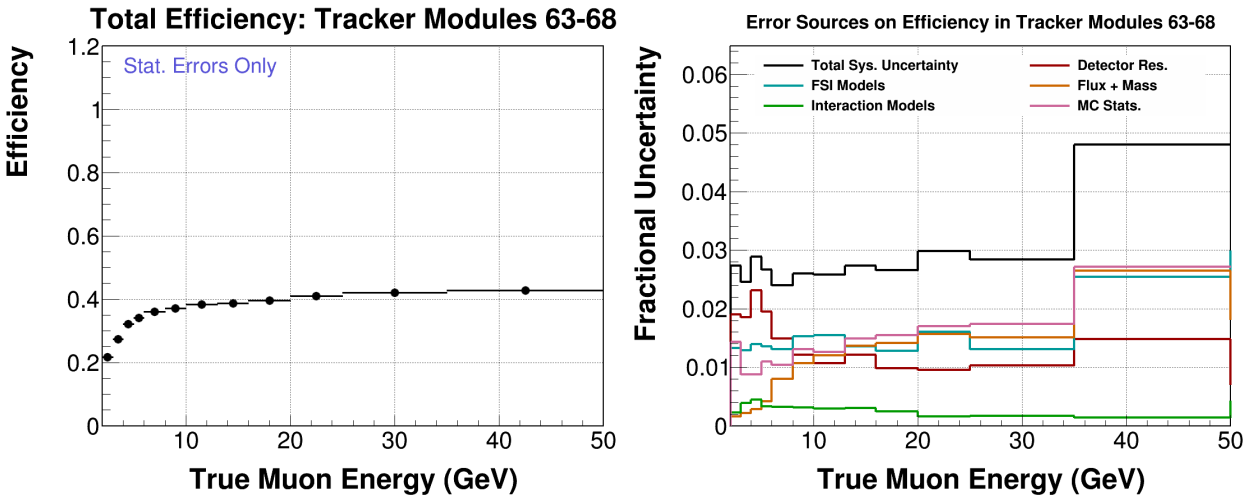

Figure E-55: Overall efficiency of events in the scintillator tracker module 63-68 as a function of true E_μ (left) and the systematic uncertainty on the overall efficiency (right).

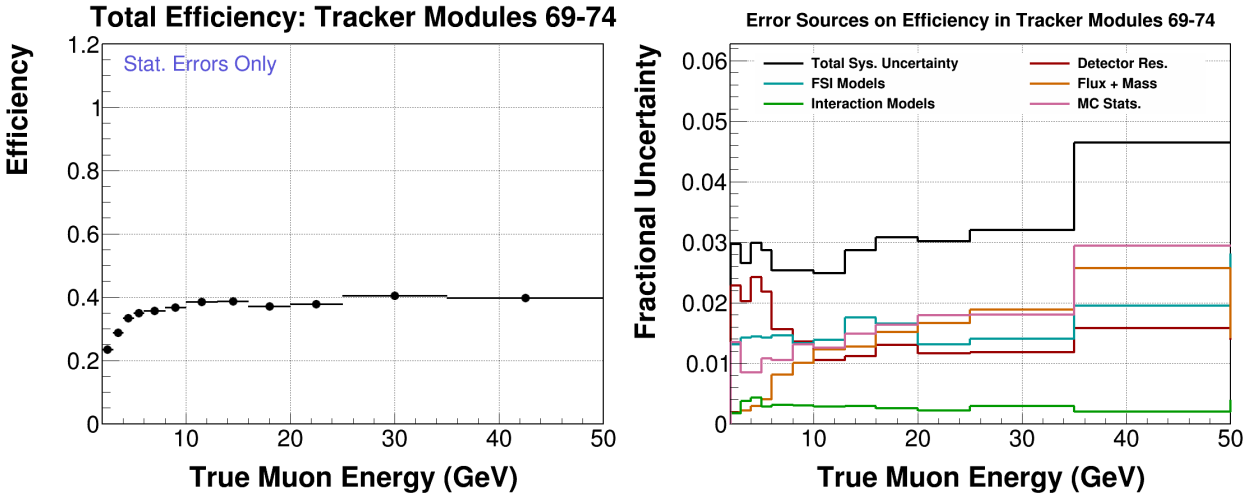

Figure E-56: Overall efficiency of events in the scintillator tracker module 69-74 as a function of true E_μ (left) and the systematic uncertainty on the overall efficiency (right).

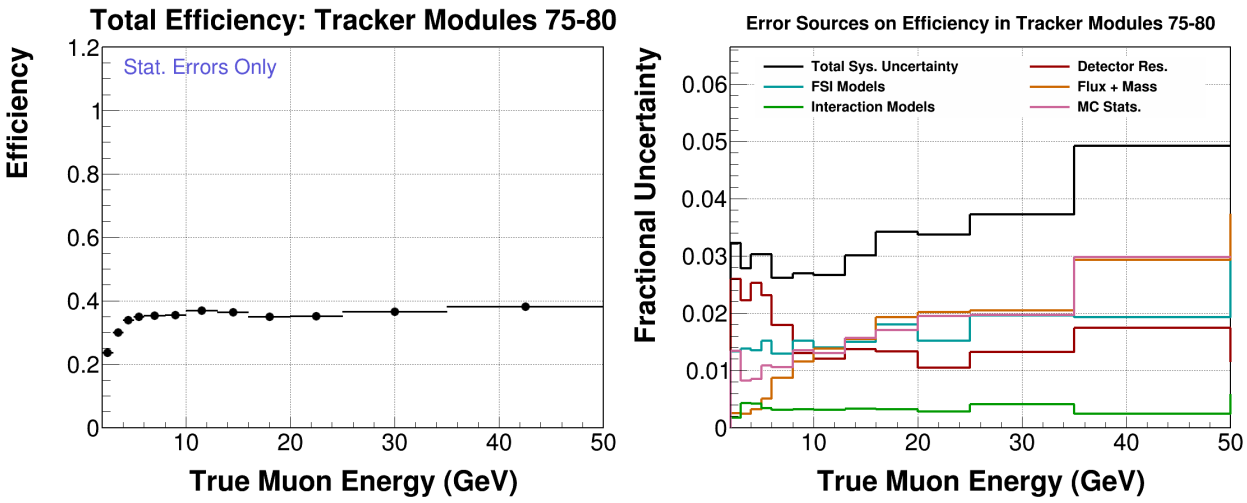

Figure E-57: Overall efficiency of events in the scintillator tracker module 75-80 as a function of true E_μ (left) and the systematic uncertainty on the overall efficiency (right).

E.4 Overall Efficiencies as a function of θ_μ

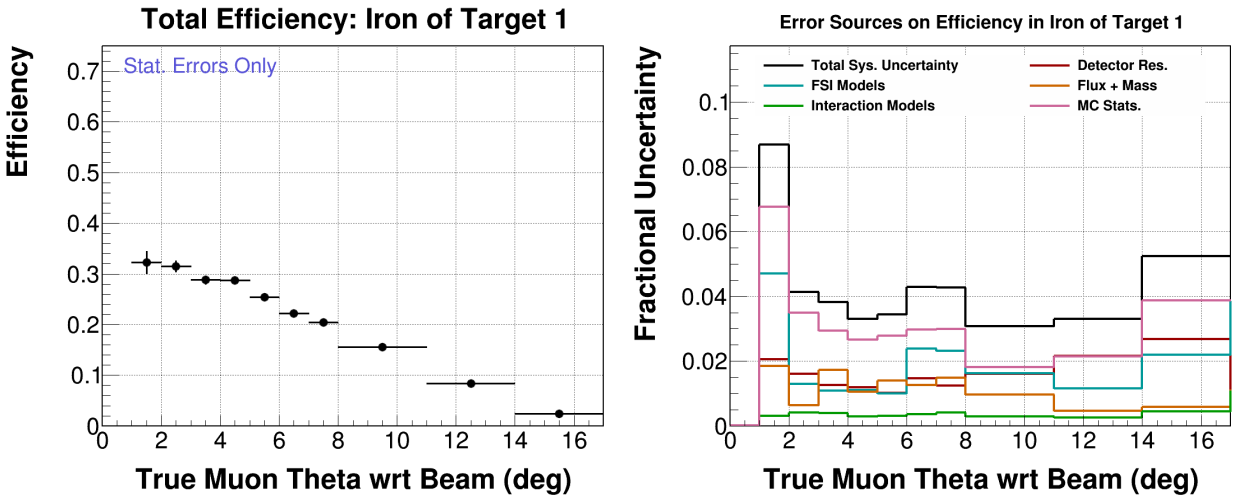

Figure E-58: Overall efficiency of events in the iron of target 1 as a function of true θ_μ (left) and the systematic uncertainty on the overall efficiency (right).

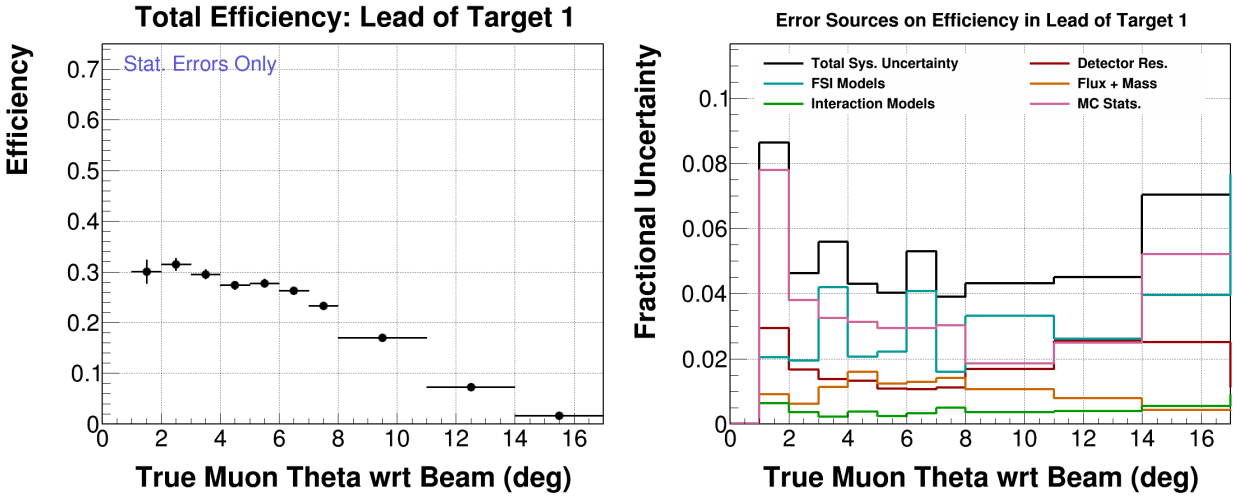

Figure E-59: Overall efficiency of events in the lead of target 1 as a function of true θ_μ (left) and the systematic uncertainty on the overall efficiency (right).

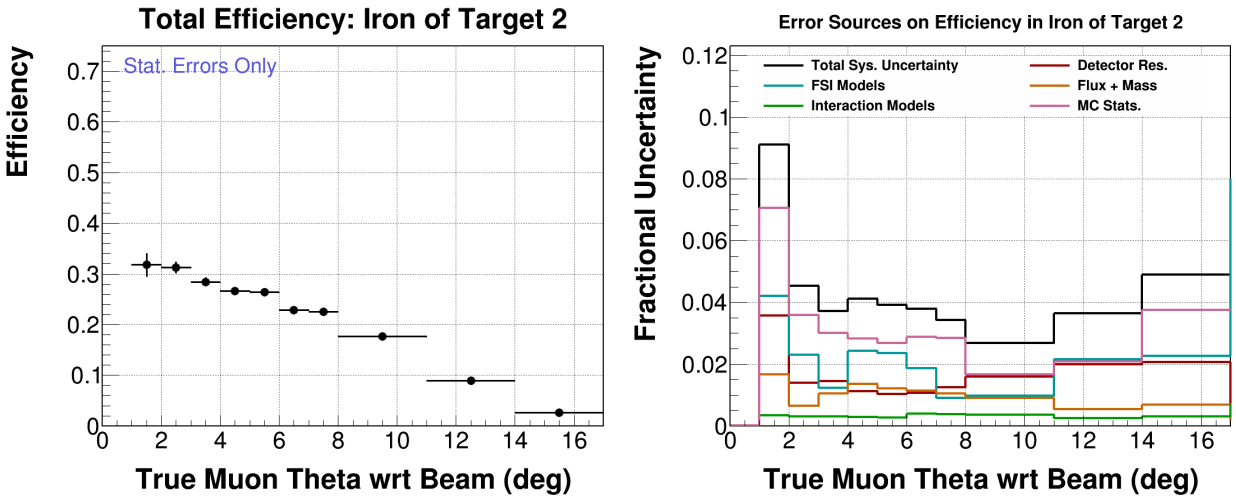

Figure E-60: Overall efficiency of events in the iron of target 2 as a function of true θ_μ (left) and the systematic uncertainty on the overall efficiency (right).

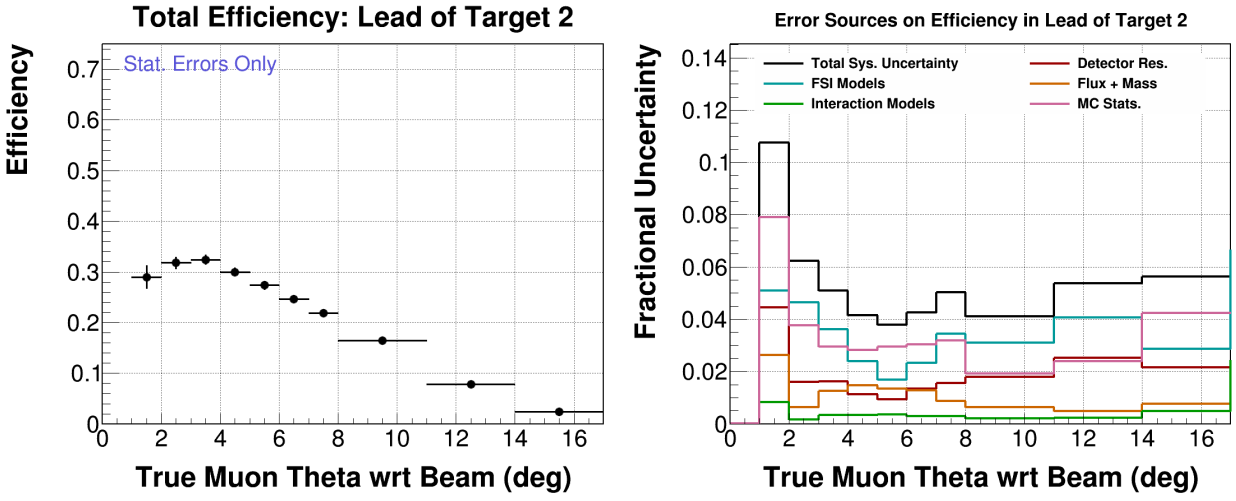

Figure E-61: Overall efficiency of events in the lead of target 2 as a function of true θ_μ (left) and the systematic uncertainty on the overall efficiency (right).

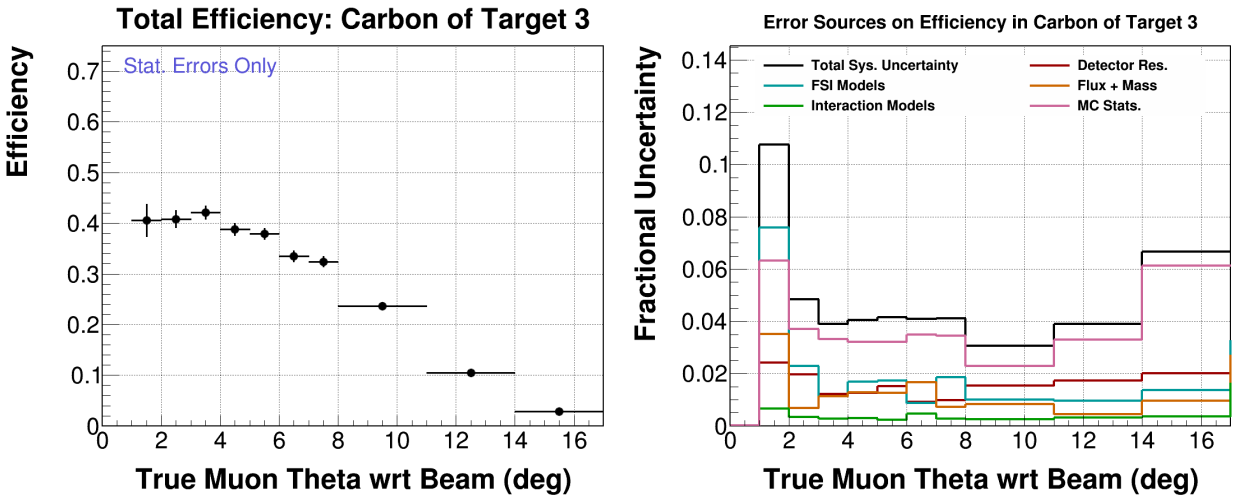

Figure E-62: Overall efficiency of events in the carbon of target 3 as a function of true θ_μ (left) and the systematic uncertainty on the overall efficiency (right).

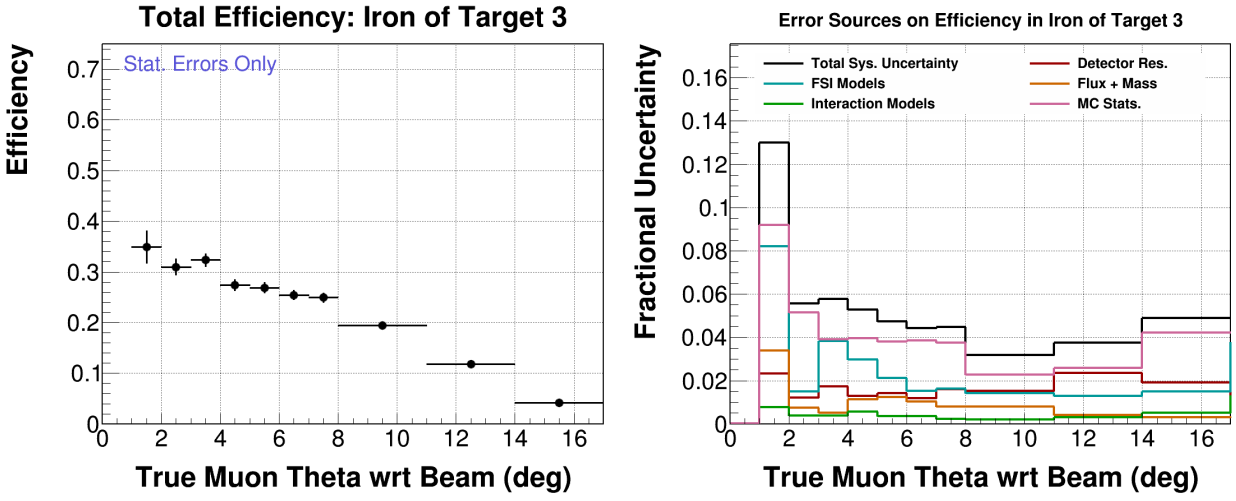

Figure E-63: Overall efficiency of events in the iron of target 3 as a function of true θ_μ (left) and the systematic uncertainty on the overall efficiency (right).

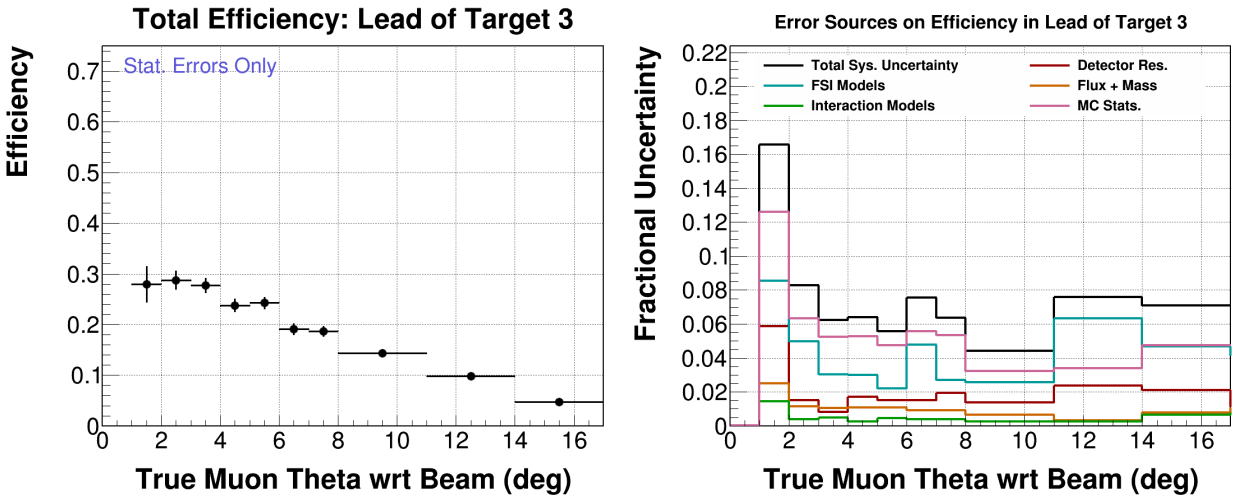

Figure E-64: Overall efficiency of events in the lead of target 3 as a function of true θ_μ (left) and the systematic uncertainty on the overall efficiency (right).

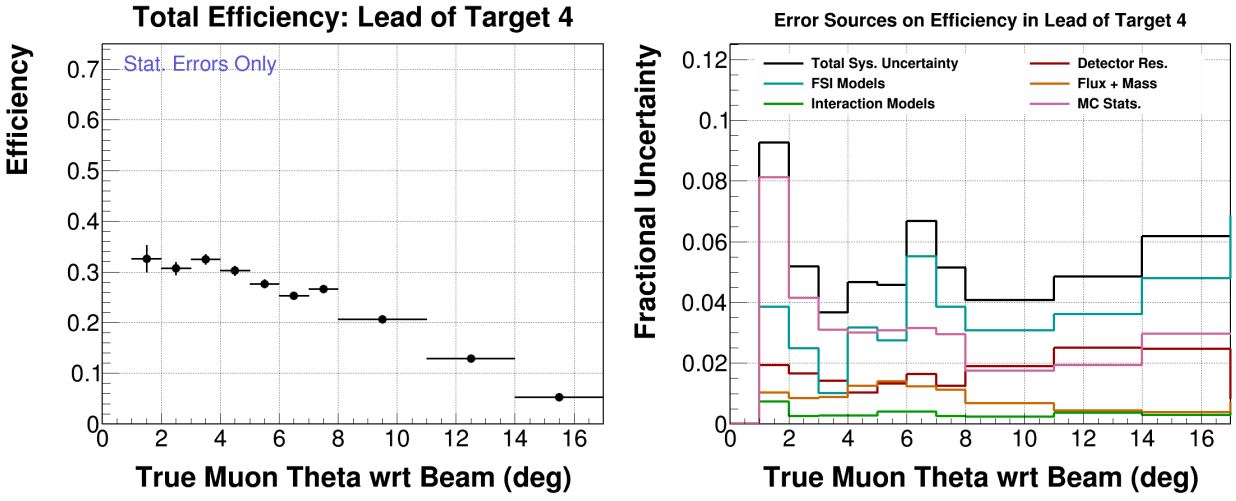

Figure E-65: Overall efficiency of events in the lead of target 4 as a function of true θ_μ (left) and the systematic uncertainty on the overall efficiency (right).

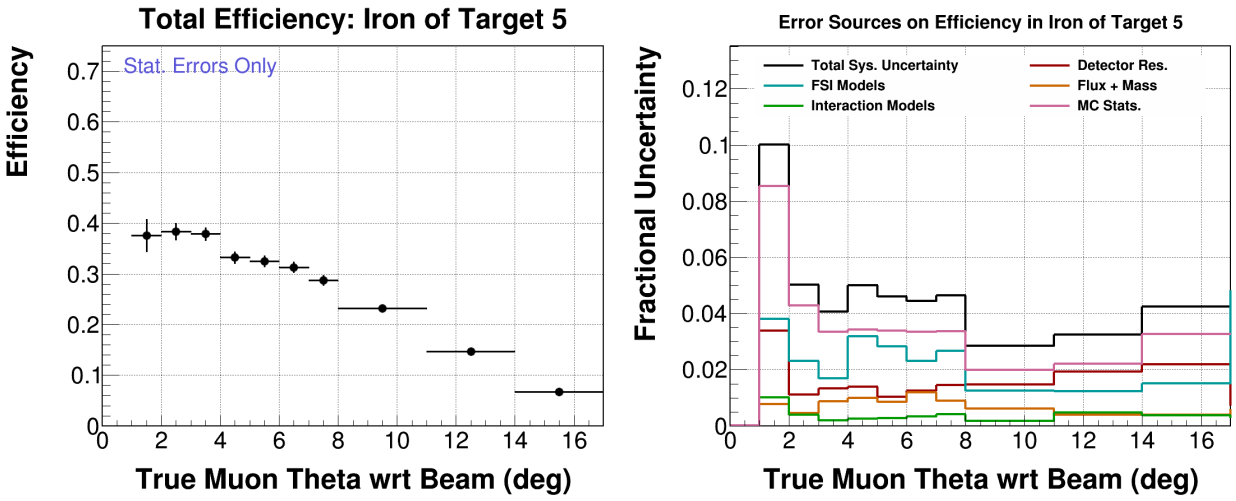

Figure E-66: Overall efficiency of events in the iron of target 5 as a function of true θ_μ (left) and the systematic uncertainty on the overall efficiency (right).

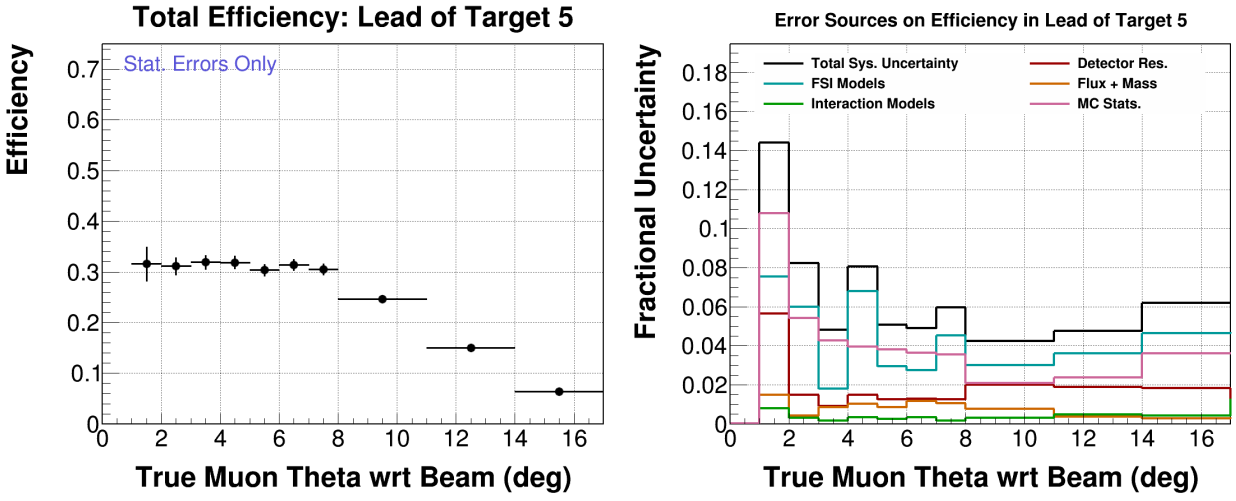

Figure E-67: Overall efficiency of events in the lead of target 5 as a function of true θ_μ (left) and the systematic uncertainty on the overall efficiency (right).

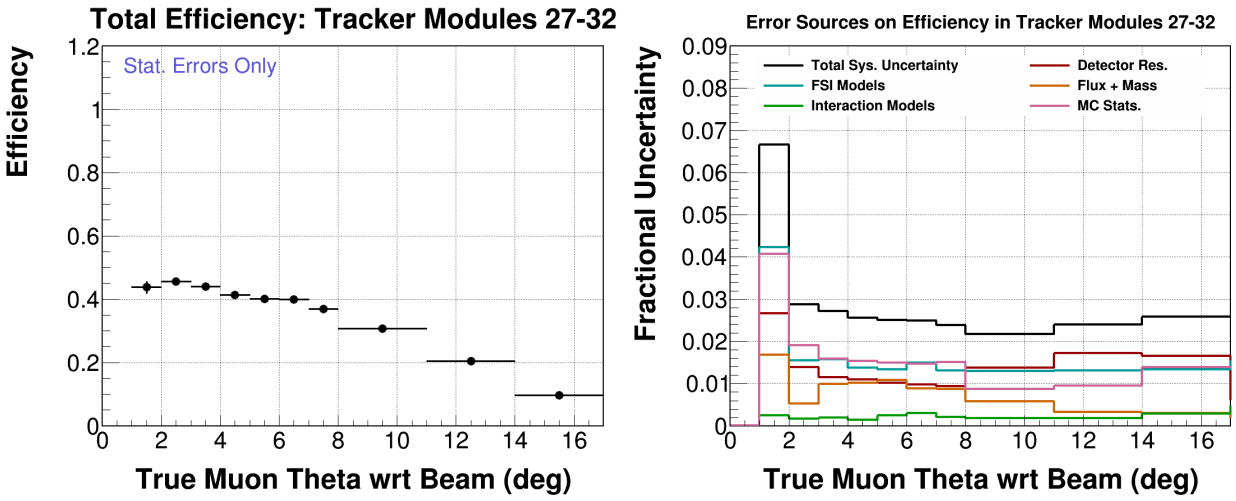

Figure E-68: Overall efficiency of events in the scintillator tracker module 27-32 as a function of true θ_μ (left) and the systematic uncertainty on the overall efficiency (right).

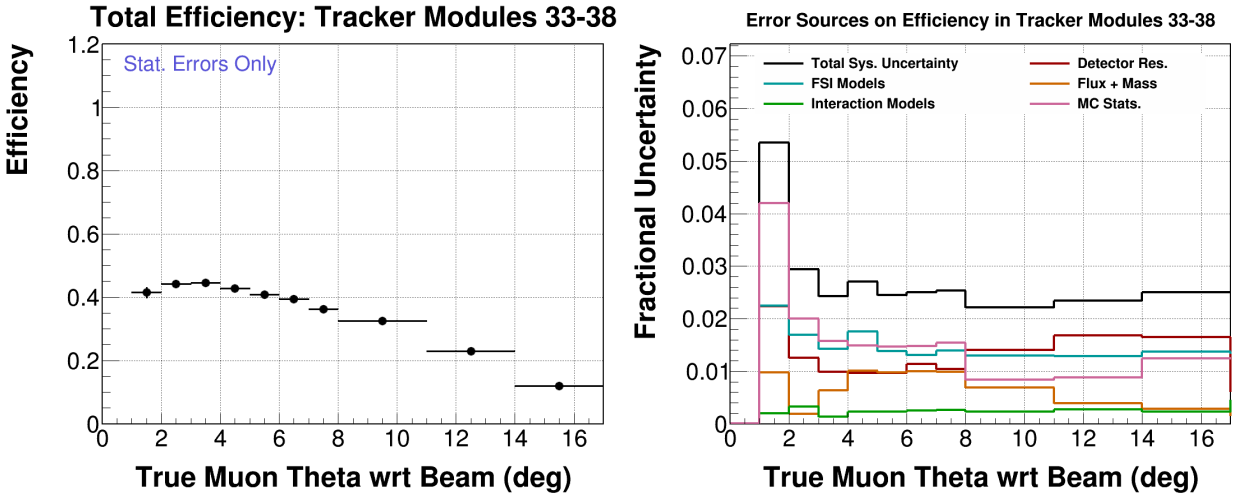

Figure E-69: Overall efficiency of events in the scintillator tracker module 33-38 as a function of true θ_μ (left) and the systematic uncertainty on the overall efficiency (right).

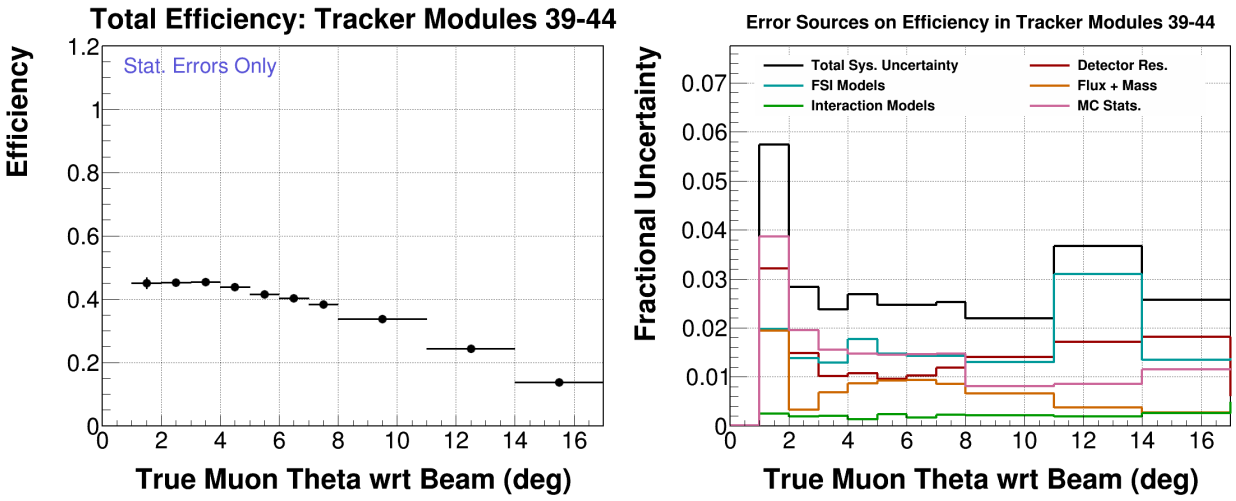

Figure E-70: Overall efficiency of events in the scintillator tracker module 39-44 as a function of true θ_μ (left) and the systematic uncertainty on the overall efficiency (right).

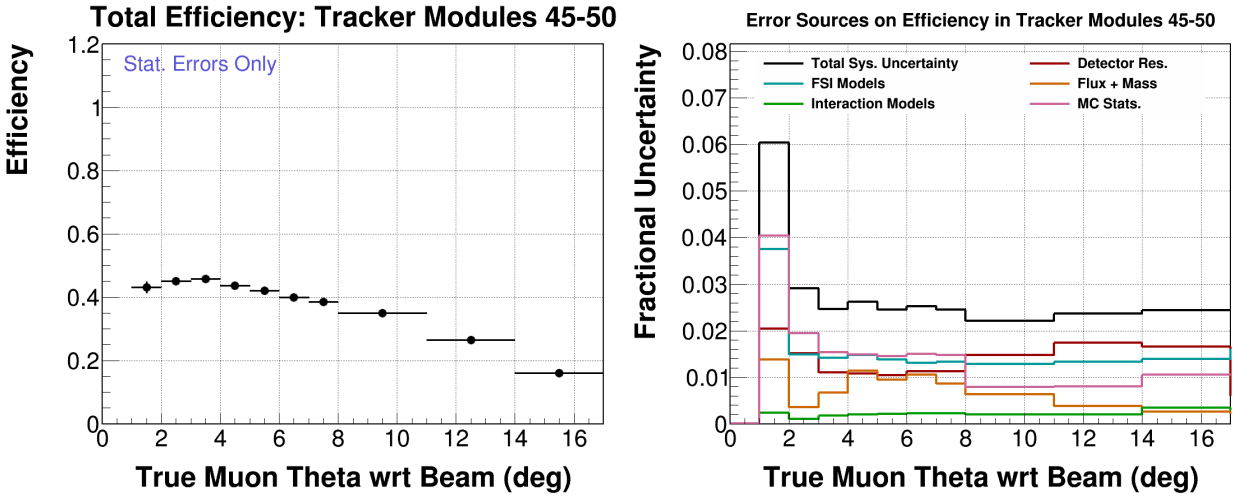

Figure E-71: Overall efficiency of events in the scintillator tracker module 45-50 as a function of true θ_μ (left) and the systematic uncertainty on the overall efficiency (right).

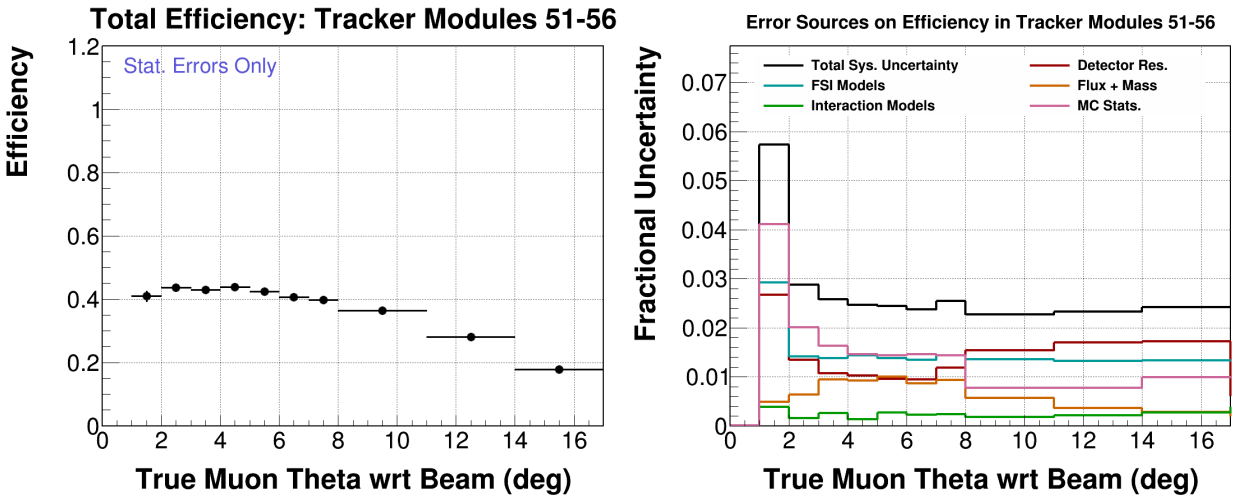

Figure E-72: Overall efficiency of events in the scintillator tracker module 51-56 as a function of true θ_μ (left) and the systematic uncertainty on the overall efficiency (right).

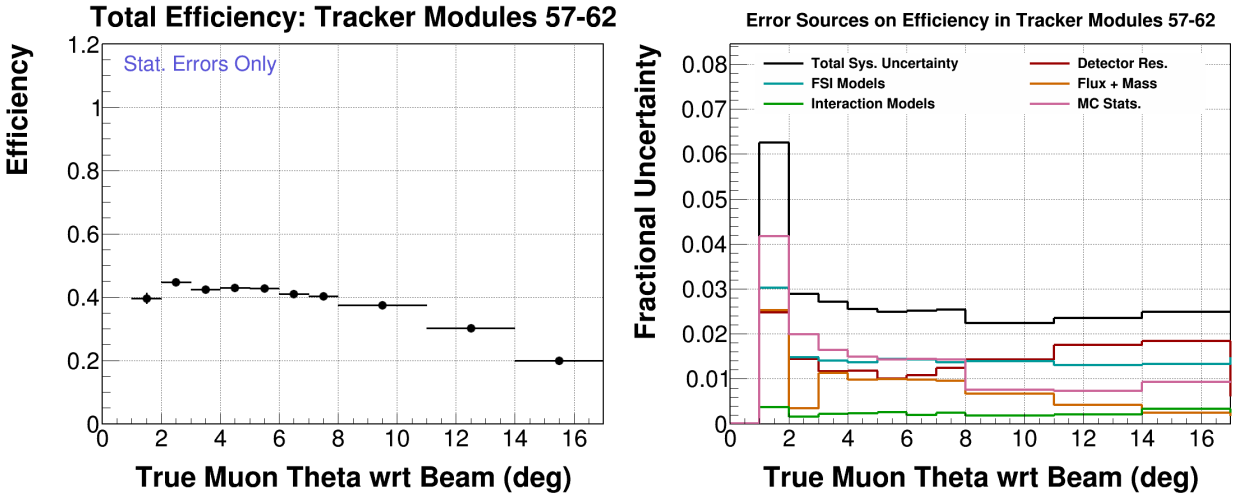

Figure E-73: Overall efficiency of events in the scintillator tracker module 57-62 as a function of true θ_μ (left) and the systematic uncertainty on the overall efficiency (right).

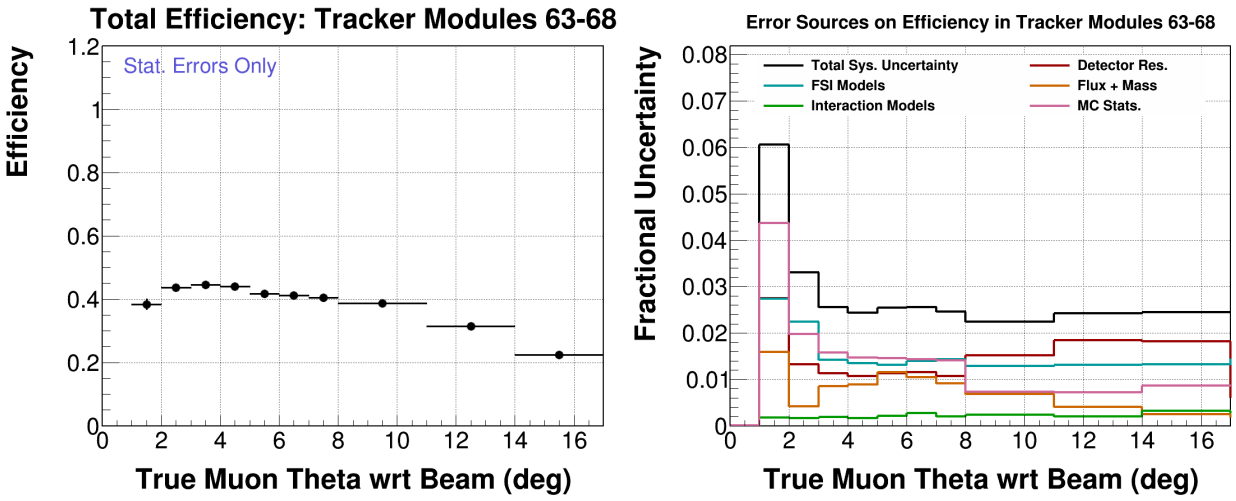

Figure E-74: Overall efficiency of events in the scintillator tracker module 63-68 as a function of true θ_μ (left) and the systematic uncertainty on the overall efficiency (right).

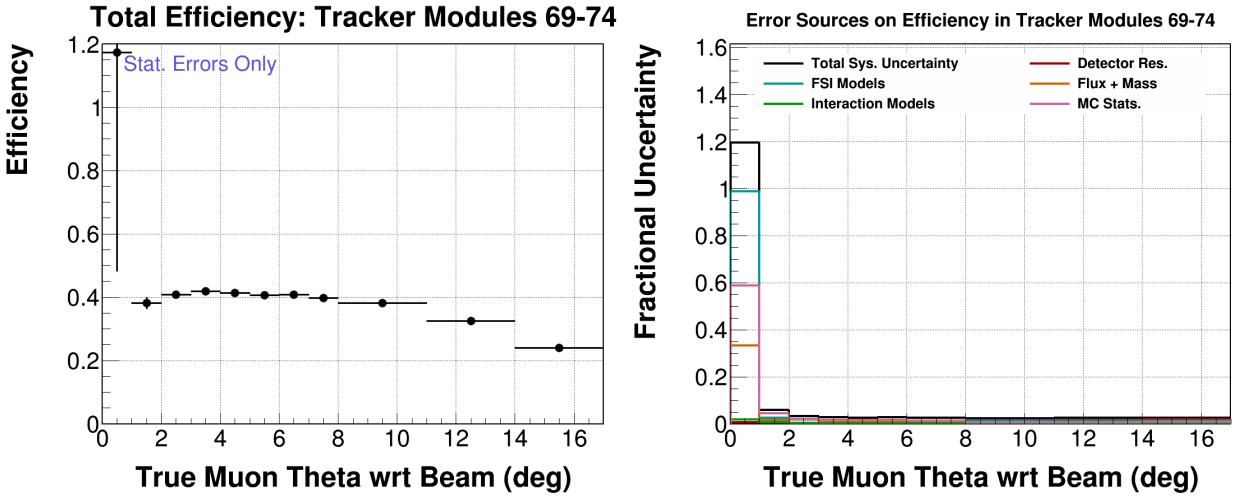

Figure E-75: Overall efficiency of events in the scintillator tracker module 69-74 as a function of true θ_μ (left) and the systematic uncertainty on the overall efficiency (right).

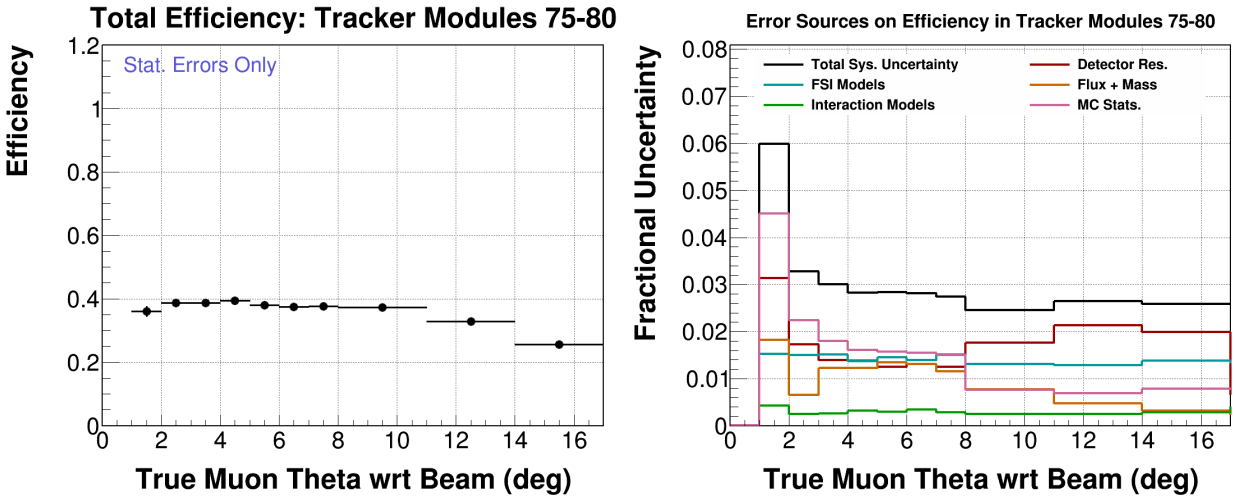

Figure E-76: Overall efficiency of events in the scintillator tracker module 75-80 as a function of true θ_μ (left) and the systematic uncertainty on the overall efficiency (right).

E.5 Overall Efficiencies as a function of Q^2

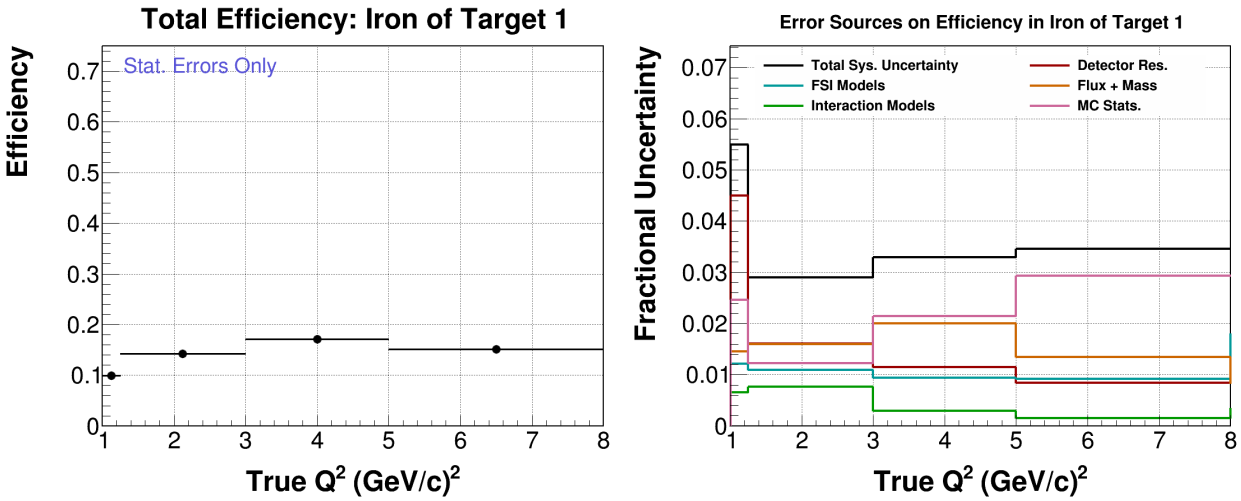

Figure E-77: Overall efficiency of events in the iron of target 1 as a function of true Q^2 (left) and the systematic uncertainty on the overall efficiency (right).

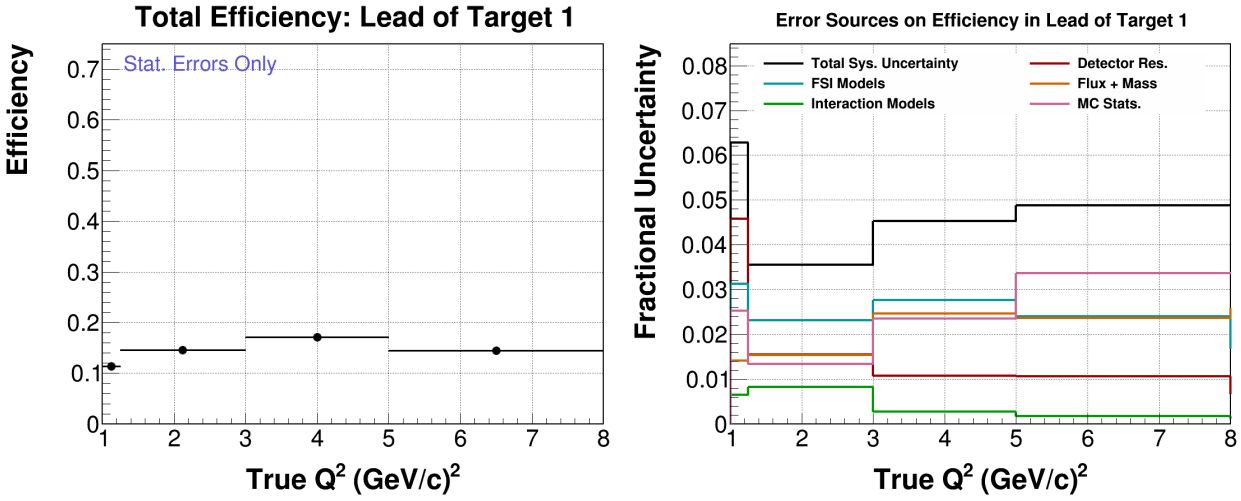

Figure E-78: Overall efficiency of events in the lead of target 1 as a function of true Q^2 (left) and the systematic uncertainty on the overall efficiency (right).

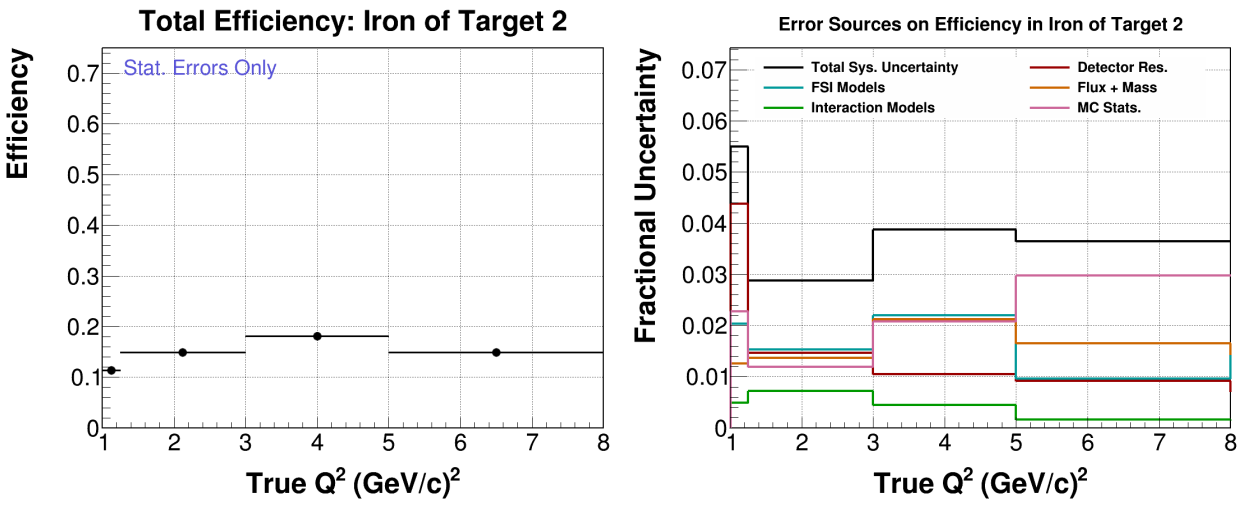

Figure E-79: Overall efficiency of events in the iron of target 2 as a function of true Q^2 (left) and the systematic uncertainty on the overall efficiency (right).

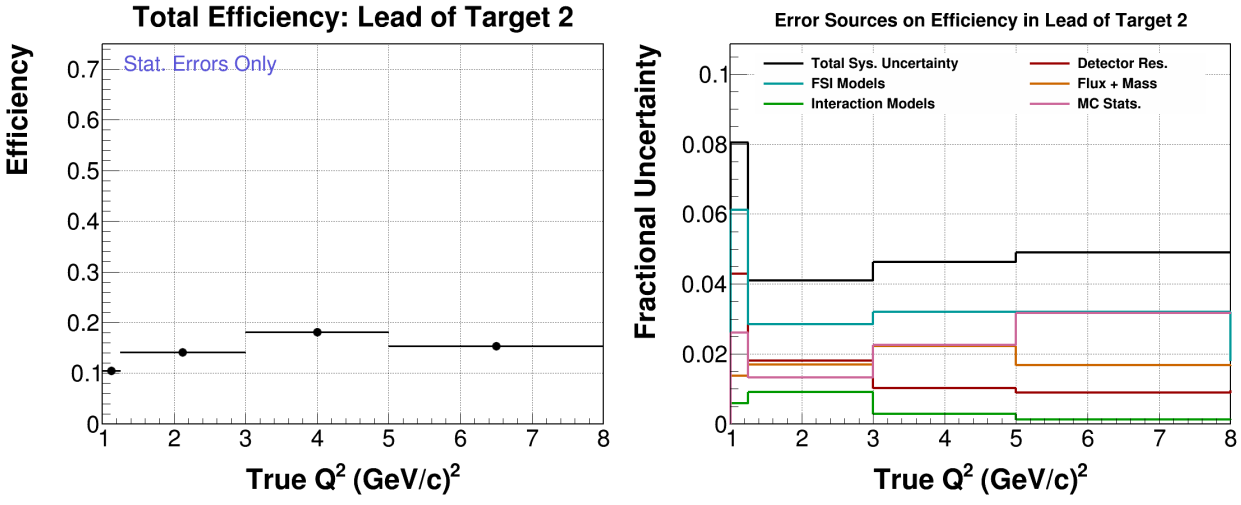

Figure E-80: Overall efficiency of events in the lead of target 2 as a function of true Q^2 (left) and the systematic uncertainty on the overall efficiency (right).

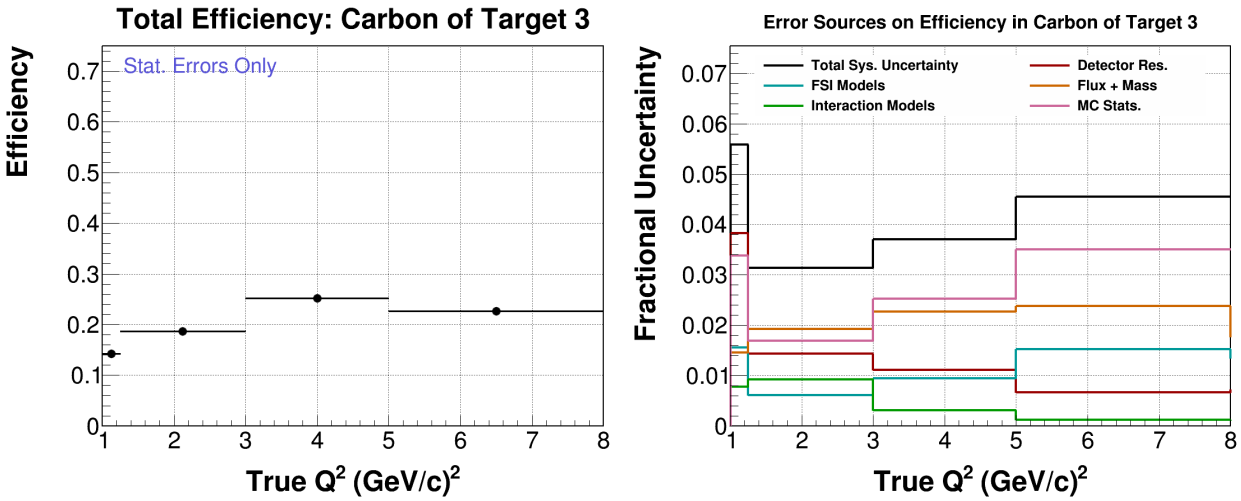

Figure E-81: Overall efficiency of events in the carbon of target 3 as a function of true Q^2 (left) and the systematic uncertainty on the overall efficiency (right).

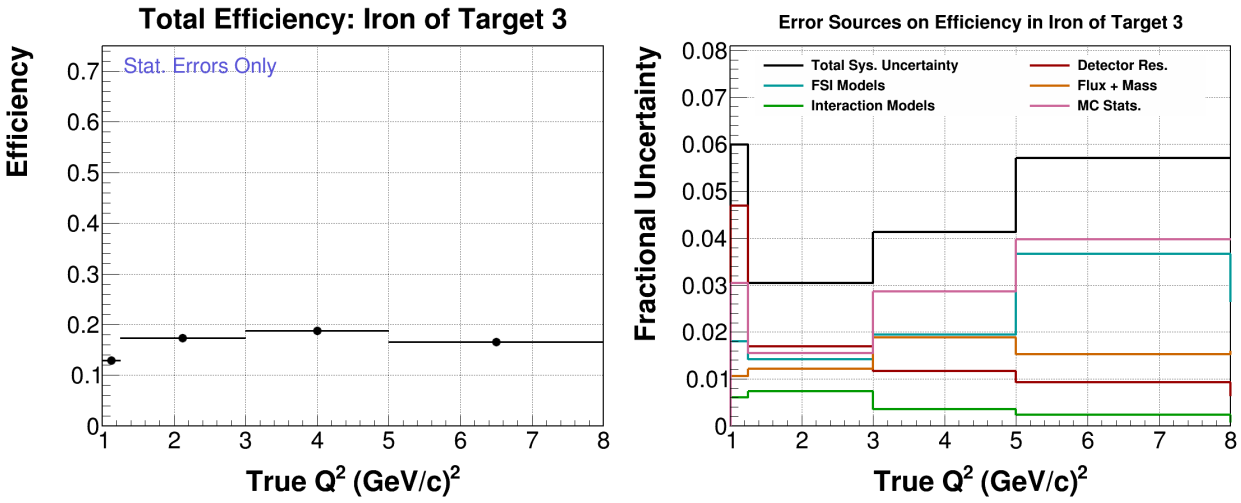

Figure E-82: Overall efficiency of events in the iron of target 3 as a function of true Q^2 (left) and the systematic uncertainty on the overall efficiency (right).

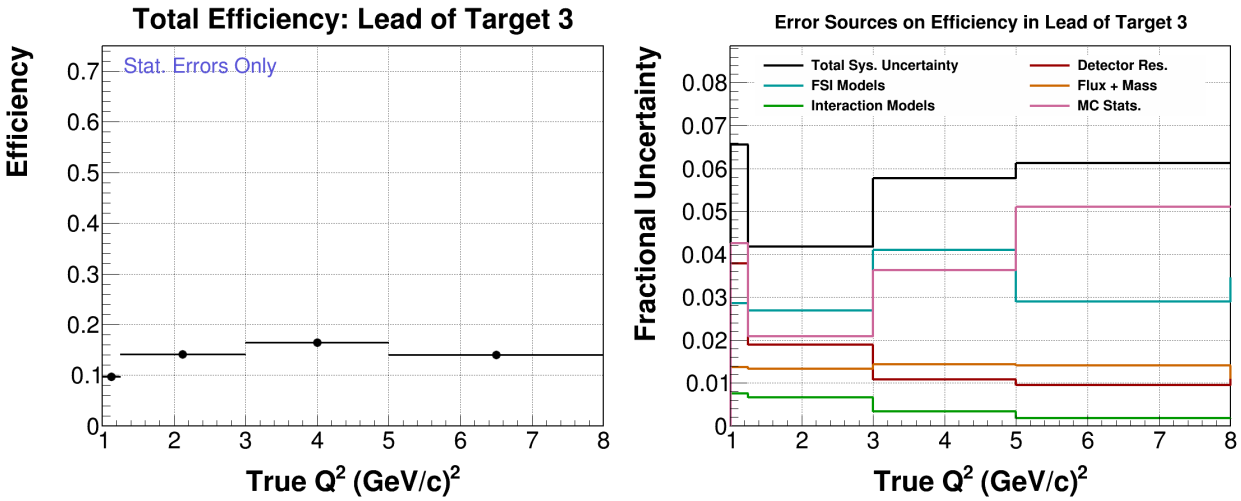

Figure E-83: Overall efficiency of events in the lead of target 3 as a function of true Q^2 (left) and the systematic uncertainty on the overall efficiency (right).

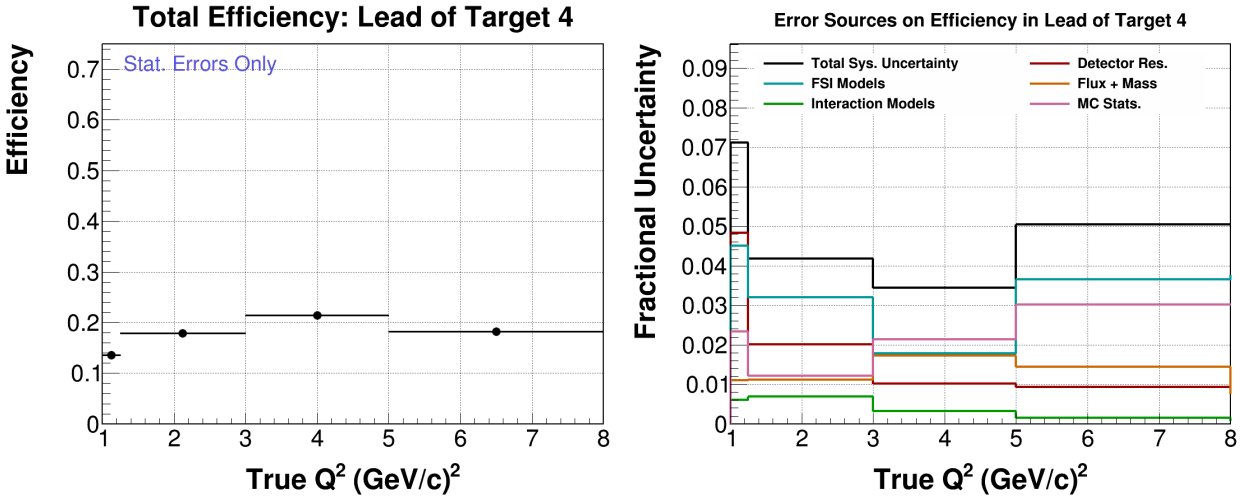

Figure E-84: Overall efficiency of events in the lead of target 4 as a function of true Q^2 (left) and the systematic uncertainty on the overall efficiency (right).

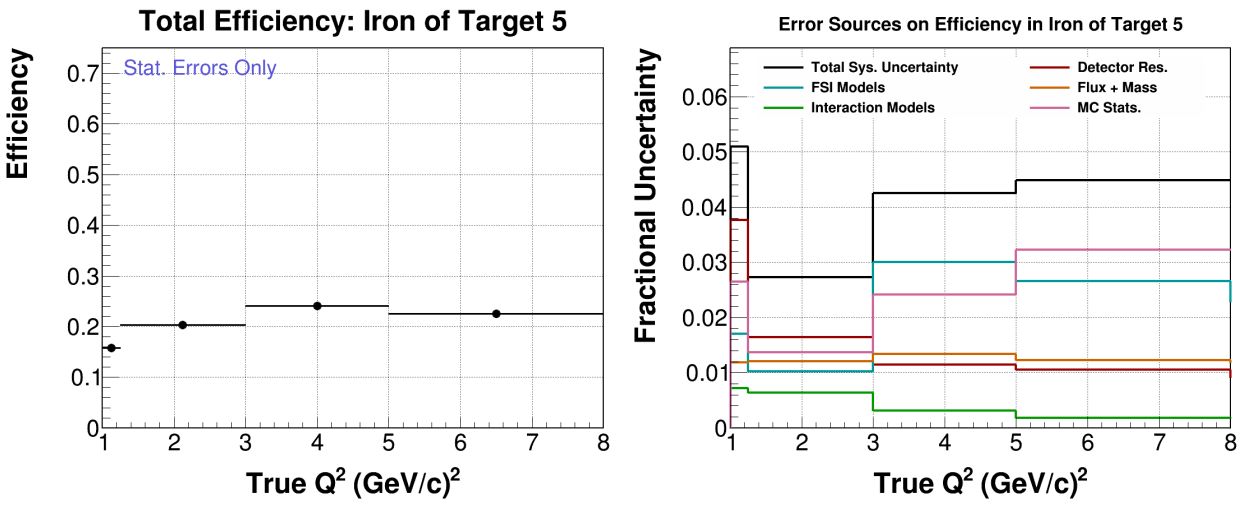

Figure E-85: Overall efficiency of events in the iron of target 5 as a function of true Q^2 (left) and the systematic uncertainty on the overall efficiency (right).

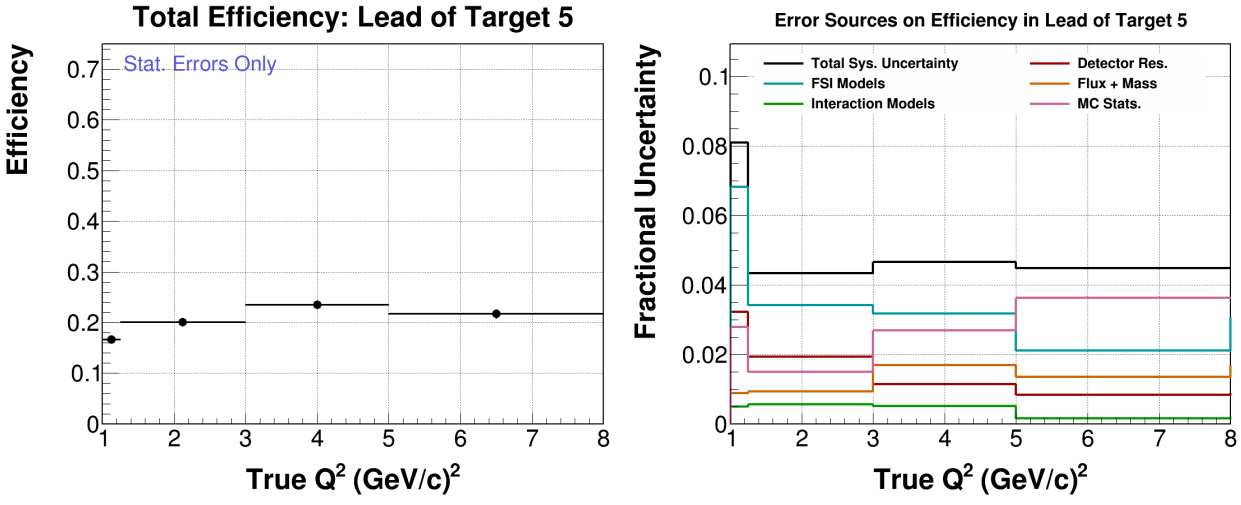

Figure E-86: Overall efficiency of events in the lead of target 5 as a function of true Q^2 (left) and the systematic uncertainty on the overall efficiency (right).

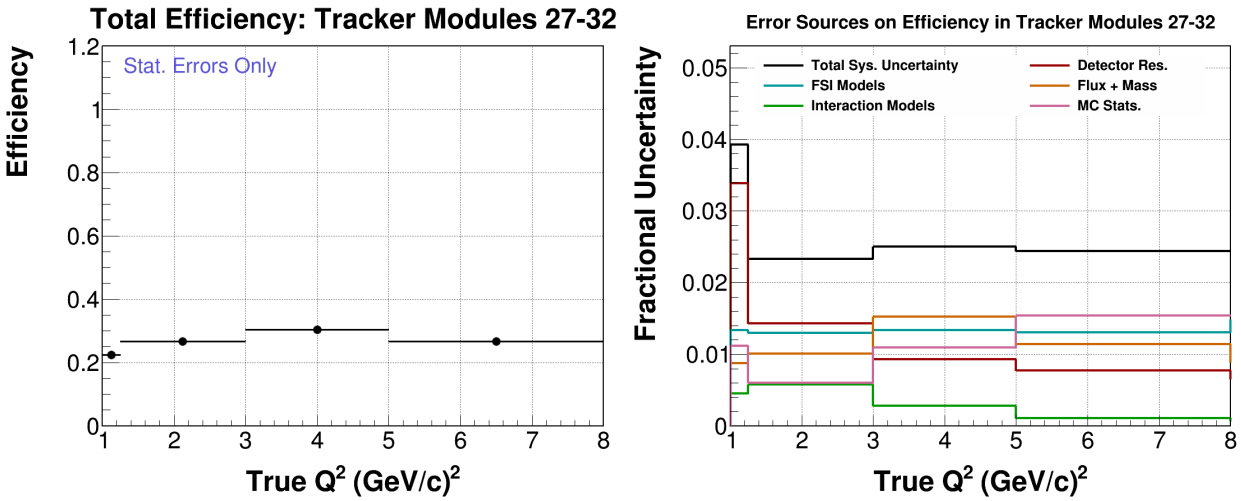

Figure E-87: Overall efficiency of events in the scintillator tracker module 27-32 as a function of true Q^2 (left) and the systematic uncertainty on the overall efficiency (right).

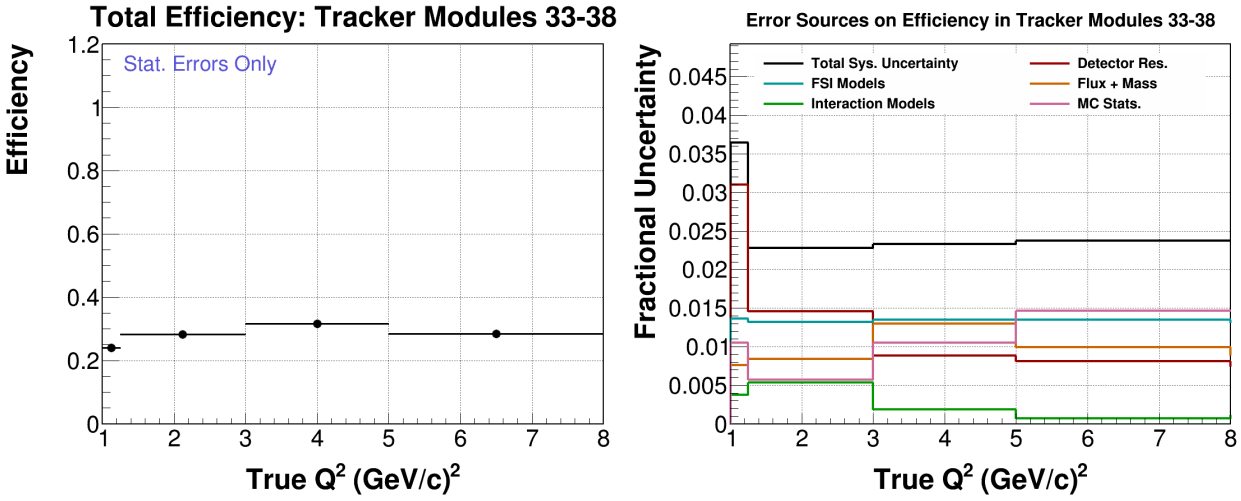

Figure E-88: Overall efficiency of events in the scintillator tracker module 33-38 as a function of true Q^2 (left) and the systematic uncertainty on the overall efficiency (right).

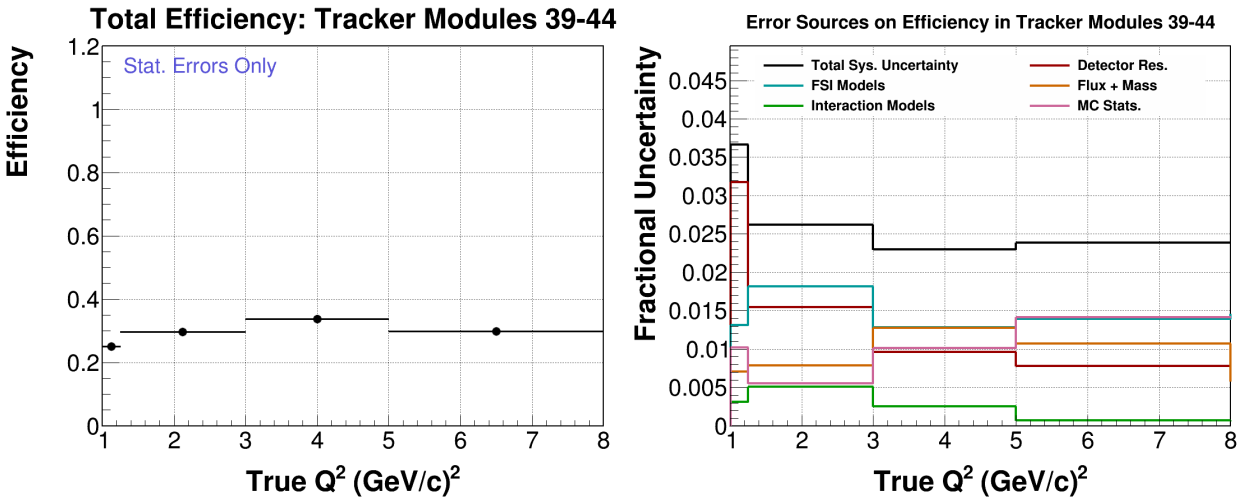

Figure E-89: Overall efficiency of events in the scintillator tracker module 39-44 as a function of true Q^2 (left) and the systematic uncertainty on the overall efficiency (right).

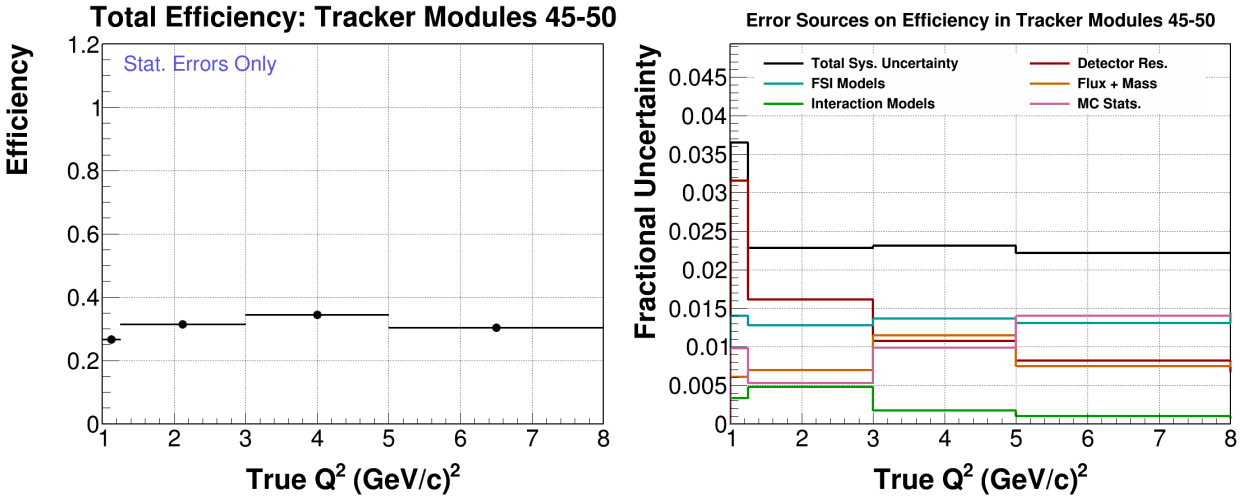

Figure E-90: Overall efficiency of events in the scintillator tracker module 45-50 as a function of true Q^2 (left) and the systematic uncertainty on the overall efficiency (right).

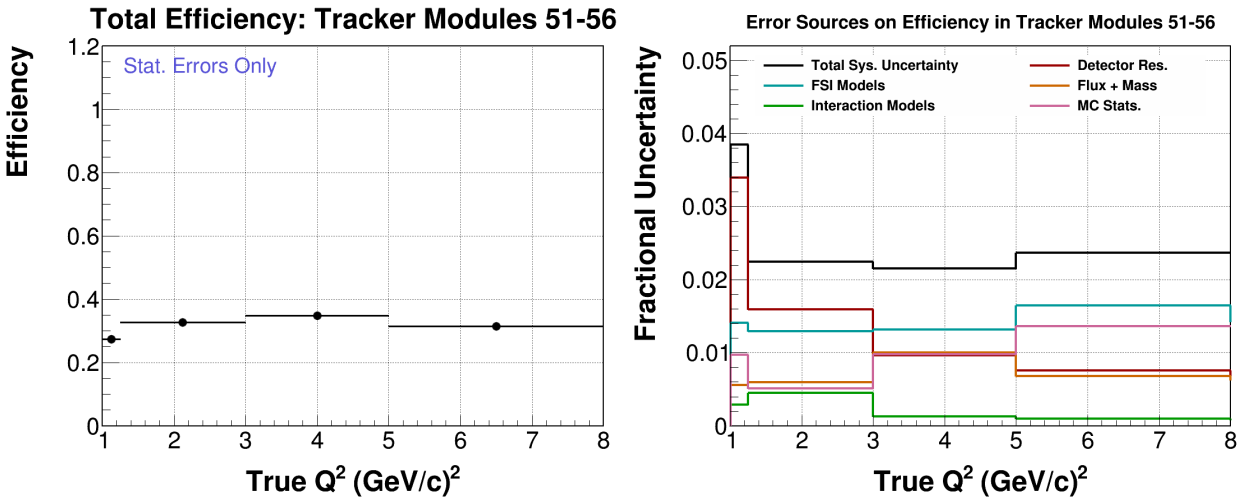

Figure E-91: Overall efficiency of events in the scintillator tracker module 51-56 as a function of true Q^2 (left) and the systematic uncertainty on the overall efficiency (right).

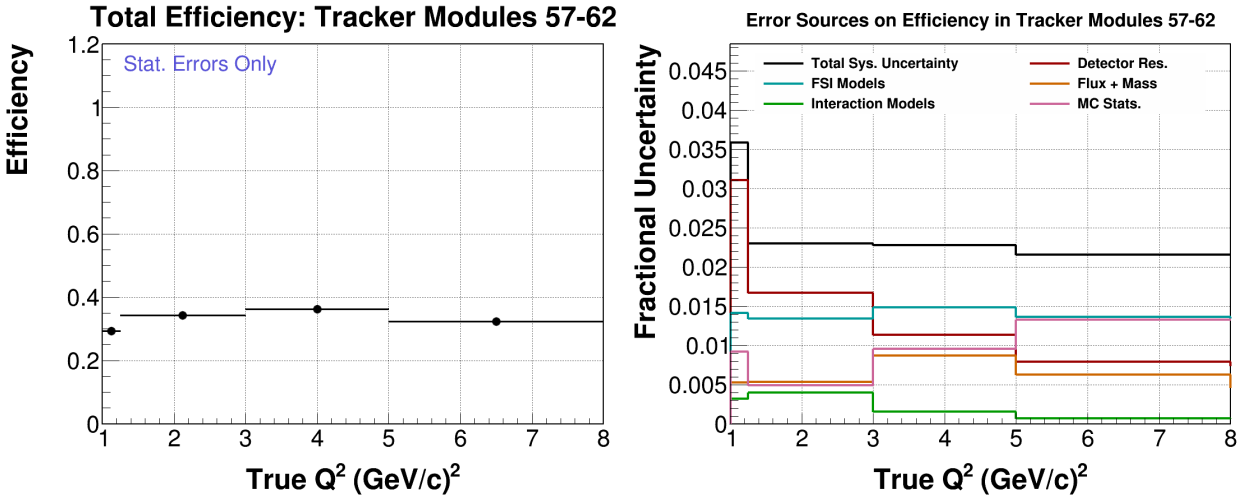

Figure E-92: Overall efficiency of events in the scintillator tracker module 57-62 as a function of true Q^2 (left) and the systematic uncertainty on the overall efficiency (right).

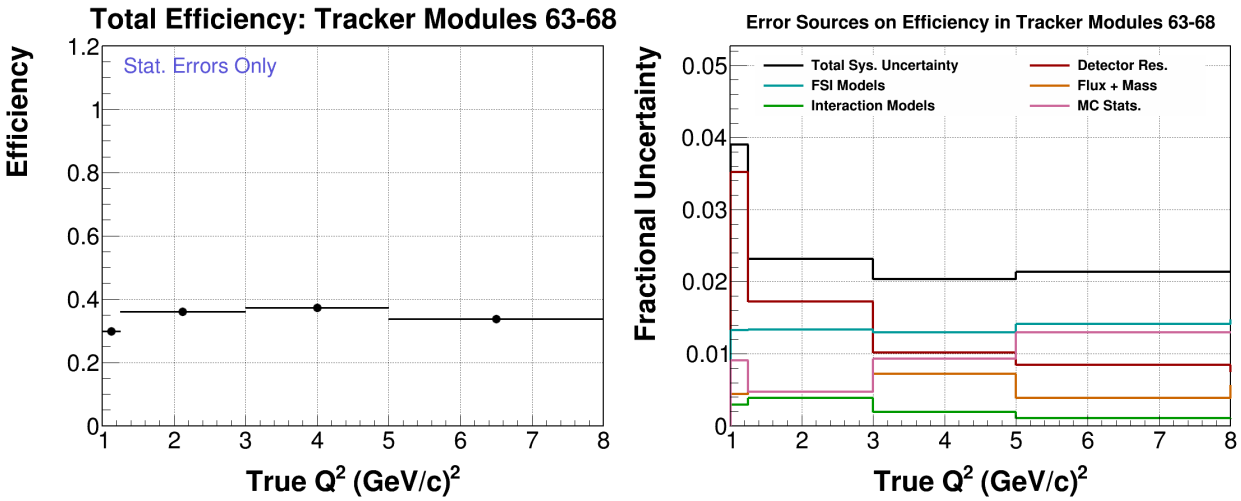

Figure E-93: Overall efficiency of events in the scintillator tracker module 63-68 as a function of true Q^2 (left) and the systematic uncertainty on the overall efficiency (right).

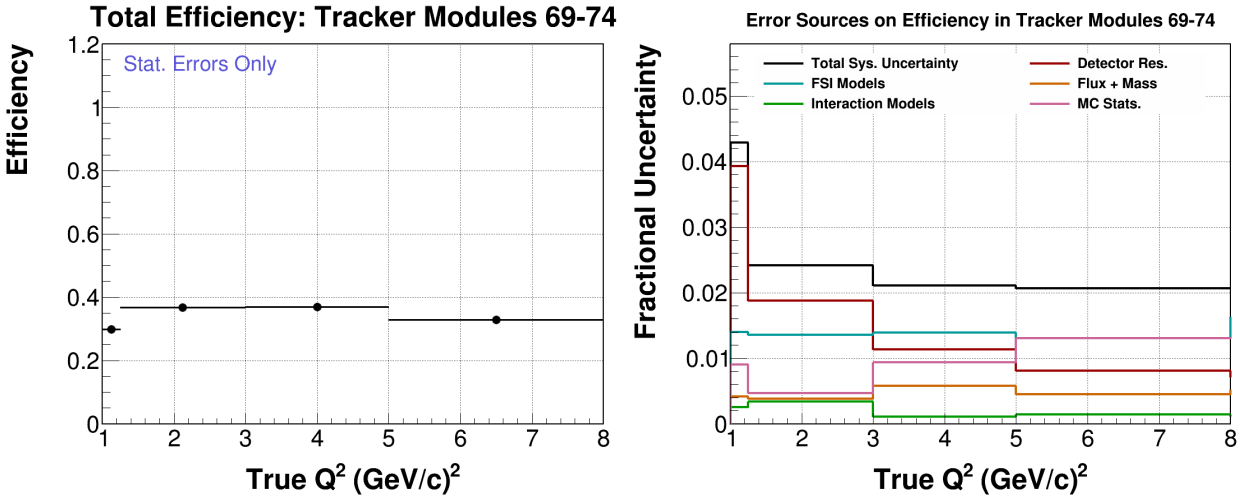

Figure E-94: Overall efficiency of events in the scintillator tracker module 69-74 as a function of true Q^2 (left) and the systematic uncertainty on the overall efficiency (right).

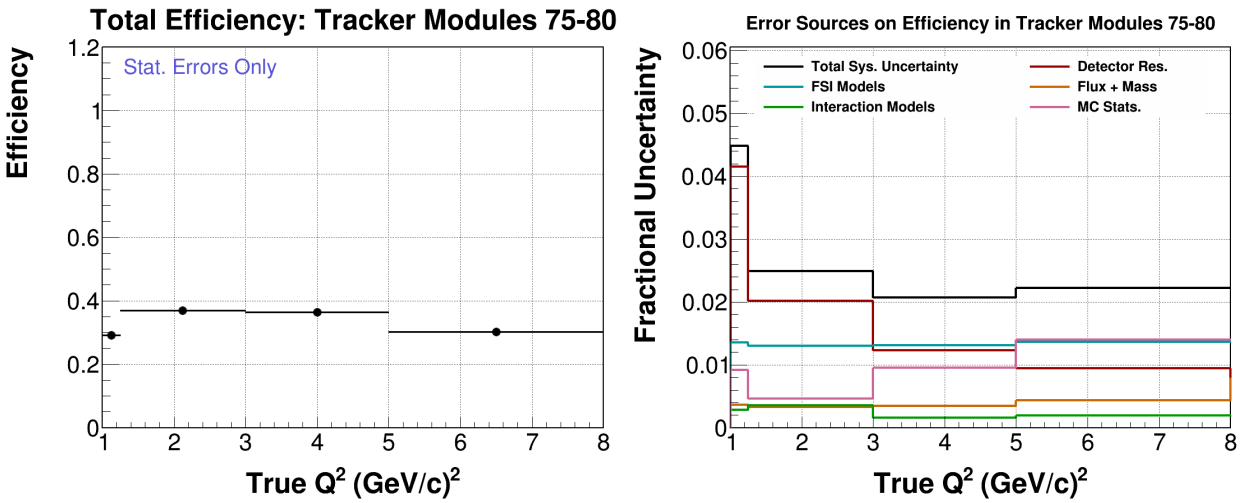

Figure E-95: Overall efficiency of events in the scintillator tracker module 75-80 as a function of true Q^2 (left) and the systematic uncertainty on the overall efficiency (right).

E.6 Overall Efficiencies as a function of W

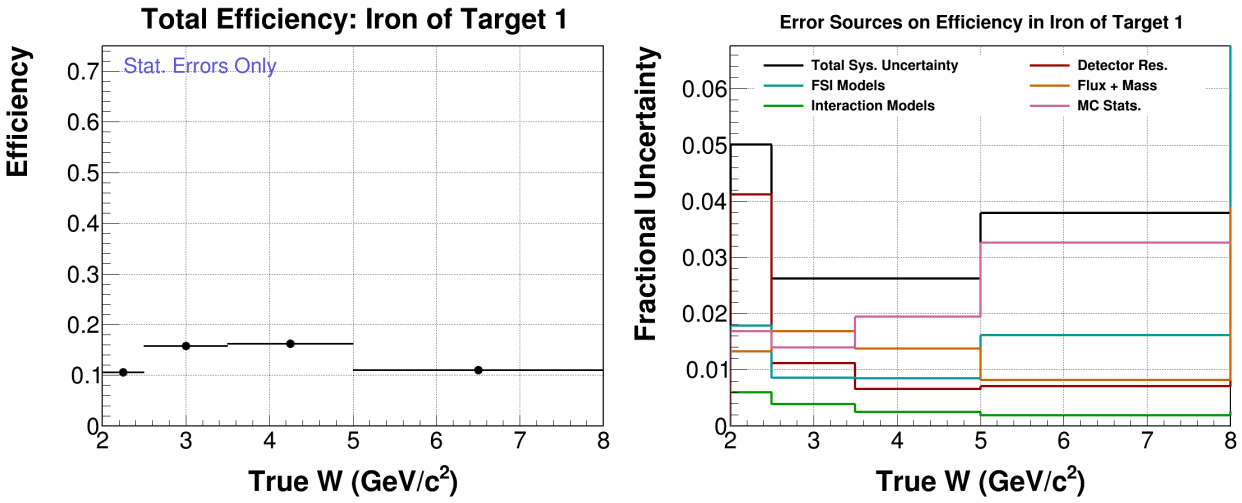

Figure E-96: Overall efficiency of events in the iron of target 1 as a function of true W (left) and the systematic uncertainty on the overall efficiency (right).

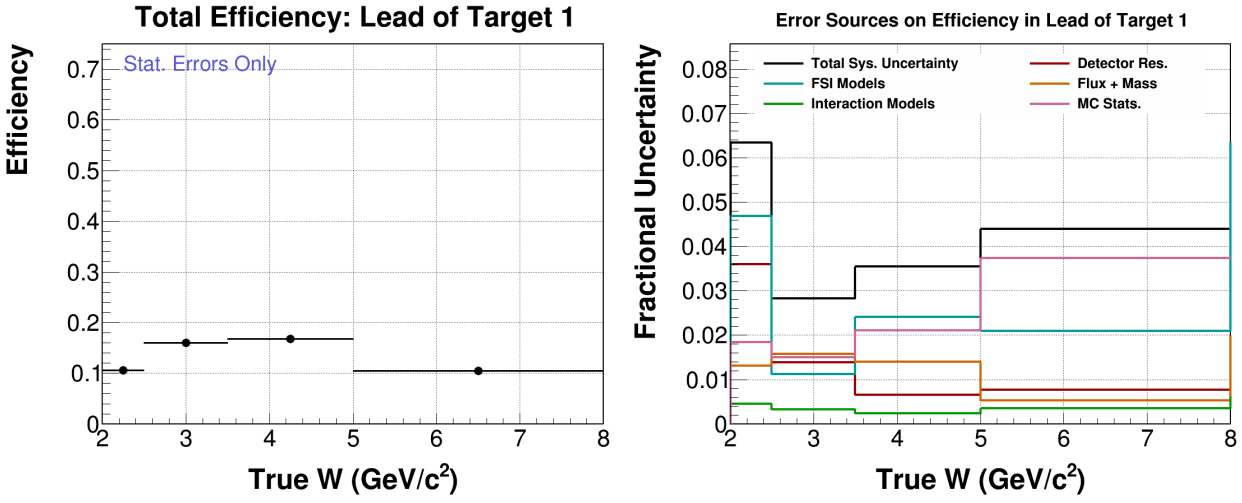

Figure E-97: Overall efficiency of events in the lead of target 1 as a function of true W (left) and the systematic uncertainty on the overall efficiency (right).

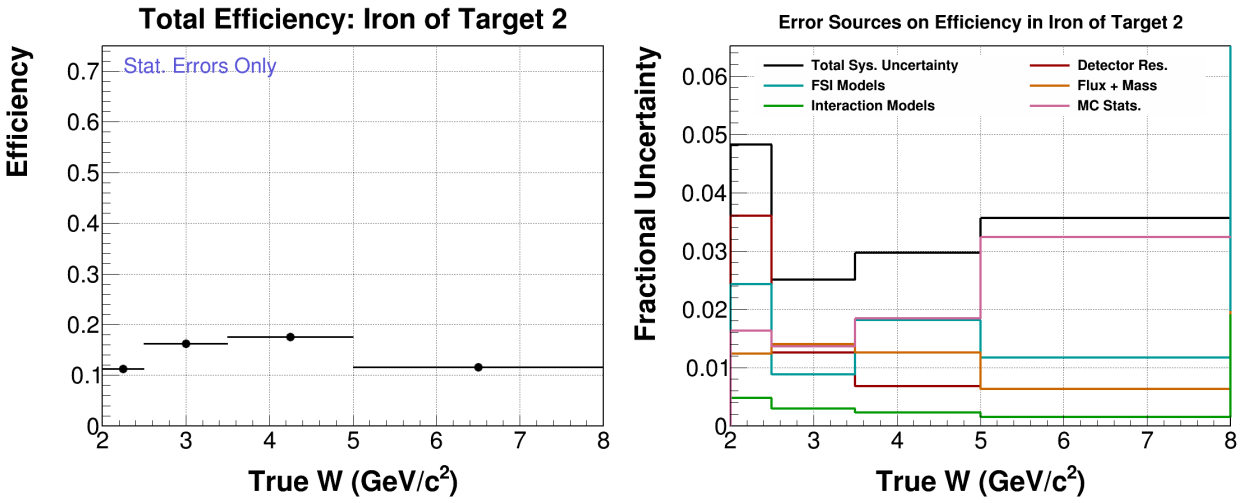

Figure E-98: Overall efficiency of events in the iron of target 2 as a function of true W (left) and the systematic uncertainty on the overall efficiency (right).

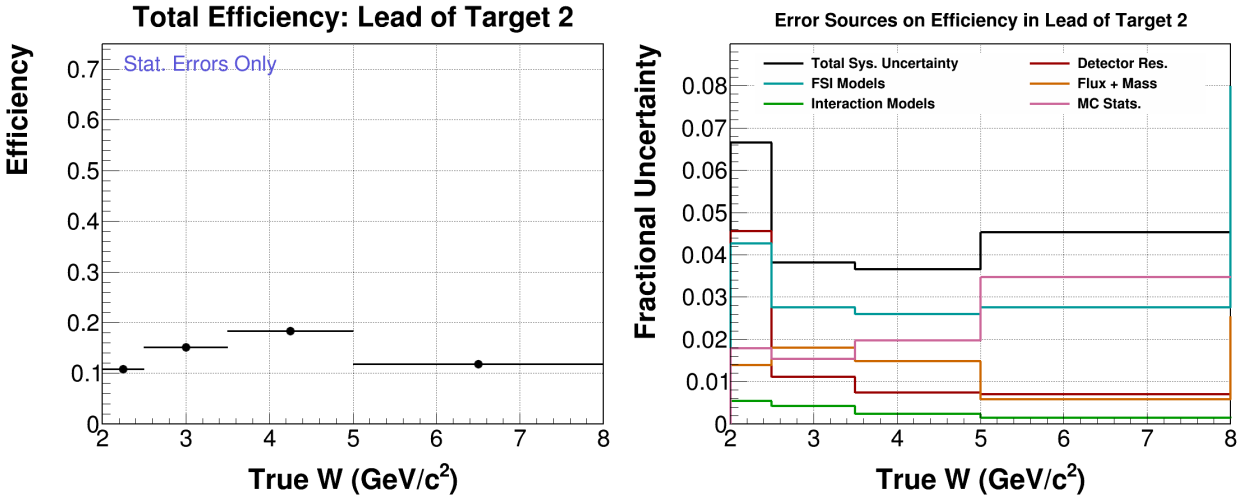

Figure E-99: Overall efficiency of events in the lead of target 2 as a function of true W (left) and the systematic uncertainty on the overall efficiency (right).

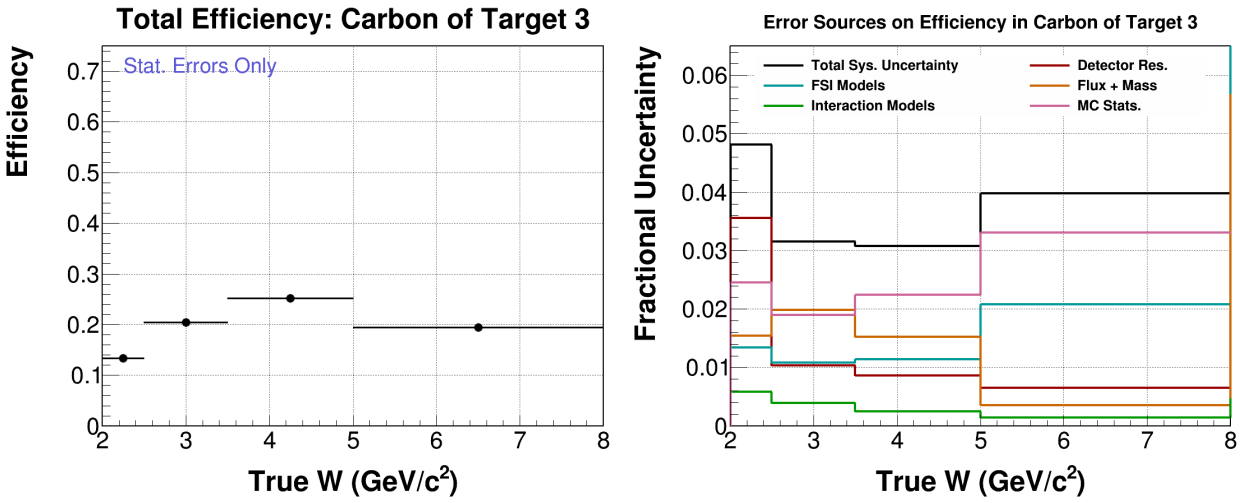

Figure E-100: Overall efficiency of events in the carbon of target 3 as a function of true W (left) and the systematic uncertainty on the overall efficiency (right).

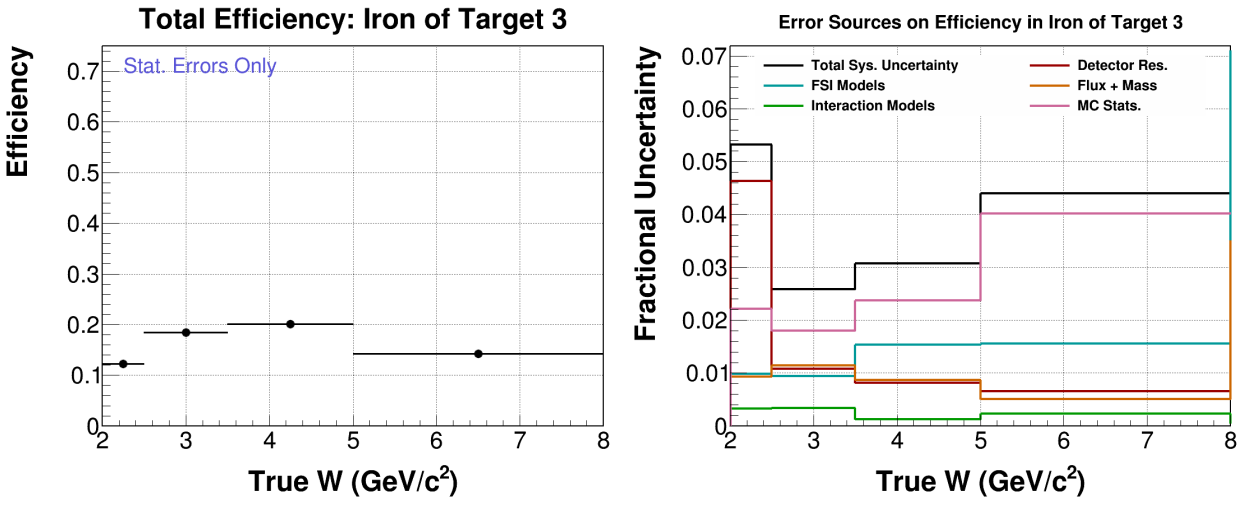

Figure E-101: Overall efficiency of events in the iron of target 3 as a function of true W (left) and the systematic uncertainty on the overall efficiency (right).

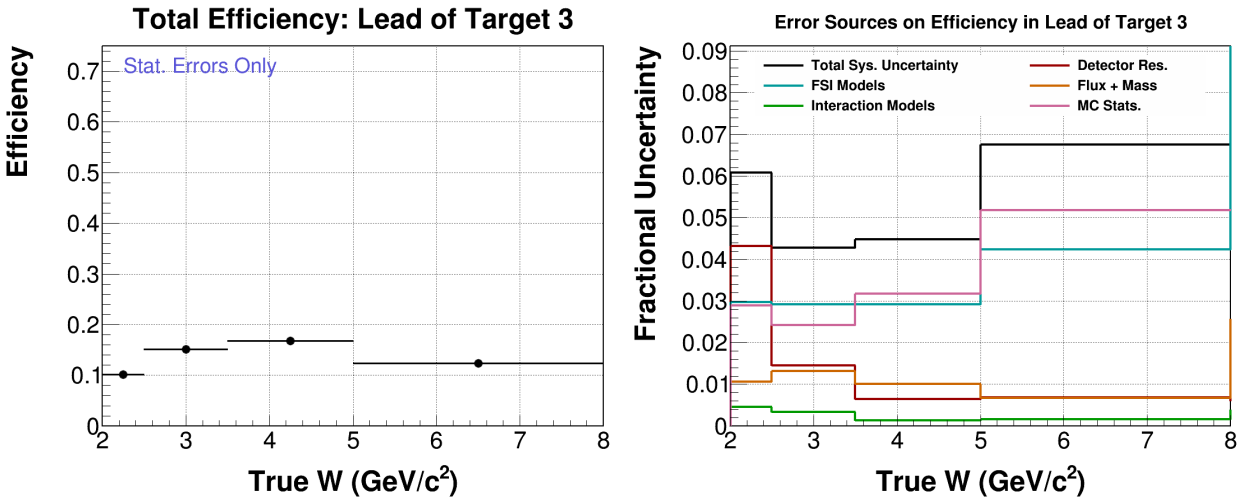

Figure E-102: Overall efficiency of events in the lead of target 3 as a function of true W (left) and the systematic uncertainty on the overall efficiency (right).

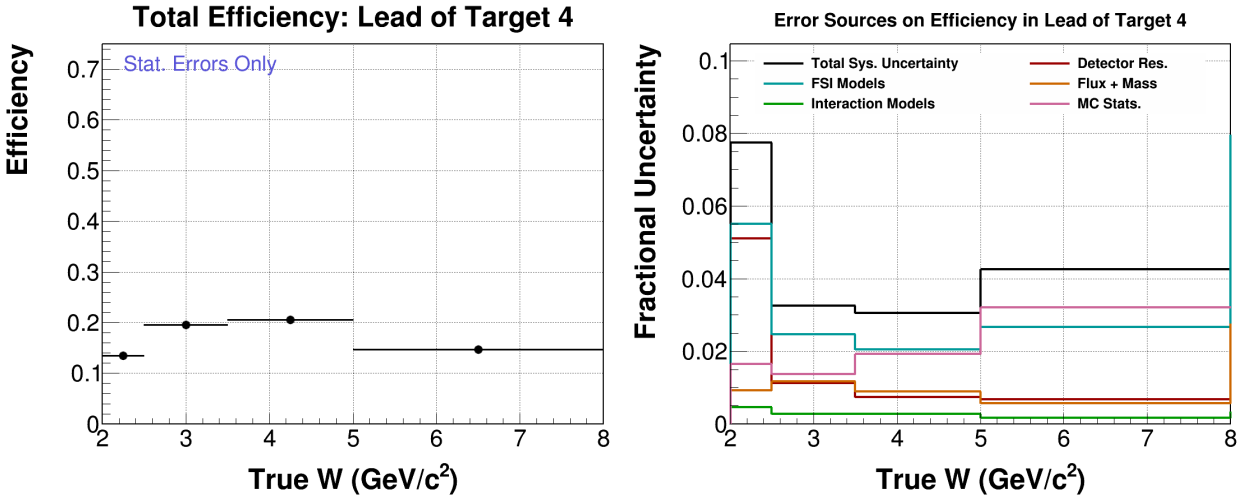

Figure E-103: Overall efficiency of events in the lead of target 4 as a function of true W (left) and the systematic uncertainty on the overall efficiency (right).

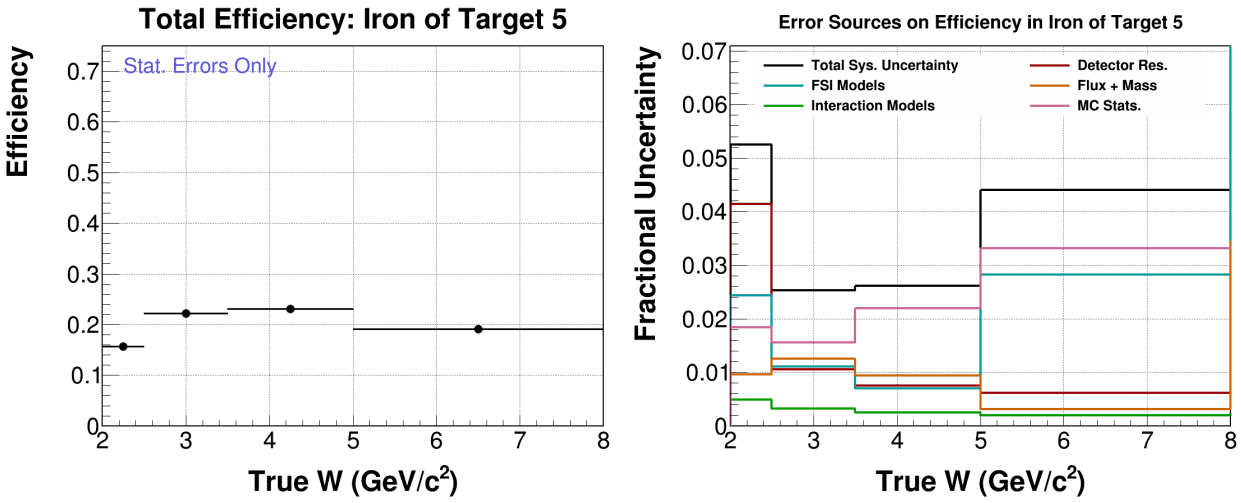

Figure E-104: Overall efficiency of events in the iron of target 5 as a function of true W (left) and the systematic uncertainty on the overall efficiency (right).

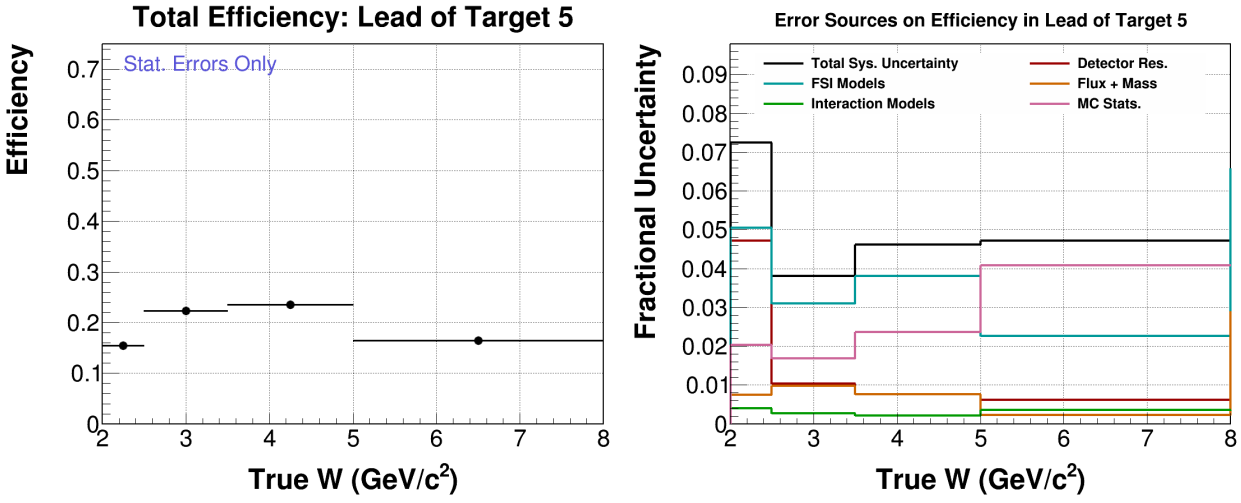

Figure E-105: Overall efficiency of events in the lead of target 5 as a function of true W (left) and the systematic uncertainty on the overall efficiency (right).

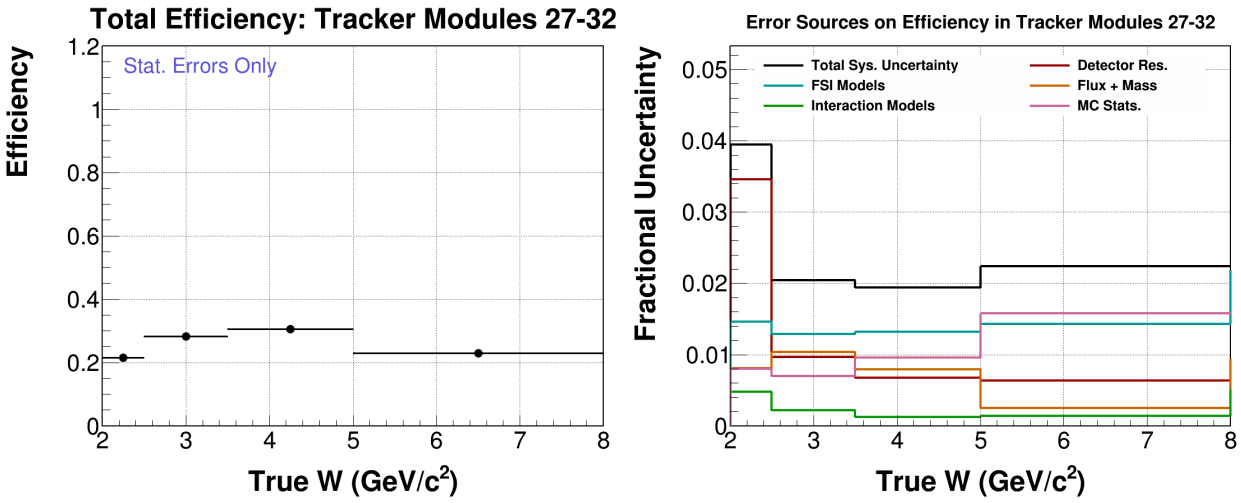

Figure E-106: Overall efficiency of events in the scintillator tracker module 27-32 as a function of true W (left) and the systematic uncertainty on the overall efficiency (right).

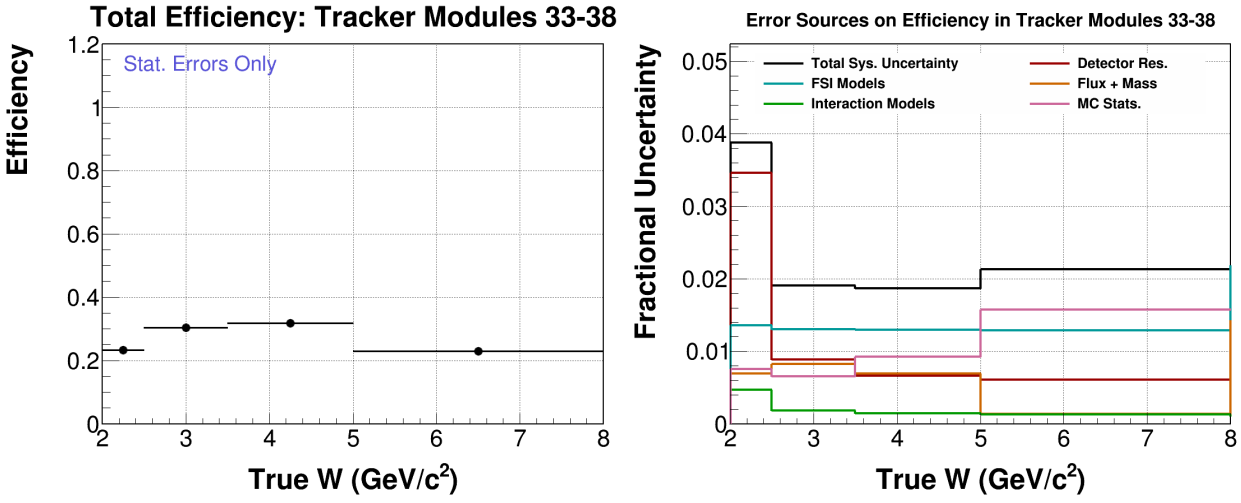

Figure E-107: Overall efficiency of events in the scintillator tracker module 33-38 as a function of true W (left) and the systematic uncertainty on the overall efficiency (right).

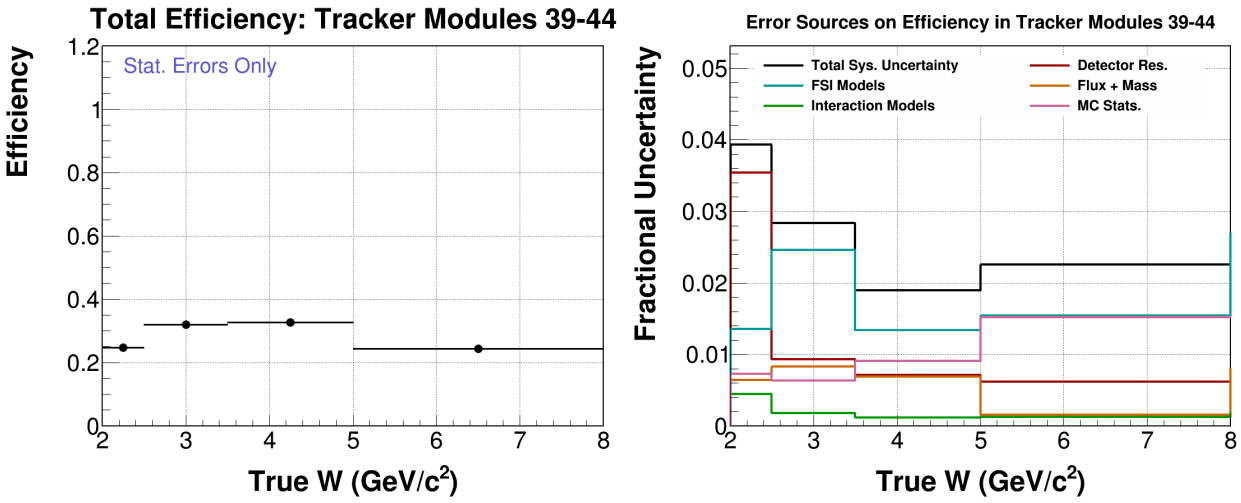

Figure E-108: Overall efficiency of events in the scintillator tracker module 39-44 as a function of true W (left) and the systematic uncertainty on the overall efficiency (right).

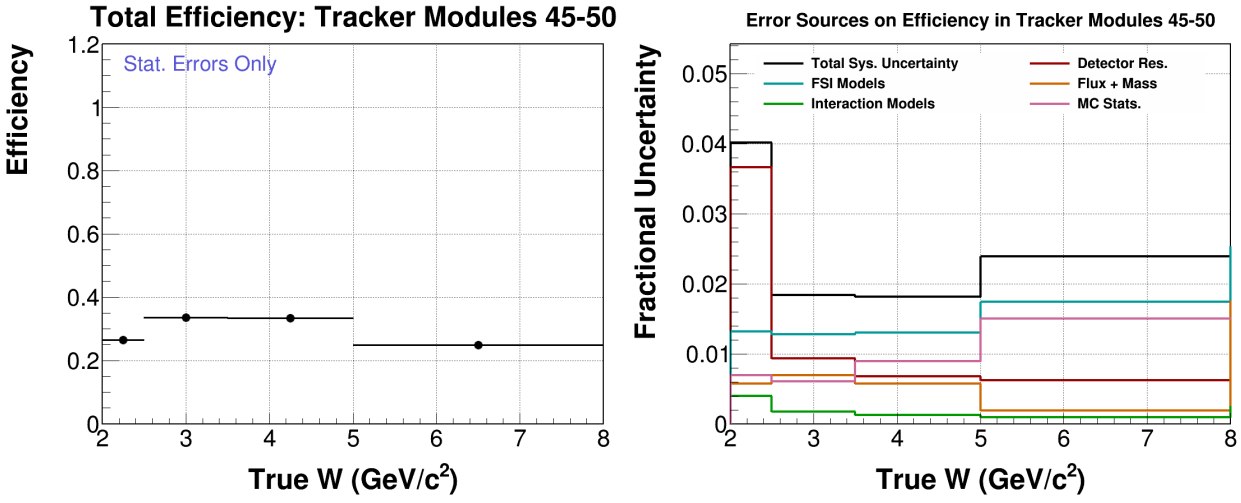

Figure E-109: Overall efficiency of events in the scintillator tracker module 45-50 as a function of true W (left) and the systematic uncertainty on the overall efficiency (right).

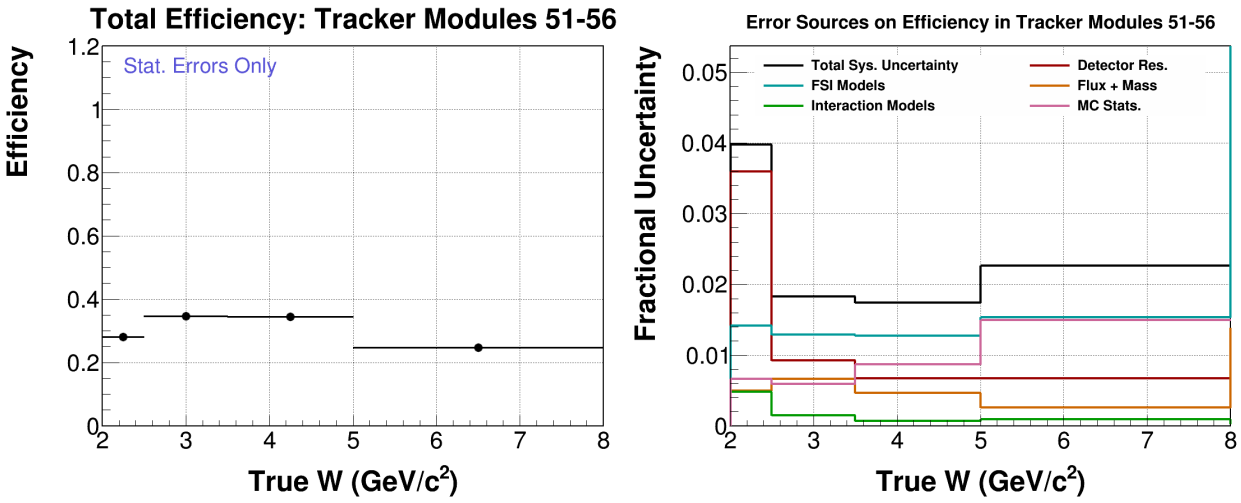

Figure E-110: Overall efficiency of events in the scintillator tracker module 51-56 as a function of true W (left) and the systematic uncertainty on the overall efficiency (right).

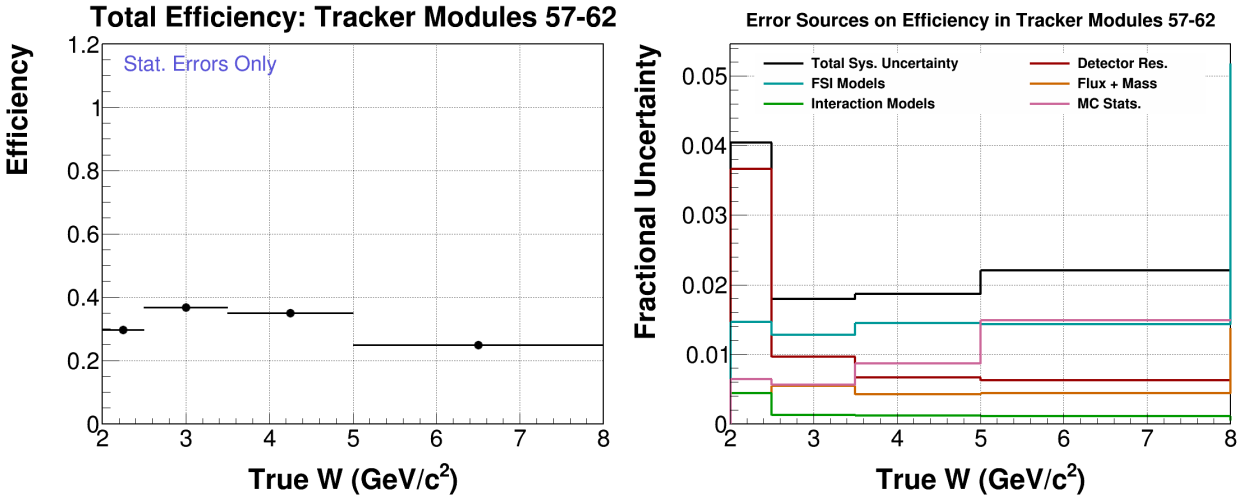

Figure E-111: Overall efficiency of events in the scintillator tracker module 57-62 as a function of true W (left) and the systematic uncertainty on the overall efficiency (right).

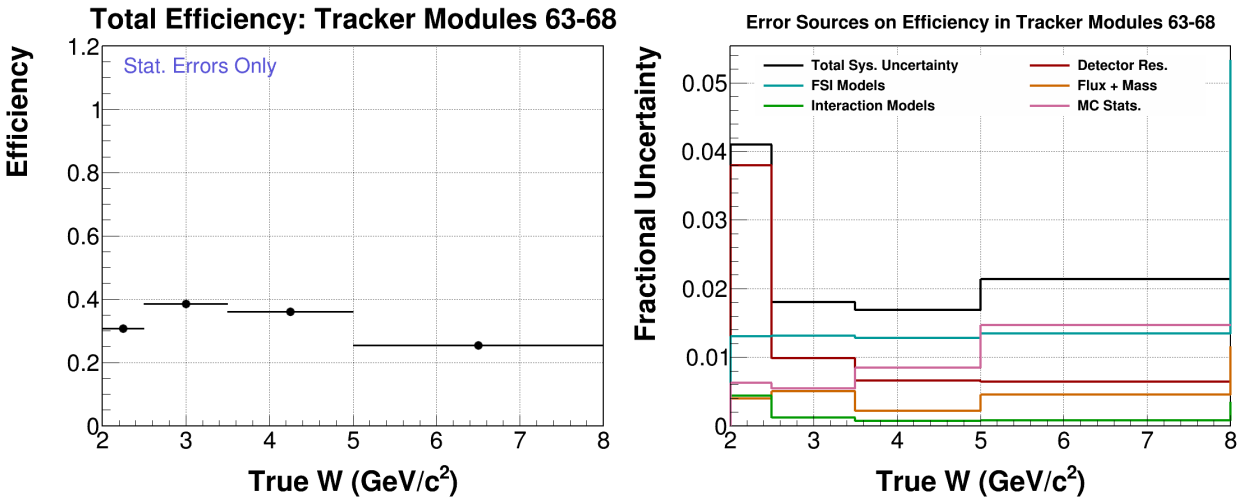

Figure E-112: Overall efficiency of events in the scintillator tracker module 63-68 as a function of true W (left) and the systematic uncertainty on the overall efficiency (right).

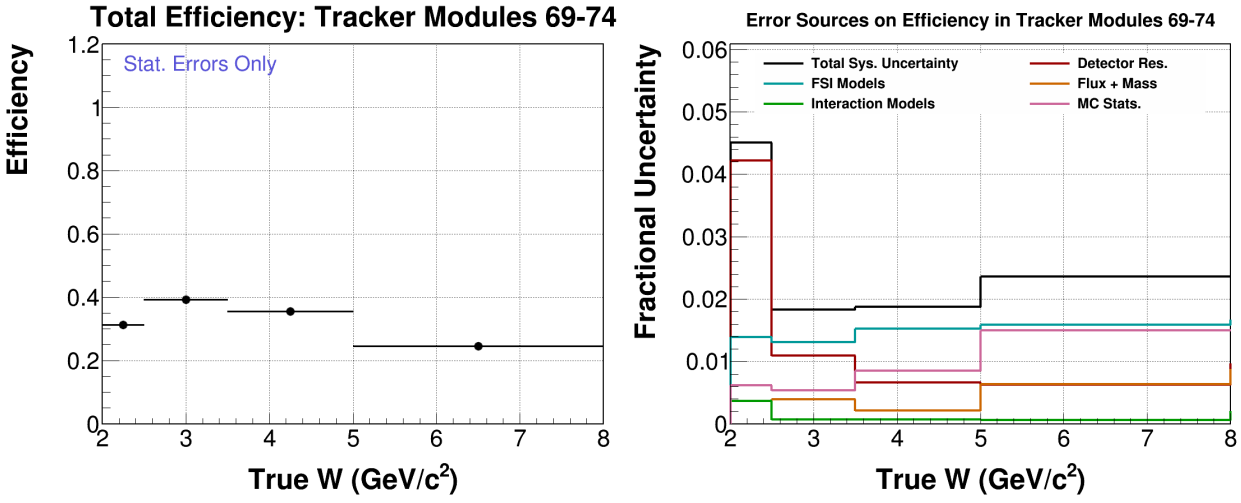

Figure E-113: Overall efficiency of events in the scintillator tracker module 69-74 as a function of true W (left) and the systematic uncertainty on the overall efficiency (right).

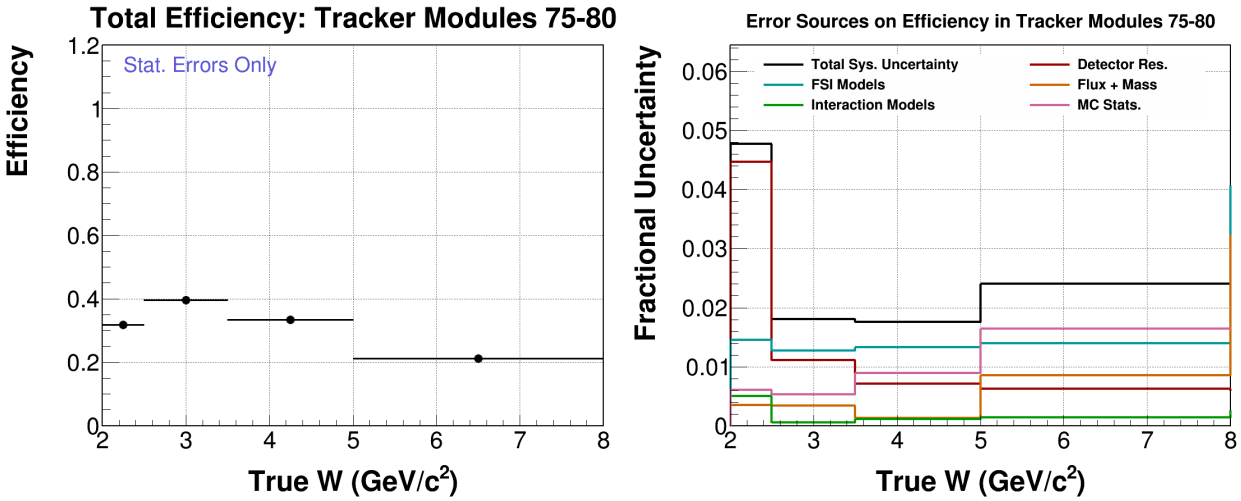

Figure E-114: Overall efficiency of events in the scintillator tracker module 75-80 as a function of true W (left) and the systematic uncertainty on the overall efficiency (right).

LIST OF REFERENCES

[1] D. Griffiths, Introduction to elementary particles, Wiley-VCH Verlag GmbH, 2009. doi:10.1002/9783527618460.

[2] C. L. Cowan, F. Reines, F. B. Harrison, H. W. Kruse, A. D. McGuire, Detection of the free neutrino: a confirmation, Science 124 (3212) (1956) 103–104. arXiv:http://science.sciencemag.org/content/124/3212/103.full.pdf, doi:10.1126/science.124.3212.103.
URL http://science.sciencemag.org/content/124/3212/103

[3] B. T. Cleveland, T. Daily, R. Davis, Jr., J. R. Distel, K. Lande, C. K. Lee, P. S. Wildenhain, J. Ullman, Measurement of the Solar Electron Neutrino Flux with the Homestake Chlorine Detector, The Astrophysical Journal 496 (1998) 505–526. doi:10.1086/305343.

[4] Y. Fukuda, et al., Evidence for oscillation of atmospheric neutrinos, Phys. Rev. Lett. 81 (1998) 1562–1567. doi:10.1103/PhysRevLett.81.1562.
URL https://link.aps.org/doi/10.1103/PhysRevLett.81.1562

[5] Q. R. Ahmad, et al., Direct evidence for neutrino flavor transformation from neutral-current interactions in the sudbury neutrino observatory, Phys. Rev. Lett. 89 (2002) 011301. doi:10.1103/PhysRevLett.89.011301.
URL https://link.aps.org/doi/10.1103/PhysRevLett.89.011301

[6] T. Katori, M. Martini, Neutrino nucleus cross sections for oscillation experiments, J. Phys. G45 (1) (2018) 013001. arXiv:1611.07770, doi:10.1088/1361-6471/aa8bf7.

[7] T. M. Collaboration, Hep portfolio review: Minerva proposal, internal Document (2018).
URL https://minerva-docdb.fnal.gov/cgi-bin/private/RetrieveFile?docid=17418

[8] S. L. Glashow, Partial Symmetries of Weak Interactions, Nucl. Phys. 22 (1961) 579–588. doi:10.1016/0029-5582(61)90469-2.

[9] S. Weinberg, A model of leptons, Phys. Rev. Lett. 19 (1967) 1264–1266. doi:10.1103/PhysRevLett.19.1264.
URL https://link.aps.org/doi/10.1103/PhysRevLett.19.1264

[10] Wikipedia, Standard model of elementary particles (2006).
URL https://commons.wikimedia.org/wiki/File:Standard_Model_of_Elementary_Particles.svg

[11] B. Kayser, Majorana neutrinos and their electromagnetic properties, Phys. Rev. D 26 (1982) 1662–1670. doi:10.1103/PhysRevD.26.1662.
URL https://link.aps.org/doi/10.1103/PhysRevD.26.1662

[12] J. Lykken, Big boost for fermilabs short-baseline neutrino experiments (2018).
URL http://news.fnal.gov/2018/06/big-boost-for-fermilabs-short-baseline-neutrino-experiments/

[13] K. Abe, et al., Combined analysis of neutrino and antineutrino oscillations at t2k, Phys. Rev. Lett. 118 (2017) 151801. doi:10.1103/PhysRevLett.118.151801.
URL https://link.aps.org/doi/10.1103/PhysRevLett.118.151801

[14] P. Adamson, et al., Constraints on oscillation parameters from ν_e appearance and ν_μ disappearance in nova, Phys. Rev. Lett. 118 (2017) 231801.
doi:10.1103/PhysRevLett.118.231801.
URL https://link.aps.org/doi/10.1103/PhysRevLett.118.231801

[15] D. C. Colley, et al., Cross-sections for Charged Current Neutrino and Anti-neutrino Interactions in the Energy Range 10-GeV to 50-GeV, Z. Phys. C2 (1979) 187.
doi:10.1007/BF01474659.

[16] W. G. Seligman, A next-to-leading-order qcd analysis of neutrino-iron structure functions at the tevatron, Ph.D. thesis, Columbia University (1 2007).

[17] D. C. Colley, et al., Cross-sections for Charged Current Neutrino and Anti-neutrino Interactions in the Energy Range 10-GeV to 50-GeV, Z. Phys. C2 (1979) 187.
doi:10.1007/BF01474659.

[18] J. G. Morfin, et al., Total Cross-sections and Nucleon Structure Functions in the Gargamelle SPS Neutrino / Anti-neutrino Experiment, Phys. Lett. 104B (1981) 235–238. doi:10.1016/0370-2693(81)90598-0.

[19] A. S. Vovenko, et al., -, Sov. J. Nucl. Phys. 30 (1979) 527.

[20] V. B. Anikeev, et al., Total cross-section measurements for muon-neutrino, anti-muon-neutrino interactions in 3-GeV - 30-GeV energy range with IHEP-JINR neutrino detector, Z. Phys. C70 (1996) 39–46. doi:10.1007/s002880050078.

[21] P. Adamson, et al., Neutrino and antineutrino inclusive charged-current cross section measurements with the minos near detector, Phys. Rev. D 81 (2010) 072002.
doi:10.1103/PhysRevD.81.072002.
URL https://link.aps.org/doi/10.1103/PhysRevD.81.072002

[22] Q. Wu, et al., A Precise measurement of the muon neutrino-nucleon inclusive charged current cross-section off an isoscalar target in the energy range 2.5 ¡ E(nu) ¡ 40-GeV by NOMAD, Phys. Lett. B660 (2008) 19–25. arXiv:0711.1183,
doi:10.1016/j.physletb.2007.12.027.

[23] M. Tzanov, et al., Precise measurement of neutrino and antineutrino differential cross sections, Phys. Rev. D 74 (2006) 012008. doi:10.1103/PhysRevD.74.012008.
URL https://link.aps.org/doi/10.1103/PhysRevD.74.012008

[24] N. J. Baker, P. L. Connolly, S. A. Kahn, M. J. Murtagh, R. B. Palmer, N. P. Samios, M. Tanaka, Total cross sections for $\nu_\mu n$ and $\nu_\mu p$ charged-current interactions in the 7-foot bubble chamber, Phys. Rev. D 25 (1982) 617–623.
doi:10.1103/PhysRevD.25.617.
URL https://link.aps.org/doi/10.1103/PhysRevD.25.617

[25] D. S. Baranov, et al., Measurements of the $\nu_\mu N$ Total Cross-section at 2-GeV - 30-GeV in Skat Neutrino Experiment, Phys. Lett. 81B (1979) 255–257. doi:10.1016/0370-2693(79)90536-7.

[26] S. Ciampolillo, et al., Total Cross-section for Neutrino Charged Current Interactions at 3-GeV and 9-GeV, Phys. Lett. 84B (1979) 281–284. doi:10.1016/0370-2693(79)90303-4.

[27] Y. Nakajima, et al., Measurement of inclusive charged current interactions on carbon in a few-GeV neutrino beam, Phys. Rev. D83 (2011) 012005. arXiv:1011.2131, doi:10.1103/PhysRevD.83.012005.

[28] S. J. Barish, et al., Study of neutrino interactions in hydrogen and deuterium: Description of the experiment and study of the reaction $\nu + d \to \mu^- + p + p_s$, Phys. Rev. D 16 (1977) 3103–3121. doi:10.1103/PhysRevD.16.3103.
URL https://link.aps.org/doi/10.1103/PhysRevD.16.3103

[29] D. Allasia, et al., Investigation of exclusive channels in /-deuteron charged current interactions, Nuclear Physics B 343 (2) (1990) 285 – 309. doi:https://doi.org/10.1016/0550-3213(90)90472-P.
URL http://www.sciencedirect.com/science/article/pii/055032139090472P

[30] N. J. Baker, A. M. Cnops, P. L. Connolly, S. A. Kahn, M. J. Murtagh, R. B. Palmer, N. P. Samios, M. Tanaka, Study of the isospin structure of single-pion production in charged-current neutrino interactions, Phys. Rev. D 23 (1981) 2495–2498. doi:10.1103/PhysRevD.23.2495.
URL https://link.aps.org/doi/10.1103/PhysRevD.23.2495

[31] T. Kitagaki, et al., High-energy quasielastic $\nu_\mu n \to \mu^- p$ scattering in deuterium, Phys. Rev. D 28 (1983) 436–442. doi:10.1103/PhysRevD.28.436.
URL https://link.aps.org/doi/10.1103/PhysRevD.28.436

[32] S. Bonetti, et al., Study of Quasielastic Reactions of Neutrino and anti-neutrino in Gargamelle, Nuovo Cim. A38 (1977) 260–270. doi:10.1007/BF02730023.

[33] A. A. Aguilar-Arevalo, et al., First measurement of the muon neutrino charged current quasielastic double differential cross section, Phys. Rev. D 81 (2010) 092005. doi:10.1103/PhysRevD.81.092005.
URL https://link.aps.org/doi/10.1103/PhysRevD.81.092005

[34] V. Lyubushkin, et al., A study of quasi-elastic muon neutrino and antineutrino scattering in the nomad experiment, The European Physical Journal C 63 (3) (2009) 355–381. doi:10.1140/epjc/s10052-009-1113-0.
URL https://doi.org/10.1140/epjc/s10052-009-1113-0

[35] H. G. Bohlen, et al., Inelastic scattering of20ne and12c on58ni and the three-body continuum, Zeitschrift für Physik A Atoms and Nuclei 320 (2) (1985) 237–251. doi:10.1007/BF01881271.
URL https://doi.org/10.1007/BF01881271

[36] J. Brunner, et al., Quasielastic nucleon and hyperon production by neutrinos and antineutrinos with energies below 30 gev, Zeitschrift für Physik C Particles and Fields 45 (4) (1990) 551–555. doi:10.1007/BF01556267.
URL https://doi.org/10.1007/BF01556267

[37] D. Casper, The Nuance neutrino physics simulation, and the future, Nucl. Phys. Proc. Suppl. 112 (2002) 161–170, [,161(2002)]. arXiv:hep-ph/0208030, doi:10.1016/S0920-5632(02)01756-5.

[38] J. A. Formaggio, G. P. Zeller, From eV to EeV: Neutrino Cross Sections Across Energy Scales, Rev. Mod. Phys. 84 (2012) 1307–1341. arXiv:1305.7513, doi:10.1103/RevModPhys.84.1307.

[39] C. Giunti, C. W. Kim, Fundamentals of Neutrino Physics and Astrophysics, University Press, 2007.

[40] W. K. Tang, Bjorken scaling (2009).
URL http://www.scholarpedia.org/article/Bjorken_scaling

[41] J. D. Bjorken, Asymptotic sum rules at infinite momentum, Phys. Rev. 179 (1969) 1547–1553. doi:10.1103/PhysRev.179.1547.
URL https://link.aps.org/doi/10.1103/PhysRev.179.1547

[42] J. I. Friedman, H. W. Kendall, Deep inelastic electron scattering, Annual Review of Nuclear Science 22 (1) (1972) 203–254.
arXiv:https://doi.org/10.1146/annurev.ns.22.120172.001223, doi:10.1146/annurev.ns.22.120172.001223.
URL https://doi.org/10.1146/annurev.ns.22.120172.001223

[43] B. Carithers, P. Grannis, Discovery of the top quark, SLAC Beam Line 25N3 (1995) 4–16, [SLAC Beam Line25,4(1995)].

[44] F. J. P. Soler, C. D. Froggatt, F. Muheim (Eds.), Neutrinos in particle physics, astrophysics and cosmology. Proceedings, 61st Scottish Universities Summer School in Physics, SUSSP61, St. Andrews, UK, August 8-23, 2006, 2009.
URL http://www.crcpress.com/product/isbn/9781420082395

[45] A. V. Manohar, An Introduction to spin dependent deep inelastic scattering, in: Lake Louise Winter Institute: Symmetry and Spin in the Standard Model Lake Louise, Alberta, Canada, February 23-29, 1992, 1992, pp. 1–46. arXiv:hep-ph/9204208.

[46] C. Patrignani, et al., Review of Particle Physics, Chin. Phys. C40 (10) (2016) 100001. doi:10.1088/1674-1137/40/10/100001.

[47] H. Georgi, H. D. Politzer, Freedom at moderate energies: Masses in color dynamics, Phys. Rev. D 14 (1976) 1829–1848. doi:10.1103/PhysRevD.14.1829.
URL https://link.aps.org/doi/10.1103/PhysRevD.14.1829

[48] B. Z. Kopeliovich, J. G. Morfin, I. Schmidt, Nuclear Shadowing in Electro-Weak Interactions, Prog. Part. Nucl. Phys. 68 (2013) 314–372. arXiv:1208.6541, doi:10.1016/j.ppnp.2012.09.004.

[49] J. I. Friedman, Deep inelastic scattering: Comparisons with the quark model, Rev. Mod. Phys. 63 (1991) 615–627. doi:10.1103/RevModPhys.63.615.
URL https://link.aps.org/doi/10.1103/RevModPhys.63.615

[50] D. F. Geesaman, K. Saito, A. W. Thomas, The nuclear emc effect, Annual Review of Nuclear and Particle Science 45 (1) (1995) 337–390.
arXiv:https://doi.org/10.1146/annurev.ns.45.120195.002005,
doi:10.1146/annurev.ns.45.120195.002005.
URL https://doi.org/10.1146/annurev.ns.45.120195.002005

[51] Z. Ahmed, et al., New precision limit on the strange vector form factors of the proton, Phys. Rev. Lett. 108 (2012) 102001. doi:10.1103/PhysRevLett.108.102001.
URL https://link.aps.org/doi/10.1103/PhysRevLett.108.102001

[52] J. J. Aubert, et al., The ratio of the nucleon structure functions $f2_n$ for iron and deuterium, Phys. Lett. 123B (1983) 275–278. doi:10.1016/0370-2693(83)90437-9.

[53] G. Berlad, A. Dar, G. Eilam, Quark-parton model of nuclear production, Phys. Rev. D 22 (1980) 1547–1573. doi:10.1103/PhysRevD.22.1547.
URL https://link.aps.org/doi/10.1103/PhysRevD.22.1547

[54] A. Bodek, J. L. Ritchie, Fermi-motion effects in deep-inelastic lepton scattering from nuclear targets, Phys. Rev. D 23 (1981) 1070–1091.
doi:10.1103/PhysRevD.23.1070.
URL https://link.aps.org/doi/10.1103/PhysRevD.23.1070

[55] A. Bodek, J. L. Ritchie, Further studies of fermi-motion effects in lepton scattering from nuclear targets, Phys. Rev. D 24 (1981) 1400–1402.
doi:10.1103/PhysRevD.24.1400.
URL https://link.aps.org/doi/10.1103/PhysRevD.24.1400

[56] L. L. Frankfurt, M. I. Strikman, High-Energy Phenomena, Short Range Nuclear Structure and QCD, Phys. Rept. 76 (1981) 215–347.
doi:10.1016/0370-1573(81)90129-0.

[57] K. Ackerstaff, et al., Nuclear effects on R = σ_L / σ_T in deep inelastic scattering, Phys. Lett. B475 (2000) 386–394, [Erratum: Phys. Lett.B567,339(2003)].
arXiv:hep-ex/9910071,
doi:10.1016/j.physletb.2003.06.044,10.1016/S0370-2693(99)01493-8.

[58] J. Gomez, et al., Measurement of the A-dependence of deep inelastic electron scattering, Phys. Rev. D49 (1994) 4348–4372. doi:10.1103/PhysRevD.49.4348.

[59] J. Seely, et al., New measurements of the EMC effect in very light nuclei, Phys. Rev. Lett. 103 (2009) 202301. arXiv:0904.4448, doi:10.1103/PhysRevLett.103.202301.

[60] K. Rith, Present Status of the EMC effect, Subnucl. Ser. 51 (2015) 431–449. arXiv:1402.5000.

[61] D. Higinbotham, et al., The emc effect still puzzles after 30 years.

[62] I. Cloet, W. Bentz, A. Thomas, Emc and polarized emc effects in nuclei, Physics Letters B 642 (2006) 210–217.

[63] A. M. Cooper-Sarkar, et al., An Investigation of the Emc Effect Using Anti-neutrinos Interactions in Deuterium and Neon, Phys. Lett. 141B (1984) 133–139. doi:10.1016/0370-2693(84)90576-8.

[64] H. Abramowicz, et al., Precision measurement of $sin^2\theta_W$ from semileptonic neutrino scattering, Phys. Rev. Lett. 57 (1986) 298–301. doi:10.1103/PhysRevLett.57.298. URL https://link.aps.org/doi/10.1103/PhysRevLett.57.298

[65] J. Hanlon, R. Burnstein, H. Rubin, M. Kalelkar, E. B. Brucker, P. F. Jacques, E. Koller, R. J. Plano, P. E. Stamer, C. Chang, S. Kunori, G. Snow, D. Son, D. Zieminska, T. Kafka, W. Mann, A. Napier, J. Schneps, T. Kitagaki, Y. Yanokura, Comparison of cross sections from deep-inelastic neutrino scattering on neon and deuterium, Physical review D: Particles and fields 32 (1985) 2441–2444.

[66] J. Guy, et al., A study of the emc effect using neutrino and antineutrino interactions in neon and deuterium, Zeitschrift für Physik C Particles and Fields 36 (3) (1987) 337–348. doi:10.1007/BF01573927. URL https://doi.org/10.1007/BF01573927

[67] J. Mousseau, et al., Measurement of Partonic Nuclear Effects in Deep-Inelastic Neutrino Scattering using MINERvA, Phys. Rev. D93 (7) (2016) 071101. arXiv:1601.06313, doi:10.1103/PhysRevD.93.071101.

[68] M. Arneodo, et al., The q2 dependence of the structure function ratio f2sn/f2c and the difference rsn rc deep inelastic muon scattering, Nuclear Physics B 481 (1) (1996) 23 – 39. doi:https://doi.org/10.1016/S0550-3213(96)90119-4. URL http://www.sciencedirect.com/science/article/pii/S0550321396901194

[69] R. Smith, E. Moniz, Neutrino reactions on nuclear targets, Nuclear Physics B 43 (1972) 605 – 622. doi:https://doi.org/10.1016/0550-3213(72)90040-5. URL http://www.sciencedirect.com/science/article/pii/0550321372900405

[70] A. Kayis-Topaksu, et al., Leading order analysis of neutrino induced dimuon events in the CHORUS experiment, Nucl. Phys. B798 (2008) 1–16. arXiv:0804.1869, doi:10.1016/j.nuclphysb.2008.02.013.

[71] O. Samoylov, et al., A Precision Measurement of Charm Dimuon Production in Neutrino Interactions from the NOMAD Experiment, Nucl. Phys. B876 (2013) 339–375. arXiv:1308.4750, doi:10.1016/j.nuclphysb.2013.08.021.

[72] M. Tzanov, et al., Precise measurement of neutrino and antineutrino differential cross sections, Phys. Rev. D 74 (2006) 012008. doi:10.1103/PhysRevD.74.012008.
URL https://link.aps.org/doi/10.1103/PhysRevD.74.012008

[73] K. Kovařík, I. Schienbein, F. I. Olness, J. Y. Yu, C. Keppel, J. G. Morfín, J. F. Owens, T. Stavreva, Nuclear corrections in neutrino-nucleus deep inelastic scattering and their compatibility with global nuclear parton-distribution-function analyses, Phys. Rev. Lett. 106 (2011) 122301. doi:10.1103/PhysRevLett.106.122301.
URL https://link.aps.org/doi/10.1103/PhysRevLett.106.122301

[74] K. Kovařík, A. Kusina, T. Ježo, D. B. Clark, C. Keppel, F. Lyonnet, J. G. Morfín, F. I. Olness, J. F. Owens, I. Schienbein, J. Y. Yu, ncteq15: Global analysis of nuclear parton distributions with uncertainties in the cteq framework, Phys. Rev. D 93 (2016) 085037. doi:10.1103/PhysRevD.93.085037.
URL https://link.aps.org/doi/10.1103/PhysRevD.93.085037

[75] P. Adamson, et al., The NuMI Neutrino Beam, Nucl. Instrum. Meth. A806 (2016) 279–306. arXiv:1507.06690, doi:10.1016/j.nima.2015.08.063.

[76] R. M. Zwaska, Accelerator Systems and Instrumentation for the NuMI Neutrino Beam (Page 5, Figure 1-2), Ph.D. thesis, Texas U. (2005). doi:10.2172/879065.
URL http://lss.fnal.gov/cgi-bin/find_paper.pl?thesis-2005-73

[77] Nuruzzaman, POT for the Medium Energy Run, internal Document (2017).
URL http://minerva-docdb.fnal.gov:8080/cgi-bin/ShowDocument?docid=12813

[78] Fermilab, Fermilab accelerator complex (2016).
URL http://www.fnal.gov/pub/science/particle-accelerators/images/accel-complex-animation.gif

[79] A. Norrick, Approved me flux plots, internal Document (2017).
URL https://minerva-docdb.fnal.gov/cgi-bin/private/ShowDocument?docid=9956

[80] Fermilab, Numi magnetic focusing horns (2017).
URL http://targets.fnal.gov/NuMI_horns.html

[81] L. Aliaga, , et al., Design, calibration, and performance of the minerva detector, Nuclear Instruments and Methods in Physics Research Section A: Accelerators, Spectrometers, Detectors and Associated Equipment 743 (2014) 130 – 159. doi:https://doi.org/10.1016/j.nima.2013.12.053.
URL http://www.sciencedirect.com/science/article/pii/S0168900214000035

[82] Minos Collaboration, D. G. Michael, P. Adamson, T. Alexopoulos, W. W. M. Allison, G. J. Alner, K. Anderson, C. Andreopoulos, M. Andrews, R. Andrews, , et al., The

magnetized steel and scintillator calorimeters of the MINOS experiment, Nuclear Instruments and Methods in Physics Research A 596 (2008) 190–228. arXiv:0805.3170, doi:10.1016/j.nima.2008.08.003.

[83] H. Budd, The MINERvA Experiment, in: TIPP 2011: Technology and Instrumentation in Particle Physics, 2011, p. 5.
URL https://indico.cern.ch/event/102998/contributions/17172/attachments/10549/15428/tipp_11_v3.pdf

[84] E. Gallas, J. Li, Polishing optical fibers for the D0 ICD in Run II, FERMILAB Reportsdoi:10.2172/2304.

[85] H. P. K.K., Photomultiplier Tubes - Basics and Applications, Hamamatsu Photonics K.K., Electron Tube Division, 2007.

[86] G. N. Perdue, et al., The MINERνA Data Acquisition System and Infrastructure, Nucl. Instrum. Meth. A694 (2012) 179–192. arXiv:1209.1120, doi:10.1016/j.nima.2012.08.024.

[87] S. M. Ross, et al., Peirce's criterion for the elimination of suspect experimental data , Journal of Engineering Technology.

[88] R. Bradford, WBS9 Closeout, internal Document (2010).
URL https://minerva-docdb.fnal.gov/cgi-bin/private/RetrieveFile?docid=4604

[89] N. Tagg, et al., Performance of 64-anode photomultipliers for use with wavelength-shifting optical fibres, Nucl. Instrum. Meth. A539 (2005) 668–678. arXiv:physics/0408055, doi:10.1016/j.nima.2004.11.003.

[90] C. Andreopoulos, et al., The GENIE neutrino Monte Carlo generator, Nuclear Instruments and Methods in Physics Research Section A: Accelerators, Spectrometers, Detectors and Associated Equipment 614 (1) (2010) 87 – 104. doi:http://dx.doi.org/10.1016/j.nima.2009.12.009.
URL http://www.sciencedirect.com/science/article/pii/S0168900209023043

[91] L. Aliaga Soplin, Neutrino Flux Prediction for the NuMI Beamline, Ph.D. thesis, William-Mary Coll. (2016). doi:10.2172/1250884.
URL http://lss.fnal.gov/archive/thesis/2000/fermilab-thesis-2016-03.pdf

[92] S. Agostinelli, et al., GEANT4: A Simulation toolkit, Nucl. Instrum. Meth. A506 (2003) 250–303. doi:10.1016/S0168-9002(03)01368-8.

[93] M. P. Guthrie, R. G. Alsmiller, H. W. Bertini, Calculation of the capture of negative pions in light elements and comparison with experiments pertaining to cancer radiotherapy, Nucl. Instrum. Meth. 66 (1968) 29–36. doi:10.1016/0029-554X(68)90054-2.

[94] B. Andersson, G. Gustafson, B. Nilsson-Almqvist, A model for low-pt hadronic reactions with generalizations to hadron-nucleus and nucleus-nucleus collisions, Nuclear Physics B 281 (1) (1987) 289 – 309. doi:https://doi.org/10.1016/0550-3213(87)90257-4.
URL http://www.sciencedirect.com/science/article/pii/0550321387902574

[95] C. Alt, et al., Inclusive production of charged pions in p+C collisions at 158-GeV/c beam momentum, Eur. Phys. J. C49 (2007) 897–917. arXiv:hep-ex/0606028, doi:10.1140/epjc/s10052-006-0165-7.

[96] J. M. Paley, et al., Measurement of Charged Pion Production Yields off the NuMI Target, Phys. Rev. D90 (3) (2014) 032001. arXiv:1404.5882, doi:10.1103/PhysRevD.90.032001.

[97] J. M. Paley, Numi target hadron production measurement in mipp, Journal of Physics: Conference Series 136 (4) (2008) 042037.
URL http://stacks.iop.org/1742-6596/136/i=4/a=042037

[98] G. Bellettini, Proton-nuclei cross sections at 20 GeV, Nucl. Phys. 79 (1966) 609–624. doi:10.1016/0029-5582(66)90267-7.

[99] R. P. Feynman, Very high-energy collisions of hadrons, Phys. Rev. Lett. 23 (1969) 1415–1417. doi:10.1103/PhysRevLett.23.1415.

[100] T. Bohlen, F. Cerutti, M. Chin, A. Fasso, A. Ferrari, P. Ortega, A. Mairani, P. Sala, G. Smirnov, V. Vlachoudis, The {FLUKA} code: Developments and challenges for high energy and medical applications, Nuclear Data Sheets 120 (2014) 211 – 214. doi:http://dx.doi.org/10.1016/j.nds.2014.07.049.

[101] N. Abgrall, et al., Measurements of Cross Sections and Charged Pion Spectra in Proton-Carbon Interactions at 31 GeV/c, Phys. Rev. C84 (2011) 034604. arXiv:1102.0983, doi:10.1103/PhysRevC.84.034604.

[102] D. S. Barton, et al., Experimental Study of the a-Dependence of Inclusive Hadron Fragmentation, Phys. Rev. D27 (1983) 2580. doi:10.1103/PhysRevD.27.2580.

[103] S. M. Seun, Measurement of $\pi - K$ ratios from the NuMI target, Ph.D. thesis, Harvard U. (2007).
URL http://lss.fnal.gov/cgi-bin/find_paper.pl?thesis-2007-61

[104] A. Ferrari, P. R. Sala, A. Fasso, J. Ranft, FLUKA: A multi-particle transport code (Program version 2005), SLAC Reports.

[105] B. Baatar, et al., Inclusive production of protons, anti-protons, neutrons, deuterons and tritons in p+C collisions at 158 GeV/c beam momentum, Eur. Phys. J. C73 (4) (2013) 2364. arXiv:1207.6520, doi:10.1140/epjc/s10052-013-2364-3.

[106] P. Skubic, et al., Neutral Strange Particle Production by 300-GeV Protons, Phys. Rev. D18 (1978) 3115–3144. doi:10.1103/PhysRevD.18.3115.

[107] Z. Pavlovic, Observation of Disappearance of Muon Neutrinos in the NuMI Beam, Ph.D. thesis, Texas U. (2008).
URL http://lss.fnal.gov/cgi-bin/find_paper.pl?thesis-2008-59

[108] L. Aliaga Soplin, Neutrino Flux Prediction for the NuMI Beamline (Page 176. Figure 5-14), Ph.D. thesis, William-Mary Coll. (2016). doi:10.2172/1250884.
URL http://lss.fnal.gov/archive/thesis/2000/fermilab-thesis-2016-03.pdf

[109] D. Rimal, Improvements in the NuMI Flux Prediction at MINERvA (slide 6), in: APS April Meeting 2018, 2018, p. 6.
URL https://absuploads.aps.org/presentation.cfm?pid=14108

[110] J. Park, Neutrino-electron scattering in minerva for constraining the numi neutrino flux, Ph.D. thesis, Rochester U. (2013).

[111] J. Devan, et al., Measurements of the Inclusive Neutrino and Antineutrino Charged Current Cross Sections in MINERvA Using the Low-ν Flux Method, Phys. Rev. D94 (11) (2016) 112007. arXiv:1610.04746, doi:10.1103/PhysRevD.94.112007.

[112] A. Bodek, U. Sarica, D. Naples, L. Ren, Methods to Determine Neutrino Flux at Low Energies:Investigation of the Low ν Method, Eur. Phys. J. C 72 (2012) 1973. arXiv:1201.3025, doi:10.1140/epjc/s10052-012-1973-6.

[113] M. Collaborations, Minerva status report and request for antineutrino running, internal Document (2017).
URL https://minerva-docdb.fnal.gov/cgi-bin/private/ShowDocument?docid=16296

[114] A. Bodek, J. L. Ritchie, Fermi-motion effects in deep-inelastic lepton scattering from nuclear targets, Phys. Rev. D 23 (1981) 1070–1091. doi:10.1103/PhysRevD.23.1070.
URL http://link.aps.org/doi/10.1103/PhysRevD.23.1070

[115] A. Bodek, U. K. Yang, Higher twist, xi(omega) scaling, and effective LO PDFs for lepton scattering in the few GeV region, J. Phys. G29 (2003) 1899–1906. arXiv:hep-ex/0210024, doi:10.1088/0954-3899/29/8/369.

[116] D. Rein, L. M. Sehgal, Neutrino Excitation of Baryon Resonances and Single Pion Production, Annals Phys. 133 (1981) 79–153. doi:10.1016/0003-4916(81)90242-6.

[117] L. W. Whitlow, S. Rock, A. Bodek, E. M. Riordan, S. Dasu, A Precise extraction of R = sigma-L / sigma-T from a global analysis of the SLAC deep inelastic e p and e d scattering cross-sections, Phys. Lett. B250 (1990) 193–198. doi:10.1016/0370-2693(90)91176-C.

[118] M. Glck, E. Reya, A. Vogt, Dynamical parton distributions revisited, Eur. Phys. J. C5 (1998) 461–470. arXiv:hep-ph/9806404, doi:10.1007/s100529800978,10.1007/s100520050289.

[119] R. P. Feynman, M. Kislinger, F. Ravndal, Current matrix elements from a relativistic quark model, Phys. Rev. D3 (1971) 2706–2732. doi:10.1103/PhysRevD.3.2706.

[120] K. S. Kuzmin, V. V. Lyubushkin, V. A. Naumov, Axial masses in quasielastic neutrino scattering and single-pion neutrinoproduction on nucleons and nuclei, Acta Phys. Polon. B37 (2006) 2337–2348. arXiv:hep-ph/0606184.

[121] Z. Koba, H. B. Nielsen, P. Olesen, Scaling of multiplicity distributions in high-energy hadron collisions, Nucl. Phys. B40 (1972) 317–334. doi:10.1016/0550-3213(72)90551-2.

[122] T. Sjostrand, S. Mrenna, P. Z. Skands, PYTHIA 6.4 Physics and Manual, JHEP 05 (2006) 026. arXiv:hep-ph/0603175, doi:10.1088/1126-6708/2006/05/026.

[123] B. Andersson, G. Gustafson, G. Ingelman, T. Sjostrand, Parton Fragmentation and String Dynamics, Phys. Rept. 97 (1983) 31–145. doi:10.1016/0370-1573(83)90080-7.

[124] D. S. Baranov, et al., An Estimate For The Formation Length of Hadrons in Neutrino Interactions, PHE 84-04.

[125] S. G. Mashnik, A. J. Sierk, K. K. Gudima, M. I. Baznat, CEM03 and LAQGSM03: New modeling tools for nuclear applications, J. Phys. Conf. Ser. 41 (2006) 340–351. arXiv:nucl-th/0510070, doi:10.1088/1742-6596/41/1/037.

[126] H. W. Bertini, M. P. Guthrie, News item results from medium-energy intranuclear-cascade calculation, Nucl. Phys. A169 (1971) 670–672. doi:10.1016/0375-9474(71)90710-X.

[127] G. N. Perdue, Event Reconstruction in MINERvA (slide 15) , internal Document (2015).
URL https://minerva-docdb.fnal.gov/cgi-bin/private/RetrieveFile?docid=10017

[128] R. Fruhwirth, Application of Kalman filtering to track and vertex fitting, Nucl. Instrum. Meth. A262 (1987) 444–450. doi:10.1016/0168-9002(87)90887-4.

[129] W. D. Hulsbergen, Decay chain fitting with a Kalman filter, Nuclear Instruments and Methods in Physics Research A 552 (2005) 566–575. doi:10.1016/j.nima.2005.06.078.

[130] D. Michael, et al., The magnetized steel and scintillator calorimeters of the minos experiment, Nuclear Instruments and Methods in Physics Research Section A: Accelerators, Spectrometers, Detectors and Associated Equipment 596 (2008) 190?228.

[131] R. Ospanov, A measurement of muon neutrino disappearance with the MINOS detectors and NuMI beam, Ph.D. thesis, The University of Texas at Austin (2008).

[132] T. M. Collaboration, Neutrino Oscillation Physics at Fermilab: The NuMI-MINOS Project, FERMILAB Technical Reports.

[133] L. Aliaga, et al., MINERvA neutrino detector response measured with test beam data, Nucl. Instrum. Meth. A789 (2015) 28–42. arXiv:1501.06431, doi:10.1016/j.nima.2015.04.003.

[134] I. Goodfellow, Y. Bengio, A. Courville, Deep Learning, MIT Press, 2016, http://www.deeplearningbook.org.

[135] C. M. Bishop, Pattern Recognition and Machine Learning (Information Science and Statistics), 1st Edition, Springer, 2007.
URL http://www.amazon.com/Pattern-Recognition-Learning-Information-Statistics/dp/0387310738%3FSubscriptionId%3D13CT5CVB80YFWJEPWS02%26tag%3Dws%26linkCode%3Dxm2%26camp%3D2025%26creative%3D165953%26creativeASIN%3D0387310738

[136] M. A. Nielsen, Neural Networks and Deep Learning, Determination Press, 2015.

[137] S. Har-peled, D. Roth, D. Zimak, Constraint classification: A new approach to multiclass classification and ranking, in: In Advances in Neural Information Processing Systems 15, 2002, pp. 365–379.

[138] E. Alpaydin, Introduction to Machine Learning, 2nd Edition, Adaptive Computation and Machine Learning, The MIT Press, 2009.
URL https://mitpress.mit.edu/books/introduction-machine-learning-second-edition

[139] K. P. Burnham, D. R. Anderson, Model selection and multimodel inference: a practical information-theoretic approach, 2nd Edition, Springer, 2002.

[140] D. M. Hawkins, The problem of overfitting, J. Chem. Inf. Comput. Sci. 44 (1) (2004) 1–12.

[141] C. M. Bishop, Pattern recognition and machine learning, 5th Edition, Information science and statistics, Springer, 2007.
URL http://www.worldcat.org/oclc/71008143

[142] T. Fawcett, An introduction to roc analysis, Pattern Recognition Letters 27 (8) (2006) 861 – 874, rOC Analysis in Pattern Recognition.
doi:https://doi.org/10.1016/j.patrec.2005.10.010.
URL http://www.sciencedirect.com/science/article/pii/S016786550500303X

[143] L. Le Cun, Y.and Bottou, Y. Bengio, P. Haffner, Gradient-Based Learning Applied to Document Recognition, Proc. of the IEEE.

[144] A. Krizhevsky, I. Sutskever, G. E. Hinton, Imagenet classification with deep convolutional neural networks, in: F. Pereira, C. J. C. Burges, L. Bottou, K. Q. Weinberger (Eds.), Advances in Neural Information Processing Systems 25, Curran Associates, Inc., 2012, pp. 1097–1105.

URL http://papers.nips.cc/paper/
4824-imagenet-classification-with-deep-convolutional-neural-networks.pdf

[145] M. Plotke, Before any kernel convolution (2013).
URL https://en.wikipedia.org/wiki/File:Vd-Orig.png

[146] M. Plotke, Edge detection (2013).
URL https://en.wikipedia.org/wiki/File:Vd-Edge3.png

[147] K. Fukushima, Neocognitron: A hierarchical neural network capable of visual pattern recognition, Neural Networks 1 (2) (1988) 119 – 130.
doi:https://doi.org/10.1016/0893-6080(88)90014-7.
URL "http://www.sciencedirect.com/science/article/pii/0893608088900147"

[148] T. D. Pham, D. E. Lee, K. R. Park, Multi-national banknote classification based on visible-light line sensor and convolutional neural network, Sensors 17 (7).
URL http://www.mdpi.com/1424-8220/17/7/1595

[149] Y. LeCun, B. Boser, J. S. Denker, D. Henderson, R. E. Howard, W. Hubbard, L. D. Jackel, Backpropagation applied to handwritten zip code recognition, Neural Computation 1 (4) (1989) 541–551. doi:10.1162/neco.1989.1.4.541.

[150] N. Srivastava, G. Hinton, A. Krizhevsky, I. Sutskever, R. Salakhutdinov, Dropout: A simple way to prevent neural networks from overfitting, Journal of Machine Learning Research 15 (2014) 1929–1958.
URL http://jmlr.org/papers/v15/srivastava14a.html

[151] K. Simonyan, A. Zisserman, Very deep convolutional networks for large-scale image recognition, CoRR abs/1409.1556. arXiv:1409.1556.
URL http://arxiv.org/abs/1409.1556

[152] R. Al-Rfou, et al., Theano: A python framework for fast computation of mathematical expressions, CoRR abs/1605.02688. arXiv:1605.02688.
URL http://arxiv.org/abs/1605.02688

[153] Y. Jia, E. Shelhamer, J. Donahue, S. Karayev, J. Long, R. B. Girshick, S. Guadarrama, T. Darrell, Caffe: Convolutional architecture for fast feature embedding, CoRR abs/1408.5093. arXiv:1408.5093.
URL http://arxiv.org/abs/1408.5093

[154] M. Abadi, et al., TensorFlow: Large-scale machine learning on heterogeneous systems, software available from tensorflow.org (2015).
URL https://www.tensorflow.org/

[155] R. Brun, F. Rademakers, Root an object oriented data analysis framework, Nuclear Instruments and Methods in Physics Research Section A: Accelerators, Spectrometers, Detectors and Associated Equipment 389 (1) (1997) 81 – 86, new Computing Techniques in Physics Research V.

doi:https://doi.org/10.1016/S0168-9002(97)00048-X.
URL http://www.sciencedirect.com/science/article/pii/S016890029700048X

[156] The HDF Group, Hierarchical Data Format, version 5, http://www.hdfgroup.org/HDF5/ (1997-NNNN).

[157] B. G. Tice, et al., Measurement of Ratios of ν_μ Charged-Current Cross Sections on C, Fe, and Pb to CH at Neutrino Energies 2-20 GeV, Phys. Rev. Lett. 112 (23) (2014) 231801. arXiv:1403.2103, doi:10.1103/PhysRevLett.112.231801.

[158] F. James, M. Winkler, MINUIT Users Guide, http://seal.web.cern.ch/seal/documents/minuit/mnusersguide.pdf (2004).

[159] J. Mousseau, First Search for the EMC Effect and Nuclear Shadowing in Neutrino Nucleus Deep Inelastic Scattering at MINERvA, Ph.D. thesis, Florida U (2015). doi:10.1007/978-3-319-44841-1.
URL http://lss.fnal.gov/archive/thesis/2000/fermilab-thesis-2015-27.pdf

[160] G. D'Agostini, A multidimensional unfolding method based on Bayes' theorem, Nuclear Instruments and Methods in Physics Research A 362 (1995) 487–498. doi:10.1016/0168-9002(95)00274-X.

[161] J. Mousseau, Genie cross section weight note, internal Document (2013).
URL https://minerva-docdb.fnal.gov/cgi-bin/private/RetrieveFile?docid=7565

[162] C. Patrick, Measurement of the Antineutrino Double-Differential Charged-Current Quasi-Elastic Scattering Cross Section at MINERvA, Ph.D. thesis, Northwestern U. (2016). doi:10.1007/978-3-319-69087-2.
URL http://lss.fnal.gov/archive/thesis/2000/fermilab-thesis-2016-04.pdf

[163] B. Tice, Analysis of charged current neutrino interactions on nuclear targets, internal Document (2013).
URL https://minerva-docdb.fnal.gov/cgi-bin/private/RetrieveFile?docid=8854

[164] A. Norrick, Our detector is too heavy: The saga, internal Document (2016).
URL https://minerva-docdb.fnal.gov/cgi-bin/private/RetrieveFile?docid=11686

BIOGRAPHICAL SKETCH

Marianette Wospakrik earned her Bachelor of Science in physics from the Bandung Institute of Technology (ITB), Indonesia in 2008. During the following three years, she was employed at PT Freeport Indonesia, Tembagapura, Indonesia. In August 2011, she entered the physics graduate program at the University of Florida. She was awarded a Master of Science from University of Florida in the spring of 2013 and she received her Ph.D. from the University of Florida in the summer of 2018.